Transactions of the ASME®

Technical Editor, T. H. OKIISHI
Associate Technical Editors
Aeromechanical Interaction
R. E. KIELB (1996)
Gas Turbine
E. M. GREITZER (1994)
Heat Transfer
M. G. DUNN (1996)
Nuclear Engineering
H. H. CHUNG (1996)
Power
P. H. GILSON (1996)
Turbomachinery
N. A. CUMPSTY (1995)

BOARD ON COMMUNICATIONS
Chairman and Vice-President
R. D. ROCKE

Members-at-Large
T. BARLOW, T. DEAR, L. KEER, J. KITTO, W. MORGAN, E. M. PATTON, S. PATULSKI, R. E. REDER, R. SHAH, A. VAN DER SLUYS, F. M. WHITE, J. WHITEHEAD

OFFICERS OF THE ASME
President, J. H. FERNANDES
Executive Director
D. L. BELDEN
Treasurer
R. A. BENNETT

PUBLISHING STAFF
Mng. Dir., Publ.,
CHARLES W. BEARDSLEY
Managing Editor,
CORNELIA MONAHAN
Sr. Production Editor,
VALERIE WINTERS
Production Assistant,
MARISOL ANDINO

Transactions of the ASME, Journal of Turbomachinery (ISSN 0889-504X) is published quarterly (Jan., Apr., July, Oct.) for $130.00 per year by The American Society of Mechanical Engineers, 345 East 47th Street, New York, NY 10017. Second class postage paid at New York, NY and additional mailing offices. POSTMASTER: Send address change to Transactions of the ASME, Journal of Turbomachinery, c/o THE AMERICAN SOCIETY OF MECHANICAL ENGINEERS, 22 Law Drive, Box 2300, Fairfield, NJ 07007-2300.
CHANGES OF ADDRESS must be received at Society headquarters seven weeks before they are to be effective. Please send old label and new address.
PRICES: To members, $40.00, annually; to nonmembers, $130.00. Add $24.00 for postage to countries outside the United States and Canada.
STATEMENT from By-Laws. The Society shall not be responsible for statements or opinions advanced in papers or ... printed in its publications (B7.1, Par. 3).

INDEXED by Applied Mechanics Reviews and Engineering Information, Inc.
Canadian Goods & Services Tax Registration #126148048

Journal of Turbomachinery

Published Quarterly by The American Society of Mechanical Engineers

VOLUME 116 • NUMBER 2 • APRIL 1994

TECHNICAL PAPERS

ANNOUNCEMENTS

Spanwise Transport in Axial-Flow Turbines: Part 1—The Multistage Environment

K. L. Lewis
Whittle Laboratory,
University of Cambridge,
Cambridge, United Kingdom

Selected experimental results, obtained from a detailed investigation into the flow fields within two low-speed multistage turbines, are presented. A repeating stage condition occurred typically after two stages, with the secondary flows an important factor in the low aspect ratio geometry. A tracer gas technique was employed to identify the dominant mechanisms of spanwise transport and their relative significance. In the first stages of both machines, tracer transport was more intense near the endwalls than at midspan, while in the multistage environment the transport was approximately constant across the whole span. The convective influence of classical secondary flow, shroud leakage, and wake passage through a downstream blade was identified and shown to be as significant as turbulent diffusion in effecting cross-passage and spanwise transport. The data show that spanwise transport should be included within any throughflow model and are used to calibrate two scaling models. These models are presented in Part 2, where the influence of incorporating spanwise transport into a throughflow model is investigated.

Introduction

The repeating stage condition, which has been known for some time to exist within multistage compressors, is one in which the velocity profiles entering and leaving the stage are similar (Smith, 1970). Although several studies of single and one and a half stage turbines have been published in the literature (Sharma et al., 1988; Joslyn and Dring, 1992a, 1992b; Boletis and Sieverding, 1991) no detailed study of the flow field deep within a multistage turbine has been performed. It was not known whether the repeating stage condition existed in a multistage turbine, although the flow field was thought to be highly three dimensional, turbulent, and unsteady, possibly quite unlike the designer's intent. The multistage environment as distinct from that of a single stage is influenced by increased endwall boundary layer skew, spanwise gradients of vorticity, increased free-stream turbulence and spanwise transport.

Endwall inlet skew affects the strength of classical secondary flow and the subsequent flow angle and loss distribution (Bindon, 1980; Walsh and Gregory-Smith, 1987). In turn the endwall skew is strongly influenced in shape and magnitude by the secondary flow and leakage from the preceding blade row (Boletis and Sieverding, 1991). This is particularly evident if the blade row spacing is small and the flow fields in the respective blade rows closely coupled. Circumferential nonuniformities generated by wakes and vortices from upstream blade rows can also have an affect. This is particularly true in low aspect ratio geometries where secondary flow effects are present across the whole span. Sharma et al. (1988) showed that the convection of rotor hub vortices through the second stator of a one and a half stage turbine affected the performance of the stator markedly, with underturning at the endwalls and overturning at midspan. Clearance flows can influence the performance of a downstream blade row with the overturning (absolute frame) associated with the rotor tip clearance being preserved through the succeeding stator (Boletis and Sieverding, 1991).

Spanwise gradients of vorticity play a significant role in affecting the secondary flow through a downstream blade row (Horlock, 1977). When these gradients become fully developed, the repeating stage condition is approached. This can only occur once endwall loss generation is balanced by the flux of loss away from the endwalls. Spanwise transport therefore plays an important role in the development of the repeating stage condition (Gallimore, 1986). In the multistage environment, turbulence produced by "vortex cutting" (Binder, 1985) and shear within upstream boundary layers and wakes (Gallimore and Cumpsty, 1986) increases the free-stream turbulence level. This accentuates mixing and hence spanwise transport. Similarly, any flow feature that has a spanwise velocity component will redistribute flow across the span (Adkins and Smith, 1982). This includes classical secondary flow, wakes, shed vorticity, and clearance/leakage flows.

This paper is divided into two parts. In Part 1 selected results, obtained from two low aspect ratio turbines that were tested in a new multistage turbine facility, are presented. These include measurements downstream of each blade row, which show the development of the flow field through the turbine.

Contributed by the International Gas Turbine Institute and presented at the 38th International Gas Turbine and Aeroengine Congress and Exposition, Cincinnati, Ohio, May 24-27, 1993. Manuscript received at ASME Headquarters March 10, 1993. Paper No. 93-GT-289. Associate Technical Editor: H. Lukas.

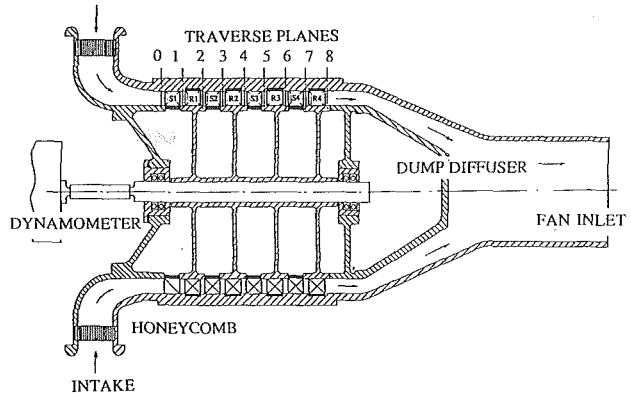

Fig. 1 Schematic of Cambridge multistage turbine: four-stage configuration

Tracer gas distributions are shown and together with the aerodynamic measurements, are used to identify the dominant mechanisms of spanwise transport within the two turbines. The Hinze (1959) model of turbulent diffusion is used to estimate the magnitude of the spanwise transport from the tracer distributions. The data are used in the second part of this paper to develop two expressions that allow the scaling of an effective diffusion coefficient based on turbine geometric parameters and performance. The coefficient is used in a spanwise transport model, which has been incorporated in a throughflow code. The resulting influence on the throughflow model's predictive capability is demonstrated by the application of the model to three other turbine applications.

Definitions

It is useful at this stage to define commonly used terminology to avoid confusion and misunderstanding. Primary flow is defined as the streamtube flow that is predicted by an axisymmetric inviscid rotational analysis. For reasons of consistency with past turbine literature, secondary flow is defined as inviscid classical secondary flow due to stream surface warp. Any other flow feature that is neither primary nor secondary flow is referred to directly. In three-dimensional flows, spanwise transport can take place by spanwise convection and turbulent diffusion. Turbulent diffusion is defined as any random unsteadiness that is not correlated to shaft speed.

Experimental Facility

The new multistage turbine facility (Fig. 1) at the Whittle Laboratory, University of Cambridge was used as the primary research tool. The facility was designed to model a high-pressure steam turbine and has a hub-to-casing ratio of 0.85 with a casing diameter of 1.0 m. Air is ingested through the radial inlet and honeycomb straightener and turned by the inlet contraction into the axial direction. After passing through the turbine the air is ducted into the intake of a centrifugal fan. An eddy-current dynamometer absorbs the rotor power and allows the measurement of torque. Stationary frame circumferential and radial traversing is possible behind each blade row, measuring planes 0 to 8 in Fig. 1. The traverse planes allow a maximum circumferential travel of one quadrant with the quadrant behind each stator offset by 90 deg relative to the quadrant behind each rotor. The axial distance of all traverse planes downstream of the respective trailing edge plane is 16 percent of stator axial chord. More details are available from Lewis (1993).

Table 1 Turbine geometric parameters

Casing diameter, D_c	1.00	
Hub diameter, D_h	0.85	
Blade-Row Spacing, $\Delta z/C_{z,stator}$	0.33	
	LL Turbine	
	Stator	Rotor
Number of stages	4	
Chord, C	0.098	0.108
Axial Chord, C_z	0.075	0.083
Aspect Ratio, H/C	0.763	0.694
Blade Inlet Angle	0^o	0^o
Cos^{-1}(o/p) Measured at Hub,	68.9^o	$-69.5°$
Casing	66.9^o	-68.1^o
Blade Number	33	30
	HL Turbine	
Number of stages	3	
Chord, C	0.108	0.119
Axial Chord, C_z	0.075	0.083
Aspect Ratio, H/C	0.694	0.630
Blade Inlet Angle	-33^o	33^o
Cos^{-1}(o/p) Measured at Hub,	74.5^o	-74.7^o
Casing	72.8^o	-73.1^o
Blade Number	31	28

The design parameters of the two turbine builds, *LL* and *HL*, are given in Table 1. Both builds are 50 percent reaction and have repeating geometry. The major difference between the two builds is an increase in stage loading, $\Delta h_o/U^2$ from 1.0 to 1.5. This is achieved by the introduction of interstage swirl in the *HL* turbine. The *HL* turbine has one less stage in order to keep the total output power from the two turbines approximately constant. The blades are radial with no twist and are shrouded at rotor casing and stator hub (Fig. 2). The stator and rotor blade geometries, nondimensionalized by chord, are identical; the chord ratio C_{st}/C_r is 0.9091. Shroud seal clearance, effected by abradable seals, was nominally 1.0 percent of midspan throat width in both builds. The rotor hubs extend upstream to the preceding stator trailing edge plane and downstream to the next stator leading edge plane. The rotor casing shroud extends from the leading edge to the trailing edge planes of the rotor blades. Intrablade row gap was 33 percent of stator axial chord in both builds. The leading edges of all stators were circumferentially aligned to each other as were the leading edges of the rotors. As flow into both turbines was axial, the first blade row of the *HL* turbine, stator 1, operated at negative incidence. This did not result in any large-scale separation from the pressure surface or increased losses.

Nomenclature

C = chord
D = diameter
h = enthalpy
H = span
L = length scale
o = throat opening
p = pitch
P = concentration
r = radial spread
U = blade speed
V = absolute velocity
x, y, z = rectangular coordinates
ϵ = diffusion coefficient

Subscripts

0 = total
c = casing
cv = convection
d = turbulent diffusion
h = hub
r = rotor
sf = secondary flow
s = stage
st = stator

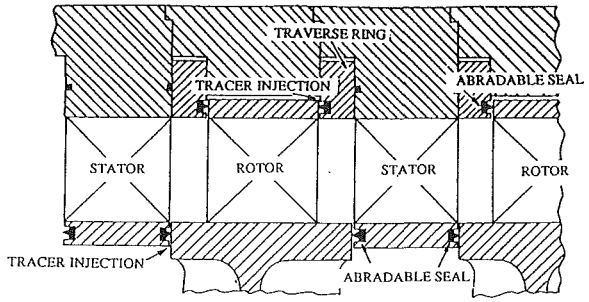

Fig. 2 Schematic of multistage environment and shrouded geometry

Experimental Techniques

The experimental program consisted of two series of tests, the first involving a detailed study of the flow field within the two turbines. This included measurements behind each blade row with a five-hole pneumatic probe to establish the time-mean velocity field. In the second series of tests, a tracer gas technique was used to give a measure of the spanwise transport. Ethylene was injected into the flow through a crooked L-shaped probe of 0.56 mm outside diameter, which minimized probe interference effects (Gallimore, 1985). Due to the limited circumferential travel of each traverse plane, it was not possible to mount the injection probe within the traverse ring upstream of a blade row and to sample immediately downstream of the same blade passage. The injection probe was therefore inserted directly through the casing limiting any circumferential movement and the number of injection points. Sampling was performed through a Kiel total pressure probe yawed to the previously measured mass-averaged flow angle. Ethylene concentration was determined by passing the sample through a flame ionization detector, which gave a time-mean value. All measured concentrations were nondimensionalized by the peak local concentration.

Both turbines were tested at their design flow coefficient of 0.384 but at different rotor wheel speeds: the *LL* turbine at 830 rpm and the *HL* turbine at 680 rpm. The corresponding Reynolds numbers based on stator chord and midspan exit velocity were 2.6×10^5 and 3.3×10^5, respectively.

Interpretation of Tracer Distributions

Although the tracer gas technique gives a direct measure of transport within a flow field, the interpretation of the resulting distributions is not always straightforward. It is useful to consider the influence that secondary flow, turbulent diffusion, and the sampling plane have on the measured distribution of a tracer. In addition, it is appropriate to explain the techniques used to estimate the magnitude of the transport mechanisms from the tracer distributions.

The Hinze (1959) model of diffusion from a point source in a uniform flow is considered. If the turbulence is homogeneous and isotropic and the velocity vector is axial and therefore normal to the traverse plane, the tracer distribution will consist of concentration contours that are circular and concentric. The distribution can be approximated by measuring the radius r to a contour of concentration P to give a turbulent diffusion coefficient ϵ_d

$$\frac{\epsilon_d}{V_z L_s} = -\frac{r^2}{4L_s z \ln P} \tag{1}$$

where L_s is the stage length and z the streamline distance from the point of injection to the traverse plane. If a uniform spanwise velocity V_y is superimposed on the uniform axial velocity flow field, the core, defined as the point where peak concentration is measured, will be transported in the spanwise direction. The concentration contours will still be circles in a plane normal to the streamwise velocity vector but this will no longer be normal to the traverse plane.

A similar argument can be applied when the flow is turned tangentially by the action of a blade row. The streamwise vector is no longer normal to the traverse plane, the effect being particularly pronounced downstream of stators. The tracer distribution, as measured in the traverse plane, will be circumferentially distorted with respect to the true distribution. The distortion could be artificially removed by scaling the circumferential distance by the cosine of the mean flow angle. This would imply different transit times for some particles and as tracer distribution is directly proportional to particle transit time, an equally erroneous interpretation could result. For this reason, the distributions are presented as measured in the traverse plane and the circumferential distortion accepted but noted. As this study was primarily involved with spanwise transport, the limitation was acceptable.

Assuming nonuniform spanwise and pitchwise perturbation velocities are superimposed on the uniform velocity flow field, contour distortion will take place in the direction of increasing perturbation velocity. Determining the magnitude of the diffusion coefficient from the resulting contours becomes more difficult. By taking the shortest distance from the core to contour P as being representative of r, an estimate of the diffusion coefficient ϵ_d can be determined by using Eq. (1). This assumes no net transport of tracer by convective mechanisms in this direction. Some circumferential scaling based on the cosine of the mean flow angle is necessary when the shortest distance r has a circumferential component and the streamwise vector is not normal to the traverse plane. This technique was used to determine ϵ_d across a stator blade row.

Estimating ϵ_d through a rotor from distributions obtained by injecting and sampling tracer in the absolute frame is substantially more difficult. The circumferential distortion that results from differing particle transit times (Denton and Usui, 1981) cannot simply be filtered out or overlooked. Assuming, however, that an *effective* diffusion coefficient ϵ, which includes the influence of both convective (ϵ_{cv}) and diffusive (ϵ_d) mechanisms, can be defined such that

$$\epsilon = \epsilon_d + \epsilon_{cv} \tag{2}$$

the Hinze model, Eq. (1), can be applied to the *circumferentially averaged* tracer distribution to obtain a value for ϵ. As the rotor is moving with respect to the tracer source, the estimated value of ϵ can be viewed as being representative of a passage-mean, the quantity required for axisymmetric modeling purposes. In general the spanwise profile, which results from the circumferential averaging, will be skewed, indicating that the spanwise transport is anisotropic. This violates one of the assumptions in the Hinze model but in the absence of a better model, Eq. (1) is applied to the profile, either side of the peak, to obtain two values of ϵ. A weighted mean of the two values, based on the integrated areas under the spanwise profile either side of the peak, is taken as representative of the effective diffusion coefficient ϵ at the radius of injection. If ϵ is a true passage-mean, any spanwise shift in the core will be predicted by a throughflow model. Admittedly this shift will be small in the present high hub to casing ratio geometry. If the tracer source is immersed in a flow feature that has a strong spanwise velocity component associated with it, for example, a stator blade wake, then a spanwise shift will occur. This is, however, due to a local effect and cannot be considered as being representative of the passage mean. The approach taken is to assume that ϵ is a true passage-mean and to neglect any spanwise shift.

Assuming that the diffusion coefficient ϵ_d is the same through the rotor as through the stator and hence measurable, an estimate of ϵ_{cv} can be obtained from Eq. (2). This is a reasonable assumption considering that both turbines are 50 percent reaction and has been confirmed by measurements of turbulence

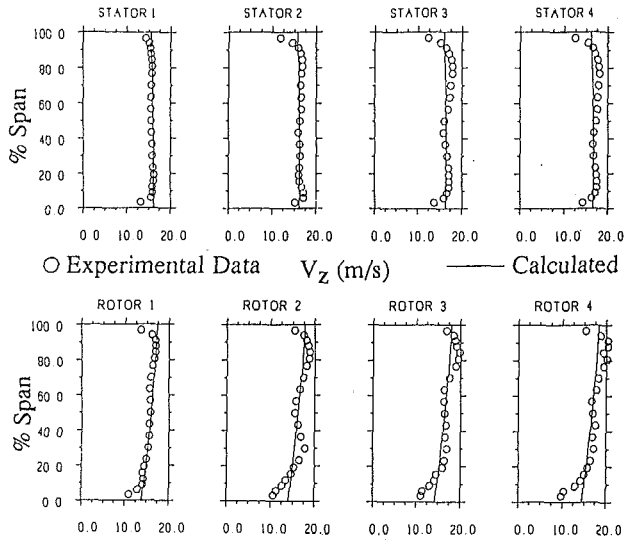

Fig. 3 Development of axial velocity distributions through *LL* turbine

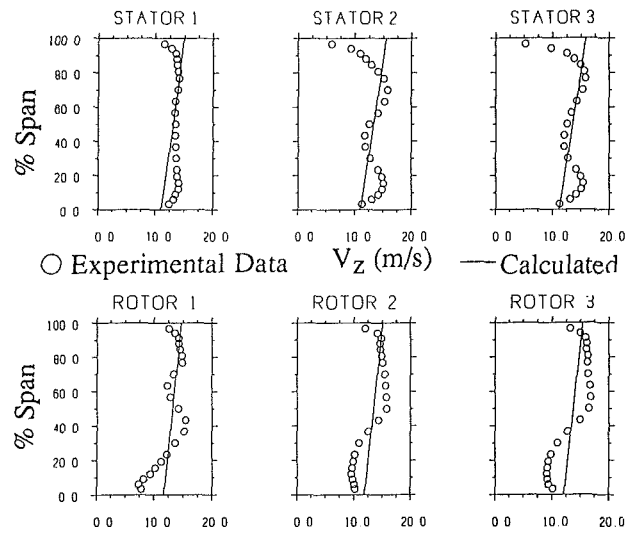

Fig. 4 Development of axial velocity distributions through *HL* turbine

intensity and length scale, which together define turbulent viscosity and hence ϵ_d (Lewis, 1993): The turbulent viscosity downstream of the rotor in the repeating stage was of the same level as that downstream of the stator. A similar technique for estimating ϵ_{cv} could be applied to the distributions obtained by injecting through the stators. As, however, there is no relative circumferential motion of the tracer source to the blade passage, the resulting distribution cannot be taken as being representative of a passage-mean. Any core shift that occurs cannot be neglected and has to be accounted for in estimating ϵ_{cv}. As the latter would require another model and set of assumptions, this was avoided.

Contour distortion due to anisotropic turbulence remains to be considered (Li and Cumpsty, 1990). In general, anisotropic turbulence exists within regions that have strong velocity gradients, notably boundary layers and vortex regions. In a turbine, the boundary layers are thin and the extent of anisotropic turbulence from this source is limited. The flow field in the vicinity of classical secondary flow vortices is, however, strongly anisotropic (Gregory-Smith and Biesinger, 1992). In the results section, it is shown that anisotropy is present but appears to be limited and should not invalidate the application of the Hinze model.

To summarize, ϵ_d is evaluated by applying Eq. (1) to the distributions obtained by injecting tracer through the stators. It is assumed that this value is approximately equal to the turbulent diffusion coefficient through the rotors. An effective distribution coefficient ϵ is determined from the circumferentially averaged distribution obtained by injecting tracer through the rotors. Equation (2) is applied to obtain ϵ_{cv}. This analysis technique is based on some sweeping approximations and assumptions. Obviously there will be regions within the flow field where significant deviations from the assumptions occur but these assumptions are shown in the next section to be generally acceptable.

Aerodynamic Measurements

The circumferentially averaged distributions of axial velocity, as determined by five-hole probe measurement downstream of each blade row of the *LL* turbine, are shown in Fig. 3, and the corresponding distributions for the *HL* turbine are shown in Fig. 4. The calculated data show the design intent and are based on a streamline curvature prediction using exit flow angles determined from measured values of $\cos^{-1}(o/p)$.

The influence of classical secondary flow was observed downstream of each blade row with the associated overturning (low axial velocity) at the endwalls and underturning (high axial velocity) toward 30 percent and 70 percent span (Figs. 3 and 4). The flow field was relatively well ordered with no atypical features similar to those observed by Sharma et al. (1988). The annulus boundary layers were extremely thin with the reduction in axial velocity at the endwalls mainly due to increased turning, as indicated by the flow angle variation (Lewis, 1993). The secondary flows represented by velocity variation from the design intent developed rapidly from the first stage toward the repeating stage condition. This condition was achieved after two stages in the *LL* turbine but only one and a half in the *HL* turbine. The greatest variation from design intent in both turbines occurred downstream of the rotors in the hub region. This indicated the presence of very strong hub vortices as confirmed by slant hot-wire measurements (Lewis, 1993). In the *LL* turbine, maximum underturning (minimum axial velocity) occurred close to the endwall suggesting that the hub vortex had not moved far off the hub. The presence of the casing vortex, although less obtrusive than the hub vortex, was still observable. In the *HL* turbine the maximum overturning (minimum axial velocity) occurred at 15 percent span, indicating that the hub vortex had moved considerably away from the endwall toward midspan. The casing vortex was far less significant downstream of rotors 2 and 3 than rotor 1. The secondary flow downstream of the stators in both turbines showed equal development of the hub and casing secondary flow vortices toward the repeating stage condition.

A repeating stage can only occur when the spanwise gradients of entropy have become fully developed and once endwall loss generation is balanced by the flux of loss away from the endwalls (Gallimore, 1986). The existence of the repeating stage suggests that spanwise transport is significant in the multistage environment and that secondary flow is a dominant mechanism. In the next section, tracer gas results are used to identify other dominant mechanisms.

Tracer Gas Results

To study spanwise transport deep within a multistage turbine, it was necessary to define a stage that represented this environment. The repeating stage was defined as representative and in the *LL* turbine, investigations were focused on the third stage. As the *HL* turbine has only three stages, the flow field within the second rotor and third stator was injected with tracer. This seemed reasonable as the repeating stage condition occurred in the *HL* turbine after one and a half stages. All

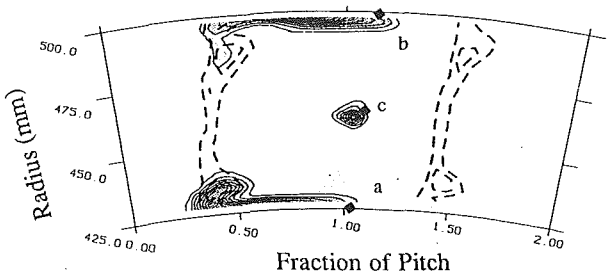

Fig. 5 Tracer gas distribution downstream of stator 1 *LL* turbine (injection in plane 0, midpitch: hub, casing, midspan, sampling in plane 1, contours 10–90 percent, interval 10 percent)

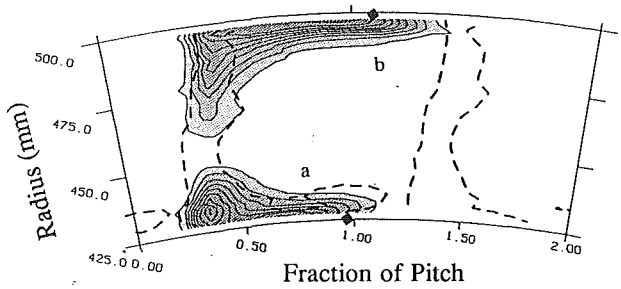

Fig. 6 Tracer gas distribution downstreamof stator 3 *LL* turbine (injection in plane 4, midpitch: hub, casing, sampling in plane 5, contours 10–90 percent, interval 10 percent)

testing was performed at the same turbine operating points as described earlier. Only the results that are of particular interest are shown with a more comprehensive set contained in Lewis (1993).

Transport Within Stator Blade Rows. Tracer distributions, obtained by injection through the first stator of each turbine build, seemed appropriate as datums against which other tracer distributions could be compared. The results for stator 1, *LL* turbine, when tracer was injected at hub, midspan, and casing at plane 0 and sampled in plane 1 are shown in Fig. 5. The solid symbols indicate the position of injection and contours of total pressure the location of wakes and other high loss regions. Figure 5(*a*) shows the result obtained when tracer was injected into a streamline close to the hub endwall and at midpitch and Fig. 5(*c*) by injecting tracer at midpitch midspan. The core (Fig. 5*a*) was entrained by the endwall boundary layer and swept toward the suction surface of the stator blade into the hub secondary flow vortex. The turbulent diffusion, as represented by spacing of the contours, was greater around the hub vortex (Fig. 5*a*), with the vortex containing transported endwall boundary layer fluid, than at midspan (Fig. 5*c*). The diffusion above the hub endwall was very similar to that at midpitch midspan (Fig. 5*c*) indicating that the new boundary layer formed after vortex lift off is very thin (Sieverding, 1985). A similar result to Fig. 5(*a*) was obtained when tracer was injected into a streamline close to the casing endwall (Fig. 5*b*). The bulk transport and entrainment of tracer into the casing vortex was, however, not as large. A possible explanation is that the tracer was injected into the outer part of the boundary layer, part of which was swept into the casing vortex and part of which became entrained in the new boundary layer that developed after the vortex lift-off line (Denton and Usui, 1981). The diffusion at midpitch midspan (Fig. 5*c*) was small with the free-stream turbulence level at inlet being 0.5 percent (Lewis, 1993). Slight distortion of the contours toward the casing was evident, probably due to probe interference, and in the circumferential direction, due to the sampling plane angle. In both cases, the distortion was not too significant.

The results of ethylene tracing through the third stator of the *LL* turbine, with injection at plane 4 and sampling at plane 5, are shown in Fig. 6. Contours of total pressure are superimposed to delineate high loss regions, the contour interval being the same as in Fig. 5. The aerodynamic differences between stators 1 and 3 are detailed by Lewis (1993) but it can be seen that the wake of stator 3 was broader and the secondary vortices not as distinct as those of stator 1. The latter is due to the time-averaging nature of the pneumatic probe and the movement of the convected features in the unsteady environment. With tracer being injected close to the hub endwall (Fig. 6*a*) the tracer core was entrained by the secondary flow and swept up into the hub vortex. A second peak was located on the endwall, suggesting that some of the tracer was injected into the outer part of the incoming boundary layer, forming the new endwall boundary layer referred to earlier. The increased free-stream turbulence associated with the multistage environment resulted in greater contour spread away from the endwall than in Fig. 5(*a*). In the vicinity of the vortex core, increased turbulent diffusion was evident. Some distortion of the tracer contours occurred within the vortex, with the contours being more tightly compressed to the left of the core. This could be related to the transport of the vortex along the blade suction surface, which would tend to limit diffusion toward the suction surface and is a form of anisotropy. A similar distortion can be seen in Fig. 5(*a*); in both cases the extent is limited.

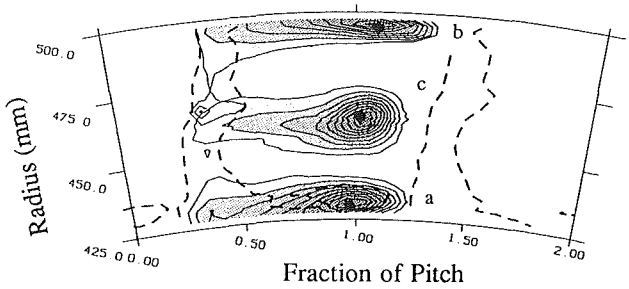

Fig. 7 Tracer gas distriution downstream of stator 3 *LL* turbine (injection in plane 4, midpitch: 5 mm off hub, 5 mm off casing, midspan, sampling in plane 5, contours 10–90 percent, interval 10 percent)

Injecting into the streamline close to the casing endwall (Fig. 6*b*) resulted in similar but greater secondary flow entrainment to that in Fig. 5(*b*). This was probably due to the strongly skewed boundary layer that developed when the rotor shroud leakage flow was re-injected back into the mainstream flow. The peak concentration, however, still occurred on the casing endwall. There was significant spanwise transport within the casing vortex and wake of the stator blade, with the 10 percent concentration contour extending to midspan. Again the turbulent diffusion away from the solid surfaces was enhanced by the increased freestream turbulence.

The cores obtained by injecting 5 mm away from the hub and casing regions (Figs. 7*a* and 7*b*) were convected through the blade row with little cross-passage or spanwise movement relative to their injection points. The contours close to the endwalls were, however, elongated toward the suction surface indicating the action of cross-passage flow. In the vicinity of the blade wake, spanwise convection associated with hub and casing secondary flow was evident. This was particularly noticeable with casing injection (Fig. 7*b*) where the 10 percent contour extended to almost midspan. This was caused by the strong skew in the casing boundary layer, which entrained fluid toward and onto the suction surface. The influence of turbulent diffusion was apparent in all directions. The spanwise spread from the casing tracer core (Fig. 7*b*) was less than that of the hub core (Fig. 7*a*), perhaps indicating the convected influence of the secondary flows generated by the upstream rotor. The rotor hub vortex was significantly stronger than the casing

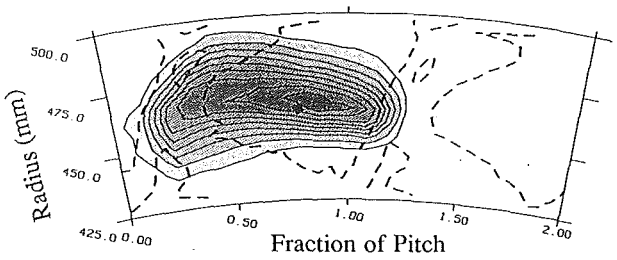

Fig. 8 Tracer gas distribution downstream of stator 3 *HL* turbine (injection in plane 4, midpitch: midspan, sampling in plane 5, contours 10–90 percent, interval 10 percent)

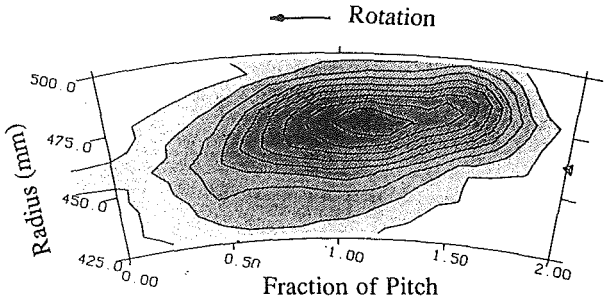

Fig. 9 Tracer gas distribution downstream of rotor 2 *HL* turbine (injection in plane 3, midpitch: midspan, sampling in plane 4, contours 10–90 percent, interval 10 percent)

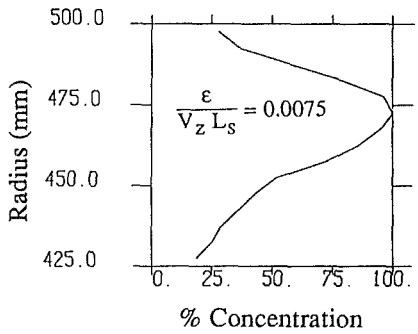

Fig. 10 Circumferentially averaged tracer gas distribution downstream of rotor 2 *HL* Turbine (injection in plane 3, midpitch: midspan, sampling in plane 4)

vortex (Fig. 3) and whether the hub vortex was convected or converted into turbulence, flow in the hub region would have experienced greater spanwise transport.

Injection at midpitch midspan (Fig. 7*c*) showed that diffusion was the dominant transport mechanism with the contours forming almost concentric circles close to the core. Approximately twice as much tracer spread occurred in the spanwise direction as in Fig. 5(*c*); this was indicative of the increased free-stream turbulence level, which from hot wire measurements was 2–3 percent at stator exit (Lewis, 1993). There was strong circumferential distortion of the lower concentration contours toward the suction surface, which can be partly explained by the influence of the traverse plane not being normal to the streamwise direction, although the contours toward the pressure surface were not similarly distorted. This suggests that a convective mechanism transported tracer toward the suction surface and away from the pressure surface. Anisotropic turbulence was discounted due to the location and magnitude of the effect. In a turbine, the wake generated by an upstream blade row has a slip velocity relative to the mean flow, which would entrain tracer toward the suction surface (Kerrebrock and Mikolajczak, 1970). If the rotor hub vortex had been convected through stator 3 without losing its structure, the tracer would also have been transported toward the suction surface, although more radial spreading than that seen in Fig. 7(*c*) would have occurred toward the hub.

Similar tracer distributions were obtained in the *HL* turbine, with the effect of increased secondary flow and turbulent diffusion apparent. For conciseness, only one distribution is presented: Figure 8 shows the tracer distribution obtained by injection in plane 4, midpitch and midspan of stator 3, and sampling in plane 5. Total pressure contours are superimposed to identify the wake and secondary flow regions. The dominant effect was the unequal circumferential and radial distortion of the contours toward the suction surface indicative of a convective mechanism transporting flow toward the suction surface (cf. Fig. 7c). By applying the Hinze model, Eq. (1), and assuming a Schmidt number of unity, the average turbulence intensity through stator 3 was estimated to be approximately 6 percent. From hot-wire measurements the turbulence intensity at inlet to stator 3 was 12–13 percent and 4–5 percent at exit.

Transport Within Rotor Blade Rows. Tracer distribution downstream of any blade row is based on the time it takes for a particle to pass through that blade row. As there is relative motion between the tracer source and a rotor, particles passing through a rotor are also circumferentially displaced, with the extent of displacement proportional to the transit time. For example, particles that enter a relative streamline, which passes close to the suction surface, are displaced circumferentially less than those that pass over the pressure surface. Assuming rotor rotation is to the left, particles that have experienced a short transit time lie to the right of the tracer core and conversely tracer to the left of the core has experienced a longer transit time. The tracer distribution obtained by injecting at midspan and midpitch of stator 2, *HL* turbine, in plane 3 and sampling in plane 4 is shown in Fig. 9. The open symbol indicates the radial location of injection but not the circumferential location, which was to the right of the traverse window. Substantial spreading occurred in both the spanwise and circumferential directions with the core having moved radially outward from the tracer source toward the casing. The effects of the two transport mechanisms, turbulent diffusion and convection, were almost inseparable. Tracer became entrained in the rotor blade boundary layer with the contours being stretched in the direction of rotation, indicating a long transit time, beyond the sampling area and toward the hub. To the right of the core, the contours were also elongated but in a direction counter to that of rotation toward the casing, indicating a short transit time. The rotation of the contours about the core could have been caused by stream surface warp associated with the hub vortex. As the rotor hub vortex was very strong with maximum underturning occurring at 50 percent span and the casing vortex almost indistinguishable (Fig. 4), the stream surface rotation would have extended to beyond midspan. The profile of the circumferentially averaged tracer distribution was skewed (Fig. 10) with the core having moved toward the casing as already noted. The area-mean of the effective diffusion coefficient ϵ/V_zL_s obtained by the method described earlier was 0.0075.

When tracer was injected in other spanwise locations substantial spreading of the tracer contours occurred in all directions with interpretation as difficult as in Fig. 9. The circumferentially averaged profiles were used in a similar manner to that of Fig. 10 to obtain estimates for the effective diffusion coefficient ϵ/V_zL_s, which were assumed to represent the passage-mean values at the radius of injection. Before discussing these, the final distributions obtained by injecting tracer into the shroud leakage flows are presented.

Shroud Leakage. The two turbines had shrouded blades and hence experienced shroud leakage. The leakage flow was

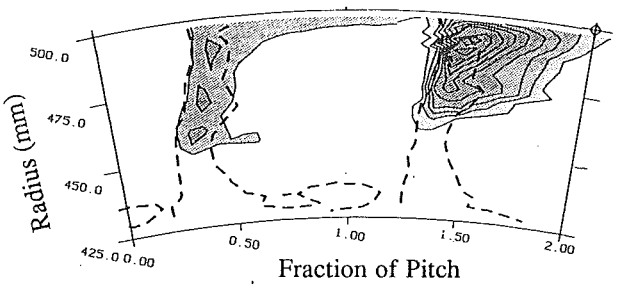

Fig. 11 Tracer gas distribution downstream of stator 3 *LL* turbine (injection in rotor 2 shroud cavity, sampling in plane 5, contours 10-90 percent, interval 10 percent)

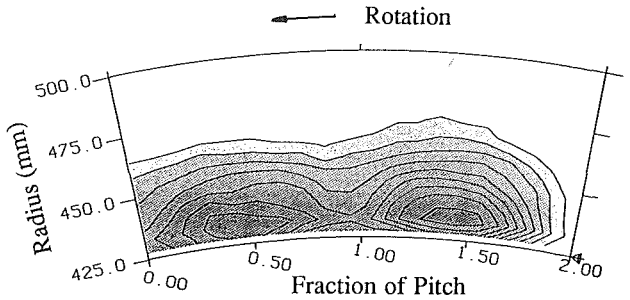

Fig. 12 Tracer gas distribution downstream of rotor 2 *HL* turbine (injection in stator 2 shroud cavity, sampling in plane 4, contours 10-90 percent, interval 10 percent)

traced after re-injection back into the main flow and subsequent transport through the succeeding blade row. The distribution obtained when tracer was injected into the cavity of the casing shroud (Fig. 2) of rotor 2, *LL* turbine and sampled downstream of stator 3 is shown in Fig. 11. Substantial tangential shear of the fluid and significant mixing of the tracer occurred within the shroud cavity. The tracer entered two adjacent passages when the seeded fluid was re-injected back into the main flow. The leakage flow constituted the inner part of the casing boundary layer, which was then swept on to the suction surface of the stator blade. Within the casing vortex, tracer was transported to beyond midspan, with the tracer core positioned at 90 percent span. Significant tracer was also observed in the right-hand passage away from the suction surface (Fig. 11), which suggests that some of the leakage flow retained the spanwise component of the re-injection velocity and was convected beyond the casing boundary layer. As this leakage flow had a tangential velocity component as well, it was transported toward the suction surface.

Injecting of tracer into the hub shroud cavity (Fig. 2) of stator 2, turbine *HL* and sampling downstream of rotor 2 in plane 4 resulted in the distribution shown in Fig. 12. The same phenomenon of mixing within the shroud cavity occurred with the point source becoming a line source on re-injection back into the main flow. The leakage flow was transported to midspan in an almost circumferentially uniform manner, with tracer detected far to the left of the traverse window in the direction of rotation. Two cores were situated off the endwall, exactly one blade pitch apart, suggesting that the leakage flow responded to the local circumferential pressure variation established at the stator trailing edge plane and became periodic.

Estimates of Diffusion Coefficients ϵ, ϵ_d, ϵ_{cv}. Estimation of the diffusion coefficients ϵ, ϵ_d, and ϵ_{cv} from the tracer distributions was explained earlier and a summary of the estimates derived from the *LL* turbine data is shown in Fig. 13. These are presented as a function of spanwise position of injection. Values for the turbulent diffusion coefficient ϵ_d/V_zL_s obtained downstream of stator 3 ranged from 0.0005 to 0.0009. The

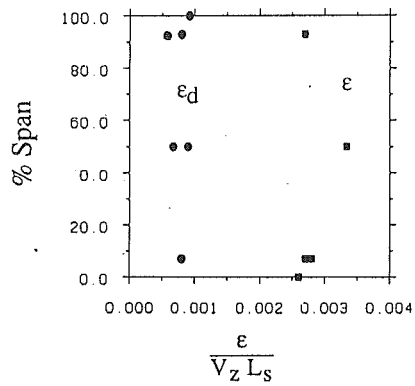

Fig. 13 Estimates of ϵ_d and ϵ from tracer distributions downstream stator 3 and rotor 3, *LL* turbine

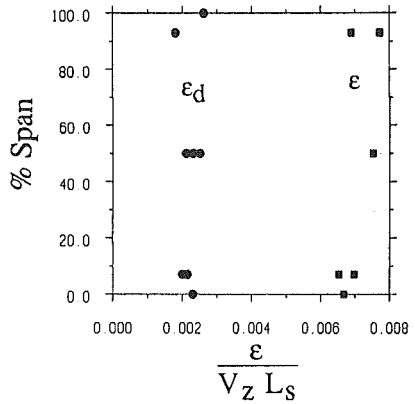

Fig. 14 Estimates of ϵ_d and ϵ from tracer distributions downstream stator 3 and rotor 2, *HL* turbine

scatter in the data reflects the difficulty in measurement but also the very complex, three-dimensional flow field in a multistage environment. The range of effective diffusion coefficient ϵ/V_zL_s, obtained downstream of rotor 3, is from 0.0026 to 0.0034. The data show less scatter probably because of the passage averaging that was effected by injecting and sampling with stationary instrumentation through a rotating blade row. If it is assumed that ϵ_d remained constant through the repeating stage, then an effective diffusion coefficient due to convective flows can be determined. A typical value for ϵ_{cv}/V_zL_s is 0.0021. Significant variation of either ϵ_d or ϵ across the span is not evident.

Figure 14 shows similar data for the *HL* turbine. Values of ϵ_d/V_zL_s downstream of stator 3, and ϵ/V_zL_s downstream of rotor 2, range from 0.0018–0.0026 and 0.0066–0.0078, respectively. A typical value of ϵ_{cv}/V_zL_s is 0.005. Again the spanwise transport appears to be fairly uniform across the whole span.

Discussion and Conclusion

In the first stator of each turbine, spanwise transport was confined to the endwall regions where secondary flow was active. The free-stream turbulence was low and toward midspan the bulk of the flow was inviscid and two dimensional. In the multistage environment the flow field became very complex and three dimensional with significant deviation from the design intent. This was particularly evident in the more heavily loaded *HL* turbine. The aerodynamic and tracer gas results indicated that within the multistage environment, defined by the repeating stage, significant spanwise transport occurred across the whole span. Although the tracer technique gave a direct indication of the transport, quantitative data were dif-

ficult to obtain when several mechanisms were superimposed on each other. The tracer distributions indicated that turbulent diffusion was fairly uniform across the whole span and although the presence of anisotropy was identified in the vicinity of the secondary flow vortices, the influence on tracer distribution appeared to be limited. Applying the Hinze model to the tracer contours gave results that correlated well with the turbulence intensities measured independently with a hot-wire.

The estimated values of the turbulent diffusion coefficient ϵ_d/V_zL_s are slightly less than those measured by Gallimore and Cumpsty (1986) in two multistage compressors (0.0018 and 0.0038 in compressors A and B, respectively). Considering the distinctly different aerodynamic environments that are involved, this is somewhat surprising. A multistage compressor environment is characterized by strong adverse pressure gradients, thick boundary layers and wakes, and possibly, regions of stalled flow. These in turn result in significant production of turbulence. Conversely in a multistage turbine the flow is continuously re-accelerated, the blade boundary layers are relatively thin, and the endwall boundary layers are re-energized in every blade row by vortex lift-off. This suggests that a significant proportion of the turbulence is produced by "vortex cutting" (Binder, 1985). Although this mechanism is present in any turbine, it is obviously more dominant in low aspect ratio geometries.

With the effect of turbulence anisotropy being limited, the significant distortion of the contours was primarily due to convective mechanisms, including wake passage, secondary flow, and leakage flow. Wake passage effects cross-passage transport although some spanwise transport can also result if the wake has a spanwise velocity component. Leakage flow, on re-injection back into the main flow, becomes part of the endwall boundary layer and as such participates in the generation of secondary flow. Although very strong hub vortices developed within the rotors of both turbines, there did not appear to be a significant increase in spanwise transport in these regions.

The data presented in Figs. 13 and 14 indicate the magnitude of the relevant diffusion coefficients. In both turbines the convective diffusion coefficient ϵ_{cv} is approximately twice that of turbulent diffusion ϵ_d. When the amount of flow turning performed in turbines is considered and compared to that obtained in compressors, the result is not too surprising. This data are used to calibrate simple scaling models presented in Part 2 of this paper. The approach taken is to consider that spanwise transport is a result of both turbulent diffusion (ϵ_d) and secondary flow (ϵ_{sf}). Application of the data assumes that the effective diffusion coefficient due to all spanwise convection ϵ_{cv} is equivalent to that due to secondary flow ϵ_{sf}. This is not rigorously correct but it can be argued that secondary flow is the dominant convective mechanism. For engineering purposes the approximation is acceptable. In Part 2 the effect of incorporating spanwise transport is found to be important in modeling the redistribution of losses and the attenuation of temperature profiles.

Acknowledgments

The author would like to thank Professor Denton for his advice and Mr. Hooper of the Whittle Laboratory, for his help in commissioning and running the multistage turbine facility. This work was financially supported by the Science and Engineering Research Council and NEI Parsons of the United Kingdom.

References

Adkins, G. G., and Smith, L. H., 1982, "Spanwise Mixing in Axial Flow Turbomachines," ASME *Journal of Engineering for Power*, Vol. 104, p. 97.

Binder, A., 1985, "Turbulence Production Due to Secondary Vortex Cutting in a Turbine Rotor," ASME *Journal of Engineering for Gas Turbines and Power*, Vol. 107, pp. 1039–1046.

Bindon, J. P., 1980, "Exit Plane and Suction Surface Flows in an Annular Cascade With a Skewed Inlet Boundary Layer," *International Journal of Heat and Fluid Flow*, Vol. 2, No. 2, p. 57.

Boletis, E., and Sieverding, C. H., 1991, "Experimental Study of the Three-Dimensional Flowfield in a Turbine Stator Preceded by a Full Stage," ASME JOURNAL OF TURBOMACHINERY, Vol. 113, p. 1.

Denton, J. D., and Usui, S., 1981, "Use of a Tracer Gas Technique to Study Mixing in a Low Speed Turbine," ASME Paper No. 81-GT-86.

Gallimore, S. J., 1985, "Spanwise Mixing in Axial-Flow Compressors," PhD thesis, Department of Engineering, University of Cambridge, United Kingdom.

Gallimore, S. J., and Cumpsty, N. A., 1986, "Spanwise Mixing in Multistage Axial-Flow Compressors: Part 1—Experimental Investigation," ASME JOURNAL OF TURBOMACHINERY, Vol. 108, p. 2.

Gallimore, S. J., 1986, "Spanwise Mixing in Multistage Axial-Flow Compressors: Part 2—Throughflow Calculations Including Mixing," ASME JOURNAL OF TURBOMACHINERY, Vol. 108, p. 10.

Gregory-Smith, D. G., and Biesinger, Th., 1992, "Turbulence Evaluation Within the Secondary Flow Region of a Turbine Cascade," ASME Paper No. 92-GT-60.

Hinze, J. O., 1959, *Turbulence*, McGraw-Hill, New York.

Horlock, J. H., 1977, "Recent Developments in Secondary Flow," AGARD-CP-214, *Secondary Flow in Turbomachines*, The Hague.

Joslyn, D., and Dring, R., 1992a, "Three-Dimensional Flow in an Axial Turbine: Part 1—Aerodynamic Mechanisms," ASME JOURNAL OF TURBOMACHINERY, Vol. 114, pp. 61–70.

Joslyn, D., and Dring, R., 1992b, "Three-Dimensional Flow in an Axial Turbine: Part 2—Profile Attenuation," ASME JOURNAL OF TURBOMACHINERY, Vol. 114, pp. 71–78.

Kerrebrock, J. L., and Mikolajczak, A. A., 1970, "Intra-stator Transport of Rotor Wakes and Its Effect on Compressor Performance," ASME Paper No. 70-GT-39.

Lewis, K. L., 1993, "Aerodynamics of Shrouded Multistage Turbines," PhD thesis, Department of Engineering, University of Cambridge, United Kingdom.

Li, Y. S., and Cumpsty, N. A., 1991, "Mixing in Axial-Flow Compressors: Part 2—Measurements in a Single Stage Compressor and a Duct," ASME JOURNAL OF TURBOMACHINERY, Vol. 113, p. 166.

Sharma, O. P., Renaud, E., Butler, T. L., Milsaps, K., Dring, R. P., and Joslyn, H. D., 1988, "Three-Dimensional Unsteady Flow in an Axial-Flow Turbine," *Journal of Propulsion and Power*, Vol. 1, p. 29.

Sieverding, C. H., 1985, "Recent Progress in Understanding the Basic Aspects of Secondary Flows in Turbine Blade Passages," ASME *Journal of Engineering for Power*, Vol. 107, p. 248.

Smith, L. H., 1970, "Casing Boundary Layers in Multistage Axial Flow Compressors," *Brown Boveri: Flow Research on Blading*, Elsevier, Amsterdam.

Walsh, J. A., and Gregory-Smith, D. G., 1987, "The Effect of Inlet Skew on the Secondary Flows and Losses in a Turbine Cascade," *Proceedings of IMechE—Efficiency Predictions and Improvement*, Paper No. C275/87, p. 15.

Spanwise Transport in Axial-Flow Turbines: Part 2—Throughflow Calculations Including Spanwise Transport

K. L. Lewis
Whittle Laboratory,
University of Cambridge,
Cambridge, United Kingdom

In Part 1 of this paper, a repeating stage condition was shown to occur in two low aspect ratio turbines, typically after two stages. Both turbulent diffusion and convective mechanisms were responsible for spanwise transport. In this part, two scaling expressions are determined that account for the influence of these mechanisms in effecting spanwise transport. These are incorporated into a throughflow model using a diffusive term. The inclusion of spanwise transport allows the use of more realistic loss distributions by the designer as input to the throughflow model and therefore focuses attention on areas where losses are generated. In addition, modeling of spanwise transport is shown to be crucial in predicting the attenuation of a temperature profile through a turbine.

Introduction

Part 1 of this paper described an experimental investigation into the flow fields found in two low aspect ratio, low-speed multistage turbines. It was observed that the time-mean flow adjusts through the machine as the spanwise gradients of entropy and total pressure develop until a repeating stage condition is reached. The distance over which this development takes place is typically that of two stages. As a significant proportion of the loss within a low aspect ratio turbine is generated on the endwalls, the existence of a repeating stage suggests that the rate of generation of endwall loss, in a global sense, balances the flux of loss away from the endwall regions. Spanwise transport is therefore significant and important. The tracer gas results presented in Part 1 indicate that in a multistage environment, both turbulent diffusion and classical secondary flow are responsible for spanwise redistribution. In the modeling of spanwise transport it is therefore necessary to consider both mechanisms.

The most common approach for designing turbomachinery is to approximate the flow field as a series of axisymmetric concentric streamtubes. Until fairly recently there was little recognition within streamline curvature schemes that the flow was three dimensional and highly turbulent. Adkins and Smith (1982) presented a method that assumed spanwise transport between streamtubes was due to deterministic secondary flows. Gallimore and Cumpsty (1986) argued that turbulent diffusion was the dominant spanwise transport mechanism with Gallimore (1986) presenting a streamline curvature model based on this premise. Wisler et al. (1987) and Leylek and Wisler (1991) demonstrated that both mechanisms were present with turbulent diffusion being dominant in the midspan region. Toward the endwall, secondary flow effects were of comparable magnitude.

Subsequent to this debate, a number of papers have been dedicated to throughflow modeling that introduced either or both spanwise transport mechanisms (reviewed by Wennerstrom, 1991). Most investigations to date have concentrated on the application of spanwise transport models to the prediction of multistage compressor flow fields; little attention has been focused on the modeling of spanwise transport in turbines and its significance to flow field prediction.

Assuming these models are still valid, any of the throughflow models that include spanwise mixing could be applied directly to the prediction of the turbine flow field. Unfortunately most approaches depend on some semi-empiricism and the models have been tuned for compressor flow field prediction. In this paper two expressions are presented that enable the scale of spanwise transport due to the two mechanisms of turbulent diffusion and classical secondary flow to be estimated. A simple model of spanwise transport has been implemented in the updated streamline curvature scheme of Denton (1978) and this scheme is used to predict the flow fields of the turbines presented in Part 1 and three other applications. The dominant effect of spanwise transport on the radial variation of efficiency and total temperature is demonstrated.

Modeling of Spanwise Redistribution in Streamline Curvature Calculations

From a review of the published literature, throughflow models developed for turbine geometries are not as capable of predicting main flow features as those developed for compressors. To the author's knowledge there are few, if any,

Contributed by the International Gas Turbine Institute and presented at the 38th International Gas Turbine and Aeroengine Congress and Exposition, Cincinnati, Ohio, May 24-27, 1993. Manuscript received by the ASME Headquarters March 10, 1993. Paper No. 93-GT-290. Associate Technical Editor: H. Lukas.

schemes that can predict the secondary flows in a multistage turbine beyond the use of empirical corrections. This reflects the difficulty in applying inviscid vortex theory to a flow field that in general experiences high turning, distortion of the Bernoulli surfaces, and very thin boundary layers. It also reflects the difficulty in applying boundary layer theory to predict endwall boundary layers that are highly skewed. Methods are available that can predict the flow field through a single blade row with boundary layers that are *a priori* defined (Hawthorne and Novak, 1969; Glynn et al. 1977; Glynn, 1982; Gregory-Smith and Okan, 1991). These are claimed to be fairly successful for a single blade row but Hunter (1979) showed that if the method of Hawthorne and Novak (1969) was extended to even a single stage, the predictions became less accurate. This is probably true of all schemes.

The approach taken in this study is that of simplicity at the expense of sophistication and rigor. A model is developed that allows the scale of spanwise transport to be easily estimated, and incorporated within an existing throughflow scheme. This enables a clear picture to emerge in terms of the influence of spanwise transport in turbines, from which further throughflow model development can follow.

The experimental results in Part 1 showed that spanwise transport takes place due to both turbulent diffusion and convective mechanisms. Spanwise transport, however, can only be included within a throughflow model by the introduction of a diffusive term; no mass, by definition, can be transferred across a streamtube boundary. The spanwise transport of variable Q is modeled by

$$V_m \frac{\partial Q}{\partial m} = \epsilon \frac{\partial^2 Q}{\partial y^2} \tag{1}$$

where m refers to the meridional direction. Equation (1) is based on a simplified transport formulation and has a similar form to the model used by Adkins and Smith (1982). The diffusion coefficient ϵ is an effective diffusion coefficient determined by contributions from both turbulent diffusion and spanwise convection. In the two low aspect ratio turbines described in Part 1, classical secondary flows were seen to be dominant in effecting spanwise convection and the effective diffusion coefficient is modeled as

$$\epsilon = \epsilon_d + \epsilon_{sf} \tag{2}$$

where ϵ_{sf} is based on classical secondary flow considerations. A conceptual objection to Eqs. (1) and (2) may well arise as the equations implicitly assume that secondary flows, which are inviscid, can be modeled by a diffusive term. Any spanwise convection will, however, have a redistributing effect on the spanwise distribution of property Q and, based on physical considerations, be of a diffusive nature to the first order. A more rigorous approach would be to model secondary flow as a convective mechanism by the consideration of the S3 transverse plane (De Ruyck et al., 1988). This method, which is based on a quasi-three-dimensional approach, becomes very complex and ultimately improved predictive capability is not guaranteed. In terms of simplicity and ease of implementation, the model represented by Eqs. (1) and (2) is preferred. A choice is now faced in terms of how ϵ_d and ϵ_{sf} should be determined and distributed across the span.

Scaling Model for ϵ_d. A similar approach to that of Gallimore and Cumpsty (1986) is taken in determining an appropriate value for ϵ_d. The production of turbulence is directly related to the generation of loss and therefore entropy. If a repeating stage is considered within a multistage turbine, the turbulence level at inlet to the stage is the same as at exit. Loss is still generated within the stage and therefore the rate of turbulence production must be balanced by the rate of turbulence decay. Although the turbulence may not be initially isotropic, it is presumed that in the global sense the turbulence can be treated as homogeneous and isotropic. This has been shown in Part 1 to be an acceptable approximation. Within the repeating stage each streamtube experiences the same increase in entropy and change in enthalpy. This does not mean that the rate of generation of entropy in each streamtube is necessarily the same. Assuming two-dimensional, incompressible flow and applying the Second Law of Thermodynamics

$$T_3 \Delta s = \Delta h_0 - \Delta p_0 / \rho$$

the definition of isentropic efficiency

$$\eta = \Delta h_0 / \Delta h_{0s} = \Delta h_0 / (\Delta h_0 + T_3 \Delta s)$$

and the Euler work equation across the rotor

$$-\Delta h_0 = U V_z (\tan \alpha_3 - \tan \alpha_2) = U V_z (\tan \alpha_1 - \tan \alpha_2)$$

gives the entropy increase in each streamtube

$$T_3 \Delta s = U V_z (\tan \alpha_2 - \tan \alpha_1)(1 - \eta)/\eta \tag{3}$$

Equation (3) is representative of the entropy production over the stage if the stagnation temperature is constant over the whole span at inlet. The rate of entropy production can be considered to be proportional to the production rate of turbulent kinetic energy. Due to the repeating stage condition, it must also be proportional to the dissipation rate of turbulent kinetic energy. The dissipation rate of turbulent kinetic energy per unit volume over the whole stage is therefore given by

Nomenclature

A = constant
C = blade chord
h = enthalpy, semi-span blade height
L = length scale
m = meridional
$\dot{m}$ = mass flow
o = throat opening
p = blade pitch, pressure
p' = projected blade pitch = $p \cos \beta_2$
Q = dependent variable
Re = Reynolds number = $V_z L_s / \epsilon$
s = entropy
s, n, b = intrinsic absolute coordinates
s^*, n^*, b^* = intrinsic relative coordinates
T = temperature
U = blade speed
V = absolute velocity
w = secondary flow velocity perturbation
x, y, z = rectangular coordinates
α = absolute flow angle, axial reference
β = relative flow angle, axial reference
δ = inlet boundary layer thickness
Δ = expression defined by Eq. (6)
ϵ = diffusion coefficient
η = efficiency
λ = secondary flow kinetic energy
ν = kinematic viscosity
ρ = density
ϕ = dissipation rate of turbulent kinetic energy
ψ = secondary flow stream function
ω = vorticity

Subscripts

0 = total
1 = inlet
2 = stator exit
3 = rotor exit
d = turbulent diffusion
p = profile
sf = secondary flow
s = stage, isentropic

Table 1 Comparison of estimated and experimental values of ϵ_d/V_zL_s

Turbine Build	Calculated	Experimental
LL	0.0009	0.0007-0.0009
HL	0.0020	0.0018-0.0026

$$\phi = A_d \dot{m} T_3 \Delta s / \rho \Delta \mathrm{Vol}$$

where A_d is the proportionality constant, ΔVol the volume of the stage, and $\dot{m}$ the mass flow rate.

Assuming an eddy viscosity formulation and a typical length scale L_d of the turbulent eddies, a form of turbulent viscosity can be determined

$$\nu_d = (A_d\phi)^{1/3} L_d^{4/3}$$

$$= \left(\frac{A_d U V_z^2 (\tan\alpha_2 - \tan\alpha_1)(1-\eta)}{\eta L_s}\right)^{1/3} L_d^{4/3}$$

where L_s is the stage length. Assuming a Schmidt number of unity and nondimensionalizing, an expression for ϵ_d is obtained

$$\frac{\epsilon_d}{V_z L_s} = \tilde{A}_d \left(\frac{U(\tan\alpha_2 - \tan\alpha_1)(1-\eta)}{\eta V_z}\right)^{1/3} \left(\frac{L_d}{L_s}\right)^{4/3} \quad (4)$$

where $\tilde{A}_d$ is a modified constant of proportionality. Besides $\tilde{A}_d$, the one variable that is not known in the design phase is the length scale L_d. It can be seen from Eq. (4) that it has a significant influence on the predicted level of ϵ_d and must therefore be approximated correctly. L_d has the same order of magnitude as δ, the boundary layer thickness, which is dependent on several parameters including blade loading. An estimate of the momentum thickness θ^* can be determined from the profile loss coefficient Y_p, blade pitch p, and blade exit flow angle α_2

$$\theta^* = \frac{Y_p p \cos\alpha_2}{2}$$

Assuming a turbulent boundary layer and a (1/7)th power law the boundary layer thickness δ is related to θ^* by $\delta = (72/7)\,\theta^*$. The length scale L_d in Eq. (4) is estimated by

$$L_d = 5 Y_p p \cos\alpha_2$$

To establish an appropriate value of $\tilde{A}_d$, the experimental data presented in Figs. 13 and 14 of Part 1 were used. The midspan design values of α_1, α_2, Y_p and the measured overall efficiencies were used in Eq. (4) to estimate ϵ_d. The efficiency of the repeating stage should, strictly speaking, be used, but based on experimental measurements the differences were not large (Lewis, 1993). A comparison of the experimental data and estimated values obtained by setting $\tilde{A}_d$ to 0.2 is presented in Table 1.

Scaling Model for ϵ_{sf}. The approach taken in this paper is to assume that the redistribution process attributable to secondary flow has a nature similar to turbulent mixing. Based on this premise, an eddy viscosity concept is used to define an effective viscosity coefficient due to secondary flow, ν_{sf}. The assumption is acceptable within the confines of the spanwise transport model, Eqs. (1) and (2), even though secondary flow is an inviscid mechanism. The application of the eddy viscosity approximation and a Schmidt number of unity allows ϵ_{sf} to be prescribed by a velocity scale and a length scale. The velocity scale is represented by the secondary flow kinetic energy λ and the length scale L_{sf}, by some appropriate measure of the secondary flow vortices

$$\epsilon_{sf} = A_{sf}\sqrt{\lambda} L_{sf} \quad (5)$$

where A_{sf} is a constant.

The secondary kinetic energy is determined by applying inviscid vortex theory to the uniform density flow through a rotating linear cascade. The analysis is based on that of Hawthorne (1955) and is contained in Appendix 1. If the velocity profile at inlet to the cascade is assumed to consist of a linear gradient with boundary layer thickness δ_1 and a free-stream velocity of V_1, the mean secondary kinetic energy is

$$\lambda = \frac{V_1^2 \Delta^2 p'}{h} f\left(\frac{\delta_1}{p'}\right)$$

where

$$\Delta = \frac{-\sin(\alpha_1 - \beta_1)\cos\beta_1}{\cos\beta_2} + \frac{\cos(\alpha_1 - \beta_1)}{\cos\beta_1 \cos\beta_2}\left(\frac{\sin 2\beta_2 - \sin 2\beta_1}{2} + \beta_2 - \beta_1\right) \quad (6)$$

and $f(\delta/p')$ is a series expansion given in the appendix. It has the form shown in Fig. 1. This expression for λ is based on a stationary wall being upstream of the rotating cascade. A similar expression, representing the case of a rotating wall upstream of a stationary cascade is presented in Appendix 1. The two expressions (A1) and (A3) model the general cases of flow into a rotor and stator, respectively.

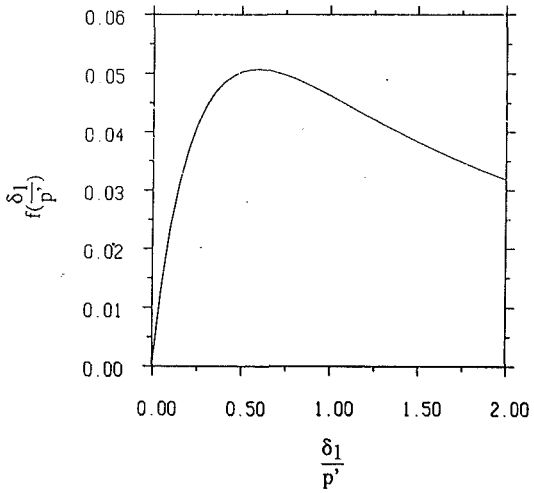

Fig. 1 Series expansion $f(\delta/p')$ as a function of inlet boundary layer thickness

The maximum possible size of the secondary flow vortex will be determined by the throat of the cascade. This can be approximated by p' (Fig. A1). Substituting for λ, L_{sf}, and nondimensionalizing gives

$$\frac{\epsilon_{sf}}{V_z L_s} = A_{sf}\left(\frac{\Delta^2 p' f\left(\frac{\delta}{p'}\right)}{h V_z \cos^2\alpha_1}\right)^{1/2} \frac{p'}{L_s} \quad (7)$$

A similar analysis yields the effective diffusion coefficient ϵ_{sf} downstream of a stationary cascade. It has exactly the same form as Eq. (7) except Δ is determined by Eq. (A3) and the absolute flow angle at inlet α_1 is replaced by the relative flow angle β_1. The experimental data presented in Part 1 were used to establish an appropriate value of A_{sf}. The exit flow angles based on $\cos^{-1}(o/p)$ of the two turbine builds were used as input to the Denton throughflow code to obtain the corresponding inlet angles. This analysis was performed about the third rotor of the *LL* turbine and the second rotor of the *HL* turbine. The values calculated at hub and tip were used to determine the parameters in Eq. (7) and hence for each build two separate values of ϵ_{sf}. As the boundary layer thickness in the multistage environment is difficult to define and therefore measure, the peak value (0.05) of the function $f(\delta/p')$ was used. The experimental data of Figs. 13 and 14, Part 1, show a degree of scatter but indicate that spanwise transport is fairly

Table 2 Comparison of estimated and experimental values of $\epsilon_{sf}/V_z L_s$

Turbine Build	Estimated Hub	Estimated Tip	Experimental
LL	0.0027	0.0015	0.0016-0.0026
HL	0.0071	0.0051	0.0042-0.0056

uniform across the span. The latter trend is reflected by the calculated values of ϵ_{sf}, shown in Table 2 with A_{sf} set equal to 0.02.

Implementation of Spanwise Transport Model

From the preceding analysis it is possible to estimate ϵ_d and ϵ_{sf}. These are average quantities and a method of distribution across the span has to be considered. In this study a linear distribution of ϵ_{sf} and a constant distribution of ϵ_d across the span were used. The local value of ϵ_{sf} was determined by applying Eq. (7) to the hub and casing regions of each blade row and assumed to extend from midchord of the particular blade row to midchord of the succeeding blade row.

In Part 1, it was shown that the stages upstream of the repeating stage experience a reduced level of free-stream turbulence. A modified form of Eq. (2) is therefore suggested, which allows the application of the scaling model to the initial stages of a multistage turbine

$$\epsilon = (\epsilon_d + \epsilon_{sf}) \tanh\left(\frac{z}{1.5L_s}\right) \tag{8}$$

The modification in Eq. (8) is somewhat arbitrary but can be justified by Fig. 2. This shows the variation of the estimated level of ϵ through the two turbine builds reported in Part 1 based on Eq. (8). The agreement with experimental data is considered acceptable.

The spanwise transport model is written into a subroutine that is called by the throughflow model after the inviscid distributions of stagnation enthalpy, entropy, and angular momentum at each quasiorthogonal have been calculated. The transport equation, Eq. (1), is discretized using finite differences and solved for the same quantities using the local meridional velocity and value of ϵ defined by Eqs. (4), (7), and (8). A zero gradient boundary condition is used in evaluating the diffusive terms at the endwalls.

Application of Throughflow Model Incorporating Spanwise Transport

One of the most important effects of spanwise transport in multistage compressors is the redistribution of entropy across the span (Adkins and Smith, 1982; Gallimore, 1986). This must also be true to some extent in multistage turbines. An investigation was made using the *LL* turbine data described in Part 1 of this paper. The measured rotor and stator relative flow angles were used as input to the modified streamline curvature code. Two different methods were used to distribute the loss coefficient, determined by the built-in loss correlations, across the span. The resulting distributions for rotor 3 are shown in Fig. 3(*a*). The first distribution is based on a linear distribution of secondary loss superimposed on the local profile loss and is the standard option available in the throughflow model (Denton, 1978). This method results in very flat loss distributions. The second method involves a parabolic distribution from endwall to midspan of secondary loss superimposed on the local profile loss. The level of secondary loss coefficient was adjusted until the integrated value across the span was the same as in the first method. In this way the same total loss is approximately generated by each method. Additional loss is introduced by the throughflow model to account for shroud leakage; the distribution was constant for both cases. The throughflow model was run without spanwise transport using

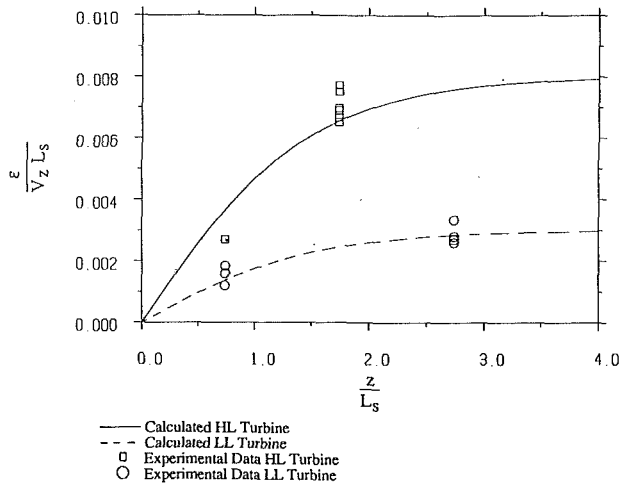

Fig. 2 Estimation of midspan effective diffusion coefficient through *LL* and *HL* turbines

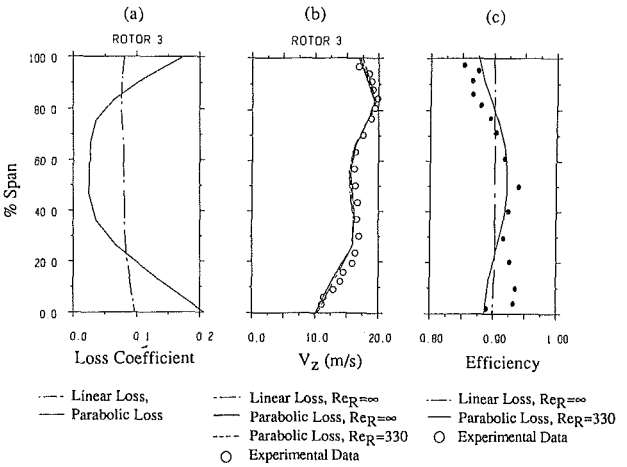

Fig. 3 Spanwise distributions in *LL* turbine of (*a*) rotor 3 loss coefficient; (*b*) axial velocity downstream of rotor 3, and (*c*) stage 3 efficiency

the two distribution methods. The predicted axial velocity profiles are compared with experimental data in Fig. 3(*b*). The prescribed exit angle distributions, which were based on measured data, ensure good predictions of the axial velocity in both cases. Although the loss distributions are significantly different, the effect on the axial velocity distribution is negligible except in the endwall regions. The introduction of spanwise transport has a minor influence on the axial velocity profile (Fig. 3*b*). The Reynolds number based on effective diffusion coefficient at rotor midspan, axial velocity, and stage length was $Re_R = 330$. The spanwise distribution of efficiency (Fig. 3*c*) is strongly influenced, however, by both loss distribution and spanwise transport. By concentrating the secondary losses toward the endwalls, the parabolic loss distribution lowers the spanwise efficiency in these locations. The linear loss distribution results in a flat efficiency distribution that is virtually independent of spanwise transport. The parabolic loss distribution and spanwise transport gives improved prediction over the region 30–100 percent span as compared to the linear distribution. The converse is true from hub to 30 percent span.

As the scaling model described by Eq. (4) contains η, the stage efficiency, it is important that the coupling between the overall loss generation and spanwise transport is weak. The magnitude of this coupling was estimated by applying the parabolic loss distributions (Fig. 3*a*) as input to the throughflow model with and without spanwise transport. The efficiency, based on mass-averaged quantities at inlet and exit

from the turbine, dropped by 0.2 percent from 91.0 percent when spanwise transport was included. Efficiencies based on throughflow calculations without spanwise transport can therefore be used as input to Eq. (4), to determine the appropriate level of ϵ_d.

The streamline curvature code has been applied to three other applications, which have strong gradients across the annulus of either a scalar or stagnation temperature at inlet. The attenuation of these profiles was thought to be strongly influenced by spanwise transport. Joslyn and Dring (1992a, 1992b) studied the attenuation of an axisymmetric concentration profile in a one and a half stage low-speed turbine, the profile at inlet simulating the spanwise temperature profile typically found at entry to a high-pressure turbine. The turbine has a hub-to-tip ratio of 0.8 and an aspect ratio of approximately 1. The transport of a scalar variable based on Eq. (1) was included in the throughflow scheme. The measured stator and rotor relative angles were used as input together with the measured concentration profile at inlet. The calculated efficiency was used to determine an appropriate level of ϵ_d and the measured flow angles at rotor hub and tip to determine ϵ_{sf}. The Reynolds number Re_R based on effective diffusion coefficient at rotor midspan was 210. The calculated concentration profiles are compared to the test data in Fig. 4 downstream of stator 1, rotor 1, and stator 2, respectively. The main area of discrepancy is downstream of the rotor, where the calculated profile suggests that the scaling models give transport coefficients that are too low. This, to a certain extent, reflects the simplicity of the approach but it is doubtful whether a more sophisticated model would do better, without tuning. The experimental results are somewhat surprising as the very strong hub vortex within the rotor does not appear to introduce significant spanwise transport of the tracer in this region. It is thought that the physics of this phenomenon can only be captured by a full three-dimensional calculation. Nevertheless, the profiles calculated by the throughflow model reflect the attenuation of the concentration profile reasonably well.

In the last two test cases it was assumed that the results and scaling models obtained from the low-speed research were applicable to higher speed machines of similar loading and Reynolds number. This is a reasonable assumption as compressibility effects influence the spanwise redistribution mechanisms of convection and diffusion in a second-order fashion (Gallimore, 1986). If however, a nonuniform temperature profile exists at inlet to a stage, the secondary flow through the rotor can be modified markedly (Hawthorne, 1974). This is not necessarily a compressibility effect as a similar influence is observed in incompressible stratified flows and is related to the density variation. As the scaling model for ϵ_{sf} is based on vorticity generated in a uniform density flow, it is not strictly applicable to a flow field with a nonisothermal inlet profile. It is however thought that the *scale* (which is shown later to be more important than the precise value) of ϵ_{sf} predicted by assuming an isothermal flow would still be approximately correct. The following two cases are approached from this perspective.

The second application is based on the experimental study of the flow through a single-stage turbine with a nonuniform radial temperature profile at inlet (Schwab and Stabe, 1983). The test turbine was a 0.767 scale model of the first stage of a two-stage core turbine designed for a modern high bypass ratio engine. It had a hub-to-tip ratio of 0.858 and an aspect ratio of approximately one. The maximum to minimum variation of the temperature profile was 16 percent of the mean temperature. Design flow angles were used as input to the throughflow code and the scaling models. The calculated efficiency was used in Eq. (4). The attenuation of the inlet temperature profile with and without spanwise transport calculated at a traverse plane 0.76 m downstream of the rotor are compared in Fig. 5(*a*). The Reynolds number based on the effective diffusion coefficient at rotor exit was $Re_R = 350$. When span-

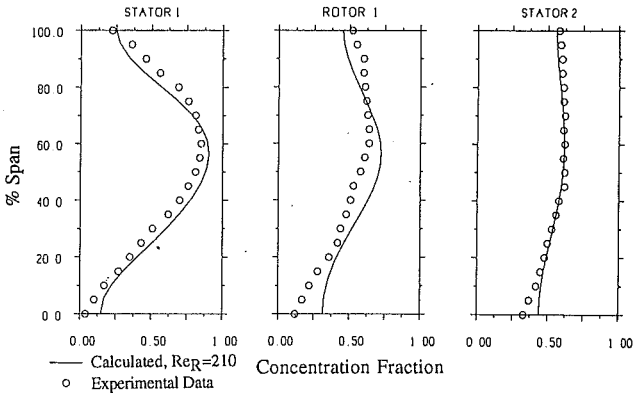

Fig. 4 Attenuation of concentration profile through one and a half stage turbine downstream of each row (Joslyn and Dring, 1990b)

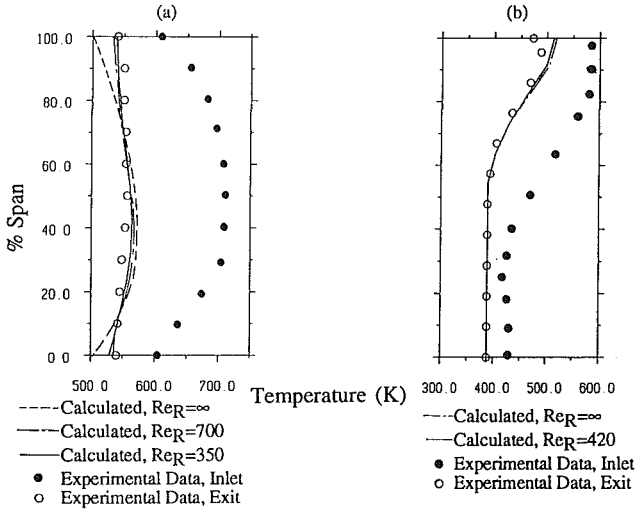

Fig. 5 Temperature profile attenuation through: (*a*) single-stage turbine (Schwab and Stabe, 1983); and (*b*) Berkeley two-stage turbine (Curtis and Halliday, 1969)

wise transport is included the temperature profile is well predicted. If spanwise transport is set to zero, $Re_R = \infty$, the endwall temperatures are underpredicted by approximately 50 K and the midspan region overpredicted by 30 K. By scaling the effective diffusion coefficient, Eq. (2), by 0.5 ($Re_R = 700$) the relative insensitivity of the calculations to the precise level of spanwise transport is apparent.

The final test case is based on data obtained from a steam mixed-flow turbine situated in the Berkeley nuclear power plant (Curtis and Halliday, 1969). The two-stage turbine is supplied steam from two sources: the inner part of the span, from the upstream high-pressure turbine, and the outer part, by fresh steam obtained from a second heating loop directly from the reactor. In this turbine the maximum to minimum temperature variation at inlet is 33 percent of the mean temperature. At inlet the hub to tip ratio was 0.8 and the aspect ratio 2.2. The Denton throughflow code has the option of perfect gas properties or steam properties, the latter being used in this case. Design flow values were used as input to the throughflow model and the scaling models, the calculated efficiency as input to Eq. (4). The Reynolds number based on effective diffusion coefficient was $Re_R = 420$. From the experimental data a significant temperature profile still exists at exit from the second stage as seen in Fig. 5(*b*). The calculated temperature profile, with spanwise transport included, shows improved agreement between experiment and calculation, the difference not being substantial. This reflects the reduced significance of spanwise transport in a higher aspect ratio turbine even though

the Reynolds number Re_R is approximately the same as in the previous test case.

Discussion

The results of the calculations presented here demonstrate the importance of including spanwise mixing in streamline curvature methods. This allows the use of more realistic loss distributions where the loss is concentrated at source and not distributed across the span. It has been common practice to distribute secondary losses more uniformly across the span, which tends to mask their importance and significance. Two-dimensional design has now advanced to the stage that significant reductions in profile loss are hard to achieve; the major area of potential loss reduction involves the unloading of endwalls through the use of three-dimensional blade design. The introduction of spanwise transport is important in focusing attention on the significant areas of loss production.

Gas turbines in general operate with a spanwise temperature profile at inlet to the first-stage turbine. This is a result of tailoring of the combustor exit profile by dilution air within the combustor. The attenuation of this profile, as the flow passes through the turbine, is important to the designer as it influences the distribution of cooling and thermal stressing. The rate of attenuation is controlled by work extraction, which is calculated by any throughflow model, and spanwise transport. It has been shown that far better agreement between experimental data and predictions is obtained when spanwise transport is included. The scaling models used to determine the magnitude of spanwise transport are simple expressions based on the kinetic energies of turbulence and secondary flow. The influence of strong temperature gradients, which is not taken into account, will result in the generation of different secondary flows, the strength of which will depend on the spanwise gradients of temperature and pressure. The fact that good agreement is obtained indicates that the correct scale of spanwise transport is predicted, but not necessarily the correct value. This degree of insensitivity, reflected in Fig. 5(*a*), is well known from multistage compressor calculations (Gallimore, 1986): Including a reasonable amount of spanwise transport improves the quality of the calculations considerably.

The incorporation of spanwise transport into a throughflow model gives the designer the capability to predict temperature profile attenuation early in the design phase. The method presented in this paper is simple and a more rigorous approach might improve the quality of prediction. Ultimately, the success of any prediction will be governed by the basic assumptions on which throughflow models are based, the point at which three-dimensional multistage schemes come into their own.

Conclusions

The experimental evidence of the repeating stage as shown in Part 1 strongly suggests that spanwise transport is important and significant in low aspect ratio multistage turbines. Spanwise transport redistributes endwall losses toward midspan by two mechanisms: turbulent diffusion and convection. It is necessary to model both of these mechanisms to generate the correct scale of transport. By incorporating a model of spanwise transport in a throughflow scheme it is possible to prescribe more realistic loss distributions across the span and thereby focus attention on where the losses are generated.

Calculations of the flow within three turbines showed that it is necessary to include the effects of spanwise transport in throughflow models in order to predict the correct attenuation of a spanwise temperature or scalar profile. Agreement with experimental data, considering the simplicity of the spanwise transport model, was good. The ability to predict this attenuation early in the design phase will aid the designer in considering spanwise distribution of cooling and thermal stressing.

Acknowledgments

The author would like to thank Professors Denton and Horlock for their advice and encouragement. This work was financially supported by the Science and Engineering Research Council and NEI Parsons of the United Kingdom.

References

Adkins, G. G., and Smith, L. H., 1982, "Spanwise Mixing in Axial Flow Turbomachines," ASME *Journal of Engineering for Power*, Vol. 104, p. 97.

Curtis, E. M., and Halliday, M., 1969, "Some Preliminary Results of Traversing No. 2 Turbine at Berkeley Nuclear Power Station," Central Electricity Generating Board Report No. RD/M/N396, Research and Development Department, Marchwood Engineering Laboratories, United Kingdom.

Denton, J. D., 1978, "Throughflow Calculations for Transonic Axial Flow Turbines," ASME *Journal of Engineering for Power*, Vol. 100, p. 212.

De Ruyck, J., Hirsch, Ch., and Segaert, P., 1988, "Secondary Flows and Radial Mixing in Axial Compressors," AGARD-CP-469, *Secondary Flows in Turbomachines*.

Gallimore, S. J., and Cumpsty, N. A., 1986, "Spanwise Mixing in Multistage Axial-Flow Compressors: Part 1—Experimental Investigation," ASME JOURNAL OF TURBOMACHINERY, Vol. 108, p. 2.

Gallimore, S. J., 1986, "Spanwise Mixing in Multistage Axial-Flow Compressors: Part 2—Throughflow Calculations Including Mixing," ASME JOURNAL OF TURBOMACHINERY, Vol. 108, p. 10.

Glynn, D. R., Spurr, A., and Marsh, H., 1977, "Secondary Flow in Axial Flow Turbomachinery," AGARD-CP-214, *Secondary Flow in Turbomachines*, The Hague.

Glynn, D. R., 1982, "Calculation of Secondary Flow in Cascades Including Effects of Bernoulli Surface Distortion," *International Journal of Heat and Fluid Flow*, Vol. 3, No. 2, p. 73.

Gregory-Smith, D. G., and Okan, M. B., 1991, "A Simple Method for the Calculation of Secondary Flows in Annular Cascades," IMechE Conference: Turbomachinery—Latest Developments in a Changing Scene, Paper No. C423/008.

Hawthorne, W. R., 1955, "Some Formulae for the Calculation of Secondary Flow in Cascades," Department of Engineering Report, University of Cambridge, United Kingdom.

Hawthorne, W. R., and Novak, R. A., 1969, "The Aerodynamics of Turbomachinery," *Annual Review of Fluid Mechanics*, Vol. 1, Palo Alto, CA, p. 341.

Hawthorne, W. R., 1974, "Secondary Vorticity in Stratified Incompressible Fluids in Rotating Systems," Aeronautical Research Council Report ARC35.695.

Horlock, J. H., and Lakshminarayana, B., 1973, "Secondary Flows: Theory, Experiment and Application in Turbomachinery Aerodynamics," *Annual Review of Fluid Mechanics*, Vol. 5, p. 247.

Hunter, I. H., 1979, "Endwall Boundary Layer Flows and Losses in Axial Turbomachines," PhD Thesis, Department of Engineering, University of Cambridge, United Kingdom.

Joslyn, D., and Dring, R., 1992a, "Three-Dimensional Flow in an Axial Turbine Part 1—Aerodynamic Mechanisms," ASME JOURNAL OF TURBOMACHINERY, Vol. 114, pp. 61-70.

Joslyn, D., and Dring, R., 1992b, "Three-Dimensional Flow in an Axial Turbine: Part 2—Profile Attenuation," ASME JOURNAL OF TURBOMACHINERY, Vol. 114, pp. 71-78.

Lewis, K. L., 1993, "Aerodynamics of Shrouded Multistage Turbines," PhD thesis to be submitted, Department of Engineering, University of Cambridge, United Kingdom.

Leylek, J. H., and Wisler, D. C., 1991, "Mixing in Axial-Flow Compressors: Conclusions Drawn From Three-Dimensional Navier–Stokes Analyses and Experiments," ASME JOURNAL OF TURBOMACHINERY, Vol. 113, p. 139.

Schwab, J. R., and Stabe, R. G., 1983, "Analytical and Experimental Study of Flow Through an Axial Turbine Stage With a Nonuniform Inlet Radial Temperature Profile," AIAA Paper No. 83-1175.

Wennerstrom, A. J., 1991, "A Review of Predictive Efforts for Transport Phenomena in Axial Flow Compressors," ASME JOURNAL OF TURBOMACHINERY, Vol. 113, p. 175.

Wisler, D. C., Bauer, R. C., and Okiishi, T. H., 1987, "Secondary Flow, Turbulent Diffusion and Mixing in Axial-Flow Compressors," ASME JOURNAL OF TURBOMACHINERY, Vol. 109, p. 455.

APPENDIX

The rate of generation of secondary kinetic energy is determined by considering inviscid vortex theory and applying it to the general case of uniform density flow through a rotating cascade. The analysis is based on that of Hawthorne (1955) and is considered in the intrinsic relative coordinate system s^*, n^*, b^*, shown in Fig. A1. If the relative Bernoulli surfaces are assumed cylindrical, the development of the absolute vorticity resolved along the relative streamline s^* is given by (Horlock and Lakshminarayana, 1973)

$$\omega^*_{s2}=\frac{\omega^*_{s1}\cos\beta_1}{\cos\beta_2}+\frac{\omega^*_{n1}}{\cos\beta_1\cos\beta_2}\left(\frac{\sin 2\beta_2-\sin 2\beta_1}{2}+\beta_2-\beta_1\right)$$

where subscripts 1 and 2 refer to cascade inlet and exit stations. For a rotor, in the general case, the upstream wall will be stationary and the incoming vorticity, defined by $\omega = \omega_{n1} = \partial V_1/\partial b$, has to be resolved into the relative streamwise s^* and normal n^* directions

$$\omega^*_{s1}=-\omega_{n1}\sin(\alpha_1-\beta_1)$$

$$\omega^*_{n1}=\omega_{n1}\cos(\alpha_1-\beta_1)$$

The absolute vorticity resolved in the relative streamwise direction becomes

$$\omega^*_{s2}=\omega_{n1}\Delta$$

where

$$\Delta=\frac{-\sin(\alpha_1-\beta_1)\cos\beta_1}{\cos\beta_2}+\frac{\cos(\alpha_1-\beta_1)}{\cos\beta_1\cos\beta_2}\left(\frac{\sin 2\beta_2-\sin 2\beta_1}{2}+\beta_2-\beta_1\right) \quad \text{(A1)}$$

By defining a secondary stream function ψ where $w_n = \partial\psi/\partial b^*$ and $w_b = -\partial\psi/\partial n^*$ a series solution can be found to the Poisson equation

$$\frac{\partial^2\psi}{\partial n^{*2}}+\frac{\partial^2\psi}{\partial b^{*2}}=-\omega^*_{s2}$$

where $\psi = \Sigma^{\infty}_{k=1,3,5}\psi_k \sin k\pi b^*/p'$ and ψ_k is given by a similar series. The boundary conditions, $\psi = 0$ where $n^* = 0$ and $n^* = p'$; $\psi = 0$ where $b^* = 0$ and $b^* = h$ define the complete solution for ψ

$$\psi=\sum_{k=1,3,5}^{\infty}\psi_k\sin k\pi b^*/p'$$

where for $0 < b^* < \delta$

$$\psi_k=\frac{4\Delta p'^2V_1}{(k\pi)^3\delta}\left(1-e^{-k\pi b^*/p'}-e^{-k\pi b^*/p'}\sinh k\pi b^*/p'\right)$$

and for $\delta < b^* < h$

$$\psi_k=\frac{4\Delta p'^2V_1}{(k\pi)^3\delta}e^{-k\pi b^*/p'}(\cosh k\pi b^*/p'-1)$$

Using the series expansion for ψ and its definition in terms of the secondary velocities w_n and w_b, the mean kinetic energy λ of the secondary flow is given by

$$\lambda=\frac{\int_0^{p'}\int_0^h\frac{1}{2}(w_n^2+w_b^2)\partial n^*\partial b^*}{\int_0^{p'}\int_0^h\partial n^*\partial b^*}$$

If the velocity profile is assumed to consist of a linear gradient with boundary layer thickness δ_1 and a free-stream velocity of V_1, λ becomes

$$\lambda=\frac{V_1^2\Delta^2p'}{h}f\left(\frac{\delta_1}{p'}\right) \quad \text{(A2)}$$

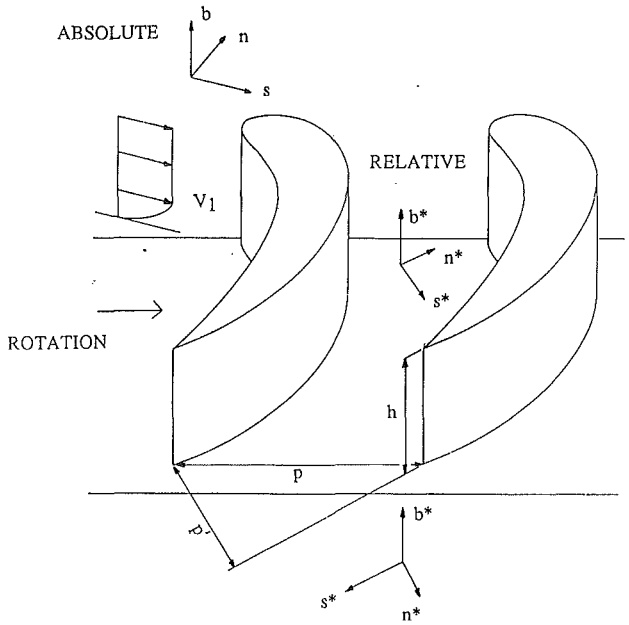

Fig. A1 Rotating cascade with stationary upstream wall

where $f(\delta_1/p')$ is a series expansion

$$f\left(\frac{\delta_1}{p'}\right)=8\left(\frac{p'}{\delta_1}\right)^2\cdot\sum_{k=1,3,5}^{\infty}\frac{1}{(k\pi)^5}\left(k\pi\delta_1/p'-1+e^{-k\pi\delta_1/p'}(2-\cosh k\pi\delta_1/p')\right)$$

$f(\delta_1/p')$ has the form shown in Fig. 1.

A similar analysis can be performed for the stator. In the general case, the upstream wall will be rotating, and the incoming absolute vorticity resolved in the intrinsic relative coordinate system is $\omega = \omega^*_{n1} = \partial W_1/\partial b$. This has to be converted back into the absolute streamwise and normal directions

$$\omega_{s1}=-\omega^*_{n1}\sin(\beta_1-\alpha_1)$$

$$\omega_{n1}=\omega^*_{n1}\cos(\beta_1-\alpha_1)$$

The absolute vorticity becomes

$$\omega_{s2}=\omega^*_{n1}\Delta$$

where

$$\Delta=\frac{-\sin(\beta_1-\alpha_1)\cos\alpha_1}{\cos\alpha_2}+\frac{\cos(\beta_1-\alpha_1)}{\cos\alpha_1\cos\alpha_2}\left(\frac{\sin 2\alpha_2-\sin 2\alpha_1}{2}+\alpha_2-\alpha_1\right) \quad \text{(A3)}$$

The mean kinetic energy λ is

$$\lambda=\frac{W_1^2\Delta^2p'}{h}f\left(\frac{\delta_1}{p'}\right) \quad \text{(A4)}$$

The series expansion $f(\delta_1/p')$ is the same as in the rotor case.

The Unstable Behavior of Low and High-Speed Compressors

I. J. Day
Whittle Laboratory,
University of Cambridge,
Cambridge, United Kingdom

C. Freeman
Rolls-Royce plc,
Derby, United Kingdom

By far the greater part of our understanding about stall and surge in axial compressors comes from work on low-speed laboratory machines. As a general rule, these machines do not model the compressibility effects present in high-speed compressors and therefore doubt has always existed about the application of low-speed results to high-speed machines. In recent years interest in active control has led to a number of studies of compressor stability in engine-type compressors. The instrumentation used in these experiments has been sufficiently detailed that, for the first time, adequate data are available to make direct comparisons between high-speed and low-speed compressors. This paper presents new data from an eight-stage fixed geometry engine compressor and compares them with low-speed laboratory data. The results show remarkable similarities in both the stalling and surging behavior of the two machines, particularly when the engine compressor is run at intermediate speeds. The engine results also show that, as in the laboratory tests, surge is precipitated by the onset of rotating stall. This is true even at very high speeds where it had previously been thought that surge might be the result of a blast wave moving through the compressor. This paper therefore contains new information about high-speed compressors and confirms that low-speed testing is an effective means of obtaining insight into the behavior of high-speed machines.

Introduction

Although stall and surge have been one of the most persistent problems in the history of aero-engine design, the study of these disturbances in high-speed machines has received relatively little attention. There are two reasons for this: First, high-speed testing is expensive, and, second, there is a natural reluctance to study a phenomenon that is not part of successful compressor design. Much of the work on stall and surge has thus been done in the laboratory at low speed.

By testing at low speed, the implicit assumption is made that compressibility is not an important factor and the results can be read across to high-speed machines. Until now there has not been a systematic study to prove that this assumption is correct. Some high-speed data do exist, e.g., Mazzawy (1980), Reis and Blocker (1987), Small and Lewis (1985), and Hosny and Steenken (1986), but, in general, the effects of compressibility have not been studied in any detail.

In historical terms, the experimental work on low-speed machines, and particularly the little that has been done on high-speed machines, has concentrated on the effects of the fully developed disturbance. Surge has been studied to assess the effects of reversed flow on structural loading, and stall, to examine recovery problems and fatigue stressing of the blades. In recent times, however, the emphasis has shifted away from the study of the fully developed disturbance to concentrate on how these disturbances came into being, i.e., the inception process.

Contributed by the International Gas Turbine Institute and presented at the 38th International Gas Turbine and Aeroengine Congress and Exposition, Cincinnati, Ohio, May 24–27, 1993. Manuscript received at ASME Headquarters February 12, 1993. Paper No. 93-GT-26. Associate Technical Editor: H. Lukas.

Epstein et al. (1986) published a paper suggesting that active control could be applied to stall and surge to extend the useful operating range of the compressor. The implementation of active control relies on the idea that if stall and surge can be shown to begin from small perturbations, it should be possible, by the introduction of artificially induced "friendly" perturbations, to create conditions in which the original perturbation can be held in check. This concept has therefore prompted a whole new series of experiments on stall and surge inception. Laboratory tests show that the instabilities do indeed begin as small perturbations and that the inception process is ordered and well defined (Day, 1993). This work is now being followed up by detailed experiments on engine compressors to see if this is also true at high speed. The first of these experiments is presented here to give a back-to-back comparison of stall inception processes in low and high-speed compressors.

Stall and Surge

In general term, *rotating stall* is a disturbance that affects the flow in the region of the compressor blading. The disturbance, once initiated, rotates about the compressor, causing severe blade vibration and, above all, a drop in overall pressure rise. In an engine, as opposed to a compressor rig, rotating stall, in all but its minor forms, will seriously restrict the flow into the combustion area leading to overheating and deceleration of the engine. Restarting of the stalled engine is then not possible until the stall cell has been cleared and normal flow conditions restored. This usually requires an almost complete shutdown of the engine. In high-speed rigs, where the compressor is driven by an electric motor, blade vibration and

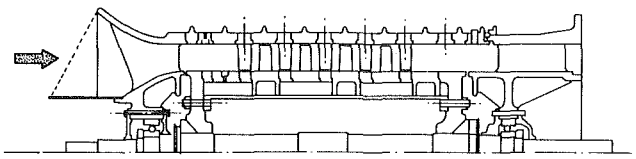

0.5 METRES

LOW SPEED LABORATORY C106 COMPRESSOR	
NUMBER OF STAGES:	4
HUB/TIP RATIO:	0.75
REYNOLDS NUMBER:	1.7×10^5
SPEED OF ROTATION:	3000rpm

Fig. 1 The Wittle Laboratory's C106 low-speed compressor

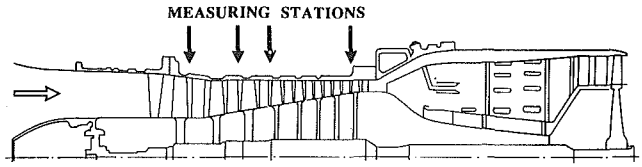

ROLLS-ROYCE VIPER ENGINE Mk 522	
NUMBER.OF STAGES:	8
SLS THRUST:	3330 lbf
COMPRESSOR PRESSURE RATIO:	5:1
SHAFT SPEED:	13850 rpm

Fig. 2 View of Viper engine showing compressor layout and pressure transducer positions

temperature rise are the most serious consequences of rotating stall.

Surge, on the other hand, is an oscillation of the mass flow through the compressor and only occurs where a significant amount of pressure energy is stored downstream of the compressor. This is usually the case in an engine at high speed, where the combustion chambers act as an energy reservoir. In industrial situations this also happens where there is significant duct work at the compressor exit. Because surge only occurs where there is storage capacity downstream of the compressor, it is usually referred to as an "installation" or "system" instability. In the past, a lot of time and energy has been spent modeling surge as a one-dimensional disturbance. Much can be learned using this approach; however, it is becoming abundantly clear that in an axial compressor, surge is actually the consequence of a two-dimensional instability, i.e., rotating stall (Day, 1991). Thus, a compressor may go into stall or surge depending on the speed of rotation and the geometry of the installation, but both types of disturbance are the result of the same fundamental inception process.

In the work that flows, we will examine the general behavior of a low-speed laboratory compressor and then compare this with the results from the high-speed tests. An engine compressor operates over a wide speed range and it is obviously not practical to consider all possible operating conditions. For convenience the results have therefore been divided into three categories: low, medium, and high-speed behavior.

Experimental Facilities

The experimental results in this paper were derived from two sources: the low-speed compressor at the Whittle Laboratory, and a Viper compressor tested as part of a complete engine on a test bed at Rolls-Royce.

The Wittle Laboratory compressor, designated the C106, is a low-speed machine of incompressible design having four identical stages preceded by a lightly loaded set of inlet guide vanes. The hub-casing radius ratio is 0.75 and the speed the rotation is 3000 rpm, giving a rotor Reynolds number of 1.7×10^5. The blading is of modern controlled diffusion design and is representative of current HP compressor practice. An outline drawing of the compressor is given in Fig. 1.

The high-speed compressor used in this study is part of a fully operational Rolls-Royce Viper engine. The engine has a single spool and the compressor is of fixed geometry design, i.e., there are no variable vanes. The speed of rotation from idle to full speed ranges from 4000 to 13,850 rpm, and the hub-casing ratio changes from 0.5 at inlet to 0.85 for the last blade row. The flow rate through the compressor is measured using a calibrated test-bed inlet and standard instrumentation. Details of the engine are shown in Fig. 2.

In the case of the laboratory compressor, the operating point can be moved up and down a fixed speed characteristic simply by changing the setting of the downstream throttle valve. The pressure rise is low and the flow is basically incompressible. Changing the compressor speed therefore has little effect other than to change the Reynolds number. In the engine, however, special steps are necessary to change the compressor working line. The engine has neither a physical throttling device, nor the inclination to rotate at fixed speed while other conditions are being varied. The usual method of pushing an engine compressor beyond the stability limit is to use a technique known as fuel spiking. This involves the removal of the normal fuel management system so as to allow the sudden injection of excess fuel into the combustion chamber. The rapid overfueling raises the back pressure on the compressor and, before the shaft has time to accelerate fully, the compressor is driven into stall or surge. For most engines this technique is effective at low and medium speeds, but at full speed the process leads to detrimental overheating and cannot be used.

In the current experiments, the problem of how to change the working line of the compressor at high speed was overcome by major modifications to the engine. Extra air from an outside source was injected into the combustion area via a ring manifold system with twelve inlet ports. In this way the compressor could be forced to go unstable at more or less fixed speed by suddenly increasing the amount of air being injected, i.e., ramp injection. At lower speeds instability could also be induced by injecting air at a steady rate while the engine is decelerated to a point where the back pressure is more than the compressor can support. Both the ramped injection and steady blowing techniques were used in the experiments reported here.

To study the processes by which the compressor becomes unstable, and the events subsequent to instability, numerous circumferential direction. In the laboratory tests, circumferential arrays of six hot wires were used, hot wires having the advantage of being able to explore the full height of the annulus. In the engine tests hot wires could not be used because of the harsh environment, and pressure transducers were used instead, five per circumferential array. Unlike the low-speed compressor, flow conditions change along the length of the compressor in the high-speed case and therefore circumferential arrays were necessary at four or five axial stations.

Stage Matching in a High-Speed Compressor

The flow through the laboratory compressor is essentially incompressible and therefore all stages receive air at the same Cx/U and perform in the same way, all moving toward or away from stall at the same time. This is not true for the engine compressor, however, where the annulus is not parallel and compressibility effects are important. Prior to instability the stages experience different loading conditions depending on the speed of rotation of the machine. At low speeds, the air entering the compressor is incompletely compressed in the front stages with the result that the rear stages receive air at a higher

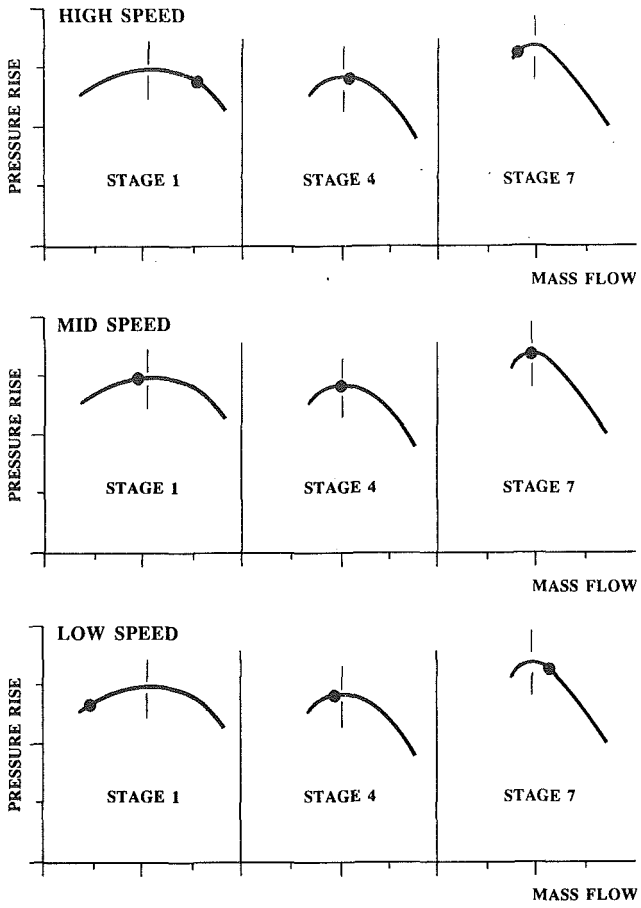

Fig. 3 Engine compressor performance predictions showing the operating points for the front, middle, and rear stages at low, medium, and high speeds

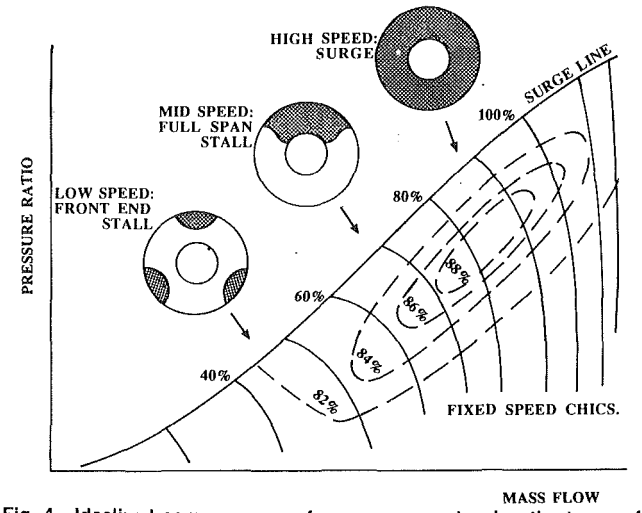

Fig. 4 Idealized compressor performance map showing the types of instability encountered at various speeds

than design Cx/U, thus pushing the operating point for these stages away from stall. At high speeds, on the other hand, the front stages compress the air so effectively that the rear stages receive air at a lower than usual Cx/U, thus forcing them to operate close to stall. This shifting of peak stage loading as the compressor speed changes is illustrated in Fig. 3.

In Fig. 3, three groups of stage characteristics, representing conditions at the front, middle, and rear of a compressor, are shown for low, medium, and high speeds. These characteristics were derived by predictive means and on each one a dot is used to indicate the operating condition for that particular stage while the compressor as a whole is operating at the stability limit. It can be seen that in the low-speed range, the front stage operates to the left of the peak of the characteristic while the rear stage operates farthest from the point of instability. In the mid-speed range, all three stages in this case are similarly loaded and the compressor may be considered to be well matched from front to back. At top speed it is the rear stage that operates closest to the point of instability while the front stage is well away from stall.

The position of the stage that is most heavily loaded, and that is most likely to cause stall, thus shifts from the front to the rear of the compressor as the speed goes up. This phenomenon is well known in high-speed compressors (Cumpsty, 1990), and in subsequent sections it will be shown how this shift in stage loading affects the stall and surge behavior of the compressor.

Overall Performance After Instability

Before considering the process by which the flow through the compressor becomes unstable, it will be useful to examine the overall behavior of the high-speed compressor after instability has set in. To this end, Fig. 4 shows a number of fixed speed pressure rise characteristics for an imaginary compressor at various operating conditions. Together with the efficiency curves, these lines constitute the overall performance map of the compressor. The map is bounded at the upper edge by the so-called "surge line." This is a general term used to describe the locus of all points at which the flow becomes unstable either through surge or stall. At low speeds the compressor experiences a type of post-stability disturbance known as "front end stall." This is generally a disturbance of light intensity that does not hinder the startup process of the compressor, unless it degenerates into single cell rotating stall. At higher speeds, say between 65 and 85 percent of full speed, the compressor will go into rotating stall at the surge line. In this case the disturbance is severe and the abrupt loss of efficiency means that the engine must be shut down to prevent the turbine overheating. At still higher speeds, the combined compression and combustion systems hold sufficient stored energy for the engine to surge. This process results in repetitive cycles involving temporary flow reversal, unless, as can happen at maximum speed, combustor flame-out occurs and then only the first part of the first flow reversal cycle is observed.

The types of compressor behavior described here can be illustrated in more detail by looking at the actual results from the Viper compressor, Fig. 5. (It should be noted that the instrumentation used for these measurements is standard test cell equipment and is of limited dynamic range. Some transient features of the stalling behavior are therefore lost, but the overall trends are well represented.) Figure 5 shows the experimentally determined working line of the compressor and the surge line. Also shown are the trajectories of the compressor operating points immediately before and after instability. As previously explained, the operating point of the compressor does not move from the working line to the surge line along any particular path. The path depends on the technique used to induce instability.

Considering the various test runs in turn, we start with runs 1 and 2 where the working line and surge line are close together. At these low speeds the compressor operates in stall all the time; this type of stall being "front end stall," which is relatively light and is not severe enough to prevent the compressor from being accelerated to a higher speed. If overfueling occurs while operating in this condition, however, a change to fully developed rotating stall, affecting the whole compressor, will occur with the result that the engine will have to be shut down. This change from "front end stall" to rotating stall will be illustrated in detail in a later section.

In the mid-speed range, as for tests 3 and 4, overfueling the engine pushes the operating point over to the surge line where

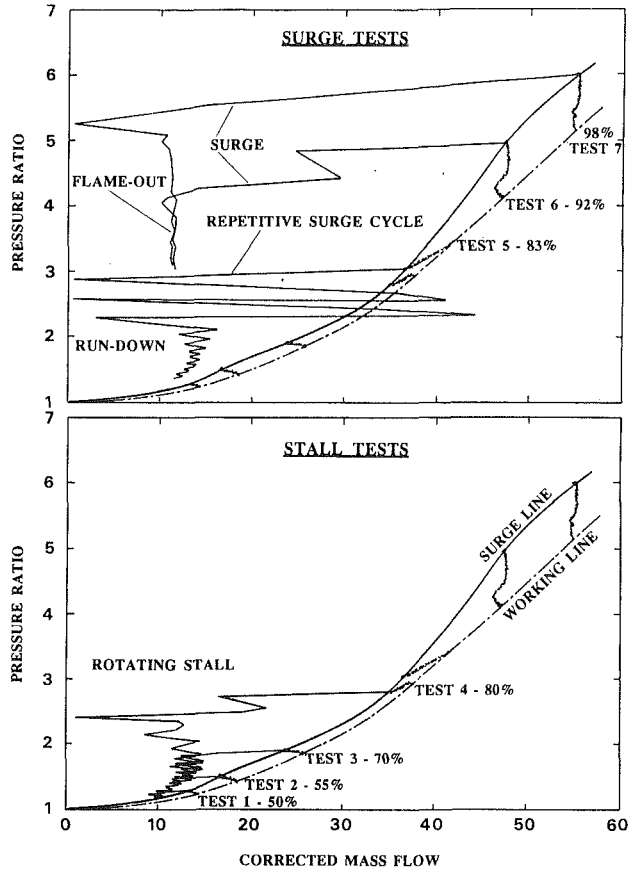

Fig. 5 Viper performance map showing the post-stability trajectory of the compressor working point at various speeds (figure is in two parts to improve clarity)

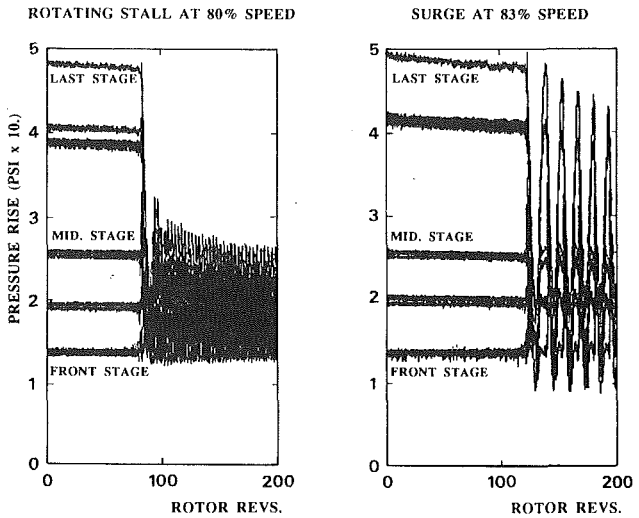

Fig. 6 Examples of rotating stall and surge in the Viper compressor separated by a small change in speed. The plots show pressure measurements from five circumferential positions at various stations along the length of the compressor.

rotating stall is initiated. Once stalling occurs, the compressor mass flow drops suddenly with an accompanying drop in pressure rise and the engine is again forced to shut down. The type of stall that occurs at this speed is known as single cell full span stall, or "locked-in stall," and is responsible for an abrupt loss of efficiency. The stall cell extends as a single axial disturbance throughout the length of the compressor and rotates around the annulus at about 50 percent of rotor speed.

If the engine speed is increased slightly, but stays within the mid-speed range, for example test 5 in Fig. 5, a disturbance of very different proportions occurs when the compressor is pushed beyond the point of instability. Here surge is encountered for the first time and the flow through the compressor undergoes a number of violent oscillations before the fuel is cut and the compressor slows down. In the low-speed laboratory compressor, this type of oscillation can be sustained indefinitely, but in an engine environment the risk of structural damage means that rapid shut-down is essential.

It is interesting to note that the change in speed between runs 4 and 5 in Fig. 5 is relatively small, yet the change in compressor behavior is remarkable. The same thing was observed by Greitzer (1976) in the testing of his low-speed compressor when it was noted that the speed range separating rotating stall and surge is very narrow. In the context of the Viper tests, Fig. 6 illustrates both the narrowness of the speed divide and the dramatic difference in compressor behavior. This figure shows the recorded pressure levels from circumferential arrays of probes at various stations along the length of the compressor. The left-hand side of the figure, at 80 percent speed, shows the compressor going into rotating stall, while the right-hand side, at 83 percent speed, shows the distinctive one-dimensional oscillations associated with surge. The speed range separating these two pictures is just 3 percent.

Returning to Fig. 5, it can be seen that a further change in compressor behavior occurs as we approach full speed, runs 6 and 7. Here, a repetitive surge cycle does not occur, as for test 5, because the initial mass flow fluctuation is so vigorous that the engine experiences a flame-out, followed by a rapid drop in rotational speed. Surge at this speed therefore consists of just the first part of a surge cycle, i.e., a sudden reversal of flow followed by rotating stall as the engine coasts to a standstill.

Having considered the question of stage loading prior to instability, and the overall behavior of the compressor after instability, we now consider the instability process itself, i.e., the details of the inception process through which the flow becomes unstable.

Stall Inception in the Laboratory Compressor

A number of detailed studies of stall inception in low-speed compressors have been conducted in recent years. It has been found that there are two distinctly different mechanisms by which axisymmetric flow becomes unstable. The first mechanism to be identified was that associated with modal perturbations. The theoretical work behind the identification of these modes was done by Moore and Greitzer (1986) and the experimental validation by McDougall et al. (1990), Garnier et al. (1991), and Day (1993). In this type of stall inception small velocity perturbations of circumferential length scale appear in the flow just prior to stall. The perturbations rotate around the annulus and grow over a number of revolutions until the perturbation itself becomes so intense as to be recognizable as a stall cell. The speed with which the modal perturbation rotates remains relatively steady from first detection right through to the fully developed state.

An example of stall occurring via a modal perturbation is illustrated in Fig. 7 where six hot wires are used around the circumference of the compressor to track the development of the mode. In this figure, the perturbation is first visible at about rotor revolution 10, and over the next twelve revolutions grows to maturity as a single, full-span stall cell. The rotational speeds marked in the figure show that there is no change in frequency during the development process. This type of stall cell thus originates from an infinitesimally small disturbance and can therefore be adequately modeled by linear theory.

The second mechanism by which the flow may become unstable is via the growth of a small localized disturbance, which appears without precursive build-up, and which grows quickly

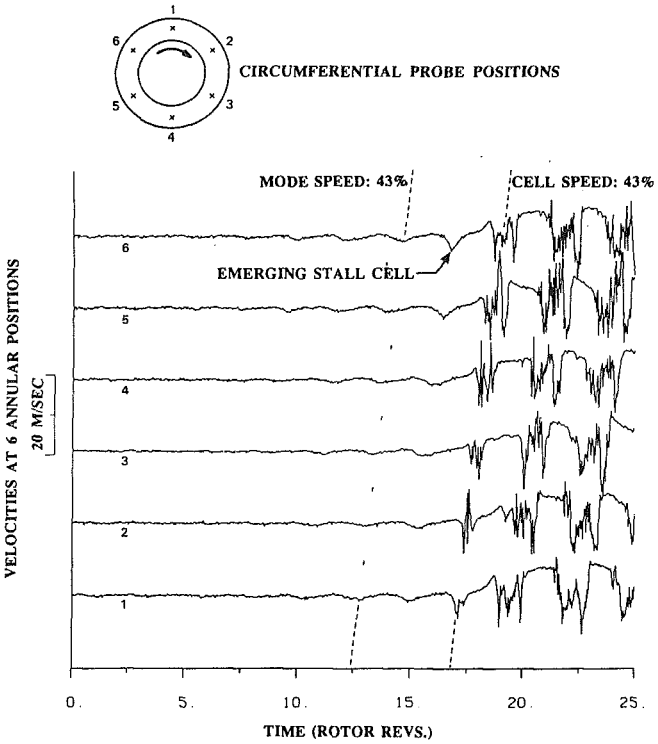

Fig. 7 Example of rotating stall originating from a model perturbation in the low-speed compressor

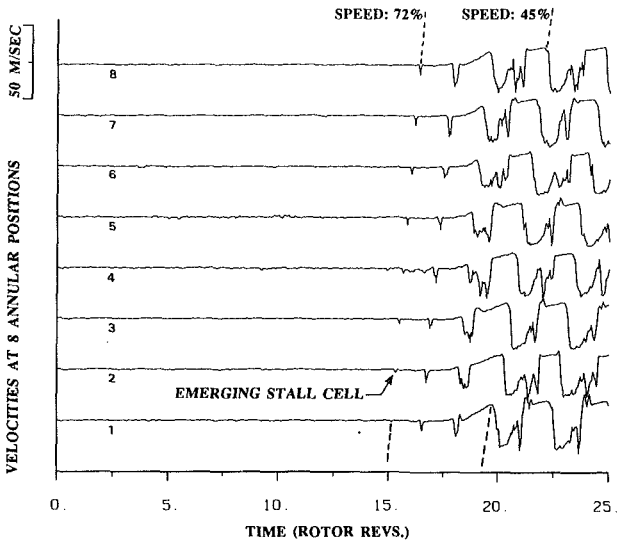

Fig. 8 Example of rotating stall originating from a localized disturbance in the low-speed compressor

to engulf a large part of the annulus. This type of stall inception was first identified by Day (1993) and can be visualized as a patch of locally separated flow initially affecting just the tips of one or two blades. An example is given in Fig. 8 where the first sign of instability occurs on wire 2 at rotor revolution 15. At this point the instability is very small, but it grows to become a fully developed stall cell in just six rotor revolutions. It is important to note that the speed of rotation of the disturbance changes markedly as it grows in size, i.e., from 72 percent at outset to just 45 percent when mature. The change in speed provides a useful means of identifying this type of stall inception.

Of the two stall inception processes outlined above, the second is the most representative of what is observed in the Viper compressor. The measurements in Fig. 8 will therefore

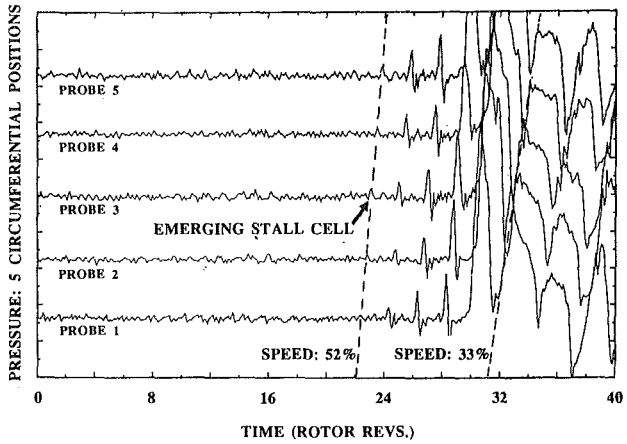

Fig. 9 Stall inception in the engine compressor at midspeed measured at five circumferential positions near the front of the compressor. The stalling pattern originates from a localized disturbance.

be used as the starting point for assessing the similarities between the laboratory compressor and the Viper engine.

Stall Inception in the Engine at Midspeed

It will be recalled that in the midspeed range, 75 to 85 percent of full speed, all of the stages in the engine compressor are approximately matched near the surge line and all approach instability at the same time. This is much the same as what happens in the laboratory compressor where the flow is incompressible and all the stages are equally loaded. It is therefore in this speed range that we should expect to see the greatest similarity in the behavior between the low-speed and high-speed compressors. Figure 9 shows measurements from the engine using five pressure transducers equally spaced about the annulus near the front of the compressor. Because wall-mounted pressure transducers were used instead of hot wires, the initial perturbations peak upward instead of downward; nevertheless, there is no mistaking the similarity of the stall development patterns in Figs. 8 and 9.

In Fig. 9 a small localized disturbance appears at revolution 24 and grows to become a single fully developed stall cell. As in Fig. 8, the speed of rotation is high at the beginning and lower when the cell is fully developed. It may therefore be concluded that in this speed range the engine and the laboratory compressor behave in very similar ways, each stalling as the result of a small localized stall cell, which rotates quickly at first, but slows down as it grows in size. Figure 9 is thus the first clear picture we have of stall inception in an engine compressor and suggests that, in this instance at least, stall inception is via a localized disturbance rather than a modal perturbation.

The lead-in traces in Fig. 9, from rotor revolutions 0 to 24, are more turbulent than those in Fig. 8 (for the laboratory compressor) and therefore it is reasonable to ask if some form of modal perturbation is not perhaps present in the background noise. This is a possibility; however, Fourier analysis in one and two dimensions has failed to yield any sign of a coherent disturbance in this region. Other tests for modal coherence, based on radar identification techniques, have also found no evidence of precursive model disturbances.

Surge Inception in the Laboratory Compressor

Even though it is a low-speed compressor, the C106 can be made to surge, rather than stall, if a large plenum is interposed between the compressor exit and the throttle. The additional energy stored in the plenum means that a surge cycle will be set up as soon as the compressor goes into rotating stall. Experiments demonstrating the part played by rotating stall in

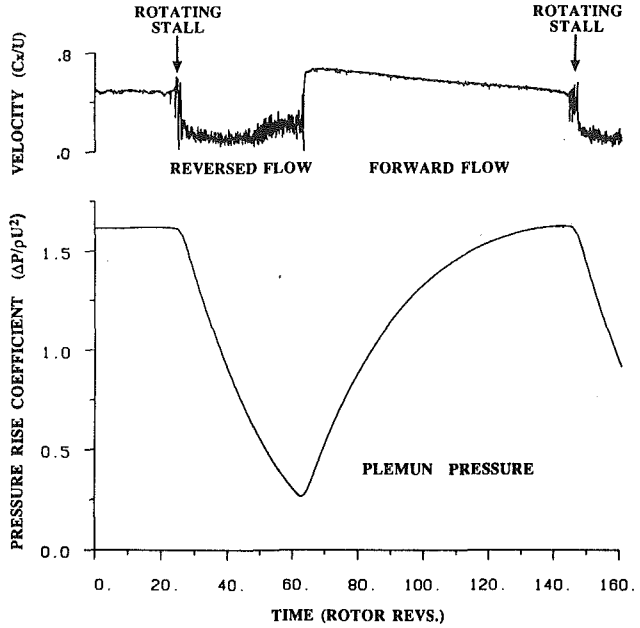

Fig. 10 Velocity at the front of the compressor, and pressure in the plenum, as measured during surge in the low speed compressor. The surge cycle begins with rotating stall.

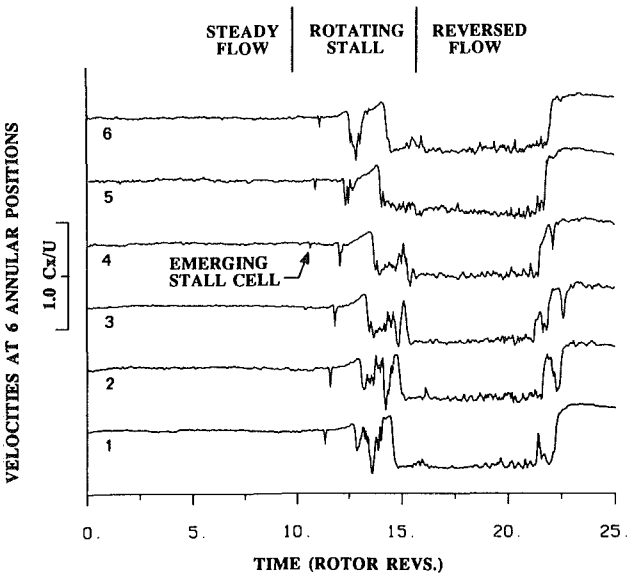

Fig. 11 Details of the rotating stall at the start of the surge cycle in the low speed compressor, using six hot wires ahead of the first rotor. (These measurements are for an event similar to, but not the same as, the one shown in Fig. 10. A smaller plenum was used here.)

initiating surge have been reported by Day (1991), and a set of representative measurements for the laboratory compressor is given in Fig. 10.

Figure 10 shows the first, and part of the second, of a series of repeating surge cycles. The upper trace is from a hot wire positioned upstream of the first rotor and records the axial velocity in the compressor, while the lower trace shows the corresponding pressure variation in the plenum chamber. For the first 25 revolutions of the traces shown, the compressor operates in a stable manner at peak pressure rise. At revolution 25 the flow becomes unstable and a burst of rotating stall is observed, followed by a dramatic fall in plenum pressure. The rotating stall itself is short lived and is soon replaced by axisymmetric reversed flow (Day, 1991). About 40 revolutions after the start of the cycle the compressor unstalls and the plenum pressure begins to rise. Provided the throttle has not

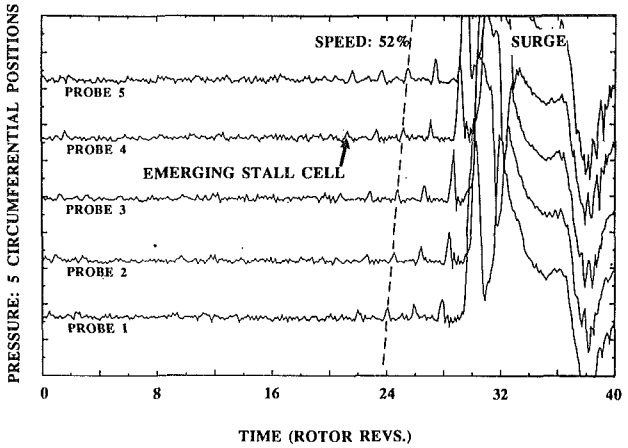

Fig. 12 Engine pressure measurements at mid-speed showing rotating stall at the start of the surge cycle

been moved since the cycle began, a second surge cycle will be initiated when the compressor stalls again at peak pressure rise.

The patch of rotating stall that initiates the surge cycle is more clearly illustrated in Fig. 11. Here six hot wires around the annulus are used to monitor the circumferential movement and growth of the stall cell. It can be seen that a small localized stall cell appears, without modal build-up, opposite hot wire 3 at revolution 4, and then rotates and grows to the point where the whole of the annulus is enveloped in reversed flow. This stall inception process is exactly like that in Fig. 8, even to the point where the initial speed of the stall cell is also 72 percent. Surge in the laboratory compressor thus begins with the sam inception process associated with rotating stall.

Surge in the Engine Compressor at Medium Speed

In the Viper engine, a repetitive surge cycle is first observed when the speed reaches 83 percent of full speed, as can be seen in Fig. 5, test 5. At this speed, the stages are well matched and all approach the instability line at the same time, as is the case in the low-speed laboratory compressor. We can therefore expect that the engine will again behave in the same way as the laboratory compressor. Detailed measurements of the start of a surge cycle in the Viper compressor at 83 percent speed are shown in Fig. 12. As before, five equally spaced pressure transducers were used at the front of the compressor. It can be seen that the start of the instability process is fundamentally similar to that for rotating stall, as shown in Fig. 9. This means that surge at mid-speed in the engine compressor begins with the formation of a localized stall cell and develops in the same way as in the laboratory compressor.

The preceding figures confirm that at certain speeds, where all the engine stages are well matched, useful information about stall and surge in the engine can be obtained directly from incompressible laboratory tests. It will be shown below that although conditions at low speed and high speed in the engine are somewhat different from those in the laboratory compressor, the fundamentals of stall inception learned from the laboratory tests provide useful insight into the engine results.

Stall in the Engine Compressor at Low Speed

Having discussed the behavior of the engine compressor at midspeed where all the stages are well matched close to stall, it remains to show what happens in the engine at the lower and upper end of the speed range. We first consider conditions at low speed, i.e., as for test runs 1 and 2 in Fig. 5. It will be recalled that the front stages are the first to run into trouble at this speed, see Fig. 3, and that rotating stall is often a permanent feature of operation in this range. In this particular

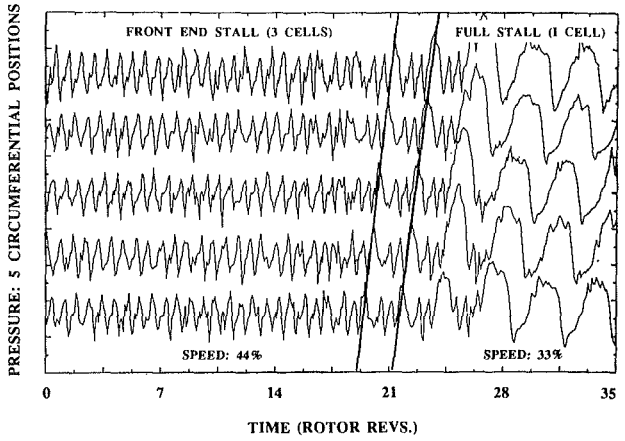

Fig. 13 Engine measurements at low speed showing a three-cell "front end stall" pattern changing to a single cell pattern. This forces the engine to be shut down.

case in the Viper compressor, three equally spaced stall cells were observed to be present right from start-up. The influence of these cells appeared to be restricted to the first three stages of the compressor. (The process by which these cells first form, i.e., their inception phase, was never observed because the cells were already present by the time the engine reached light-up speed.)

The type of stall cells seen here are not unlike the part-span cells sometimes found in lightly loaded laboratory compressors (Day, 1976). How far the cells extend down the span of the blades is not known in this case, but the similarity with part-span cells in other compressors is supported by the fact that these cells do not stop the engine from operating normally, albeit slightly inefficiently. Part-span cells do not usually cause a large loss of pressure rise and therefore their presence is not overwhelmingly detrimental to performance.

While operating with light stall at the front of the compressor, it may happen that the operating point is pushed still further into stall, for instance by sudden overfueling, in which case a larger full-span cell will develop out of the existing part-span pattern. An example of this happening is given in Fig. 13 where five pressure transducers were used around the circumference at the front of the compressor. For the first 18 revolutions the compressor operates with three small stall cells restricted to the front end of the compressor. Events in the second half of the figure show how one of the three cells grows in amplitude until the other two are swallowed up, leaving a single full-span cell rotating at a much slower speed. Parallel lines have been drawn in Fig. 13 showing how the two smaller of the three original cells are squeezed out of existence as the larger cell grows to maturity. Other measurements from farther back in the compressor confirm that the initial cells were limited to the first three stages and that the larger single cell, once formed, extended right through the length of the compressor.

Surge at High Speed in the Engine Compressor

At high speeds the engine surges in a very dramatic fashion, with a single bang and flames shooting out of the intake and exhaust. This happens for test runs 6 and 7 in Fig. 5. A repeating surge cycle does not occur at this speed, because the initial flow reversal is so vigorous that combustion is extinguished, i.e., "flame-out" occurs. Without combustion, the engine decelerates very quickly, passing through a period of rotating stall before coming to a standstill. In some engines, but fortunately not this one, structural bending as a result of the pressure loads can cause catastrophic failure.

In the past it has been suggested that this type of high-speed surge consists of a blast wave, which starts at the back of the compressor and sweeps through to the inlet at near sonic speed,

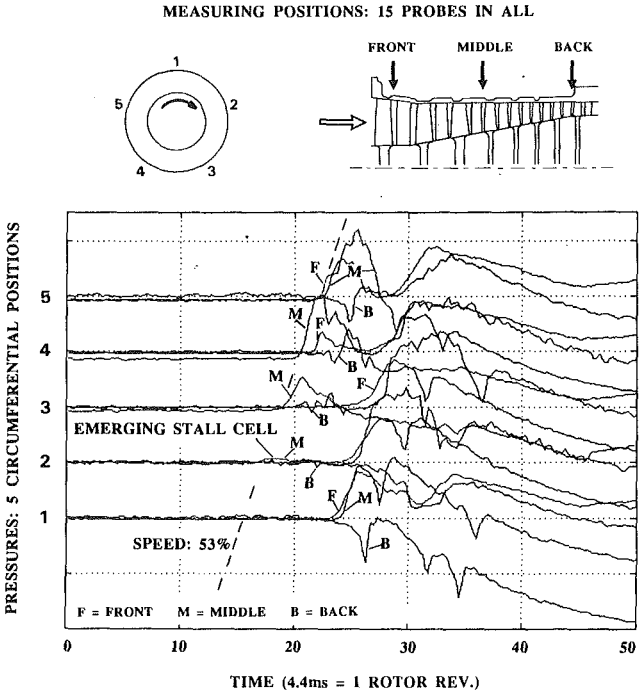

Fig. 14 Engine measurements of surge inception at high speed. This figure shows front, middle, and rear dynamic pressures at five circumferential positions. A rotating disturbance precedes the surge event.

the pressure difference across the shock front increasing as the wave approaches the front of the compressor; see Mazzawy (1980) and Cargill and Freeman (1991). In the current tests some evidence of a blast wave has been detected, but there are two other features of these tests that need to be considered first.

To begin with, the physical location of the initiating disturbance in the Viper engine was not where it was expected to be, i.e., at the rear of the compressor. The first sign of flow breakdown appears on the traces from the middle stages of the compressor. This can be seen in Fig. 14 where three pressure traces are plotted at each of five circumferential positions; one trace each for the front, middle, and rear sections of the compressor. It might have been thought from Fig. 3 that the rear stages would be the first to go unstable, but this does not appear to happen here. The first sign of instability occurs at time 18 at position 2 at the middle of the compressor. It is possible that the instability actually starts slightly farther back than the plane of the measuring probes; however, it is nonetheless interesting that in this case flow breakdown does not start at the rear of the compressor.

The second interesting thing to come out of these full-speed measurements concerns the rotational nature of the initial disturbance. Before these measurements were taken, ideas about the origins of the surge event were speculative rather than informed. The idea of a "blast wave" rushing forward from the rear of the compressor assumed some form of initiating disturbance, but just what form this disturbance would take was not known. From results like those in Fig. 14 it is now clear that the initiating disturbance is once again rotating stall. The traces in Fig. 14 show that the disturbance is roughly 53 percent of rotor speed, similar to the stall cell speeds observed at lower power settings.

The preceding results have also been studied to ascertain whether the emerging stall cell is a localized disturbance or has its origins in a modal perturbation. Modal analysis of the first 18 ms of Fig. 14 does not show any form of coherent precursive structure. In addition, the disturbance that starts the whole stalling sequence appears to be restricted to one sector of the annulus only. This suggests that, even at full speed, the onset

of instability takes the form of a localized disturbance. This observation is not only significant in its own right, but it is also important from the point of view of future active control experiments. It determines the type of control strategy that will be required and highlights the need for very fast actuator systems.

In terms of a blast wave moving forward through the compressor, it can be seen from Fig. 14 that the stall cell at the middle of the compressor has no effect on the front of the compressor until the emerging stall cell reaches circumferential position 4. Starting from Time 0 and looking along the pressure traces at circumferential position 4, it can be seen that the flow at the front of the compressor becomes disturbed about 1 ms later than conditions at the middle, i.e., the "M" trace begins to rise 1 ms before the "F" trace. The dimensions of the compressor are such that a disturbance taking this length of time to propagate from the middle of the compressor to the front will do so at a speed of 330 m/s. This is near enough to sonic velocity to suggest that some sort of "blast wave" may be present. Evidence of this type from a single measurement is however inconclusive, especially as it does not explain why conditions at the front of the compressor are the first to be affected at circumferential position 5! Further measurements are therefore necessary to obtain a complete picture of what actually happens in the compressor at very high speeds.

The topic of surge at high speed is also discussed in a companion paper by Wilson and Freeman (1994).

Conclusions

Two compressors, one a low-speed laboratory machine operating incompressibly, the other a high-speed engine compressor, have been tested to examine the similarities in the stall inception processes. In the process of making the comparisons, interesting information about stall and surge in an aero-engine compressor is presented here for the first time. The conclusions to be drawn from this work are listed below:

1 This paper shows that useful information about stall and surge can be obtained from tests on low-speed compressors. Examples have been given where precise read-across from incompressible tests to the high-speed conditions is possible

2 In the mid-speed range, all the stages in the engine compressor are evenly matched near the surge line and therefore it is reasonable to expect close similarity between the engine and laboratory tests. This has been shown to be correct for both stall and surge where the inception patterns in the two compressors are almost identical.

3 Previous work on laboratory compressors has identified two distinct mechanisms of stall inception: model perturbations and localized stalling. Throughout the engine tests it was clear that a localized disturbance initiated stall and surge, with no modal disturbances being detected at any speed.

4 At low speeds, the engine compressor is seldom free of multicell stall in the front stages. This type of stall is similar in character to the part-span stall sometimes seen in laboratory compressors. If the engine is pushed further into stall when operating in this condition, the multicell pattern coalesces to form a single more severe cell pattern, which extends throughout the whole compressor and forces the engine to be shut down.

5 Toward the upper end of the speed range the engine will surge rather than stall. Repetitive surge cycles were possible at medium to high speeds, but at top speed surging occurred with such violence that the flow reversal extinguished combustion. The results show that the repetitive type of surge is initiated by rotating stall in much the same way as in the laboratory compressor. Top speed surge has also been shown to be initiated by rotating stall, but the growth of the disturbance, and the rate at which it spreads throughout the compressor, is much faster than at lower speeds. Some, though limited, evidence exists for a "blast wave" type of pressure front moving through the compressor soon after stall inception occurs.

6 It was observed that when surge was initiated at high speed, the initial pressure perturbation did not appear at the rear of the compressor, as might have been expected, but more toward the middle of the compressor. This finding may be a feature of the particular compressor tested, but it is mentioned for reference when measurements from other compressors become available.

7 Work in the laboratory has shown that the rotational speed at which the change from stall to surge occurs is well defined. Tests on the engine likewise show an almost abrupt change from stall to surge as the speed of rotation is increased.

8 Taken as a whole, this study confirms that laboratory testing of low-speed compressors is an effective and inexpensive way of gaining insight into many aspects of the behavior of aero-engine compressors.

Acknowledgments

The financial support for the laboratory test program was provided jointly by Rolls-Royce and the SERC in the form of a cooperative grant. The engine testing was conducted at Rolls-Royce Ansty and the authors wish to express their gratitude to the test crew and especially to Mr. Ron Speddings. Grateful thanks is also extended to Dr. John Longley, Mr. Alec Wilson, and Prof. Nick Cumpsty for their generous help while preparing this paper.

References

Cargill, A. M., and Freeman C., 1991, "High-Speed Compressor Surge With Application to Active Control," ASME JOURNAL OF TURBOMACHINERY, Vol. 113, pp. 303-311.

Cumpsty, N. A., 1989, *Compressor Aerodynamics*, Longman Scientific and Technical, United Kingdom.

Day, I. J., 1976, "Axial Compressor Stall," PhD Thesis, Department of Engineering, University of Cambridge, United Kingdom.

Day, I. J., 1993, "Stall Inception in Axial Flow Compressors," ASME JOURNAL OF TURBOMACHINERY, Vol. 115, pp. 1-9.

Day, I. J., 1991, "Axial Compressor Performance During Surge," Tenth ISABE Meeting, Nottingham, ISABE Paper No. 91-7098.

Emmons, H. W., Pearson, C. F., and Grant, H. P., 1955, "Compressor Surge and Stall Propagation," *Transactions of the ASME*, Vol. 79.

Epstein, A. H., Ffowcs Williams, J. E., and Greitzer, E. M., 1986, "Active Suppression of Aerodynamic Instabilities in Turbomachines," AIAA *Journal of Propulsion and Power*, Vol. 5, No. 2, pp. 204-211.

Garnier, V. H., Epstein, A. H., and Greitzer, E. M., 1991, "Rotating Waves as a Stall Inception Indication in Axial Compressors," ASME JOURNAL OF TURBOMACHINERY, Vol. 113, pp. 290-302.

Greitzer, E. M., 1976, "Surge and Rotating Stall in Axial Flow Compressors, Parts I & II," ASME *Journal of Engineering for Power*, Vol. 98, pp. 190-217.

Hosny, W. M., and Steenken, W. G., 1986, "Aerodynamic Instability Performance of an Advanced High-Pressure-Ratio Compression Component," AIAA Paper No. 86-1619.

Ishii, H., and Kashiwabara, Y., 1989 "Surge and Rotating Stall in Axial Compressors," AIAA Paper No. 89-2683.

Mazzawy, R. S., 1980, "Surge-Induced Structural Loads in Gas Turbines," ASME *Journal of Engineering for Power*, Vol. 102, p. 162.

McDougal, N. M., Cumpsty, N. A., and Hynes, T. P., 1990, "Stall Inception in Axial Compressors," ASME JOURNAL OF TURBOMACHINERY, Vol. 112, pp. 116-125.

Moore, F. K., and Greitzer, E. M., 1986, "A Theory of Post-stall Transients in Axial Compression Systems: Part I—Development of Equations; Part II—Application," ASME *Journal of Engineering for Gas Turbines and Power*, Vol. 108, pp. 68-76; 231-239.

Paduano, J. D., Epstein, A. H., Valavani, L., Longley, J. P., Greitzer, E. M., and Guenette, G. R., 1993, "Active Control of Rotating Stall in a Low-Speed Axial Compressor," ASME JOURNAL OF TURBOMACHINERY, Vol. 115, pp. 48-57.

Reis, W., and Blocker, U., 1987, "Possibilities for On-Line Surge Suppression by Fast Guide Vane Adjustment in Axial Compressors," AGARD-CP-421.

Small, C. J., and Lewis, J. T., 1985, "High Speed Compressor Rig as a Stall Recovery Research Tool," AIAA Paper No. 85-1428.

Wilson, A. G., and Freeman, C., 1994, "Stall Inception and Development in an Axial Flow Aeroengine," ASME JOURNAL OF TURBOMACHINERY, Vol. 116, this issue, pp. 216-225.

A Review of Nonsteady Flow Models for Compressor Stability

J. P. Longley
Engineering Department,
Whittle Laboratory,
Cambridge University,
Cambridge, United Kingdom

This paper presents a review of the different approaches to modeling the nonsteady fluid dynamics associated with two-dimensional compressor flow fields. These models are used to predict the time development of flow field disturbances and have been found useful in both the study of rotating stall and the development of active control. The opportunity to digest the earlier investigations has now made it possible to express the modeling ideas using only a very simple mathematical treatment. Here, the emphasis is on the underlying physical processes that the models simulate and how the assumptions within the models affect predictions. The purpose of this work is to produce, in a single document, a description of compressor modeling techniques, so that prospective users can assess which model is the most suitable for their application.

Introduction

Surge and rotating stall are important considerations both in the design of compressors, where their occurrence represents a performance boundary, and in the operation of aeroengines, where they can occur prematurely due to inlet distortion. The time development of these phenomena is determined by nonsteady fluid dynamic processes both within the blade passages and in the flow field as a whole. Direct calculations of all aspects of the flow are impractical, because of the many length and time scales that are involved, and so models that represent the effective local compressor performance are used.

Calculations using these models can only ever be as good as the predicted performance, that is, pressure rise as a function of mass flow, and this depends on the accuracy of the component characteristics. These characteristics are not normally known with great precision. Consequently, the greatest value of these compressor models is in identifying the important physical processes and in undertaking parametric studies using generic performance correlations. This review is concerned with the details of the compressor models that are in current use, the physical mechanisms that they simulate, and the constraints on their application.

Conceptually, a compression system is represented by a series of components comprising inlet duct, compressor, exit duct, plenum, and throttle, Fig. 1. Each of these components can be modeled in different ways depending on the fluid dynamic phenomena of interest. For example, "surgelike" disturbances are primarily axisymmetric and involve variations in the mass flow through all the system components; to study these types of phenomena, the plenum and throttle are necessary, along with the dynamics of nonsteady mass storage within the plenum. "Stall-like" disturbances, on the other hand, involve a region of the compressor annulus that has a lower throughflow than the rest and only the average mass flow and average pressure rise interact with the plenum and throttle[1]; to study these phenomena it is necessary to account for the circumferential variation of flow within the compressor.

Stall is the primary disturbance (Day, 1993b) and so the modeling techniques for nonsteady flow through compressors will be discussed with reference to "stall-like" flow perturbations. These are intrinsically nonaxisymmetric and involve circumferential flow redistribution and static pressure fields that decay away from the compressor. A reliable model must simulate these effects and here, as in virtually all treatments to date, attention is limited to flow variations that are primarily in the axial and circumferential directions, often referred to as two dimensional. As a result these models are useful in the study of high hub-to-tip ratio compressors for which radially uniform flow is a reasonable approximation. A schematic representation of the inlet duct, compressor, and exit duct for a two-dimensional flow field is shown in Fig. 2.

[1]This fact has been used with generalized compressor performance characteristics, that represent the average pressure rise and mass flow in fully developed rotating stall, to take some account of two-dimensional phenomena in a one-dimensional model; for example see Bloch and O'Brien (1992).

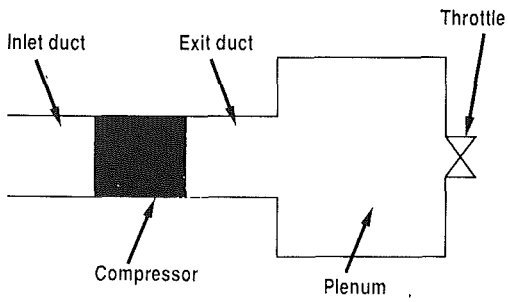

Fig. 1 Compression system components

Contributed by the International Gas Turbine Institute and presented at the 38th International Gas Turbine and Aeroengine Congress and Exposition, Cincinnati, Ohio, May 24-27, 1993. Manuscript received at ASME Headquarters February 12, 1993. Paper No. 93-GT-17. Associate Technical Editor: H. Lukas.

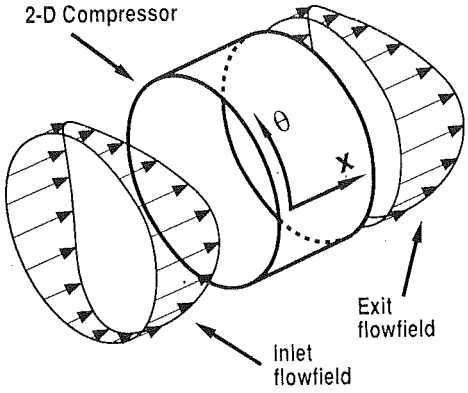

Fig. 2 Schematic representation of a two-dimensional compressor flow field

The compressor modeling techniques discussed in this paper are applicable to both large and small-amplitude flow field disturbances. However, attention is limited to the latter as this is convenient for examining nonsteady flow field behavior. An additional advantage of this restriction is that small-amplitude nonaxisymmetric disturbances do not affect the average mass flow or average pressure rise. Therefore, the compressor models and the behavior of nonaxisymmetric disturbances may be analyzed without explicit inclusion of the plenum and throttle.[2]

Although not discussed in any depth in this review, these two-dimensional compressor models are, nevertheless, applicable to nonsteady axisymmetric flow and so may be used to study surge. The compression system modeling approach for surge was developed by Greitzer (1976a, b), with a simple mass flow pressure rise relationship for the compressor and lumped parameter representations for the other components, the behavior being determined by a second-order ordinary differential equation. An important result from Greitzer's modeling is that an analogy of surge behavior is a spring-mass-damper, with surge being equivalent to a system oscillation. This type of compression system model, often referred to as a one-dimensional simulation, is still extensively used (see Pinsley et al., 1991, Gysling et al., 1991, and Simon et al., 1993) and a great deal has be learned about surge dynamics (see Moore and Greitzer, 1986, and McCaughan, 1988).

Review Structure

In this review the underlying constraints on the models to represent the average blade row performance over some length and time scales of interest are examined first. It is shown that for circumferential harmonics up to the fifth or sixth the spatial flow redistribution should be well modeled and that the temporal behavior of the lowest harmonics should be quasi-steady. Here, quasi-steady is taken to mean that the instantaneous blade loss and exit angle are identical to those for corresponding steady flow.

The quasi-steady compressor model is then derived and is, in essence, the one presented by Moore (1984a). The predicted nonsteady fluid dynamic behavior of compressor flow fields is investigated with, initially, two simplifying assumptions (perfect IGVs and high-solidity compressor exit blading) concerning the compressor and flow field interaction. These simplifications facilitate the identification of the physical mechanisms that determine circumferential propagation and growth or decay of flow field disturbances. It is then shown that in the more general case, where inlet and exit swirl variations are fully accounted for, the physical mechanisms are the same though quantitative predictions may change.

The later sections of this review consider possible consequences when the blade rows no longer respond in a quasi-steady manner. An enhanced compressor model is described that uses a simple time lag approach for nonsteady blade row response. With this enhanced model the individual circumferential modes are predicted to have distinct stability boundaries and this has been experimentally demonstrated. Finally, approximate forms of this enhanced model that are more convenient for solution are described and their merits considered.

Throughout this review, the different models are compared by using them to study the behavior of flow disturbances in a hypothetical compressor. The validity of the assumptions within the models is assessed in the light of available experimental evidence and, to this end, information is drawn from different research works. It is assumed that the reader is familiar with compression system instabilities (for stall and surge see Greitzer, 1980, and for inlet flow distortion see Longley and Greitzer, 1992).

Constraints on the Modeling Approach

The general approach to modeling compressor flow field dynamics is to take the steady-state axisymmetric performance characteristics of the individual components and to include additional terms to represent the nonaxisymmetric and nonsteady flow effects. Surge, rotating stall, and inlet flow nonuniformities are relatively large length scale and long time scale fluid dynamic phenomena compared to blade pitch length scale and blade passage convection time scale. Compressor models exploit these facts by representing the effective performance of a group of blades when averaged over the circumferential length scale and time scale of interest. The limitations on these spatial and temporal averages will be examined in this section.

Spatial Flow Field Resolution. An important constraint on two-dimensional compressor models is how large the ratio of "nonuniformity wavelength" to "blade pitch" must be for the local blade performance in nonuniform flow to be similar to what it would have been in uniform flow with the same local conditions. There is little available information on this question, although some guidance may be drawn from the studies of back pressure distortion[3] through stationary blade rows.

For a nonuniformity with wavelength shorter than a blade pitch, flow redistribution can occur freely and appreciable decay of the pressure field is expected. For a long wavelength nonuniformity imposed on a blade row, the blades themselves would restrict the circumferential redistribution and so there would be reduced axial decay of the pressure field. This is supported by O'Brien et al. (1985) who studied the interaction between a row of stators and a downstream strut. Their results showed little decay of the long length scale pressure field across the stators.

From this a rough constraint can be said to be that the circumferential length scale of the flow nonuniformity should be long enough so that a blade and its neighbors (two pitches) have similar flow conditions (within a quarter wavelength). Therefore:

$$1/4 \text{ nonuniformity wavelength} > 2 \text{ blade pitches}$$

and hence an estimate for the minimum wavelength-to-pitch ratio is eight. Taking 50 as a typical blade count, then circumferential harmonics up to the fifth or sixth should be well modeled.

Ham and Williams (1983) investigated this point experi-

[2]For large-amplitude stall-like disturbances the downstream components must be included.

[3]Most studies on convected vorticity are for nonsteady wake and blade row interaction.

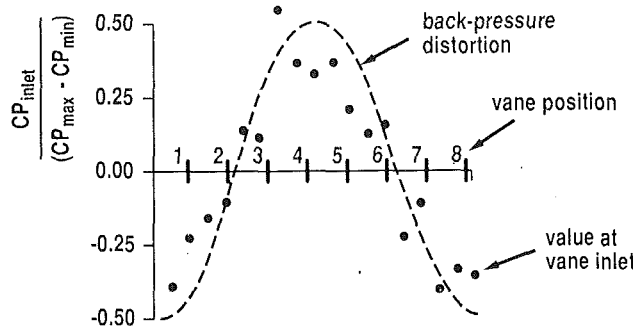

Fig. 3 *Transfer of a primarily first harmonic back-pressure distortion through eight unloaded vanes (Ham and Williams, 1983)*

mentally for a primarily[4] first circumferential harmonic back pressure distortion through eight unloaded vanes in an annulus of moderate hub-to-tip ratio. Their results, Fig. 3, indicate that although the short length scale pressure field is attenuated within the individual vane passages, the circumferential pressure nonuniformity transfers through the blade row. This is because each of the eight passages responds to the local pressure and therefore adequately defines the long length scale variation. Without the vanes the pressure nonuniformity would decay to approximately 50 percent along an axial duct.

Temporal Flow Field Resolution. There are two ways in which nonsteady flow arises. The flow in the absolute (stator) frame can be time varying, so both rotors and stators see unsteadiness, or there can be a stationary spatial nonuniformity, which appears as a time varying flow in the relative (rotor) frame. The importance of the nonsteady flow effects within the blade passages is assessed by comparing the relative sizes of the blade passage convection time, i.e., from the leading edge to trailing edge, with the disturbance passing time, i.e., the passage of the blade through one wavelength. The ratio of these two is referred to as the reduced frequency, and the flow behaves quasi-steadily at low reduced frequencies, i.e., when

$$\text{convection time} \ll \text{disturbance passing time}$$

Taking c_x and u as the blade axial chord and the axial velocity, respectively, the inequality may be written:

$$c_x/u \ll 2\pi/nf\Omega$$

where n is the spatial Fourier harmonic being considered and f is the fraction of rotor angular velocity (Ω) with which the spatial pattern moves. Thus for quasi-steady blade row performance:

$$nf \ll \frac{2\pi\phi}{c_x/r} \tag{1}$$

where $\phi = u/U$. Typically $\phi \approx 0.3$ to 0.7, $c_x/r \approx 0.15$, and nonsteady phenomena of interest have $0 < f < 1$. Under these conditions the right-hand side of Eq. (1) is approximately twelve and so for the lowest circumferential harmonics the blades are expected to behave quasi-steadily.

Blade Passage Fluid Inertia. Even when the blade flow field responds quasi-steadily there is an associated nonsteady flow effect due to the acceleration of the fluid within the blade passage. This acceleration requires a nonsteady pressure difference across the blade row that may be estimated[5] by modeling the blade passage as a parallel duct at the mean stagger angle, Fig. 4, so:

[4]A 90 deg distortion generator was used at approximately 1 radius downstream so that at the vanes the pressure field would mainly consist of the first mode only.

[5]Moore (1984a) states that the effective inertia could depend on viscous processes.

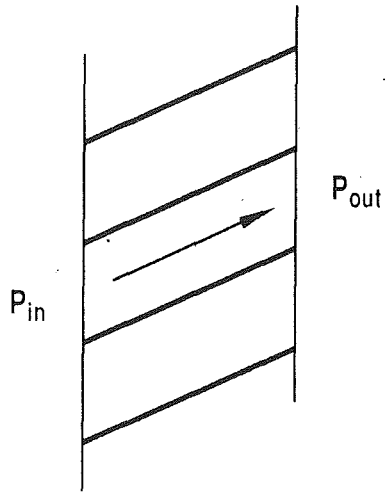

Fig. 4 **A parallel duct at the mean stagger angle can be used to estimate the inertia-driven nonsteady pressure difference**

$$(P_{in} - P_{out})_{inertia} = \rho \times \text{chord} \times \frac{\partial}{\partial t} (\text{mean relative velocity})$$

$$(P_{in} - P_{out})_{inertia} = \rho \frac{c_x}{\cos(\text{stagger})} \frac{\partial}{\partial t} \left(\frac{u_x}{\cos(\text{stagger})} \right) \Bigg|_{\text{rel to blade}}$$

Thus:

$$\frac{P_{in} - P_{out}}{\rho U^2} \Bigg|_{inertia} = \Lambda \frac{r}{U} \frac{\partial}{\partial t} \left(\frac{u_x}{U} \right) \Bigg|_{\text{rel to blade}} \tag{2}$$

where the inertia parameter is:

$$\Lambda = \frac{c_x}{r \cos^2(\text{stagger})} \tag{3}$$

Williams (1986) calculated that typical values of Λ for individual blade rows of military aeroengines are:

$\Lambda \approx 0.314 (\pm 10$ percent) for low-pressure compressor

$\Lambda \approx 0.14 (\pm 13$ percent) for high-pressure compressor

For civil engines the inertia parameters are usually within the range 0.1–0.2 for each row in the high-pressure compressor.

Quasi-Steady Compressor Model

In this review the starting point for all the models will be the blade row performance. Steady-state blade row performance is usually correlated as total pressure loss coefficient and exit deviation as functions of inlet angle, Mach number, and Reynolds number. An equivalent presentation, which is more convenient for modeling purposes, is in terms of static pressure rise and exit flow angle as functions of inlet angle and flow coefficient. Reynolds number and compressibility effects are being ignored as they are not necessary to elucidate the physical mechanisms.

For some of the models it is possible to recombine the individual blade row pressure rises into a more compact form where the overall compressor pressure rise is directly evaluated in terms of, say, the local flow coefficient at inlet. Wherever possible this will be done, as it simplifies the application of the model.

For quasi-steady flow through a stator passage, the local instantaneous static pressure rise may be related to that in steady flow by inclusion of the inertia term, Eq. (2). Thus:

$$\frac{P_{out} - P_{in}}{\rho U^2} = \frac{P_{out} - P_{in}}{\rho U^2} \Bigg|_{steady} - \Lambda_{row} \frac{\partial \phi}{\partial \tau} \tag{4a}$$

where rotor speed has been used to produce the nondimensional time $\tau = Ut/r$. The instantaneous exit angle, α_{out}, is the same as in steady flow:

$$\alpha_{out} = \alpha_{out}\Big|_{steady} \tag{4b}$$

In general, the steady-state pressure rise and outlet flow angle for each blade row are functions of the inlet angle and flow coefficient.

For a rotor row the time rate of change for the inertia term must be evaluated in the relative frame, that is:

$$\frac{\partial}{\partial \tau^{rel}} = \frac{\partial}{\partial \tau} + \frac{\partial}{\partial \theta}$$

Hence for nonuniform and nonsteady flow through a rotor:

$$\frac{P_{out} - P_{in}}{\rho U^2} = \frac{P_{out} - P_{in}}{\rho U^2}\Big|_{steady} - \Lambda_{row}\left(\frac{\partial \phi}{\partial \tau} + \frac{\partial \phi}{\partial \theta}\right) \tag{5a}$$

and

$$\alpha_{out}^{rel} = \alpha_{out}^{rel}\Big|_{steady} \tag{5b}$$

In order to proceed without introducing unwarranted complexity, it will be assumed that there is no flow field redistribution within the compressor; this is the idealized case of no axial gaps between adjacent blade rows. Consequently, the constraints of mass conservation and flow at low Mach number imply that the axial velocity[6] at each circumferential position is constant through the machine. The individual blade row pressure rises may, therefore, be combined to obtain:

$$\frac{P_2 - P_1}{\rho U^2} = \sum_{\text{all rows}} \frac{P_{out} - P_{in}}{\rho U^2}\Big|_{steady} - \lambda \frac{\partial \phi}{\partial \theta} - \mu \frac{\partial \phi}{\partial \tau} \tag{6}$$

where 1 and 2 refer, respectively, to the leading edge of the first blade row and the trailing edge of the last one. The overall inertia parameters are:

$$\lambda = \sum_{\text{rotors}} \Lambda_{row} \text{ and } \mu = \sum_{\text{all rows}} \Lambda_{row} \tag{7}$$

At each circumferential location, the summation of the individual blade row pressure rises may only be replaced by the overall static-to-static pressure rise, ψ^{ss}, evaluated at the local inlet conditions provided that the flow angles between all the blade rows correspond to those in steady uniform flow operation. The quasi-steady assumption implies that this is true, and so Eq. (6) may be rewritten:

$$\frac{P_2 - P_1}{\rho U^2} = \psi^{ss}(\phi, \alpha_1)\Big|_{steady} - \lambda \frac{\partial \phi}{\partial \theta} - \mu \frac{\partial \phi}{\partial \tau} \tag{8a}$$

where $\phi(\theta, \tau)$ and $\alpha_1(\theta, \tau)$ are the local values of the flow coefficient and inlet swirl angle at the compressor. Similarly, the compressor exit flow angle, α_2, may be written:

$$\alpha_2 = \alpha_2(\phi, \alpha_1)\Big|_{steady} \tag{8b}$$

The dependence on both ϕ and α_1 have been explicitly included to emphasize that no assumptions have been made concerning the swirl sensitivity of the compressor.

It is convenient, as was done by Hynes and Greitzer (1987) and was implicit in Moore (1984a), to express the compressor performance in terms of the total-to-static pressure rise. This is achieved by subtracting off an inlet dynamic head from both sides of Eq. (8*a*) to give:

$$\frac{P_2 - Pt_1}{\rho U^2} = \psi^{ts}(\phi, \alpha_1)\Big|_{steady} - \lambda \frac{\partial \phi}{\partial \theta} - \mu \frac{\partial \phi}{\partial \tau} \tag{8c}$$

where the total-to-static pressure rise is $\psi^{ts} = \psi^{ss} - \phi^2/(2\cos^2\alpha_1)$. The exit flow angle is, of course, still determined by Eq. (8*b*).

Simplified Behavior of Flow Field Disturbances

The quasi-steady compressor model can be used to examine the predicted behavior of nonaxisymmetric flow field disturbances within compressors. In this section it will be shown that as a consequence of the nonsteady fluid dynamics of compressor flow fields any nonaxisymmetric disturbance will be circumferentially propagated and that its amplitude may grow or decay.

The physical mechanisms that determine the circumferential propagation and growth or decay of "stall-like" phenomena will be examined and, to minimize the mathematical complexity, two simplifying assumptions concerning compressor performance will be utilized. The first one is that the compressor pressure rise does not depend upon the inlet swirl angle, eliminating α_1 from Eqs. (8*a*, *b*, *c*). This represents the idealized case of a compressor operating with perfect IGVs, ones where the flow is isentropic and the IGV exit angle is constant. The second assumption is that the compressor exit flow angle, α_2, stays constant, and would be the idealized case of high-solidity exit blading.[7] Equations (8*b*, *c*) become:

$$\frac{P_2 - Pt_1}{\rho U^2} = \psi^{ts}(\phi)\Big|_{steady} - \lambda \frac{\partial \phi}{\partial \theta} - \mu \frac{\partial \phi}{\partial \tau} \tag{9a}$$

$$\alpha_2 = \text{const} \tag{9b}$$

For the purposes of the present discussions it is sufficiently general to consider small amplitude flow field disturbances and so the equation may be linearized about a uniform axisymmetric flow to obtain:

$$\frac{\delta P_2}{\rho U^2} - \frac{\delta Pt_1}{\rho U^2} = \frac{d\psi^{ts}}{d\phi}\delta\phi - \lambda \frac{\partial}{\partial \theta}(\delta\phi) - \mu \frac{\partial}{\partial \tau}(\delta\phi) \tag{10}$$

where $\delta(\ )$ denotes the perturbed quantity. Any flow field disturbance can be expressed by a Fourier decomposition and, because of linearity, the harmonics may be considered individually. Thus the flow coefficient perturbation at the compressor may be taken as:

$$\delta\phi = \text{REAL}(a\, e^{in\theta + i\omega\tau}) \tag{11}$$

with similar expressions for other perturbed quantities. For $n \neq 0$ this represents an n-lobed harmonic wave-form that, depending on the associated value of ω, moves around the annulus at fraction $f = -\omega/n$ of rotor speed and therefore resembles a stall-like disturbance. (Although not of interest here, surgelike disturbances correspond to $n = 0$ and to study these the plenum and throttle are required.)

To solve Eq. (10), to find the value of ω required in Eq. (11), it is necessary to relate the changes in flow, $\delta\phi$, to those in exit pressure δP_2 and inlet total pressure δPt_1. For the case of constant height annular inlet and exit ducts the linearized equations of motion can be solved analytically; see Appendix A. In the inlet duct only potential flow perturbations can be created by the compressor and these decay upstream. Solving the nonsteady form of the Bernoulli equation for axial flow in the inlet duct ($\alpha_1 = 0$) gives that at the leading edge of the first blade row (Eq. (A5)):

$$\frac{\delta Pt_1}{\rho U^2} = -\frac{1}{|n|}\frac{\partial}{\partial \tau}(\delta\phi) \tag{12}$$

with δPt_1 and $\delta\phi$ each varying with time and circumferential position.

In the exit duct the only allowed disturbances are a decaying

[6] Assuming constant height compressor annulus.

[7] No assumption, other than quasi-steady and no internal flow field redistribution, has been made concerning the blade rows within the compressor.

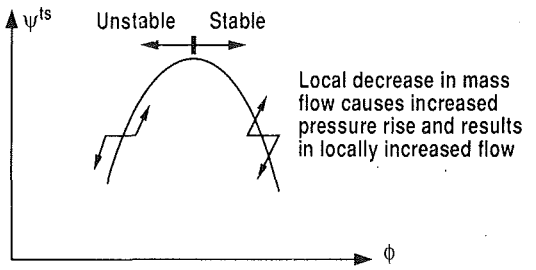

Fig. 5 Static argument showing why negative slopes are stable while positive ones are unstable

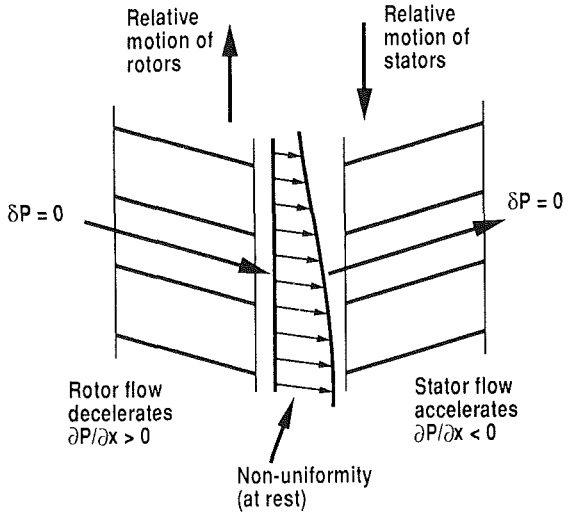

Fig. 6 Rotors and stators pass in opposite directions through a moving flow nonuniformity. The requirement to match these pressure differences determines the propagation rate.

potential field and vorticity associated with the variation in compressor loading around the annulus. For fixed compressor exit flow angle ($\delta\alpha_2 = 0$, the high-solidity assumption), Eq. (A9) gives:

$$\frac{\delta P_2}{\rho U^2} = \frac{1}{|n|}\frac{\partial}{\partial \tau}(\delta\phi) \tag{13}$$

Essentially Eqs. (12) and (13) represent the impedances of the inlet and exit flow fields (in this case it has been assumed that the ducts are long enough for the nonaxisymmetric pressure field to decay completely). Combining the above gives the differential equation that determines the time development of the small-amplitude nonaxisymmetric perturbation:

$$\left[\left(\frac{2}{|n|}+\mu\right)\frac{\partial}{\partial \tau}+\lambda\frac{\partial}{\partial \theta}\right]\delta\phi = \frac{d\psi^{ts}}{d\phi}\delta\phi \tag{14}$$

Growth or Decay. The differential operator on the left-hand side of the equation above represents the time rate of change in a frame of reference rotating around the annulus at fraction $\lambda/(2/|n|+\mu)$ of rotor speed. In this reference frame the equation becomes:

$$\left(\frac{2}{|n|}+\mu\right)\frac{\partial}{\partial \tau^{\text{ref}}}\delta\phi = \frac{d\psi^{ts}}{d\phi}\delta\phi \tag{15}$$

Solutions to the equation above are exponential growth or decay of a nonaxisymmetric disturbance depending upon the sign of $d\psi^{ts}/d\phi$. The predicted stability boundary for rotating stall is therefore at the peak of the total-to-static pressure rise characteristic, a condition first presented by Dunham (1965) through considerations of distortion transfer.

The zero slope stability boundary may be explained by a static style argument based on changes in the local mass flow and pressure rise, Fig. 5. On the negatively sloped pressure rise mass flow characteristic a local increase in mass flow causes a decrease in pressure rise. This causes the flow to decelerate, and the disturbance decays. On a positively sloped characteristic the opposite is true, and so any circumferential disturbance is amplified. Although appealing, this argument does not consider the impact of flow field dynamics, nor does it explain why it is the total-to-static characteristic that is important; this will be returned to later.

Experimental evidence to support the zero slope stability boundary is limited because of difficulties in estimating the slope of the characteristic. However, in experimental investigations where unstalled operation beyond the usual stability boundary was possible[8] (Longley and Hynes, 1990; Day, 1993b; Paduano et al., 1993; Haynes et al., 1993) the natural stability boundary was very close to the zero slope condition.

Circumferential Propagation. The derivation of the quasi-steady compressor model has assumed only that the flow disturbance has a long circumferential length scale. As a consequence of the fluid dynamics any nonaxisymmetric disturbance that is of potential form in the upstream flow field will be circumferentially propagated at a rate that depends primarily on λ and μ, the inertia parameters, and does not involve the slope of the characteristic.

The physical processes that determine circumferential propagation may thus be examined by considering the case where the slope of the total-to-static characteristic is zero. For this condition Eq. (14) may be rewritten as:

$$\left(\frac{2}{|n|}+\mu-\lambda\right)\left[\frac{\partial}{\partial \tau}\right]\delta\phi = -\lambda\left[\frac{\partial}{\partial \tau}+\frac{\partial}{\partial \theta}\right]\delta\phi \tag{16}$$

The left-hand side contains the inertia in the stationary components: inlet and exit flow fields ($2/|n|$) and the stationary blades ($\mu-\lambda$). The right-hand side contains the inertia in the rotors (λ) and the time rate of change in their frame of reference. Thus the propagation rate is set by the constraint that the inertia-induced pressure perturbations in the absolute and relative frames must balance; this was first suggested by Cumpsty and Greitzer (1982).

When viewed in the frame of reference of the flow nonuniformity, the rotors and stators pass in opposite directions, Fig. 6. As drawn, the flow in the rotor passages experiences a deceleration associated with the velocity nonuniformity so there must be an inertia-driven pressure increase across the blade row in addition to the pressure rise due to flow turning. In the stators (and the inlet and exit flow fields) the flow accelerates and so a decreasing axial pressure gradient is required. Thus it is possible for there to be a circumferential pressure nonuniformity within the compressor, which must accompany the velocity nonuniformity, while still satisfying no pressure perturbation far upstream or downstream.

Increasing the propagation rate (which is always less than rotor speed) reduces the rotor inertia effect while increasing the stator one, and the rotation rate of the nonuniformity is that which will balance the pressure fields. If inertia is the sole mechanism, then stall-cell propagation rates must be between zero and rotor speed since the time rate of change must be opposite for the rotors and stators.

Evidence to support the importance[9] of inertia in determining circumferential propagation speeds is provided by studies of fully developed rotating stall. Cumpsty and Greitzer (1982) examined compressor performance at the trailing edge of a fully developed rotating stall cell and, as confirmation that the inertia-driven nonsteady pressure fields must be matched, pre-

[8]These were achieved by some form of active or passive flow field stabilization.

[9]Later it will be shown that nonsteady blade row performance can also have a significant effect.

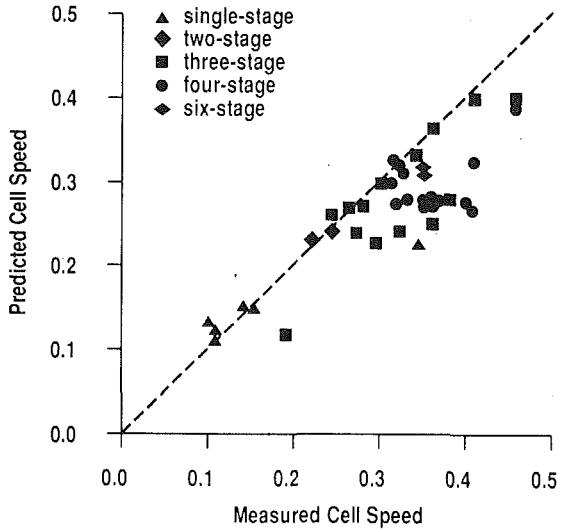

Fig. 7 Comparison between predicted, based on inertia, and measured stall cell speeds (Cumpsty and Greitzer, 1982)

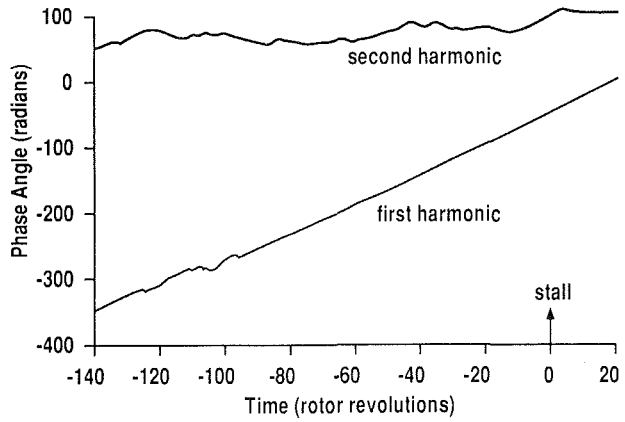

Fig. 8 Time history of the phase of the first and second circumferential harmonics measured upstream of a compressor (Garnier et al., 1991)

dicted stall cell speeds, Fig. 7. The predicted stall cell speeds are generally lower than the measured ones and this suggests that other phenomena may be important.

Moore (1984a) examined the theoretical basis for rotating stall, using ideas similar to those above, and developed the essential form of the quasi-steady compressor model. He showed that the model exhibited both small and large-amplitude stall-like phenomena and that it could correlate stall cell speeds.

Verification of the existence of small-amplitude circumferentially propagating wavelike disturbances comes from examining the behavior of flow field disturbances at operating points close to the compressor stability boundary. McDougall et al. (1990) were first in presenting the Fourier decomposition of velocity measurements, from an array of six equally spaced transduces upstream of a single-stage compressor, that showed the growth and decay of propagating disturbances with amplitude approximately 1/2 to 1 percent of mean flow velocity. Garnier et al. (1991) obtained similar results upstream of a three-stage compressor, Fig. 8. The first mode was well defined for approximately 100 rotor revolutions prior to stall, while the second mode showed no conclusive propagating disturbances (attributed to signal-to-noise limitations).

Alternate Approaches. An important consideration in the modeling of compressors is the calculation of the impedances for the inlet and exit flow fields. In the above the impedances,

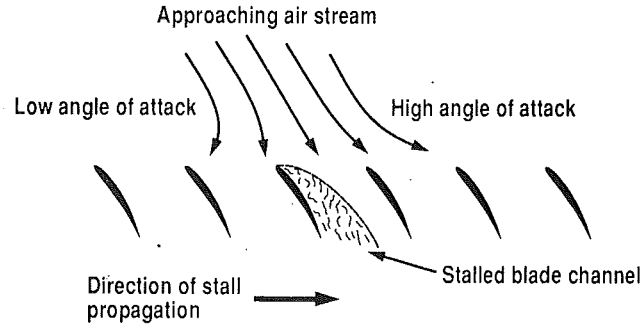

Fig. 9 Stall propagation mechanism pictured as upstream redistribution associated with blockage within blade passages (Iura and Rannie, 1954)

Eqs. (12) and (13), were obtained by solving the linearized equations of motion for flow in a constant height annular duct. Historically several alternate approaches have been taken in evaluating these impedances.

Emmons et al. (1955) analyzed disturbances in an isolated cascade and assumed that there would be no static pressure perturbation in the exit flow field. The effect of this assumption is to change the inertia of the absolute flow field and so a different propagation rate is predicted. The conditions under which the exit static pressure would be uniform in a constant height duct were examined by Greitzer (1976c), and are that the nonuniformity must be stationary in the frame of reference of the high-solidity exit blade row (see Eq. (A9)).

Moore (1984a) took a slightly different approach for solving the flow fields by introducing an empirical relationship between the axial and tangential velocity perturbations. The relationship matches the one derived above for the lowest circumferential harmonic, which is usually the most important in fully developed rotating stall. The effect of this is to modify the propagation rate for the higher modes slightly. Moore also introduced an impedance scale factor, usually called "m," that would allow for a sudden expansion in duct height as might be the case of a large dump diffuser immediately downstream of the compressor.

Variations in Inlet and Exit Swirl

The simplified examination of the quasi-steady compressor model suggests that the propagation rate is set only by considerations of fluid inertia. This is contrary to the classical explanation for stall-cell propagation proposed by Iura and Rannie (1954) and Emmons et al. (1955), Fig. 9. They argued that it was the upstream flow field redistribution caused by increased blockage within a blade passage that was important. In this section the simplifying assumptions of perfect IGVs (isentropic, fixed exit angle) and high-solidity compressor exit blades will be relaxed so that both the effects of fluid inertia and changes in incidence can be assessed.

In the inlet flow field the disturbances are of a potential form and so any axial velocity perturbation, $\delta\phi$, has associated with it both tangential velocity (in quadrature) and angle changes. These changes of flow coefficient and inlet angle not only affect the pressure rise, $\psi^{ts}(\phi, \alpha_1)$, but also the compressor exit flow angle $\alpha_2(\phi, \alpha_1)$. For this most general interaction between the compressor model[10] and the inlet and exit flow fields the equation (derived in Appendix B) that determines the behavior of small-amplitude disturbances is:

$$\left[\left(\frac{2}{|n|}+\mu\right)\frac{\partial}{\partial\tau}+R\,\frac{\partial}{\partial\theta}\right]\delta\phi = S\delta\phi \qquad (17a)$$

The rotation term is:

[10]The blades are still assumed to respond quasi-steadily and there is no internal flow field redistribution.

Table 1 Parameters at design for the hypothetical single-stage and four-stage compressors used in the illustrative examples

Flow Coefficient	0.60
Stage Loading ($\Delta ht/U^2$)	0.4
Reaction	60%
Inlet Flow Angle (α_1)	18.43°
Rotor Inlet Angle (α_1^{rel})	-53.13°
Rotor Exit Air Angle (α_2^{rel})	-33.69°
Stator Inlet Angle (α_2)	45.00°
Stator exit Air Angle (α_3)	18.43°
Inertia Parameter (Λ per row)	0.2

$$R = \lambda - \frac{\partial \psi^{ts}}{\partial \alpha_1}\frac{\cos^2 \alpha_1}{\phi |n|} + \frac{\phi}{|n|}\sec^2 \alpha_2 \left(\sin \alpha_1 \cos \alpha_1 \frac{\partial \alpha_2}{\partial \alpha_1} - \phi \frac{\partial \alpha_2}{\partial \phi} \right) \quad (17b)$$

and the modified slope of the total-to-static pressure rise characteristic is:

$$S = \frac{\partial \psi^{ts}}{\partial \phi} - \frac{\partial \psi^{ts}}{\partial \alpha_1}\frac{\sin \alpha_1 \cos \alpha_1}{\phi} - \phi \frac{\partial \alpha_2}{\partial \alpha_1}\frac{\cos^2 \alpha_1}{\cos^2 \alpha_2} \quad (17c)$$

Equation (17*a*) is of the same form as that derived earlier, Eq. (14), and so the qualitative behavior of flow field disturbances is unchanged though propagation speed and growth rate will be altered.

Whether growth or decay of a disturbance occur is determined by $S/(2/|n| + \mu)$, where S many be thought of as the effective slope of the total-to-static characteristic. The stability boundary is no longer at zero slope on the total-to-static pressure rise characteristic; it is however still the same for all circumferential harmonics. The rate of propagation is now determined by $R/(2/|n| + \mu)$ and depends on both inertia and swirl sensitivity. The propagation mechanism is, however, still one of balancing pressure perturbations that now have two causes. The inertia term generates a pressure perturbation corresponding to the velocity change, while swirl sensitivity has a similar effect as it creates a pressure perturbation associated with the incidence change.

Example of Swirl Sensitivity. As modeled above the blade passage fluid inertia is an easily defined quantity while those of swirl sensitivity and the slope of the pressure rise characteristic depend strongly on the compressor design. For instance, compressors with high-solidity IGVs are usually regarded as insensitive to small variations[11] of inlet swirl. The exact shape of the total-to-static pressure rise characteristic depends on the values of the blade row deviation and total pressure losses (increasing deviation and loss make the slope of the characteristic become more positive) and these are influenced by blade design. In this section a hypothetical compressor design will be used to demonstrate the probable sizes of these effects.

For the present purposes only a representative compressor is required, and so it is sufficient to use a simple empirical correlation (Howell, 1965) to determine the variations in blade loss coefficient and exit deviation. The compressor stage design parameters are listed in Table 1 and the inertia parameter was set at $\Lambda = 0.2$ per row, in accordance with the earlier discussion. Both a single-stage and four-stage configuration will be examined, and their predicted pressure rise characteristics are shown in Fig. 10; note the difference in slopes between the total-to-static and static-to-static curves.

The stability boundary and the circumferential propagation rate are calculated for four configurations of each compressor. The reference case is with perfect IGVs and high-solidity exit blading (the propagation rate is therefore given by Eq. (14)) and the other cases correspond to relaxing either or both of these constraints. When the perfect IGVs are removed (so there is no upstream blade row) the bulk inlet swirl of the flow is changed to the value that was produced at the exit of the IGVs. The rotor blades, therefore, operate with the same mean incidence and the comparison is an assessment of the effects of flow field redistribution rather than changes due to modified preswirl. Without the high-solidity exit constraint, the compressor exit angle is taken to be the air outlet angle of the last blade row.[12]

For the single-stage compressor the calculated propagation rate and the slope of the total-to-static characteristic at the stability boundary are shown in Fig. 11. Removing the perfect

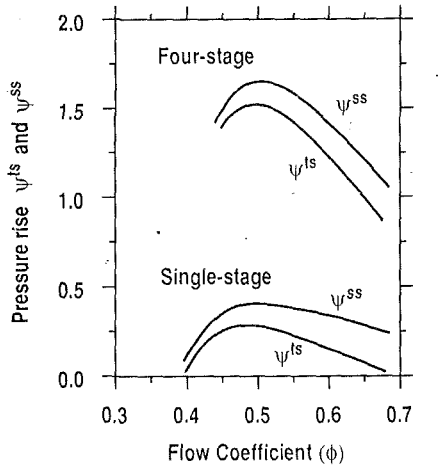

Fig. 10 Pressure rise characteristics for the hypothetical single-stage and four-stage compressors

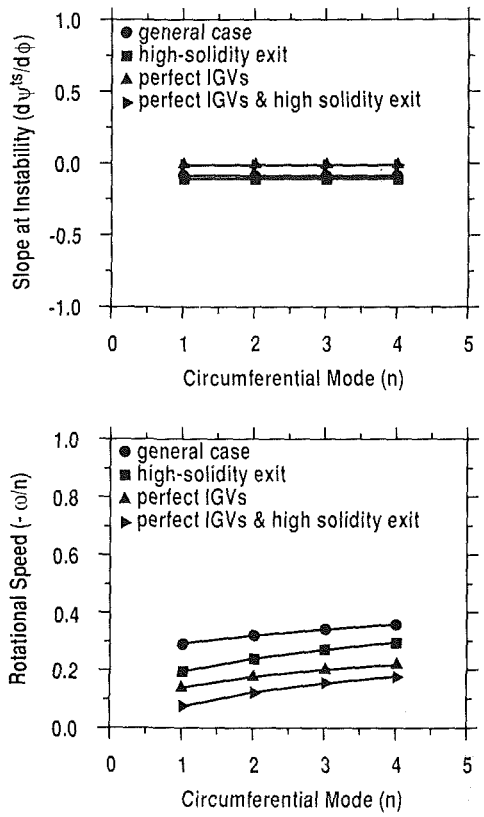

Fig. 11 Effects of swirl sensitivity for the hypothetical single-stage compressor

[11]For large-amplitude flow disturbances, such as inlet distortion and fully developed rotating stall, a circumferential portion of the IGVs can have separated flow and result in high loss and exit angle deviation.

[12]The small change in exit angle has only a minor effect on the pressure rise characteristic because the flow is normally near axial.

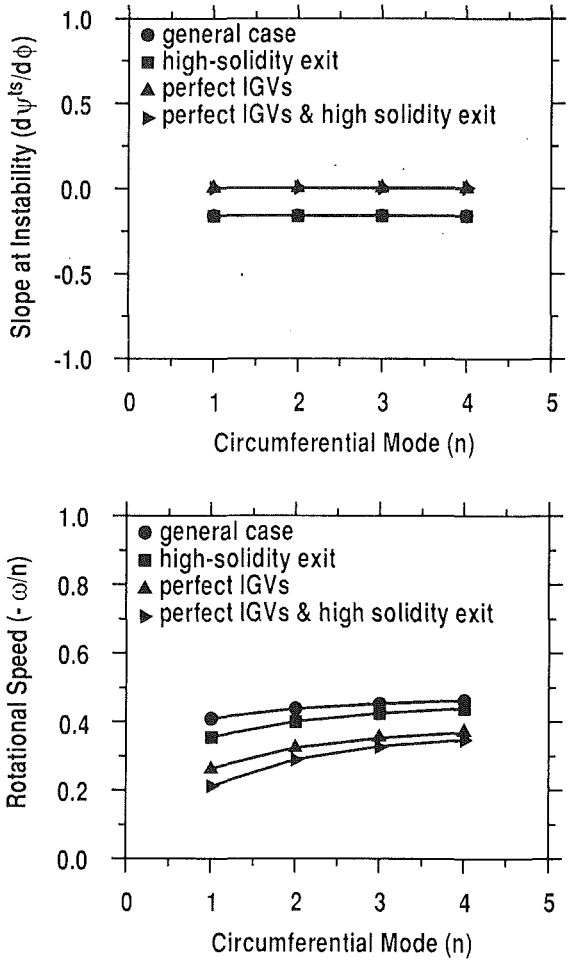

Fig. 12 Effect of swirl sensitivity for the hypothetical four-stage compressor

IGVs increases the predicted propagation rate. For this hypothetical compressor, as with many others, increasing the inlet swirl angle decreases the flow turning through the rotor and thereby produces a reduced pressure rise ($\partial\psi^{ts}/\partial\alpha_1 < 0$). This relationship between the pressure rise change and the flow angle perturbation causes an increase in the propagation rate (positive term in Eq. (17*b*)) and also a marginally decreased stability of the flow field (positive term in Eq. (17*c*)). This is confirmed by the negative slope of the total-to-static characteristic at instability and corresponds to approximately a 1 percent increase in flow coefficient for the characteristics of Fig. 10.

Relaxing the high solidity exit blading constraint similarly increases the propagation rate (through the $\partial\psi^{ts}/\partial\phi$ term) but has very little effect on the stability boundary because, for this compressor, $\partial\alpha_2/\partial\alpha_1 \approx 0.06$, which is small compared to the other terms.

To investigate whether these effects are important in multistage compressors, a similar study for a four-stage configuration is shown in Fig. 12. The results are comparable, the first mode propagation rate is approximately doubled and the stability boundary is at an increased flow coefficient of 1/2 percent.

Enhanced Compressor Model

The quasi-steady compressor model has been examined both with simplifying assumptions concerning the flow field interaction (perfect IGVs and high-solidity exit blading) and also in its most general form. For the first four circumferential modes the predicted propagation rates varied substantially between the different configurations, there was no preferential circumferential length scale[13] and the stability boundary was always near the peak of the total-to-static characteristic.

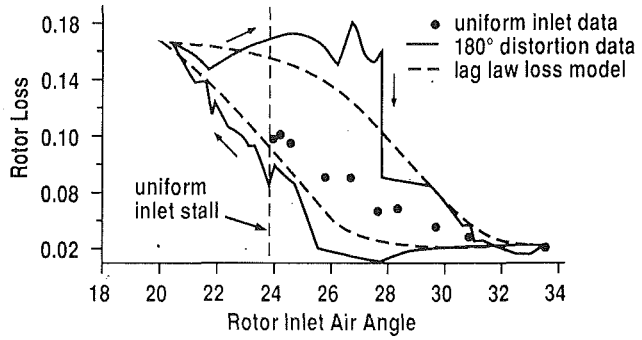

Fig. 13 Comparison of steady and nonsteady operation on pressure loss as a function of incidence. Also shown is the lag law prediction (Mazzawy, 1977).

The quasi-study assumption relies on the flow field disturbances being long length scale, and therefore low reduced frequency. However, the higher the circumferential harmonic, the more likely it is that the blade pressure losses and exit deviation will respond nonsteadily. An enhanced compressor model will now be examined that incorporates some account of these nonsteady flow effects and accounts for axial gaps between adjacent blade rows.

Nonsteady Loss and Deviation. The steady-state pressure rise across a blade row can be written as:

$$\left.\frac{P_{\text{out}} - P_{\text{in}}}{\rho U^2}\right|_{\text{steady}} = \frac{1}{2}\phi^2(\tan^2\alpha_{\text{in}} - \tan^2\alpha_{\text{out steady}}) - \text{LOSS}_{\text{steady}} \quad (18a)$$

where

$$\text{LOSS}_{\text{steady}} = \frac{Pt_{\text{in}} - Pt_{\text{out}}}{\rho U^2} \quad (18b)$$

and all quantities are in the frame of reference of the blade. An approach for modeling the nonsteady response of a blade row is to apply a time lag to the loss and deviation. (This lag law was originally used by Emmons et al., 1955, to predict the time rate of change of flow area.) Thus the static pressure rise across a blade row in nonuniform nonsteady flow may be modeled by:

$$\frac{P_{\text{out}} - P_{\text{in}}}{\rho U^2} = \frac{1}{2}\phi^2(\tan^2\alpha_{\text{in}} - \tan^2\alpha_{\text{out}}) - \text{LOSS} \quad (19a)$$

with

$$\tau_{\text{loss}}\frac{\partial}{\partial\tau}\text{LOSS} = \text{LOSS}_{\text{steady}} - \text{LOSS} \quad (19b)$$

and

$$\tau_{\text{dev}}\frac{\partial}{\partial\tau}\alpha_{\text{out}} = \alpha_{\text{out steady}} - \alpha_{\text{out}} \quad (19c)$$

All quantities are evaluated in the frame of reference of the blade row in question. Equations (19*b*, *c*) have the effect of reducing the amplitude of response compared to the case with no time lags.

Values for the time constants, τ_{loss} and τ_{dev}, are chosen based on consideration of the response time of the blade boundary layers. Assuming that the boundary layers adjust as soon as the disturbance passes through the blade row, then the time constant is expected to be of the order of the blade passage convection time, i.e.:

[13]The stability boundary is independent of the mode number.

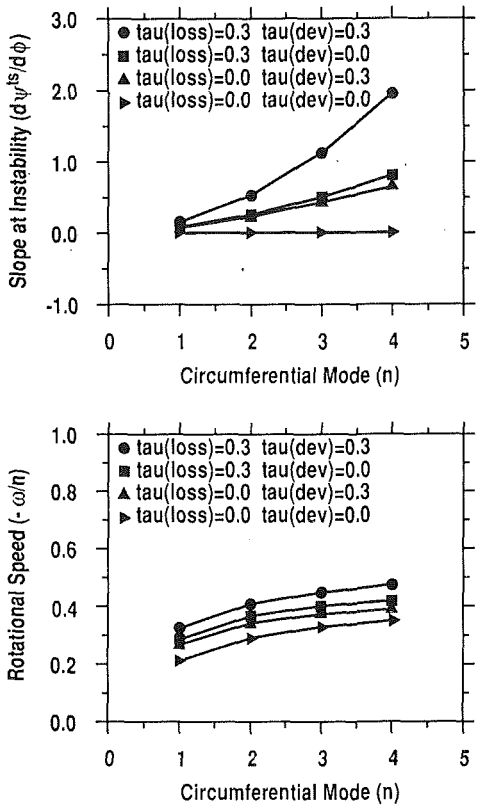

Fig. 14 Effects of pressure loss and deviation time lags on the hypothetical four-stage compressor (with perfect IGVs and high-solidity exit blading)

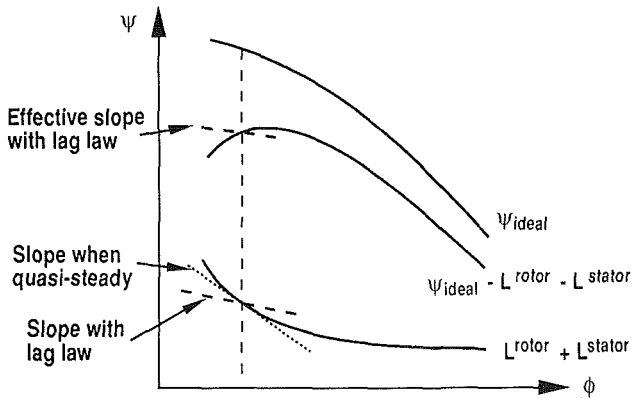

Fig. 15 Lag law reduces the effect of the pressure losses and thereby makes the effective slope of the characteristic more negative (stable)

$$\tau_{\text{loss}} = \tau_{\text{dev}} = \frac{c_x}{r}\frac{1}{\phi} \tag{20}$$

Some investigations into these lag laws for nonsteady blade row performance have been undertaken for disturbances of large amplitude. Nagano et al. (1971) experimentally studied the variation of blade loss and deviation for a compressor operating in rotating stall. They concluded that while the pressure loss time lag (τ_{loss}) was approximately the convection time, the deviation time lag (τ_{dev}) varied across the range of zero to three times convection time.

Mazzawy (1977) developed the multiple segment parallel compressor model and included a pressure loss time lag. The justification for doing so was experimental measurements of rotor loss as a function of incidence both in steady and nonsteady (nonuniform) flow; these are shown in Fig. 13 along with the variation predicted using the lag law (Eq. (19)). The validity of this time lag model for small amplitude disturbances is inferred by the comparison of Haynes et al. (1994) shown later.

Example of Time Lags. The effects of pressure loss and blade deviation time lags are compared using the hypothetical four-stage compressor in the configuration with perfect IGVs and high-solidity exit blading as the reference case. The time lag was set approximately equal to the convection time, so $\tau_{\text{loss}} = \tau_{\text{dev}} = 0.3$ (assuming $c_x/r \approx 0.15$ and $\phi \approx 0.5$). For the cases with and without time lags, the propagation rate and slope of the characteristic at the stability boundary are shown in Fig. 14. Both pressure loss and deviation time lags increase the propagation rate and stabilize the higher modes, with their combined effect being approximately the sum of the individual ones.

The higher the mode the greater the stabilizing effect of nonsteady blade row response, as indicated by a more positive slope of the total-to-static characteristic. This ordering is consistent with the higher modes having higher reduced frequency. This separation of the individual mode stability boundaries was first suggested by Stenning and Kriebel (1958) and experimentally verified by Haynes et al. (1994).

The increased propagation rate may be explained by interpreting the reduced amplitude of response due to time lag as, in some sense (see later section), a larger blade passage fluid inertia and thereby increasing the speed. The reduction in the amplitude of the total pressure loss perturbation has the effect of making the time-averaged characteristic more negatively sloped, Fig. 15, and hence more stable (deviation time lag has a similar effect).

Example of Blade Row Gaps. In all of the models described above it has been assumed that there is no internal flow field redistribution, i.e., $\delta\phi_1 = \delta\phi_2$. This can only ever be an approximation as there must be some clearance between adjacent blade rows. The larger the gaps the less the coupling (nonaxisymmetric and nonsteady flow field interaction) between the stages; see Turner (1959), Ham and Williams (1983), and Longley and Hynes (1990).

The presence of gaps has several effects: First, internal circumferential flow redistribution changes both the amplitude of the perturbation through the compressor and the incidences on the blade rows within the compressor (Longley, 1990). Second, the interaction pressure fields between adjacent components can decay resulting in an effective "decoupling" of the compressor blade rows. This can affect the stability of the system in either a beneficial or detrimental way (see Longley and Hynes).

Conceptually, including the effects of gaps into a compressor model is straightforward. Each gap between the blade rows is considered as an annular volume and the equations of motion linearized to obtain solutions, similar to what was done in the inlet and exit ducts. Within each gap there are three unknowns corresponding to the vortical perturbation and the two potential perturbations (upstream and downstream decaying pressure fields). There are three boundary conditions specified at the upstream end of the gap, namely matching the flow angle, mass flow, and pressure perturbations, and so the unknowns may be found. The implementation of the model, however, becomes more complicated than the preceding compact models, e.g., Eq. (9), as each blade row and gap must be explicitly analyzed.

For the four-stage compressor, with perfect IGVs and high-solidity exit blading, the effect of gaps of length $x/r = 0.05$ ($c_x/r \approx 0.15$) are shown in Fig. 16. The propagation rate is slightly increased and the individual modes have different stability boundaries. The gaps appear longer for the higher modes and therefore the compressor behaves more like four individual compressor stages. An individual stage has its total-to-static

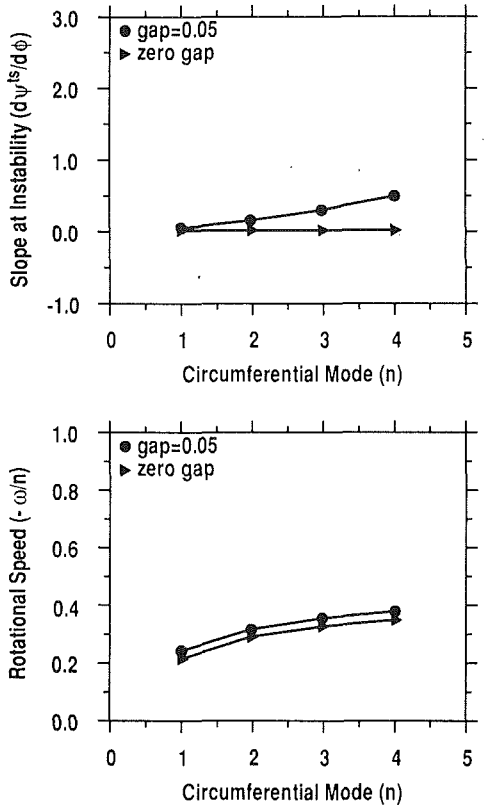

Fig. 16 Effect of inter-blade-row gaps on the hypothetical four-stage compressor (perfect IGVs and high-solidity exit blading)

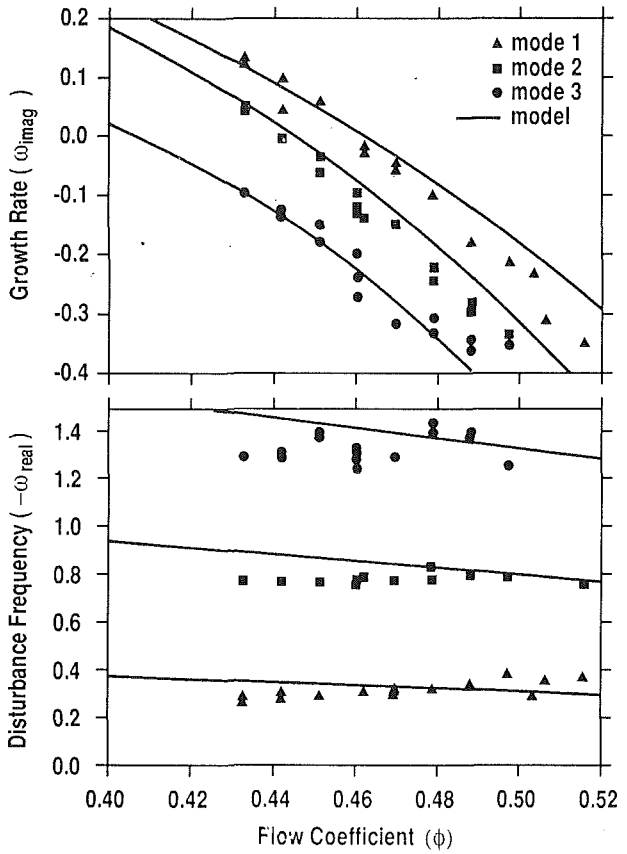

Fig. 17 Comparison of measured and calculated, with lagged pressure losses, frequency and growth rate for a compressor (Haynes et al., 1993)

pressure rise peak at a lower flow than the overall compressor (assuming identical stages) and therefore the decoupling stabilizes the higher modes.

Simplified Forms of Compressor Model

The inclusion of time lags and inter-blade-row gaps increases the complexity of the model and it becomes both computationally expensive and requires extensive information about the individual compressor blade rows. In many instances this information is either not available or the application does not warrant such effort. Therefore, approximate methods have been developed that include some of the advantages of the enhanced model.

Lagged Losses and Quasi-Steady Deviation. When both pressures and flow angles differ from their steady-state values, an explicit row-by-row analysis is required. If, however, only the total pressure losses are lagged, i.e., $\tau_{dev} = 0$, then all flow angles are quasi-steady and the individual blade rows can be recombined (see Chue et al., 1989, and Hendricks and Gysling, 1992) to give:

$$\frac{P_2 - P_1}{\rho U^2} = \psi^{ss}_{ideal} - L^{rotor} - L^{stator} - \lambda \frac{\partial \phi}{\partial \theta} - \mu \frac{\partial \phi}{\partial \tau} \qquad (21a)$$

$$\alpha_2 = \alpha_2(\phi, \alpha_1)|_{steady} \qquad (21b)$$

with

$$\tau_{loss} \frac{\partial}{\partial \tau} L^{stator} = L^{stator}_{steady} - L^{stator} \qquad (21c)$$

and

$$\tau_{loss} \left(\frac{\partial}{\partial \tau} + \frac{\partial}{\partial \theta} \right) L^{rotor} = L^{rotor}_{steady} - L^{rotor} \qquad (21d)$$

In the above ψ^{ss}_{ideal} represents the ideal (isentropic) pressure rise due to flow turning (first part on right-hand side of Eq. (18)) and L^{rotor}, L^{stator} are the overall total pressure losses for the rotors and stators, respectively ($\psi^{ss} = \psi^{ss}_{ideal} - L^{rotor}_{steady} - L^{stator}_{steady}$).

A comparison between the calculated and measured propagation and growth rates for small-amplitude flow field disturbances was undertaken by Haynes et al. (1993) for a three-stage compressor that appeared to have little unsteady deviation effect, Fig. 17. The calculations were based upon decomposing the measured pressure rise performance, ψ^{ss}, into the ideal pressure rise and loss terms and then solving the set of Eqs. (21). The experimental measurements were obtained by actively controlling the compressor and extracting the flow field dynamics from the controlled system. The comparisons indicate that with an appropriate choice of the time constant (1.5 × convection time) the growth rates and propagation speeds for the first three modes were well predicted across a range of flow coefficients.

Effective Inertia Parameters. As mentioned above one interpretation of the effects of time lags is to increase the blade passage fluid inertia. In this section approximate relationships are derived that determine the modified, or effective, inertia parameters.

For the case of quasi-steady exit angles but time lagged pressure losses Eq. (21*c*) can be rearranged as:

$$L^{stator} = \frac{L^{stator}_{steady}}{1 + \tau_{loss} \frac{\partial}{\partial \tau}}$$

For a single temporal frequency and small values of τ_{loss} this can be approximated for the stator by:

$$L^{stator} = L^{stator}_{steady} - \tau_{loss} \frac{\partial}{\partial \phi} L^{stator}_{steady} \frac{\partial \phi}{\partial \tau}$$

and for the rotor by:

$$L^{\text{rotor}} = L^{\text{rotor}}_{\text{steady}} - \tau_{\text{loss}} \frac{\partial}{\partial \phi} L^{\text{rotor}}_{\text{steady}} \left(\frac{\partial \phi}{\partial \tau} + \frac{\partial \phi}{\partial \theta} \right)$$

Substituting these into Eq. (21*a*) and rearranging gives:

$$\frac{P_2 - P_1}{\rho U^2} = \psi^{ss} - \lambda_{\text{eff}} \frac{\partial \phi}{\partial \theta} - \mu_{\text{eff}} \frac{\partial \phi}{\partial \tau} \tag{22a}$$

where

$$\lambda_{\text{eff}} = \lambda - \tau_{\text{loss}} \frac{\partial}{\partial \phi} L^{\text{rotor}}_{\text{steady}} \tag{22b}$$

and

$$\mu_{\text{eff}} = \mu - \tau_{\text{loss}} \frac{\partial}{\partial \phi} (L^{\text{rotor}}_{\text{steady}} + L^{\text{stator}}_{\text{steady}}) \tag{22c}$$

These effective inertia parameters were first presented by Chue et al. (1989).

Following a similar approach, Strang (1991) suggested that the effects of time lags on blade deviation could be approximated by:

$$\lambda_{\text{eff}} = \lambda - \tau_{\text{dev}} \sum_{\text{rotors}} \phi^2 \frac{\sin \alpha_{\text{out}}}{\cos^3 \alpha_{\text{out}}} \frac{\partial \alpha_{\text{out}}}{\partial \phi} \tag{23a}$$

$$\mu_{\text{eff}} = \mu - \tau_{\text{dev}} \sum_{\text{all rows}} \phi^2 \frac{\sin \alpha_{\text{out}}}{\cos^3 \alpha_{\text{out}}} \frac{\partial \alpha_{\text{out}}}{\partial \phi} \tag{23b}$$

The assumption made in deriving the above is that the change in flow angle due to time lag affects only the pressure rise in that blade row and not any of the downstream ones.

In both of these approximations modifying the values of the inertia parameters to λ_{eff} and μ_{eff} yields a model of identical structure to the quasi-steady one. Therefore the only differences will be modified propagation and amplitude of the growth rates but no preferential circumferential length scale (all the modes will share the same stability boundary near the peak of the total-to-static characteristic).

Discussion

Compressors are predicted to behave like circumferential wave propagators for the time development of nonaxisymmetric (stall-like) disturbances. This is in contrast to the oscillatory nature associated with axisymmetric surgelike phenomena within compression systems. The circumferential propagation rate is determined by the requirement to balance the nonsteady pressure perturbations across the moving and stationary blade rows with those in the inlet and exit flow fields.

The mechanisms that drive these pressure perturbations are the inertia of the fluid within the flow field, the effects of incidence on the blade row pressure rise, and nonsteady viscous effects. The inertia effect will always be present while the incidence and viscous effects will, to some extent, depend on the blade design. In the examples shown the propagation rate can be approximately doubled depending upon how the blade rows are modeled.

The growth or decay of circumferentially propagating flow field disturbances is related to the slope of the total-to-static pressure rise characteristic, the swirl sensitivity of the compressor, and the nonsteady blade row response. For the first circumferential mode the predicted stability boundary is close to the peak of the total-to-static characteristic and has little dependence on nonsteady flow effects. In the examples included, the nonsteady blade response has a stabilizing influence on the higher modes and therefore only the low-order circumferential modes are expected to be detected prior to instability.

Velocity and Pressure Perturbations. In this review much has been made of the relationships between velocity and pressure perturbations, and the different types will now be summarized. Whenever the pressure perturbation is determined by the time derivative of the absolute axial velocity perturbation, e.g., Eq. (13), the quantity is inertial and affects the amount of the compressor flow field that the other forces (propagation and growth or decay) must drive.

If the relationship is a simple proportionality, e.g., $\delta P = c\delta\phi$, then it affects the stability of the flow field, with a destabilizing effect if they are in-phase ($c > 0$) and stabilizing effect when they are in anti-phase ($c < 0$). (This is essentially the argument used for positive slopes being unstable while negative ones are stable.) Whenever pressure and velocity are in quadrature, e.g., $\delta P = \partial/\partial\theta\delta\phi$, the effect is to propagate the disturbance circumferentially. An example of this latter effect is the acceleration of the fluid in a rotor blade passage when it passes through a spatial flow nonuniformity.

These ideas concerning velocity and pressure relationships will now be used to demonstrate that some physical mechanisms, in this case inlet swirl sensitivity, may affect both propagation and stability depending on the compressor design.

In the inlet flow field the disturbance is of potential form and so the axial and tangential velocity perturbations are in quadrature. For small values of mean inlet swirl angle, the inlet angle perturbation ($\delta\alpha_1$) is determined by the tangential velocity change and is therefore in quadrature with the axial velocity. For this case, the pressure rise perturbation associated with $\delta\alpha_1$ will affect the propagation rate. For compressors with large values of inlet swirl, the angle perturbation will be primarily associated with the axial velocity change. Therefore the swirl sensitivity pressure perturbation will be in-phase or antiphase with the velocity change and consequently will affect the stability.

This dual effect of swirl sensitivity is confirmed by both Eqs. (17*b*), propagation rate, and (17*c*), growth or decay, having a $\partial\psi^{ts}/\partial\alpha_1$ term with a coefficient depending on the size of α_1.

Stability Argument. Gysling (1992) examined compressor stability in terms of the net mechanical energy input into the flow field. A compressor puts energy into a nonaxisymmetric flow field disturbance whenever the total-to-total characteristic has a positive slope ($\partial\psi^{tt}/\partial\phi > 0$). Mechanical energy can escape since some of it is convected away by the nonsteady vortical disturbance in the exit flow field, and instability will only therefore occur when the compressor puts in more energy than can be convected away (or dissipated in losses). In rough terms, the vortical field carries energy at a rate ϕ, the convection speed, and so instability occurs approximately when:

$$\frac{d\psi^{tt}}{d\phi} \approx \phi$$

or equivalently, since $\psi^{tt} \approx \psi^{ts} + 1/2\phi^2$, when:

$$\frac{d\psi^{ts}}{d\phi} \approx 0$$

This is the zero slope of the total-to-static pressure rise characteristic condition that was deduced from Eq. (14) and observed in the later studies of low-order modes in the hypothetical compressor.

Relaxing the high-solidity exit blading constraint can change (depending on the size of $\partial\alpha_2/\partial\alpha_1$) the balance between the decaying potential field (which carries no net energy) and the shed vorticity, thus affecting the stability boundary. It is not yet known whether this could be a feasible approach to active control, which as implemented by Paduano et al. (1993) and Haynes et al. (1994) has only used $\partial\psi^{ts}/\partial\alpha_1$ in Eq. (17*c*).

Other Flow Perturbations. The stability of the flow field

has been considered by analyzing two-dimensional (stall-like) disturbances that have a long circumferential length scale. However, flow field stability requires that all types of flow disturbances be stable. It can be shown (for instance, see Hynes and Greitzer, 1987) that one-dimensional (surgelike) disturbances go unstable at points on the positively sloped part of the total-to-static characteristic. This would suggest that stall-like disturbances are expected to grow prior to surge, and this has been observed (see Day, 1993b).

Other types of flow field disturbances that have not yet received extensive modeling are short length scale (similar to blade pitch) two-dimensional and three-dimensional (with radial variation of flow properties) ones. If any of these become unstable before long length scale two-dimensional ones then the compressor will have a different stability boundary.

Day (1993a) exhibited results that show rotating stall developing from a "spike" or "pip" (three-dimensional and short circumferential length scale) in some cases while from a "modal-wave" (two-dimensional) in others. These short length scale disturbances are observed to propagate at approximately 75 percent of rotor speed (much faster than long length scale two-dimensional ones) and it is not yet known what mechanisms determine their behavior.

Other Effects. Emmons et al. (1955) observed that the propagation rates for linearized disturbances have a weak dependence on the spatial mode; see Eq. (14). They argued that the propagation rate for fully developed rotating stall must be set by nonlinear effects as more than one spatial harmonic is involved.

Although examined in terms of small amplitude disturbances, the models described above have been successfully used to study nonlinear phenomena, i.e., ones with large amplitude flow disturbances (see Moore, 1984b, c; Hynes and Greitzer, 1987). Longley (1990) experimentally verified that the nonlinear flow field redistribution associated with inlet distortion could be adequately simulated using the quasi-steady model. Longley also identified the circumferentially propagating, growing, and decaying waves that had been predicted by Hynes and Greitzer.

The effects of compressibility have not been investigated in this review. However, the fluid dynamic phenomena (inertia and nonsteady response) that these models simulate are not restricted to low Mach number flows, though their implementation will differ. Consequently compressible versions of these models have been developed (LINEARB, 1980; Kodama, 1986; Bonnaure, 1991), though verification of their predictions is harder. Compressibility only introduces additional physical phenomena at high Mach numbers (shocks and choking), and these have been discussed by Mazzawy (1980) and modeled by Cargill and Freeman (1991).

Conclusions

Important contributions toward understanding the behavior of flow field disturbances can be made by examining the models for nonsteady flow within compressors. These models have also been successfully used to calculate the time development of flow field disturbances though, as shown by the included examples, the propagation rate depends strongly on the assumptions made within the model. The calculated stability boundary for the first mode is, however, always near the peak of the total-to-static characteristic, while for higher circumferential modes the nonsteady blade row response can have a substantial stabilizing effect.

The final choice of compressor model depends upon the amount of information that is available, though it appears that nonsteady blade row response must be modeled for quantitative comparisons.

Experimentally it has been observed that rotating stall can result from a short length scale three-dimensional disturbance and these types of phenomena are not addressed by the models described above. Areas where further research could be beneficial are the modeling of nonsteady blade row response to moderate reduced frequency disturbances and the modeling of three-dimensional flow phenomena.

Acknowledgments

The author is greatly indebted to Dr. T. P. Hynes and Prof. E. M. Greitzer for the innumerable discussions on all aspects of compressor performance. The encouragement of Prof. N. A. Cumpsty and Prof. A. H. Epstein in preparing this review is also acknowledged. Finally, sincere thanks must go to the staff and students of various research establishments for their many questions concerning compressor modeling and to Dr. I. J. Day for his valuable comments on an early form of this paper.

References

Bloch, G. S., and O'Brien, W. F., 1992, "A Wide-Range Axial-Flow Compressor Stage Performance Model," ASME Paper No. 92-GT-58.

Bonnaure, L. P., 1991, "Modelling High Speed Multistage Compressor Stability," M.S. Thesis, Department of Aeronautics and Astronautics, MIT, Cambridge, MA.

Cargill, A. M., and Freeman, C., 1991, "High-Speed Compressor Surge With Application to Active Control," ASME JOURNAL OF TURBOMACHINERY, Vol. 113, pp. 303–311.

Chue, R., Hynes, T. P., Greitzer, E. M., Tan, C. S., and Longley, J. P. 1989, "Calculations of Inlet Distortion Induced Compressor Flowfield Instability," *Int. J. Heat Fluid Flow*, Vol. 10, No. 3, Sept.

Cumpsty, N. A., and Greitzer, E. M., 1982, "A Simple Model for Compressor Stall Cell Propagation," ASME *Journal of Engineering for Power*, Vol. 104, pp. 170–176.

Day, I. J., 1993a, "Stall Inception in Axial Flow Compressors," ASME JOURNAL OF TURBOMACHINERY, Vol. 115, pp. 1–9.

Day, I. J., 1993b, "Active Suppression of Rotating Stall and Surge in Axial Compressors," ASME JOURNAL OF TURBOMACHINERY, Vol. 115, pp. 40–47.

Durham, J., 1965, "Non-axisymmetric Flows in Axial Compressors," *Mechanical Engineering Science*, Monograph No. 3, Oct.

Emmons, H. W., Pearson, C. E., and Grant, H. P., 1955, "Compressor Surge and Stall Propagation," *Transactions of the ASME*, Vol. 77, pp. 455–469.

Garnier, V. H., Epstein, A. H., and Greitzer, E. M., 1991, "Rotating Waves as a Stall Inception Indication in Axial Compressors," ASME JOURNAL OF TURBOMACHINERY, Vol. 113, pp. 290–301.

Greitzer, E. M., 1976a, "Surge and Rotating Stall in Axial Flow Compressors, Part I: Theoretical Compression System Model," ASME *Journal of Engineering for Power*, Vol. 98, pp. 190–198.

Greitzer, E. M., 1976b, "Surge and Rotating Stall in Axial Flow Compressors, Part II: Experimental Results and Comparison With Theory," ASME *Journal of Engineering for Power*, Vol. 98, pp. 199–217.

Greitzer, E. M., 1976c, "A Note on Compressor Exit Static Pressure Maldistribution in Asymmetric Flow," Cambridge University Engineering Dept. Report CUED/A-Turbo/TR 79.

Greitzer, E. M., 1980, "Review—Axial Compressor Stall Phenomena," ASME *Journal of Fluids Engineering*, Vol. 102, June.

Gysling, D. L., Dugundji, J., Greitzer, E. M., and Epstein, A. H., 1991, "Dynamic Control of Centrifugal Compressor Surge Using Tailored Structures," ASME JOURNAL OF TURBOMACHINERY, Vol. 113, pp. 710–722.

Gysling, D. L., 1992, private communication.

Ham, C. J., and Williams, D. D., 1983, "Some Applications of Actuator and Semi-actuator Disk Theory to the Problem of Intake/Engine Compatibility," Paper No. 83-TOKYO-IGTC-50.

Haynes, J. M., Hendricks, G. J., and Epstein, A. H., 1994, "Active Stabilization of Rotating Stall in a Three-Stage Axial Compressor," ASME JOURNAL OF TURBOMACHINERY, Vol. 116, this issue, pp. 226–239.

Hendricks, G. J., and Gysling, D. L., 1992, "A Theoretical Study of Sensor-Actuator Schemes for Rotating Stall Control," Paper No. AIAA 92-3486.

Howell, A. R., 1965, "Aerodynamic Design of Axial Flow Compressors," NASA SP36.

Hynes, T. P., and Greitzer, E. M., 1987, "A Method for Assessing Effects of Circumferential Flow Distortion on Compressor Stability," ASME JOURNAL OF TURBOMACHINERY, Vol. 109, pp. 371–379.

Iura, T., and Rannie, W. D., 1954, "Experimental Investigations of Propagating Stall in Axial-Flow Compressors," *Transactions of ASME*, Vol. 76, pp. 463–471.

Kodama, H., 1986, "Performance of Axial Compressor With Nonuniform Exit Static Pressure," ASME JOURNAL OF TURBOMACHINERY, Vol. 108, pp. 76–81.

LINEARB, 1980, "Linearised Two-Dimensional, Actuator Disk and Semi-actuator Disk Computer Code," Rolls-Royce Report, United Kingdom.

Longley, J. P., 1990, "Measured and Predicted Effects of Inlet Distortion on Axial Compressors," ASME Paper No. 90-GT-214.

Longley, J. P., and Hynes, T. P., 1990, "Stability of Flow Through Multistage Axial Compressors," ASME JOURNAL OF TURBOMACHINERY, Vol. 112, pp. 126–132.

Longley, J. P., and Greitzer, E. M., 1992, "Inlet Distortion Effects in Aircraft Propulsion System Integration," AGARD Lecture Series LS-183, May.

McCaughan, X. X., 1988, "Application of Bifurcation Theory to Axial Flow Compressor Instability," ASME JOURNAL OF TURBOMACHINERY, Vol. 110, pp. 426–433.

McDougall, N. M., Cumpsty, N. A., and Hynes, T. P., 1990, "Stall Inception in Axial Compressors," ASME JOURNAL OF TURBOMACHINERY, Vol. 112, pp. 116–125.

Mazzawy, R. S., 1977, "Multiple Segment Parallel Compressor Model for Circumferential Flow Distortion," ASME *Journal of Engineering for Power*, Vol. 99, Apr.

Mazzawy, R. S., 1980, "Surge-Induced Structural Loads in Gas Turbines," ASME *Journal of Engineering for Power*, Vol. 102, pp. 162–168.

Moore, F. K., 1984a, "A Theory of Rotating Stall of Multistage Axial Compressors: Part I—Small Disturbances," ASME *Journal of Engineering for Power*, Vol. 106, pp. 313–320.

Moore, F. K., 1984b, "A Theory of Rotating Stall of Multistage Axial Compressors: Part II—Finite Disturbances," ASME *Journal of Engineering for Power*, Vol. 106, pp. 321–326.

Moore, F. K., 1984c, "A Theory of Rotating Stall of Multistage Axial Compressors: Part III—Limit Cycles," ASME *Journal of Engineering for Power*, Vol. 106, pp. 327–336.

Moore, F. K., and Greitzer, E. M., 1986, "A Theory of Post-stall Transients in Axial Compression Systems: Parts I and II," ASME *Journal of Engineering for Gas Turbines and Power*, Vol. 108, pp. 68–76; 231–240.

Nagano, S., Machida, Y., and Takata, H., 1971, "Dynamic Performance of Stalled Blade Rows," Japan Society of Mechanical Engineering, Paper #11, presented at Tokyo Joint International Gas Turbine Conference, Tokyo, Japan, Oct.

O'Brien, W. F., Ng, W.-F., and Richardon, S. M., 1985, "Calculation of Unsteady Fan Rotor Response Caused by Downstream Flow Distortions," *Journal of Propulsion*, Vol. 1, No. 6, Nov.–Dec.

Paduano, J., Epstein, A. H., Valavani, L., Longley, J. P., Greitzer, E. M., and Guenette, G. R., 1993, "Active Control of Rotating Stall in a Low-Speed Axial Compressor," ASME JOURNAL OF TURBOMACHINERY, Vol. 115, pp. 48–56.

Pinsley, J. E., Guenette, G. R., Epstein, A. H., and Greitzer, E. M., 1991, "Active Stabilization of Centrifugal Compressor Surge," ASME JOURNAL OF TURBOMACHINERY, Vol. 113, pp. 723–732.

Simon, J. S., Valavani, L., Epstein, A. H., and Greitzer, E. M., 1993, "Evaluation of Approaches to Active Compressor Surge Stabilization," ASME JOURNAL OF TURBOMACHINERY, Vol. 115, pp. 57–67.

Stenning, A. H., and Kriebel, A. R., 1958, "Stall Propagation in a Cascade of Airfoils," *Transactions of the ASME*, Vol. 80, p. 777.

Strang, E. J., 1991, "Influence of Unsteady Losses and Deviation on Compression System Stability With Inlet Distortion," M.S. Thesis, Department of Aeronautics and Astronautics, MIT, Cambridge, MA.

Turner, R. C., 1959, "The Effect of Axial Spacing on the Surge Characteristics of Two Mismatched Axial Compressor Stages," Aeronautical Research Council, CP No. 431.

Williams, D. D., 1986, "Review of Current Knowledge on Engine Response to Distorted Inflow," AGARD-CP-400, Munich, Germany.

APPENDIX A

Flow Field Impedances

In this appendix the relationships between the flow coefficient perturbation, $\delta\phi(\xi, \theta, \tau)$,[14] and the pressure and flow angle perturbations in the inlet and exit flow fields are derived. The assumption made is that the equations of motion may be linearized, and a single Fourier disturbance of the form $e^{in\theta + i\omega\tau}$ with $n \neq 0$ will be considered.

Inlet Flow Field. The compressor can only create localized flow disturbances and these must be of the potential form that decays upstream. The nondimensional axial ($\delta\phi$) and tangential ($\delta\nu$) velocity perturbations in the inlet flow field may thus be expressed:

$$\delta\phi = \frac{\partial}{\partial\xi}(\delta\Phi) \quad \text{and} \quad \delta\nu = \frac{\partial}{\partial\theta}(\delta\Phi)$$

where the velocity potential is:

$$\delta\Phi(\xi, \theta, \tau) = A(\xi)e^{in\theta + i\omega\tau}$$

Since $\nabla^2\delta\Phi = 0$, then for upstream decaying disturbances $A(\xi) = ae^{|n|\xi}$ and so $\delta\phi = |n|\delta\Phi$.

The tangential perturbation is:

$$\delta\nu = \frac{1}{|n|}\frac{\partial}{\partial\theta}(\delta\phi) \tag{A1}$$

To evaluate the corresponding perturbation in angle, $\delta\alpha$, the definition $\nu = \phi \tan\alpha$ is linearized:

$$\delta\nu = \delta\phi \tan\alpha + \phi \sec^2\alpha\, \delta\alpha \tag{A2}$$

and so:

$$\delta\alpha = \frac{\cos^2\alpha}{\phi}\left(\frac{1}{|n|}\frac{\partial}{\partial\theta}(\delta\phi) - \delta\phi \tan\alpha\right) \tag{A3}$$

The nonsteady form of the Bernoulli equation (for disturbance of assumed form) is:

$$\frac{\partial}{\partial\tau}(\delta\Phi) + \frac{\delta Pt}{\rho U^2} = \text{const} \tag{A4}$$

and therefore:

$$\frac{\delta Pt}{\rho U^2} = -\frac{1}{|n|}\frac{\partial}{\partial\tau}(\delta\phi) \tag{A5}$$

The equations above (A1 to A5) are valid everywhere in the upstream flow field, and so to specify the relationships at the leading edge of the first blade row it is only necessary to apply a subscript "1" to the appropriate quantities.

Exit Flow Field. In the exit duct there is a convected vortical disturbance along with a downstream decaying potential field. Two of the equations of motion are:

Axial Momentum:

$$\frac{\partial}{\partial\tau}\delta\phi + \phi\frac{\partial}{\partial\xi}\delta\phi + \nu\frac{\partial}{\partial\theta}\delta\phi = -\frac{\partial}{\partial\xi}\frac{\delta P}{\rho U^2}$$

Continuity:

$$\frac{\partial}{\partial\xi}\delta\phi + \frac{\partial}{\partial\theta}\delta\nu = 0$$

Eliminating the axial derivative and using $\nu = \phi \tan\alpha$ gives:

$$\frac{\partial}{\partial\tau}\delta\phi - \phi\frac{\partial}{\partial\theta}\delta\nu + \phi \tan\alpha\frac{\partial}{\partial\theta}\delta\phi = -\frac{\partial}{\partial\xi}\frac{\delta P}{\rho U^2} \tag{A6}$$

The pressure field decays downstream and therefore is of the form:

$$\frac{\delta P}{\rho U^2} = be^{-|n|\xi + in\theta + i\omega\tau}$$

so:

$$\frac{\partial}{\partial\xi}\frac{\delta P}{\rho U^2} = -|n|\frac{\delta P}{\rho U^2} \tag{A7}$$

Combining Eqs. (A6) and (A7) gives:

$$|n|\frac{\delta P}{\rho U^2} = \frac{\partial}{\partial\tau}\delta\phi + \phi\left(\tan\alpha\frac{\partial}{\partial\theta}\delta\phi - \frac{\partial}{\partial\theta}\delta\nu\right) \tag{A8}$$

Substituting Eq. (A2) and rearranging gives:

$$\frac{\delta P}{\rho U^2} = \frac{1}{|n|}\frac{\partial}{\partial\tau}\delta\phi - \frac{\phi^2}{|n|}\sec^2\alpha\frac{\partial}{\partial\theta}\delta\alpha \tag{A9}$$

This equation is valid everywhere in the downstream flow field, but will only be applied at the trailing edge of the last blade row of the compressor, denoted by subscript "2." (It is worth noting that this equation is also valid in the relative frame provided that all the quantities are relative and that the time rate of change is interpreted in the relative frame.)

[14] Nondimensional axial distance is ξ = (axial distance)/radius.

APPENDIX B

Compressor and Flow Field Interaction

The most general form of interaction between the inlet and exit flow fields and the quasi-steady compressor model is derived in this appendix. The total-to-static pressure rise of the compressor is now $\psi^{ts}(\phi, \alpha_1)$ and so the linearized form of Eq. (9*a*) becomes:

$$\frac{\delta P_2}{\rho U^2} - \frac{\delta Pt_1}{\rho U^2} = \frac{\partial \psi^{ts}}{\partial \phi}\,\delta\phi + \frac{\partial \psi^{ts}}{\partial \alpha_1}\,\delta\alpha_1 - \lambda\,\frac{\partial}{\partial \theta}\,(\delta\phi) - \mu\,\frac{\partial}{\partial \tau}\,(\delta\phi) \qquad \text{(B1)}$$

An expression for $\delta\alpha_1$ in terms of $\delta\phi$ is given by Eq. (A3) and the inlet flow field impedance ($\delta Pt_1/\rho U^2$ in terms of $\delta\phi$) is still given by Eq. (A5). In the exit flow field, however, $\alpha_2 = (\phi, \alpha_1)$ and so when linearized becomes:

$$\delta\alpha_2 = \frac{\partial \alpha_2}{\partial \phi}\,\delta\phi + \frac{\partial \alpha_2}{\partial \alpha_1}\,\delta\alpha_1 \qquad \text{(B2)}$$

Therefore, the exit impedance becomes (from Eq. (A9)):

$$\frac{\delta P_2}{\rho U^2} = \frac{1}{|n|}\,\frac{\partial}{\partial \tau}\,\delta\phi - \frac{\phi^2}{|n|}\,\sec^2\alpha_2\left(\frac{\partial \alpha_2}{\partial \phi}\,\frac{\partial}{\partial \theta}\,\delta\phi + \frac{\partial \alpha_2}{\partial \alpha_1}\,\frac{\partial}{\partial \theta}\,\delta\alpha_1\right) \qquad \text{(B3)}$$

Combining Eqs. (B1), (B2), and (B3) with (A3) and (A5) gives, after rearrangement:

$$\left[\left(\frac{2}{|n|} + \mu\right)\,\frac{\partial}{\partial \tau} + R\,\frac{\partial}{\partial \theta}\right]\delta\phi = S\delta\phi \qquad \text{(B4}a\text{)}$$

where:

$$R = \lambda - \frac{\partial \psi^{ts}}{\partial \alpha_1}\,\frac{\cos^2\alpha_1}{\phi\,|n|} + \frac{\phi}{|n|}\,\sec^2\alpha_2\left(\sin\,\alpha_1\,\cos\,\alpha_1\,\frac{\partial \alpha_2}{\partial \alpha_1} - \phi\,\frac{\partial \alpha_2}{\partial \alpha}\right) \qquad \text{(B4}b\text{)}$$

and:

$$S = \frac{\partial \psi^{ts}}{\partial \phi} - \frac{\partial \psi^{ts}}{\partial \alpha_1}\,\frac{\sin\,\alpha_1\,\cos\,\alpha_1}{\phi} - \phi\,\frac{\partial \alpha_2}{\partial \alpha_1}\,\frac{\cos^2\alpha_1}{\cos^2\alpha_2} \qquad \text{(B4}c\text{)}$$

Stall Inception and Development in an Axial Flow Aeroengine

A. G. Wilson

C. Freeman

Rolls-Royce plc,
Derby, United Kingdom

This paper describes the phenomenon of stall and surge in an axial flow aeroengine using fast response static pressure measurements from the compressor of a Rolls-Royce VIPER engine. It details the growth of flow instability at various speeds, from a small zone of stalled fluid involving only a few blades into the violent surge motion of the entire machine. Various observations from earlier theoretical and compressor rig results are confirmed by these new engine measurements. The main findings are as follows: (1) The point of stall inception moves rearward as engine speed increases, and is shown to be simply related to the axial matching of the compressor. (2) The final unstable operation of the machine can be divided into rotating stall at low speed and surge or multiple surge at high speed. (3) The inception process is independent of whether the final unstable operation is rotating stall or multiple surge. (4) Stall/surge always starts as a circumferentially small flow disturbance, rotating around the annulus at some fraction of rotor speed.

Introduction

A great deal of work has been expended in recent years to understand the nature of stall and surge in axial flow compressors. Most of the work has centered on theoretical calculations and on low and high-speed compressor measurements in a rig environment, which are not necessarily representative of surge/stall in a real engine. For a complete picture of stall/surge the compressor cannot be treated as an isolated component. Rather, stall/surge is a system instability heavily dependent on the environment in which the compressor is operating. This is clearly seen in the work of Greitzer (summarized by Moore and Greitzer, 1985), where the entire compressor is modeled by a single characteristic. In spite of this, few data have been published from compressors in an engine environment. The objective of this paper is to start to fill this gap by presenting a fairly broad range of results from a highly instrumented engine compressor.

It was decided to put sufficient instrumentation into a high-speed axial flow engine to trace the inception of stall/surge. The Rolls-Royce VIPER engine was chosen as a test vehicle because of the relatively small size and simple single-shaft geometry.

Kulite pressure transducers were chosen for tracing the flow disturbances, being sufficiently rugged to survive the engine environment. Data were collected at 4000 points per second on a 32 channel A-D converter, and fed to a PC-compatible COMPAQ computer. The data were recorded in a 4-s-long rolling buffer, frozen manually on hearing a surge/stall event.

Various methods were developed to analyze the time histories of the pressure measurements. Three types of plot were chosen for this paper as being particularly suitable for showing qualitatively the stall/surge inception process. These are described in the appendix.

Our particular interest is in stall inception: the very start of the stall/surge event. This is distinct from the general event in that the time scales are short, down to two rotor revolutions for our engine at top speed. Thus it may be expected that the start of the stall event is heavily dependent on local conditions around the point of inception. This paper shows that inception can be traced to a localized area within the compressor, and further that the point of inception moves with speed in the same way that would be predicted by a conventional stage matching argument.

It is intended to use the test results presented here as the basis for a model of the stall/surge inception process. This work is beyond the scope of the present paper.

Test Rig

The Rolls-Royce VIPER engine chosen for the experimental work (Fig. 1) generates a thrust of 14.7 kN at a shaft speed of 13,800 rpm. The compressor is a 0.7-m-long eight-stage machine with DCA blading, giving an overall pressure ratio of 5:1. A typical midstage at the 100 percent speed surge point operates at about $Va/U = 0.64$, with a rotor relative exit angle of 26 deg and a stator absolute exit angle of 22 deg at midspan. The compressor has an IGV giving 25 deg of preswirl, and an OGV at exit to return the flow to axial. The Mach number varies from just over 0.9 at rotor 1 tip to 0.4 at compressor exit. The outer radius of the compressor is constant from stage 1 exit rearward at 0.216 m.

Figure 1 also shows the positions of the primary instrumentation. Following the work of Day (1993), which showed that flow instabilities start as circumferentially small regions of stalled flow, the compressor was instrumented with rings of five Kulite static pressure transducers, more or less equi-

Contributed by the International Gas Turbine Institute and presented at the 38th International Gas Turbine and Aeroengine Congress and Exposition, Cincinnati, Ohio, May 24-27, 1993. Manuscript received at ASME Headquarters February 12, 1993. Paper No. 93-GT-2. Associate Technical Editor: H. Lukas.

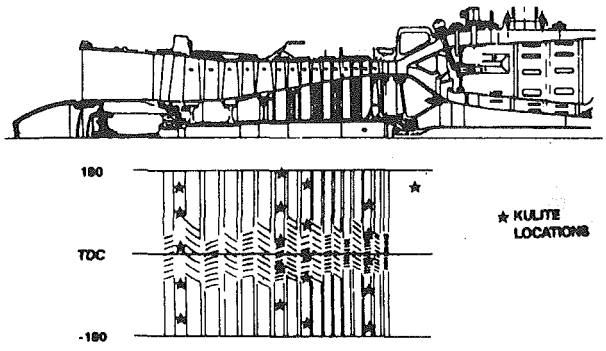

Fig. 1 VIPER test engine

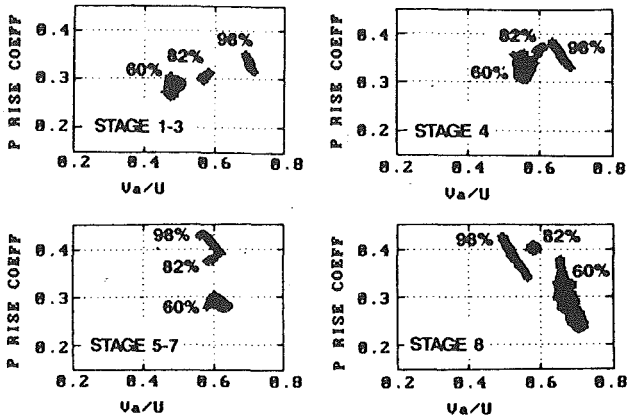

Fig. 2 Compressor stage characteristics

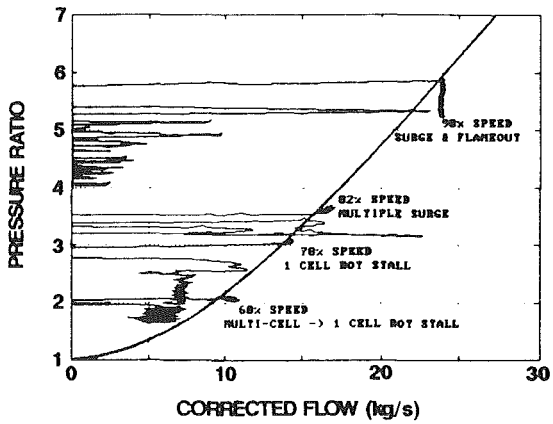

Fig. 3 Overall compressor characteristics

spaced around the outer wall of the annulus. Rings of transducers were placed upstream of the first rotor, above the third stator, above the fourth stator, and above the seventh stator. A further Kulite was placed in the exit duct. Mass flow was measured by an airmeter at compressor inlet, with a Druck pressure transducer.

In order to investigate the stall/surge behavior of the machine it was necessary to raise the working line artificially. At low speed this can be achieved by rapid overfueling. To raise the working line at higher speeds a large pressure vessel was used to inject high-pressure air (up to 2000 kPa) through a control valve into the combustion chamber. At intermediate speeds the surge line could be approached gently by injecting air at insufficient pressure to stall the machine and then decelerating slowly. At top speeds this process caused unacceptably long periods of high jet pipe temperature, and so higher pressure air was injected, causing an immediate engine surge.

The Kulite measurements were averaged circumferentially to produce the stage characteristics presented in Fig. 2. These are approximations to individual stage characteristics for typical stages between the Kulite rings, taken from transient measurements at three speeds while approaching surge/stall. Although they are only approximate, they do show the expected form. At low speed the front stages appear to be operating on a positively sloping characteristic, while all the later stages are operating on a negative slope. At higher speeds the front stages move away from stall, whereas the rear stages move further up their characteristics. The stage 5–7 characteristic starts to turn over at 98 percent speed. Note, however, that the last stage always operates on a negative slope, even at top speed (98 percent nominal).

Analysis of Surge/Stall Regimes

Figure 3 shows overall transient compressor characteristics for the VIPER compressor during surge at a range of speeds, based on Druck pressure measurements in the airmeter and at compressor exit. No account is taken of inertia in the mass flow calculation, so the flow is only approximate. Note also that an instrumentation problem affected the 78 percent speed characteristic: The absolute level of flow for this characteristic has been factored down to be consistent with other data at similar speeds. Nonetheless Fig. 3 demonstrates the different stall/surge regimes of the VIPER compressor.

At low to midspeeds (60–80 percent design speed) the mean compressor operating point simply drops during the stall transient to a lower level of flow and pressure ratio.

At intermediate speeds (around 80 percent speed) there is a sharp dichotomy in stall/surge behavior, along the lines of the theoretical model of Moore and Greitzer (1985). Below 81 percent speed the event is as described above. Above 81 percent speed the engine develops violent multiple surge, where the mean flow and pressure rise drop to around zero, and then climb again to near their presurge levels. Only the mass flow variations are captured by the slow response measurements presented in Fig. 3 (fast response pressure measurements are presented later, Fig. 7). The whole cycle repeats itself over and over, in this case to the end of the data record.

At high speeds (above 88 percent speed), the pressure rise and flow drop to near zero without climbing again. The engine also requires relighting. It can be inferred that the initial surge is sufficiently violent to cause a flameout, preventing a multiple surge as seen between 81 and 88 percent speed.

Figure 3 cannot give a complete picture of stall/surge, because the flow at all speeds is substantially nonaxisymmetric during surge. The following sections detail the nonaxisymmetric transient behavior of the flow that gives rise to the changes in mean level plotted in Fig. 3.

Low-Speed Stall Event. At low speed the engine was stalled by overfueling. The compression system moves through various regimes of rotating stall, both before and after reaching the surge line (defined conventionally as the point of irretrievable breakdown of the flow structure).

Figure 4(*a*) maps out static pressure around the outer annulus wall during the overfueling, but prior to reaching the surge line at 60 percent speed. The five axial planes correspond to the Kulite measurement planes upstream of the first rotor, above the third stator, above the fourth stator, above the seventh stator, and in the exit duct. The pressure at each stage is shown relative to a datum level at the start of the event. The compressor turns in a clockwise direction viewed from the front, which is from left to right on Fig. 4(*a*). Appendix 1 gives details of how the plot is constructed from the available static pressure data. The four patches of high static pressure at the

front of the compressor represent four areas of low axial momentum fluid, or stall cells. Time histories of the various Kulite measurements show that the cells are rotating at slightly different rates, but all at around 57 percent of rotor speed. Each cell has a "tail" of low pressure reaching part way along the length of the compressor. This picture is consistent with the existence of a number of stalled blade passages, limited circumferentially to the region of each individual stall cell, and axially to a region between the first measurement at rotor 1 entry and the second above stator 3. These blade passages are incapable of supporting the pressure ratio of the unstalled passages, giving a low-pressure area downstream, and a high-pressure area upstream. Note that the stall cell is limited to the front of the compressor. It may be even more limited in extent than Fig. 4(*a*) suggests, as there are no pressure measurements between the first rotor and the third stator blade row.

Figure 4(*b*) shows the same map 50 ms (7 rotor revolutions) later, as the compressor is just crossing the surge line. Note that the origin of the x axis has been shifted around the compressor relative to Fig. 4(*a*), according to the procedure in Appendix 1. This keeps the disturbance from moving across the page on successive plots, and allows its development to be followed more easily. One of the stall cells has disappeared almost entirely, leaving three irregularly spaced cells with the one on the right much the strongest, reaching almost axially to the back of the compressor. The next figure shows it to have deepened further 125 ms (17 rotor revs) later. The high static pressure area in the middle of the compressor indicates more stalled blade rows toward the back of the machine, left in the wake of the stall cell as it rotates around the annulus.

By Fig. 4(*d*), just 12.5 ms (1.7 rotor revs) later, the strongest cell has grown significantly. The leading edge of the cell still proceeds at much the same rate, but the trailing edge lags further and further behind, until in this frame it is about to swallow one of the other two cells. This large cell slows to about 40 percent rotor speed, swallowing both of the smaller cells. Figure 5 shows the pressure map (on a new scale), having achieved a stable rotating stall condition 12.5 ms (1.7 rotor revs) after Fig. 4(*d*), with what was the original stall cell occupying over half the circumference. The pressure ratio has dropped from about 2 to 1.5; hence the low pressure at the back of the compressor.

Figures 4(*b–d*) and 5 all show a significant region of high static pressure at compressor exit axially aligned with the trailing edge of the stall cell. A similar phenomenon occurs at higher speeds (e.g., Figs. 9*d*, 11*d*, 15c), with a related low-pressure region at the leading edge of the stall cell. This is not considered in detail in this paper. It is noted, however, that the flow in the duct between the compressor and combustor is axial. The phenomenon can then be explained as the result of low-momentum fluid emanating from the rotating stall cell.

Figure 6 shows the change from 3 stall cells to 1 (corresponding to the data in Figs. 4*c* to 4*d* and 5) in a different format. Here the rotor 1 inlet pressure is plotted around the annulus with time moving out from the center (see the appendix for a complete description of the plot). The stall cells move around the annulus with time, giving rise to the spirals. Three cells are visible at the center of the plot. Two of these keep

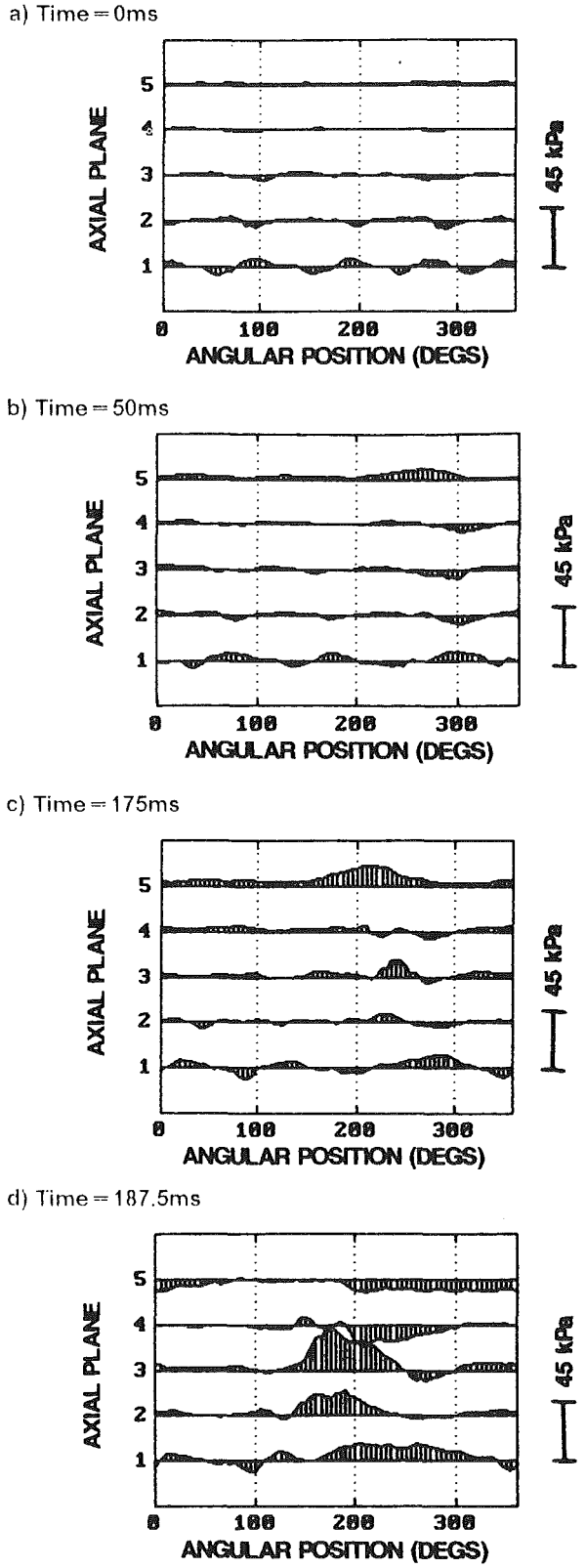

Fig. 4 Static pressure maps at 60 percent speed development of stall cell

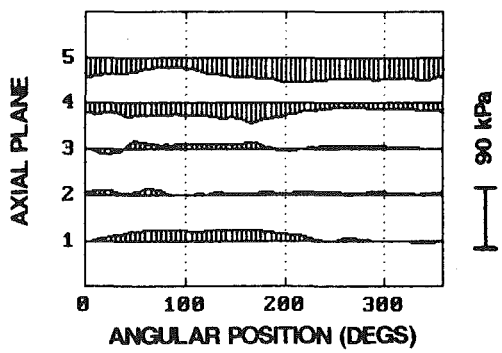

Fig. 5 Static pressure map at 60 percent speed (time = 200 ms) stable rotating stall

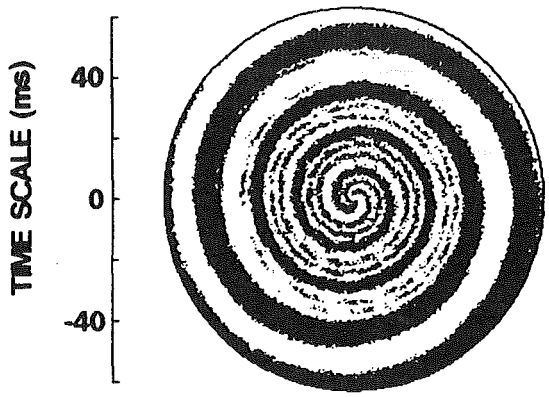

Fig. 6 Rotor 1 inlet static pressure at 60 percent speed

roughly constant in size while the third grows stronger. The two smaller cells eventually die out, leaving only the one large cell, which develops into stable rotating stall.

The low-speed results show that the compression system moves relatively slowly through various regimes of rotating stall. Even on the stable side of the surge line the compressor exhibits stable rotating stall, with four stall cells limited to the front of the compressor. During the stall transient these four cells reduce to three, one of which spreads axially to the back of the machine, and then grows circumferentially. The front edge of this strong cell rotates at a fairly constant speed, while the trailing edge slows down, swallowing the weaker cells. The final operating condition is single-cell rotating stall at a far lower pressure ratio and flow. The whole event occurs over a period of roughly 200 ms, or 30 rotor revolutions.

Midspeed Stall/Surge. There is a sharp change in stall/surge behavior at around 81 percent speed. Up to this speed the compression system develops stable single-cell rotating stall. Above this speed the engine goes into violent multiple surge. This is illustrated in Fig. 7, which shows time histories from each of the Kulites at each of the five measurement planes, normalized at each axial plane to the same starting value. Figure 7(*a*) shows a stall event at 78 percent speed. The engine has been decelerated slowly from 90 percent speed with air injected into the combustion chamber at a constant pressure of 500 kPa. The compressor exit pressure is seen to drop dramatically and remain at a new lower level. Figure 7(*b*) shows a similar event with a slightly higher level of air injection (700 kPa), causing the engine to hit the surge line at 82 percent speed. This time the overall pressure ratio drops nearly to unity, before climbing back to almost its original level. This process is repeated indefinitely, the gradual drop in peak pressure being related to a slow run-down in engine speed. Close inspection of the pressure rise prior to each surge shows that each stage in turn reaches its normal operating point, starting with the front stage and moving backward. This is consistent with a conventional stage matching argument that the rear stages are operating near choke until the front stages begin to produce some pressure rise.

Figure 8 shows a "spiral plot" of the static pressure at stage 4 during the 82 percent speed multiple surge event (see the appendix for a description of this plot). Beneath this are the time traces of the individual Kulite measurements on the same scale. The spiral plot shows the onset of rotating stall as a spiral at the start of the event, which dies away as the pressure level drops. The disturbance remains broadly axisymmetric until the pressure returns to almost the same value as before the surge. Rotating stall is again shown as the pressure begins to drop, and returns at the same point on each successive stall. It is important to note that rotating stall is the first sign of any disturbance for the first surge event, whereas the compressor exit pressure (not shown on Fig. 8) starts to drop before

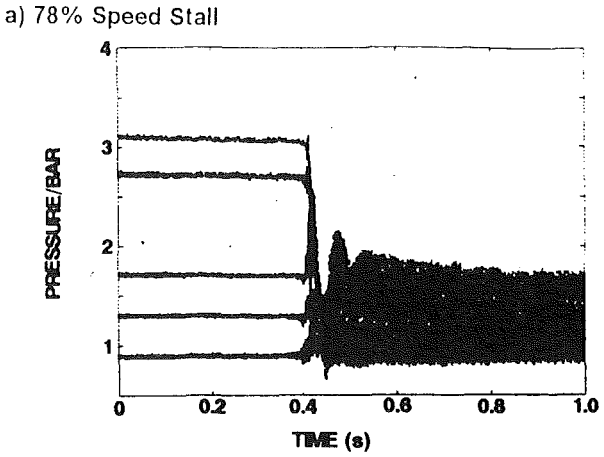

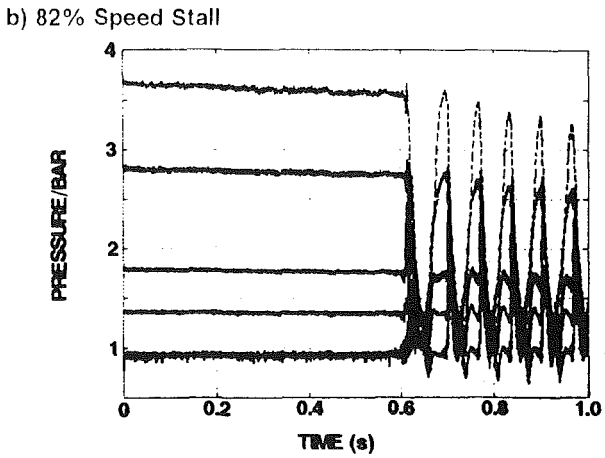

Fig. 7 Comparison of two midspeed stall/surge events

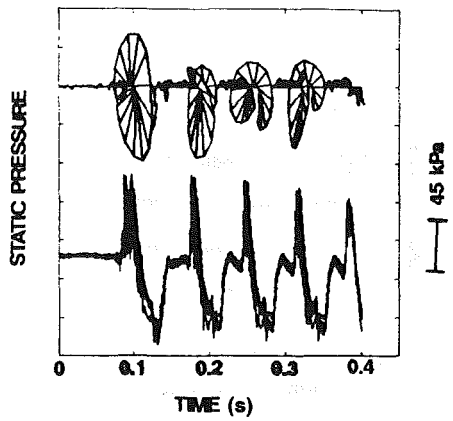

Fig. 8 Stator 4 exit static pressure at 82 percent speed

the onset of rotating stall in the second and subsequent surges of the multiple event.

Figures 9 and 10 show static pressure maps at various times during the stall event at 78 percent speed. The first sign of any disturbance (Fig. 9*a*) is again at the front of the compressor. This is consistent with the stage characteristics in Fig. 2, which show the front stages of the machine to be furthest toward stall at this speed. The stall cell is rotating at roughly 56 percent of rotor speed. Like the low-speed data, the cell spreads almost axially to the back of the machine, only this time much more quickly (Figs. 9*b–d*, at 5 ms intervals, or roughly 1 rotor revolution). Having grown axially, it proceeds to grow circumferentially, as shown in Fig. 10. Figure 10(*a*) is the same as

Fig. 9(*d*), but with a new pressure scale. Eventually it occupies about half the circumference and settles into stable rotating stall (Figs. 10*c*, 10*d*).

Figures 11 and 12 show static pressure maps for the 82 percent speed event. The initial stall cell rotational speed is slightly higher than the 78 percent speed event, scaling almost exactly with rotor speed. Figures 11 and 12 are taken at the same time intervals as Figs. 9 and 10, and are notable in that they show an almost identical pattern of stall cell development, even though the subsequent history is entirely different. In this case the stall cell continues to grow circumferentially until the flow becomes axisymmetric once more (Fig. 12*c*). Having be-

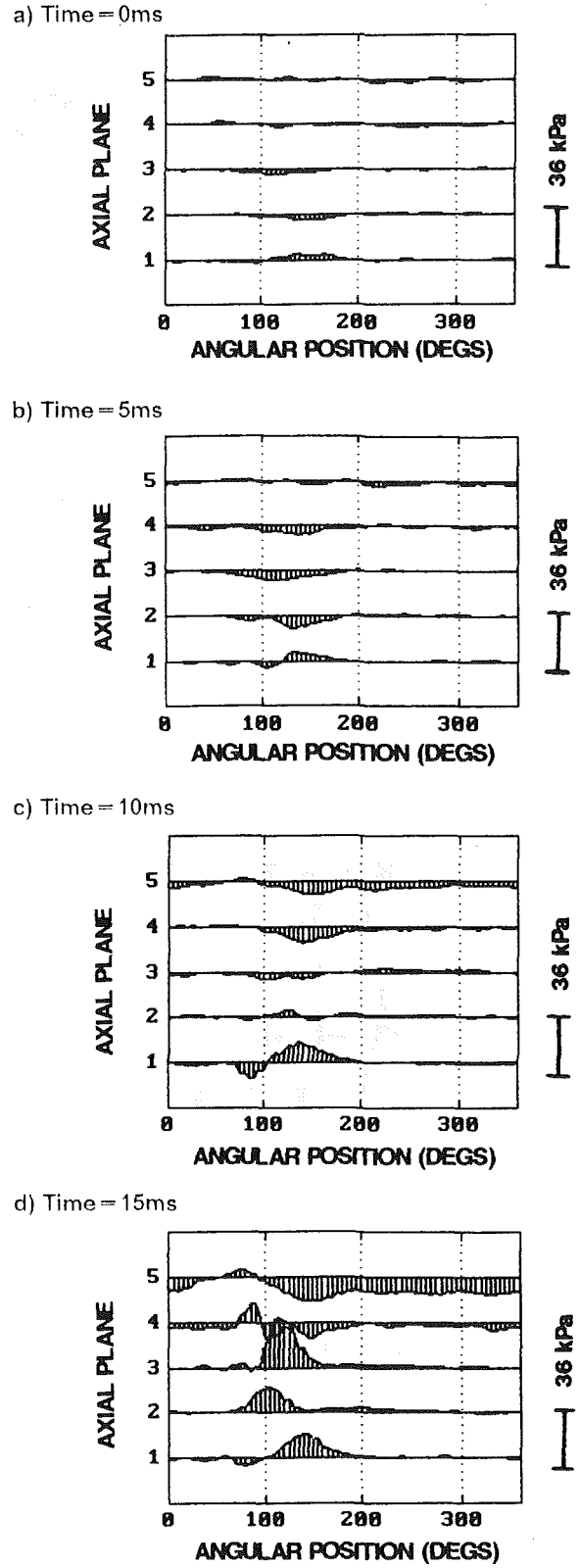

Fig. 9 Static pressure maps at 78 percent speed: development of stall cell

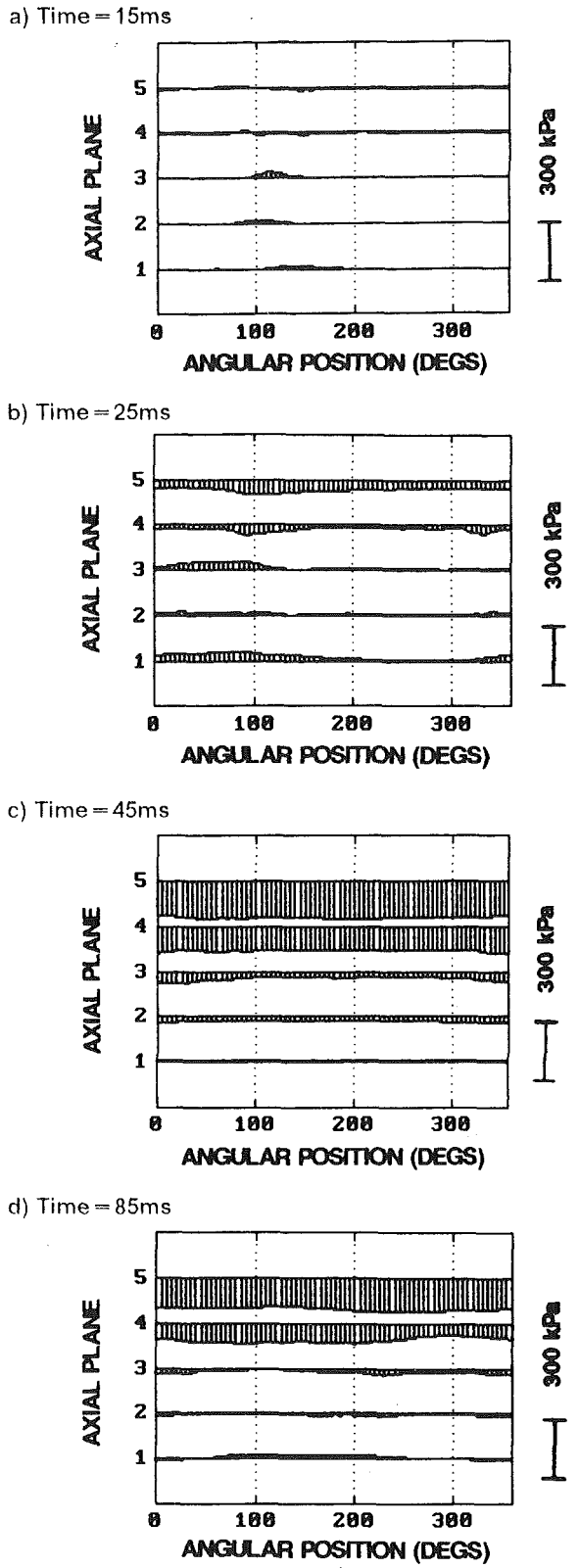

Fig. 10 Static pressure maps at 78 percent speed (ctd): growth of stall cell into stable rotating stall

come axisymmetric, the flow returns to almost the same flow and pressure ratio as before the event, before repeating the cycle. Figure 12(*d*) shows the pressure map 85 ms (16 rotor revs) into the event, where the pressure at the back is almost back to the original level.

The different post-stall behavior in the 78 percent and 82 percent speed events is highlighted in Figs. 13 and 14. Static pressure maps are shown for the first three axial planes only, on an expanded scale, at an equivalent point in the two events (just after the times of Figs. 10*c* and 12*c*, respectively). Figure 13 shows the stall cell still to be present at 78 percent speed, whereas at 82 percent speed Fig. 14 shows the flow to be much more uniform circumferentially.

The difference in post-stall behavior above and below 81

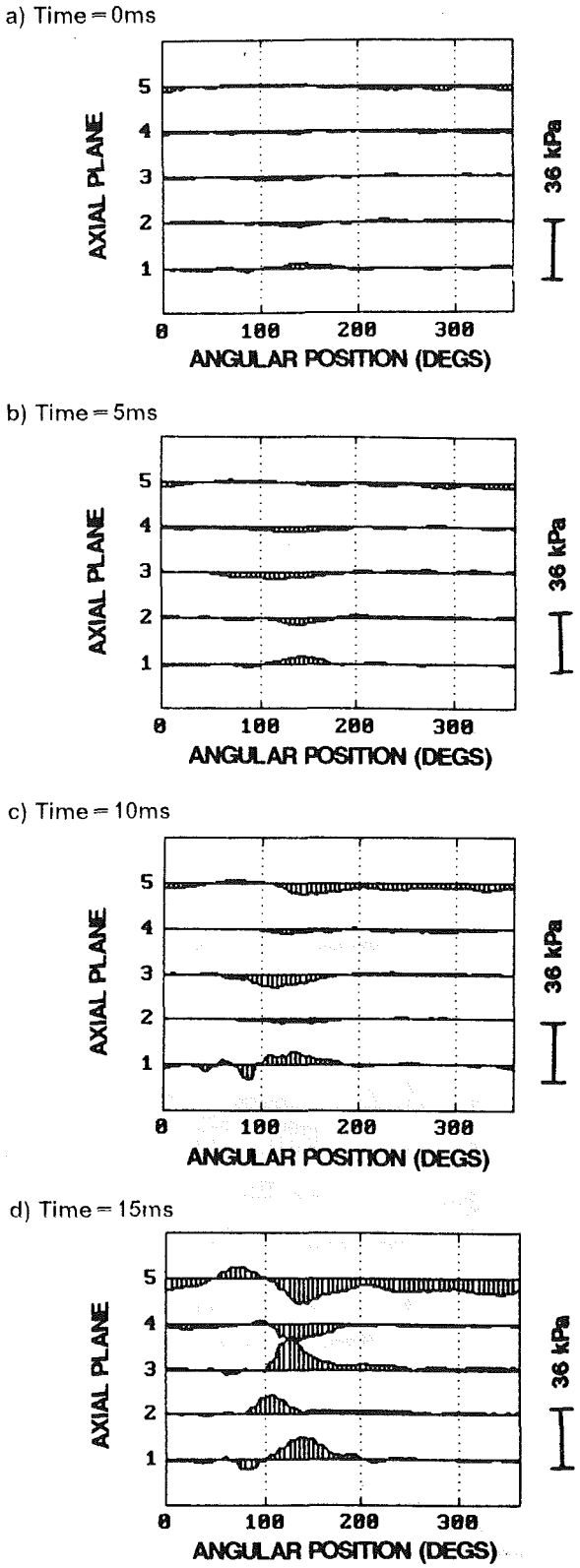

Fig. 11 Static pressure maps at 82 percent speed: development of stall cell

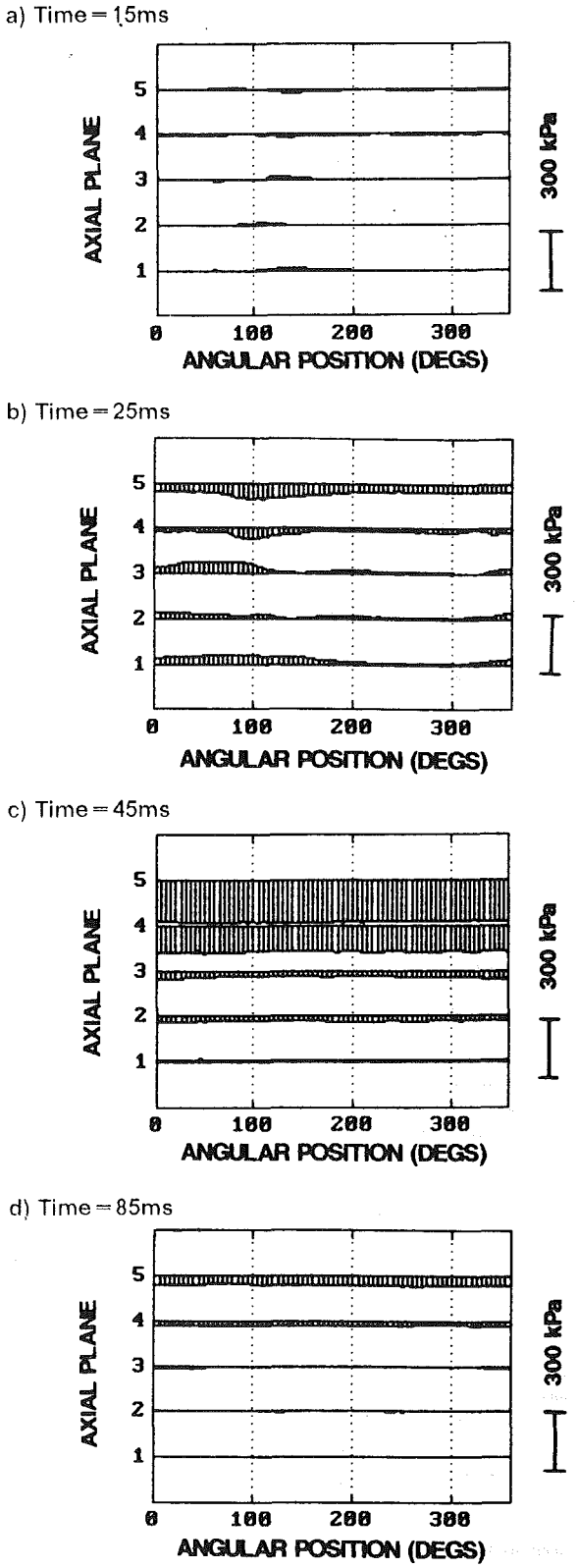

Fig. 12 Static pressure maps at 82 percent speed (ctd): growth of stall cell, then axisymmetric flow

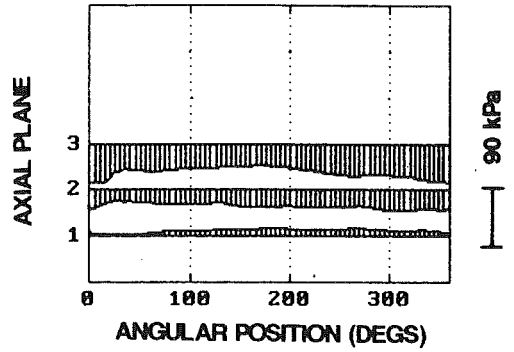

Fig. 13 Static pressure map at 78 percent speed (time = 47.5 ms): stable rotating stall—axial planes 1-3 only

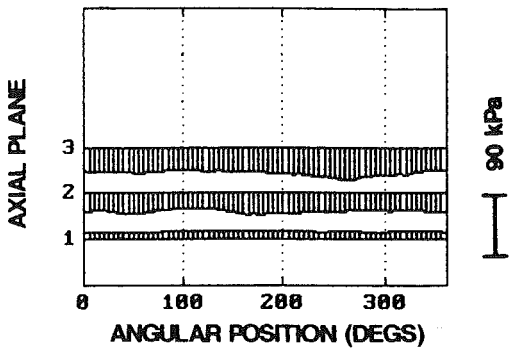

Fig. 14 Static pressure map at 82 percent speed (time = 47.5 ms): almost axisymmetric flow—axial planes 1-3 only

percent speed confirms the picture of surge/stall proposed by Greitzer (summarized by Moore and Greitzer, 1985). The stall inception process, however, is almost identical on either side of this critical speed. Events at 78 and 82 percent speed both start with a rotating stall cell at the front of the compressor, which grows rapidly to the back of the compressor and then circumferentially. Below 81 percent speed the circumferential growth stops, to leave a single rotating stall cell, with the compressor operating steadily in the mean, but at a much lower overall pressure ratio and flow. Above this speed the flow becomes axisymmetric once more, and the overall pressure ratio drops to nearly unity, before climbing again to almost the same operating point as before, and repeating. The time scale of the stall/surge inception process is in both cases around 35 ms or 6.6 rotor revolutions.

High-Speed Surge. Surge events are fastest at high speed. The engine was stalled at 98 percent speed by injecting air at 1000 kPa into the combustion chamber. Figure 15 shows static pressure maps at intervals of 2 ms (0.45 rotor revs) at the start of the event. Figure 16 shows the subsequent development on a smaller pressure scale. The start of the surge event is indicated by the high pressure around stage 4 in Fig. 15(*a*). This is consistent with a region of stalled blade passages between the middle of the compressor and stator 7, with the unstalled passages unable to produce the required pressure rise, giving rise to a high-pressure region upstream and a low-pressure region downstream. This picture is again compatible with the stage characteristics (Fig. 2), which reach peak pressure rise in the region between stages 4 and 7, while the upstream and downstream characteristics have a clear negative slope.

The stall cell, rotating initially at about 47 percent of rotor speed, grows extremely rapidly, first in the axial direction and then circumferentially until the whole annulus is affected and the flow becomes more and more axisymmetric (Fig. 16*d*). The pressure ratio drops away rapidly to near unity. Unlike the 82 percent speed case, the initial surge is violent enough to produce a flameout, preventing a multiple surge. The stall inception process is much faster than at lower speeds. From the first sign of a disturbance to a significant drop in overall pressure ratio takes about 10 ms or 2.25 rotor revs (roughly 1 revolution of the stall cell).

Figure 17 shows the stage 4 static pressure as a "spiral plot" (see the appendix for a complete description of this plot). The

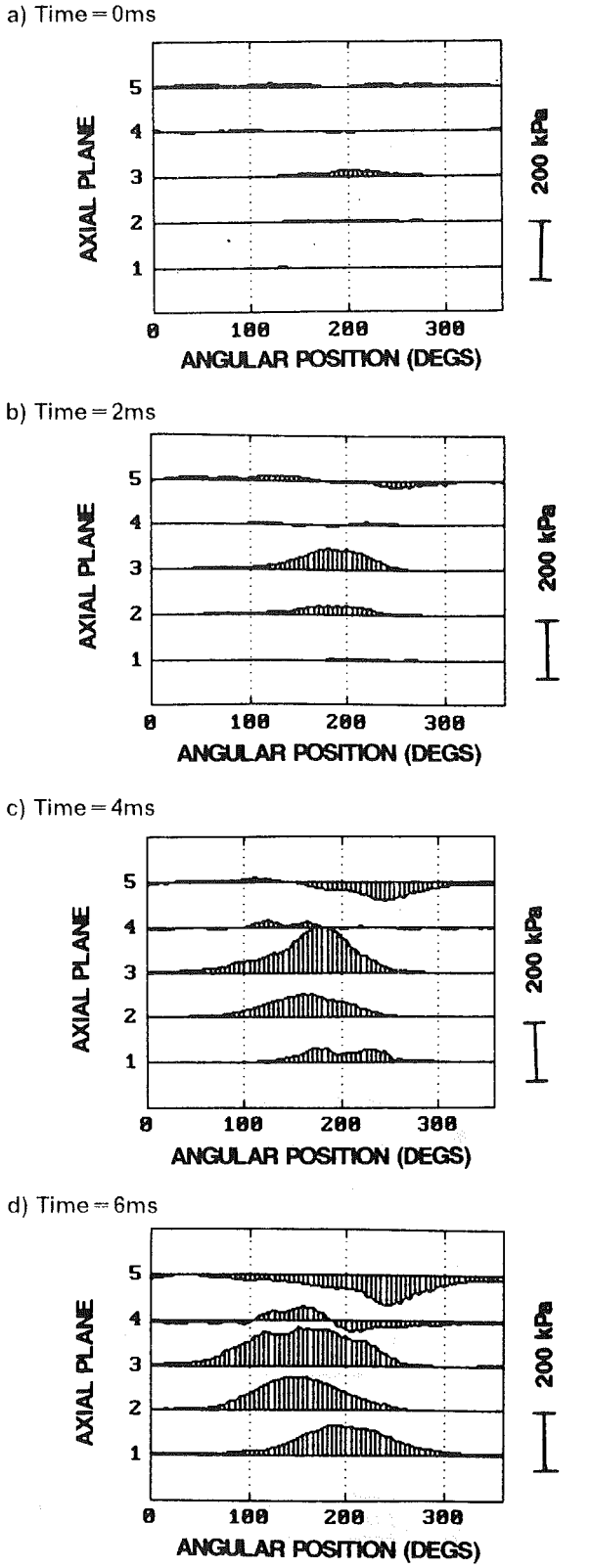

Fig. 15 Static pressure maps at 98 percent speed: growth of stall cell

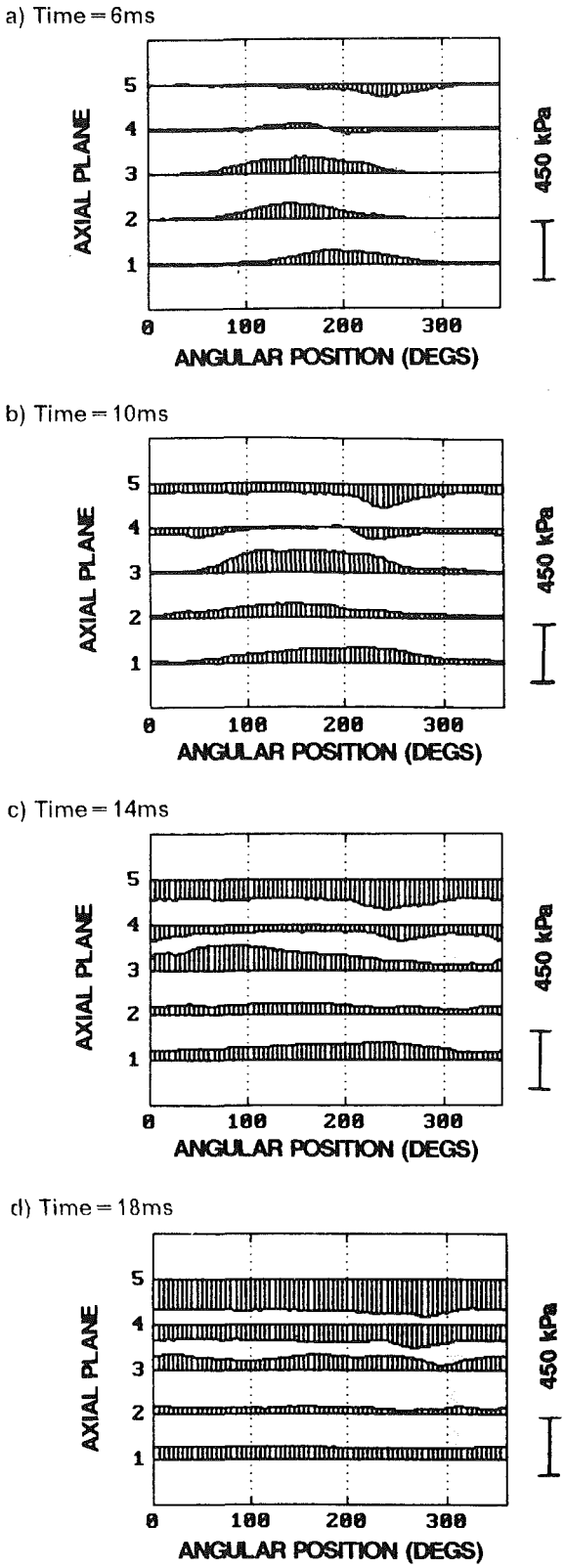

Fig. 16 Static pressure maps at 98 percent speed (ctd): development of stall cell

time histories of the five Kulites at this position are shown beneath to the same scale. The rotating stall continues into the region where the pressure level is dropping severely, and then dies away as the pressure level falls. Note the size of the pressure disturbances: a rise of 150 kPa in the stall cell region from a base level of only 220 kPa.

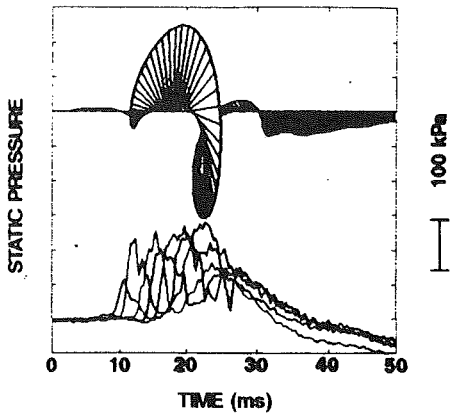

Fig. 17 Stator 4 exit static pressure at 98 percent speed

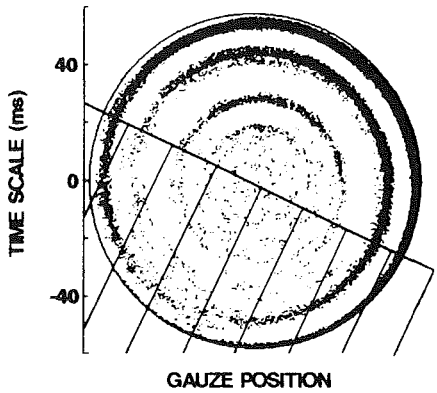

Fig. 18 Stator 4 exit static pressure at 98 percent speed, highpass filtered to 10 Hz, showing effect of inlet distortion gauze

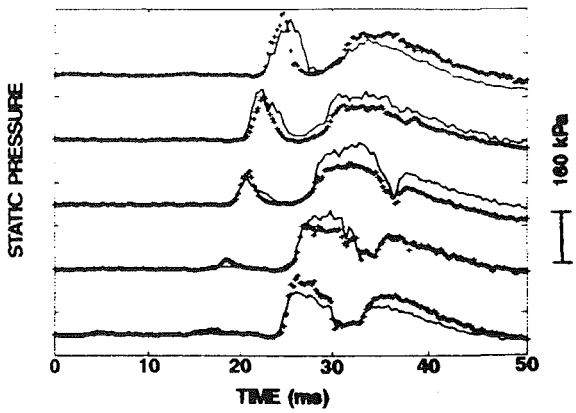

Fig. 19 Stator 4 exit static pressure traces: two events at 98 percent speed

Inlet Distortion at High Speed

Figure 18 shows static pressure above stator 4 during a surge at 98 percent speed, with an inlet distortion gauze fitted over the bottom half of the annulus (the position is marked more accurately on the plot). Time is increasing outward from the center. The spirals represent stall cells rotating at about half compressor speed, as for the undistorted case. The gauze has the effect of attenuating the depth of the stall cell: Each cell diminishes as it enters the region downstream of the gauze, and then grows again in the clean flow area. This is consistent with the observations of Longley and Greitzer (1992). In this case (Fig. 18), the first cell disappears entirely in the gauze region, and a second cell grows that eventually initiates the surge event. Thus the effect of the gauze, apart from degrading

the overall surge pressure ratio, is to provide a stabilizing influence on the compressor, such that the initiation of stall/surge takes place over a longer time scale.

Repeatability

Figure 19 shows time histories of all five Kulite measurements at stage 4 (separated by an arbitrary amount on the y axis) during two separate surge events at 98 percent speed. The first event, shown by the solid lines, was brought about by injecting air at 1000 kPa into the combustion chamber. The second, shown by the crosses, was started by injecting air at 2000 kPa, thus approaching the surge line much more quickly. The matching on the time scales was chosen to give the best fit. To improve the fit further Kulite 3 from the first case was plotted over Kulite 1 from the second, Kulite 4 over Kulite 2, and so on. This shows that stall inception on this engine is not tied to a particular circumferential position, although at lower speeds (where the surge line is approached much more slowly), there was evidence of preferred circumferential positions.

The two sets of traces in Fig. 19 show remarkable agreement. Even some of the minor changes in pressure are mirrored in the two events. Similar repeatability was observed at lower speeds too. The two midspeed events reported earlier, for example, show almost identical patterns of stall inception.

Concluding Remarks

This paper lays out the stall/surge behavior of a compression system in a high-speed axial flow engine. Surge/stall on the VIPER engine is shown to be a deterministic event with clearly defined features varying with speed. Rotating stall is found to exist at the start of every stall/surge event, with the point of inception moving axially rearward with increasing speed in accordance with conventional stage matching principles.

Many of the ideas about surge and stall from compressor rig and theoretical studies have been confirmed: that stall/surge starts with a rotating stall cell of limited circumferential area (Day, 1993), that the compression system ends up in rotating stall or multiple surge depending on speed (Moore and Greitzer, 1985), and that rotating stall is visible at the start of every surge/stall event (Day, 1991; Riess and Bloecker, 1987).

At low speed the "stall point" is identified as a change in the type of rotating stall from multiple cells limited to the front of the compressor to a single cell reaching axially along the entire length of the machine. At intermediate speeds a dichotomy in the stall/surge behavior is seen along the lines of that described by Moore and Greitzer (1985). Up to 81 percent speed the engine settles into stable rotating stall. At higher speeds there is a multiple surge. These events start, however, with an almost identical pattern of stall inception, with initially a single cell of rotating stall starting at the front of the machine. At still higher speeds the inception point moves toward the rear of the machine, and a multiple surge is prevented by flameout.

Acknowledgments

The authors would like to thank Rolls-Royce plc for permission to publish this paper. Thanks are also due to the Department of Trade and Industry and the Defence Research Agency, Pyestock, for part-funding the work.

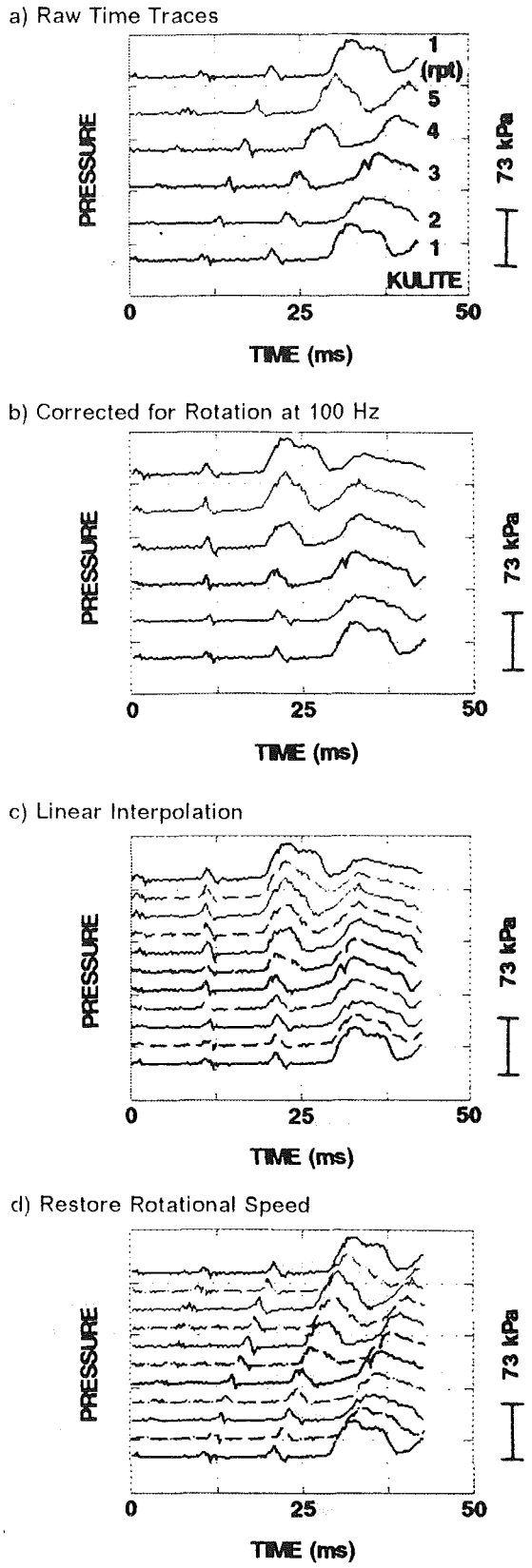

Fig. 20 Static pressure interpolation procedure

References

Day, I. J., 1991, "Axial Compressor Performance During Surge," AIAA Paper No. 91-7098.

Day, I. J., 1993, "Stall Inception in Axial Flow Compressors," ASME JOURNAL OF TURBOMACHINERY, Vol. 115, pp. 1-9.

Longley, J. P., and Greitzer, E. M., 1992, "Inlet Distortion Effects in Aircraft Propulsion System Integration," AGARD Lecture Series LS-183, May.

Moore F. K., and Greitzer, E. M., 1985, "A Theory of Post Stall Transients in Axial Compression Systems, Parts I, II," ASME *Journal of Engineering for Gas Turbines and Power*, Vol. 108, pp. 68-76, 231-239.

Riess, W., and Bloecker, U., 1987, "Possibilities for On-Line Surge Suppression by Fast Guide Vane Adjustment in Axial Compressors," *AGARD Conference Proceedings 421*, 69th Symposium of PEP.

APPENDIX

Description of Graphs

Three types of graph are presented in this paper that require explanation. The first is the map of static pressure around the compressor casing (e.g., Fig. 4*a*). The data for this graph come entirely from the rings of Kulite measurements along the compressor and the single Kulite at compressor exit. Many of the data presented in this paper are related to flow disturbances, which rotate fast around the compressor, but change slowly in time (relative to the time taken for the disturbance to get from one measurement position to the next). In these circumstances the type of interpolation used can be significant.

Figure 20 demonstrates the interpolation procedure used to calculate the static pressure at intermediate circumferential positions for the static pressure maps such as Fig. 4(*a*). Figure 20(*a*) shows the raw pressure traces from the five measurements at rotor 1 inlet at 78 percent speed, spaced evenly on the y axis with the first one repeated at the top. Because the initial disturbance is so sharp, interpolating linearly between the traces at any one time would give a totally erroneous picture, spreading out the disturbance or even showing two peaks instead of one. However, once the rate of rotation of the disturbance is known or has been deduced, the time traces can be corrected for the rotation as in Fig. 20(*b*). This procedure allows a linear interpolation to be performed (Fig. 20*c*) along a direction in which the disturbance is changing only gradually. Figure 20(*d*) shows the raw and interpolated traces with the rotational speed restored. The static pressure maps such as Fig. 4(*a*) use data interpolated in this way at 5 deg intervals around the compressor at each of the five measurement planes.

It is easier to trace the development of the disturbances if they are kept stationary on the x axis for successive time steps. This was achieved by moving the origin of the x axis between plots around the annulus at the same (constant) rate of rotation as used in the interpolation procedure. A circumferential offset was then chosen for each speed to position the disturbance in the center of the picture, although changes in the rotational speed of a stall cell as it develops mean that over a period of time it does move off center. Changes in rotational speed also affect the quality of the interpolation. Once the disturbance gets circumferentially large, however, the effect of the poorer interpolation is quite small.

The second type of graph is seen in Fig. 6. The same type of interpolation is used as for the static pressure maps, although in this case for only one measurement position. A polar plot is produced, where time increases radially, and the circumferential position reflects the true geometry of the compressor, viewed from the front. A high pressure level is represented by a high density of points on the plot. The pressures are measured relative to a datum at the start of the event, with only positive values shown. Plotted in this way, a positive pressure disturbance moving around the compressor with time shows itself as a spiral. The inner edge of the spiral represents the leading edge of the disturbance as it moves around the compressor, and the outer edge is the back of the disturbance.

The third type of graph is used for Figs. 8 and 17. In these figures the first (circumferential) harmonic of the pressure signal is plotted in a complex plane perpendicular to a time axis inclined into the page at an angle of 20 deg. For a single-cell disturbance this means, broadly speaking, that the "spokes" within the spiral shape are of a size proportional to the size of the pressure disturbance, and point along the direction of maximum pressure. Thus a single-cell rotating stall, for example, where the direction of maximum pressure moves around the annulus with time, would be seen as a spiral around the zero level. The individual Kulite measurements are shown underneath the spirals to the same scale (though shifted to an arbitrary level). In order to produce smooth spirals, the data were filtered to roughly once/rev frequency. This process introduces a very slight delay to the spiral plots relative to the Kulite measurements.

Note the difference in time scales between Figs. 8 and 17. The former plots data over several repeating surges, whereas the latter plots data for a single surge event. The "spokes" in Fig. 8 are 1 ms apart. In Fig. 17 they are 1/4 ms apart.

Active Stabilization of Rotating Stall in a Three-Stage Axial Compressor

J. M. Haynes

G. J. Hendricks

A. H. Epstein

Gas Turbine Laboratory,
Massachusetts Institute of Technology,
Cambridge, MA 02139

A three-stage, low-speed axial research compressor has been actively stabilized by damping low-amplitude circumferentially traveling waves, which can grow into rotating stall. Using a circumferential array of hot-wire sensors, and an array of high-speed individually positioned control vanes as the actuator, the first and second spatial harmonics of the compressor were stabilized down to a characteristic slope of 0.9, yielding an 8 percent increase in operating flow range. Stabilization of the third spatial harmonic did not alter the stalling flow coefficient. The actuators were also used open loop to determine the forced response behavior of the compressor. A system identification procedure applied to the forced response data then yielded the compressor transfer function. The Moore–Greitzer two-dimensional stability model was modified as suggested by the measurements to include the effect of blade row time lags on the compressor dynamics. This modified Moore–Greitzer model was then used to predict both the open and closed-loop dynamic response of the compressor. The model predictions agreed closely with the experimental results. In particular, the model predicted both the mass flow at stall without control and the design parameters needed by, and the range extension realized from, active control.

Introduction

Axial flow compressors suffer from inherent hydrodynamic instabilities known as surge and rotating stall. Surge is a one-dimensional mass flow disturbance involving the entire compression system, while rotating stall has a two- or three-dimensional structure rotating about and local to the compressor blading. Both are large-amplitude disturbances, disrupting compressor operation and imposing large structural loads, and so are unacceptable in routine compressor operation.

A useful theoretical model of compressor hydrodynamic stability started with Emmons et al. (1955) and has evolved through Moore and Greitzer (1986). In this analysis, surge and rotating stall are simply the mature form of the natural oscillatory modes of the compression system. Surge is the lowest (zero) order mode and rotating stall is the higher order modes. This model predicts that these hydrodynamic disturbances start at very small amplitude (during which time the modes may be considered as linear and decoupled) but quickly grow into their large-amplitude form, surge, and rotating stall (which exhibit nonlinear behavior and whose dynamics are coupled). Thus, the stability of the compressor is equivalent to the stability of these small-amplitude waves that exist prior to stall. Garnier et al. (1991), McDougal et al. (1990), and Etchevers (1992) presented experimental data showing the existence of these low-amplitude waves and their evolution into stall in several axial compressors. More recently, Paduano and Gysling (1992) have shown that the details of the time evolution of the disturbances, especially the wave form, is quite sensitive to the shape of the compressor pressure rise versus mass flow characteristic.

Epstein et al. (1989) first suggested that surge and rotating stall could be prevented by using active feedback control to damp the hydrodynamic disturbances while they are still at small amplitude. Aside from reducing the control authority required, control of the fluid disturbances while they still are at very low amplitude permits incipient surge and rotating stall to be treated and controlled separately (since their behavior will be linear and decoupled). Active suppression of surge was subsequently demonstrated experimentally on centrifugal compressors by Ffowcs Williams and Huang (1989) and Pinsley et al. (1991), and on an axial compressor by Day (1993). Paduano et al. (1993a) demonstrated active suppression of rotating stall in a single-stage low-speed compressor. By damping the small amplitude traveling waves rotating about the annulus prior to stall, they increased the stable flow range of the compressor by 25 percent.

The data of Paduano et al. provide strong experimental evidence that at least the qualitative structure of the hydrodynamic stability theory is appropriate for this type of compressor and that, indeed, rotating stall can evolve from small-amplitude traveling waves since damping these waves prevents the formation of rotating stall. In those experiments, the traveling waves were decomposed into separate spatial harmonics with each harmonic controlled individually. This showed that

Contributed by the International Gas Turbine Institute and presented at the 38th International Gas Turbine and Aeroengine Congress and Exposition, Cincinnati, Ohio, May 24–27, 1993. Manuscript received at ASME Headquarters March 17, 1993. Paper No. 93-GT-346. Associate Technical Editor: H. Lukas.

Table 1 MIT three-stage axial compressor design parameters

Tip Diameter (mm.)	610
Hub-to-Tip Ratio	0.88
Design Average Reaction	0.75
Design Flow Coefficient	0.59
Pressure Rise Coefficient (@design)	2.03
Efficiency (@design)	84.3%
Stalling Flow Coefficient	0.460

	No. of Blades	Chord (mm.)	Camber (degrees)	Stagger (degrees)	Tip Clearance* (mm)	Leading Edge Blade Angle* (degrees)	Trailing Edge Blade Angle* (degrees)
Inlet Guide Vanes	125	20	11.0	8.1		0	10.0
IGV to CV Gap		6					
Control Vanes	12	81	0.0	8.1		8.1	8.1
CV to R1 Gap		13					
Rotor 1	54	45	17.0	42.8	0.97	50.0	41.0
R1 to S1 Gap		20					
Stator 1	85	31	27.0	11.0	0.81	18.0	-1.0
S1 to R2 Gap		20					
Rotor 2	55	45	18.0	43.5	0.94	54.5	36.5
R2 to S2 Gap		20					
Stator 2	88	31	25.0	12.0	0.94	27.5	2.5
S2 to R3 Gap		20					
Rotor 3	49	51	20.0	44.6	0.89	58.0	38.0
R3 to S3 Gap		18					
Stator 3	90	31	53.0	5.5	0.86	36.5	-17.0

*Measured by Gamache CV = Control Vane IGV = Inlet Guide Vane

the linear and decoupled behavior predicted by the theory did indeed occur. The theory, however, predicted that all spatial harmonics go unstable at the same mass flow, while the experiment showed that the lower the harmonic, the higher the mass flow at instability. This behavior has an important implication for active control since it means that all spatial harmonics need not be simultaneously controlled in order to realize an increase in compressor operating range, greatly simplifying the physical realization of such a control system.

In the work presented herein, we extend the experimental single-stage work of Paduano by applying the same active control techniques to a three-stage, low-speed research compressor. Both open-loop forced response and closed-loop actively stabilized data are presented. We also extend the two-dimensional, incompressible hydrodynamic stability theory of Moore and Greitzer to include nonideal effects such as time lags associated with the development of viscous losses and deviations. These modifications have the effect of separating in mass flow the inception of the instabilities of individual spatial harmonics as observed by Paduano. We then show that this theory does an excellent job in quantitatively predicting both the open and closed-loop dynamic behavior of the three-stage compressor. This includes predicting the natural stall point (inception of rotating stall without control) and predicting both the controller parameters required and the improvement in mass flow range gained from active control. Finally, we make some comments on the utility of an actively stabilized machine for exploration of compressor dynamics.

Experimental Apparatus. A 0.6 m dia., three-stage low-speed axial research compressor was adapted for use as a test article in these experiments. Work in this rig was previously reported by Gamache (1985), Lavrich (1988), and Garnier et al. (1991). The blading details are given in Table 1. The control scheme adopted was that used by Paduano et al. in which the traveling waves of axial velocity are detected by a circumferential array of hot wires just upstream of the compressor and individually actuated vanes upstream of the rotor are used to generate the rotating disturbance structure required for control. The test compressor was appropriately modified by moving the inlet guide vanes (IGVs) sufficiently far upstream so that control vanes could be placed between the IGVs and the first rotor. In this arrangement, the inlet guide vanes produce the mean swirl while the unchambered control vanes provide the time and circumferential variations needed to stabilize the compressor. Each of the twelve control vane assemblies con-

Nomenclature

A_n = coefficient of nth spatial harmonic of flow coefficient perturbation
L = total pressure loss
δL = perturbation in total pressure loss
n = spatial harmonic number
P = static pressure
P_t = total pressure
δP = pressure perturbation
r = compressor annulus mean radius
R = feedback gain
s_n = $(\alpha_n - i\omega_n)r/U$
t = time
U = rotor linear velocity at the mean radius
Z = complex gain $= Re^{i\beta}$
α = disturbance growth rate
β = feedback phase angle
γ = control vane stagger angle
θ, ϑ = circumferential coordinate
λ = inertia parameter for compressor rotors
μ = inertia parameter for compressor
ρ = fluid density
τ = characteristic time
$\bar{\tau}$ = nondimensional characteristic time
ϕ = flow coefficient = axial velocity/wheel speed
$\delta\phi$ = flow coefficient perturbation
ψ = total-to-static pressure rise
ψ_t = torque coefficient = torque/(annulus area$\cdot\rho U^2 r$)
ω = disturbance frequency

Subscripts

e = exit
i = inlet
ideal = ideal (Euler's equation)
IGV = inlet guide vane
isen = isentropic
n = harmonic number
r = rotor
s = stator
1 = upstream of IGVs
2 = downstream of control vanes

Superscripts

$\bar{}$ = time average
$\tilde{}$ = spatial Fourier coefficient

sisted of NACA 65-0009 cast epoxy airfoils, cantilevered from a hollow core, high torque-to-inertia DC servo motor (Fig. 1). Instrumentation included circumferential hot wire, total pressure, and static pressure arrays mounted throughout the compressor (Fig. 2). Additional measurements consisted of rotor speed and torque, average compressor mass flow (from a venturi), and rig housekeeping. The net measurement precision of the flow coefficient (ϕ), the pressure rise coefficient (ψ), the torque coefficient (ψ_t), and the rotor speed were all ± 0.3 percent or better. Control vane angles were measured to ± 0.05 deg. On the stable portion of the compressor characteristic near the point of instability, the signal-to-noise ratios of the first three spatial harmonics were 46 dB, 29 dB, and 23 dB, respectively.

The control system hardware is illustrated in Fig. 3. The signals from the eight hot-wire anemometers mounted about the compressor circumference are filtered by four-pole Bessel filters set at 1000 Hz, which is 25 times the shaft frequency, ω_s. The signals are then digitized by a 16-bit A/D system in an 80486 computer, which implements the control laws and outputs the commanded control vane positions to individual vane position control systems. These consist of closed loop, PID position servos, one for each channel, feeding 350 W servo amplifiers, which drive the DC servo motors. Optical encoders mounted on each motor provide a vane position signal to the position servos. The vane servo loops operated at 50 ω_s (2000 Hz), while the entire control loop in the computer was operated at 12.5 ω_s (500 Hz). The control vane system dynamic response was determined by driving the vane array with a pseudo-random binary signal with a minimum frequency of 2.5 ω_s (100 Hz), while the compressor was operated near its stall point. These measurements showed that the transfer function of the flow actuation system could be modeled quite closely by two second-order systems in series with a natural frequency of 170 Hz and a damping ratio of 0.35. This yields a frequency response flat to ± 3 dB up to 3 ω_s (120 Hz). The first spatial harmonic of rotating stall is approximately 0.3 ω_s (12.5 Hz) in this compressor.

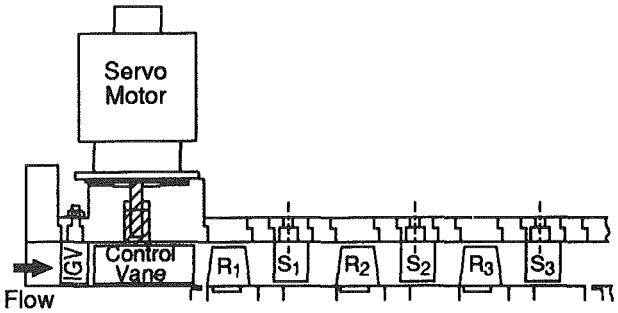

Fig. 1 Three-stage compressor arrangement with individually activated high-speed control vanes

The rotating stall control algorithms were similar to those used by Paduano. At each time step, the anemometer data are digitized and linearized into axial velocity; a discrete spatial Fourier transform is then used to decompose the eight velocity measurements into spatial harmonics (only modes 1, 2, and 3 were examined here); a separate control law is then implemented on each spatial harmonic; and then an inverse discrete Fourier transform on the spatial harmonics is taken to yield individual blade position commands to each of the twelve control vane position control systems.

A simple proportional control law was implemented in these experiments. For each spatial harmonic n, the change in control vane stagger angle, γ, is proportional to the measured change in axial velocity, V.

$$|\delta\gamma_{\text{vane}}|_n = Z_n V_n \tag{1}$$

where Z_n is the complex constant of proportionality

$$Z_n \equiv R_n e^{i\beta_n} \tag{2}$$

R_n represents the gain of the controller, while β_n is the phase angle between the measured velocity perturbation and commanded stagger angle change for each harmonic. With this harmonic by harmonic control scheme, β_n is a spatial lead that can account for both lags in the control system and the dynamics of the compressor. The total change in vane stagger angle is then simply the sum of the deflections calculated for the individual harmonics being studied (1, 2, or 3 in this case). Paduano established the optimum gain and phase for each harmonic empirically. Here, as will be shown later, theory can be used to calculate the optimum feedback gain and phase with results closely matching those found experimentally.

Steady-State Compressor Performance. In addition to the active stabilization experiments, steady-state measurements were taken both to assess the compressor operating characteristics and to establish the aerodynamic parameters needed as input to the analytical modeling and control law design. These included measurements of the speedline shape, the torque efficiency, and the influence of control vane stagger angle (γ)

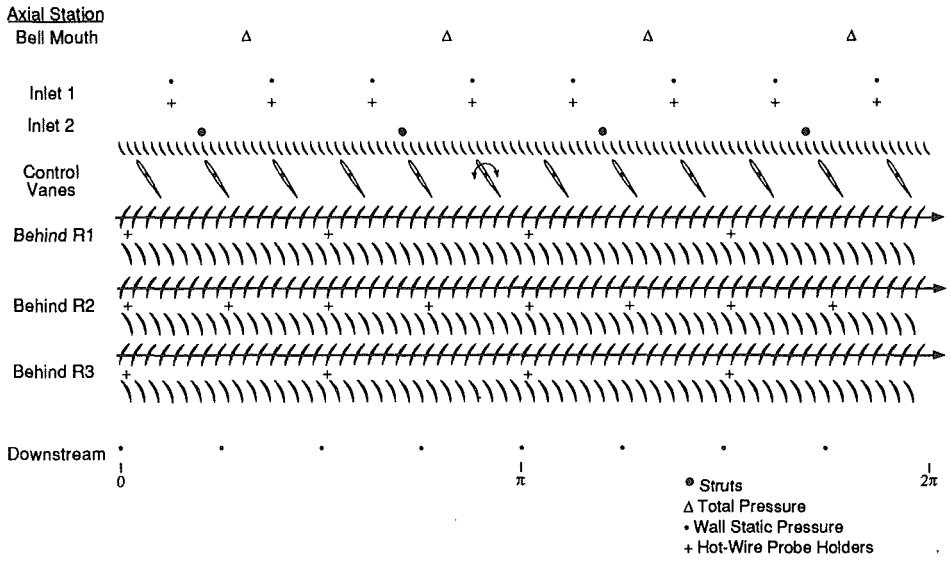

Fig. 2 Layout of compressor blading and instrumentation

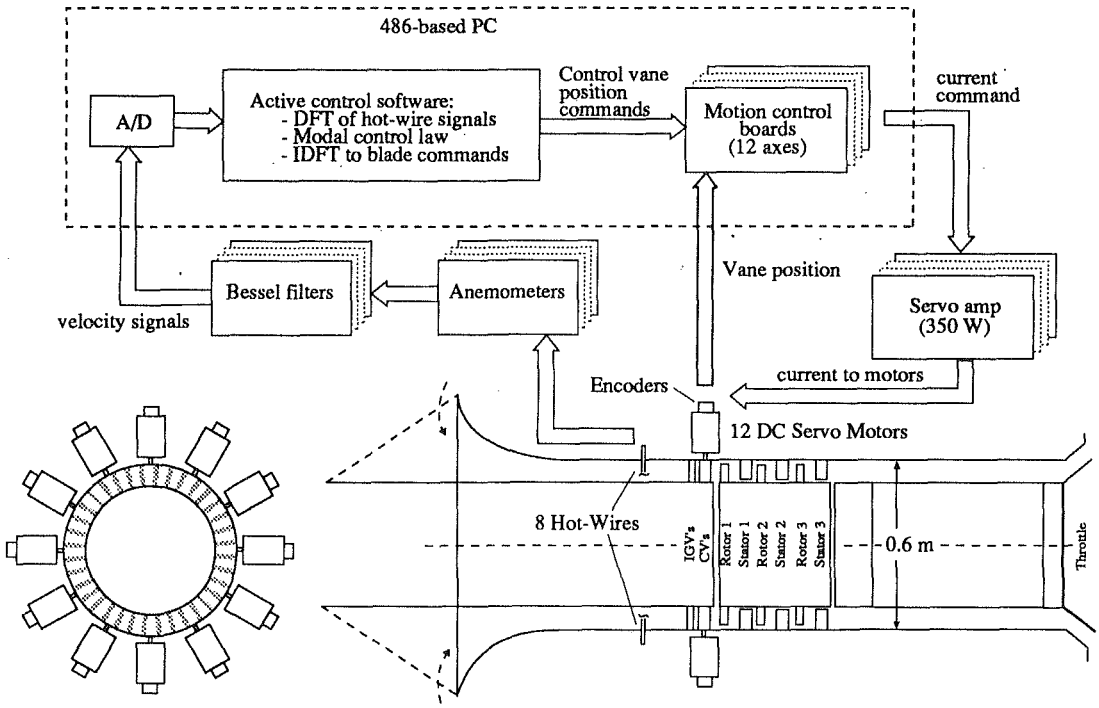

Fig. 3 Closed-loop control feedback path

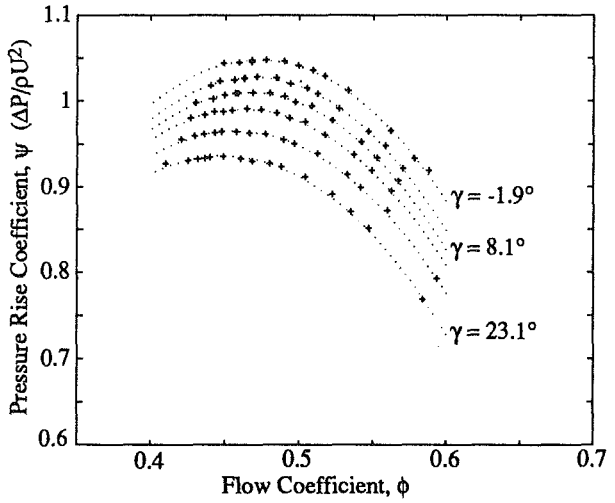

Fig. 4 The influence of uniform control vane stagger angle (γ) on the compressor characteristic at 5 deg intervals of γ

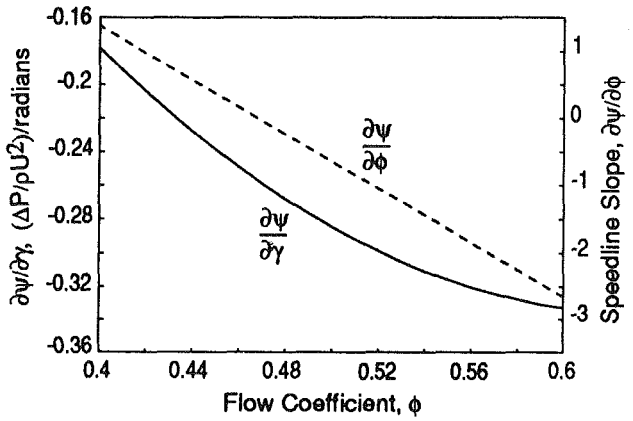

Fig. 5 Variation of speedline slope ($\partial\psi/\partial\phi$) and control vane angle pressure rise influence ($\partial\psi/\partial\gamma$) measured for the three-stage compressor

on the nondimensional pressure rise coefficient (ψ). Specifically, the $\partial\psi/\partial\gamma$ values required by the theory were derived from measurements of the steady-state influence of vane stagger on compressor pressure rise, as illustrated in Fig. 4. The resultant values of $\partial\psi/\partial\gamma$ and $\partial\psi/\partial\phi$ are shown in Fig. 5. Data in the normally unstable low flow area were taken while the compressor was stabilized with feedback control.

Compressor Performance With Active Stabilization. Active feedback stabilization of the first two spatial harmonics was implemented as described above. The results using the optimum feedback gain and phase found are illustrated on the speedline in Fig. 6. Control of the first harmonic yields a range increase of 3 percent, while control of the first and second harmonics together increase that to 8 percent. At this point, the speedline slope is 0.9. The compressor torque efficiency continues to decrease smoothly in the actively stabilized region.

It is useful to examine the time history of the transient into stall as an aid in understanding the instability evolution process. The time history of the axial velocity measured by the eight sensors about the compressor circumference is shown in Fig. 7 for the unstabilized compressor. Here, the smooth growth of the first spatial harmonic wave is quite apparent for the 15 rotor revolutions illustrated before stall (it is highlighted by the parallel dotted lines in the figure). When the first spatial harmonic is actively suppressed (Fig. 8), the stall inception process is different in that it occurs at a lower mass flow and that the low-amplitude waves growing prior to stall have one half the wavelength, as can be readily seen by comparing Figs. 7 and 8. The second spatial harmonic goes unstable now and triggers the rotating stall when the first harmonic is stabilized.

A useful tool for examining the wave growth is a discrete spatial Fourier transform of the axial velocities measured about the compressor annulus at each instant in time. This yields a complex Fourier coefficient for each spatial harmonic, the magnitude of which represents the instantaneous strength of that spatial wave, and the phase of which is a measure of the instantaneous angular position of the wave. Thus, a straight

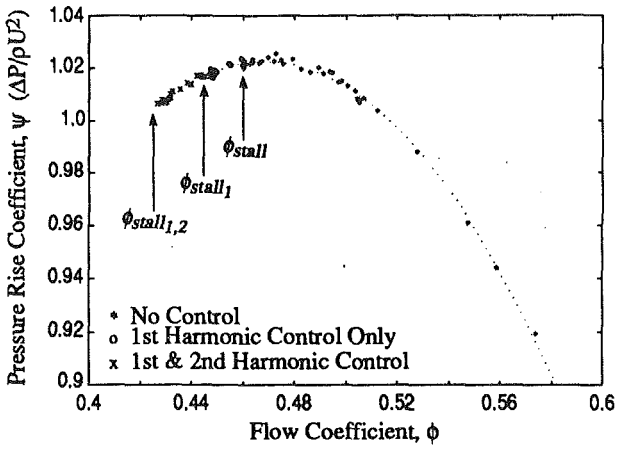

Fig. 6 Active stabilization of the first and second spatial harmonics decreases stalling mass flow by 8 percent

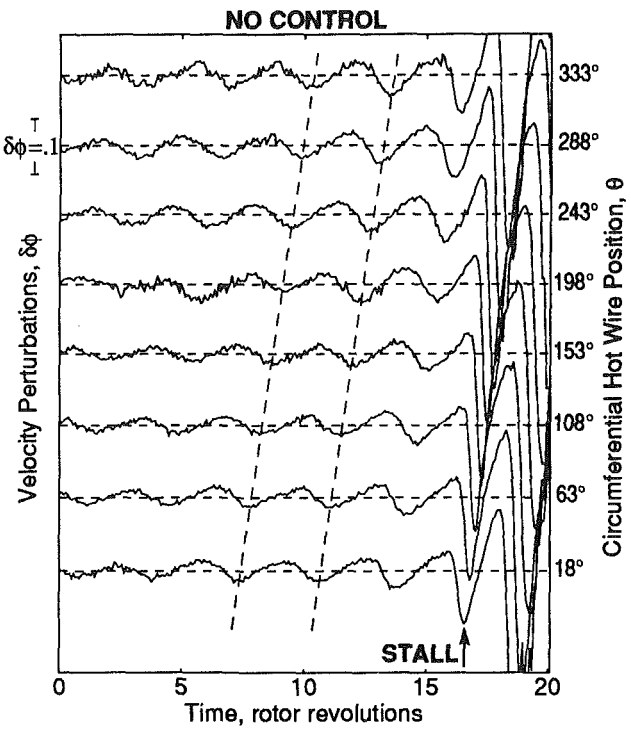

Fig. 7 Stall inception flow field around compressor annulus at midspan, measured upstream of the IGVs when $\phi = 0.46$, with no control

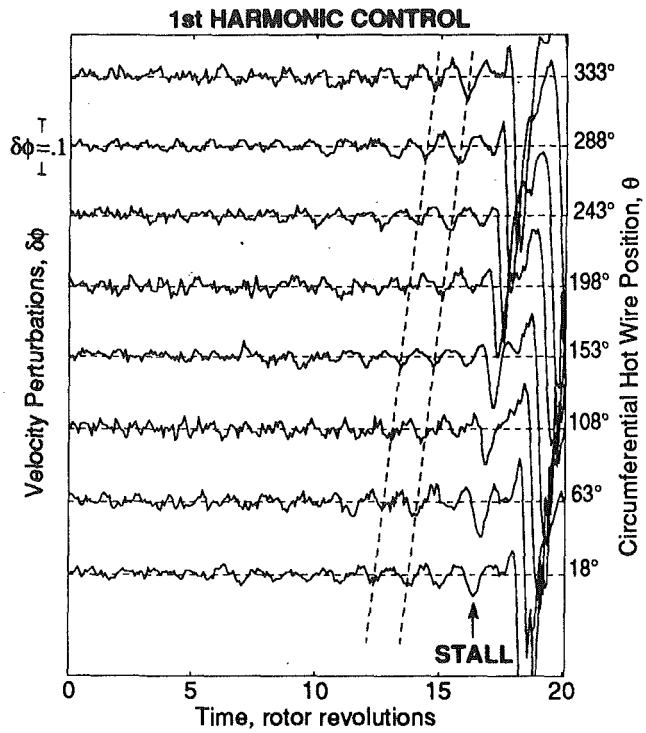

Fig. 8 Stall inception flow field around compressor annulus at midspan during first harmonic control, measured upstream of the IGVs when $\phi = 0.45$

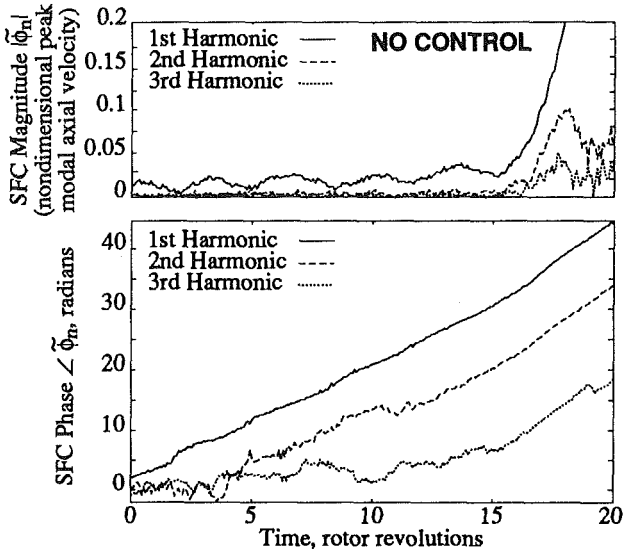

Fig. 9 Magnitude and phases of the first three spatial Fourier coefficients (SFC) calculated from the stall inception flow field at midspan (calculated from the data of Fig. 7)

line phase history indicates that the wave is traveling at constant angular velocity. This behavior can be seen in Fig. 9, which presents the spatial Fourier coefficients calculated from the unstabilized data of Fig. 7. The first harmonic position does change at a constant rate for some 15 revolutions before stall. (Note that the compressor is unwrapped here so that 2π radians represents one revolution of the wave, 4π radians two revolutions, and so on.) Examination of the magnitudes of the first three spatial harmonics in Fig. 9 shows that the first is the strongest and that it grows to large amplitude before the second and third do. This uncontrolled compressor has a single lobed stall (primarily first harmonic) at this mass flow. When the first harmonic is actively stabilized, however, the Fourier coefficient of the second harmonic is strongest prior to stall (Fig. 10). Once stall starts, though, the first harmonic quickly dominates. Indeed, examination of the time history in Fig. 8 shows that once the fully developed rotating stall is established, it is a single lobed stall.

A time history of the compressor under first and second harmonic control is shown in Fig. 11 and the corresponding spatial Fourier coefficients in Fig. 12. Here, the instability appears to grow from both the first and second harmonic, with the third harmonic weaker. Again, the fully developed stall is primarily single lobed. Although the third harmonic does not appear to play a dominant role in Fig. 12, simultaneous stabilization of the first three harmonics was implemented with results shown in Figs. 13 and 14. No increase in

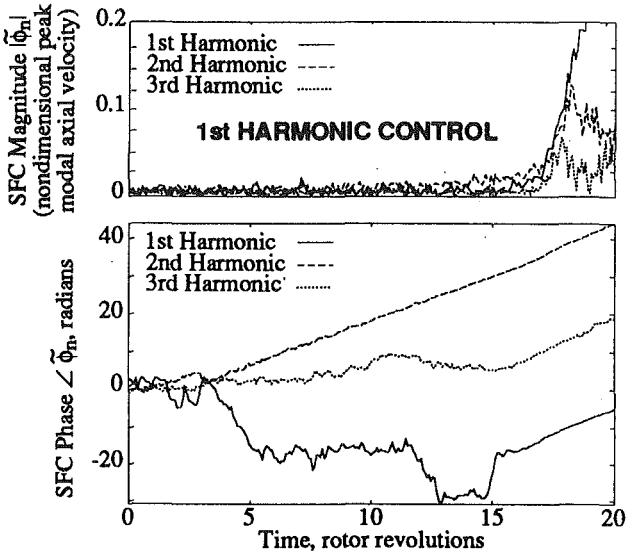

Fig. 10 Magnitude and phases of the first three spatial Fourier coefficients calculated from the stall inception flow field at midspan during first harmonic control (calculated from the data of Fig. 8)

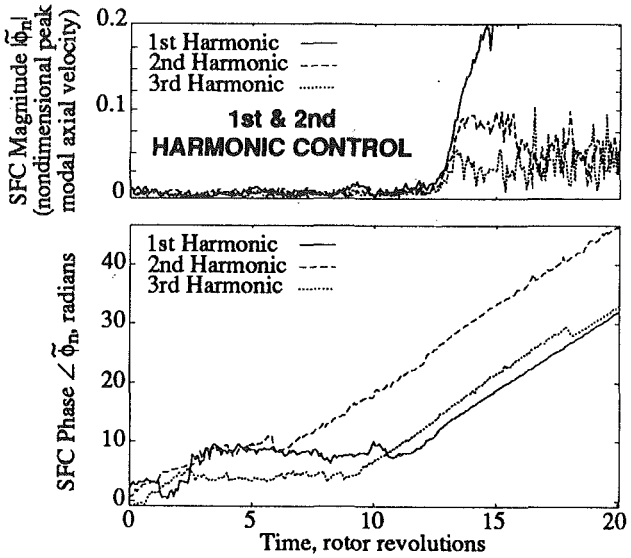

Fig. 12 Magnitude and phases of the first three spatial Fourier coefficients calculated from the stall inception flow field at midspan during optimal first and second harmonic control (calculated from the data of Fig. 11)

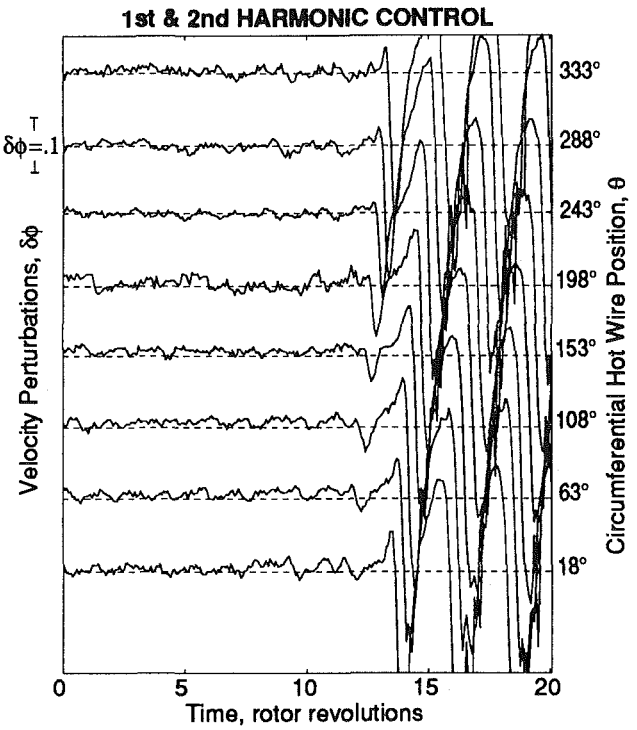

Fig. 11 Stall inception flow field around compressor annulus during optimal first and second harmonic control, measured upstream of the IGVs when $\phi = 0.43$

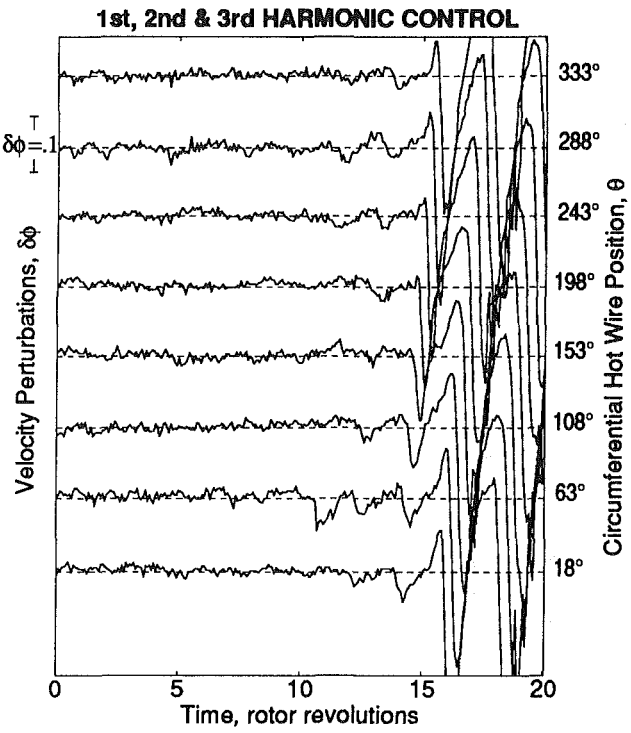

Fig. 13 Stall inception flow field around compressor annulus during optimal first, second, and third harmonic control, measured upstream of the IGVs when $\phi = 0.43$

stable flow range is achieved over control of only the first and second harmonics. The relative roles played by the three spatial harmonics is not clear from the data in Fig. 14, although the first harmonic does appear to grow first.

We have now presented experimental data showing that a low-speed multistage axial compressor can be actively stabilized and illuminating the stall inception processes in this machine. We will now use these data as an aid in refining an analytical model of instability inception and show both how this model can quantitatively predict many details of stall inception and how the model can be used to design an active control system.

Modeling

The two-dimensional, incompressible theory formulated by Moore and Greitzer to describe rotating stall implies that, at the inception of the instability, small-amplitude traveling waves develop in the compressor annulus, grow in magnitude, and eventually develop into rotating stall cells. In this analysis of instability inception, an arbitrary axial velocity disturbance is decomposed into its Fourier spatial harmonics, which can then be analyzed independently, since the equations describing the evolution of the instability are linear. If the compressor is assumed to operate in a quasi-steady manner, i.e., pressure

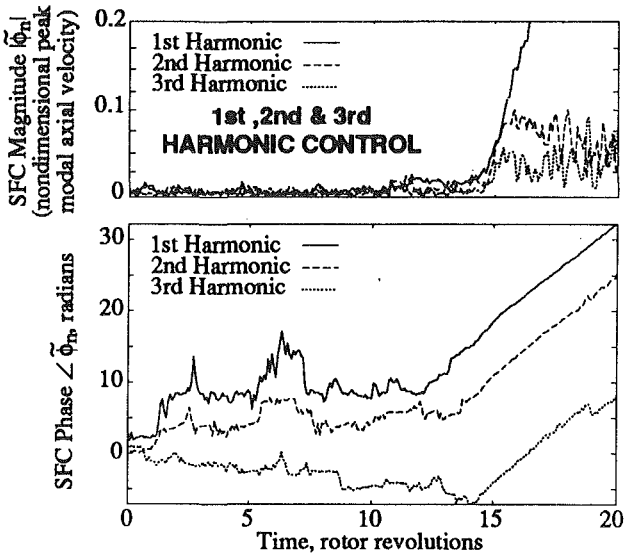

Fig. 14 Magnitude and phases of the first three spatial Fourier coefficients calculated from the stall inception flow field at midspan during optimal first, second, and third harmonic control (calculated from the data of Fig. 13)

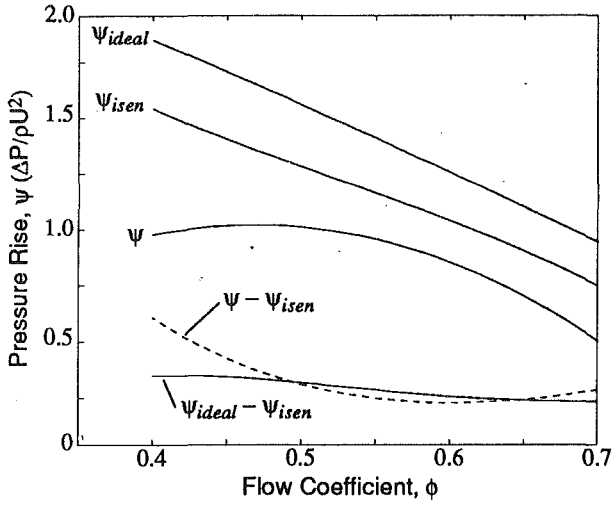

Fig. 15 The difference between the ideal pressure rise (ψ_{ideal}) and the isentropic pressure rise (ψ_{isen}) is due to deviation, while the difference between the measured pressure rise (ψ) and ψ_{isen} is due to total pressure losses

rise is a function of flow coefficient only, this model predicts that all the spatial harmonics of the flow coefficient perturbation become unstable at the operating point where the total-to-static pressure rise characteristic (ψ versus ϕ) becomes positively sloped. Disturbances are damped where the characteristic is negatively sloped, and amplified where the characteristic is positively sloped, with the growth or decay rate of the perturbation being determined by the magnitude of the slope.

Contrary to the assumptions of the above model, airfoils do not respond instantaneously to changes of incidence, and it has been observed in experiments (Nagano et al., 1971; Mazzawy, 1977) that the pressure rise across a compressor does not respond instantaneously to variations in flow coefficient. As will be shown, this finite response time of the compressor pressure rise has a stabilizing effect on flow perturbations, stabilizing higher harmonics to a greater extent than lower ones. When the quasi-steady assumption in the model is relaxed, and allowance is made for finite blade-passage flow response times, the spatial harmonics becoming unstable sequentially, with higher harmonics become unstable at larger positive slopes of the compressor total-to-static pressure-rise characteristic (i.e., lower flow coefficients). This is the behavior observed in the experiments on both the three-stage compressor being discussed, and previous experiments on a single-stage compressor (Paduano, 1991; Paduano et al., 1993a).

In the following sections, the model is extended to include the finite response time and the results are compared to experimental data.

Accounting for Blade Row Pressure Losses, Deviation, and Blockage

Current two-dimensional models of compressor stability like that of Moore and Greitzer are quite simplified. In these analyses, the compressor is described only in terms of the slope of its pressure rise–mass flow characteristic and the inertia of the fluid in the blade rows. The effects of physical phenomena important to the compressor designer such as stagnation pressure losses, deviations, blockage, and characteristic airfoil response times had not been treated explicitly in these models since few data were available to evaluate their influence on compressor stability. The actively stabilized compressor rig is a tool with which such data may be acquired so that we can now evaluate the relative importance of these phenomena and modify the analysis accordingly.

To start, we will quantify the effects of deviation, blockage, and airfoil unsteady response on the measured compressor pressure rise. In an ideal compressor with none of the above, the ideal pressure rise (ψ_{ideal}) can be calculated with the Euler equation and decreases monotonically with increasing flow coefficient, as can be seen in Fig. 15. The difference between this ideal pressure rise and the actual measured one (ψ) is due to the combined effects of lack of flow turning (due to both deviation as specified in Carter's rule and blockage, which is the result of viscous effects) and total pressure losses (viscous dissipation in all compressors plus shock losses in transonic machines). To separate the two effects, consider the case when the compressor is operating isentropically so that all of the shaft work goes into stagnation pressure rise. This isentropic stagnation pressure rise (ψ_{isen}) can be calculated from the measured shaft torque, ψ_t, as:

$$\psi_{isen} = \left[\frac{\psi_t}{\phi} - \frac{\phi^2}{2\cos^2\epsilon_e}\right] \tag{3}$$

where ϵ_e is the exit flow angle from the last stator. The isentropic pressure rise characteristic of this compressor is shown in Fig. 15. The loss in pressure rise represented by the difference between the ideal (ψ_{ideal}) and the isentropic (ψ_{isen}) pressure rises must be due to lack of turning (i.e., deviation and blockage). The loss in pressure rise represented by the difference between the isentropic rise (ψ_{isen}) and the measured rise (ψ) must be due to total pressure losses (viscous dissipation). These are illustrated in Fig. 15.

The important information in Fig. 15 is that, for the three-stage compressor considered here, the total pressure losses due to dissipation, ($\psi - \psi_{isen}$), increase significantly with reduction of flow coefficient over the range of interest (to the left of the peak of the measured characteristic). On the other hand, the loss due to the deviation ($\psi_{ideal} - \psi_{isen}$) is relatively flat over this range. Thus, we would expect the influence of dissipation on compressor stability to be considerably larger than that of deviation. Both were modeled and, in fact, the influence of deviations proved negligible so that in the following sections we will only discuss the role of dissipation. We have not studied the generality of this observation to all compressors but have merely exploited it to simplify the modeling (more details may be found in Haynes, 1993). We note, however, that Longley

and Hynes (1990) reported deviation to be more important in their compressor than the one studied here.

Modeling Compressor Transient Behavior

Dissipation influences compressor stability because of the time lags the viscous flow introduces. An instantaneous change in mass flow (axial velocity) abruptly changes the compressor blading angle of attack. The flow over the blades does not change instantaneously, however; rather it evolves to the new steady state over a time period on the order of the bulk convection time through the blade rows. Emmons et al. (1955) suggested modeling the evolution of losses as a first-order lag. For the step reduction in ϕ, the change in stagnation pressure loss δL is then given by:

$$\delta L_{\text{transient}} = \delta L_{\text{quasi-steady}}(1 - e^{-t/\tau}) \tag{4}$$

where τ is the characteristic time.

Since the instantaneous stagnation pressure losses reflect the time lags associated with the flow within the compressor blade passages, the compressor pressure rise must as well. To illustrate this point, consider an instantaneous reduction in flow coefficient when the compressor is operating on a positively sloped portion of the characteristic (Fig. 16). Immediately after the reduction in flow coefficient, the stagnation pressure loss is at its initial value, so that the actual pressure rise follows as a curve parallel to the isentropic pressure rise (ψ_{isen}), as shown in Fig. 16. The transient slope is thus less than the steady-state one, so that the compressor is more stable than it is in steady state at the same mass flow. In the operating range where the compressor characteristic slope is positive (and the compressor unstable), the transient slope can be negative (and thus the compressor stable) if the transient time constant is low enough (i.e., if the reduced frequency is high). This has important implications for the inception of rotating stall since the stability of disturbances is dependent on the effective slope of the pressure rise characteristic. Specifically, inclusion of the time lag can increase compressor stability.

Compressor Stability Modeling

The analytical model used in this study is an extension to the one described by Moore (1984), Hynes and Greitzer (1987), and Epstein et al. (1989). The analysis is two dimensional, which is appropriate since the machine under consideration has a high hub-to-tip ratio. The inlet flow field is undistorted (uniform inlet total pressure), and the inlet and exit ducts are assumed long, so that end effects, i.e., reflection and scattering of the disturbance wave from the ends, are not important. In addition, the tip speed of the compressor is assumed to be low enough for the flow field to be considered incompressible.

In the analysis an arbitrary flow perturbation, $\delta\phi$, is assumed to be of the form:

$$\delta\phi = \sum_{n=1}^{\infty} A_n e^{s_n t} e^{in\vartheta}, \tag{5}$$

where

$$s_n = \frac{(\alpha_n - i\omega_n)r}{U} \tag{6}$$

The rotation rate of the nth spatial harmonic nondimensionalized by the rotor rotational speed is represented by $\omega_n r/nU$, while $\alpha_n r/U$ represents the nondimensionalized growth rate of the nth spatial harmonic. When the above form of the flow coefficient perturbation is substituted into the differential equations describing the dynamics of the fluid in the compression system, the analysis yields an eigenvalue problem in s_n, with the growth and rotation rates of each spatial harmonic determined from the solution to the eigenvalue problem. If the real part of s_n is negative, the spatial harmonic is damped,

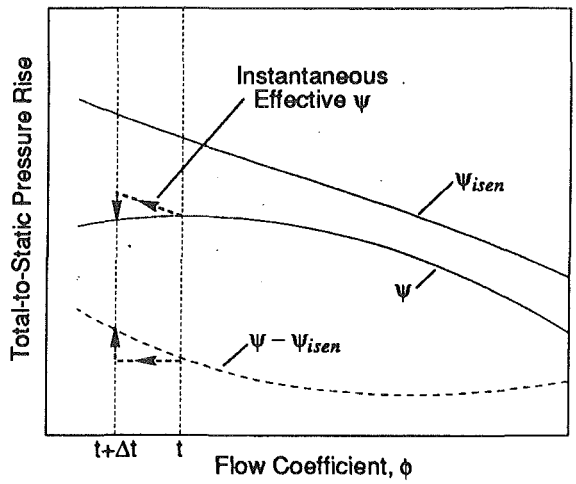

Fig. 16 Compressor time lags temporarily decrease the effective slope of the compressor characteristic during a transient, as illustrated starting at time, t

and the compressor operation is stable; if the real part of s_n is positive, the spatial harmonic grows exponentially, so that the compressor is unstable. Details of the extension of the stability modeling to account for finite compressor response time can be found in Appendix A.

The analysis must then be extended to include the effects of active feedback control. Control is implemented by the temporal and spatial variation of the control vane stagger angles in response to a measured inlet axial velocity distribution. The spatial variation in the control vane stagger angle has two effects on the compressor inlet flow. The first is an inlet flow angle variation to the first rotor with an associated variation in pressure rise. The second is a variation in flow blockage in the compressor, which is a consequence of the variation in blade passage geometry around the annulus of the compressor. Paduano et al. (1993a) developed a semi-actuator disk model of the control vanes that accounts for both of these effects. In the present study, this vane model is retained, but the compressor model is extended to account for the finite response time of the compressor pressure rise to both axial velocity fluctuations and control vane deflections. The modeling of the actuation system includes the time delay between velocity sensing and the control command to the guide vane servo-motors, and the dynamic response of the control vane/servo-motor assembly to the controller command. To illustrate the analysis technique, a derivation of the model with a simplified version of the controller and actuator dynamics is given in Appendix B.

System Identification of Compressor Dynamics

Paduano showed that the response of compressor flow perturbations to control vane deflections can be expressed in transfer function form as

$$\frac{\delta\phi_1}{\delta\gamma} = \frac{(iG_n s + A_n + iB_n)(a_{n1} + a_{n2}s + a_{n3}s^2 + \ldots + a_{nj}s^j)}{(s - C_n - iD_n)(b_{n1} + b_{n2}s + b_{n3}s^2 + \ldots + b_{nk}s^k)} \tag{7}$$

where s represents the complex frequency (growth rate and rotation speed) of the forcing function; $\delta\gamma$, the control vane deflection wave; and ϕ_1 refers to the flow coefficient at the measurement station. The transfer function developed from the compression system model in Appendix B can be written in an equivalent form, hence, the model parameters can be related directly to those determined experimentally. In particular, C_n corresponds to the growth rate α_n, and D_n to the rotation rate ω_n of the nth spatial harmonic. $(-B_n/G_n)$ and (A_n/G_n) represent the growth rate and frequency of the forced

perturbation wave at which the actuation system is ineffective at producing a flow perturbation response. (This is defined as a *zero* of the actuation system.) In addition, G_n represents the effectiveness of the compression system to control vane forcing over the frequency range. The parameters A_n, B_n, C_n, D_n, and G_n therefore completely specify the open-loop behavior of the compressor/actuation system. The parameters in Eq. (7) were experimentally determined using a least-squares algorithm to fit the form of the transfer function to the measured dynamic response of the compressor. The accuracy of the theoretical model as a quantitative predictive tool could therefore be established by comparing the experimentally determined parameters to those predicted theoretically.

Open-Loop Identification Methodology

In the development of the hydrodynamic stability model, it is assumed that the spatial harmonics of disturbance waves are decoupled, so that a linear model could be used. This assumption should be valid for the experimental identification studies so long as both the forcing and response disturbances are small in amplitude. Since the compressor characteristic slope plays an important role in the dynamics, a unique transfer function exists at each steady-state operating point for each spatial harmonic of the disturbance wave. In the experiment, the forced response was determined with the compressor operating in both the stable and normally unstable range. In the normally unstable operating range, the compressor was operated under closed-loop active control. Under active control, it is the dynamic response of the combination of the compressor and the control system that is measured; therefore, it is necessary also to characterize the dynamics of the control system accurately, so that the compressor transfer can be deduced from measurements of the overall system.

The basic approach is to excite the compressor with a well-characterized disturbance (a small-amplitude sine wave deflection of the control vanes traveling about the circumferences at various speeds is a simple example). To generate the data presented herein, on the normally stable portion of the compressor map, a pseudo-random binary excitation signal with a bandwidth 1.25 times the rotor's rotational frequency was used to excite the dynamics of the first three spatial harmonics. Identification studies of harmonics higher than three would have required control vane forcing at a frequency beyond the bandwidth of the actuation system. The transfer function was then determined from simultaneous discrete-time measurements of the control vane deflections, and flow field velocity perturbations around the compressor annulus, using a spectral method. The transfer function of each spatial harmonic resembled a second-order dynamic system, which is equivalent to a first-order system with complex coefficients of the form,

$$\frac{\delta\phi_1}{\delta\gamma} = \frac{iG_n s + A_n + iB_n}{s - C_n - iD_n} \tag{8}$$

which indicates that the additional terms in Eq. (7) do not affect the transfer function significantly. From the order of magnitude of the coefficients of the additional terms in the theoretical model, one can deduce that they will not affect the shape of the transfer function significantly over the range of forcing frequencies that was used in the experiment. Figures 17 and 18 show a least-squares fit of the transfer function of the form in Eq. (8) to the experimental data. The fidelity of fit indicates that the form of Eq. (8) is quite appropriate for this compressor. The fit parameters that therefore form the dynamic model of this compressor are given in Table 2.

When the spatial harmonic of interest was stabilized by closed-loop control, the transfer function could not be determined directly in the above manner. In this case, the parameters describing the open-loop performance were calculated using

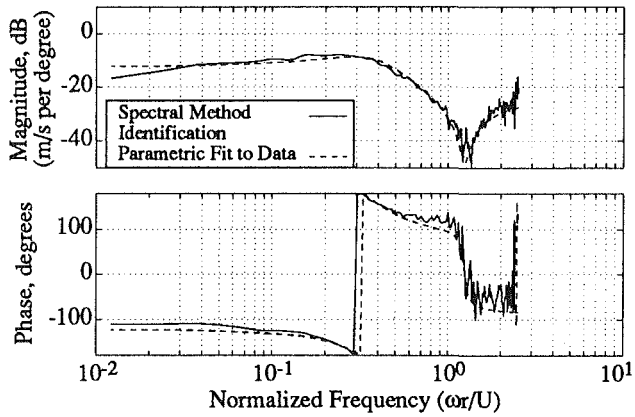

Fig. 17 Estimate of compressor transfer function for first harmonic at $\phi = 0.49$ (6 percent above the stalling flow coefficient)

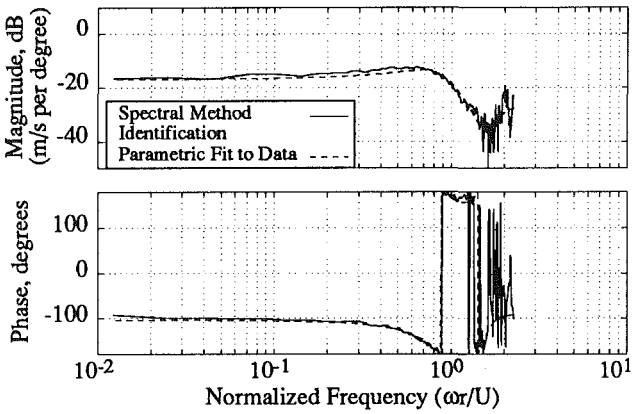

Fig. 18 Estimate of compressor transfer function for second harmonic at $\phi = 0.49$ (6 percent above the stalling flow coefficient)

Table 2 Parameter identification data

		1st Harmonic						
ϕ	Percent Difference from ϕ_{stall}	$C_1 = \alpha_1$	$D_1 = \omega_1$	A_1	B_1	G_1	Re(zero)= $-B_1/G_1$	Im(zero)= A_1/G_1
0.488	6.0	-0.1839	0.329	-0.0709	0.00280	-0.0573	0.0489	1.238
0.462	0.4	-0.0303	0.304	-0.0650	0.00375	-0.0515	0.0728	1.262
0.432	-6.0	0.1320	0.270	-0.0463	0.00943	-0.0329	0.2865	1.406
		2nd Harmonic						
ϕ	Percent Difference from ϕ_{stall}	$C_2 = \alpha_2$	$D_2 = \omega_2$	A_2	B_2	G_2	Re(zero)= $-B_2/G_2$	Im(zero)= A_2/G_2
0.488	6.0	-0.2829	0.790	-0.1119	-0.01525	-0.0872	-0.1749	1.283
0.460	0.0	-0.1223	0.762	-0.1032	-0.00446	-0.0724	-0.0616	1.426
0.432	-6.0	0.0510	0.781	-0.0684	0.00345	-0.0431	0.0799	1.587

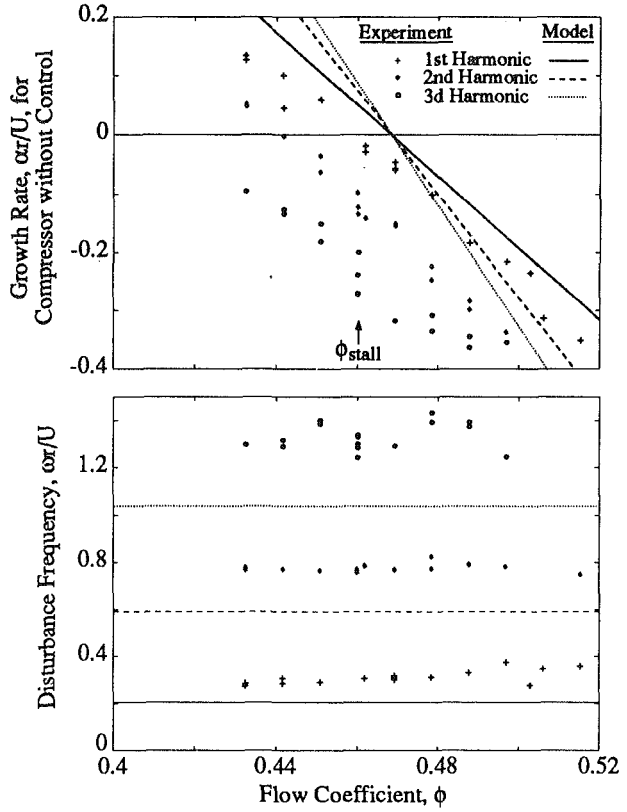

Fig. 19 Measured wave growth and rotational rates compared with predictions of the unmodified Moore-Greitzer model for the first three spatial harmonics

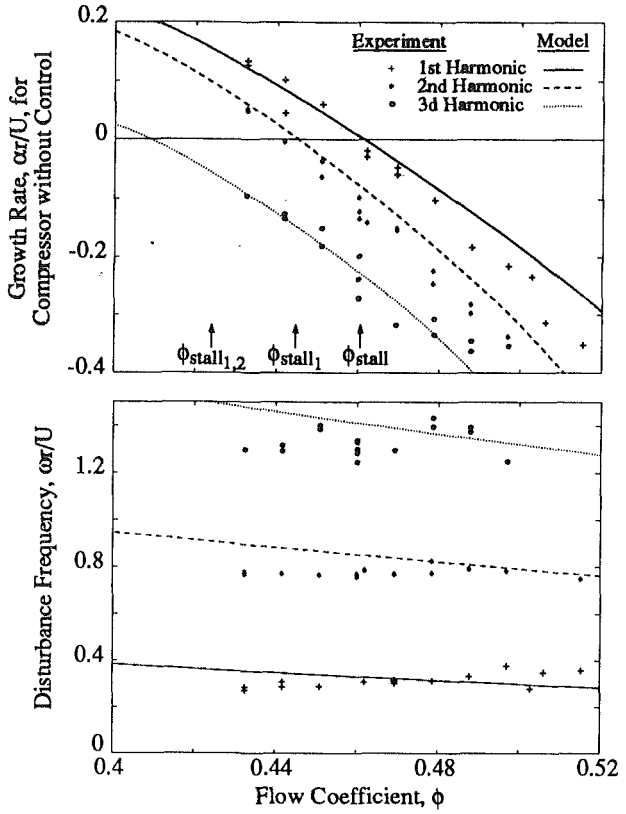

Fig. 20 Measured wave growth and rotational rates compared with predictions of the model modified to account for compressor time lags. The arrows denote the experimentally determined rotating stall initiation points.

an instrumental-variable modeling technique adapted to compressor identification by Paduano et al. (1993b). This method required an accurate model of the actuator dynamics, and a quantitative estimate of time delays in the feedback system. The actuator dynamics were determined from measurements of the response of control vane motion to the command signal. The open-loop transfer function of the compressor was then measured by superimposing a forcing signal on the vane control signal. The accuracy of the instrumental-variable method was checked continually by comparing the vane deflections with those simulated by the actuator dynamic model. The open-loop dynamic parameters of the compressor could then be obtained from the commanded forcing perturbation, the actual vane deflections, and measurements of velocity perturbations upstream of the compressor. The details of the procedure are described by Haynes (1993).

Comparing Open-Loop Measurements and Predictions

The symbols in Fig. 19 show the growth rates and frequencies of the first three spatial harmonics of a disturbance wave determined from the experimental identification studies. Negative values of $\alpha_n r/U$ represent temporal decay of a spatial harmonic while positive values represent exponential growth. The experimental data show that the spatial harmonics of the disturbance wave become unstable sequentially as ϕ is decreased, with higher harmonics becoming unstable at lower flow coefficients. The spacing of the neutral stability points ($\alpha_n = 0$) of the spatial harmonics is important for active control of rotating stall in compressors, since it gives an indication of the range extension that could be achieved for each additional spatial harmonic that is controlled.

With no control, the identification data indicates that rotating stall would be triggered by the growth of the first spatial harmonic where $\alpha_1 = 0$ at a flow coefficient of $\phi = 0.46$. The time history of spatial harmonic coefficients shown in Fig. 9 does indeed show that a coherent first-harmonic perturbation appears first here and grows in amplitude before the higher harmonics do.

Figure 19 shows the prediction of the unmodified Moore–Greitzer model (which does not include the effects of finite compressor time response) that all the spatial harmonics of the disturbance wave become unstable at the same flow coefficient, $\phi = 0.468$, which is the peak of the total-to-static pressure rise characteristic. Also, the model underpredicts the rotational frequencies of the spatial harmonics. The model modified to include finite response times, however, gives much better agreement with the experimental data (Fig. 20). Since the exact values of the compressor blade row time lags needed by the model were not known a priori, a parametric study was done to determine the effect of their variation on the resultant theoretical predictions. In Fig. 20, the blade row response times $\bar{\tau}_s$ and $\bar{\tau}_r$ are set equal to 1.5 times the blade passage convection times, which gave the best agreement of the model with the experimental data. It is important to note that the growth and rotation rates of all three harmonic disturbances (six quantities in total) predicted by the model show good agreement with data when only one constant is adjusted, the blade row time lag. Furthermore, the value required to match the data, 1.5 times the blade passage convection time, is within the range found by Nagano et al. (1971) whose experiments to characterize the response time produced values of between 1 and 1.5. This supports the hypothesis that finite pressure rise response time is the physical mechanism causing the sequential destabilizing of the spatial harmonics of the flow coefficient perturbation.

Predicting Closed-Loop Compressor Behavior

As was discussed above, the modified compressor stability

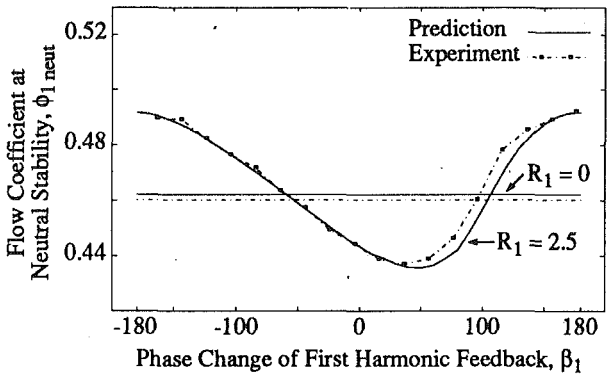

Fig. 21 The influence of the first spatial harmonic controller phase angle, β_1, on stalling flow coefficient at two controller gains, R

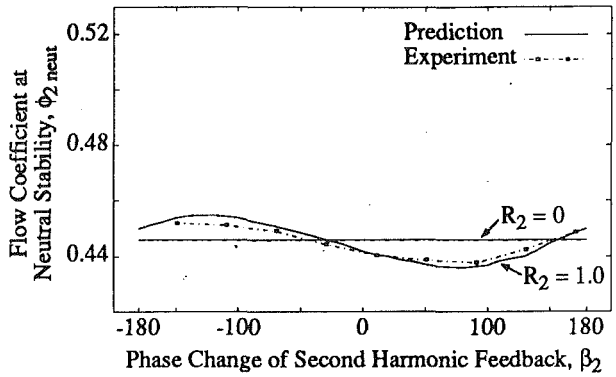

Fig. 22 The influence of the second spatial harmonic controller phase angle, β_2, on stalling flow coefficient at two controller gains, R

model does a good job of predicting the open-loop dynamics of the system, implying that the compressor dynamics are appropriately represented. This model adapted to the closed-loop system should then be able to predict both the behavior of the compressor under active control as well as the influence of control system design parameters on that behavior. Details of the closed-loop model are given in Appendix B.

Figure 21 shows the boundary between stable and unstable operation of the compressor operating under closed loop active control of the first spatial harmonic, as the phase of the control vane deflection wave is varied relative to that of the measured velocity perturbation wave. The flow coefficient at which the spatial harmonic becomes unstable with no feedback control (gain, $R = 0$) is also shown. The operating range of the compressor is thus extended for those phases for which the closed-loop stability boundary is lower than the uncontrolled neutrally stable flow coefficient. The control system has a destabilizing effect on the compressor where the stability boundary is greater. The optimum feedback phase is that which gives the largest range extension and corresponds to the trough of the closed-loop stability curve.

The model prediction and the experimental results in Fig. 21 agree closely. The agreement for control of the second spatial harmonic is close as well (Fig. 22), suggesting that the model is indeed an accurate representation of the stabilized compressor dynamics.

Discussion and Summary

We have presented herein details of the closed-loop control of a three-stage low-speed research compressor. In addition to being an end unto itself, the actively stabilized compressor is a powerful research tool for use in the understanding of compressor dynamics. In particular, such a machine facilitates the accurate measurement of the compression system dynamics with a combination of forced response experiments and system identification methodology. We have found the adoption of controls formalization to be a great aid in this area of fluid mechanics research.

Two approaches were taken to establish the compressor dynamics: (1) experimental measurement and identification, and (2) an analytical hydrodynamic two-dimensional stability model of the flow field. The experimental data were used to determine the relative importance of fluid phenomena included in the modeling. In this case, compressor time lags due to losses proved to be important while those stemming from deviation and blockage were not. The Moore–Greitzer stability model when suitably modified to include these time lags accurately predicted the open-loop onset of stall as well as the behavior of the stabilized compressor. This implies that, to the degree to which these results may now be generalized, a tool now exists for predicting the rotating stall point in high hub-to-tip ratio compressors for which compressibility is not important.

What limits the improvement in compressor operating range achievable with active stabilization, and are these limits predicted by theory? As the compressor operating point is moved to lower mass flows and the characteristic slope increases, the controller gain must be increased. At some point, however, the bandwidth and control authority of the stabilization system will be inadequate to maintain stability. The drop-off of control authority with frequency is exacerbated with variable angle control vane actuators because of unfavorable dynamic behavior. The vanes change the flow angle into the rotor (the primary control mechanism) but also the convergent/divergent passages formed between vanes (depending on stagger angle distribution) simultaneously introduce an additional circumferential flow variation which influences the compressor stability. These two effects have differing frequency response and sign, so as the vane frequency is increased, they can cancel each other, reducing the net control authority. When the control loop is closed by sensing axial velocity upstream of the control vanes (as is the case here), a nonminimum phase zero is introduced limiting controller effectiveness. (Calculations indicated that moving the sensors downstream of the control vanes can alleviate this problem by altering the system phase lags and thereby increase the stable compressor operating range. This has yet to be verified experimentally, however.)

The limits imposed by actuator effectiveness and sensor placement notwithstanding, the theory predicts that the controller gain (R) could be increased by a factor of two over the values used in this work with a concomitant increase in stable operating range. Experimentally, however, the higher controller gain yielded no improvement in performance. Why? One possibility is that the zero order mode (surge) plays a role. Also, at the higher gain, the model indicates that there is very little margin for error in the setting of the feedback parameters, while we know that, at the very least, there is uncertainty in such parameters as the characteristic slope ($\partial\psi/\partial\phi$) and control authority ($\partial\psi/\partial\gamma$), whether derived from aerodynamic theory or parametric fits. In addition, considerable noise (uncharacterized unsteadiness) is present on all measurements in a multistage compressor. Thus, we attribute the difference between the theoretical and empirical gain limits to modeling uncertainty (a sophisticated way of saying that we are not certain of the cause). Control theorists have developed a considerable body of knowledge concerning the design of controllers for systems with parametric uncertainty, but we have yet to apply it in this case.

Since control of the first two harmonics conforms quite closely to theory at the lower gains, Hendricks and Gysling (1994) have used this modeling approach to examine the performance of alternate actuators in controlling this compressor.

They predicted that a circumferential array of jets at the compressor inlet in place of the control vanes should by particularly effective, stabilizing the compressor down to a characteristic slope of 4, over four times that achievable with control vanes, with a concomitant increase in stable flow range. Work is proceeding on an experimental verification of this analysis.

Overall, we believe that the good agreement between the experiment and theory presented herein indicates that it is now possible to assess analytically the influence of active compressor stabilization on the dynamics of the type of machine tested. Work is ongoing to extend the modeling and experiment to include low hub-to-tip ratio compressors (a three-dimensional stability model), to account for the effects of compressibility, and to treat the influence of inlet distortion on actively stabilized compressors.

Acknowledgments

The authors wish to thank Professors J. D. Paduano and E. M. Greitzer for much help and thoughtful discussion. This work was supported by the Air Force Office of Scientific Research, Major D. Fant, technical monitor.

References

Day, I. J., 1993, "Active Suppression of Rotating Stall and Surge in Axial Compressors," ASME JOURNAL OF TURBOMACHINERY, Vol. 115, pp. 40–47.

Emmons, H. W., Pearson, C. E., and Grant, H. P., 1955, "Compressor Surge and Stall Propagation," *ASME Transactions*, Vol. 79, pp. 455–469.

Epstein, A. H., Ffowcs Williams, J. E., and Greitzer, E. M., 1989, "Active Suppression of Aerodynamic Instabilities in Turbomachines," *Journal of Propulsion and Power*, Vol. 5, No. 2, pp. 204–211.

Etchevers, O., 1992, "Evaluation of Rotating Stall Warning Schemes for Axial Compressors," M.S. Thesis, Department of Aeronautics and Astronautics, MIT, Cambridge, MA.

Ffowcs Williams, J. E., and Huang, X., 1989, "Active Stabilization of Compressor Surge," *Journal of Fluid Mechanics*, Vol. 204, pp. 245–262.

Gamache, R. N., 1985, "Axial Compressor Reversed Flow Performance," Ph.D. Thesis, Department of Aeronautics and Astronautics, MIT, Cambridge, MA.

Garnier, V. H., Epstein, A. H., and Greitzer, E. M., 1991, "Rotating Waves as a Stall Inception Indication in Axial Compressors," ASME JOURNAL OF TURBOMACHINERY, Vol. 113, pp. 290–301.

Haynes, J., 1993, "Active Control of Rotating Stall in a Three-Stage Axial Compressor," M.S. Thesis, Department of Mechanical Engineering, MIT, Cambridge, MA.

Hendricks, G. J., and Gysling, D. L., 1994, "A Theoretical Study of Sensor-Actuator Schemes for Rotating Stall Control," *AIAA J. of Propulsion & Power*, Vol. 10, No. 1, pp. 101–109.

Hynes, T. P., and Greitzer, E. M., 1987, "A Method for Assessing Effects of Circumferential Flow Distortion on Compressor Stability," ASME JOURNAL OF TURBOMACHINERY, Vol. 109, pp. 371–379.

Lavrich, P. L., 1988, "Time Resolved Measurements of Rotating Stall in Axial Flow Compressors," MIT GTL Report No. 194.

Longley, J. P., and Hynes, T. P., 1990, "Stability of Flow Through Multistage Axial Compressors," ASME JOURNAL OF TURBOMACHINERY, Vol. 112, pp. 126–132.

Mazzawy, R. S., 1977, "Multiple Segment Parallel Compressor Model for Circumferential Flow Distortion," ASME *Journal of Engineering for Power*, Vol. 99, No. 2.

McDougal, N. M., Cumpsty, N. A., and Hynes, T. P., 1990, "Stall Inception in Axial Compressors," ASME JOURNAL OF TURBOMACHINERY, Vol. 112, pp. 116–125.

Moore, F. K., 1984, "A Theory of Rotating Stall of Multistage Axial Compressors: Part I—Small Disturbances," ASME *Journal of Engineering for Gas Turbines and Power*, Vol. 106, pp. 313–320.

Moore, F. K., and Greitzer, E. M., 1986, "A Theory of Post-stall Transients in Axial Compressors: Part I—Development of the Equations," ASME *Journal of Engineering for Gas Turbines and Power*, Vol. 108, pp. 68–76.

Nagano, S., Machida, Y., and Takata, H., 1971, "Dynamic Performance of Stalled Blade Rows," Japan Society of Mechanical Engineering Paper JSME 11, presented at the Tokyo Joint International Gas Turbine Conference, Tokyo, Japan.

Paduano, J. D., 1991, "Active Control of Rotating Stall in Axial Compressors," Ph.D. Thesis, Department of Aeronautics and Astronautics, MIT, Cambridge, MA.

Paduano, J. D., and Gysling, D. L., 1992, "Rotating Stall in Axial Compressors: Nonlinear Modeling for Control," presented at the SIAM Conference on Control and Its Applications, Minneapolis, MN, Sept.

Paduano, J. D., Epstein, A. H., Valavani, L., Longley, J. P., Greitzer, E. M., and Guenette, G. R., 1993a, "Active Control of Rotating Stall in a Low-Speed Axial Compressor," ASME JOURNAL OF TURBOMACHINERY, Vol. 115, pp. 48–56.

Paduano, J., Valavani, L., and Epstein, A. H., 1993b, "Parameter Identification of Compressor Dynamics During Closed-Loop Operation," ASME *Journal of Dynamic Systems, Measurement, and Control*, Vol. 115, pp. 694–703.

Pinsley, J. E., Guenette, G. R., Epstein, A. H., and Greitzer, E. M., 1991, "Active Stabilization of Centrifugal Compressor Surge," ASME JOURNAL OF TURBOMACHINERY, Vol. 113, pp. 723–732.

APPENDIX A

Compressor Stability Model Including Transient Behavior

In this model, the pressure rise across a compressor is modified by the pressure difference required to overcome the inertia of the fluid within the blade channels when the flow within the compressor is unsteady. If one assumes that the flow within the blade passages is one dimensional, the unsteady pressure rise across the compressor can be written as (Moore, 1984; Hynes and Greitzer, 1987):

$$\frac{P_e - P_{ti}}{\rho U^2} = \psi - \lambda \frac{\partial \phi}{\delta \vartheta} - \frac{\mu r}{U} \frac{\partial \phi}{\partial t} \tag{A1}$$

where:

$$\psi = \psi_{\text{isen}} - L_r - L_s \tag{A2}$$

ψ_{isen} is the isentropic stagnation pressure rise across the compressor and L_r and L_s are the rotor and stator stagnation pressure losses. The inertias of the fluid in the rotors and in the compressor are represented by λ and μ, respectively. At the inception of rotating stall, the flow coefficient through the compressor is modified by a small perturbation $\delta\phi$ so that:

$$\begin{aligned} \phi &= \bar{\phi} + \delta\phi & \psi_{\text{isen}} &= \bar{\psi}_{\text{isen}} + \frac{d\bar{\psi}_{\text{isen}}}{d\phi}\,\delta\phi \\ P_e &= \bar{P}_e + \delta P_e & L_s &= \bar{L}_s + \delta L_s \\ P_{ti} &= \bar{P}_{ti} + \delta P_{ti} & L_r &= \bar{L}_r + \delta L_r \end{aligned} \tag{A3}$$

The compressor pressure rise perturbation equation is therefore:

$$\frac{\delta P_e - \delta P_{ti}}{\rho U^2} = \frac{d\bar{\psi}_{\text{isen}}}{d\phi}\,\delta\phi - \delta L_s - \delta L_r - \lambda \frac{\partial(\delta\phi)}{\partial \vartheta} - \frac{\mu r}{U}\frac{\partial(\delta\phi)}{\partial t} \tag{A4}$$

$$\bar{\psi}_{\text{isen}} = \bar{\psi} + \bar{L}_r + \bar{L}_s \tag{A5}$$

where $\bar{\psi}$ is the steady, axisymmetric total-to-static pressure rise including losses, and $\bar{L}_s$ and $\bar{L}_r$ the steady stator and rotor stagnation pressure losses, respectively. The stator transient stagnation pressure loss perturbation, δL_s, is given by the differential equation:

$$\tau_s \frac{\partial(\delta L_s)}{\partial t} = \frac{\partial \bar{L}_s}{\partial \phi}\,\delta\phi - \delta L_s \tag{A6}$$

The rotor transient stagnation pressure loss, δL_r, is calculated in a reference frame rotating with the rotor:

$$\tau_r\left(\frac{\partial(\delta L_r)}{\partial t} + \frac{U}{r}\frac{\partial(\delta L_r)}{\partial \vartheta}\right) = \frac{\partial \bar{L}_r}{\partial \phi}\,\delta\phi - \delta L_r \tag{A7}$$

In this analysis, a general perturbation in flow coefficient of the form:

$$\delta\phi = \sum_{n=1}^{\infty} A_n e^{(\alpha_n - i\omega_n)t} e^{in\vartheta} \tag{A8}$$

is considered. Each spatial harmonic of the perturbation can be considered separately, so only the nth spatial harmonic:

$$\delta\phi_n = A_n e^{(\alpha_n - i\omega_n)t} e^{in\vartheta} \tag{A9}$$

will therefore be examined.

The variables describing the evolution of the perturbation can be nondimensionalized as follows:

$$\bar{t} = \frac{tU}{r},\quad \bar{\tau} = \frac{\tau U}{r},\quad s_n = \frac{(\alpha_n - i\omega_n)r}{U}, \tag{A10}$$

where U is the rotor speed and r is the average radius of the

compressor annulus, so that the equations describing the perturbation become:

$$\frac{\delta P_e - \delta P_{ti}}{\rho U^2} = \frac{d\bar{\psi}_{\text{isen}}}{d\phi}\,\delta\phi_n - \delta L_s - \delta L_r - \lambda\,\frac{\partial(\delta\phi)}{\partial\vartheta} - \mu\,\frac{\partial(\delta\phi)}{\partial\bar{t}} \tag{A11}$$

$$\bar{\tau}_s\,\frac{\partial(\delta L_s)}{\partial\bar{t}} = \frac{\partial\bar{L}_s}{\partial\phi}\,\delta\phi_n - \delta L_s \tag{A12}$$

$$\tau_r\left(\frac{\partial(\delta L_r)}{\partial\bar{t}} + \frac{\partial(\delta L_r)}{\partial\vartheta}\right) = \frac{\partial\bar{L}_r}{\partial\phi}\,\delta\phi_n - \delta L_r \tag{A13}$$

$$\delta\phi_n = A_n e^{s_n\bar{t}} e^{in\vartheta} \tag{A14}$$

The upstream stagnation and downstream static pressure perturbations are given by the expressions (Epstein et al., 1989):

$$\frac{\delta P_{ti}}{\rho U^2} = -\frac{1}{|n|}\,\frac{\partial(\delta\phi_n)}{\partial\bar{t}}, \tag{A15}$$

and

$$\frac{\delta P_e}{\rho U^2} = \frac{1}{|n|}\,\frac{\partial(\delta\phi_n)}{\partial\bar{t}} \tag{A16}$$

Substitution of Eqs. (A15), (A16), and (A14) into Eqs. (A11)–(A13) produces a generalized, complex eigenvalue problem in s_n:

$$(A - s_n B)\delta\bar{x} = 0 \tag{A17}$$

where:

$$A = \begin{pmatrix} \frac{1}{\zeta}\left(\frac{d\bar{\psi}_{\text{isen}}}{d\phi} - in\lambda\right) & -\frac{1}{\zeta} & -\frac{1}{\zeta} \\ \frac{1}{\bar{\tau}_s}\frac{d\bar{L}_s}{d\phi} & -\frac{1}{\bar{\tau}_s} & 0 \\ \frac{1}{\bar{\tau}_r}\frac{d\bar{L}_r}{d\phi} & 0 & -\left(in + \frac{1}{\bar{\tau}_r}\right) \end{pmatrix} \tag{A18}$$

$$B = \begin{pmatrix} 1 & 0 & 0 \\ 0 & 1 & 0 \\ 0 & 0 & 1 \end{pmatrix} \tag{A19}$$

$$\delta\bar{x} = \begin{pmatrix} \delta\phi_n \\ \delta L_s \\ \delta L_r \end{pmatrix} \tag{A20}$$

$$\zeta = \left(\frac{2}{|n|} + \mu\right) \tag{A21}$$

and

$$\bar{\psi}_{\text{isen}} = \bar{\psi} + \bar{L}_r + \bar{L}_s \tag{A22}$$

The solution to the eigenvalue problem yields the growth and rotation rates of the perturbation wave. If the real part of s_n is negative, the disturbance is damped, representing stable operation of the compressor. If the real part of s_n is positive, the disturbance grows exponentially, representing unstable operation. For the uncontrolled compressor the growth rate of the perturbation is determined by the slope of the total-to-static pressure rise characteristic.

We must now fit this model to our data. The steady-state compressor slope, $d\bar{\psi}/d\phi$, is determined from a polynomial fit to the measured pressure rise data. The total pressure loss across the compressor is estimated from the difference between the isentropic pressure rise characteristic and the measured one. A polynomial fit to this estimate is then used to determine the slopes of the rotor and stator loss curves, $d\bar{L}_r/d\phi$ and $d\bar{L}_s/d\phi$. For the particular build of the three-stage compressor that was considered (75 percent reaction), it was assumed that 75 percent of the steady total pressure losses occurred across the rotors, and 25 percent across the stators. The time constants $\bar{\tau}_s$ and $\bar{\tau}_r$ were related to the convection time of the bulk flow through the blade channels. Since the values of these constants were not measured, a parametric study was done by varying these constants about the blade passage convection time. The best agreement with the experimental data was obtained with the time constants set to 1.5 times the blade passage convection time.

APPENDIX B

Compressor Stability Model Including Active Control

In an actively controlled compressor, the relation between pressure and velocity perturbations can be manipulated by the actuator. Analysis of the movable inlet guide vane actuator involves determining relations between the actuation and perturbations in velocity and pressure introduced into the flow field. The actuator is modeled using quasi-steady actuator disk theory. A detailed model of the compressor with control vane control is given by Paduano (1991) and Paduano et al. (1993), and is outlined here, with modifications to account for finite compressor response times. With control vanes and quasi-steady compressor response the compressor perturbation equation for each spatial harmonic can be written as:

$$\frac{\delta P_e - \delta P_{t2}}{\rho U^2} = \frac{\partial\psi}{\partial\phi}\,\delta\phi_2 + \frac{\partial\psi}{\partial\gamma}\,\delta\gamma - \lambda\,\frac{\partial(\delta\phi_2)}{\partial\vartheta} - \mu\,\frac{\partial(\delta\phi_2)}{\partial\bar{t}} \tag{B1}$$

where

$$\frac{\delta P_e}{\rho U^2} = \frac{1}{|n|}\,\frac{\partial(\delta\phi_2)}{\partial\bar{t}} \tag{B2}$$

and

$$\frac{\delta P_{t2}}{\rho U^2} = \frac{\delta P_{t1}}{\rho U^2} - \mu_{igv}\,\frac{\partial}{\partial\bar{t}}\left(\delta\phi_2 + \frac{1}{2}\,\phi\mu_{igv}\,\frac{\partial(\delta\gamma)}{\partial\vartheta}\right) \tag{B3}$$

with

$$\delta\phi_2 = \delta\phi_1 - in\phi\mu_{igv}\delta\gamma \tag{B4}$$

and

$$\frac{\delta P_{t1}}{\rho U^2} = -\frac{1}{|n|}\,\frac{\partial(\delta\phi_1)}{\partial\bar{t}} \tag{B5}$$

Here $\delta\gamma$ represents an angular displacement of the inlet guide vanes from their mean position. When the quasi-steady assumption is relaxed, and the finite compressor response times are modeled, the compressor perturbation equation can be written as:

$$\frac{\delta P_e - \delta P_{t2}}{\rho U^2} = \frac{\partial\bar{\psi}_{\text{isen}}}{\partial\phi}\,\delta\phi_2 + \frac{\partial\bar{\psi}_{\text{isen}}}{\partial\gamma}\,\delta\gamma - \delta L_s - \delta L_r - \lambda\,\frac{\partial(\delta\phi_2)}{\partial\vartheta} - \mu\,\frac{\partial(\delta\phi_2)}{\partial\bar{t}} \tag{B6}$$

where the transient losses, δL_s and δL_r, are now modeled by the following equations:

$$\bar{\tau}_s\,\frac{\partial(\delta L_s)}{\partial\bar{t}} = \frac{\partial\bar{L}_s}{\partial\phi}\,\delta\phi_2 - \delta L_s \tag{B7}$$

$$\bar{\tau}_r\left(\frac{\partial(\delta L_r)}{\partial\bar{t}} + \frac{\partial(\delta L_r)}{\partial\vartheta}\right) = \frac{\partial\bar{L}_r}{\partial\phi}\,\delta\phi_2 + \frac{\partial L_r}{\partial\gamma}\,\delta\gamma - \delta L_r \tag{B8}$$

The system of equations above can be written as a transfer function between the flow perturbation at the measurement location upstream of the IGVs, $\bar{x}_{hw}$, and the control vane deflection $\delta\gamma$,

$$\frac{\delta\phi_{1,hw}}{\delta\gamma} = in\mu_{igv}\phi e^{-|n|\bar{x}_{hw}} + \frac{\dfrac{\partial\bar{\psi}_{\text{isen}}}{\partial\gamma} - \dfrac{\partial\bar{L}_r/\partial\gamma}{1+\bar{\tau}_r(s+in)} - in\mu_{igv}\phi s\left(\dfrac{1}{|n|} + \dfrac{\mu_{igv}}{2}\right)}{\zeta s + in\lambda - \dfrac{\partial\bar{\psi}_{\text{isen}}}{\partial\phi_2} - \dfrac{\partial\bar{L}_s/\partial\phi_2}{1+s\bar{\tau}_s} - \dfrac{\partial\bar{L}_r/\partial\phi_2}{1+\bar{\tau}_r(s+in)}}\,e^{-|n|\bar{x}_{hw}} \tag{B9}$$

Control is implemented by sensing the axial velocity perturbation, $\delta\phi_1$, upstream of the inlet guide vanes. The measured signal is then processed by the controller, which commands the control vanes to introduce a suitable perturbation into the flow field. With the proportional feedback scheme that was employed in the experiment, the measured signal is modified in amplitude and shifted spatially in phase. This is implemented analytically as follows:

$$\delta\gamma|_c = Ze^{-|n|\bar{x}_{hw}}\delta\phi_1 \tag{B10}$$

$$Z = \mathrm{Re}^{-i\beta_n} \tag{B11}$$

where R is the gain in amplitude of the signal, and β_n is the spatial phase shift of the commanded signal relative to the measured signal. In practice, nonideal behavior causes the output from the actuator to differ from the command given by the controller. The nonideal actuator dynamics were determined experimentally by measuring the transfer function of the actuator motion relative to an input command signal, and then fitting an appropriate dynamic model to the transfer function. As a simple example, assume that the dynamics of the actuator can be modeled by a second-order differential equation,

$$\frac{\partial^2(\delta\gamma)}{\partial\bar{t}^2} + 2\zeta_a\omega_a\frac{\partial(\delta\gamma)}{\partial\bar{t}} = \omega_a^2(\delta\gamma|_c - \delta\gamma) \tag{B12}$$

where ω_n and ζ_a are the resonant frequency and damping ratio of the actuation system. (In the experiment a higher order dynamic model was required to match the measured actuator transfer function accurately.) With axial velocity sensing upstream of the control vanes, the actuator equation then becomes:

$$\frac{\partial^2(\delta\gamma)}{\partial\bar{t}^2} + 2\zeta_a\omega_a\frac{\partial(\delta\gamma)}{\partial\bar{t}} = \omega_a^2(Ze^{-|n|\bar{x}_{hw}}\delta\phi_1 - \delta\gamma) \tag{B13}$$

Equations (B2)–(B8) and (B10)–(B13) produce an eigenvalue problem. Parameters in the analysis are the operating flow coefficient (which determines the slope of the pressure rise characteristic), the gain and phase of the feedback control law, and the actuator dynamic parameters. For the control vane actuator with velocity feedback, this system of differential equations reduces to the form given in Eq. (A17), where the matrices A, B, and the vector $\delta\bar{x}$ are now:

$$A = \begin{bmatrix} \frac{1}{\zeta}\left(\frac{\partial\bar{\psi}_{\mathrm{isen}}}{\partial\phi} - in\lambda\right) & -\frac{1}{\zeta} & -\frac{1}{\zeta} & \frac{1}{\zeta}\left(\frac{\partial\bar{\psi}_{\mathrm{isen}}}{\partial\gamma}\right) & 0 \\ \frac{1}{\bar{\tau}_s}\frac{\partial\bar{L}_s}{\partial\phi} & -\frac{1}{\bar{\tau}_s} & 0 & 0 & 0 \\ \frac{1}{\bar{\tau}_r}\frac{\partial\bar{L}_r}{\partial\phi} & 0 & -\left(in + \frac{1}{\bar{\tau}_r}\right) & \frac{1}{\bar{\tau}_r}\frac{\partial\bar{L}_r}{\partial\gamma} & 0 \\ 0 & 0 & 0 & 0 & 1 \\ Ze^{-|n|\bar{x}_{hw}}\omega_a^2 & 0 & 0 & X & -2\zeta_a\omega_a \end{bmatrix} \tag{B14}$$

$$B = \begin{pmatrix} 1 & 0 & 0 & \frac{in\phi\mu_{ig\nu}}{\zeta} & \left(\frac{1}{|n|} + \frac{\mu_{ig\nu}}{2}\right)0 \\ 0 & 1 & 0 & 0 & 0 \\ 0 & 0 & 1 & 0 & 0 \\ 0 & 0 & 0 & 1 & 0 \\ 0 & 0 & 0 & 0 & 1 \end{pmatrix} \tag{B15}$$

$$\delta\bar{x} = \begin{pmatrix} \delta\phi_2 \\ \delta L_s \\ \delta L_r \\ \delta\gamma \\ \partial(\delta\gamma)/\partial\bar{t} \end{pmatrix} \tag{B16}$$

with:

$$\zeta = \left(\frac{2}{|n|} + \mu\right) \tag{B17}$$

$$\bar{\psi}_{\mathrm{isen}} = \bar{\psi} + \bar{L}_r + \bar{L}_s \tag{B18}$$

and

$$X = \omega_a^2(Ze^{-|n|\bar{x}_{hw}}in\phi\mu_{ig\nu} - 1) \tag{B19}$$

There are five eigenvalues for each spatial harmonic of the disturbance, and the system is stable when the real part of each of the eigenvalues is negative.

Developments in Centrifugal Compressor Surge Control—A Technology Assessment

K. K. Botros

J. F. Henderson

NOVACOR Research & Technology Corp., Calgary, Alberta, Canada

There are a number of surge control schemes in current use for centrifugal compressors employed in natural gas transmission systems. Basically, these schemes consist of a set of detection devices that either anticipate surge or detect it at its inception, and a set of control devices that act to prevent surge from occurring. A patent search was conducted in an attempt to assess the level and direction of technology development over the last 20 years and to define the focus for future R&D activities. In addition, the paper presents the current state of technology in three areas: surge control, surge detection, and surge suppression. Patent data obtained from on-line databases showed that most of the emphasis has been on surge control rather than on detection and control and that the current trend in surge control will likely continue toward incremental improvement of a basic or conventional surge control strategy. Various surge suppression techniques can be grouped in two categories: (i) those that are focused on better compressor interior design, and (ii) others that attempt to suppress surge by external and operational means.

1 Introduction

Surge is a known dynamic instability in axial and centrifugal compressors, which is characterized as a one-dimensional (planar) flow disturbance in the compressor and associated piping system. It results in severe vibration and damage to the compressor unit as well as reduced efficiency. Considerable effort has been expended in the past to understand the phenomenon and control it. The literature describes a large number of surge control techniques, the majority of which employ the basic concept of restricting the operation of the compressor to the right of the surge limit by a margin defined by what is called "surge control line" or "control line" for short. This line is shown in Fig. 1, where point 1 indicates the minimum flow permitted through the compressor when an antisurge control is in effect. Obviously, when these techniques are successfully employed, surge will not take place during the operation of the compressor since it is restricted from crossing the surge control line.

Another technique which has the advantage of extending the operating range of the compressor is based on detecting incipient surge as the compressor approaches the surge limit (e.g., point 2 on Fig. 1). In this case a signal from the detection device is used to drive a surge controller, which, in turn, will act to prevent the unit from crossing the surge limit, for example, by opening a recycle valve. This technique will be defined as "detection and control," as opposed to "control" based merely on the safety margin defined by the control line.

In recent years there have also been innovative attempts to suppress surge beyond the surge limit, i.e., to operate the compressor at point 3 in Fig. 1. Some of these attempts involve modifications to the design of the compressor interiors, while others involve addition of external devices on the compressor

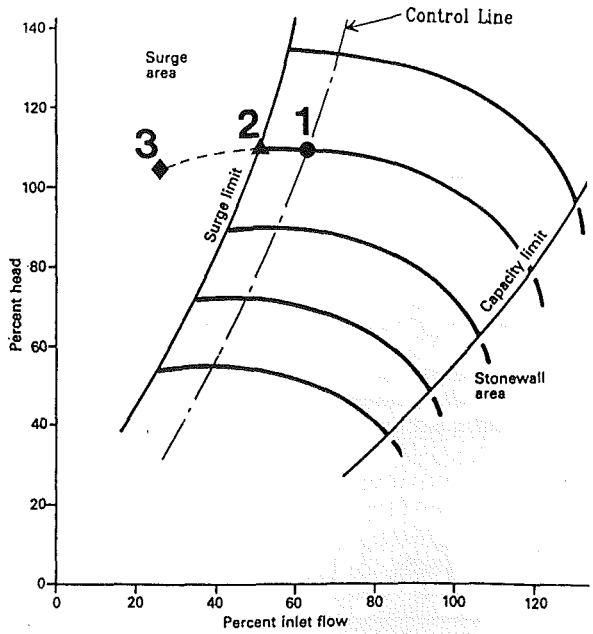

Fig. 1 Typical centrifugal compressor performance map showing surge limit and surge control line

Contributed by the International Gas Turbine Institute and presented at the 38th International Gas Turbine and Aeroengine Congress and Exposition, Cincinnati, Ohio, May 24–27, 1993. Manuscript received at ASME Headquarters February 12, 1993. Paper No. 93-GT-8. Associate Technical Editor: H. Lukas.

suction or discharge, which shift the occurrence of surge to much lower flow rates.

In this review an attempt is made to determine the current state of the art and current trends in centrifugal compressor surge control technology by studying the patent literature. Patent activity trends and citations have been determined across technical areas, countries, and companies. In addition, technological information contained in some full patent documents has been evaluated. For the most part, these documents represent a unique and rich source of current state-of-the-art information, new ideas, and problem-solving technology. For instance, about 70 to 80 percent of US patents issued in the last 10 to 15 years likely contain technology that has not been disclosed in the nonpatent literature [1]. Finally, a brief technical overview of the various techniques and methods employed in surge control, and detection and suppression will be discussed.

2 Patent Trends

Patent abstracts were located by searching four on-line databases from the mid-1960s to the present: Claims/U.S. Patent Abstracts, Derwent World Patents Index, APIPAT (American Petroleum Institute) and TULSA (Petroleum Abstracts). The search concepts used for each database differed somewhat but were generally along the following lines:

Centrifugal or rotating compressor(s) and (surge or surging or pulsation or pulsating or surges)
or
Compressor(s) and surge control
or
Surge detection and compressor(s)

Patent abstracts obtained using the search concepts above were then scanned for relevance to give a set of 67 abstracts judged to be highly comprehensive and relevant to the study. Copies of some of the full patent documents were purchased for further evaluation.

Patent trend analysis was based on the following assumptions. First, patent activity can be used as an indicator of the amount of technological activity in a technology, country, or company [2–4]. Second, the number of companies obtaining patents in a selected technology can be used as an indicator of the level of interest in the technology. Third, when these two trends are correlated with one another, it can be estimated whether a technology is in the development stage, the research or perfection stage, or the fully mature or declining stage [1]. Fourth, the number of times that a patent has been cited by later patents can be used as an indicator of the technological importance or value of the patent [5–7]. Fifth, when citations are correlated with patent counts, technological innovation and strength can be assessed across technologies, countries, and companies [8, 9]. In the US patent system, any prior disclosures of technology that might anticipate the claimed invention and preclude the issuance of a patent, which might be similar to the claimed invention and limit the scope of patent protection, or which generally reveal the state of the technology to which the invention is directed must be cited by the examiner on the front page of the patent. The number of times a US patent has been cited on the front pages of later US patents is assumed to be a measure of its technological importance or value.

Information on citations was provided by patent abstracts obtained from the Claims/U.S. Patent Abstract database, which includes citation counts as a standard information item in each US patent. Since this measure is all-inclusive, it will capture the value spilled over to other technical areas as well as the value for and in terms of surge control and surge detection in centrifugal compressors. This limitation in the citation data used in the present study must be recognized when drawing conclusions about the technological importance or value of patented inventions.

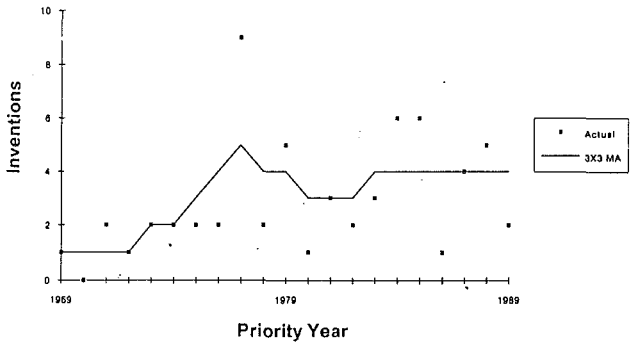

Fig. 2 Basic patented inventions in surge control and/or detection

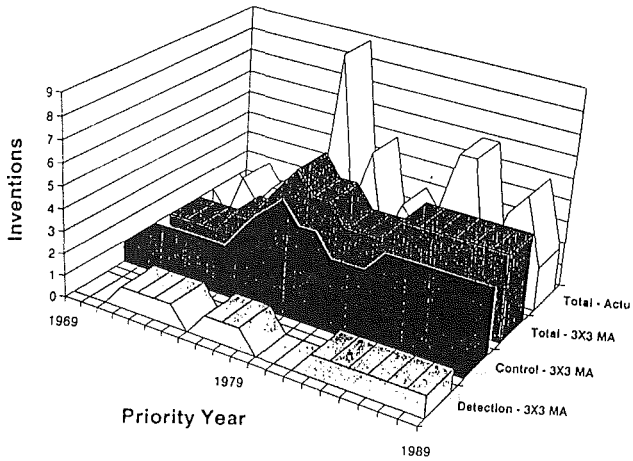

Fig. 3 Basic patented inventions in surge control and/or detection across technology

(i) **Technological Activity and Interest.** Figure 2 shows the number of basic patented inventions plotted against their priority years. Both actual data and data that were smoothed using three year by three year moving averages are displayed. Smoothing was used to improve the visibility of the patenting pattern. The priority year was used because this is the year closest to the time when the R&D was carried out. Furthermore, the priority year is not influenced by the examination procedure at a patent office, which has nothing to do with the innovation process.

This figure shows that patent activity increased through the 1970s and has been decreasing/stable since then. It is believed that apparent growth in technological activity through 1977 was associated with the spectacular rise in the prices of petroleum and other fossil fuels coupled with increased utilization of natural gas, computers, and advanced process control procedures.Technological progress during the 1980s seems to have involved incremental improvement. A major invention opening up a new high-payoff hot topic for technological research and development does not seem to have been made.

Figure 3 shows the actual and smoothed trends in basic patented inventions displayed in Fig. 2 as well as the distribution of basic patented inventions across surge control and surge detection technologies. The data indicate that most of the technological activity has been connected with surge control rather than with surge detection and that there is no trend in either case at the present time. Three possible explanations might account for the observed emphasis on surge control. First, there is more scope for technological progress in surge control than in surge detection. Second, control based on surge detection has not yet found wide acceptance in the industry. Third, a promising or breakthrough invention opening up intensive technological activity along the lines of surge detection has not yet been made.

Table 1 US patented inventions across technical areas

	Basic Inventions		Citation Frequency
	1970-89 #	1985-89 % of 1970-89	1970-89
Technology			
Surge Control	37	32	5
Surge detection	10	30	2
Surge detection & control	3	0	13
Technical Approach			
Bleeding	14	36	4
Diffuser guide vanes	1	0	4
Inlet guide vanes	1	0	1
Recycling	14	36	7
Application			
Air compressors	4	0	6
Aircraft	3	67	1
Gas conveyors	3	0	10
Gas turbine engines	2	0	3
Power plants	2	0	1
Refrigeration	4	25	5

Table 1 shows the patenting of basic inventions in the US across technical areas. Three indicators of technological innovation and strength are used: the number of US patented inventions made since 1970, those patented in the last five years as a percentage of patenting in the last two decades, and the citation frequency. The second parameter, which can be called a 5 yr/20 yr growth figure, stresses recent growth in a technology and can spot "hot technical areas." The citation frequency is the average number of times that a set of patented inventions has been cited by later patents and indicates the technological importance of a set of inventions.

As already shown by Fig. 3, the results in Table 1 indicate that most of the technological activity has been connected with surge control rather than with either surge detection or surge detection and control technologies. Technological activity connected with surge control and surge detection seems to be more or less stable at the present time and surge detection and control technology no longer seems to be receiving attention. However, patented inventions connected with surge detection and control have been relatively highly cited.

About two thirds of the patent abstracts revealed more specific technical approaches in development for preventing surge. The areas of bleeding, venting or blow-off and of recycling have received most of the attention. Furthermore, technological activity seems to be increasing in both areas at the present time. The latter observation indicates that the percentage of patents that specify a technical approach is increasing, which in turn suggests that emphasis in research and development is shifting from overall technology to specific technical approaches and that the overall technology is in a perfection stage. The observation that designs of diffuser guide vanes and inlet guide vanes seem to have received virtually no attention suggests that preventing surge is viewed to be an operating problem rather than a design problem. On average, patented inventions in recycling have been cited somewhat more frequently than those in bleeding.

About one third of the patent abstracts specified an area of application, while the remaining were more general. Technological activity seems to have been more or less uniformly distributed across several of the revealed applications. However, only aircraft and refrigeration seem to be receiving attention at the present time and the former appears to be a "hot topic." Patented inventions connected with gas conveyors have been relatively highly cited, while those connected with refrigeration have been cited more frequently than those connected with aircraft.

Figure 4 shows the number of companies that have been patenting plotted against priority year using both actual data and data smoothed by using three year by three year moving averages. By and large company activity has been increasing over the entire period of time, which points to growing interest in the technology over time.

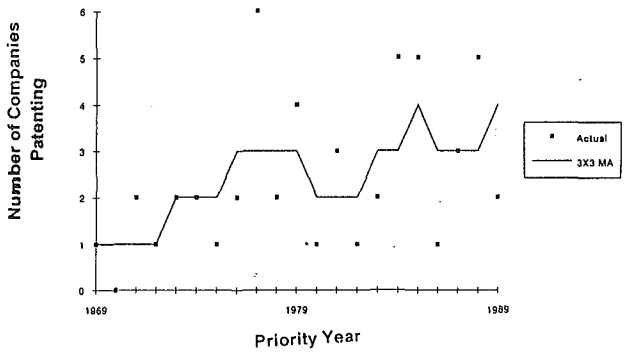

Fig. 4 Company activity in surge control and/or detection

In summary, the following observations arise from the above findings. First, patent activity, which indicates technological activity, is currently stable/decreasing. Second, company activity, which indicates interest in the technology, is increasing/stable at the present time. Third, technological effort seems to be shifting from the overall technology to specific technical approaches, which are generally related to operation rather than interior design of centrifugal compressors. These observations in combination indicate that the technology seems to be in a research or perfection stage rather than in a development stage or a fully mature or declining stage.

Finally, it is believed that principal advances during the foreseeable future will be in surge control, which involves recycling rather than in surge detection or surge detection and control.

***(ii)* Technological Innovation and Strength by Country.** Table 2 shows the patenting of basic inventions in both the world and the United States across the geographic locations of patent assignees. The countries are ranked according to the number of inventions patented in the world since 1970 and are assessed using the same indicators of technological innovation and strength as in Table 1.

The information in Table 2 indicates that most of the technological activity has been in the US followed by the former USSR and Germany. At the present time, activity in the US seems to be stable/decreasing, activity in the former USSR seems to be virtually zero, and activity in Germany seems to be increasing. Patented inventions made in both the US and Germany have been cited at more or less the same frequencies.

These findings indicate that the US is currently at the forefront in terms of technological innovation and strength followed by Germany, which seems to be establishing a stronger position in the technology at the present time.

***(iii)* Technological Innovation and Strength by Company.** Table 3 ranks companies holding two or more US patented inventions according to the number patented in the US since 1970. The companies are assessed using the same indicators of technological innovation and strength as in Tables 1 and 2. It is seen that five companies hold four or more patented inventions. At the present time, activities by Compressor Controls Corporation and United Technologies Corporation seem to be decreasing/stable, activity by MAN Gutehoffnungshutte GMBH DE in Germany seems to be increasing, and activities by Babcock & Wilcox Co. and Sundstrand Corporation seem to be virtually zero. On average, patented inventions held by Compressor Controls Corporation, Babcock & Wilcox Co., Phillips Petroleum Co., and Simmonds Precision Products Inc. were cited eight or more times. The lower citation frequency observed for patented in-

Table 2 Patented inventions in surge detection and/or control

	Patented In the World		Patented In the U.S.		
	Basic Inventions		Basic Inventions		Citation Frequency
Location	1970-89 #	1985-89 % of 1970-89	1970-89 #	1985-89 % of 1970-89	1970-89
Total	60	30	48	31	5
United States	43	26	41	24	6
Former USSR	8	13	0	0	0
Germany	5	80	4	100	4
United Kingdom	1	100	1	100	2
Japan	1	100	0	0	0
Netherlands	1	0	1	0	0
France	1	0	1	0	3

ventions held by MAN Gutehoffnungshutte GMBH DE might arise in part from the fact that they have not been around for as long as those held by the other companies referred to above.

These findings suggest that MAN Gutehoffnungshutte GMBH DE in Germany seems to be emerging as one of the top companies in terms of technological innovation and strength.

(*iv*) **Observed Trends.** The following trends arise from the findings reported above:

- It is believed that centrifugal compressor surge control technology is now in a research or perfections stage rather than in a development stage or a fully mature or declining stage.
- The emphasis in research and development seems to be shifting from the overall technology to specific technological approaches for preventing surge and possibly to specific applications with more fine details distinguishing between many variations in the basic technology.
- It is expected that principal advances during the foreseeable future will be along the following two lines: first, surge control that involves recycling rather than surge detection and control and second, new or improved operating procedures for compressors rather than new or improved compressor interior designs.
- The top companies in terms of technological innovation and strength seem to be located in the United States and Germany.

3 Developments in Anti-surge Control

As mentioned in the introduction, the anti-surge control system is based on the concept of operating the compressor away from the surge limit. In pipeline application, this is accomplished by opening the recycle valve before the surge limit is reached. To provide a safety margin, the recycle valve is opened when the compressor approaches a control line placed to the right of the surge limit on the compressor performance map. The margin between the surge limit and the control line must be minimized to obtain maximum operating flexibility and high efficiency. On the other hand, the margin must not be too small to take account of the inaccuracies of the transmitters and analog or digital signal processors, and the dynamic response of the controller and the actuator on the recycle valve. This margin is typically around 10 percent of the actual flow at the surge limit [10]. The current anti-surge control technology seems to have accepted this 10 percent margin for system reliability and safety reasons. The challenge is still out, however, to reduce this margin for a wider operating range and higher efficiency compression without sacrificing reliability or safety.

Various anti-surge control systems differ either in the way the control line is defined or in the parameters measured to define the relative location of the operating point with respect to the control line. All literature reviewed and patents searched revealed that the anti-surge control systems can be grouped in the following categories:

(*i*) Conventional anti-surge control.
(*ii*) Flow/rotational speed (Q/N) technique.
(*iii*) Microprocessor and PLC based controller.
(*iv*) Control without flow measurements.

A brief account and analysis of activities in these four categories is given below.

Table 3 Top companies in US patenting

	Basic Inventions		Citation Frequency
Patent Assignee	1970-89 #	1985-89 % of 1970-89	1970-89
Compressor Controls Corp.	5	20	9
United Technologies Corp.	5	20	1
MAN Gutehoffnungshutte GMBH DE	4	100	4
Babcock & Wilcox Co.	4	0	9
Sundstrand Corp.	4	0	6
Allied-Signal Inc.	2	100	1
Phillips Petroleum Co.	2	50	8
Westinghouse Elec. Corp	2	50	4
Elliott Turbomachinery Co. Inc	2	50	3
Simmonds Precision Prod Inc.	2	0	12
Borg Warner Corp	2	0	5
Dresser Industries Inc	2	0	5

(*i*) **Conventional Anti-surge Control.** This is widely used with variable speed centrifugal compressors and is based on measurements of compressor inlet flow and differential pressure across the compressor. Consequently, the technique is called "Flow/ΔP_c," and is illustrated in Fig. 5. In this system, the signal from the flow element, which is normally a differential pressure (ΔP_o) is shown to be proportional to the differential pressure across the compressor [10]. In general, a linear relationship is used to describe the control line in the form $\Delta P_o = k_1 \cdot \Delta P_c + k_2$.

Consequently, this system is also called "ratio/bias," based on this relationship. The advantages of this conventional system are that it is simple and is very practical since it is independent of compressor speed and suction pressure. However, care should be taken to account for varying inlet temperature, gas composition, and molecular weight as they affect the location of the control line and hence the surge margin [10–12]. Figure 5 shows a temperature compensator as an example.

There are many variations in this basic concept of anti-surge control, which resulted in quite a few patented inventions listed in Table 4. In this table the assignee company name is shown and a brief description of the variation is given. For example, in the patent assigned to Bendix Corporation, the dynamic pressure on the suction side ($P_{os} - P_s$) is used instead of the flow signal, while the difference between discharge total pressure and suction static pressure ($P_{od} - P_s$) is used instead of merely the static differential [13]. Another variation is the

Table 4 Variations of conventional surge control

Company	Technique	Ref.
1. Bendix Corp.	$(P_{os}-P_s) > k(P_{od}-P_s)$	[13]
2. MAN Gutehoffnungshutte	- correction signal is added to the integral part for quick open of the recycle valve and cancelled when closed	[14,15]
3. Compressor Control Corp.	- relay backup to open the valve quickly in case of rapid disturbance	[16,17]
	- control constants are proportional to the rate of approaching the control line	[18]
3. Babcock & Wilcox	- flow is measured on the discharge side by means of orifice meter	[19]
	- adaptive gain depending on the location of the operating point with respect to control line	[20]
	- feed forward signal from the base load anticipating control line crossing	[21,22]
4. Sundstrand Corp.	- flow is measured at discharge with a nozzle	[23]
5. Simmonds Precision	- additional information is obtained from sensing the horsepower	[24]
6. Agar Inst.	- conventional	[25]
7. Phillips Petroleum Co.	- conventional	[26]
8. Elliot Turbomachinery Co.	- conventional	[27]
9. United Technologies Corp.	- conventional	[28]
10. Siemens AG	- conventional	[29]
11. Gas Reproc. Res. Des	- conventional	[30]

addition of a correction signal to the integral part of the controller for quick opening of the recycle (or bleed) valve, which is canceled when the valve is closing [14, 15]. Control systems by Compressor Control Corporation [16–18] feature a relay backup to open the recycle valve quickly in case of rapid disturbance [17]. Also in their patent [18], it is shown that a more effective control system is achieved with controller constants that are proportional to the rate of approach to the control line.

Other patented variations in the conventional anti-surge control are by Babcock & Wilcox Co. [19–22]. The flow signal was provided by means of an orifice plate on the discharge side [19], giving the advantage of lower pressure losses compared to that if it was on the suction side. Adaptive gain depending on the location of the operating point with respect to the control line was demonstrated to provide more stable system [20]. Another interesting concept based on a feed forward signal from the base load anticipating control line crossing was employed successfully [21, 22]. As the concept of measuring the flow on the discharge side was proven, another patented invention was introduced by Sundstrand Corporation [23], where the flow was measured by means of a venturi nozzle on the discharge side to minimize further the pressure loss from the flow element. Additional information is also added to the surge controller along with the basic flow and ΔP_c signals to improve the quality of the output signal. An example of this is the addition of the compressor horsepower to the ΔP_c signal in the invention by Simmonds Precision Products Inc. [24].

Table 4 lists other patented inventions based primarily on the conventional anti-surge control concept described above and are included here for completion purposes. These are referenced in [25–30].

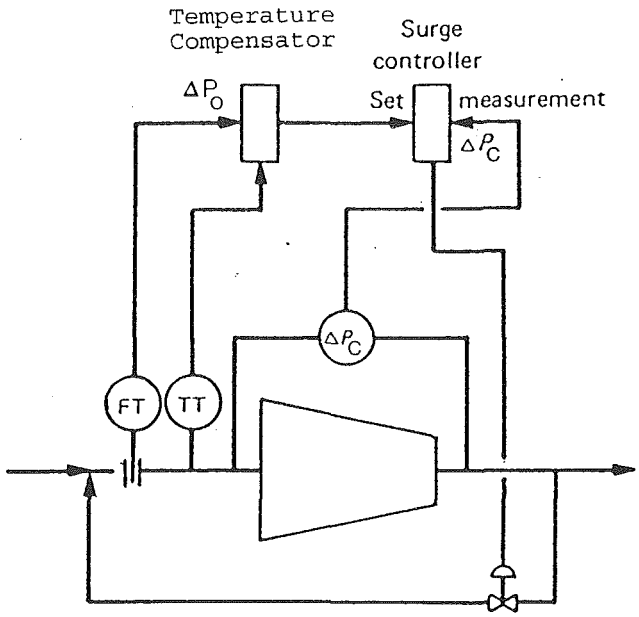

Fig. 5 Conventional surge control system

Two observations are worth mentioning in the analysis of the different variations of this conventional anti-surge control systems listed in Table 4. These are, first, the obvious trend and emphasis on quick opening of the recycle valve to cope with any disturbance that may arise during operation of the compressor unit. The other observation is the fact that the control constants are variables, which depend on the severity of the disturbance or the rate of approach to the control line. But what is common in all of these systems is the basic concept of "flow/ΔP," which is referred to as the conventional system.

***(ii)* Q/N Technique.** In this technique, the fan law characteristics of centrifugal compressors are applied in that the compressor performance characteristics are reduced to a single characteristic if the actual flow through the compressor (Q) is normalized with respect to its rotational speed (N) and the adiabatic or polytropic head across the compressor (H) is normalized with respect to (N^2). The control line is therefore reduced to a control point and at which the ratio $(Q/N)_c$ will be a constant value regardless of the compressor speed. Therefore, in a surge control system the (Q/N) ratio measured by the controller at the compressor operating conditions is compared with the constant $(Q/N)_c$ at the control point. When the measured ratio is less than $(Q/N)_c$, a signal is sent to the recycle valve to open. Examples of systems based on this technique are referenced in [31, 32]. Although pressure and temperature signals are not directly needed in this case, compensators have to be employed to correct for suction temperature, pressure, and gas gravity to determine precisely the actual flow (Q). This technique may hold promise for further development and successful implementation in the future.

***(iii)* Microprocessor and PLC Based Controller.** The conventional anti-surge control systems, despite their inherent simplicity, have a serious limitation in that they only work if the flow signal (ΔP_o) is proportional to the differential pressure across the compressor (ΔP) along the control line. If the compressor performance characteristics show that this relationship between ΔP_o and ΔP is far from linear, a direct comparison between the compressor operating point on the performance map in relation to the control line ought to be made in the controller. This can be accomplished by calculating both the actual flow and the adiabatic or polytropic head across the compressor. Such calculation requires measurements of pa-

rameters other than ΔP_o and ΔP, e.g., temperature, suction pressure, and other stored information on gas composition and properties, and also use of the compressor performance map. Microprocessor or computer-based controllers lend themselves readily to this requirement. The majority of newly designed anti-surge controllers, whether they are provided by the compressor manufacturers or developed by the operating companies themselves, are of this type, and in many cases Programmable Logic Control (PLC) based controllers are employed. The main advantage of such systems is that no inherent assumptions are made in the definition of the control line, which can be located anywhere on the performance map with any chosen margin with respect to the surge limit. Examples of computer based anti-surge controllers are given in [33–35].

***(iv)* Control Without Flow Measurements.** Flow measurements often pose serious problems for anti-surge control. The signal is generally noisy, inaccurate, and in some cases, nonlinear and nonrepeatable. Furthermore, generally the flow measurement elements constitute a pressure loss element and hence a waste of energy. For these reasons it is advantageous to have a surge control system that avoids measuring the flow to the compressor. This was accomplished by making use again of the compressor fan law in which the compressor characteristics are reduced to a single characteristic by means of the normalization discussed earlier. Instead of the Q/N ratio used in (*ii*) above, it is also possible to use (H/N^2) if the characteristic is steep enough on the H-Q diagram to have an appreciable difference between (H/N^2) at the control point and that of the compressor operating point. In this case pressures both upstream and downstream of the compressor are measured along with the compressor rotating speed. The controller can be further simplified by using the pressure ratio P_r $(=P_d/P_s)$ as a process variable and comparing it to a set point corresponding to the speed of the compressor [36]. Another technique uses torque and speed instead of H and N. Here the torque and speed are continuously monitored by a noncontacting sensor system including three equi-spaced gears, two of which are mounted on a reference sleeve mounted on the shaft of the compressor at a position spaced from the third gear [37]. Relative movement of the three gears is monitored by sensors, which through appropriate circuitry produce signals directly related to the shaft horsepower and speed, which in turn are fed to the anti-surge controller. In these two systems, not only is the flow through the compressor not measured but also the sensor system does not create any pressure or energy losses and hence is considered to be efficient.

In concluding this section, it may be fair to say that the current anti-surge control technology is based on a control line margin of 10 percent, and technological progress has been concentrated on a tighter control around this 10 percent margin. Adaptation of advanced process control ideas, such as adaptive gain, feed forward, and variable control constants dependent on the disturbance or rate of approach have been implemented. Almost all of the new anti-surge controllers are now computer-based controllers, which permit better definition and location of the compressor operating point in relation to the control line. Lastly, it was also observed through the literature review that proper selection of the control parameters and constants (i.e., tuning of the controller) requires good assessment of the mechanical components of the system (i.e., the compressor itself and the recycle valve and line). The dynamic interaction between the control components and the recycle system needs better understanding.

4 Control Based on Detection of Surge

A number of anti-surge control systems have been described based on detection of incipient surge first and use the signal from such detection system in the surge controller to drive an output signal to open the recycle valve. There are numerous innovative techniques and ideas for surge detection, which are used for surge control purposes. Schemes based on monitoring vibrations of the compressor usually fail because of difficulties in distinguishing between vibrations arising from incipient surge and from other sources. This gives rise to the problem of false surge indications due to vibrations coming from other sources, such as the transients experienced in start-up of the compressor. Therefore, most of the successful techniques are based on monitoring various variations in flow, pressure, temperature, speed, or other parameters at the compressor suction or discharge, along with their time derivatives or frequency of oscillations. These parameters are compared to threshold values defining the incipient surge and are fed to the surge controller. An overview of these various techniques is given below.

One technique of surge detection is by sensing the temperature rise beyond a predetermined value in a space located within the impeller chamber of the compressor, but outside the gas flow path [38]. Specifically, a thermistor is carried by the casing and exposed to the space between the impeller disk and the hub side of the casing. It is claimed that the temperature rise occurring when the compressor is at incipient surge is caused by the increased heat produced by reduced compressor efficiency, and the inability of the reduced gas flow to remove the heat. Therefore, it is important that the temperature sensor is not located in the gas flow path or on the discharge since at surge or incipient surge the discharge temperature will actually go down.

Another technique for surge detection by means of temperature sensors was disclosed in [39], where the inlet temperature rate of change or rise is computed and compared to a predetermined value, which is a function of other operating parameters such as rotor speed and discharge pressure in order to guard against false detection. A similar technique was applied in [40], where the inlet temperature rise is monitored by means of two thermocouples having different response times. The temperature rise is determined by subtracting the low-response output from the high-response output and compared to a threshold value. Obviously, the last two techniques rely on inlet temperature rise during surge, which is perhaps due to either reversed flow, which is a characteristic of deep surge, or to the increased heat produced by the compressor which somehow is transmitted to the inlet temperature sensors. One of the authors has observed the latter during an experiment that involves surge suppression by means of closed couple throttling.

Another group of surge detection techniques entails measurements of pressures and derivatives thereof, and is by far the most exhaustively investigated technique for surge detection. Numerous systems were developed and patented, which differ in the specific location of the pressure probe(s) and in the manipulation of the pressure signals particularly with respect to time. Therefore, it may be possible to divide this group into the following categories: (*i*) systems that use the pressure signals directly; or (*ii*) systems that rely on time derivatives of the pressure signals; and (*iii*) systems based on dynamic pressure fluctuations, i.e., pressure pulsations.

An example of the first category is the system disclosed in [41], which is suited for centrifugal compressors with vaned diffusers. In this system, three pressures are sensed: static pressure on the pressure side of the diffuser's vane (P_2), static pressure on the suction side of the vane (P_3), and a reference pressure (P_1). An output signal equal to $(P_1-P_2)/(P_1-P_3)$ is compared to a threshold value indicative of surge. Another technique meant for a fan-jet aircraft engine is based on measuring distortions in the total pressure downstream of the fan [42]. A third detection technique is based on measuring the differential pressure between the hub side pressure in the vicinity of the diffuser inlet and the shroud side pressure [43]. Again, the controller compares this differential pressure to a set point value for surge control.

The second category uses time derivatives of pressure signals as a surge detector. A simple system described in [44], for example, differentiates the discharge pressure with respect to time and if a surge condition is ensuing, the absolute value of the differentiated signal is greater than a reference value. To account for the level of pressure itself, the ratio of the time derivative of the pressure to the pressure itself is used instead [45]. A similar system was proposed for a refrigeration compressor, which uses time derivative of the pressure rise across the compressor along with other parameters from the electric driver [46].

The last category of surge detectors based on pressure measurements makes use of the pressure pulsation amplitudes and frequencies in or around the compressor. An early system of this type was disclosed in [47], which produces a signal that depends on discharge pressure fluctuations and their frequencies. Three Russian technologies were later developed that are also based on measuring pulsating pressures with some variations. For example, the system in [48] compensates for the effect of compressor shaft speed through a comparator, while that in [49] has a counter for measuring the frequency of oscillations. The system in [50] has dynamic pressure transducers located on the impeller disk, which measure the pulsating pressure inside the impeller for surge detection.

Other surge detection systems are based on combinations of pressure, speed, and also velocity. At the onset of surge, flow reversal near the wall at impeller exit takes place, and a surge detection system based on placing a velocity reversal probe there was developed in [51]. Another is based on measuring the tangential and radial pressure gradients near the wall at the impeller inlet [52], which are indicative of reversed flow near the wall upstream of the impeller. This system is good for compressors without inlet guide vanes. A system based on time derivatives of both the compressor speed and the discharge pressure was disclosed in [53], where a "surging" signal is formed if the time derivative of the speed above its setting coincides with a lagged signal representing the pressure derivative rise above its signal.

As can be seen from the above number of innovative techniques for surge detection and control, numerous ideas now exist and the technology is not starving for new techniques or systems. However, each of these techniques is rather specific to a certain machine and compression system. This is because different compressors exhibit different behaviors and signature patterns during incipient surge, and thus any attempt to implement a specific technique to a different type of compressor or system would likely be unsuccessful. Therefore, the technology is awaiting a major breakthrough invention for a general system that can be applied to almost every centrifugal compressor or compression system. Additionally, the signal(s) measured when the compressor is near its incipient surge is compared to a predetermined setting in the controller to decide on the action signal. Generally, a proper setting is very difficult to determine at different operating conditions and actual compressor surge tests are necessary to assure correct setting.

Another aspect of surge control by means of detection is the lack of high response mechanical components to prevent the compressor from going into deep surge once incipient surge is detected. In particular, the response time of the recycle valve to open is far beyond that of the surge detection and control system. Consequently, a surge control system based on detection of incipient surge and then control always runs the risk of driving the compressor unit into a damaging surge. As a result, this technique has not found wide acceptance, particularly in the gas transmission industry where system reliability and safety are of primary importance. Again, unless a reliable technique is developed that can be applied to a wide range of compressor types and system configurations, the road to surge control by means of detection will not be reached.

5 Developments in Surge Suppression

The surge phenomenon in centrifugal compressors limits their operating range and can prevent operation at maximum efficiency, which may lie at or close to the surge line. In addition, anti-surge control systems, described in section 3 above, further limit the operation of the compressor and also result in loss of energy as a consequence of gas recycling during surge protection operation. Surge detection and control described in section 4 runs the risk of damaging the unit due to the lack of high response mechanical components for gas recycling, i.e., the recycle valve and its actuator.

The nonpatent literature describes a considerable amount of work carried out in an attempt to understand and identify the various mechanisms and causes for the surge phenomenon. As the knowledge increased in this area, novel ideas emerged for suppressing surge as much as possible. This has also been driven by the obvious motivation to increase the operating range of the compressor by extending the surge limit to the minimum possible flow. This section attempts to describe briefly the various techniques and methods that are available in the literature and aimed at influencing the surge limit to a lower limit.

Since the compressor surge phenomenon is both machine and system dependent, the various methods described here for surge suppression can be grouped into two categories: (*i*) those methods that affect the internal design of the compressor unit itself and can be implemented during the manufacture of the compressor; and (*ii*) those methods and techniques that are considered operational and affect the system design where modifications of or additions to the connecting system of a particular compressor can be made to suppress surge and extend its limit during operation. The following is a brief description of the various methods in each category.

(*i*) Design Methods. Different design techniques have been suggested to improve the stability of the impeller, diffuser, and casing geometry. The most effective way to increase impeller stability, which has also received considerable investigation, is to use a backward leaned angle at impeller exit (often called backsweep). The higher this angle, the steeper the negative slope of the performance curve, and the better the blade loading [54]. The number of impeller blades also has an effect on the surge limit. Gottschalk [55] found that there is a minimum number of blades for rotating stall to occur. Flynn and Weber [56] were able to lower the surge limit by 60 percent by means of thickening the impeller blades on the suction side to prevent separation of the flow.

Another technique for extending the surge limit by better design of the compressor components is by stabilizing the diffuser. One way to suppress surge in a compressor with a vaneless diffuser is by reducing the diffuser exit width [57]. In compressors with vaned diffusers, experimental data by Japikse [58] show the effects of decreasing the number of vanes on lowering the surge limit at the cost of 2 percent loss in total pressure rise due to the presence of stronger shocks. Different shapes particularly at the diffuser's inlet were found to have an effect on the surge limit [59]. To cope with variations of the flow velocity and angle coming out from the impeller, Bammert et al. [60] changed the vane inlet geometry of the diffuser from the hub side to the shroud side, which resulted in improvement in both compressor range and efficiency. Also, the ratio between the radius of the leading edge of the diffuser vane to the rotor outlet radius has an effect on the surge limit. Which direction this effect might be is still under investigation as contradictory results were obtained by different investigators [61, 62]. Another technique for enhancing the surge margin is by what is called "porous diffuser," which is based on linking of the diffuser throats by a communicating manifold. This equalizes the pressures in the diffuser throats and hence prevents any one diffuser from reaching its limiting (stalling)

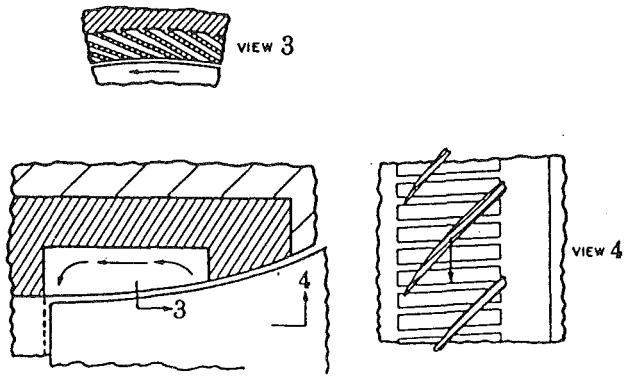

Fig. 6 Inclined axial grooves at impeller inlet for surge limit improvement [66]

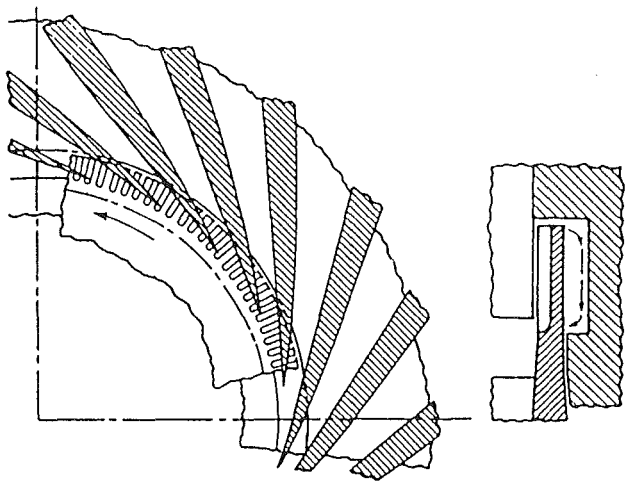

Fig. 7 Casing treatment at impeller exit proposed by Jansen et al. [66]

condition before any other, thereby extending the range to stall of the diffuser and compressor system as a whole [63]. Different designs of compressor volutes [64] and locations of the scroll tongue with respect to compressor circumference in cases where the scroll is very close to the impeller outlet [65] were also found to be possible methods to postpone surge.

Casing treatments that were first applied to axial compressors have been extended to centrifugal compressors. Some successful applications are reported by Jansen and co-workers [66], where inclined axial grooves at impeller inlet (as shown in Fig. 6) give a remarkable improvement in surge limit for a medium pressure rise compressor. In a patent by Wiggins and Walz [67], circumferential grooves were also proved successful in suppressing surge. Casing treatment at impeller exit and vaned diffuser casing treatment with radial slots in the external hub section (Fig. 7) give unsatisfactory results in terms of moving the surge limit, but the flow rate at choking was markedly increased [66]. A more successful diffuser casing treatment is proposed by Amann and co-workers [68] for vaned diffusers. A circumferential slot, connected to annular chamber (Fig. 8) was effective in suppressing surge. A more uniform pressure distribution with lower pulsation levels was observed with this treatment, which has a favorable effect on the surge limit.

Lastly, rotating vaneless diffusers are claimed to smooth out any distortion in the entry flow profiles from the impeller outlet to the diffuser inlet, and hence improve the surge limit [69]. However, only a small change in surge limit and a positive influence on efficiency was observed.

***(ii)* Operational Methods.** Another way to influence the compressor surge limit is by the use of additional devices or components attached to the compressor either on the suction

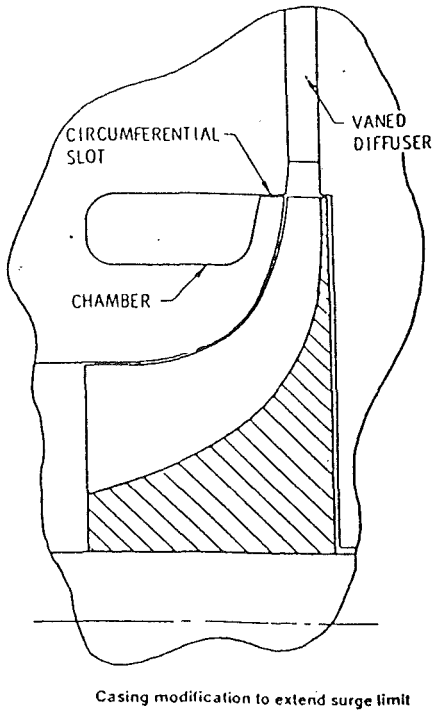

Fig. 8 Circumferential slot connected to chamber at impeller exit for surge suppression (Amann et al. [68])

or the discharge side. Imposed prerotation in the proper direction seems to suppress surge and decrease the energy input for compression. Prewhirl also accentuates the negative slope of the performance curve, similar to backswept blades. Prewhirl can be achieved by means of inlet guide vanes (IGV) [59, 70] or by reinjecting gas from the discharge side to the inlet side using directional nozzles [71]. One drawback of the IGV is an inherent pressure loss. The IGV are also used to control the right amount of prewhirl required by means of variable setting. The mechanical setup and control for the reinjection are simpler than for variable IGV; however, the amount of reinjection is not negligible. A similar concept is used at the outlet of the compressor upstream of the diffuser vanes. In this case, an annular row of freely movable (floating) vanes is aligned with the flow direction and has the effect of preventing surge conditions [77].

Another operational means to suppress surge was described by Dussourd and co-workers [72], who demonstrated that a resistance element placed very close to the compressor discharge changes the performance curve of the combined compressor/resistance in such a way that the negative slope part of the curve is extended over a larger region. It is also believed that the presence of such resistance dynamically separates the compressor from the system capacitance which is the basic component for surging. Epstein and co-workers [73] and Pinsely [74] extended the principle of throttling and applied active control to the throttling element, which was allowed to oscillate in a manner dictated by the control system in order to modulate the measured oscillating pressure. Their system was composed of a plenum chamber resembling the combustion chamber of an aeroengine. Simon [75] showed that proper choice of sensor as well as actuator crucially affects the ability to stabilize these systems, and that those actuators most closely coupled to the compressor appear most effective. Jungowski and Weiss [76] further extended the concept and applied it successfully to suppress surge of a centrifugal compressor connected to a piping network. They demonstrated that passive throttling can be as effective as active throttling, as is demonstrated in Fig. 9.

In conclusion, most of the research and innovative ideas

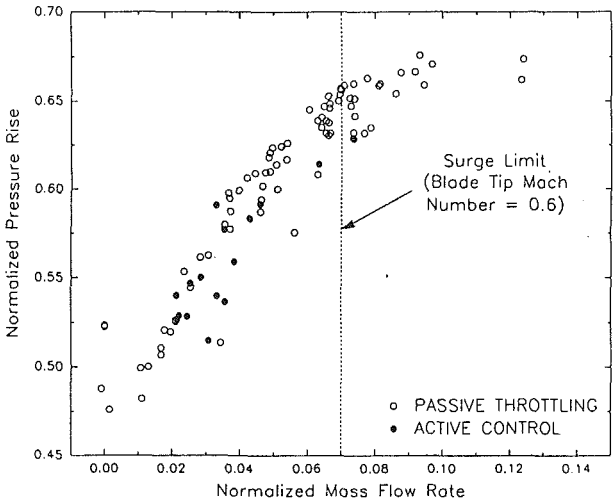

Fig. 9 Comparison between passive and active throttling for surge suppression (Jungowski and Weiss [76])

mentioned above were on a trial-and-error basis leading to disappointing as well as encouraging results. The challenge is still ahead to find the most effective surge suppression method, technique, or device that is effective in suppressing surge and extending the operating region substantially without sacrificing much in terms of efficiency.

6 Concluding Remarks

The overview assessment presented in this paper allows the following conclusions to be drawn:

(*a*) Centrifugal compressor surge control technology seems to be in a perfection stage. Most of the current and future activities will be directed toward incremental improvements in existing technology. These improvements involve better engineering application and embodiments such as different sensors and computational methods. Additionally an old approach based on using normalization techniques needs to be revisited as it can offer reliable control systems in some cases. It is believed that during the next decade principal advances will be along the lines of digital computer methods, sensors, and actuators. Inventions that might involve combination of different concepts such as a system where surge detection can be combined with temporal surge suppression for a period of time long enough to bring another low response but more efficient surge control system on line. This might place the whole surge control technology in a developmental stage and open up opportunities for further innovations. Unfortunately, there is no patent that points to such possibilities.

(*b*) Effective and safe techniques for detection based on surge control do not yet exist and are still a challenge. The main obstacles are: (*i*) the signals from detection devices are not sufficiently reliable, (*ii*) the detection techniques are rather specific to certain machines and compression systems, and (*iii*) the response of the mechanical components such as the recycle valve and its actuator is not fast enough (e.g., the time to open the recycle valve needs to be reduced by an order of magnitude to respond quickly to the detection signal without the risk of driving the compressor into deep surge once incipient surge is detected). As a result, the prospect that control based on detection of surge will find widespread commerical use is believed to be poor.

(*c*) Various surge suppression techniques for use in specific types of compressors now exist in some laboratories and the technology seems to be in a research stage. Surge suppression requires a truly significant inventive concept which would be applicable to many types of compressors while maintaining acceptable reliability and energy efficiency of the overall compression system as compared to conventional control technology.

Acknowledgments

The work presented here is initiated and supported by NOVA CORPORATION OF ALBERTA, and permission to publish it is hereby acknowledged. The assistance of B. Clibbon and S. Veness in devising search concepts and searching on-line patent databases is very much appreciated.

References

1 Marmor, A. C., Lawson, W. S., and Terapane, J. F., "The Technology Assessment and Forecast Program of the United States Patent and Trademark Office," World Patent Information, Vol. 1, No. 1, 1979, pp. 15–23.

2 Griliches, Z., "Patent Statistics as Economic Indicators: A Survey," *Journal of Economic Literature*, Vol. XXVIII, Dec. 1990, pp. 1661–1707.

3 Wilson, R. M., "Patent Analysis Using Online Databases—I. Technological Trend Analysis," *World Patent Information*, Vol. 9, No. 1, 1987, pp. 18–26.

4 Wilson, R. M., "Patent Analysis Using Online Databases—II. Competitor Activity Monitoring," *World Patent Information*, Vol. 9, No. 2, 1987, pp. 73–78.

5 Narin, F., Noma, E., and Perry, R., "Patents as Indicators of Corporate Technological Strength," *Research Policy*, Vol. 16, 1987, pp. 143–155.

6 Narin, F., Carpenter, M. P., and Woolf, P., "Technological Performance Assessment Based on Patents and Patent Citations," *IEEE Transactions on Engineering Management*, Vol. EM-31, No. 4, 1984, pp. 172–183.

7 Carpenter, M. P., Narin, F., and Woolf, P., "Citation Rates to Technologically Important Patents," *World Patent Information*, Vol. 3, No. 4, 1981, pp. 160–163.

8 Trajtenberg, M., "Patents, Citations and Innovations: Tracing the Links," National Bureau of Economic Research, Cambridge, MA, Working Paper No. 2457, 1987.

9 Mogee, M. E., "Using Patent Data for Technology Analysis and Planning," *Research Technology Management*, Vol. 34, No. 4, 1991, pp. 43–49.

10 White, M. H., "Surge Control for Centrifugal Compressors," *Chemical Engineering*, Dec. 1992, pp. 54–62.

11 Boyce, P. B., et al., "Tutorial Session on Practical Approach to Surge and Surge Control," *Proceeding of the 12th Turbomachinery Symposium*, Texas A&M University, 1983, pp. 145–173.

12 Kolnsberg, A., "Reasons for Centrifugal Compressor Surging and Surge Control," ASME *Journal of Engineering for Power*, Vol. 101, 1979, pp. 79–86.

13 Middleton, E. J. (Bendix Corp.), "Air Compressor Surge Control Apparatus," US Patent 3473727, 1969.

14 Wilfried, B. (MAN Gutehoffnungshutte), "Device for Control of a Turbocompressor," US Patent 4968215, 1990.

15 Wilfried, B. (MAN Gutehoffnungshutte), "Method and Apparatus for Controlling Turbocompressors to Prevent Surge," US Patent 4831534, 1989.

16 Rutshtein, A., and Staroselsky, N. (Compressor Control Corp.), "Method and Apparatus for Antisurge Protection of a Dynamic Compressor," US Patent RE30329, 1980, reissue of US 4046490.

17 Staroselsky, N. (Compressor Control Corp.), "Method and Apparatus for Preventing Surge in a Dynamic Compressor," US Patent 4142838, 1979.

18 Mirsky, S., Reinke, P. A., and Staroselsky, N. (Compressor Control Corp.), "Method and Apparatus for Preventing Surge in a Dynamic Compressor," US Patent 4949276, 1990.

19 Agarwal, S. C. (Babcock & Wilcox Co.), "Centrifugal Compressor Surge Control System," US Patent 4464720, 1984.

20 Keyes, M. A., and Saffer, J. J. (Babcock & Wilcox Co.), "Adaptive Gain Compressor Surge Control System," US Patent 4697980, 1987.

21 Enterline, L. L., and Kaya, A. (Babcock & Wilcox Co.), "Integrated Control of Output and Surge for a Dynamic Compressor Control," US Patent 4562531, 1985.

22 Dziubakowski, D. J., Keyes, M. A., and Saffer, J. J. (Babcock & Wilcox Co.), "Compressor Surge Control Method," US Patent 4900232, 1990.

23 Schuh, P. A. (Sundstrand Corp.), "Gas Turbine Engine/Load Compressor Power Plants," US Patent 4834622, 1989.

24 Abbey, W. C. (Simonds Precision Inc.), "Surge Control for Centrifugal Compressor," US Patent 4203701, 1980.

25 Zanker, K. J., and Agar, J. (Agar J Instr. Ltd.), "Centrifugal Compressor Surge Prevention—By Maintaining Fixed Relationship Between Two Signals Dependent on Gas Flow," GB Patent 790221, 1979; US Patent 4156578, 1979.

26 Bellinger, R. M., and Clayton, H. A. (Phillips Petroleum Co.), "Compressor Surge Control System," US Patent 4230437, 1980.

27 Condrac, E., and Hohlweg, W. C. (Elliot Turbomachinery Co. Inc.), "Method and Apparatus for Regulating Power Consumption While Controlling Surge in a Centrifugal Compressor," US Patent 4586870, 1986.

28 Goodman, R. B., and Perkinson, R. H. (United Technologies Corp.), "High Frequency Surge Controller for Compressor—Has Surge Valve Biassed as Function of Inlet Guide Vane Angle, Ambient Pressure and Ambient Temp," EP Patent 301993, 1989; CN Patent 1030968, 1989.

29 Ewe, K., and Linzenkirk, E. (Siemens AG), "Control System for Axial Flow Air Compressor—Feeds Signal From Anti-Surge Control to Main Control to Improve Stability," DE Patent 2739229, 1979.

30 Bocharov, V. I., Tereschen, V. P., and Savin, V. F. (Gas Reproc Res Des), "Anti-Surge Mechanism for Centrifugal Compressor—Has Transducer

for Specific Gravity of Gas and Multiplication Unit Linked to Transducers," SU Patent 909328, 1982.

31 Agahi, R., and Swearingenm, J. S. (Rotoflow Corp.), "Surge Control System," US Patent 5002459, 1991.

32 Lawless, B. S., and Stickel, J. E. (Exxon Research and Engineering Co.), "Surge Control in Compressors," US Patent 4971516, 1990.

33 Hobbs, J. W. (Phillips Petroleum Co.), "Constraint Control for a Compressor System," US Patent 4807150, 1989.

34 Ramos, E. J., "Microprocessor Applications in Gas Turbines and Centrifugal Compressors," ISA Paper #87-1011, 1987.

35 Bergen, D. P., and Vermilya, R., "Microprocessor Theory and Application for Turbomachinery," Solar Turbine Inc., 1986.

36 Glennon, T. F., and Sarphie, T. E. (Sundstrand Corp.), "Surge Control for Variable Speed-Variable Geometry Compressors," US Patent 4164035, 1979.

37 Weitz, P. G. (Simmonds Precision Products Inc.), "Surge Control System," US Patent 3876326, 1975.

38 Watson, T. E., and Smailwood, P. R. (Westinghouse Electric Corp.), "Method and Apparatus of Surge Detection and Control in Centrifugal Gas Compressors," GB Patent 2052645, 1980.

39 Preti, E., and Ripy, H. W. (United Technology Corp.), "Surge Detector for Gas Turbine," US Patent 4137710, 1979.

40 Gaston, J. R. (Dresser Industries Inc.), "System, Apparatus, and Method for Detecting and Controlling Surge in a Turbo Compressor," US Patent 4594051, 1986.

41 Clark, J. C., and Perrone, G. L. (The Garrett Corp.), "Apparatus and Methods for Preventing Compressor Surge," US Patent 4662817, 1987.

42 Callahan, D. J., et al. (United Technologies Corp.), "Engine Surge Prevention System," US Patent 4550564, 1985.

43 Adachi, Y., and Oka, T. (Daiken Inds Ltd.), "Surging Prediction Device for Centrifugal Compressor," EP Patent 435294, 1991.

44 Faulkner, D. T., Glennon, T. F., and Sarphie, T. E. (Sundstrand Corp.), "Compressor Surge Control With Pressure Rate of Change Control," US Patent 4164034, 1979.

45 Collins, B. J. (Rolls Royce Motor Cars Ltd. GB), "Control Systems for Gas Turbine Aeroengines," US Patent 4603546, 1986.

46 Hagerman, R. T., and Lowe, M. M. (Borg-Warner Corp.), "Method and Apparatus for Detecting Surge in Centrifugal Compressors Driven by Electric Motors," US Patent 4581900, 1986.

47 Blutinger, B., and Stalker, R. W. (Navistar International Corp.), "Turbine Surge Detection System," US Patent 3963367, 1976.

48 Akulshin, Y. U. D., Izmailov, R. A., and Seleznev, K. P. (Lengd Poly), "Surge Indicator for Centrifugal Compressor," SU Patent 830009, 1981.

49 Semenov, Y. U. A., "Centrifugal Compressor Surge Indicator," SU Patent 840492, 1981.

50 Belyanovsk, E. S., Izmailov, R. A., and Seleznev, K. P. (Ind Dwelling Cons), "Compressor Pre-surge Condition Determination Method," SU Patent 1321927, 1987.

51 Boyce, M. P. (Howell Instruments Inc.), "Method and Apparatus for Compressor Surge Control," US Patent 3901620, 1975.

52 Fradin, C. F. (Office National D'Etudes et de Recherches Aerospatiales FR), "Methods and Apparatus for Avoiding Surging Phenomena in Compressors," US Patent 4205941, 1980.

53 Heinismann, M. G., Kochrov, V. I., and Nakhshin, G. S., "Compressor Anti-Surge Protection by Comparison of Gas Pressure and Rotor Rotational Speed Derivatives With Settings to Form Signal," SU Patent 985450, 1982.

54 Cumpsty, N. A., "Compressor Aerodynamics," Longman Scientific & Technical, 1989.

55 Gottschalk, M., "Investigations on the Stability of the Characteristic of Radial Flow Fans," *Proceedings of the 4th Conference on Fluid Machinery*, Budapest, pp. 459–475, 1972.

56 Flynn, P., and Weber, H., "Design and Test of an Extremely Wide Flow Range Compressor," ASME Paper No. 79-GT-80.

57 Ludtke, K., "Aerodynamic Tests on Centrifugal Process Compressors—The Influence of the Vaneless Diffuser Shape," ASME *Journal of Engineering for Power*, Vol. 102, No. 4, 1983, pp. 902–909.

58 Japikse, D., "The Influence of Diffuser Inlet Pressure Field on the Range and Durability of Centrifugal Compressor Stages," *Centrifugal Compressors, Flow Phenomena and Performance*, AGARD CP 282, Paper 13, 1980.

59 Whitefield, A., Wallace, F. J., and Atkey, R. C., "The Effect of Variable Geometry on the Operating Range and Surge Margin of a Centrifugal Compressor," AME 76-DT-98, 1976.

60 Bammert, K., Jansen, M., and Rautenberg, M., "On the Influence of the Diffuser Inlet Shape on the Performance of a Centrifugal Compressor Stage," ASME Paper No. 83-GT-3, 1983.

61 Pampareen, R. C., "The Use of Cascade Technology in Centrifugal Compressor Vaned Diffuser Design," ASME Paper No. 72-GT-9, 1972.

62 Dean, R. C., "The Fluid Dynamic Design of Advanced Centrifugal Compressors," CREARE TN 153, Sept. 1973.

63 Raw, J. A., "Surge Margin Enhancement by a Porous Throat Diffuser," *Canadian Aeronautics and Space Journal*, Vol. 32, No. 1, Mar. 1986.

64 Stiefel, W., "Experiences in the Development of Radial Compressors," *Advanced Radial Compressors*, VKI Lecture Series 50, May 1972.

65 Lipski, W., "The Influence of Shape and Location of the Tongue of Spiral Casing on the Performance of Single Stage Radial Pumps," *Proc. 6th Conference on Fluid Machinery*, Budapest, 1979, pp. 673–682.

66 Jansen, W., Carter, A. F., and Swarden, M. C., "Improvements in Surge Margin for Centrifugal Compressors," *Centrifugal Compressor, Flow Phenomena and Performance*, AGARD Cp 282, Paper 19, 1980.

67 Wiggins, J. V., and Waltz, G. L., "Centrifugal Compressor Vaneless Space Casing Treatment," US Patent 4063848, 1977.

68 Amann, C. A., Nordenson, G. E., and Skellenger, G. D., "Casing Modification for Increasing the Surge Margin of a Centrifugal Compressor in an Automotive Turbine Engine," ASME *Journal of Engineering for Power*, Vol. 97, 1975, pp. 329–336.

69 Rodgers, C., and Mnew, H., "Experiments With a Model Free Rotating Vaneless Diffuser," ASME *Journal of Engineering for Power*, Vol. 97, 1975, pp. 231–242.

70 Rodgers, C., "Centrifugal Compressor Inlet Guide Vanes for Increased Surge Margin," ASME JOURNAL OF TURBOMACHINERY, Vol. 113, 1991, pp. 696–702.

71 Kyrtatos, N., and Watson, N., "Application of Aerodynamically Induced Prewhirl to a Small Turbocharger Compressor," ASME *Journal of Engineering for Power*, Vol. 102, No. 4, 1980, pp. 943–950.

72 Dussourd, J. L., Pfrannenbecker, G. W., and Singhania, S. K., "An Experimental Investigation of the Control of Surge in Radial Compressors Using Close Coupled Resistance," ASME *Journal of Fluids Engineering*, Vol. 99, No. 1, 1977, pp. 64–76.

73 Epstein, A. H., Ffowcs Williams, J. E., and Greitzer, E. M., "Active Suppression of Aerodynamic Instabilities in Turbomachines," *J. Propulsion*, March–April, 1989, pp. 204–211.

74 Pinsely, J., "Active Control of Centrifugal Compressor Surge," M.S. Thesis, Dept. of Aeronautics and Astronautics, Massachusetts Institute of Technology, Cambridge, MA, 1988.

75 Simon, J. S., Valavani, L., Epstein, A. H., and Greitzer, E. M., "Evaluation of Approaches to Active Compressor Surge Stabilization," ASME JOURNAL OF TURBOMACHINERY, Vol. 115, 1993, pp. 57–67.

76 Jungowski, W. M., Weiss, M. H., and Price, G. R., "Pressure Oscillations Occurring in a Centrifugal Compressor System With and Without Passive and Active Surge Control," to be presented at the 39th International Gas Turbine & Aeroengine Congress & Exposition, Turbo-Expo, The Hague, Netherlands, June 13–16, 1994.

77 Blackburn, R. B. (Caterpillar Tractor Co.), "Self-Aligning Vanes for a Turbomachine," U.S. Patent 3957392, 1976.

The Operational Stability of a Centrifugal Compressor and Its Dependence on the Characteristics of the Subcomponents

R. Hunziker

G. Gyarmathy

Turbomachinery Laboratory,
ETH Swiss Federal Institute of Technology,
Zurich, Switzerland

A centrifugal compressor was tested with three different diffusers with circular-arc vanes. The vane inlet angle was varied from 15 to 30 deg. Detailed static wall pressure measurements show that the pressure field in the diffuser inlet is very sensitive to flow rate. The stability limit regularly occurred at the flow rate giving the maximum pressure rise for the overall stage. Mild surge arises as a dynamic instability of the compression system. The analysis of the pressure rise characteristic of each individual subcomponent (impeller, diffuser inlet, diffuser channel,...) reveals their contribution to the overall pressure rise. The diffuser channels play an inherently destabilizing role while the impeller and the diffuser inlet are typically stabilizing. The stability limit was mainly determined by a change in the characteristic of the diffuser inlet. Further, the stability limit was found to be independent of the development of inducer-tip recirculation.

Introduction

It is common industrial practice to adapt the optimal range of operation of centrifugal impellers to different users by combining them with diffusers of different geometry. Also, variable geometry diffusers are widely used to satisfy customer demand for broad range. There is great interest in reducing the empiricism involved in these approaches by establishing criteria for the influence of key geometric factors on the stability limit of the stage, all the more since maximum efficiency in centrifugal compressors usually occurs close to this limit and therefore the necessity of a surge margin results in a reduced operating efficiency.

Flow instabilities have been studied extensively. Rotating stall, a frequently observed flow phenomenon, sometimes, but not necessarily, precedes surge. Experimental data with vaneless diffuser rotating stall are given, for example, in Jansen (1964), Abdelhamid (1983), Frigne and Van Den Braembussche (1984), and Rieder (1987). Rotating stall occurring in the impeller is described, for example, in Frigne and Van Den Braembussche (1984), Ariga et al. (1987), and Kämmer and Rautenberg (1982, 1986). Another type of flow instability, mild surge, also has been observed prior to the occurrence of "deep" surge (Emmons et al., 1955; Amann et al., 1975). Intermittent mild surge cycles can be part of the whole deep surge cycle (Toyama et al., 1977; Dean and Young, 1977; Fink et al., 1991). Greitzer (1981) reviews the literature concerning different types of instabilities and provides criteria for the static and dynamic stability of the system comprising the compressor, the piping, and the user. Based on the physical mechanisms for dynamic instability, various passive and active control concepts have been proposed or realized (Pinsley et al., 1991; Gysling et al., 1991; Simon et al., 1993).

In the literature many parameters determining compressor stability have been advanced; see, for example, the review by Elder and Gill (1985). Some of these parameters concern the impeller, some the diffuser. Often the semi-vaneless space is stated as the most critical element of a centrifugal compressor stage where the flow breaks down if a critical level of diffusion or a critical value of pressure recovery is exceeded (e.g., Kenny, 1972; Toyama et al., 1977; Came and Herbert, 1980; Elder and Gill, 1985). But such critical values are not able to explain surge line shifts caused solely by changes in the diffuser channel geometry (Japikse, 1980; Clements and Artt, 1987).

The above-mentioned work of Greitzer (1981) points out that for simple compression systems with a sufficiently large B-parameter a simple stage-stability parameter based on empirical pressure rise versus flow rate data can be deduced. The criterion states that the limit of dynamic stability coincides with the maximum of the total-to-static pressure rise characteristic. This argument can be extended to the individual components of the stage, indicating the components that are potentially unstable (Dean, 1974; Japikse, 1984). A typical unstable subcomponent is the diffuser channel.

In diffuser design the (laboratory) two-dimensional diffuser data of Reneau et al. (1967) and Runstadler et al. (1975) are commonly used. They show the relationship of geometry, pressure recovery, stalled regimes, and inlet blockage. Comparisons of radial diffuser channel data and two-dimensional duct or pipe diffuser data show principal agreement but discrepancies exist in the level of pressure recovery (Yoshinaga et al., 1980; Japikse and Osborne, 1986). There are several reasons

Contributed by the International Gas Turbine Institute and presented at the 38th International Gas Turbine and Aeroengine Congress and Exposition, Cincinnati, Ohio, May 24-27, 1993. Manuscript received at ASME Headquarters March 10, 1993. Paper No. 93-GT-284. Associate Technical Editor: H. Lukas.

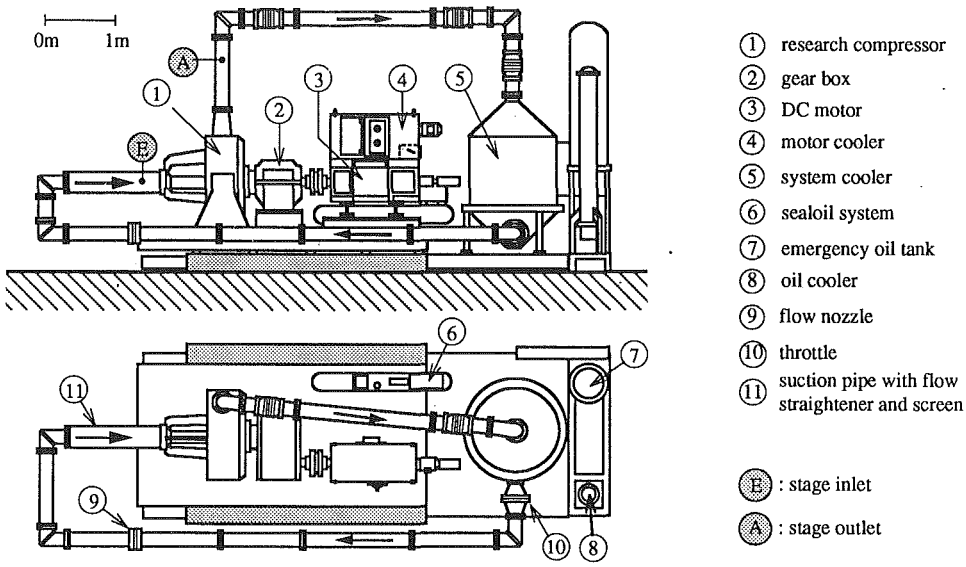

Fig. 1 General view of the test rig

for these discrepancies, e.g., difference in aspect ratio or difference in turbulence structures. Also the range of blockage values typical of radial diffusers was not completely covered by the duct data and the inflow conditions may differ significantly.

Detailed measurements of wall pressure distributions and of flow velocity fields in radial diffusers (e.g., Krain, 1981; Jansen, 1982; Stein and Rautenberg, 1988) provide insight into the complex flow structures existing within the vaneless and semi-vaneless space. Investigations in isolated diffuser test rigs are reported in Baghdadi and McDonald (1975), Dutton et al. (1986), and Filipenco (1991). Information on the overall performance of diffusers and diffuser subcomponents are given, for example, in Kenny (1972), Rodgers (1982), Japikse and Osborne (1986), and Clements (1987).

Experimental Setup and Instrumentation

The experiments were performed on a closed-loop test rig using air. The single-stage centrifugal compressor is driven by a 440 kW DC motor coupled to a two-stage gear box. The maximum rotational speed is limited to 22,000 rpm by the shaft seal. The flow rate is controlled by a throttle. The pressure in the suction pipe was set to 960 mbar and the inlet temperature was held at 24°C. Figure 1 shows the test rig. A flow straightener mounted in the suction pipe ensures axial flow at the stage inlet.

The cross-sectional view of the stage in Fig. 2 and the picture in Fig. 3 reveal more details of the compressor stage. The main data of the unshrouded impeller used in the present tests were:

Impeller tip diameter d_2	280 mm
Full/splitter blades	11/11 (total 22)
Exit blade angle	30 deg back lean
Exit width	17 mm

The vaned diffuser investigated consists of two parallel walls and 24 circular-arc vanes. By adjusting the diffuser vanes by turning them around a pin fixing the leading edge different diffuser configurations can be realized. The center of the leading edge is at radius $r_B/r_2 = 1.16$. Three different diffusers were investigated by setting the vane angle α_{Bvane} at the leading edge to 15, 25, and 30 deg. A diffuser channel is sketched in Fig. 4 and the main parameters of the diffuser are listed in Table 1. It is a common practice to describe radial diffusers by the area ratio AR and by the ratio of length l to inlet width h, or alternatively by the divergence angle 2θ. The relationship between 2θ and l/h is given by:

$$2\theta = 2\text{atn}\left(\frac{AR-1}{2l/h}\right) \tag{1}$$

The radial diffuser is followed by a large toroidal collecting chamber providing a virtually uniform circumferential pressure distribution.

The overall performance of the compressor was determined by conventional wall pressure taps and temperature probes in

Nomenclature

A = geometric area
A_{eff} = effective area
AS = diffuser aspect ratio $= b/h_C$
AR = diffuser area ratio
Bl = diffuser throat blockage
b = diffuser width (axial)
Cp = pressure recovery coefficient
Dp = pressure rise coefficient
d = diameter
h = diffuser channel height (perpendicular to a mean streamline)
L = length of diffuser vane
l = diffuser channel length
Mu = peripheral Mach number
p_{dyn} = dynamic pressure
p = pressure
R = gas constant
r = radius
T = temperature
t = diffuser vane thickness
u = circumferential speed
V = volumetric flow rate
α_{Bvane} = diffuser vane setting angle
Δp = pressure difference
2θ = diffuser channel divergence angle
κ = isentropic coefficient
ρ = density
φ = flow coefficient

Subscripts

2 = impeller outlet
3 = diffuser outlet ($r_3/r_2 = 1.79$)
A = stage outlet
B = diffuser vane leading edge ($r_B/r_2 = 1.16$)
C = diffuser throat
D = diffuser channel exit
E = stage inlet
K = curvature

Superscripts

o = stagnation

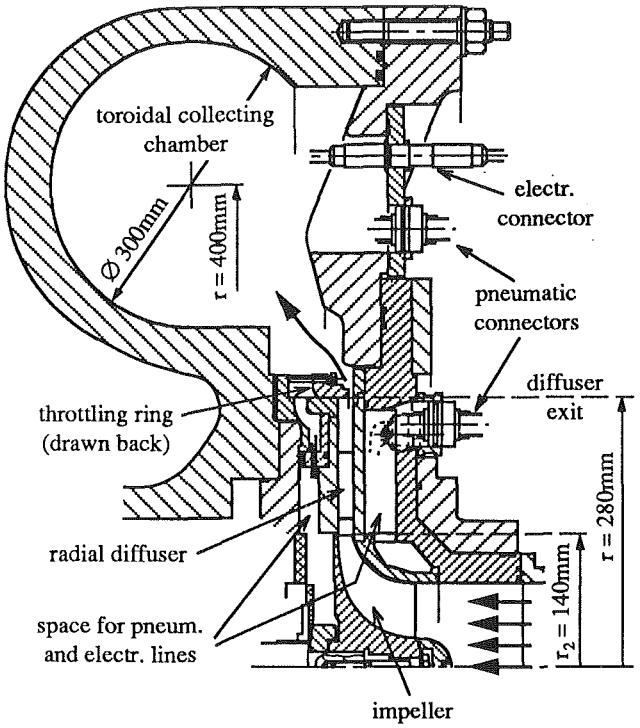

Fig. 2 Cross-sectional view of the centrifugal compressor stage

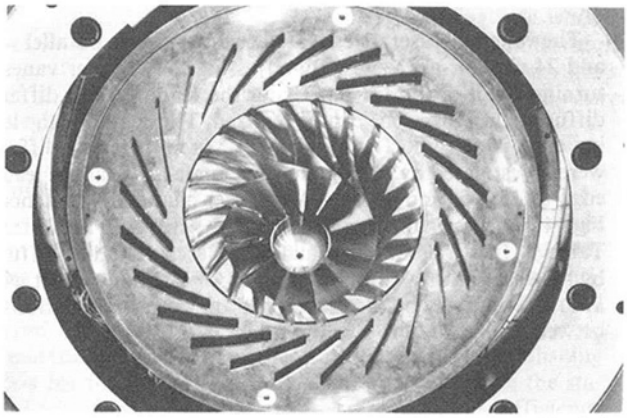

Fig. 3 View of centrifugal impeller and vaned radial diffuser (25 deg)

the suction pipe and in the outlet tube. Along the casing contour as well as in the front and rear diffuser wall a large number of wall pressure taps are located. All wall-tap pressure data were taken by means of a multichannel pressure data acquisition system with about 250 ports. The accuracy of this system is about 1 mbar. All the temperature and pressure data are collected by a μVax computer.

Any wall pressure fluctuations caused by flow instabilities as rotating stall or surge are detected by high-frequency response pressure transducers placed in the diffuser entry region, whose signals are amplified, filtered (cut off frequency 10 kHz) and recorded on a multichannel tape. Afterward the signals are processed using a two-channel frequency analyzer. From the frequency information and the phase shift of the signals of two circumferentially displaced transducers the type of instability (rotating stall or surge) can be diagnosed.

Performance Map

For each of the three diffuser configurations, the measurements were taken at four different speeds. The rotational speed of the impeller is expressed by a peripheral Mach number Mu:

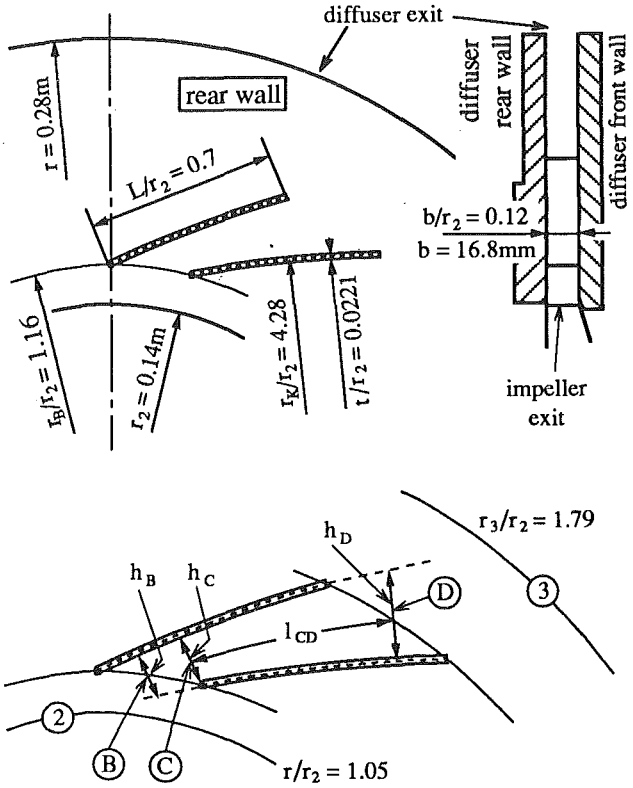

Fig. 4 Sketch of the vaned diffuser

Table 1 Geometric data of diffusers

$\alpha_{B\ vane}$	AR_{BD}	l_{BD}/h_B	$2\theta_{BD}$	AR_{CD}	l_{CD}/h_C	$2\theta_{CD}$
15°	2.95	10.2	10.9°	2.37	6.5	12.0°
25°	2.14	5.9	11.1°	1.90	4.2	12.1°
30°	1.96	4.9	11.3°	1.79	3.7	12.2°

$$\mathrm{Mu} = \frac{u_2}{\sqrt{\kappa R T_E^Q}} \tag{2}$$

The dimensionless flow coefficient φ used instead of the volumetric flow rate $\dot{V}$ is defined by:

$$\varphi = \frac{\dot{V}}{d_2^2 u_2} \tag{3}$$

The performance map in terms of volume flow rate and total pressure ratio, with Mu and diffuser vane setting angle as parameters, are shown in Fig. 5. This map will be discussed in detail below.

As can be seen, the operational range of the compressor stage can be significantly extended to lower flow rates by lowering the vane setting angle. Simultaneously the flow range (maximum flow rate-minimum flow rate) becomes smaller.

The width of the diffuser throat, which of course changes with the vane setting angle, clearly determines the maximum (or "choking") flow rate at each speed line. The minimum safely achievable flow rate is fixed by the occurrence of flow instabilities, mild surge, or deep surge.

At low rotational speed, for example Mu = 0.5 or lower, inducer rotating stall seems to be responsible for the triggering of deep surge (Ribi and Gyarmathy, 1993). Another typical problem of the impeller flow, a recirculation zone at the impeller inlet occurring at $\varphi < 0.05$, affects only the onset of mild surge at low speeds in case of the 25 and 30 deg configurations.

At the higher rotational speeds, however, mild surge appears

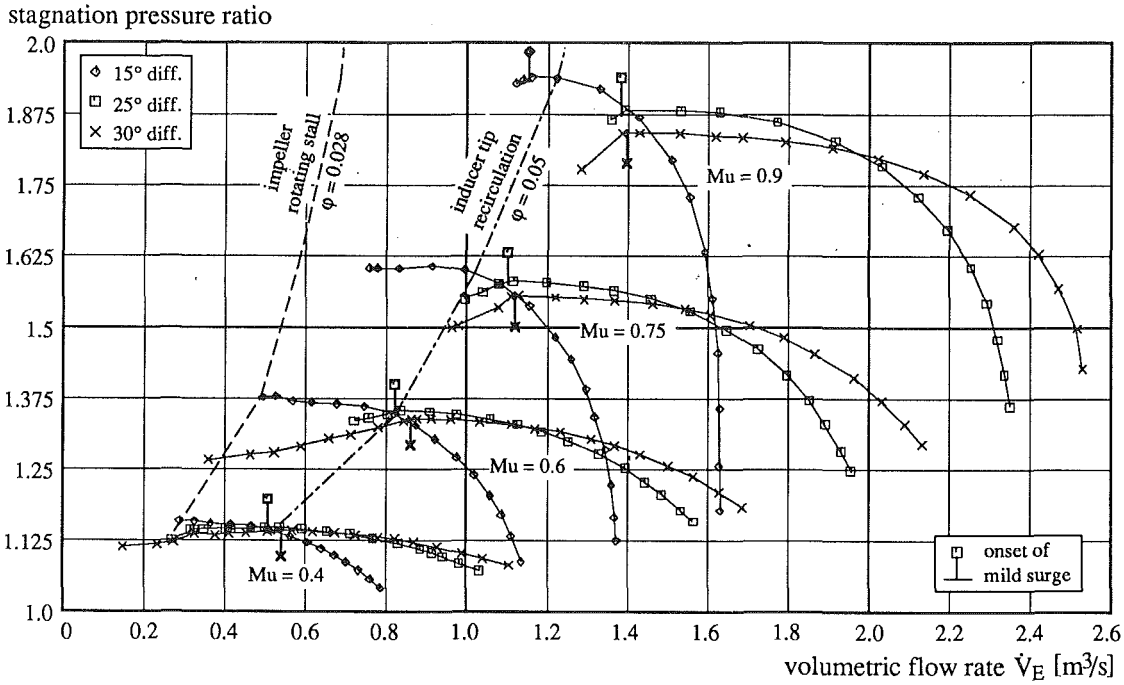

Fig. 5 Performance map

Table 2 Summary of instability types observed

Speed	Diffuser Vane Setting		
	15°	25°	30°
Mu = 0.9	φ<0.050 impeller recirculation φ<0.047 mild surge at max. of stage characteristic φ=0.046 deep surge is triggered	φ<0.057 mild surge at max. of stage characteristic φ=0.055 deep surge is triggered	φ<0.057 mild surge at max. of stage characteristic φ=0.053 deep surge is triggered
Mu = 0.75	φ<0.05 impeller recirculation No mild surge φ=0.037 deep surge is triggered	φ<0.054 mild surge at max. of stage characteristic φ=0.049 deep surge is triggered	φ<0.055 mild surge at max. of stage characteristic φ=0.047 deep surge is triggered
Mu = 0.6	φ<0.050 impeller recirculation φ=0.028 deep surge is triggered by impeller rotating stall	φ<0.050 mild surge at max. of stage characteristic φ=0.044 deep surge is triggered	φ<0.052 mild surge at max. of stage characteristic φ=0.022 deep surge is triggered
Mu = 0.4	φ<0.050 impeller recirculation No mild surge φ=0.028 deep surge is triggered by impeller rot. stall	φ<0.050 impeller recirculation φ<0.050 mild surge φ=0.028 deep surge is triggered by impeller rot. stall	φ<0.050 impeller recirculation φ<0.050 mild surge φ=0.028 deep surge is triggered by impeller rot. stall

in the 25 and 30 deg configurations at higher flow rates than any of the flow disturbances associated with the impeller. On the other hand, with the 15 deg diffuser, mild surge was observed to start at a flow rate where impeller tip recirculation already existed. Therefore the diffusers play a much stronger role in limiting the stable flow range than the impeller. The observations are summarized in Table 2 in terms of φ.

The maximum achievable stage pressure ratio at any given speed is seen to increase with decreasing vane stagger angle. There are two reasons for this. First, the impeller produces more head at lower flow rate φ as result of blade back lean. Second, the pressure recovery in the diffuser channel becomes higher as a result of the changes in the main geometric dimensions of the diffuser.

As mentioned above, the stability limit for mild surge regularly occurs, in accordance with Greitzer's theory, at the flow rate giving maximum pressure rise in the overall stage. Here the slope of the stage characteristic is zero. Figure 6 shows the time traces of static pressure at stage inlet (PVE), at diffuser entry (PDE1), and at diffuser outlet (PDA). At the top of the figure the time mean flow rate is indicated. At diffuser entry (PDE1) high-frequency pressure fluctuations associated with the impeller are dominant. If the flow rate $\dot{V}$ falls short of 1.10 m³/s (the value corresponding to the maximum of the stage characteristic at Mu = 0.75) a periodic pressure oscillation arises as seen in the traces PVE and PDA. The frequency of 19 Hz corresponds to an acoustic resonance of the whole compression system and remains the same at other rotational speeds. This oscillation is synchronous over the circumference. For these reasons these pressure fluctuations have to be interpreted as mild surge. Further decreasing the flow rate results in an increase of the amplitude of the pressure fluctuations at constant frequency. The accompanying flow oscillations have been analyzed by Ribi and Gyarmathy (1993).

Pressure Fields in the Diffuser

About 60 static wall pressure taps distributed over the shroud

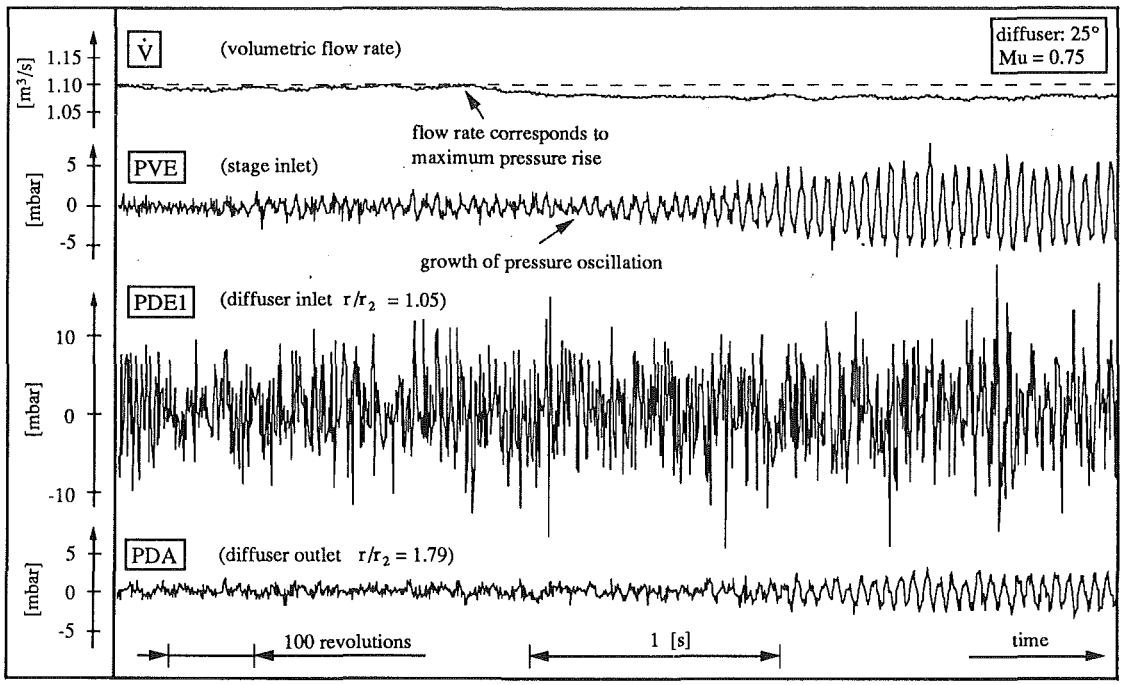

Fig. 6 Typical pressure traces during the onset of mild surge

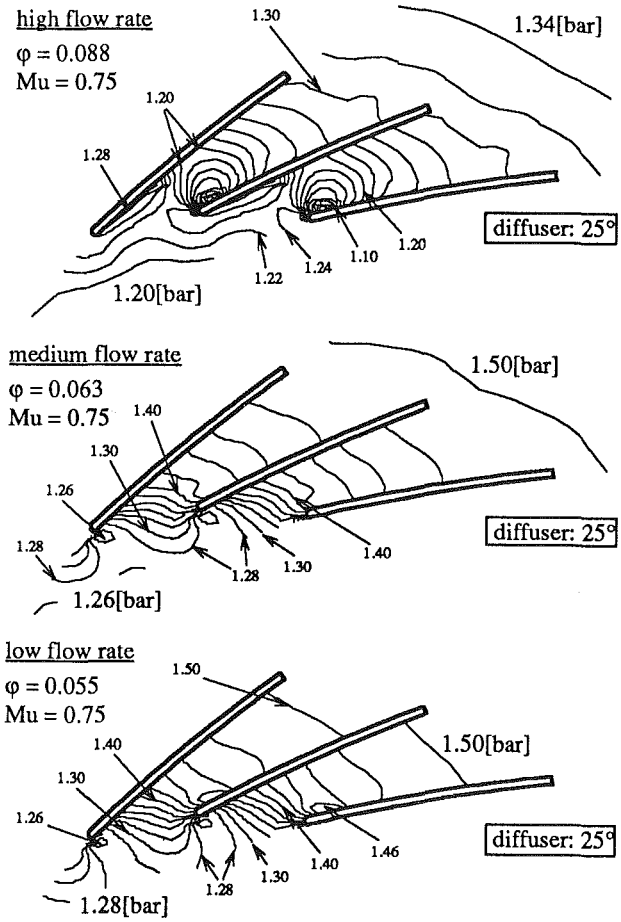

Fig. 7 Isobars within the 25 deg diffuser at three different operating conditions

side of the radial diffuser provide wall pressure distributions. Figure 7 shows the wall pressure fields of three different operating conditions. These measured distributions correspond to those calculated and described in Dalbert et al. (1993).

At high flow rate (Fig. 7, top) there is a strong local acceleration when the steep inlet flow turns into the diffuser channels. In the semi-vaneless space a pressure gradient acts against the vanes. Minimum pressure exists on the outward facing side of the vanes (which is normally referred to as the "pressure side"). Local flow separation behind the leading edge on the pressure side may exist. Downstream of the throat the flow becomes more and more one dimensional.

At medium and low flow rate (Fig. 7, center and bottom) there is a continuous and regular pressure rise in the semi-vaneless space and in the channel. A local pocket of low pressure exists on the suction side near the leading edge. This indicates a turning of the incident flow from a more tangential direction into the channel.

The static pressure field in the vaneless and semi-vaneless space is very sensitive to flow rate. At low flow rate the stationary static pressure field set up by the vanes is most uneven in circumferential direction. This may stimulate impeller blade vibration.

Component and Subcomponent Characteristics

Since mild surge occurs at the maximum of the stage overall pressure rise characteristic, it is interesting to examine the characteristics of each component and subcomponent of the compressor in order to determine which components influence the stage characteristics significantly. First the stage is divided into the components impeller, diffuser, and collector. Afterward the diffuser is subdivided into vaneless and semi-vaneless space, diffuser channel, and vanelessspace downstream of the channels.

The characteristics obtained from an analysis of the pressure measurements are given for each component in a dimensionless form as:

$$Dp = \frac{\Delta p}{\rho_E u_2^2/2} \tag{4}$$

Here Δp is the static pressure rise in the component. The static pressures in planes 2, C, D, and 3 as indicated in Fig. 4 are mean values averaged over several tappings. In planes C and D the wall pressure data are averaged along the lines h_C

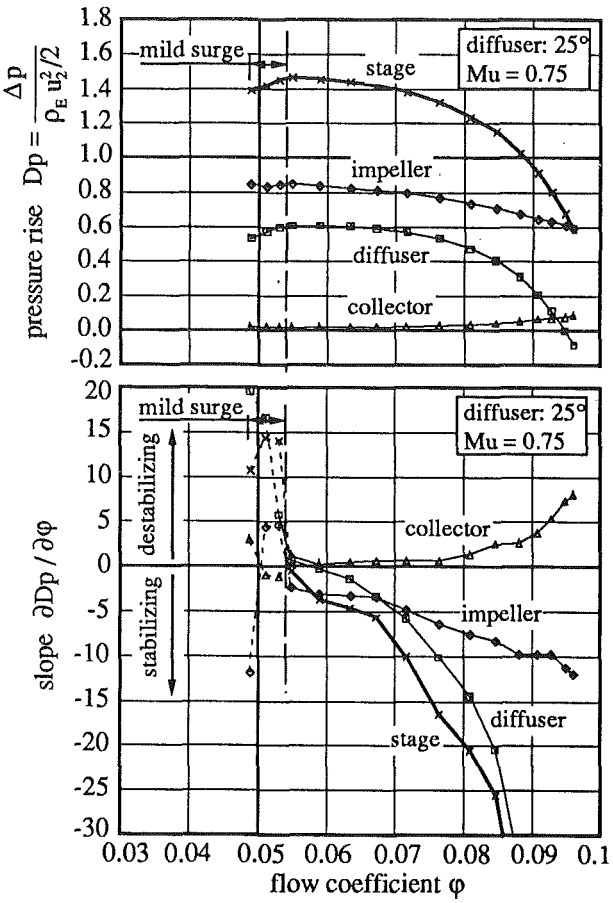

Fig. 8 Characteristics of the components and slopes of the characteristics (with 25 deg diffuser)

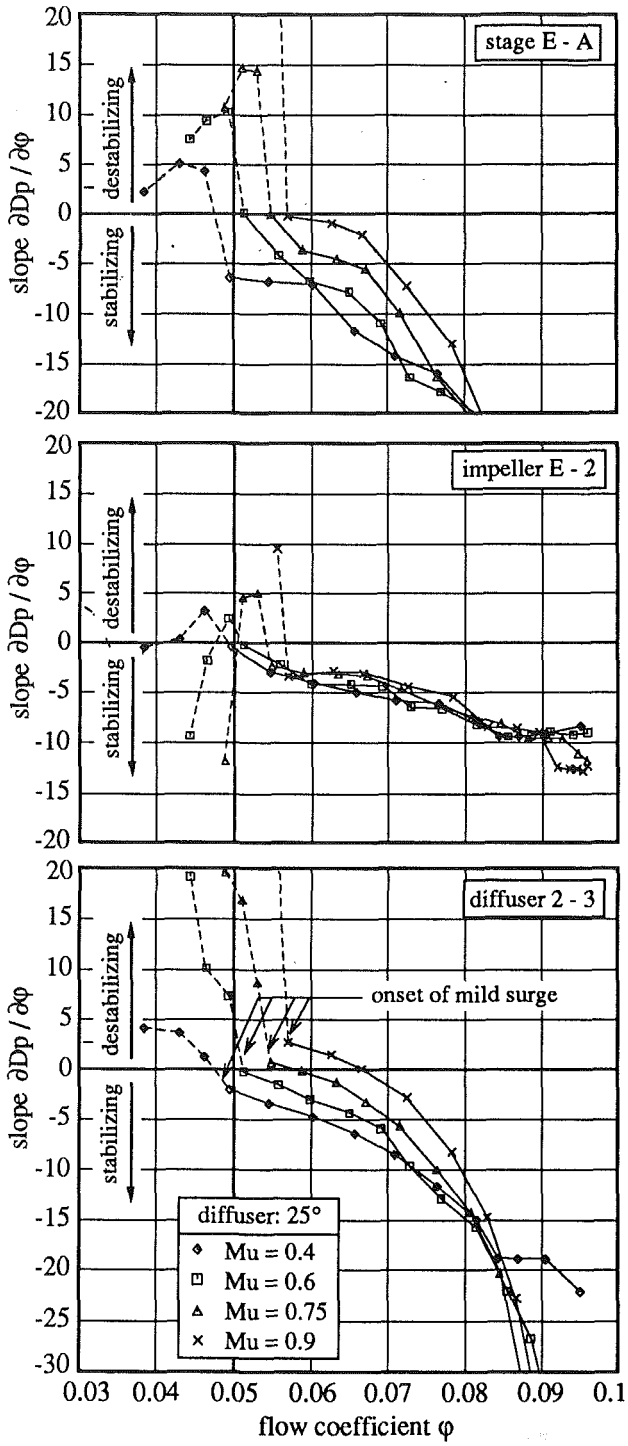

Fig. 9 Slope of the stage, impeller, and diffuser characteristics (with 25 deg diffuser) at different speeds

and h_D, respectively. In planes 2 and 3 the data are averaged in circumferential direction.

In a similar way to Dean (1974) or Japikse (1984) a stability parameter of the component is obtained as $\partial Dp/\partial\varphi$. This parameter corresponds to the slope of the dimensionless pressure rise characteristic of the component.

The classical (Greitzer) stability theory identifies the stability limit with the peaking of the total-to-static pressure rise characteristic of the stage. Since the flow velocity at the stage inlet (E) is low, the difference between total and static pressure in plane E is small. Therefore it is of little importance if the total-to-static or the static-to-static pressure in rise characteristic of the stage is used. Taking the latter approach for simplicity, both the impeller and the diffuser characteristics are taken static-to-static. The characteristics of the diffuser subcomponents and of the collector are static-to-static in both cases.

As discussed in detail by Greitzer (1981), positively sloped characteristics are to be avoided generally. Of particular interest is the identification of those "culprit" components or subcomponents, which contribute a positively sloped characteristic, and of those stabilizing components that have a strongly negative slope. This analysis and identification have been carried out for the configurations tested.

Figure 8, upper part, shows the Dp characteristics of the individual components for one configuration. The lower part shows the Dp slope. The impeller has a stabilizing effect over the whole stable operating range. Since the impeller has 30 deg back-swept blades, this observation is plausible. The diffuser has a strong stabilizing effect at high flow rate but is slightly destabilizing at low flow rate. The collector acts as a destabilizer at high flow rate but is neutral at medium and low flow rates.

The influence of the rotational speed on the slopes of the characteristics of the stage, the impeller, and the 25 deg diffuser is documented in Fig. 9. Instabilities set in at zero stage slope. While the slope for the impeller is almost independent of the peripheral Mach number Mu, there is a dependence for the diffuser. At low speed the diffuser is stabilizing over the whole stable operating range of the stage. With increasing Mu the diffuser acts more and more destabilizing at low flow rate.

Figure 10 gives the slopes of the impeller and diffuser characteristics for the three different stages at Mu = 0.9. Since the same impeller was used in the three cases, there are no differences in the impeller characteristics. But with the 15 deg diffuser, where stable stage operation with inducer tip recirculation was possible ($\varphi < 0.05$), the impeller acts destabil-

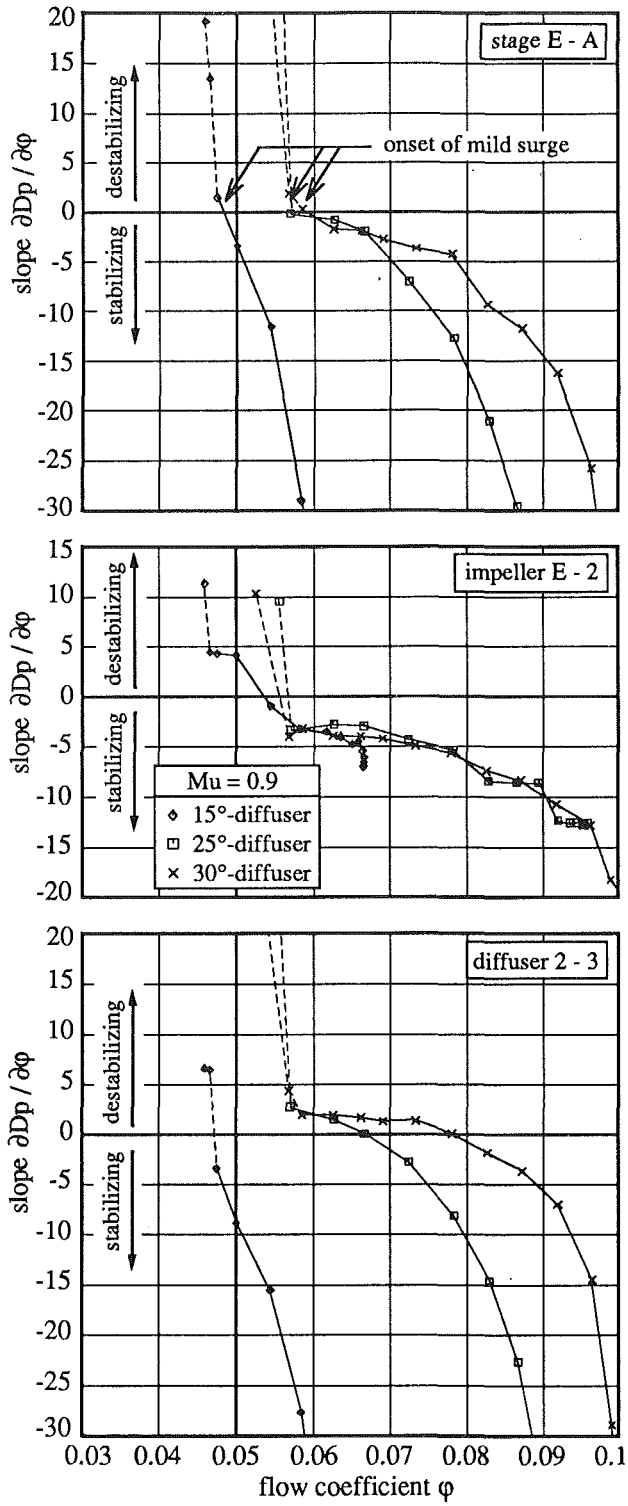

Fig. 10 Slope of the stage, impeller, and diffuser characteristics for the three diffuser vane settings, at Mu = 0.9

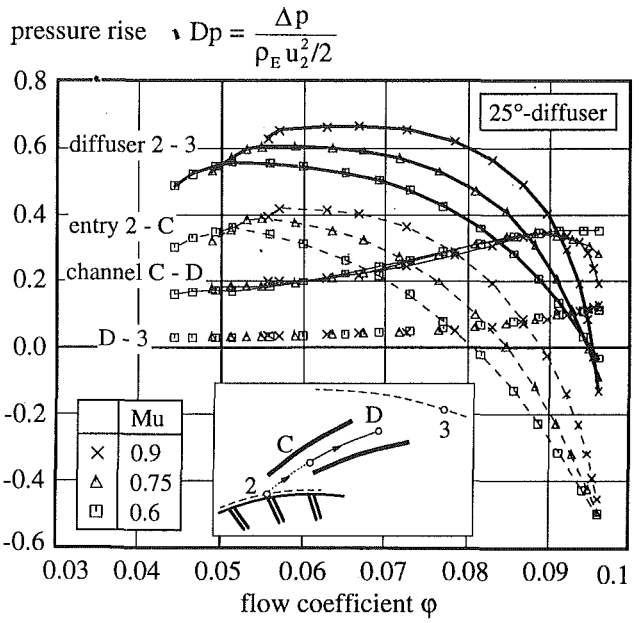

Fig. 11 Characteristics of the 25 deg diffuser and its subcomponents at different speeds

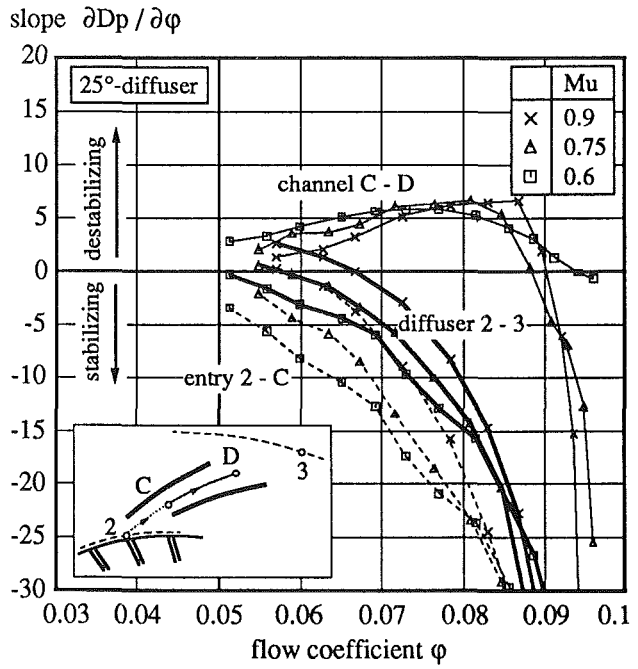

Fig. 12 Slopes of the characteristics of the 25 deg diffuser and its subcomponents at different speeds

izing, whereas in this stage the diffuser is always stabilizing. With the other two stages (25 and 30 deg) the situation is reversed. Here the impeller is always stabilizing but the diffusers are destabilizing at reduced flow rate. Of course at high flow rate the diffusers are also stabilizing.

In the same manner, the diffuser can be analyzed in sections. This reveals the contribution of the diffuser subcomponents to the characteristic slope. For three diffuser elements, the diffuser inlet (comprising the vaneless and semi-vaneless space, 2-*C*), the diffuser channel (*C* – *D*) and the vaneless space downstream of the channel (*D* – 3), the characteristics *Dp* are shown in Fig. 11 for the stage with the 25 deg diffuser. The slopes are plotted in Fig. 12.

The diffuser inlet appears to be the most stabilizing element of the stage over a wide flow range. This agrees with Japikse (1984). But with decreasing flow rate this element acts less and less stabilizing, especially if Mu is high.

The diffuser channel is always destabilizing, except at high flow rate and high Mu where the flow is accelerating at the channel entry (throat). No significant effect of Mach number on the slope of the characteristics can be seen.

The vaneless space downstream of the diffuser channel is slightly destabilizing.

Figures 13 and 14 show the diffuser element *Dp* characteristics for the 15 and 30 deg diffuser, respectively. Essentially

the same trends appear. The channel is mainly destabilizing, the vaneless space downstream of the channel is also destabilizing. The diffuser's entry region is stabilizing over a wide range, but the strength of this effect decreases during throttling. The example of the 30 deg diffuser (Fig. 14) shows that this element is also able to act destabilizing at reduced flow rate.

Of great interest is the observation that the diffuser channel with the smallest throat area and with the longest channel (highest l/h_C) having the highest ratio AR is the most destabilizing one.

Diffuser Channel Performance

The pressure recovery in the diffuser channel is defined as:

$$Cp = \frac{\Delta p_{C-D}}{p_C^o - p_C} \tag{5}$$

It differs from Dp in referring the pressure rise to the actual inlet velocity head. This pressure recovery coefficient is usually compared with those of Reneau et al. (1967) and Runstadler et al. (1975) who tested different diffuser geometries. It is well known that inlet blockage is a main parameter. Therefore the pressure recovery coefficient is plotted versus the diffuser throat blockage Bl_C in Fig. 15. Similar plots are given in the literature (e.g., Japikse and Osborne, 1986; Clements, 1987; Verdonk, 1978). The blockage definition used is:

$$Bl_C = 1 - \frac{A_{\text{eff C}}}{A_C} \tag{6}$$

The area $A_{\text{eff C}}$ effectively used by the flow is calculated using the diffuser throat static pressure, the stagnation pressure measured in the diffuser vane leading edge (by means of a pitot probe), and the continuity equation.

The present data points in the vertical bands correspond to high flow rate. The more horizontal portion corresponds to operating conditions between best efficiency and surge. The latter data show approximately the level indicated by Reneau or Runstadler, but the tendencies are different. Unfortunately their laboratory data do not cover the interesting range for most centrifugal compressor diffusers in terms of geometry or blockage. The slight increase in pressure recovery at increasing blockage is supposed to be due to two effects. First, since the pitot probe only indicates the stagnation pressure in the flow core, any changes in the stagnation pressure *distribution* are not recognized correctly. This may result in an overestimation

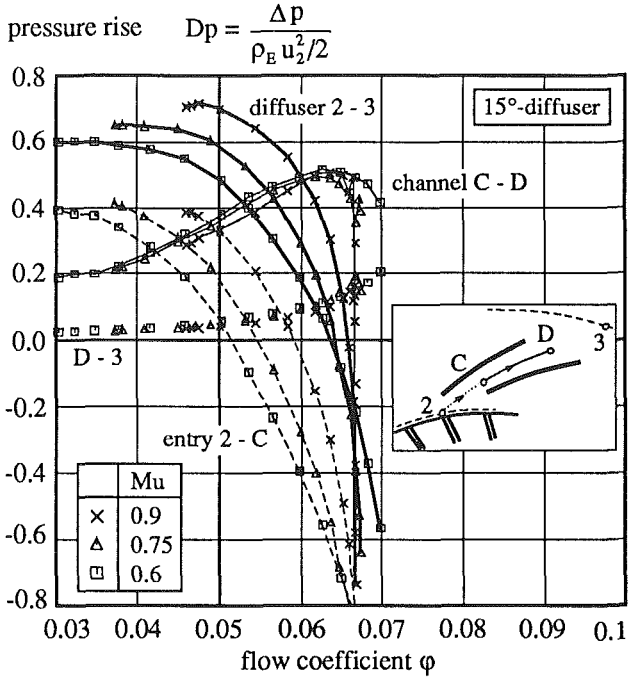

Fig. 13 Characteristics of the 15 deg diffuser and its subcomponents at different speeds

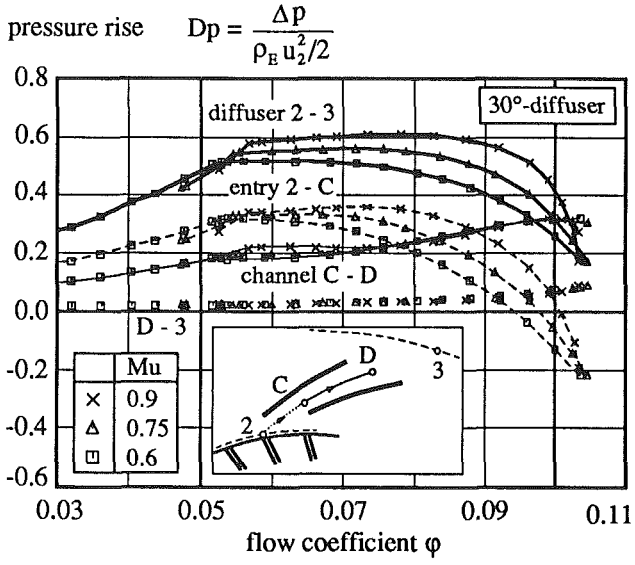

Fig. 14 Characteristics of the 30 deg diffuser and its subcomponents at different speeds

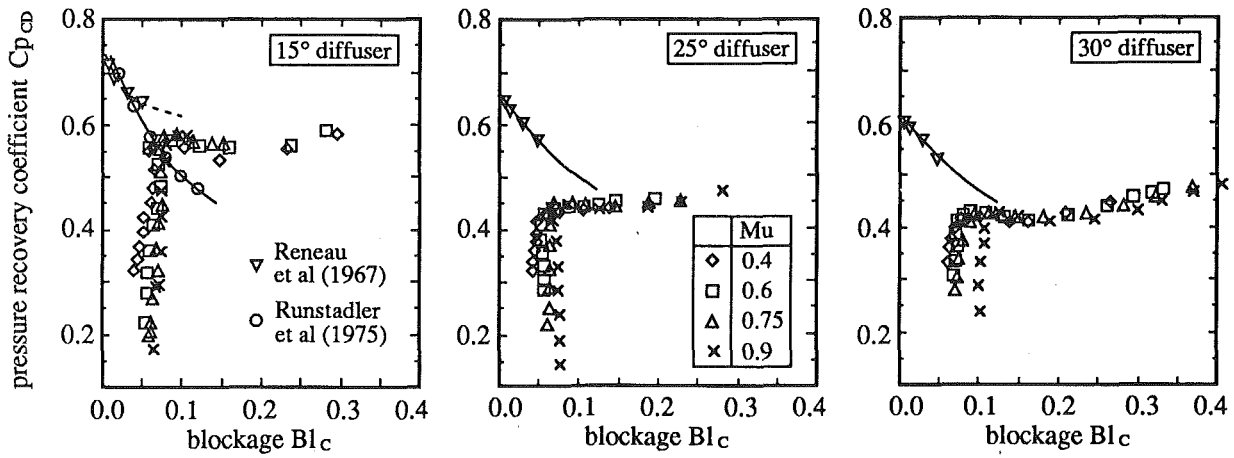

Fig. 15 Channel pressure recovery Cp_{C-D} vs. diffuser throat blockage Bl_C

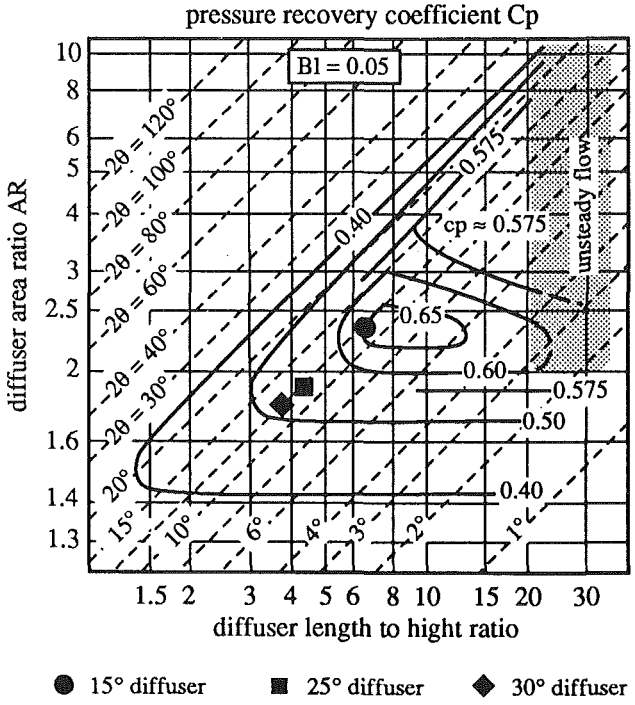

Fig. 16 Comparison of diffuser channel geometry

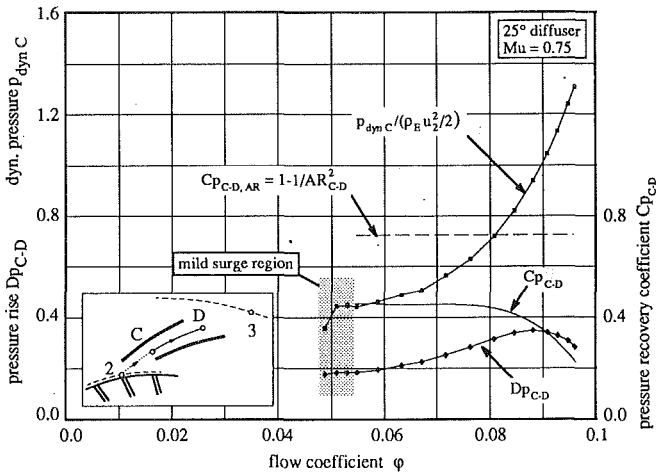

Fig. 17 Conversion of dynamic pressure $P_{dyn\,C}$ in the diffuser channel

of the pressure recovery. Second, the pressure recovery in the channel of a radial diffuser is caused not only by deceleration but by blade forces (deflection) too. This may in fact increase the recovery coefficient.

Channels with higher AR and higher l/h_C exhibit higher recovery coefficients in the horizontal portion in Fig. 15 (reduced flow rate). This trend is in agreement with laboratory diffuser data. For comparison the geometries of the diffuser channels are plotted in the diffuser map of Reneau et al. (1967) in Figure 16.

There exists a relationship between the channel pressure rise Dp_{C-D} and the channel pressure recovery coefficient Cp_{C-D} as:

$$Dp_{C-D} = Cp_{C-D}\frac{p^0 - p_C}{\rho_E u_2^2/2}$$

The fraction term represents the dimensionless dynamic pressure in the diffuser throat. For a given diffuser inlet geometry, especially a given throat area, its dependence on flow rate is fixed and shown in Figure 17 as the top curve. Using the Dp_{C-D} curve plotted in Figure 11 the above relationship yields the curve Cp_{C-D}. This is seen to fall short of the theoretical value $Cp_{C-D,AR}$, calculated from the area ratio. A geometric increase in AR will normally increase Cp and Dp and act toward destabilization.

Note that the ordinate of the curve Dp_{C-D} and the normalized pressure head curve is a direct measure of the utilization of impeller exit velocity in the channel part of the diffuser. This ratio appears to be fairly constant over flow rate, except for the deterioration seen at high flow.

Summarizing, the surge line movements connected with geometric changes of the diffuser channel reported in the literature (Japikse, 1984; Clements and Artt, 1987) can be understood as the consequence of basic physical mechanisms of diffusing flow in the radial diffuser. Thereby the general observation that the radial diffuser affects the surge line (Came and Bellamy, 1982) is substantiated. Diffusers designed for low pressure recovery result in an improved stability of the stage whereas diffusers for high pressure recovery results in smaller flow ranges.

Conclusions

- Mild surge, as a dynamic instability of the compression system, arises at the flow rate giving the maximum overall stage pressure rise characteristic (zero slope), in perfect compliance with Greitzer's stability theory for high B-parameter values.
- The static wall pressure field in the vaneless and semivaneless space as well as slightly downstream of the diffuser throat is very sensitive to flow rate.
- The backswept impeller is a typically stabilizing stage element. With inlet recirculation the impeller becomes destabilizing.
- The diffuser entry region is a strong stabilizing subcomponent over a wide flow range. This stabilizing influence decreases as the flow is reduced. This is the influence that mainly determines the stability limit.
- The diffuser channels play an inherently destabilizing role. The relationship of diffuser geometry and channel pressure recovery with the strength of the destabilizing effect of the channels substantiates experiments published in the literature showing surge line movements caused by changes in the diffuser channel geometry.
- With adjustable fixed-length diffuser vanes the higher total pressure ratios are obtained with lower vane stagger angle.

Acknowledgments

The authors would like to thank the Swiss Kommission für die Förderung der Wissenschaftlichen Forschung (KWF) for financial support, and ABB Turbo Systems, Sulzer Escher Wyss, Sulzer Innotec, and Sulzer Brothers Winterthur for their technical cooperation and their financial support. The authors wish to thank Mrs. D. Aeppli for typing this manuscript.

References

Abdelhamid, A. N., 1983, "Effects of Vaneless Diffuser Geometry on Flow Instability in Centrifugal Compression Systems," *Canadian Aeronautics and Space Journal*, Vol. 29, No. 3, pp. 259–266.

Amann, C. A., Nordenson, G. E., and Skellenger, G. D., 1975, "Casing Modification for Increasing the Surge Margin of a Centrifugal Compressor in an Automotive Turbine Engine," ASME *Journal of Engineering for Power*, Vol. 97, pp. 329–336.

Ariga, I., Masuda, S., and Ookita, A., 1987, "Inducer Stall in a Centrifugal Compressor With Inlet Distortion," ASME JOURNAL OF TURBOMACHINERY, Vol. 109, pp. 27–35.

Baghdadi, S., and McDonald, A. T., 1975, "Performance of Three Vaned Radial Diffusers With Swirling Transonic Flow," ASME *Journal of Fluids Engineering*, Vol. 97, pp. 155–173.

Came, P. M., and Bellamy, A. G., 1982, "Design and Performance of Advanced Large Turbochargers," IMechE C37/82.

Came, P. M., and Herbert, M. V., 1980, "Design and Experimental Per-

formance of Some High Pressure Ratio Centrifugal Compressors," AGARD, CP-282, Paper No. 15.

Clements, W. W., and Artt, D. W., 1981, "The Influence of Diffuser Channel Geometry on the Flow Range and Efficiency of a Centrifugal Compressor," *Proceedings of the Institution of Mechanical Engineers*, Vol. 201, pp. 145–152.

Clements, W. W., 1987, "A Theoretical and Experimental Study of Diffusion Levels in Centrifugal Compressor Stage," PhD Thesis, University of Belfast.

Dalbert, P., Gyarmathy, G., and Sebestyen, A., 1993, "Flow Phenomena in a Vaned Diffuser of a Centrifugal Stage," ASME Paper No. 93-GT-53.

Dean, R. C., 1974, "The Fluid Dynamic Design of Advanced Centrifugal Compressors," Lecture Notes, Von Karman Institute, Brussels, Mar.

Dean, R. C., and Young, L. R., 1977, "The Time Domain of Centrifugal Compressor and Pump Stability and Surge," ASME *Journal of Fluids Engineering*, Vol. 99, pp. 53–63.

Dutton, J. C., Piemsomboon, P., and Jenkins, P. E., 1986, "Flowfield and Peformance Measurements in a Vaned Radial Diffuser," ASME *Journal of Fluids Engineering*, Vol. 108, pp. 141–147.

Elder, R. L., and Gill, M. E., 1985, "A Discussion of the Factors Affecting Surge in Centrifugal Compressors," ASME *Journal of Engineering for Gas Turbines and Power*, Vol. 107, pp. 499–506.

Emmons, H. W., Pearson, C. E., and Grant, H. P., 1955, "Compressor Surge and Stall Propagation," *ASME Transactions*, Vol. 77, 455–469.

Filipenco, V. G., 1991, "Experimental Investigation of Flow Distortion Effects on the Performance of Radial Discrete-Passage Diffusers," GTL Report 206, Gas Turbine Laboratory, MIT.

Fink, D. A., Cumpsty, N. A., and Greitzer, E. M., 1992, "Surge Dynamics in a Free-Spool Centrifugal Compressor System," ASME JOURNAL OF TURBOMACHINERY, Vol. 114, pp. 321–332.

Frigne, P., and Van Den Braembussche, R., 1984, "Distinction Between Different Types of Impeller and Diffuser Rotating Stall in a Centrifugal Compressor With Vaneless Diffuser," ASME *Journal of Engineering for Gas Turbines and Power*, Vol. 106, pp. 468–474.

Greitzer, E. M., 1981, "The Stability of Pumping Systems—The Freeman Scholar Lecture," ASME *Journal of Fluids Engineering*, Vol. 103, 1981, pp. 193–242.

Gysling, D. L., Dugundji, J., Greitzer, E. M., and Epstein, A.H., 1991, "Dynamic Control of Centrifugal Compressor Surge Using Tailored Structures," ASME JOURNAL OF TURBOMACHINERY, Vol. 113, pp. 710–722.

Jansen, M., 1982, "Untersuchungen an beschaufelten Diffusoren eines hochbelasteten Radialverdichters," Ph.D Thesis, University of Hannover, Germany.

Jansen, W., 1964, "Rotating Stall in a Vaneless Diffuser," ASME *Journal of Basic Engineering*, Vol. 86, pp. 750–758.

Japikse, D., 1980, "The Influence of Diffuser Inlet Pressure Fields on the Range and Durability of Centrifugal Compressor Stages," AGARD CP-282, Paper No. 13.

Japikse, D., 1984, "A Critical Evaluation of Stall Concepts for Centrifugal Compressors and Pumps—Studies in Component Performance, Part 7," presented at the ASME Conference on Stall and Surge in Compressors and Pumps.

Japikse, D., and Osborne, C., 1986, "Optimization of Industrial Centrifugal Compressors, Part 6B: Studies in Component Performance—Laboratory Development of Eight Stages From 1972 to 1982," ASME Paper No. 86-GT-222.

Kämmer, N., and Rautenberg, M., 1982, "An Experimental Investigation of Rotating Stall Flow in a Centrifugal Compressor," ASME Paper No. 82-GT-82.

Kämmer, N., and Rautenberg, M., 1986, "A Distinction Between Different Types of Stall in a Centrifugal Compressor Stage," ASME *Journal of Engineering for Gas Turbines and Power*, Vol. 108, pp. 83–92.

Kenny, D. P., 1972, "A Comparison of the Predicted and Measured Performance of High Pressure Ratio Centrifugal Compressor Diffusers," ASME Paper No. 72-GT-54.

Krain, H., 1981, "A Study on Centrifugal Impeller and Diffuser Flow," ASME *Journal of Engineering for Power*, Vol. 103, pp. 688–697.

Pinsley, J. E., Guenette, G. R., Epstein, A. H., and Greitzer, E. M., 1991, "Active Stabilization of Centrifugal Compressor Surge," ASME JOURNAL OF TURBOMACHINERY, Vol. 113, pp. 723–732.

Reneau, L. R., Johnson, J. P., and Kline, S. J., 1967, "Performance and Design of Straight, Two-Dimensional Diffusers," ASME *Journal of Basic Engineering*, Vol. 89, pp. 141–150.

Ribi, B., and Gyarmathy, G., 1993, "Impeller Rotating Stall as a Trigger for the Transition From Mild to Deep Surge in a Subsonic Centrifugal Compressor," ASME Paper No. 93-GT-234.

Rieder, M., 1987, "Das instationäre Strömungsverhalten von Radialverdichterstufen mit langsamläufigen Laufrädern und schaufellosen Diffusoren im Pumpgrenzbereich," Ph.D. Thesis, University of Stuttgart.

Rodgers, C., 1982, "The Performance of Centrifugal Compressor Channel Diffusers," ASME Paper No. 82-GT-10.

Runstadler, P. W., Dolan, F. X., and Dean, R. C., 1975, "Diffuser Data Book," Creare Technical Note TN-186.

Simon, J. S., Valavani, L., Epstein, A. H., and Greitzer, E. M., 1993, "Evaluation of Approaches to Active Compressor Surge Stabilization," ASME JOURNAL OF TURBOMACHINERY, Vol. 115, pp. 57–67.

Stein, W., and Rautenberg, M., 1988, "Analysis of Measurements in Vaned Diffusers of Centrifugal Compressors," ASME JOURNAL OF TURBOMACHINERY, Vol. 110, pp. 115–121.

Toyama, K., Runstadler, P. W., Jr., and Dean, R. C., Jr., 1977, "An Experimental Study of Surge in Centrifugal Compressors," ASME *Journal of Fluids Engineering*, Vol. 99, pp. 115–131.

Verdonk, G., 1978, "Vaned Diffuser Inlet Flow Conditions for a High Pressure Ratio Centrifugal Compressor," ASME Paper 78-GT-50.

Yoshinaga, Y., Gyobu, I., Mishina, H., Koseki, F., and Nishida, H., 1980, "Aerodynamic Performance of a Centrifugal Compressor With Vaned Diffusers," ASME *Journal of Fluids Engineering*, Vol. 102, pp. 486–493.

A Rotating Laser-Doppler Anemometry System for Unsteady Relative Flow Measurements in Model Centrifugal Impellers

M. Abramian
Pratt & Whitney Canada,
Mississauga, Ontario, Canada

J. H. G. Howard
Department of Mechanical Engineering,
University of Waterloo,
Waterloo, Ontario, Canada

The behavior of the relative flow in centrifugal turbomachines is extremely complex due to the existence of various fluid dynamic phenomena and their interaction. At design and off-design operating conditions, the relative flow is subject to stationary unsteadiness, which includes the flow separation and wakes associated with passage pressure gradients, secondary flows, and boundary layer stability. It is also subject to periodic unsteadiness from the rotating stall and the cyclic flow phenomena induced by the casing. This paper describes the mechanical and optical design of a rotating laser-Doppler anemometry system, which allows direct measurement of the relative flow by means of an optical derotator. By isolating the impeller rotational frequency from the sampling frequency, it allows direct time-averaged measurements of the stationary behavior of the relative flow along with the ensemble (phase)-averaged measurements of its periodic behavior. Its success is demonstrated with measurements conducted in a low specific speed centrifugal impeller fitted with a single volute. Sample results of the time-averaged blade-to-blade variation of total relative velocities along with their associated turbulence intensities are reported. The (periodic) cyclic variations of the impeller exit flow, induced by the volute at low flow rates, are also presented for the suction and pressure sides.

Introduction

The lack of available data for verification of analytical and numerical models, along with the quest for better understanding of the flow behavior inside turbomachinery components, has created a separate research area, which involves the development of new instrumentation and measurement techniques to allow accurate quantitative description of general, unsteady flow in regions that are difficult to access.

In the *rotating coordinate system*, the behavior of the relative flow can be recognized in two categories:

- *Stationary unsteadiness*, which is the flow separation and wakes associated with the passage pressure gradients, secondary flows, and boundary layer stability, and
- *Periodic unsteadiness*, which is the rotating stall and the cyclic flow phenomena induced by the volute casing.

According to the ergodicity theorem, for a stationary random process, such as homogeneous isotropic turbulence, the time average of a signal U is equal to ensemble (phase) average of its value over all records, i.e.,

$$\overline{U}_{\text{time average}} = \lim_{T\to\infty} \frac{1}{2T}\int_{-T}^{T} U(t)\,dt = \overline{U}_{\text{ensemble}} = \frac{\lim\limits_{N\to\infty}\sum\limits_{1}^{N} U(t)}{N} \quad (1)$$

With respect to the stationary (absolute) location, however, a stationary flow in the relative system will produce a (nonstationary) periodic signal on which a fluctuating signal, due

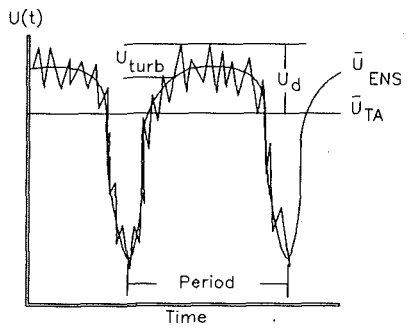

Fig. 1 Analysis of a nonstationary signal obtained from a fixed location

Contributed by the International Gas Turbine Institute and presented at the 38th International Gas Turbine and Aeroengine Congress and Exposition, Cincinnati, Ohio, May 24-27, 1993. Manuscript received at ASME Headquarters February 12, 1993. Paper No. 93-GT-11. Associate Technical Editor: H. Lukas.

to turbulence, may be superimposed. In the absolute system, considering U_{TA} as the long-time-average, and U_{ENS} as the ensemble average, the total signal $U(t)$ is comprised of:

$$U(t) = \overline{U}_{TA} + \overline{U}_{ENS} + U_{turbulence} \quad (2)$$

Considering U_d as disturbance (fluctuating) velocity from the mean time-average velocity (Fig. 1):

$$U_d = U_{turb} + (U_{ENS} - U_{TA}) \quad (3)$$

The rms values associated with each fluctuating component are:

$$\text{rms}(U_d)^2 = \text{rms}(U_{turb})^2 + \text{rms}(U_{ENS} - U_{TA})^2 + 2(U_{turb})(U_{ENS} - U_{TA})) \quad (4)$$

The analysis technique described above has been used extensively to discriminate between rms turbulence levels associated with periodic fluctuations and those due to true turbulence within the rotating passages. Without including the last term in Eq.(4), i.e., assuming that the turbulent velocity fluctuations are independent of the periodic wake fluctuations, Evans (1975) demonstrated a difference of 2–3 times in the turbulence fluctuations between a stalled and an unstalled axial rotor while the periodic fluctuations stayed the same. Raj and Lakshminarayana (1976) used a triple hot-wire probe and investigated the wakes shed by a row of axial rotor blades and compared the wake velocity deficit to that shed by an equivalent stationary blade row.

It can be seen that by conducting measurements in the rotating frame of reference and isolating the impeller rotational frequency, the stationary unsteadiness of the relative flow is maintained as stationary and can be quantified by time-averaging the continuous signal without further assumptions. According to the ergodicity theorem, ensemble (phase) averaging will, also, provide the same information with respect to the angular (phase) orientation of the impeller and, further, allow additional periodic unsteadiness, such as those caused by rotating stall or when the impeller is operating in a circumferentially nonuniform environment induced by the casing, to be quantified by periodic averaging in the relative coordinate system.

In the past, several attempts have been undertaken to allow quantitative description of the relative flow within a rotating passage by either ensemble (spatial or phase) average techniques using laser-Doppler anemometry (LDA) from a stationary point or rotating (hot wire, pitot) probes for direct measurements in the relative coordinate system (Fowler, 1968; Lennemann, 1969; Howard and Kittmer, 1975; Gorton and Lakshminarayana, 1976; Lakshminarayana, 1980; Sitaram et al., 1981).

Since the development of laser velocimetry (LV), its nonintrusive character has allowed its application to interblade measurement of rotating machines by ensemble average measurements from a stationary location and has allowed the measuring control volume, fixed at some axial or radial position, to sweep out a circumferential path within the rotating blades (Howard et al., 1980; Powel et al., 1981; Carey et al., 1985; Menon, 1987; Flack et al., 1992). Fagan and Selbach (1984) reported an (L2F) LV technique, which included capabilities of direct relative flow measurements by means of an image reversal prism. By de-rotating the passage, their system allowed measurements in regions that were generally difficult to access by blade shadowing. The main advantage of L2F system is that, because of fine focusing, the concentration of light into the illuminated regions is much greater than in LDA and allows efficient application near solid surfaces. The disadvantage of the system is that it requires a great length of time to record sufficient observations and cannot be applied to highly turbulent and reverse flows. Fagan and Selbach (1984) claimed that the application of the de-rotating prism to an LDA system may not be possible due to the extra glare associated with the prism. The application of LDA to rotating systems has been limited to those developed in axisymmetric flows in rotating cylinders with no frequency shifting capabilities (Tokoi et al., 1980; Ribando et al., 1989). In these cases a single laser beam was transferred from the stationary to the rotating system using a conventional beam splitter rotating at the speed of the cylinder. When a rotating LDA system is to be applied to the study of turbomachinery flows, frequency shifting capabilities are required, to allow it to detect reverse flows and regions of high turbulence. A rotating LDA system with frequency shifting was employed by Dunagan (1991) to investigate velocities adjacent to helicopter rotors.

Motivation

Flow analysis in an impeller passage is carried out from the perspective of the average flow at each passage location based on the relative frame of reference. It should therefore be an advantage to have a measurement system that follows the same reference frame.

Even though the LV techniques based on absolute locations can successfully measure instantaneous relative velocity, several practical difficulties are present in obtaining mean velocities and turbulence. The ensemble average technique is intended to ensure that only velocities at one physical location in the passage are measured. A compromise must be made in the chosen width of the time window for the measurement, to ensure an adequate number of data points within a reasonable number of revolutions while avoiding errors associated with high velocity gradients in the impeller passage. Turbulence measurements will be erroneously increased in the presence of velocity gradients within the measurement window. The alternative of combining measurement windows from equivalent locations in different passages introduces errors in the mean and the fluctuating values stemming from the (almost inevitable) flow variations between passages. Information about periodic unsteadiness in the passage, which occurs at impeller rotational frequency, or any harmonics of the impeller rotational frequency cannot be measured by a stationary measurement system at a single location. Measurement at multiple locations can be difficult, and in the best case only a limited number of locations can be used, leading to a limited definition of the periodic unsteadiness. Further difficulties arise in correlating measurements from these different stationary locations. Thus it is unlikely that a highly accurate mean relative velocity can be produced that reflects both the stationary and the periodic unsteadiness components.

Only by direct measurements in the rotating system can one isolate the impeller rotational frequency and ensure capturing

Nomenclature

T = time
Q = flow rate
V = total relative velocity
Z = impeller axial height (hub-to-shroud)
θ = impeller blade-to-blade coordinate
ω = impeller rotational speed
NFR = number of fringes
E = beam expansion factor
λ = wavelength
f = focal length
d_{e-2} = beam waist at the focal point
U_{TA} = time average mean of a signal
U_{ENS} = ensemble (phase) average mean of a signal
U_{turb} = signal fluctuations due to stationary turbulence

Subscripts

1 = inlet
2 = exit
b = blade

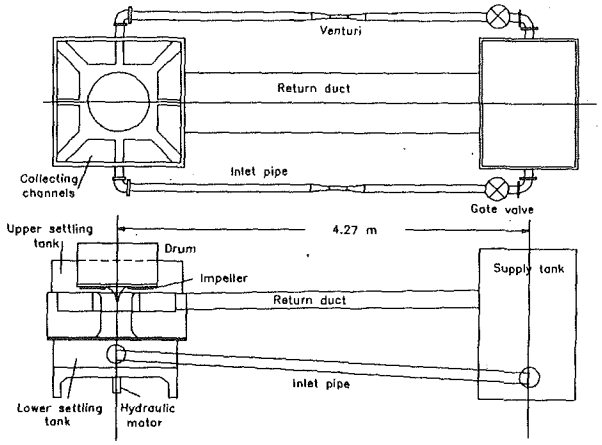

Fig. 2 Schematic diagram of the test rig

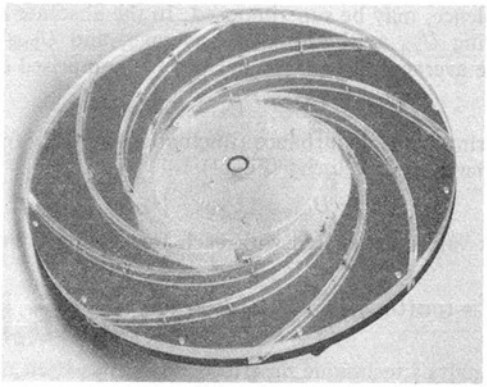

Fig. 3 Test impeller

all the information of the fluctuating components that may occur as harmonics of the impeller rotational frequency. In this case the measurement is limited to the size of the measurement control volume (probe volume) so the problem with velocity gradients is effectively avoided. Of course, when it is desired to separate the periodic unsteadiness, such as the cyclic flow phenomena induced by the volute and rotating stall, from the remaining signal, it is necessary to ensemble average according to the orientation of the impeller within the casing at the instant of measurement. This is easily carried out as a data processing task, and the window size for the ensemble averaging can be as small as is needed to define the periodic pattern, making it equivalent to a very large number of stationary locations. The importance of direct measurements in the rotating frame also arises in quantifying higher order moments such as Reynolds shear stress, which requires simultaneous sampling of instantaneous u and v components. The more accurate average value requires a continuous signal over all the circumferential locations during the impeller rotation, while separation of the periodic variation is possible as before if desired.

Objective

The objective of the present research project is to develop an experimental technique to investigate the unsteady behavior of the relative flow in a series of low specific speed, backward swept, radial impellers, by optically modifying a conventional single-component laser-Doppler anemometry system to allow direct measurements in the relative coordinate system. The conventional system is modified by incorporating a triple reflection Dove prism, rotating at half the speed of the impeller, in order to de-rotate the image of the passage and allow the two (shifted and unshifted) beams to be transferred from stationary to rotating system while maintaining their orientation. The two beams are further transferred to a desired radial location by means of a rotating periscope. An on-board (rotating) microcomputer is included to control stepping motors and allow a two-dimensional (R, θ) traversing during rotation.

By changing the orientation of the prism with respect to the impeller, both mean and rms values of the radial and tangential velocity components are measured separately. Sample results of the time-averaged total relative velocity vectors and turbulence intensities are presented for an impeller operating without the volute describing the stationary behavior of the relative flow in a circumferentially uniform environment. Sample ensemble-averaged measurements of the impeller exit flow at very low (near shut-off) flow rate, when fitted with a single volute, are also presented, which demonstrates the success of the experimental technique in quantifying the cyclic variation of the impeller flow, induced by the volute, under off-design flow rate.

The primary objective of this paper is to demonstrate the success and capabilities of the experimental technique, which may be enhanced by further modifications to a two-component system, and applied to other impeller designs to obtain more information toward optimum design procedure. It may also be applied to fundamental investigations of boundary layers subject to system rotation and surface curvature.

Experimental Apparatus

Test Rig. The schematic diagram of the test rig is shown in Fig. 2. It is a closed-circuit arrangement consisting of a reservoir tank and a test section. The test section itself consists of an upper settling tank, open to atmosphere, and a lower settling tank. The upper and lower settling tanks are connected through a draft tube in which there is an axial flow inducer (connected to the impeller) providing swirling flow to the impeller inlet. A vertical shaft extending from the lower to the upper settling tank is used to drive the impeller by means of a hydraulic motor. The impeller is mounted at the upper end of the shaft, above the inducer and inside the upper settling tank. The volute (when employed) is mounted around the impeller and fastened to the tank at four locations. The rpm is measured by a torque meter mounted between the hydraulic motor and the main shaft. Through one of the supply pipes, the test impeller circulates the water from the reservoir to the lower settling tank, up through the draft tube, through the impeller, into the upper settling tank, and back to the reservoir via an inclined rectangular duct. Each supply pipe is fitted with a gate valve and an internal venturi meter in order to control and measure different flow rates. The large-diameter low-speed rig has been designed specifically to allow the upper surfaces of either the impeller back-face or the volute to be directly exposed to the air. This served to make possible various flow visualization and special velocity measurement methods. In the past, both locally traversed hot-film probes and laser-Doppler velocimetry have been used to measure velocities in the impeller passage (Howard and Lennemann, 1971; Howard et al., 1980), and the volute (Howard et al., 1987).

Test Impeller. The impeller for the present investigation, designed to model a hypothetical low specific speed aircraft fuel pump is shown in Fig. 3. It was formed by fitting eight backward swept blades between two (upper and lower) shrouds. The angles vary linearly with radius from 15 deg (tangential) at the inlet to 30 deg (tangential) at the exit. The blade axial height varies inversely with radius in a slight curvature on the lower shroud. It is entirely manufactured from plastic to allow flow visualization studies to be conducted inside the rotating passages (Abramian, 1986; Howard et al., 1987). The hub of the one complete passage of the original impeller was removed

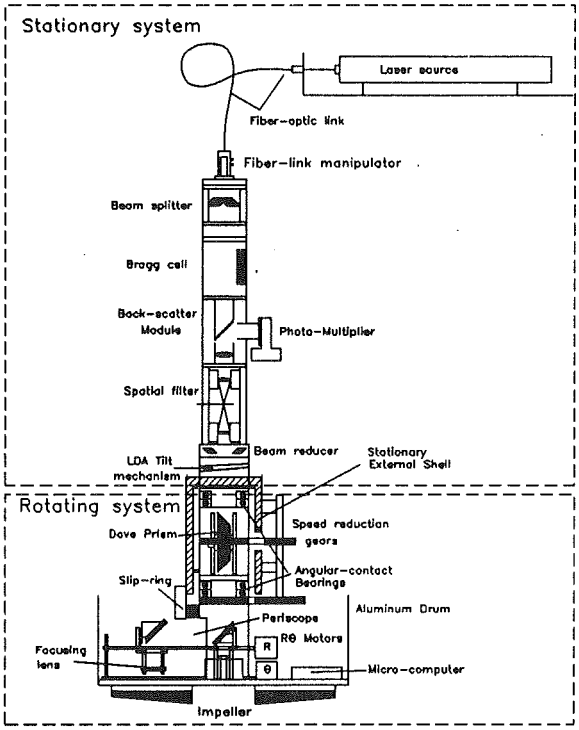

Fig. 4 Schematic drawing of the experimental technique

by machining and replaced by a conventional (window) glass to allow complete access of the LDV probe to the entire passage.

Experimental Technique and Instrumentation

The schematic diagram of the overall LDA system used for the present investigation is shown in Fig. 4. It is comprised of the laser, its fiber-optically-linked transmission to stationary dual-beam optics, and the rotating optics in the relative system required for transferring the beams from stationary to any desired location in the relative frame. Details of the stationary and rotating optical systems are as follows.

Stationary Optical System. The stationary optical system includes the laser source, its fiber optical link, and the conventional one-component LDA optics. The LDA system used for the present investigation employs a 4 W argon ion laser for a one-component differential (dual-beam) Doppler system operating in backscatter mode with optics for beam manipulation and a counter-type signal processor.

Reverse flow detection is obtained by employing a Bragg cell (40 MHz) frequency shifter in one beam of the main optics. A down-mixer provides "effective" frequency shift from 2 kHz to 5 MHz. In addition to eliminating the directional ambiguity, frequency shifting reduces the fringe bias associated with highly turbulent, low particle density flows and enhances the signal quality of very low velocity particles. The high pass filter in the down-mixer also removes the DC component of the Doppler burst (pedestal).

Fiber Optical Link. For the present system, the initially developed link (Abramian et al., 1987) was replaced by a more efficient one, which is used to connect the laser source to the stationary optics. It consisted of two fiber manipulators and one single mode fiber. One fiber manipulator was used as a launch unit to couple the beam onto the fiber, while the second was used at the probe end to allow adjustments to the beam divergence and alignment before entering the stationary optics. The launch manipulator is placed on a special mounting bracket, which, after the initial detail alignment, allows its removal from the laser mount, without affecting the initial alignment. The single mode polarization preserving fiber produced a beam diameter of 1.35 mm, and beam divergence angle of 0.5–0.6 mrad, with coherence length of 5 m. It was fitted with two plugs at each end, which included the microlens for focusing (at the receiving end) and/or resetting the divergence angle of the beam (at the probe end). Polarization of the (exiting) beam was also possible by rotating the fiber within the plug housing. The overall system allowed coupling efficiency of ≈ 70 percent to be achieved for laser to fiber coupling.

LDA Optics. At the beginning of the probe unit, the fiber manipulator was attached to a series of conventional LDA optics to provide two parallel beams (50 mm apart) of equal intensity with frequency shifting by means of a beam splitter and a Bragg cell. Equal intensity beams were obtained by matching and optimizing the polarization of the optical fiber to the beam splitter. At the entrance, the Photo-Multiplier (PM) was "optically" isolated from the Bragg cell to avoid internal reflection and minimize background noise. In order to improve the signal to noise quality further for near-wall measurements, a spatial filter was manufactured and incorporated immediately downstream of the PM. It consists of two achromat lenses separated by $2\times$ focal length (130 mm), and a pinhole of 50 μm placed at the focal point. The axial position of one of the lenses, along with the location of the pinhole, were adjustable to allow combined optimization of the filter and the backscatter receiving optics. The pinhole diameter was experimentally optimized for maximum data rate. After the PM, the beam spacing is reduced from 50 to 22 mm, by means of a beam-reducing prism, to allow the two beams to pass through a 30 mm wide Dove prism, which served to transfer the two beams to the rotating system while maintaining their orientation.

Although the alignment and optimization of the LDA optics with each other and the optical axis of the fiber were important tasks, the combined alignment of the entire column of LDA optics with the axis of rotation was significantly difficult, simply because of the combined effects of all the different elements and their associated joints. As an attempt to allow adjustments to the LDA optical axis an "angular offset" ring arrangement was designed and incorporated at the end of the stationary system, to provide tilt and translation to the entire LDA column, and match the stationary optical axis to the axis of rotation. Different combinations of rotation between the three rings provide translation and up to 0.5 deg tilt.

A system was required to provide support to the entire optical system, and prevent the stationary optics from rotating due to the friction within the bearings. The support mechanism had to prevent rotation of the stationary optics while maintaining the overall system as a rigid body and, therefore, allowing the entire optical column to tilt and translate as a result of any transferred impeller wobble. The final design provided three degrees of freedom in translation and tilt. The concept above introduced a vibration of 1.25 Hz within the system, which was transferred to the optical fibers. Such vibrations may produce a phase shift in the light wave, causing the fringe patterns to move, and introduce an artifact velocity. A comparative study conducted by Kaufman and Fingerson (1985) showed that the artifact velocity at low vibration frequencies is proportional to cable acceleration. For the present system, the vibrational contribution to the measured rms is 0.287 mm/s.

Rotating Optical System. The rotating system design is comprised of the Dove prism for transferring the beams from stationary to rotating system, the periscope, which locates the measuring control volume at any desired location in the passage, and the microcomputer, which controls the traversing mechanism of the periscope. The entire system is attached to an aluminum disk, mounted on the impeller hub (upper sur-

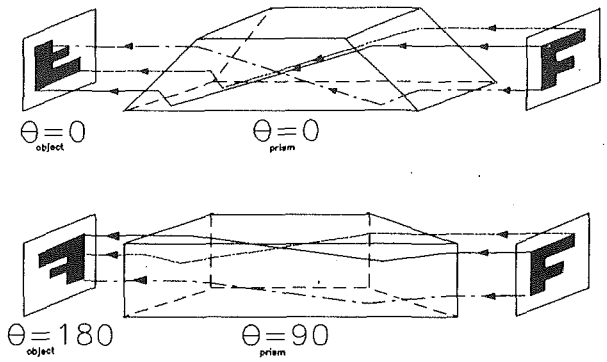

Fig. 5 Operating principal of Dove prism

face), which includes a cavity around the desired impeller passage.

Theory and Application of Dove Prism. Two possible techniques can be applied to transfer the required beams from a stationary to a rotating system. One would allow the use of a single beam transmission by a conventional beam splitter, which rotates at the same speed as the rotating system (Tokoi et al., 1980; Ribando et al., 1989). The disadvantage of this technique is that frequency shifting cannot be included since it will require a rotating Bragg cell or a diffraction grating to be incorporated into the rotating optics. Other techniques have been developed that allow the shifted and unshifted beams to be transmitted through one single mode fiber and then separated by polarization rotators (Knuhtsen et al., 1982). However, its application to a rotating system will not be successful since the rotating beam splitter will effect the polarization of the two beams. The only method that can be applied to transfer both shifted and unshifted beams separately to a rotating system is a triple reflection Dove prism or similar system such as triple mirrors used by Dunagan (1991). The principle of the Dove prism is shown in Fig. 5. Its optics are such that if rotated by 90 deg, the image of an object through the prism will rotate by 180 deg. Therefore, for a rotating object with a certain angular velocity, if the prism is rotated (in the same direction) at half the speed of the object, its image will remain stationary. The application of Dove prism to rotating systems was adapted by Lennemann (1969) for flow visualization studies inside the rotating passages of radial impellers. Successful application of the Dove prism to the present investigation required perfect alignment of the prism with first, the axis of its casing, and then with the combined axis of the LDA optics and rotation. The prism, held within its own casing, was therefore mounted on a "θ-θ" tilt adjustment mechanism, which provided two-directional tilt from the axis of rotation. A lead-screw mechanism was incorporated within the prism housing to provide translation in addition to tilt. The prism housing unit, along with the tilt adjustment mechanism, was held between two precision, double row, preloaded, angular contact bearings designed to interconnect to the pre-existing optics. The impeller speed was picked up by a timing belt directly linked to the rotating mechanism and then reduced to half by gear reduction and transferred to the prism rotating external housing unit. The gear reduction mechanism was mounted on an external shell attached to the stationary system. Both tilt and translation adjustments to the prism were possible from the external stationary shell.

Rotating Periscope. The periscope consisted of a combination of 45 deg mirror and lens combination, which transferred the two beams to any desired radial location. Both primary (on-axis) and secondary (off-axis) 45 deg mirrors included translation and tilt adjustment. The mirrors were reasonably good quality with 0.3 percent absorption and surface accuracy of $\lambda/20$. The final focusing lens was a 80 mm focal

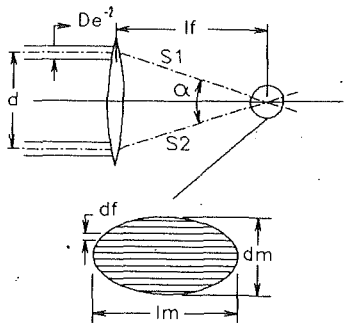

Fig. 6 Geometric parameters of the LDA

length achromat doublet lens, compensated for chromatic and spherical abberations, which focused the beams with a 31.3 deg included cone angle. Upstream of the secondary mirror a 12 mm aperture restricted the reflecting beams from the window surface to propagate further upstream while allowing the transmission of the primary beams through a 4 mm hole. The focusing lens was attached to a manual leadscrew mechanism for axial (hub-to-shroud) traversing. The R, θ traversing was conducted by an on-board microcomputer, which controlled the signals to the R, θ stepping motors.

Rotating Microcomputer. In order to allow remote control of the R, θ traversing during the measurement, an 8 bit microcomputer (MC) based on an Intel 8251 processor unit was developed and incorporated in the rotating system. The advantage of the on-board unit was that the quadrature signals required for the operation of the stepping motors were transmitted directly. The MC was connected to a stationary personal computer, via RS232 serial transmission, which served as a terminal to control the operation. The RS232 serial connection and the required electrical power were transmitted through six brass slip-ring and carbon brush arrangements. Two separate brush assemblies were placed 180 deg apart to provide constant connection during rotation and compensate for impeller wobble.

Two ports of the 8255 serial interface were connected to each stepping motor. The R traverse was a lead screw mechanism and the θ traverse incorporated a circular arc and worm gear assembly attached to the lower aluminum disk through a circular roller bearing.

The geometric parameters of the present LDA measuring control volume, described in Fig. 6, are summarized as follows:

$$D_{e-2} = 1.35 \text{ mm}$$

$$d = 22 \text{ mm}$$

$$l_f = 80 \text{ mm}$$

$$\alpha = 15.656 \text{ deg}$$

$$d_{e-2} = \frac{4\lambda f}{\pi D_{e2} E} = 38.7 \ \mu\text{m}$$

$$d_m = \frac{d_{e-2}}{\cos\left(\frac{\alpha}{2}\right)} = 39 \ \mu\text{m}$$

$$l_m = \frac{d_{e-2}}{\sin\left(\frac{\alpha}{2}\right)} = 0.284 \text{ mm}$$

$$d_f = \frac{\lambda}{2\sin\left(\frac{\alpha}{2}\right)} = 1.88 \ \mu\text{m}$$

$$\text{NFR} = \frac{d_m}{d_f} = 20$$

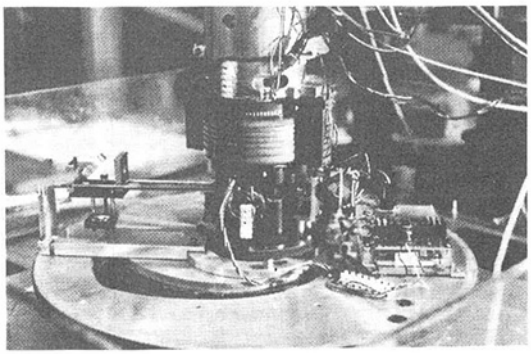

Fig. 7 Photograph of the microcomputer, rotating periscope, and the slip-ring

Air to water transmission alters the beam angle α without changing the beam spacing and the axial positions of the beams are shifted by the refractive index of water (1.333). This probe volume geometry allowed measurements within 1.5 mm away from the (hub) wall and 2 deg from the blade surface. Measurements closer to the blade surface were limited by the passage axial height.

Experimental Procedure

Optical Setup and Alignment. The success of the measurement technique was dependent on the alignment and optimization of all the optical components.

The (stationary) LDA optics were aligned and optimized for data rate using a Nebulizer as a particle generator. Optimization required adjustment to the position of the beam waist using the fiber manipulator. All stationary LDA optics were attached to a frame that held their alignment. Without the prism in place, the stationary optics were aligned with the axis of rotation using the "angular off-set" tilt adjustment mechanism. The entire LDA optics unit was then removed to allow the Dove prism, within its housing, to be attached to its tilt adjustment mechanism and the lower bearing inside the bearing housing. After placing the prism housing onto the tilt adjustment mechanism, the LDA optical column was then returned and attached to the LDA angular offset mechanism. Two vertically displaced rings, connected by lead screws, provided a support system and locked the angular offset mechanism in place. The prism was adjusted by tilt and/or translation until the two beams coincided on a target, 5 m apart, after 720 deg rotation. After rotation, the two target points generally coincided with the beams within 3–5 mm, resulting in a 0.05 deg wobble of the beams. The periscope primary mirror was adjusted (translation and rotation) to transfer the beams through their associated (4 mm) pinholes at the receiving end of the secondary mirror. The secondary mirror was then adjusted (translation and rotation) to locate the beams, through the focusing lens, within the passage. The position of the beam waist was optimized by adjusting the (axial) position of the optical fiber at the probe end until minimum beam diameter was obtained at the control volume. Extreme care had to be taken when adjusting the fiber position. If the fiber movements included an angular shift, the alignment of the overall setup with the axis of rotation was disturbed. In this case the prism was removed and the entire alignment procedure repeated. Preliminary visual inspection of the prism alignment was conducted by rotating the prism about the two bearings, with the upper optics and the impeller held stationary, to ensure that the two beams passed through their associated pinhole at the entry of the periscope secondary mirror. After the stationary external shell and the associated gear reduction mechanism were in place, with the LDA optics held stationary, the impeller was manually rotated and the alignment of the prism visually inspected by ensuring that at any angular orientation of the impeller both beams were present. The design of the periscope and the associated pinhole at its entry incorporates such tight tolerance (± 0.5 mm) that wobble associated with the misalignment of the prism will prevent the transmission of one beam.

The important factor to consider was that, when the prism was in place, care had to be taken to ensure that the initial alignment of the LDA column with the axis of rotation was not disturbed. It was practically impossible to conduct simultaneous alignment of the prism and the LDA column. In an attempt to examine the quality of the alignment and the overall LDA setup, the measuring control volume was set at the inner wall of the hub with the shift frequency set at 0.5 MHz. The impeller was then rotated at 150 (design) rpm. The shaft-angle-averaging software was used to measure the velocity (off-set frequency) as a function of circumferential angle. In the soft-

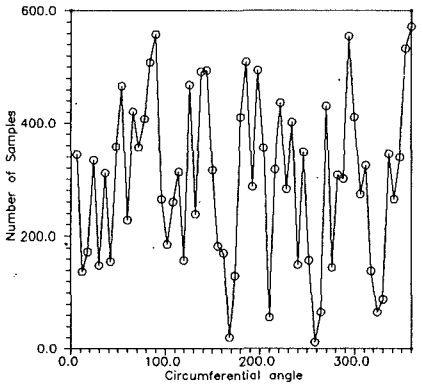

Fig. 8 Angular distribution of number of samples

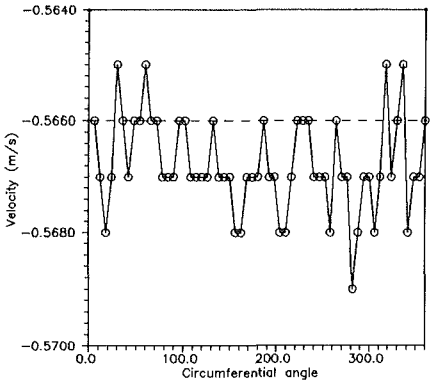

Fig. 9 Angular distribution of the offset measured velocity at the wall

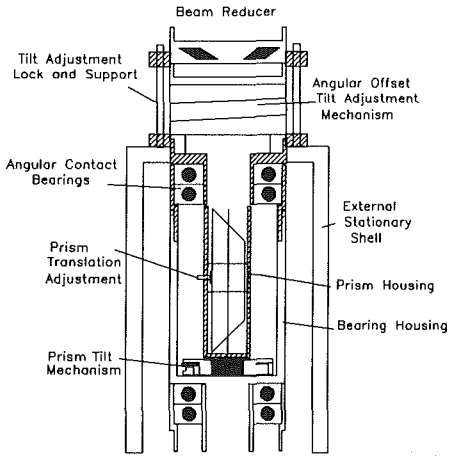

Fig. 10 Schematic description of the prism alignment mechanisms

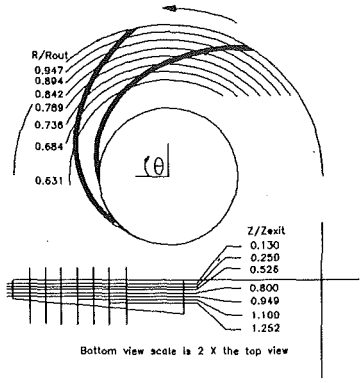

Fig. 11 Schematic drawing of the measurement locations within the impeller

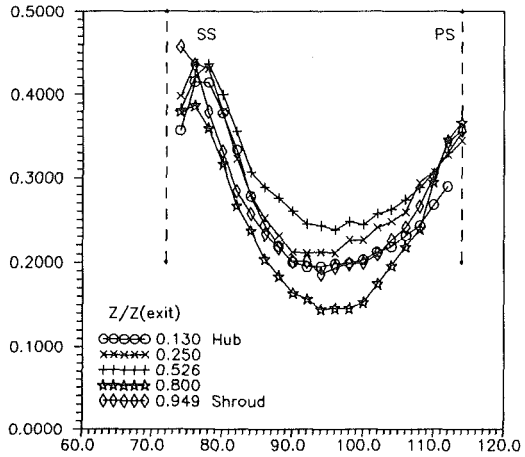

Fig. 12 Suction-pressure distribution of the radial velocity at design flow (no volute)

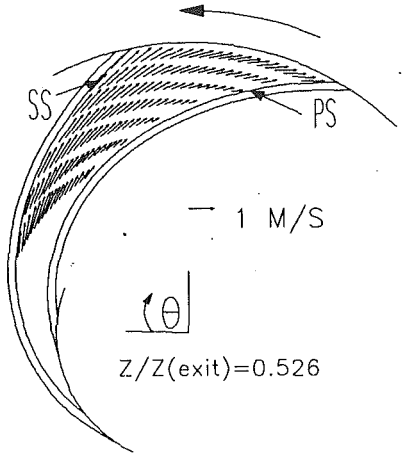

Fig. 13 Time-averaged velocity vectors at $Z/Z_{exit} = 0.526$, design flow (no volute)

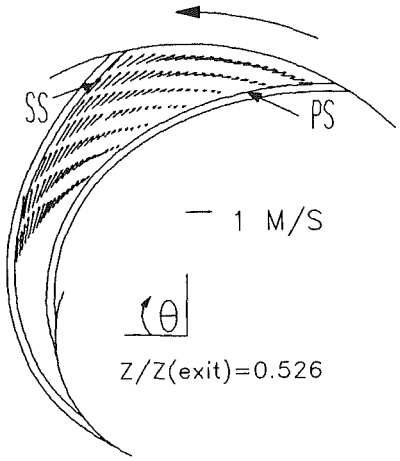

Fig. 13 Time-averaged velocity vectors at $Z/Z_{exit} = 0.526$, design flow (no volute)

ware the shift frequency was set to 0.2 MHz, which, given the conversion factor of 1.885 (m/s)/(MHz), resulted in an offset frequency of 0.3 MHz, hence, 0.5655 m/s. Results of the measurement are shown in Figs. 8 and 9 for the number of recorded samples and the ensemble-averaged velocity, respectively. Samples were taken over 20 seconds, which corresponded to approximately 50 impeller revolutions. The nonuniform distributions of the recorded samples were associated with the random movement of the control volume around the wall associated with the impeller wobble. The constant measurement of frequency also indicated the satisfactory alignment of the two beams, since any misalignment would have resulted in "loosing" one of the beams at some angular orientation and at a rate of twice the impeller rotational frequency. Slight misalignment may have resulted in a slight relative motion of the control volume against the wall, which simulated an additional movement of the fringes. The overall effect was on the order of 0.3 percent and was considered negligible since the measured rms was zero.

Continuity Verification. The blade-to-blade distribution of radial velocity, measured at the exit plane ($R/R_{out} = 0.947$) is shown in Fig. 12 for design flow. The velocity profiles were integrated to determine the overall flow and compare the integrated value to the one measured by the calibrated venturi. The total flow rate was obtained by integrating $V_{\theta z}$ (the average velocity) over the incremental area dA. The flow rate based on the integrated velocity profile is 0.487 l/s per impeller blade passage, which is 18.7 percent higher than the design flow rate of 0.410 l/s. In addition to the actual impeller flow, leakage flow contributes to the overall exit flow as well. With the impeller operating under shut-off condition, the (leakage) radial velocity was measured at the same radial location. The integrated leakage flow under shut-off condition is 0.188 l/s, which is ≈ 38 percent of the total design flow. The contribution of the leakage flow is expected to be different under different operating conditions, with its highest contribution at shut-off. It is, therefore, not possible to evaluate the exact leakage flow under design operating condition.

Sampling Rate. Maximum obtainable data rate was within 400–500 data/s. Comparison between continuous time sampling at a rate below the maximum data rate and arrival time sampling showed, for most of the flow regimes at design flow rate, a difference of 1.5 percent between the mean values. At regions of very low data rate (near pressure side separated region) arrival time sampling was conducted and its associated bias was accounted for by allowing for the particle resident time. Total sampling time for every point was varied until satisfactory probability distribution function of the signal was obtained.

Sample Measurements and Discussions

Sample plots of the time-averaged total relative velocity vectors, without the volute, are shown in Figs. 13 and 14 for the design and 50 percent of design flow conditions taken at $Z/Z_{exit} = 0.526$ (passage midheight). Hub-to-shroud distribution of the total relative velocity at the exit, along with their associated turbulence intensities, are also presented in Figs. 15 and 16. In general, in contrast to the usual expectation, the overall behavior of the impeller flow is similar to that predicted

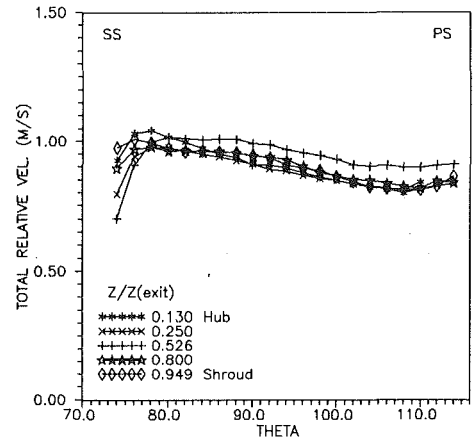

Fig. 15 Time-averaged relative velocity at $R/R_{out} = 0.947$, design flow (no volute)

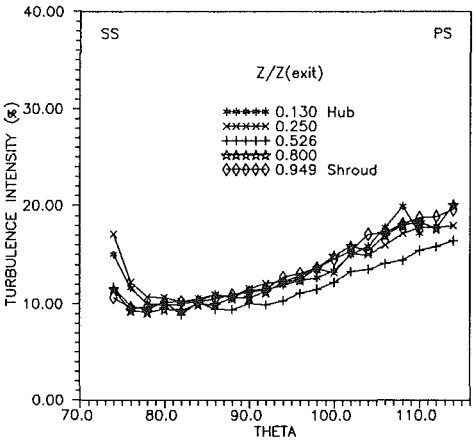

Fig. 16 Stationary turbulence intensity at $R/R_{out} = 0.947$, design flow (no volute)

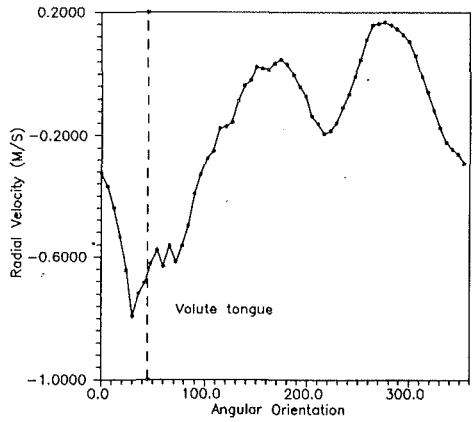

Fig. 17 Circumferential variation of the ensemble-averaged radial velocity at the pressure side, shut-off

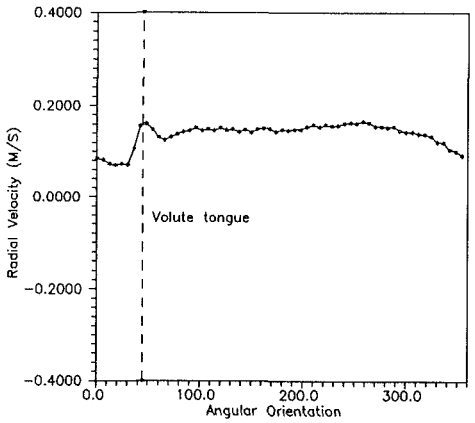

Fig. 18 Circumferential variation of the ensemble-averaged radial velocity at the suction side, shut-off

by potential flow theory. Measurements have quantified the same flow behavior observed in previous flow visualization studies (Abramian, 1986), which indicated the strong influence of the relative eddy on the passage flow. Under low flow conditions, the relative eddy results in flow separation on the pressure side of the passage followed by the reattachment and a wake-free exit. Details of the results obtained by conducting measurements at other locations (shown in Fig. 11) along with a description of the interaction between the primary and secondary flows, which results in such behavior of the relative flow, are discussed by Abramian and Howard (1994). They concluded that the inviscid behavior of the impeller passage in a reflection of its highly loaded characteristics, which results in the secondary viscous effects being dominated by the inviscid primary characteristics of the passage. Total turbulence intensity is determined by considering the average of the radial and tangential fluctuation divided by the total relative velocity (as reported by Flack et al. (1992)). Measured turbulence intensities indicate the increase of turbulence from the suction side to the pressure side associated with the dominating effect of Coriolis acceleration on the unstable region of the boundary layer. The "somewhat" high levels of turbulence are associated with the operating point of the impeller. Previous performance measurements indicated that the best-efficiency-point (b.e.p.) of the impeller occurs at 170 percent of the intended design flow. This effect is associated with the choice of exit axial width, which is higher than normal correlations and limited by the manufacturing constraints of the model pump. The overall turbulence level at the b.e.p. of the impeller is expected to be between 5 and 10 percent. The important factor to note is that, based on the present technique, the reported turbulence intensities do not include frequencies associated with the impeller rotation. The importance of this criterion becomes more significant when the impeller is operating in a circumferentially nonuniform environment, such as the one induced by the volute. Data presented by Flack et al. (1992) demonstrate the variation of the turbulence intensity of their eight different circumferential locations. The average of the turbulence intensities at those locations will not contain the effect of any periodic unsteadiness at the frequency of the impeller rotation or higher harmonics. The overall unsteadiness of the impeller passage flow will not be reflected by these measurements at fixed locations, because the flow fluctuations that occur between each angular orientation have not been included. When the impeller is operating in a nonuniform environment the order of these fluctuations may be at two or three harmonics of the impeller rotational frequency. To demonstrate the overall effect of the cyclic variation induced by the volute, under near shut-off condition, ensemble-averaged blade-to-blade measurements were conducted at the impeller exit with the impeller fitted with the volute. Results of the angular variation of the radial velocities at the pressure and the suction side are shown in Figs. 17 and 18, respectively. More detailed discussion of the power spectrum analysis along with the complete vector plots of the blade-to-blade variations are given by Abramian and Howard (1994). The angular orientation of the passage with respect to the volute was such that the volute tongue was set at 45 deg from the passage suction side. At the suction side, the passage is not significantly affected by the presence of the volute. At the pressure side, however, complete flow reversal occurs when the passage approaches the tongue followed by

an acceleration immediately past the volute tongue. After a mild reversal and recovery midway through the volute, the flow reverses again before reaching the tongue. The measurements confirmed the previous hydrogen bubble flow visualization study conducted for the same impeller using an optical triggering mechanism to determine the impeller orientation with respect to the volute (Howard et al., 1987).

Although the impeller exit flow may be periodic at any given circumferential location, in order to quantify its overall mean and fluctuating components, the ability to continuously detect their values at discrete angular locations is extremely important. Furthermore, when the impeller is operating in a circumferentially nonuniform environment, the importance of isolating any periodic fluctuation from those due to turbulence should not be overlooked. Ensemble (phase) average velocity measurements of the impeller flow from a stationary location, even at design operating conditions, may not represent the true mean and fluctuating components of relative velocity even if the (stationary) measurements are conducted at different circumferential locations.

Conclusions

A laser-Doppler anemometry measurement system has been developed that allows direct measurements of the relative velocity in model centrifugal impellers. Details of the optical and mechanical design of the system are presented. The success of the technique is demonstrated by sample measurements conducted within the rotating passages of a low specific speed impeller, with and without the volute. Although individual measurement of instantaneous velocity will be the same whether measured from the stationary or the rotating system, the present technique becomes superior in specific applications where the impeller flow is nonperiodic and other passages do not represent the same flow behavior.

The capabilities of the technique may be enhanced by further modifications toward a two-component system, which will allow quantitative description of the turbulent shear stress within the rotating passage. The periodic averaging of such a parameter based on the measurements at a stationary location can be less accurate.

Although the application of the technique is currently limited to low-speed apparatus, it is expected to contribute further toward optimum design procedure by applying it to impellers of different geometry and flow characteristics (unshrouded impeller). Impeller passage geometries that could conveniently be investigated are those where the flow has little axial component and the impeller passage backface is radial or near-radial. The technique can also be applied to fundamental investigations of turbulent boundary layers when subject to Coriolis acceleration.

Acknowledgments

The research was funded principally by a grant from the Natural Sciences and Engineering Research Council of Canada.

References

Abramian, M., 1986, "Experimental Investigation of the Volute-Impeller Interaction in a Low Specific Speed Pump," M.A.Sc. Thesis, University of Waterloo, Waterloo, Ontario, Canada.

Abramian, M., Howard, J. H. G., and Tropea, C., 1987, "A Fibre-Optically-Linked Laser-Doppler Anemometry System for Turbomachinery Fluid Flow," *Fluid Measurement and Instrumentation Forum*, ASME Fluids Engineering Conference, Cincinnati, OH, June 14-17, pp. 11-14.

Abramian, M., and Howard, J. H. G., 1994, "Experimental Investigation of the Steady and Unsteady Relative Flow in a Model Centrifugal Impeller Passage," ASME JOURNAL OF TURBOMACHINERY, Vol. 116, this issue, pp. 269-279.

Carey, C., Fraser, S. M., Rachman, D., and Wilson, G., 1985, "Studies of the Flow of Air in a Model Fixed-Flow Pump Using Laser Doppler Anemometry, Part 1: Research Facility and Instrumentation, Part 2: Velocity Measurements Within the Impeller," *National Engineering Laboratory*, Report No. 698.

Dunagan, S., 1991, "Dual-Beam Laser Velocimetry With Image Rotation," *Fluid Measurements and Instrumentation Forum*, First ASME/JSME Fluids Engineering Conference, Portland, OR, June, pp. 69-73.

Evans, R. L., 1975, "Turbulence and Unsteadiness Measurements Downstream of a Moving Blade Row," ASME *Journal of Engineering for Power*, Vol. 97, pp. 131-139.

Fagan, W., and Selbach, H., 1984, "Laser 2 Focus Flow Measurements in the Absolute and Rotating Frame Inside the Blade Row of an Axial Flow Fan," *Proceedings of the Second International Symposium on the Application of Laser Anemometry in Fluid Mechanics*, Lisbon, 16.2.

Flack, R. D., Miner, S. M., and Beaudoin, R. J., 1992, "Turbulence Measurements in a Centrifugal Pump With a Synchronously Orbiting Impeller," ASME JOURNAL OF TURBOMACHINERY, Vol. 114, pp. 350-359.

Fowler, H. S., 1968, "The Distribution and Stability of Flow in a Rotating Channel," ASME *Journal of Engineering for Power*, Vol. 90, pp. 229-236.

Gorton, C. A., and Lakshminarayana, B., 1976, "A Method of Measuring the Three-Dimensional Mean Flow and Turbulence Quantities Inside a Rotating Turbomachinery Passage," ASME *Journal of Engineering for Power*, Vol. 98, pp. 000-000.

Howard, J. H. G., and Lennemann, E., 1971, "Measured and Predicted Secondary Flows in a Centrifugal Impeller," ASME *Journal of Engineering for Power*, Vol. 93, pp. 000-000.

Howard, J. H. G., and Kittmer, C. W., 1975, "Measured Passage Velocities in a Radial Impeller With Shrouded and Unshrouded Configurations," ASME *Journal of Engineering for Power*, Vol. 97, pp. 207-213.

Howard, J. H. G., Mukker, O. S., and Naeem, T., 1980, "Laser Doppler Measurement in Radial Pump Impeller," *Measurement Methods in Rotating Components of Turbomachinery*, ASME, New York, pp. 133-138.

Howard, J. H. G., Abramian, M., and Hermann, P., 1987, "Experimental Investigation of Impeller and Volute Flow Fields for a Low Specific Speed Pump With Single and Double Volutes," *Proceedings of the ASME/JSME Thermal Engineering Conference*, Vol. 2, pp. 51-61.

Kaufman, V. V., and Fingerson, Y. Y., 1985, "Fiber Optics in LDV Applications," *International Conference on Laser Anemometry—Advances and Application*, Dec. 16-18, Manchester, United Kingdom, pp. 53-65.

Knuhsten, J., Olldag, E., and Buchhave, P., 1982, "Fiber-Optic Laser Doppler Anemometry With Bragg Frequency Shift Utilizing Polarization Preserving Single Mode Fiber," *Journal of Physics E: Scientific Instrumentation*, Vol. 15, pp. 1188-1191.

Lakshimanarayana, B., 1980, "An Axial Flow Research Compressor Facility for Flow Measurements in Rotor Passages," *Measurements Methods in Rotating Components of Turbomachinery*, ASME, New York, pp. 31-41.

Lennemann, E., 1969, "Secondary Flows in Rotating Passages," Ph.D. Thesis, University of Waterloo, Waterloo, Ontario, Canada.

Menon, R. K., 1987, "Three Component Velocity Measurements in the Interblade Region of a Fan," ASME Paper No. 87-GT-207.

Powel, J. A., Strazisar, A. J., and Seasholtz, R. G., 1981, "Efficient Laser Anemometry for Intra-rotor Flow Mapping in Turbomachinery," ASME *Journal of Engineering for Power*, Vol. 103, pp. 424-429.

Raj, R., and Lakshminarayana, B., 1976, "Three Dimensional Characteristics of Turbulent Wakes Behind Rotors of Axial Flow Turbomachinery," ASME *Journal of Engineering for Power*, Vol. 98, pp. 218-228.

Ribando, R. J., Palmer, J. L., and Scott, J. E., 1989, "Flow in Partially Filled, Rotating, Tapered Cylinder," *Journal of Fluid Mechanics*, Vol. 203, pp. 541-555.

Sideris, M. Th., and Van den Braembussche, 1987, "Influence of a Circumferential Exit Pressure Distortion on the Flow in an Impeller and Diffuser," ASME JOURNAL OF TURBOMACHINERY, Vol. 109, pp. 48-54.

Sitaram, N., Lakshminarayana, B., and Ravindranath, A., 1981, "Conventional Probes for the Relative Flow Measurements in a Turbomachinery Rotor Blade Passage," ASME *Journal of Engineering for Power*, Vol. 103, pp. 406-414.

Tokoi, H., Ozaki, N., and Harada, I., 1980, "Measurements of Velocity Profiles of Gas in a Rapidly Rotating Cylinder," *Rev. Sci. Instrum.*, Vol. 51, No. 10, pp. 1318-1322.

Experimental Investigation of the Steady and Unsteady Relative Flow in a Model Centrifugal Impeller Passage

M. Abramian
Pratt & Whitney Canada,
Mississauga, Ontario, Canada

J. H. G. Howard
Department of Mechanical Engineering,
University of Waterloo,
Waterloo, Ontario, Canada

The behavior of the relative flow in centrifugal turbomachines is extremely complex due to the existence of various fluid dynamic phenomena and their interaction. At design and off-design operating conditions, the relative flow is subject to stationary unsteadiness, which includes flow separation and wakes associated with passage pressure gradients, secondary flows, and boundary layer stability. It may also be subject to periodic unsteadiness, as are the rotating stall and cyclic flow phenomena induced by the casing. This paper describes detailed measurements of the relative velocity field in a very low specific speed centrifugal pump impeller (N_s = 515). Measurements were conducted by means of a recently developed rotating laser-Doppler anemometry system. Detailed quantitative descriptions of the mean and fluctuating components of the primary and secondary velocity fields are presented for an impeller without volute at design, 50 percent design, and shut-off conditions. The flow pattern in this low specific speed impeller with high blade loading is dominated by the relative eddy (a phenomenon also present in potential flow), which has suppressed suction side separation. The cyclic variation of the impeller exit flow, induced by the volute at low flow rates, is also presented for an impeller fitted with a volute.

Introduction

As higher operating speeds become available, smaller centrifugal impellers with higher pressure rise may be considered as replacements for multistage axial machines for gas turbine and pump applications. A low specific speed design may result from a need to eliminate multistaging. Even though turbomachines are designed to operate at their best efficiency point of operation, in many applications they are expected to have stable and efficient operation over a wide range of flow rates. As well as attaining higher efficiencies, it is desirable to make the machine less sensitive to off-design operation. Analytical models used for design, however, are often unable to predict the off-design conditions for various geometries. Improvement to the available analytical models requires a more detailed understanding and knowledge of the flow behavior in the rotating impeller passage (referred to here as relative flow).

In summary, the unsteady behavior of the relative flow can be considered under two categories:

- *Stationary unsteadiness*, which is the flow separation and wakes associated with the passage pressure gradients, secondary flows, and boundary layer stability, and
- *Periodic unsteadiness*, which is the rotating stall and the cyclic flow phenomena induced by the volute or casing.

Contributed by the International Gas Turbine Institute and presented at the 38th International Gas Turbine and Aeroengine Congress and Exposition, Cincinnati, Ohio, May 24–27, 1993. Manuscript received at ASME Headquarters March 1993. Paper No. 93-GT-430. Associate Technical Editor: H. Lukas.

Stationary Unsteadiness. The agreement of two-dimensional inviscid flow prediction with the actual flow behavior inside an impeller passage was first examined by Fischer and Thoma (1932) who conducted a series of flow visualization studies. In contrast to the prediction based on potential flow analysis, they found that reverse flow occurred, for most of the off-design conditions, at the suction side of the passage and the zone of separation increased with decreasing flow rate. This was later confirmed by other researchers and suggested that the suction side separation is due to the secondary flow of the endwall boundary layer across the passage from the pressure side to suction side, owing to the cross-passage pressure gradient (Johnson and Ginsburg, 1953; Fowler, 1968; Lennemann and Howard, 1970). For the unshrouded impeller, however, they observed pressure side separation, which was suggested to be associated with the vortex sheet generated from the blade tip, which rolled up along the blade suction side. The rolled-up vortex was also observed by Senoo et al. (1968) in mixed flow impellers. Howard and Kittmer (1975) later conducted hot-film measurements inside an impeller similar to the low-speed Lennemann (1969) impeller, and confirmed the existence of a single vortex in the unshrouded impeller. In the shrouded impeller, two counterrotating vortices swept the boundary layer along both shrouds from pressure to suction side of the passage.

Johnson and Moore (1980) considered the equation governing the development of the streamwise vorticity for incom-

pressible inviscid flow, which was originally derived by Smith (1957). Howard (1966) later developed a secondary flow model for compressible flow and Lakshminarayana and Horlock (1973) introduced generalized expressions for secondary vorticity:

$$\frac{\partial}{\partial s}\left[\frac{Q_s}{W}\right]=\frac{2}{\rho W^2}\left[\frac{1}{R_N}\frac{\partial P^*}{\partial b}+\frac{\omega}{W}\frac{\partial P^*}{\partial z'}\right] \quad (1)$$

$$P^*=\frac{1}{2}\rho W^2+p-\frac{1}{2}\rho r^2\omega^2 \quad (2)$$

The two major factors contributing to the development of streamwise vorticity are the radius of curvature R_N and rotation with angular velocity ω around the impeller axis. Large gradients of P^* give rise to secondary flows. Due to the action of the secondary flows, fluid with low P^* migrates toward the region of low reduced static pressure. The rotational effects are opposite to that of curvature for backward curve blading. Rotation induces a streamwise component of vorticity when a gradient of P^* exists in the axial direction. The effect of rotation on the radial part of an impeller causes low P^* fluid to be convected to the suction side of the passage, as measured by Moore (1973) in a rotating radial diffuser. Rotation and curvature do not result in similar secondary flows but they compete for the dominating effect on the stable location of low P^* fluid. In impellers of different design geometry, it is the competition between the curvature and rotation effects that results in the observed variations in the location and the intensity of the wake. The relative magnitudes of the two opposed secondary flows have been assessed from the Rossby number (Ro = $W/[\omega R_n]$) by Farge and Johnson (1990), who investigated the secondary flow generation in radial and backswept impellers. When Ro < 1, rotation effects dominate, and when Ro > 1, curvature effects dominate. The stable location of low P^* fluid is a function of the Ro number. Even in the backswept impellers, the stable location may be on the suction side if Ro < 1 or on the pressure side if Ro > 1. In addition to their effect on the generation of secondary vorticity, both surface curvature and system rotation can have stabilizing and/or destabilizing effects on the passage boundary layer as a function of the effect relative to the shear layer coordinates. Numerous attempts have been made to investigate the individual or combined effects of rotation and curvature on the performance of laminar and turbulent boundary layers (Johnson, 1970; Gillis et al., 1980; Bradshaw, 1973; Jeans and Johnston, 1982; Rothe and Johnston, 1976; Barlow and Johnston, 1985).

Overall, the evidence has indicated that the discharge flow of a radial impeller is highly distorted into a "jet-wake" structure, which is a result of the separation-like phenomena associated with secondary flows and stability effects. This led to the development of the "jet-wake" model introduced by Dean (1968) in which the relative flow at the exit of the impeller was divided into two regions: a jet region along the pressure side of the passage (inviscid potential core), and a wake region along the suction side (viscous low-momentum flow). Recent L2F measurements conducted on a backswept impeller by Rohne and Banzhaf (1991) allowed modifications to the classical model. In order to discriminate between the flow in these regions and those in true jets and wakes, the regions have been renamed as the primary and secondary zones (Japikse, 1985). Moore (1973) conducted detailed hot-wire velocity measurements in a rotating radial diffuser and verified the suction side separation followed by the formation of the wake. At low flow rates, an eddy (stagnation pressure point) was measured on the pressure side of the passage. Eckardt (1975, 1976) conducted similar measurements for unshrouded radial impellers and obtained similar results with the exception of a more unstable and enlarged wake region due to the secondary flows being fed through the shroud gap into the the wake. In an attempt to verify the previous results further, and to compare the results of radial to backward swept passages, Adler and Levy (1979) conducted LDA measurements in a shrouded impeller, with straight, backward swept blades. They observed a decaying jet-wake structure, which occurred on the shroud pressure side due to a distorted inlet flow. The suppression of the wake and the uniformity of the flow at the exit were suggested to be associated with the stability effects of the backward swept blades. The location and the intensity of the wake varied with the impeller geometry, operating flow, and speed. Krain (1987) conducted laser 2-Focus blade-to-blade measurements at various locations from entry to exit of a backward swept, unshrouded, centrifugal impeller. In contrast to the referenced studies, his results showed fairly uniform distribution of the meridional velocity at the inlet, followed by a distortion midway into the passage, which then recovered to a uniform distribution at the exit. Hamkins and Flack (1986) conducted shaft-angle averaged laser-Doppler anemometry in shrouded and unshrouded radial impellers with log-spiral blades fitted with a single volute. At low flow rates, the flow separation, followed by the formation of wake, had occurred on the suction side of the passage for both shrouded and unshrouded impellers.

Periodic Unsteadiness. The periodic unsteadiness of the relative flow was first observed by Fischer and Thoma (1932) during their flow visualization studies on a low specific speed radial impeller. At some critical flow rate, they observed a flow pattern known as a rotating stall. Studies conducted by Lennemann and Howard (1970) also investigated the initiation of rotating stall, relating it to secondary flows and entry boundary layer conditions. There must also be an interaction with the stationary components. Flow blockage in one passage unstalls the adjacent passage. Thus the rotating stall moves relative to the stationary elements in the direction of rotation at a lower speed than the impeller. Recent experimental investigations of Mizuki and Oosawa (1992) in low pressure ratio centrifugal compressors showed that fluctuations caused by the full-span stall occurred even during surge and affected the flow within the volute through the vaneless diffuser. They obtained good agreement between their results and those computed by the lumped parameter theory (Greitzer, 1976).

In addition to the possibility of rotating stall, when the impeller is fitted with a volute, the interaction between the volute and the impeller flow fields also results in a flow pattern that is cyclic with respect to the impeller. Under off-design low flow rates, the volute induces a nonuniform pressure dis-

Nomenclature

b = binormal direction
C_3 = normal acceleration parameter (Eq. (4))
P^* = rotary stagnation pressure (Eqs. (1) and (2))
R, r = radius
R_N = radius of curvature
Ro = Rossby number
s = streamwise distance
W = relative velocity
W_{sec} = secondary velocity normal to blade
w' = turbulent (fluctuating) velocity
X_1 = distance along passage streamline
ΔX_3 = passage normal width
Z, z' = axial direction
β = relative flow angle from meridional
ζ = streamwise vorticity
Ω_s = secondary vorticity
ω = angular velocity of rotation

Subscripts

r = radial
t = tangential

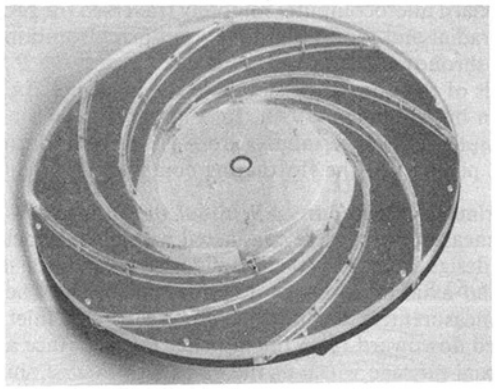

Fig. 1 Test impeller

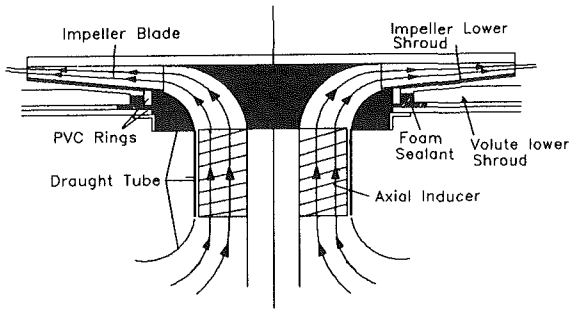

Fig. 2 Seal locations and impeller entry flow

tribution around the impeller periphery, which increases to its maximum at the throat (Abramian, 1986). The high pressures result in a reverse flow inside the impeller passage each time the passage reaches the throat. This phenomenon has been confirmed by the flow visualization studies (Howard et al., 1987), on the impeller of the present investigation.

Objective

The present study was undertaken to investigate the unsteady behavior of the relative flow in very low specific speed centrifugal pump impellers. A newly developed experimental technique, based on rotating laser-Doppler velocimetry, was incorporated to quantify the stationary and periodic behavior of the relative flow in a low specific speed, N_s = 515 (based on gpm, ft rpm), backward swept impeller. The technique employs a Dove prism, between rotating and stationary optics, which transfers the two (shifted and unshifted) beams from the stationary to the rotating system while maintaining their orientation. The specific speed is lower than those in the studies noted above except for Abramian (1986) and Howard et al. (1987).

Extensive measurements were conducted within the impeller passage at design, and 50 percent design flow. At near-shut-off flow rate, in order to describe the cyclic variation of the impeller flow induced by the volute, measurements were also conducted at the impeller exit with a single volute in place. Quantitative descriptions of the primary and secondary flows, as well as the mean and fluctuating components of the total relative flow, are presented. The periodic unsteadiness is described by vector plots of the angular variation of the relative flow and power spectrum analysis.

Experimental Apparatus

Test Rig. A detailed description of the test rig is given by Abramian and Howard (1994). It is a closed-circuit arrangement consisting of a reservoir tank and a test section. The test section itself consists of an upper settling tank, open to the atmosphere, and a lower settling tank. The upper and lower settling tanks are connected through a draft tube in which there is an axial flow inducer (connected to the impeller) providing swirling flow to the impeller inlet. The test impeller circulates the water from the reservoir up through the draft tube, into the upper settling tank, and back to the reservoir via an inclined rectangular duct. The upper settling tank serves as a dump with uniform circumferential pressure distribution when the impeller is operated without the volute.

Table 1 Impeller geometry and design parameters

Q (Design Flow Rate)	52.1 USGPM	3.287 L/S
H (Design Head Rise)	2.69 Ft.H2O	819.9 mm.H2O
ω (Design Speed)	150 RPM	
R_1 (Inlet Radius)	4.25 in.	10.79 cm.
R_2 (Exit Radius)	9.50 in.	24.13 cm.
B_1 (Inlet Blade Height)	1.06 in.	2.70 cm.
B_2 (Exit Blade Height)	0.475 in.	1.20 cm.
β_{b1} (Inlet Blade Angle)	15° Tangential	
β_{b2} (Exit Blade Angle)	30° Tangential	

Test Impeller and Volute. The impeller for the present investigation, designed to model a very low specific speed (N_s = 515) pump, such as might be used for an aircraft fuel pump, is shown in Fig. 1 and details of its design parameters and geometry are given in Table 1. It was formed by fitting eight backward swept blades between two (upper and lower) shrouds. The angles vary linearly with radius from 15 deg (tangential) at the inlet to 30 deg (tangential) at the exit. The blade axial height varies inversely with radius, resulting in a curved lower shroud. It is entirely manufactured from plastic to allow flow visualization studies to be conducted inside rotating passages (Abramian, 1986; Howard et al., 1987). The hub of the one complete passage of the original impeller was removed by machining and replaced by conventional (window) glass to allow complete access of the LDV probe to the entire passage. Details of the impeller entry conditions are shown in Fig. 2. Two PVC rings, machined to match the impeller inlet radius, were used to seal the gap between the impeller and the draft tube. The impeller exit height is greater than the normal design correlations suggest for this specific speed, due to manufacturing limitations on a scaled fuel pump. The result is a best efficiency point higher than the design flow rate. Further manufacturing limitations required the number of blades to be limited to 8. The combined effects resulted in a highly loaded impeller. The tangential loading of the impeller is on the order of 0.7 at the inlet and 6 at the exit. In the past, a similar impeller with two splitters was examined. Flow visualization studies revealed nonuniform flow in the splitter passages and its performance showed no overall improvement. The chosen impeller was selected for the present investigation since prior hydrogen bubble flow visualization studies had been conducted within its passages and the effect of the volute on its performance had been investigated. The flow visualization studies showed that, despite its highly loaded passage, flow separation occurred on the pressure side of the passage (Abramian, 1986).

The single volute was manufactured by fitting the volute vanes between two parallel shrouds. The axial height of the volute was chosen to be twice the height of the impeller blade at the exit in order to allow the impeller discharge flow to be unaffected by the boundary layer generated on the impeller and volute upper and lower shrouds. The volute was cut in half, which allowed its assembly around the impeller without removal of the impeller and its associated optics. The gap between the volute upper shroud was sealed using flexible strips. The overall performance of the impeller with and without the volute is shown in Fig. 3. The b.e.p. of the impeller without the volute is at 170 percent of the design flow, which

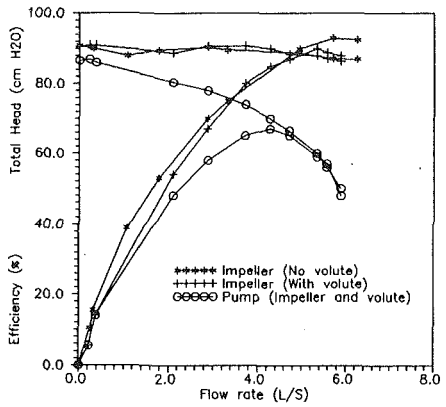

Fig. 3 Impeller and pump performance with and without volute

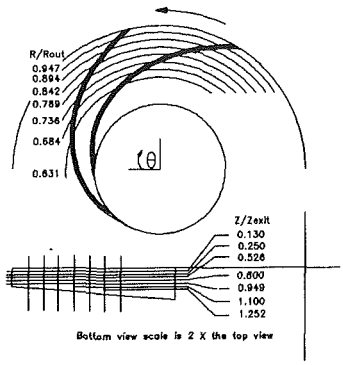

Fig. 4 Schematic description of the radial and axial measurement locations within the impeller passage

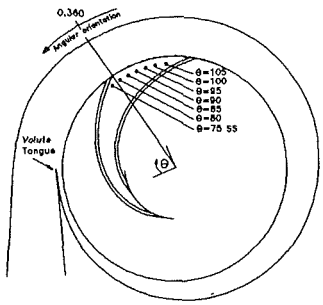

Fig. 5 Schematic description of the impeller passage orientation with respect to volute for cyclic variation measurement

is associated with the extra axial depth of the impeller at the exit. With the single volute, however, the overall pump b.e.p. occurs at ≈ 120 percent of design flow. The presence of the volute also shifted the b.e.p. of the impeller toward design flow. Detail effects of a double volute as well as the effect of the volute tongue clearance are given by Abramian (1986).

Experimental Technique and Procedure

Experimental Technique. Details of the rotating LDA system used for the present investigation are described by Abramian and Howard (1994). In general, it was comprised of the laser, its fiber optically linked transmission to stationary dual-beam optics, and the rotating optics required for transferring the beams from the stationary system to any desired location in the relative frame. The stationary LDA optics were attached to a Dove prism, which rotated at half the speed of the impeller and transferred the two (shifted and unshifted) beams from the stationary to the rotating system. A rotating periscope, which included the final focusing lens, positioned the probe volume to any desired location within the passage. An on-board microcomputer remotely traversed the probe volume in radial and tangential direction during rotation. Axial (hub-to-shroud) traverse was manual.

Details of the uncertainty levels to the present LDA system are given by Abramian (1992). In summary, based on arrival time sampling, the uncertainties are ±1.2 percent for the mean and ±2 percent for the fluctuating components.

Experimental Procedure. *Without the volute in place, extensive measurements were conducted within the impeller passage at design, and 50 percent design flow rate at a series of radial and axial locations as described in Fig. 4. The lowest radius measurement location is referred to as "inlet." Z is* measured downward from the impeller flat backface and Z_{exit} is the axial passage width at the exit (12 mm). At shut-off a complete R–Θ traverse was conducted only at midheight ($Z/Z_{exit} = 0.526$).

After the measurements of the impeller flow were completed, the volute was assembled around the impeller. An LDA diagnostic program was used to set the volute tongue at some arbitrary known (45 deg) angular orientation with respect to the impeller suction side. Shaft-angle (ensemble) averaged measurements of both radial and tangential velocities were made at 5 deg angular increments from suction to pressure side as shown in Fig. 5 (only at the passage midheight ($Z/Z_{exit} = 0.526$).

Results and Discussion

Primary Flow. A general description of the impeller flow is presented, as vector plots of the total relative velocity from hub to shroud, in Figs. 6 and 7 for design and 50 percent flow rates, respectively.

Inlet ($R/R_{out} = 0.631$). At the design flow rate, high velocities exist near the hub suction side while farther toward the shroud the flow velocity along the suction side is reduced significantly. Near the hub, the high-velocity region ($Z/Z_{exit} = 0.13$ to $Z/Z_{exit} = 0.25$) is accompanied by a strong cross-passage velocity gradient. The associated pressure gradient tends to force the flow toward the suction side. Since the associated static pressures within the passage are not quantified, velocity gradients may be a assumed to be reflection of the passage pressure gradient with constant relative total pressure.

Midway between the hub and shroud ($Z/Z_{exit} = 0.526$–0.949) the flow is forced from midpassage toward the pressure side. Near the shroud ($Z/Z_{exit} = 1.100$), with no evidence of the cross-passage velocity gradient, the flow follows both blade contours. The stronger pressure-to-suction ($P \rightarrow S$) velocity gradient near the hub may be associated with the greater Coriolis acceleration due to higher velocities. In general, the inlet flow is (axially) nonuniform and its behavior is three dimensional and distorted. The distortion may be associated with flow separation and recirculation at the true inlet near the shroud, where the flow turns from axial to radial, through the sealing rings. The flow recirculation results in a dead-water "blocked" zone concentrated at the passage midheight near the shroud. Even though the minimum measurement radius is well inside the radial portion of the passage, the effect of the recirculated dead-water zone along the shroud is extended farther downstream and results in higher velocities along the hub.

At 50 percent flow rate, the inlet flow patterns are generally the same as the design flow condition. The $P \rightarrow S$ pressure gradient near the hub, however, is much stronger, resulting in much higher velocities along the suction surface. Farther toward the shroud, the reduction of total velocity along the suction side is more significant. Unlike the design flow condition, where the $P \rightarrow S$ pressure gradient dominated only the flow near the hub, at 50 percent flow, the flow near the shroud is also affected by the $P \rightarrow S$ pressure gradient, which dominates

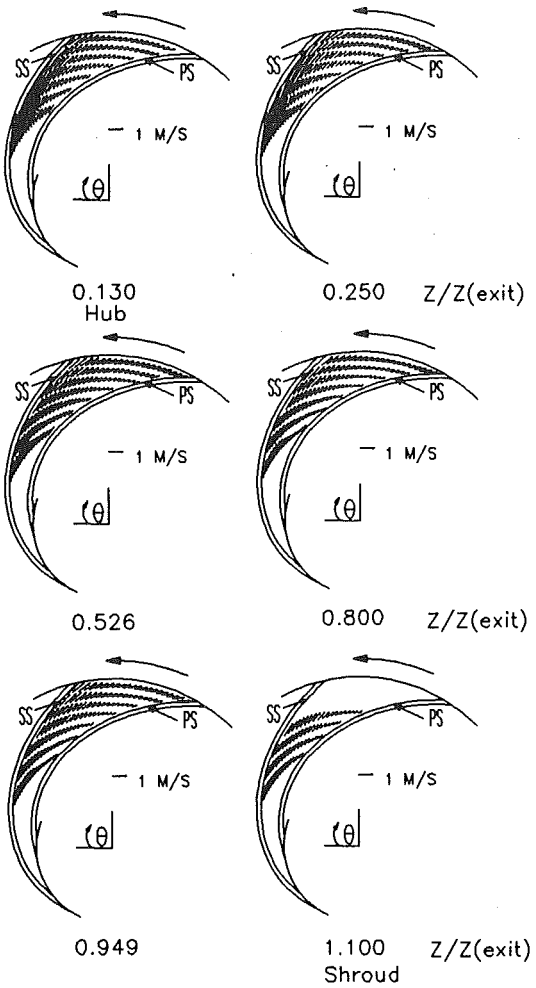

Fig. 6 Total velocity vectors at design flow

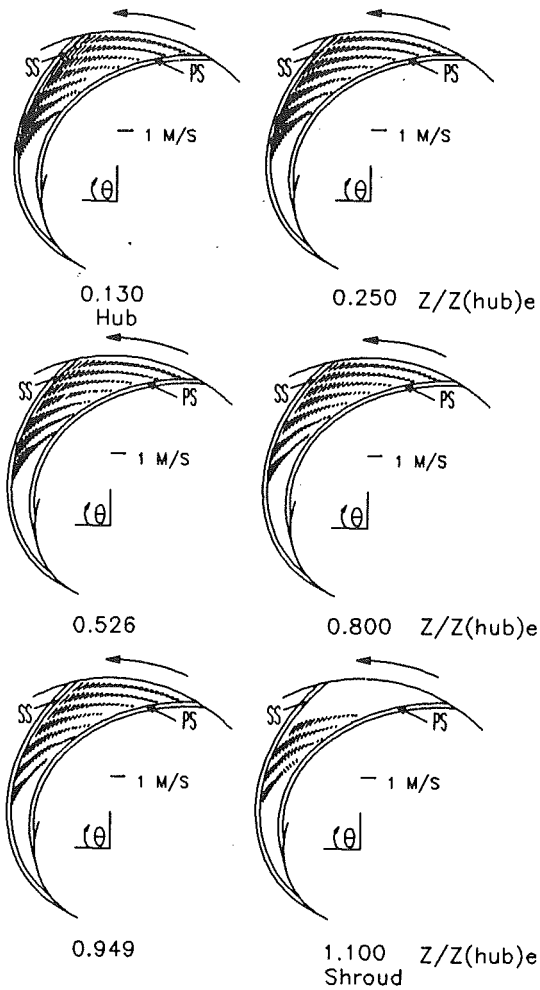

Fig. 7 Total velocity vectors at 50 percent flow

the low energy primary flow near the shroud and forces the flow along the pressure side away from the blade at $R/R_{out} = 0.631$.

Middle ($R/R_{out} = 0.684$–0.894). At the design flow rate, the flow in the middle portion of the passage is not affected by the inlet distortion and, generally, follows the blade passage with no significant three-dimensional nonuniformity. The axial (hub-to-shroud) gradient is maintained, with the high velocities along the hub suction surface while lower velocities exist near the shroud. At 50 percent flow rate, in contrast to the usual expectation, flow separation occurs along the pressure side, extending from inlet to ≈85 percent of the passage where the flow reattaches with no further extension of a low-energy wake region. The separation zone is confined along the pressure surface. Although the term "separated" is used to describe the flow pattern along the pressure side, this region is mostly a very low-velocity dead-water region with no distinct flow recirculation. The measured flow patterns at 50 percent flow are in agreement with previous hydrogen bubble flow visualization studies conducted on the present impeller (Abramian, 1986), which also indicated a dead-water zone along the pressure surface.

Exit ($R/R_{out} = 0.947$). At design flow condition, the flow at the exit region follows the passage without any significant axial or tangential distortion from hub to shroud. Near the pressure and suction surfaces, the flow follows the blade with no significant deviation. Midway between the two blades, however, the flow deviates toward the pressure side. At 50 percent flow, the separated flow along the pressure side has reattached, resulting in a uniform exit flow free from distortion and wake. The flow deviation toward the pressure side, midway between the blades, is also apparent at 50 percent flow.

In general, the overall behavior of the impeller (primary) relative flow is similar to that predicted by potential flow theory. Despite its highly loaded characteristics, under off-design (low flow) operating condition, flow separation occurs on the pressure side of the passage. The flow separation and re-attachment is confined on the pressure side with no extension of (low-momentum) wake region farther toward the exit. Except for the three-dimensional characteristics of the inlet flow, the middle and exit portions of the passage are free from secondary effects associated with the cross-passage pressure gradients.

The flow near the exit portion of the passage is being driven from pressure to suction side, at all axial planes, indicating the strong presence of the relative eddy. At 50 percent flow rate, it is the presence of the relative eddy that results in the flow reattachment prior to the exit region. In order to demonstrate the passage secondary flow patterns further, the components of the total relative velocity vectors, normal to the blade, are considered and are described in the following section.

Secondary Flow. Since traverses were conducted at constant radii rather than normal to the passage, the secondary flow distributions were obtained by considering the component of the total velocity vector along the normal to the blade angle, at any given radius. The results are shown in Fig. 8 for design condition.

Inlet to Near-Exit. At the design flow condition, the $P \rightarrow S$

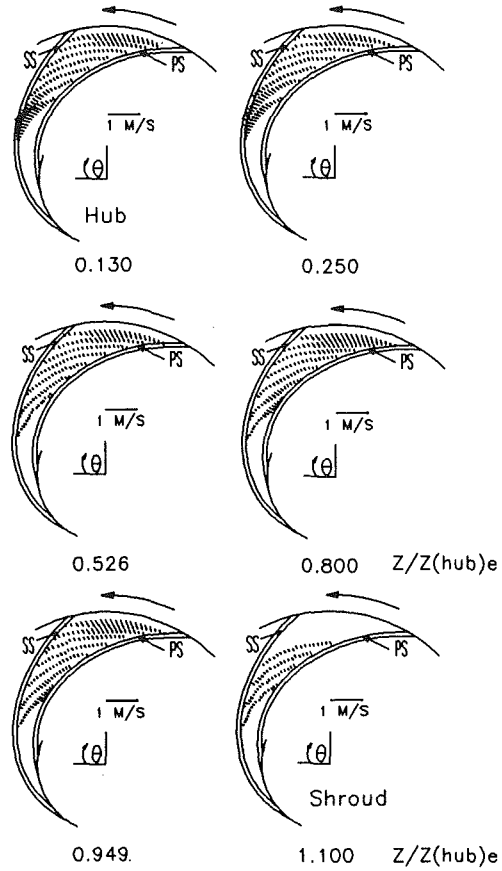

Fig. 8 Secondary flow patterns at design flow

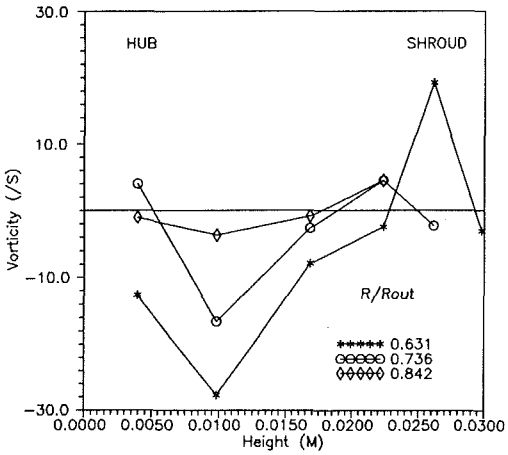

Fig. 9 Radial variation of streamwise vorticity (ζ) at design flow

pressure gradient, which forces the flow toward the suction side, exists from hub (Z/Z_{exit} = 0.13) to ≈30 percent of the passage height (Z/Z_{exit} = 0.526) toward the shroud. At Z/Z_{exit} = 0.8 and 0.949, the secondary flow is returned to the pressure side. At the shroud (Z/Z_{exit} = 1.100), there is no indication of secondary flow. The middle of the passage (R/R_{out} = 0.789–0.894) is unaffected by the secondary flow from hub to shroud. The onset and the radial variations of the secondary streamwise vorticity are further demonstrated in Fig. 9 for the design condition. The streamwise vorticity was calculated by considering the blade-to-blade average of the secondary velocity for each radii and axial plane resulting in:

$$\zeta = \frac{d[\overline{W}_{sec}]_{suction}^{pressure}}{dz}$$

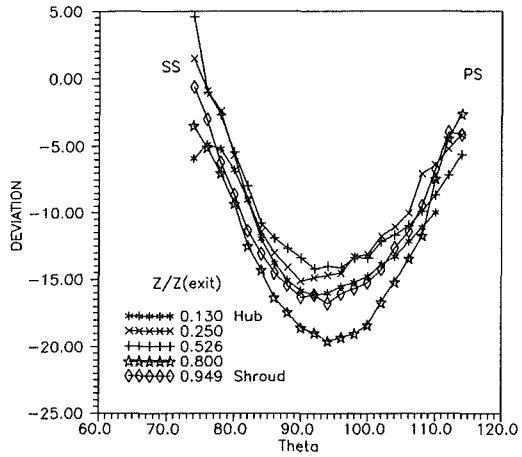

Fig. 10 Flow angle deviation ($\beta - \beta_b$) at R/R_{out} = 0.947, design flow

Negative ζ represents a counterclockwise (CCW) vortex when looking downstream. Two equally strong counterrotating vortices along the hub and the shroud are seen at the inlet region (R/R_{out} = 0.631). Although the CCW vortex along the hub weakens more slowly, near the exit (R/R_{out} = 0.842) the streamwise vorticity is nearly dissipated.

Exit. At the exit, the suction-to-pressure (relative eddy) gradient is present at all planes, which sweeps the flow toward the pressure side, with its strongest effect midway between the pressure and the suction sides. Its general pattern and strength is similar between design and 50 percent flow conditions. The effect of the relative eddy on the flow deviation at the exit is shown in Fig. 10 for R/R_{out} = 0.947 at design condition. In general, the flow near the suction and pressure side follow the blade, while up to 20 deg deviation exists at the middle. Maximum deviation occurs at Z/Z_{exit} = 0.8. The measured slip factor at R/R_{out} = 0.947 based on mass-averaged tangential and radial velocity (including leakage flow) is 0.90, in comparison with an exit slip based on Wiesner (1967) (0.835). The slip is expected to be higher at exit.

In summary, the relative flow seems to be affected by the interaction between the secondary vorticity, which is initiated at the inlet, and relative eddy (potential vortex), which gains significant strength toward the exit. Since secondary vorticity is a function of both the passage streamline curvature (centrifugal acceleration), and system rotation (Coriolis acceleration), the overall effects of curvature and rotation are examined in the following section.

Effect of Passage Curvature and System Rotation. The Rossby number ($W/\omega R_n$), Ro, which represents the ratio of centrifugal to Coriolis force, is considered to determine the dominating effect between curvature and rotation. In contrast to the usual practice, which generates a single Rossby number for an impeller, the local blade radius of curvature (R_n) along with the average measured relative velocity (W) at each radius were used to determine Ro. The highest Ro occurs at the inlet region where the blade curvature is maximum and was ≈0.4 for design and ≈0.3 for 50 percent flow conditions, indicating that, even where curvature effects are highest, the passage is mostly dominated by rotational effects. According to the conclusions made by Johnson and Moore (1980), the overall effect of the secondary flow is to convect the low P^* fluid from endwall regions into a wake. The wake will then accumulate in the most stable region of low P^* fluid, which for the radial portion of the passage will be the suction side if the Rossby number is less than 1.0. For backward swept impellers, the stable location may be on the pressure side if the Rossby number exceeds one and the curvature effects dominate. For the present impeller, despite the low Rossby numbers throughout

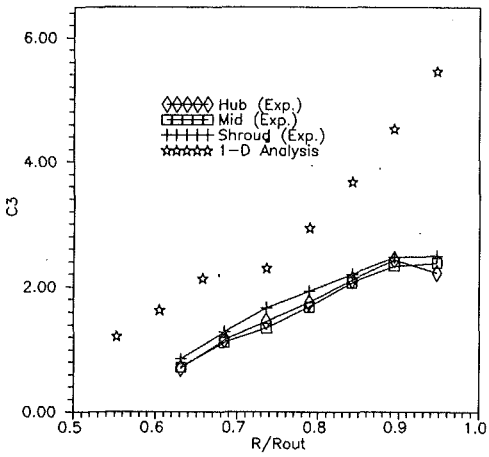

Fig. 11 Radial variation of tangential loading (C_3) at design flow

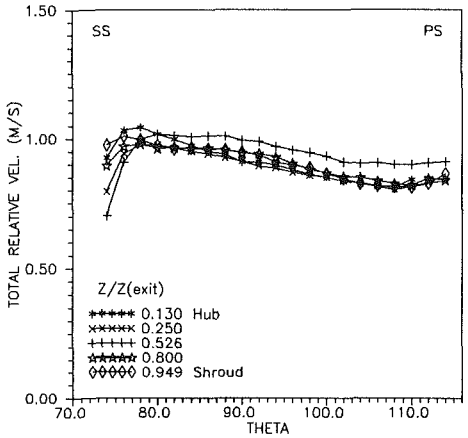

Fig. 12 Total relative velocity at R/R_{out} = 0.947, design flow (no volute)

the passage, not only is there no indication of a wake region, but the low-velocity region is confined to the pressure side as well. Such rotational domination, in a highly backward swept passage, is a reflection of the highly loaded characteristics of the impeller. The nondimensionalized normal acceleration parameter, C_3, from Howard (1978) and adapted for this passage,

$$C_3 = \Delta X_3 \left(-\frac{1}{R_n} + \frac{2\omega}{W} \right) \tag{4}$$

considers the acceleration normal to the passage direction in the blade-to-blade plane associated with both curvature and rotation. The commonly accepted limit for C_3 is considered to be ≈ 0.8, above which flow separation along the suction side is expected. For the present impeller, the value of C_3, based on the average (measured) relative velocity and passage curvature, along with a corresponding one-dimensional analysis, is shown in Fig. 11. It can be seen that, although the measured values are lower than the predicted one-dimensional values, the overall levels are considerably higher than accepted limits. The loading continues to increase from inlet to a value of ≈ 2.5 at the exit. With such a high ($P \rightarrow S$) tangential force present in the passage, not only the (low-energy) boundary layer flow at the endwall, but the (high-energy) primary flow within the passage is forced toward the suction side. As the loading increases toward the exit, the strength of the relative eddy (potential vortex) is also increased. The onset of the potential vortex is reflected in the measured radial distribution of the tangential loading, which indicates a reduction from the one-dimensional prediction prior to the passage exit, as a result of the energy exchange between the cross-passage pressure gradient and the relative eddy. The overall consequence is a low-

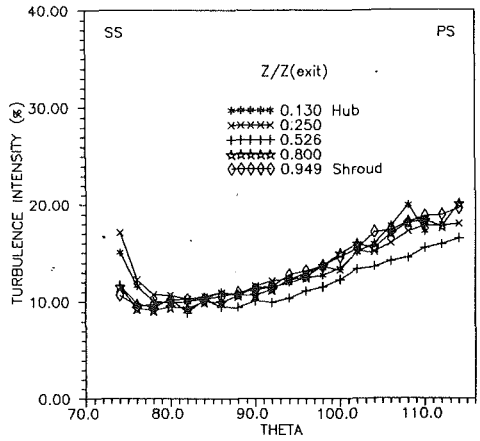

Fig. 13 Turbulence intensity at R/R_{out} = 0.947, design flow (no volute)

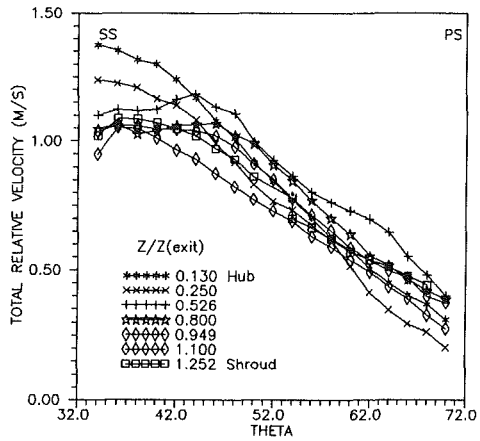

Fig. 14 Total relative velocity at R/R_{out} = 0.684, design flow (no volute)

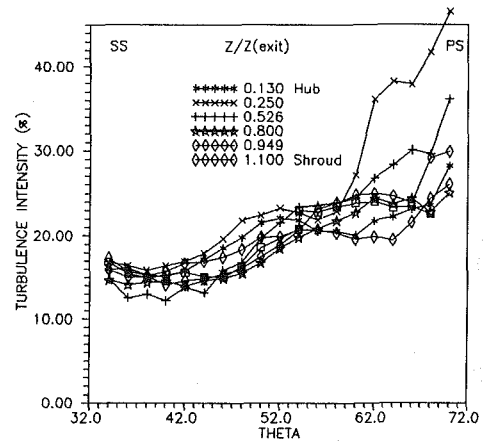

Fig. 15 Turbulence intensity at R/R_{out} = 0.684, design flow (no volute)

velocity region near the pressure side at the middle of the passage, and a uniform (attached) flow at the exit. In this particular case, the commonly accepted secondary viscous effects, which result in the accumulation of a low-momentum wake along the suction side, are overcome by the primary (inviscid) characteristics of the flow.

In light of the blade loading, it is useful to consider the probable result of adding splitters in the outer third of the blade passage. Based on the results of the present investigation, it is clearly evident that incorporating splitters would result in "breaking" the strong potential vortex, which tends to maintain the attached exit flow along the pressure surface. Although

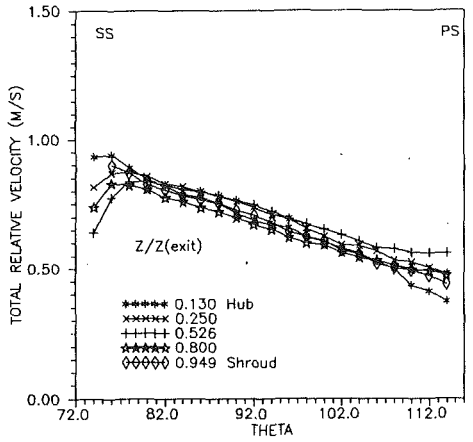

Fig. 16 Total relative velocity at R/R_{out} = 0.947, 50 percent flow (no volute)

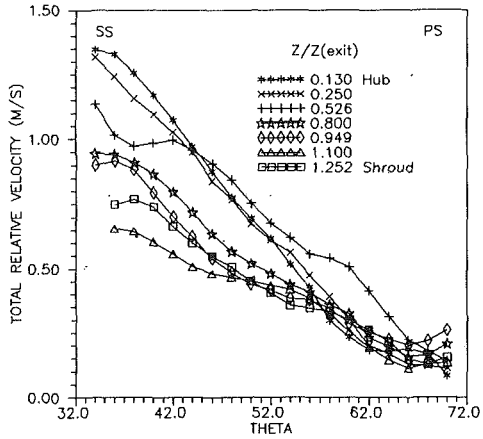

Fig. 18 Total relative velocity at R/R_{out} = 0.684, 50 percent flow (no volute)

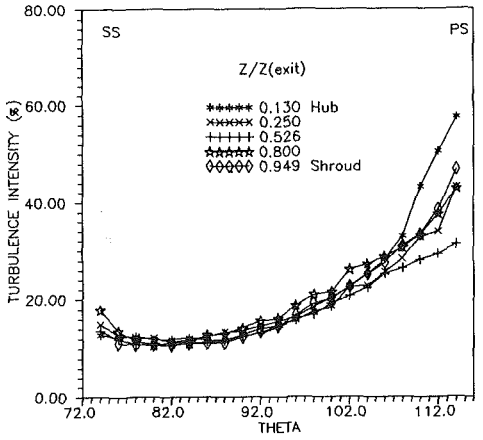

Fig. 17 Turbulence intensity at R/R_{out} = 0.947, 50 percent flow (no volute)

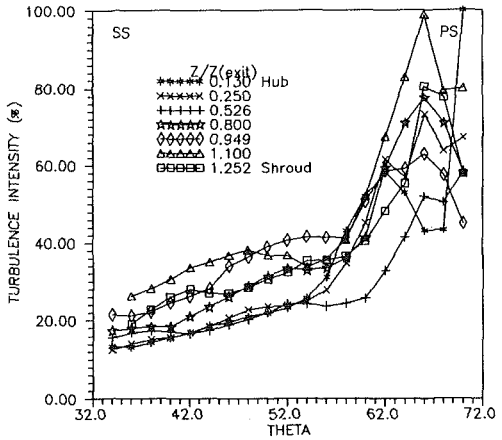

Fig. 19 Turbulence intensity at R/R_{out} = 0.684, 50 percent flow (no volute)

the potential vortex results in considerable deviation of the exit flow at the midblade region, its contribution toward maintaining the attached flow along the exit has more significance on the improved overall performance of the impeller.

In comparison to other (published) impeller flow descriptions, this peculiar behavior of the present impeller is a result of the exceptionally high loading characteristics, imposed by the design and manufacturing constraints associated with the model pump. However, it is interesting to note that the overall consequence of such a highly loaded design is a quasi-inviscid behavior of the passage flow due to the dominating effect of the primary flow characteristics over the secondary viscous effects.

Total Relative Velocity and Turbulence Intensity Distribution. The blade-to-blade distribution of the total relative velocities, from suction to pressure side, along with their corresponding turbulence intensities, are presented in Figs. 12–15 for design, and Figs. 16–19, for 50 percent flow rate, at R/R_{out} = 0.684 and R/R_{out} = 0.947.

The distributions at other radii are included in Abramian (1992). The total turbulence intensity is determined from the average tangential and radial fluctuations:

$$TI = \frac{\sqrt{\frac{(w'^2_r + w'^2_t)}{2}}}{\sqrt{W_r^2 + W_t^2}}$$

where W_r and W_t are the local mean velocities. This definition of total turbulence intensity has been recently used by Flack et al. (1992), in a similar laboratory pump but of higher specific speed, which may be used for comparison with the present results.

Design Flow. At R/R_{out} = 0.947 (Figs. 12 and 13), the total relative velocity is uniform from hub to shroud with slightly higher velocities at the passage midheight. The associated turbulence intensity is ≈10 percent near the suction side, which rises to ≈18 percent near the pressure side. At R/R_{out} = 0.684 (Figs. 14 and 15), the relative velocity gradient from blade to blade has increased and axial nonuniformity is evident. Evidence can be seen of the previously speculated recirculation, at the suction side of the passage true inlet. The turbulence intensities have risen to about 13 percent at the suction side and 30 percent at the pressure side. The intermediate radii (Abramian, 1992) display a progressive variation with radius of the velocity gradient and turbulence distributions, but axial uniformity of velocity profiles is maintained at the two outer measured radii.

50 Percent Flow. At 50 percent flow condition, the total relative velocity at the exit (Fig. 16) demonstrates higher loading across the passage. The axial distribution is nearly constant at the middle of the blade-to-blade passage. Along the suction and pressure side, a slight axial gradient exists, which, in comparison to design condition, increases the associated turbulence intensity (Fig. 17) from 17 percent at the suction side to ≈50 percent at the pressure side. The lower velocity levels at 50 percent flow conditions also contribute to the higher turbulence

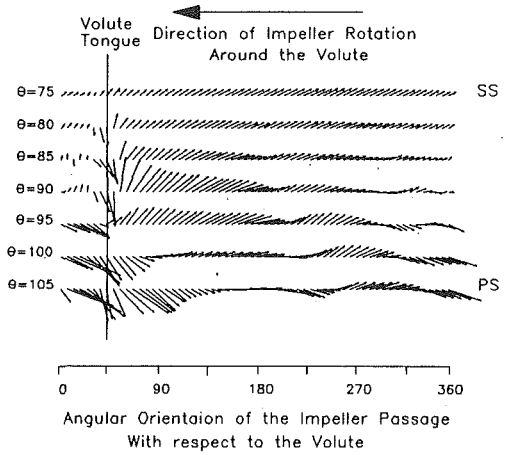

Fig. 20 Cyclic variation of the impeller flow at R/R_{out} = 0.947, near shut-off flow

levels, especially along the pressure side. At the inner measurement radius, R/R_{out} = 0.684 (Figs. 18 and 19) axial distortions are increased particularly on the suction side. The blade-to-blade velocity gradient has increased with very low velocities on the pressure side resulting in high turbulence levels (near 100 percent). At intermediate radii (Abramian, 1992), the progression between the patterns of the inner and outer radii is less uniform than the design case. The axial uniformity of velocity profile and the turbulence levels are generally maintained over the outer three measurement radii. The average velocity gradient and turbulence levels are closely similar over the inner three radii. Axial nonuniformity decreased sharply between R/R_{out} = 0.684 and 0.736.

In general, the increase of turbulent intensity, from the suction to the pressure side, indicates the dominating effect of Coriolis acceleration over centrifugal acceleration, tending to enhance the turbulence at the unstable region of the boundary layer. Although the backward curvature of the passage may have contributed toward a more moderate pressure gradient, as concluded in the previous section, it is the highly loaded characteristics of the passage that result in maintaining high turbulence levels along the pressure side. With such high loading, one might would have expected the suction (stable) side boundary layer to relaminarize. The results, however, indicate high levels ($\approx$ 10–15 percent) of turbulence intensity along the suction surface even under design operating condition. One important factor to consider is that the so-called design operating condition is the intended design point of the impeller. Results of the previously conducted performance measurements indicate that the impeller best efficiency point occurs at much higher than its intended design point. The presently reported design condition should, therefore, be considered as a partial flow operating condition. The overall consequence is a much lower than design relative velocity level and, hence, higher turbulence intensities. By considering the "best efficiency point" operating condition for the impeller alone (170 percent of the present design flow), the turbulence levels are estimated to reduce to approximately 5 percent along the suction and 10 percent along the pressure side. The relative velocity variation from inlet to exit is characterized by a significant acceleration along the pressure surface and only a modest deceleration along the suction surface, which may be a significant factor in the absence of suction side separation.

Cyclic Variation of the Relative Flow Induced by the Volute. The results of the impeller exit flow measurements, with the presence of the volute, are presented as vector plots of total relative velocity, as a function of the angular orientation of the passage with respect to the volute (Fig. 20). The vectors are presented for seven measurement locations from suction side (θ = 75 deg) to pressure side (θ = 105 deg), where θ is defined according to the impeller design geometry.

The 45 deg reference was chosen to demonstrate graphically, the flow near the tongue in a continuous line. At the suction side (θ = 75 deg), the flow continuously exits the passage throughout the entire angular orientation. Shortly before reaching the volute tongue, a slight reduction of velocity occurs. At θ = 80 deg, the relative flow reverses toward the passage just prior to reaching the tongue and then accelerates toward the exit immediately past the tongue. Further toward the pressure side, the flow reversal upstream from the tongue and the acceleration immediately downstream are more pronounced. At θ = 90 deg, midway along the volute, the initiation of flow reversal toward the passage, followed by recovery, occurs twice before complete reversal is maintained near the tongue. At the pressure side (θ = 105 deg), complete flow reversal is present for most of the circumferential locations except the second recovery, which occurs at approximately 90 deg upstream from the tongue.

The measured flow patterns are in agreement with the previous flow visualization studies conducted by Howard et al. (1987). Previously measured static pressures along the present volute circumference had indicated two high pressure regions at 50 and 180 deg downstream from the volute tongue (Abramian, 1986), which result in the second reversal and recovery of the flow midway along the volute. To demonstrate the periodic variations of the relative flow further and determine the dominating flow frequencies, measurements of the radial velocity were taken near the suction and pressure sides for power spectrum analysis. The results of the power spectrum density along with the associated profiles of radial velocity are shown in Figs. 21 and 22 for the suction and the pressure side, respectively.

At the suction side, although slight reduction of the radial velocity occurs prior to the tongue, no dominant frequencies are reflected in the power spectrum density. At the pressure side, however, the dominant frequency occurs at 2.5 Hz, which is the impeller rotational frequency, and is due to the strongest reverse flow occurring each time the passage reaches the tongue. The second frequency occurs at 5 Hz, which is a reflection of the second flow reversal and recovery occurring at the angular orientation of $\approx$ 180 deg. The third and the least dominant frequency on the pressure side occurs at 7.5 Hz which may be associated with the reversal of the passage even prior to reaching the tongue at the angular orientation of $\approx$ 330 deg.

At higher than design operating conditions, both the previous static pressure measurements conducted along the present volute outer wall (Howard et al., 1987) and those reported by Sideris and Van den Braembussche (1987) indicate the opposite variation of static pressure across the tongue.

Under high-flow operating condition, therefore, without the presence of passage reverse flow, the impeller may experience similar unsteadiness of the same order of frequencies. As an attempt to develop an analytical model to predict the volute impeller interaction, Sideris and Van den Braembussche (1987) conducted LDA measurements at (only) four circumferential locations around the volute and described the circumferential variations by ensemble-averaged values of velocity.

Although the (shut-off) flow condition above may be considered an exaggerated condition, which amplifies the cyclic variation, it clearly demonstrates the significance of the ability to conduct measurements in the rotating system. It has been shown, both experimentally and analytically, that the presence of the volute introduces circumferential variation around the impeller periphery, even at design flow conditions. Although the impeller exit flow may be periodic at any given circumferential location, in order to quantify its overall mean and fluctuating components, the ability to detect their value continuously at discrete circumferential locations is extremely important. Ensemble (phase) average velocity measurements of

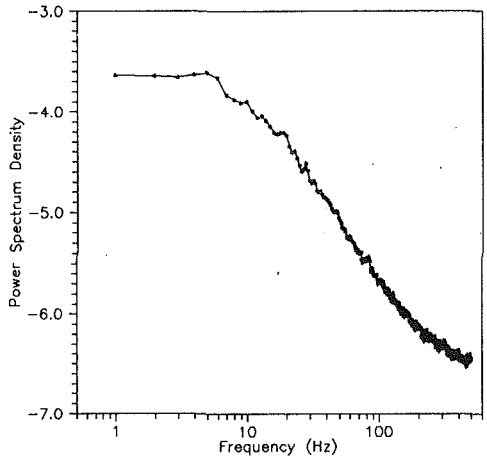

Fig. 21 Power spectrum density at the suction side (θ = 75 deg), shut-off

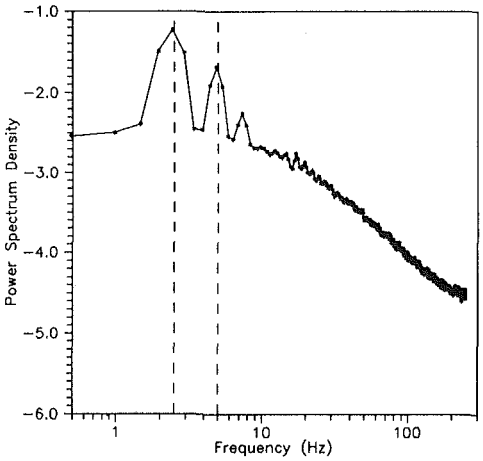

Fig. 22 Power spectrum density at the pressure side (θ = 105 deg), shut-off

the impeller flow, even at design operating conditions, may not represent the true mean and fluctuating components even if (stationary) measurements are conducted at different circumferential orientations.

Conclusions

Stationary Unsteadiness. The mean relative flow within the impeller passage, without the volute in place, is affected by a combined interaction between a secondary vorticity, initiated at the inlet, and a potential (relative) vortex, which dominates the flow at the exit. The combined effects result in a pressure side flow separation under off-design (low flow) operating condition. Due to the strong effects of the relative eddy, the separated flow reattaches to the pressure side, resulting in a uniform exit throughflow, free from wake and distortion. Although the impeller incorporates highly backward swept blades, the passage is mostly dominated by rotational effect, which is a reflection of its highly loaded characteristics imposed by design and manufacturing limitations. Such a highly loaded design results in the secondary viscous effects being dominated by the primary inviscid characteristics of the passage flow, which in turn, in contrast to the usual expectations, results in a flow field qualitatively similar to potential flow. The modest suction side diffusion rate is also important in avoiding suction side separation. The presence of the strong relative eddy has a favorable influence on the performance of the impeller under low flow operating conditions. The turbulence intensity increases from $\approx$ 10 percent on the suction side to $\approx$ 20 percent on the pressure side, indicating the dominating rotational effect on the boundary layer stability along the pressure side. The present design operating condition should, in fact, be considered as a partial flow condition since performance measurements had shown that the impeller best efficiency point occur at 170 percent of the intended design point. The overall consequences are high levels of turbulence intensities at the intended design operating point. Under (intended) 50 percent off-design flow condition, the flow separation along the pressure side results in 100 percent turbulence intensity.

Periodic Unsteadiness. Under off-design (low flow) conditions, the presence of the volute induces periodic unsteadiness, as harmonics of the impeller rotational frequency, on the pressure (unstable) side of the passage exit. The most dominant one occurs at 2.5 Hz (impeller rotational frequency) as a result of the strong flow recirculation each time the passage reaches the volute tongue. The multiple flow recovery and reversals, occurring downstream of the volute tongue, induce other periodic frequencies at two and three harmonics of the impeller rotational frequency.

Acknowledgments

The research reported here was supported by a grant from the Natural Sciences and Engineering Research Council of Canada.

References

Abramian, M., 1986, "Experimental Investigation of the Volute-Impeller Interaction in a Low Specific Speed Pump," M.A.Sc. Thesis, University of Waterloo, Waterloo, Ontario, Canada.

Abramian, M., 1992, "Experimental Investigation of the Unsteady Relative Flow in Rotating Passages of Centrifugal Impellers," Ph.D. Thesis, University of Waterloo, Waterloo, Ontario, Canada.

Abramian, M., and Howard, J. H. G., 1994, "A Rotating Laser-Doppler Anemometry System for Relative Flow Measurements in Model Centrifugal Impellers," ASME JOURNAL OF TURBOMACHINERY, Vol. 116, this issue, pp. 260–268.

Adler, D., and Levy, Y., 1979, "A Laser Doppler Investigation of the Flow Inside a Backswept, Closed, Centrifugal Impeller," IMechE *Journal of Mechanical Engineering Science*, Vol. 21, No. 1, pp. 1–6.

Barlow, R., and Johnston, J. P., 1985, "Structures of Turbulent Boundary Layers on a Concave Surface," Report #MD-47, Thermoscience Division, Mech. Eng. Dept., Stanford University, Stanford, CA.

Bradshaw, P., 1973, "Effects of Streamline Curvature on Turbulent Flow," AGARDograph No. 169.

Dean, R. C., 1968, "On the Unresolved Fluid Dynamics of the Centrifugal Compressors," ASME Paper No. 68-GT-XXX.

Eckardt, D., 1975, "Instantaneous Measurements in the Jet/Wake Discharge Flow of a Centrifugal Compressor Impeller," ASME *Journal of Engineering for Power*, Vol. 97, pp. 337–346.

Eckardt, D., 1976, "Detail Flow Investigation Within a High Speed Centrifugal Compressor Impeller," ASME *Journal of Fluids Engineering*, Vol. 98, pp. 390–402.

Farge, T. Z., and Johnson, M. W., 1990, "The Effect of Backswept on the Flow in a Centrifugal Compressor Impeller," ASME Paper No. 90-GT-231.

Fischer, K., and Thoma, D., 1932, "Investigation of the Flow Conditions in a Centrifugal Pump," *Trans. ASME*, Vol. 54, Paper No. HYD-54-8, p. 141.

Flack, R. D., Miner, S. M., and Beaudoin, R. J., 1992, "Turbulence Measurements in a Centrifugal Pump With a Synchronously Orbiting Impeller," ASME JOURNAL OF TURBOMACHINERY, Vol. 114, pp. 350–359.

Fowler, H. S., 1968, "The Distribution and Stability of Flow in a Rotating Channel," ASME *Journal of Engineering for Power*, Vol. 90, pp. 229–236.

Gillis, J. C., Johnston, J. P., Kays, W. M., and Moffat, R. J., 1980, "Turbulent Boundary Layer on a Convex Curved Surfaces," Report #HMT-31, Thermoscience Division, Mech. Eng. Dept., Stanford Unversity, Stanford, CA.

Greitzer, E. M., 1976, "Surge and Rotating Stall in Axial Flow Compressors," ASME *Journal of Engineering for Power*, Vol. 98, pp. 190–197.

Hamkins, C. P., and Flack, R. D., 1986, "Laser Velocimeter Measurements in Shrouded and Unshrouded Radial Flow Pump Impellers," ASME JOURNAL OF TURBOMACHINERY, Vol. 109, pp. 70–76.

Howard, J. H. G., 1966, "Analytical Theory of Secondary Flow in a Centrifugal Impeller," *Trans. of the Engineering Institute of Canada*, Vol. 9, No. B-1.

Howard, J. H. G., and Kittmer, C. W., 1975, "Measured Passage Velocities in a Radial Impeller With Shrouded and Unshrouded Configurations," ASME *Journal of Engineering for Power*, Vol. 97, pp. 207–213.

Howard, J. H. G., 1978, "The Use of Parameters Based on Accelerations Normal to a Relative Streamline in a Centrifugal Impeller Design," *Proceedings*

of the First International Conference on Centrifugal Compressor Technology, Madras, India, Feb. 20–23.

Howard, J. H. G., Abramian, M., and Hermann, P., 1987, "Experimental Investigation of Impeller and Volute Flow Fields for a Low Specific Speed Pump With Single and Double Volutes," *Proceedings of the ASME/JSME Thermal Engineering Conference*, Vol. 2, pp. 51–61.

Jeans, A. H., and Johnston, J. P., 1982, "The Effect of Streamwise Concave Curvature on Turbulent Boundary Layer Structure," Report #MD-40, Thermoscience Division, Mech. Eng. Dept., Stanford University, Stanford, CA.

Japikse, D., 1985, "Assessment of Single- and Two-Zone Modelling of Centrifugal Compressor Studies in Component Performance: Part 3," ASME Paper No. 85-GT-73.

Johnson, I. A., and Ginsburg, A., 1953, "Some NACA Research on Centrifugal Compressors," *Trans. ASME*, Vol. 75, p. 805.

Johnson, M. W., 1978, "Secondary Flow in Rotating Bends," ASME *Journal of Engineering for Power*, Vol. 100, pp. 553–560.

Johnson, M. W., and Moore, J., 1980, "The Development of Wake Flow in Centrifugal Impeller," ASME *Journal of Engineering for Power*, Vol. 102, pp. 382–390.

Johnston, J. P., 1970, "The Effect of Rotation on Boundary Layers in Turbomachine Rotors," Report # MD-24, Thermoscience Division, Mech. Eng. Dept., Stanford University, Stanford, CA.

Koyama, H., Masuda, S., Ariga, I., and Watanabe, I., 1979, "Stabilizing and Destabilizing Effects of the Coriolis Force on Two Dimensional Laminar and Turbulent Boundary Layers," ASME *Journal of Engineering for Power*, Vol. 101, pp. 382–390.

Krain, H., 1987, "Swirling Impeller Flow," ASME Paper No. 87-GT-19.

Lakshminarayana, B., and Horlock, J. H., 1973, "Generalized Expressions for Secondary Vorticity Using Intrinsic Coordinates," *Journal of Fluid Mechanics*, Vol. 59, pp. 97–115.

Lennemann, E., 1969, "Secondary Flows in Rotating Passages," Ph.D. Thesis, University of Waterloo, Waterloo, Ontario, Canada.

Lennemann, E., and Howard, J. H. G., 1970, "Unsteady Flow Phenomena in Rotating Centrifugal Impeller Passages," ASME *Journal of Engineering for Power*, Vol. 92, pp. 65–72.

Mizuki, S., and Oosawa, Y., 1992, "Unsteady Flow Within Centrifugal Compressor Channels Under Rotating Stall and Surge," ASME JOURNAL OF TURBOMACHINERY, Vol. 114, pp. 312–320.

Moore, J., 1973, "A Wake and an Eddy in a Rotating Radial-Flow Passage," Part 1: Experimental Observation; Part 2: Flow Model," ASME *Journal of Engineering for Power*, Vol. 95, pp. 205–219.

Rohne, K. H., and Banzhaf, M., 1991, "Investigation of the Flow at the Exit of an Unshrouded Centrifugal Impeller and Comparison With the 'Classical' Jet-Wake Theory," ASME JOURNAL OF TURBOMACHINERY, Vol. 113, pp. 654–659.

Rothe, P. H., and Johnston, J. P., 1976, "Effects of System Rotation on the Performance of Two-Dimensional Diffusers," ASME *Journal of Fluids Engineering*, Vol. 98, pp. 422–430.

Senoo, Y., Yamauguchi, M., and Nishi, M., 1968, "A Photographic Study on the Three-Dimensional Flow in a Radial Compressor," ASME *Journal of Engineering for Power*, Vol. 90, pp. 237–244.

Sideris, M. Th., and Van den Braembussche, 1987, "Influence of a Circumferential Exit Pressure Distortion on the Flow in an Impeller and Diffuser," ASME JOURNAL OF TURBOMACHINERY, Vol. 109, pp. 48–54.

Smith, A. G., 1957, "On the Generation of the Streamwise Component of Vorticity for Flows in Rotating Passages," *Aeronautical Quarterly*, Vol. 8, pp. 369–383.

Wiesner, F. J., 1967, "A Review of Slip Factors for Centrifugal Impellers," ASME *Journal of Engineering for Power*, Vol. 89, pp. 558–572.

Inviscid-Viscous Interaction Method for Three-Dimensional Inverse Design of Centrifugal Impellers

M. Zangeneh
Department of Mechanical Engineering,
University College of London,
London, United Kingdom

A three-dimensional design method for the design of the blade geometry of centrifugal compressor impellers is presented. In this method the blade shape is computed for a specified circulation distribution, normal (or tangential) thickness distribution, and meridional geometry. As the blade shapes are computed by using an inviscid slip (or flow tangency) condition, the viscous effects are introduced indirectly by using a viscous/inviscid procedure. The three-dimensional Navier-Stokes solver developed by Dawes is used as the viscous method. Two different approaches are described for incorporating the viscous effects into the inviscid design method. One method is based on the introduction of an aerodynamic blockage distribution throughout the meridional geometry, while in the other approach a vorticity term directly related to the entropy gradients in the machine is introduced. The method is applied to redesign the blade geometry of Eckardt's 30 deg backswept impeller as well as a generic high pressure ratio (transonic) impeller. The results indicate that the entropy gradient approach can fairly accurately represent the viscous effects in the machine.

1 Introduction

In recent years considerable progress has been made in our understanding of the complicated flow patterns inside centrifugal compressor impellers. The results of experimental work by Eckardt (1976, 1980) and later Krain (1988) indicate that the flow inside the impeller is dominated by complicated secondary flow patterns and gross boundary layer separation, resulting in a circumferential (the so-called jet-wake phenomenon) as well as spanwise exit flow nonuniformity. The results of these findings have been gradually incorporated into the impeller design procedures used by most manufacturers. For example, the widespread use of backswept impellers in all state-of-the-art designs and the careful design of shroud geometry has resulted in appreciable improvements in impeller performance and exit flow distribution, in particular for low specific speed machines (Krain, 1988).

However, in the case of high specific speed machines, there is little scope in optimizing the shroud curvature and therefore without careful design of the vane geometry, gross boundary layer separation and secondary flow effects will result in the formation of the nonuniform exit flow pattern with its deleterious effect on performance and stability of the machine.

In this paper, a three-dimensional impeller vane design method is presented, which should provide an efficient means of optimizing the impeller geometry. The method is based on Hawthorne et al.'s (1984) approach to the design problem, in which the blades are represented by sheets of vorticity whose strength is determined by a specified distribution of circumferentially averaged swirl velocity, or $r\bar{V}_\theta$ (directly related to the bound circulation $2\pi r\bar{V}_\theta$ and the blade loading), defined as:

$$r\bar{V}_\theta = \frac{B}{2\pi}\int_0^{2\pi/B} rV_\theta \, d\theta,$$

where B is the number of blades.

The original application of the method was confined to the design of two-dimensional cascades of infinitely thin blades in incompressible flow. The method has since been extended to the three-dimensional design of incompressible axial machines by Tan et al. (1984) and applied to the case of arbitrary meridional geometry in incompressible flow by Borges (1990) using a finite difference approach and Ghaly and Tan (1990) using the finite element approach. The finite difference arbitrary geometry method was later extended to compressible flow by Zangeneh (1991), using an approximate and an exact approach. In the approximate approach the pitchwise variation in density is neglected and as a result the algorithm is simple and efficient, while in the exact approach the density is computed throughout the three-dimensional flow field. It was found, however, that the error in blade shapes computed by the two methods is well within the manufacturing tolerances. The method was applied to the design of a high (subsonic) speed radial-inflow turbine and appreciable improvements in efficiency over conventional impellers of identical size and

Contributed by the International Gas Turbine Institute and presented at the 38th International Gas Turbine and Aeroengine Congress and Exposition, Cincinnati, Ohio, May 24-27, 1993. Manuscript received at ASME Headquarters February 19, 1993. Paper No. 93-GT-103. Associate Technical Editor: H. Lukas.

design point were obtained (Zangeneh, 1990). Recently, a compressible version of the method based on the finite volume approach was reported by Dang (1993).

The method described by Zangeneh (1991) assumes an irrotational flow through the impeller. This assumption is not very limiting in the case of most radial-inflow turbines due to the favorable pressure gradients and high Reynolds numbers. In the case of centrifugal compressors, however, the flow is dominated by viscous effects, which result in an entropy rise and a reduction in the flow turning in the impeller. An impeller designed on purely irrotational flow basis may have a lower than expected pressure rise and slip factor.

In the case of almost all inverse design methods, it is difficult to introduce the viscous effects directly into the equations of motions, as these methods rely on the inviscid slip (or tangency) condition at the blades to calculate the blade shape. One way to introduce the viscous effects into the design method is to use a viscous/inviscid interaction approach. Due to the three-dimensional nature of the flow, it is important to model the three-dimensional viscous effect and so it is possible to use, in order of decreasing accuracy and increasing computational efficiency, a three-dimensional full Navier–Stokes solver, or a parabolized N-S technique or a three-dimensional boundary layer method. For this application an approach based on a three-dimensional N-S method is described. Once the viscous method has been selected the problem is in what form the viscous information can be fed back into the design method.

In this paper we shall outline two approaches for the introduction of the viscous effects into the design method: one based on the introduction of an aerodynamic blockage distribution and the other based on the introduction of a vorticity term directly related to the entropy gradients in the impeller.

2 Description of Inverse Design Method

In the theory that will be presented the following assumptions will be made:

(*a*) The flow is steady and homenergetic (adiabatic and uniform at inlet) but not homentropic.

(*b*) The blades have zero thickness, so that they can be represented by a single sheet of vorticity. However, the blade blockage effects are accounted for by using a mean stream surface thickness parameter in the continuity equation of the mean flow.

(*c*) The working fluid is a perfect gas and the maximum meridional Mach number (based on the meridional velocity) is less than unity throughout the flow. The latter condition is a result of the fact that when the mean swirl velocity is specified the governing equation of the flow field remains elliptic as long as the Mach number based on the mean meridional velocity is less than unity (Wu, 1955). Therefore, this method (which uses central differencing to solve the flow equations) can be used for the design of high pressure ratio machines where the relative Mach number is greater than unity as long as the *meridional Mach number remains below unity* and it has already been used to design impellers with maximum relative Mach numbers of up to 1.3–1.4. The current method, however, has no shock capturing capability. The presence of the shock wave has a local and a global effect on the blade geometry. The local effect is due to the large velocity gradient across the shock wave, which if the shock is captured accurately can result in a discontinuous blade shape that is not beneficial from aerodynamic considerations. So there is perhaps an advantage in neglecting the local effect of the shock wave in the design method. The global effect, which is a result of entropy generation by the shock wave, is more important and can have an appreciable effect on the blade geometry downstream of the shockwave. This important global effect of the shock is in fact modeled in this design method through the inviscid/viscous interaction described in section 4.

2.1 Calculation of Flow Field. In this subsection, the governing equations of the mean and periodic flow will be derived. For simplicity the derivation will be based on the approximate method, in which the pitchwise-averaged density is used. But exactly the same method can be applied to the exact approach (Zangeneh, 1991).

In the absence of pitchwise variation in density, the continuity equation of the mean (or circumferentially averaged) flow is given by (Zangeneh, 1991):

$$\nabla \cdot (\bar{\rho} B_T \overline{W}) = 0, \tag{1}$$

where $\overline{W}$ is the relative mean velocity, $\bar{\rho}$ is the pitchwise average density. When the aerodynamic blockage is specified, B_T is the total blockage factor, which accounts for the combined effect of the blade blockage and aerodynamic blockage, i.e.,

$$B_T = B_{\text{blade}} \times B_{\text{Aero}} \tag{2}$$

where

$$B_{\text{blade}} = 1 - \frac{t_\theta}{r} \frac{B}{2\pi}, \tag{3}$$

t_θ is the tangential thickness, r is the radius, and B is the blade number. The normal thickness, t_n, distribution obtained from structural considerations is used in conjunction with the latest blade wrap angle distributions to compute the tangential thickness. The method for determining the aerodynamic blockage is discussed in section (4). However, when the entropy gradients are specified, B_T is equal to the blade blockage only.

The continuity equation of the mean flow, Eq. (1), can be implicitly satisfied if we define a stream function Ψ, namely

$$\overline{V}_r = -\frac{1}{rB_f}\left(\frac{\rho_i}{\bar{\rho}}\right)\frac{\partial \Psi}{\partial z}, \quad \overline{V}_z = \frac{1}{rB_f}\left(\frac{\rho_i}{\bar{\rho}}\right)\frac{\partial \Psi}{\partial r}. \tag{4}$$

where ρ_i is a reference density and Ψ is the Stokes' stream function. In this way, the mean flow velocities can be deter-

Nomenclature

B = number of blades
B_f = blockage factor
C_p = specific heat at constant pressure
$\hat{\mathbf{e}}$ = unit vector
f = blade wrap angle (θ value at the blade)
h = static enthalpy
I = rotary stagnation enthalpy or rothalpy
r = radius
(r, θ, z) = cylindrical-polar coordinate system
s = entropy
$S(\alpha)$ = sawtooth function
T = static temperature
v = periodic velocity
V = velocity
W = relative velocity
α = angular coordinate of blade surfaces
$\delta_p(\alpha)$ = periodic delta function
ρ = density
Φ = potential function
Ψ = Stokes' stream function
ω = rotational speed
Ω = absolute vorticity

Subscript

bl = at the blade
r = radial component
z = axial component (three-dimensional)
θ = tangential component

Superscripts

$\overline{\ }$ = pitchwise mean value
$+$ = relative to upper blade surface (facing $+ve\theta$)
$-$ = relative to lower blade surface (facing $-ve\theta$)

mined by calculating the stream function Ψ. An equation for the unknown stream function can be obtained by using either a dynamic or a kinematic approach. In the dynamic approach, which has been widely used in throughflow analysis methods, e.g., Marsh (1966), the components of Euler equation are used to derive an expression for the stream function. In the kinematic approach, however, a vorticity equation is used. This latter approach is more suitable to the design problem in which the bound circulation is specified. It can be shown (Zangeneh, 1991) that the bound circulation is given by

$$\Omega_b = \nabla \times V = (\nabla r\overline{V}_\theta \times \nabla\alpha)\delta_p(\alpha), \tag{5}$$

where

$$\alpha = \theta - f(r, z) = n\frac{2\pi}{B}, \quad n = 0, 1, 2, 3, \ldots \tag{6}$$

represents the blade surfaces, θ is the tangential coordinate of a cylindrical polar coordinate system and $f(r, z)$ is the angular coordinate of the point on the thin blade surface, or the so-called wrap angle. $\delta p(\alpha)$ is the periodic delta function, whose pitchwise mean is unity, so that the mean bound vorticity is given by

$$\overline{\Omega} = \nabla \times \overline{\mathbf{V}} = (\nabla r\overline{V}_\theta \times \nabla\alpha). \tag{7}$$

When entropy gradients are specified the overall mean vorticity is given by

$$\overline{\Omega} = \overline{\Omega}_b + \overline{\Omega}_f \tag{8}$$

where $\overline{\Omega}_f$ accounts for the vorticity due to entropy gradients in the flow, which are generated by viscous effects. The method used to calculate $\overline{\Omega}_f$ is discussed in detail in section (4).

Now by considering the tangential component of mean vorticity we can see that

$$\overline{\Omega}_\theta = \frac{\partial\overline{V}_r}{\partial z} - \frac{\partial\overline{V}_z}{\partial r} = \mathbf{e}_\theta \cdot (\overline{\Omega}_b + \overline{\Omega}_f) \tag{9}$$

Substituting Eqs. (4) and (7) into Eq. (9) the following equation for the unknown stream function can be derived:

$$\frac{\partial}{\partial r}\left(\frac{\rho_i}{\overline{\rho}}\frac{1}{rB_t}\frac{\partial\Psi}{\partial r}\right) + \frac{\partial}{\partial z}\left(\frac{\rho_i}{\overline{\rho}}\frac{1}{rB_t}\frac{\partial\Psi}{\partial z}\right) = \left(\frac{\partial r\overline{V}_\theta}{\partial r}\frac{\partial f}{\partial z} - \frac{\partial r\overline{V}_\theta}{\partial z}\frac{\partial f}{\partial r}\right) + \overline{\Omega_{f\theta}} \tag{10}$$

where the first term on the right-hand side is zero outside blade row and the second term is zero when the aerodynamic blockage is specified. This elliptic equation is solved subject to boundary conditions at the end walls and upstream and downstream boundaries. At the end walls (hub and shroud), the no-flow condition is satisfied by using the Dirichlet condition $\Psi = \text{const}$. The far upstream boundary condition is obtained from the specified far upstream velocity and a parallel efflux condition is used at far downstream.

The periodic flow field is determined by using the Clebsch formulation for the periodic velocity (Zangeneh, 1991), which is given as

$$\mathbf{v}(r, \theta, z) = \nabla\Phi(r, \theta, z) - S(\alpha)\nabla r\overline{V}_\theta, \tag{11}$$

where $S(\alpha)$ is the periodic sawtooth function and Φ is the potential function of the periodic flow. In the absence of circumferential variations in density (approximate approach), the periodic component of the continuity equation can be written as

$$\nabla \cdot \mathbf{v} = -\mathbf{v} \cdot \nabla \ln\overline{\rho}. \tag{12}$$

Taking the divergence of Eq. (11) and using the continuity Eq. (12) we obtain

$$\nabla^2\Phi = S(\alpha)\nabla^2 r\overline{V}_\theta + (\nabla\alpha \cdot \nabla r\overline{V}_\theta)S'(\alpha) - \mathbf{v} \cdot \nabla \ln\overline{\rho} \tag{13}$$

where the first two terms on the right-hand side will be zero outside of the blade row. Using the periodicity of the periodic flow, it is possible to express Φ in terms of a Fourier series in the tangential direction. Furthermore, the right-hand side of Eq. (13) (i.e., $S(\alpha)$ and $S'(\alpha)$) can also be expressed in terms of a Fourier series. As a result, the three-dimensional Poisson equation in Eq. (13) is reduced to a two-dimensional Helmholtz equation, which is then solved for each harmonic of the potential function. The use of a Fourier expansion in the tangential direction results in substantial savings in computational time and memory as the three-dimensional flow field is solved without the need for a grid in the tangential direction, which would also require regriding after each blade iteration.

The Helmholtz equation is solved subject to the flow tangency condition at the endwalls and zero potential condition at the far upstream and far downstream boundaries.

2.2 Calculation of Density. For a *homenergetic irreversible* flow, the energy equation in relative frame can be reduced to a constant rothalpy condition (Denton, 1986). This form of energy equation is widely used in three-dimensional Navier-Stokes calculations, e.g., Dawes (1988). Therefore the energy equation is given by:

$$I = h + \frac{1}{2}(\mathbf{W} \cdot \mathbf{W}) - \frac{1}{2}\omega^2 r^2 = \text{const} \tag{14}$$

where ω is the rotational speed and $\mathbf{W}$ is the relative velocity. By using the perfect gas relations it is possible to show that:

$$\frac{\rho}{\rho_i} = \left[1 + \frac{\omega^2 r^2 - (\mathbf{W} \cdot \mathbf{W})}{2C_pT_i}\right]^{1/\gamma - 1} \times e^{-(s - s_i/R)} \tag{15}$$

where s is the entropy and subscript i refers to a reference value. In the case of the approximate approach, the latest values of mean velocity, calculated from Eq. (4), are used in Eq. (15) to obtain a new estimate for the mean density. The exponential of the entropy term in Eq. (15) is set to unity when the aerodynamic blockage distribution is specified.

2.3 Calculation of Blade Shape. Once the flow field is determined, then it is possible to compute the blade shape by using the blade boundary condition that the blade must be aligned to the velocity vector there. This condition can be expressed as:

$$\mathbf{W}_{bl} \cdot \nabla\alpha = 0. \tag{16}$$

where $\nabla\alpha$ is a vector normal to the blade surface and $\mathbf{W}_{bl}$ is the relative velocity at the blade surface ($\mathbf{W}_{bl} = (\mathbf{W}^+ + \mathbf{W}^-)/2$, where $\mathbf{W}^+$ and $\mathbf{W}^-$ are the velocities on the upper and lower surface of the blades). Equation (16) is a first-order hyperbolic partial differential equation, which has to be integrated along the meridional projections of streamlines on the blade surface in order to find the blade shape. The integration, as in the case of other initial value problems, cannot be completed without some initial condition on f. This initial value will be called the *stacking condition of the blade*. In this method the stacking condition is implemented by giving as input, the values of the blade wrap angle f along a quasi-orthogonal, for example at the leading edge. The effect of different stacking conditions on the flow field is discussed in detail in Zangeneh (1992).

2.4 Extension to Non-free Vortex Blade Design. In some design conditions, for example for very high pressure ratio compressors, it may be necessary to specify a spanwise non-uniform loading distribution in order to optimize the performance. This type of loading distribution generates shed vorticity at the trailing edge of the blade so that the flow downstream of the blade row becomes rotational. This rotational flow is a Beltrami flow as the shed vortex lines lie along the streamlines and of course cannot support static pressure changes across them (Tan, 1981).

The enthalpy change across the blade is given by (Zangeneh, 1991):

$$h^+ - h^- = \frac{2\pi}{B}(\mathbf{W}_{bl} \cdot \nabla r\bar{V}_\theta)$$

so that the Beltrami flow downstream of the blade satisfies the following condition:

$$\mathbf{W}_{bl} \cdot \nabla r\bar{V}_\theta = 0 \tag{17}$$

where $\mathbf{W}_{bl}$ is the mean of the velocities on the upper and lower part of the trailing vortex sheet. Equation (17) can be solved to find the $r\bar{V}_\theta$ distribution downstream of the blade row.

Now if we let α to represent the blade shape inside the blade region and the trailing vortex sheet downstream of the blade, we can represent the trailing vorticity by Eq. (5). Therefore, the flow downstream of the blade can be calculated from Eqs. (10) and (13). Noting that in this case the term in brackets on the right-hand side of Eq. (10) and the first two terms on the right-hand side of Eq. (13) do not vanish downstream of the blade row. Furthermore, when solving Eq. (13), it is no longer possible to set the potential function of the periodic flow to zero at far downstream boundary. A suitable boundary condition is obtained by setting

$$\Phi_{ss} = 0$$

at the downstream boundary, where s is the meridional distance.

2.5 Design of Impellers With Splitter Blades. In some high pressure ratio applications splitter blades are used to reduce the blade loading. In conventional designs, it is common to use splitter blades with the same blade profile as the full blade located at midpitch. This choice of splitter blades is usually based on simplicity of design and manufacture rather than aerodynamic considerations. This inverse design method provides an ideal technique for optimizing the splitter blade shapes as well as the full blades.

The extension of the method to the design of impellers with splitter blades is quite straightforward. For this purpose we let

$$\alpha_1 = \theta - f_1(r, z) \quad \text{and} \quad \alpha_2 = \theta - f_2(r, z)$$

to represent the full and splitter blades, respectively. If the circulation distribution on the full blades is $2\pi r\bar{V}_\theta^1$ and that on the splitter blades is $2\pi r\bar{V}_\theta^2$, then the bound vorticity on the full and splitter blades are given by

$$\Omega_1 = (\nabla r\bar{V}_\theta^1 \times \nabla\alpha_1)\delta_p(\alpha_1)$$

and

$$\Omega_2 = (\nabla r\bar{V}_\theta^2 \times \nabla\alpha_2)\delta_p(\alpha_2)$$

so the overall bound vorticity is given by

$$\Omega_b = (\nabla r\bar{V}_\theta^1 \times \nabla\alpha_1)\delta_p(\alpha_1) + (\nabla r\bar{V}_\theta^2 \times \nabla\alpha_2)\delta_p(\alpha_2)$$

and therefore the right-hand side of Eqs. (10) and (13) are modified accordingly. The full and splitter blade shapes α_1 and α_2 are then calculated by applying the appropriate inviscid slip condition, Eq. (16).

2.6 Numerical Algorithm. The partial differential equations for the computation of the flow field, i.e., Eqs. (10) and (13) and the blade shape, Eq. (16), are solved numerically by using a finite difference approximation. An algebraic transformation to a boundary-fitted computational plane was used so that in the new curvilinear coordinate system the coordinate lines are coincident with the boundaries. The form of the differential equations in the computational plane are presented in Zangeneh (1991).

The governing equations of the flow field in the computational plane, equations corresponding to Eqs. (10) and (13), are discretized by using a second-order accurate finite difference formula. The boundary conditions are then applied and the resulting simultaneous algebraic equations are solved iteratively, using the Brandt (1977) cycle C multigrid strategy to increase the rate of convergence. More details on the discretization procedure and the form of the discretized equations can be found in Zangeneh (1991). The blade boundary condition, Eq. (17), is discretized by using the Crank–Nicholson scheme.

3 Viscous Method

For the viscous method the Navier–Stokes solver developed by Dawes (1988) was used. In this method the unsteady Reynold's averaged Navier–Stokes equations are discretized using a cell-centered finite volume formulation. The discretized equations are time-marched using an implicit "pre-processed" algorithm. In this version of the program a simple algebraic turbulence model patterned after Baldwin and Lomax (1978) is used. A two-level multigrid is used to accelerate the rate of convergence to steady state.

At the inflow boundary, the total pressure, total temperature, the swirl and pitch angles are fixed and the derivative of static pressure in the streamwise direction is set to zero. At the outflow boundary, the static pressure is held constant and other variables are extrapolated from the interior. At the solid surfaces zero normal fluxes of mass, momentum, and energy are imposed. In satisfying the wall boundary conditions, the casing wall is assumed to be stationary (as in unshrouded impellers) while the hub (including the region upstream and downstream of the blade row) rotates with the blade. A wall function is used in order to compute the wall shear stresses when the mesh is too coarse to resolve down to laminar sublayer scale.

In order to establish the accuracy of the method, the flow through Eckardt's (1980) backswept impeller was computed by using a $(17 \times 73 \times 17)$ computational grid. The predicted exit meridional velocity (nondimensionalized by the tip speed) is compared to Eckardt's measurements in Fig. 1. There is a good qualitative correlation between the predicted and measured velocity distributions. A more thorough evaluation of this viscous method for analysis of flow through radial and mixed flow turbomachines can be found from Goto (1991) and Casey et al. (1992). In terms of overall performance parameters Goto's (1991) study indicates that the method can predict the Euler head (or the exit tangential velocity at exit from the impeller) quite accurately. However, both Goto and Casey et al. show that the code fails to predict accurately the actual head (or pressure rise) in the impeller as it underestimates the amount of mixing losses in the impeller and the diffuser.

4 Viscous-Inviscid Interaction

In this section, we shall describe two different approaches for the introduction of the viscous effects into the design method. Both approaches introduce the effect of viscosity into the mean flow. One is based on the introduction of an aerodynamic blockage distribution, which is computed from the viscous results, while in the second approach, the generation of vorticity due to the entropy gradients in the flow is modeled directly by introducing an extra vorticity term related to the entropy gradients.

4.1 Aerodynamic Blockage Approach. In external flow over aerofoils, it is usually possible to distinguish between the nonuniform, high-loss, low-momentum region inside the boundary layer and the uniform, low-loss, high-momentum region outside. Under these circumstances, the aerodynamic blockage can be based on the displacement thickness of the boundary layer. However, in the case of most compressors the nonuniform flow region can sometimes occupy the whole flow passage and there are therefore difficulties in defining the boundary layer thickness. Hence an alternative definition for the aerodynamic blockage is required. One definition that does provide a good measure of the extent of nonuniformity in the

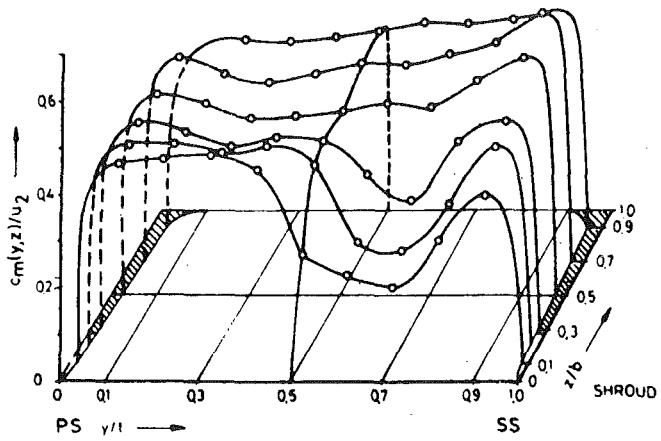

(a) Eckardt's Measurements

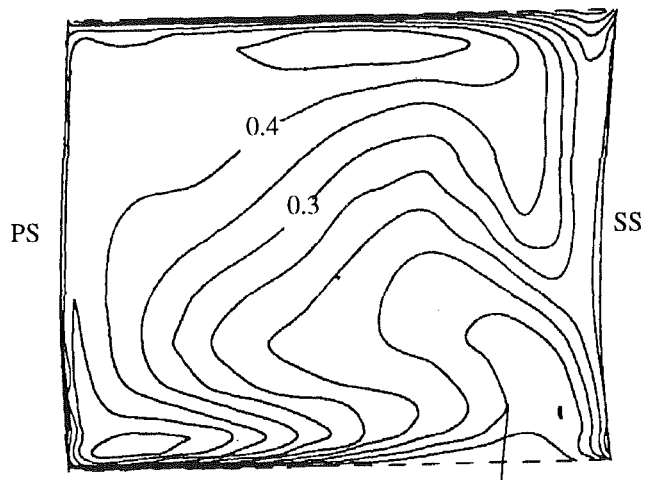

(b) Viscous Predictions

Fig. 1 Comparison of viscous calculation with Eckardt measurements

flow is the ratio of the area (pitchwise) averaged meridional velocity to the mass-averaged meridional velocity, i.e.,

$$B_{\text{aero}} = \frac{\overline{V_m^{\text{area}}}}{\overline{V_m^{\text{mass}}}} \tag{18}$$

where

$$\overline{V_m^{\text{mass}}} = \frac{2\pi \int_{\theta_p}^{\theta_s} \rho V_m V_m r \, d\theta}{2\pi \int_{\theta_p}^{\theta_s} \rho V_m r \, d\theta}$$

and

$$\overline{V_m^{\text{area}}} = \frac{2\pi \int_{\theta_p}^{\theta_s} V_m r \, d\theta}{2\pi \int_{\theta_p}^{\theta_s} r \, d\theta}$$

This definition of aerodynamic blockage is very similar to that suggested by Dring (1984) for processing of experimental measurements. For this application however, Eq. (18) is used to process the result of the three-dimensional viscous flow calculation from which the aerodynamic blockage is calculated throughout the meridional geometry of the computational domain.

4.2 Vorticity Generation and Transport Approach. In section 2.1, it was mentioned that the effects of entropy gradients in the flow are to be represented by the mean vorticity component $\bar{\Omega}_f$. In this section a method will be presented for relating $\bar{\Omega}_f$ to the entropy gradients in the machine.

It has been shown by Hawthorne (1974) that Crocco's equation of motion can be expressed as

$$\overline{\mathbf{W}} \times \bar{\Omega} = \nabla \bar{I} - \bar{T} \nabla \bar{s} - \mathbf{F}_b - \mathbf{F}_f \tag{19}$$

where Ω is the absolute vorticity vector (which is the sum of the bound vorticity and the vorticity due to the entropy gradients), I is the rothalpy, and $\mathbf{F}_b$ is the blade body force distribution. In order to obtain a consistent set of equations when entropy gradients are present, it is necessary to introduce a dissipative body force distribution $\mathbf{F}_f$ (see Horlock, 1971), which acts in the streamwise direction, but opposes the motion. Now by substituting Eqs. (7) and (8) into Eq. (19) and equating terms associated with the blade body force and dissipative force (see Dang and Wang, 1992, and Roddis and Zangeneh, 1993) it is possible to show that:

$$\mathbf{F}_b = (\overline{\mathbf{W}} \cdot \nabla r\bar{V}_\theta) \nabla \alpha - (\overline{\mathbf{W}} \cdot \nabla \alpha) \nabla r\bar{V}_\theta \tag{20}$$

and

$$\overline{\mathbf{W}} \times \bar{\Omega}_f = \nabla \bar{I} - \bar{T} \nabla \bar{s} - \mathbf{F}_f \tag{21}$$

Taking the curl of both sides of Eq. (21) we find:

$$\overline{\mathbf{W}}(\nabla \cdot \bar{\Omega}_f) - \bar{\Omega}_f \nabla \cdot \overline{\mathbf{W}} + (\bar{\Omega}_f \cdot \nabla)\overline{\mathbf{W}} - (\overline{\mathbf{W}} \cdot \nabla)\bar{\Omega}_f = -\nabla \times (\bar{T} \nabla \bar{s}) - \nabla \times \mathbf{F}_f \tag{22}$$

Using the fact that the vorticity vector is solenoidal together with vector identity for the first term on the right-hand side it is possible to derive the following expression for $\bar{\Omega}_f$:

$$(\overline{\mathbf{W}} \cdot \nabla)\bar{\Omega}_f = \Omega_f \nabla \cdot \overline{\mathbf{W}} - (\bar{\Omega} \cdot \nabla)\overline{\mathbf{W}} + (\nabla \bar{T} \times \nabla \bar{s}) + \nabla \times \mathbf{F} \tag{23}$$

Now by considering the tangential component of Eq. (23) and noting that the radial component of $\bar{\Omega}_b$ is $-(1/r\bar{V}_\theta/r\partial r)$ so that:

$$\bar{\Omega}_{fr} = \mathbf{e}_r \cdot (\bar{\Omega} - \bar{\Omega}_b) = 0$$

and similarly the axial component of $\bar{\Omega}_b$ is $(1/r\bar{V}_\theta)/(r\partial z)$ so that:

$$\bar{\Omega}_{fz} = \mathbf{e}_z - (\bar{\Omega} - \bar{\Omega}_b) = 0$$

we can derive the following PDE for $\bar{\Omega}_{f\theta}$:

$$\overline{W}_z \frac{\partial \bar{\Omega}_{f\theta}}{\partial z} + \overline{W}_r \frac{\partial \bar{\Omega}_{f\theta}}{\partial r} + \bar{\Omega}_{f\theta}\left(\frac{\partial \overline{W}_r}{\partial r} + \frac{\partial \overline{W}_z}{\partial z}\right) = \left(\frac{\partial \bar{T}}{\partial z}\frac{\partial \bar{s}}{\partial r} - \frac{\partial \bar{T}}{\partial r}\frac{\partial \bar{s}}{\partial z}\right) + \left(\frac{\partial F_{fr}}{\partial z} - \frac{\partial F_{fz}}{\partial r}\right) \tag{24}$$

This equation governs the transport of vorticity and its generation due to entropy gradients in the flow. For given values of mean velocity, temperature, and entropy it is possible to integrate Eq. (24) for $\bar{\Omega}_{f\theta}$ once the values of the dissipative body force components F_{fr}, and F_{fz} are known.

To calculate the dissipative body forces, following Horlock (1971), let us consider the streamwise component of Eq. (21), whereby:

$$\overline{\mathbf{W}} \cdot (\overline{\mathbf{W}} \times \bar{\Omega}_f) = \overline{\mathbf{W}} \cdot \nabla \bar{I} - \overline{T}\overline{\mathbf{W}} \cdot \nabla \bar{s} - \overline{\mathbf{W}} \cdot \mathbf{F}_f \tag{25}$$

As mentioned in section (2.2), if the flow is adiabatic and uniform at inlet (i.e., homenergetic) then, in spite of the dissipative effects, the energy equation can be reduced to a constant rothalpy condition. As a result the first term on the right-hand side of Eq. (25) vanishes and so we are left with the following equation for $\mathbf{F}_f$:

$$\overline{\mathbf{W}} \cdot \mathbf{F}_f = \overline{T}\overline{\mathbf{W}} \cdot \nabla \bar{s}$$

or

$$F_d = -\frac{\bar{T}}{W}\left(\overline{W}_z \frac{\partial \bar{s}}{\partial z} + \overline{W}_z \frac{\partial \bar{s}}{\partial r}\right) \tag{26}$$

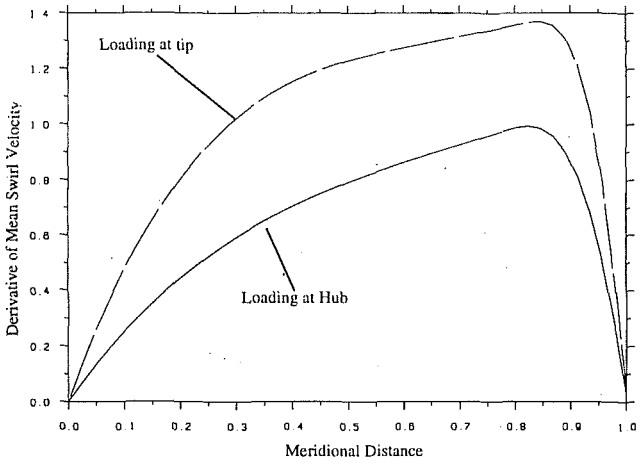

Fig. 2 Specified loading distribution

Now since $\mathbf{F}_f$ acts in the direction of $\overline{\mathbf{W}}$ then $\overline{\mathbf{W}} \times \mathbf{F}_f = 0$ so that the components of $\mathbf{F}_f$ can be found from:

$$F_{fr} = \frac{\overline{W}_r}{\overline{W}} F_d \quad \text{and} \quad F_{fz} = \frac{\overline{W}_z}{\overline{W}} F_d \tag{27}$$

The form of Eq. (25) in the transformed plane is presented in the appendix. This equation is then solved by using the Crank-Nicholson method. The initial value of $\bar{\Omega}_{f\theta}$ at the upstream boundary is set to zero, as the flow is irrotational at inlet.

5 Results

In the first application of the method we shall use it to redesign the blade geometry of Eckardt's (1980) backswept centrifugal impeller. This impeller's blade geometry may not be representative of some of the more advanced current designs, but it does provide a well-understood impeller of relatively high specific speed. The design was based on identical design point, i.e., a rotational speed of 14,000 rpm, mass flow rate of 4.54 kg/s, blade number of 20, and backsweep angle of 30 deg from radial.

The meridional geometry and the tangential thickness distribution used for the design were also identical to that of the Eckardt's impeller. A (73 × 25) meridional grid was used for the design. The grid points were clustered near the endwalls in order to resolve the sever entropy gradients; see Fig. 6(*b*).

To design for comparable overall loading the exit tangential velocity was set to 203.5 m/s. The specific distribution of $r\bar{V}_\theta$ was determined by specifying the loading distribution shown in Fig. 2 on the hub and shroud and then interpolating linearly to find the $r\bar{V}_\theta$ distribution throughout the meridional domain. For this particular design, the blade was stacked at the trailing edge plane. In this case no attempt was made to control secondary flows in the impeller. However, the method has already been successfully applied to control secondary flows in radial turbomachinery, the result of which will be reported in near future. More information on the choice of $r\bar{V}_\theta$ distribution and the stacking condition is given by Zangeneh (1992).

These input specifications were then used to compute the blade geometry by using the Actuator Duct (axisymmetric) and three dimensional *inviscid* versions of the design method (Runs C0AD and C0, respectively). For the three-dimensional design 15 harmonics of the Fourier series, representing the periodic flow, were used. The corresponding CPU times for the Actuator Duct and three-dimensional runs were 30 seconds and 33 minutes on a VAX station 4000 VLC, respectively. The mean blade angles (or wrap angles) computed by the two methods are compared in Fig. 3. The difference between the wrap angles computed by the three-dimensional and axisymmetric

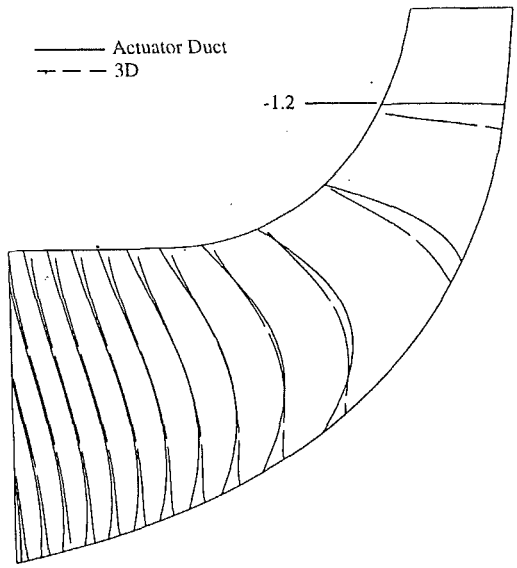

Fig. 3 Contours of mean camber angle *f*

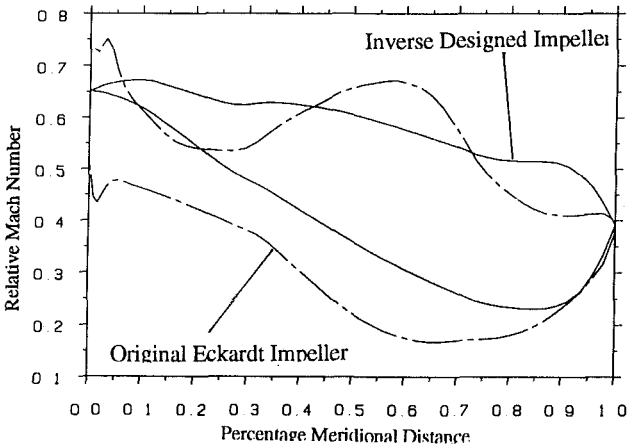

Fig. 4 Comparison of Mach number distribution shroud streamline

methods become very significant in regions of high loading near the trailing edge. The resulting Mach number distribution on the shroud streamline of the three-dimensional designed blade is presented in Fig. 4. Also shown in Fig. 4 are the Mach number distributions for the original Eckardt's impeller. These Mach number distributions were computed by Denton's (1983) inviscid three-dimensional Euler solver code using a (17 × 69 × 17) grid. Figure 4 shows that the specified loading distribution results in a smooth Mach number distribution, particularly on the shroud suction surface, where little diffusion can be observed.

In order to validate the inviscid version of the design method, the flow through the designed impeller was computed by using Denton's three-dimensional Euler code, using a (17 × 73 × 17) grid. The resulting $r\bar{V}_\theta$ distribution on the shroud predicted by the Denton code is compared with the specified distribution in Fig. 5. This excellent agreement between the predicted and specified $r\bar{V}_\theta$ distribution could be observed along all the streamlines.

The flow through the blade geometries calculated by the Actuator Duct (Run C0AD) and three-dimensional method (Run C0) were then computed by using the three-dimensional viscous method of Dawes (1988) using a (17 × 73 × 17) computational grid. In each case, the static pressure at outlet, which was located at $R/R_2 = 1.3$, was varied until the design mass flow rate was obtained. In these computations the tip clearance effects between the impeller tip and the casing were not con-

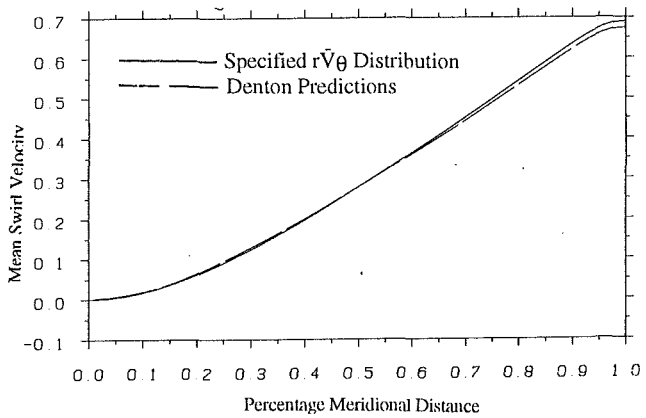

Fig. 5 Comparison of specified and computed $r\bar{V}_\theta$

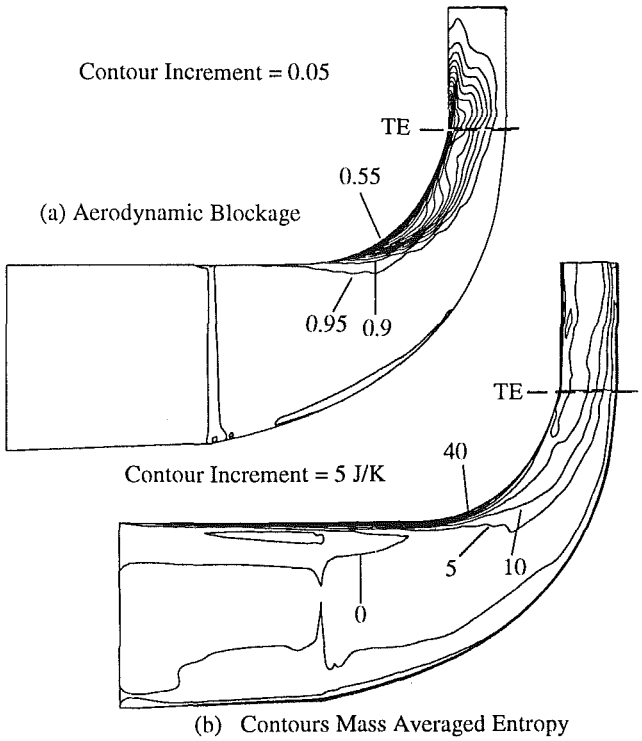

Fig. 6 Contours of aerodynamic blockage and entropy

sidered. To achieve convergence for a typical run about 2500 time steps were required. A typical calculation required about 11 hours of CPU time on VAX station 4000VLC. The overall results of these two viscous calculations are tabulated in Table 1. The predicted losses were 4.2 and 4.3 percent, respectively, for geometries C0AD and C0. These losses compare favorably with a predicted loss of 5.5 percent by the same viscous method for the original Eckardt impeller. The main difference between the geometries designed by the axisymmetric and three-dimensional methods is in the values of exit tangential velocity. The blade geometry computed by the actuator duct method results in an exit tangential velocity lower than the design value (196 m/s as opposed to 203.5 m/s). As this is a design method (in which the mean tangential velocity rather than the blade geometry is specified) the lower actual tangential velocity implies that the flow field does not fully follow the blade shape computed by the Actuator Duct method. We can therefore conclude that there is a certain amount of slip (using this term in its widest sense) in the impeller geometry computed by the AD method. The flow through the three-dimensional designed geometry, however, shows little slip as the exit tangential velocity is 205.3 m/s, very slightly higher than the design value.

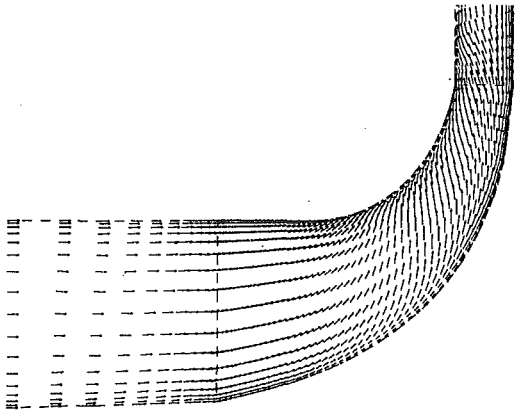

Fig. 7 Velocity vectors near suction surface—run C0 viscous predictions

Table 1 Summary of the results of viscous/inviscid interactions: low-speed impeller design

Run	m (kg/s)	V_θ (m/s)	Loss (%)
C0 AD	4.57	196	4.2
C0	4.59	206.3	4.3
C1 - Entropy	4.5	208.8	4.7
C2 - Entropy	4.51	209.2	4.6
C1 - Blockage	4.61	210.8	4.8
C2 - Blockage	4.49	214.3	4.7
C3 - Blockage	4.53	210.1	4.9

The results of this viscous calculation for the three-dimensional geometry (Run C0) were then used to compute the aerodynamic blockage distribution (using Eq. (18)) and the mass-weighted tangentially averaged entropy distribution in the impeller as shown in Fig. 6. The results in Fig. 6(*a*) indicate that the aerodynamic blockage is negligible everywhere apart from a relatively small region near and on the shroud starting from the meridional bend. This picture is further confirmed by the distribution of mass-averaged entropy, which shows an accumulation of low-momentum, high-loss fluid in this region. The main mechanism for the accumulation of low-momentum fluid in this region can be explained by considering the velocity vector plots on the pressure and suction surfaces. The velocity vectors on the suction surface are presented in Fig. 7. The velocity vectors on the pressure surface are almost identical to that shown in Fig. 7 and therefore are not presented. This plot indicates that the flow is *fully attached*, but there is a strong secondary flow moving low-momentum fluids toward the shroud, thereby resulting in the accumulation of low-momentum fluids in this region.

The aerodynamic blockage distribution and the entropy gradients, shown in Fig. 6, were then used in the corresponding versions of the design program to compute the blade shape. The CPU time for the blockage method is similar to that required for the inviscid method. However, the introduction of the vorticity term due to entropy gradients does slow down the convergence rate and more blade iterations are required to reach convergence. In this case 2 hours and 10 minutes of CPU time on VAX 4000 was required.

In Fig. 8, the mean camber angles (or wrap angles) computed by the aerodynamic blockage and entropy gradient methods are compared with the inviscid results. The wrap angles computed by the two former methods are similar at the hub, but differ considerably near the tip. The meriodional velocity at the trailing edge as predicted by the different versions of the

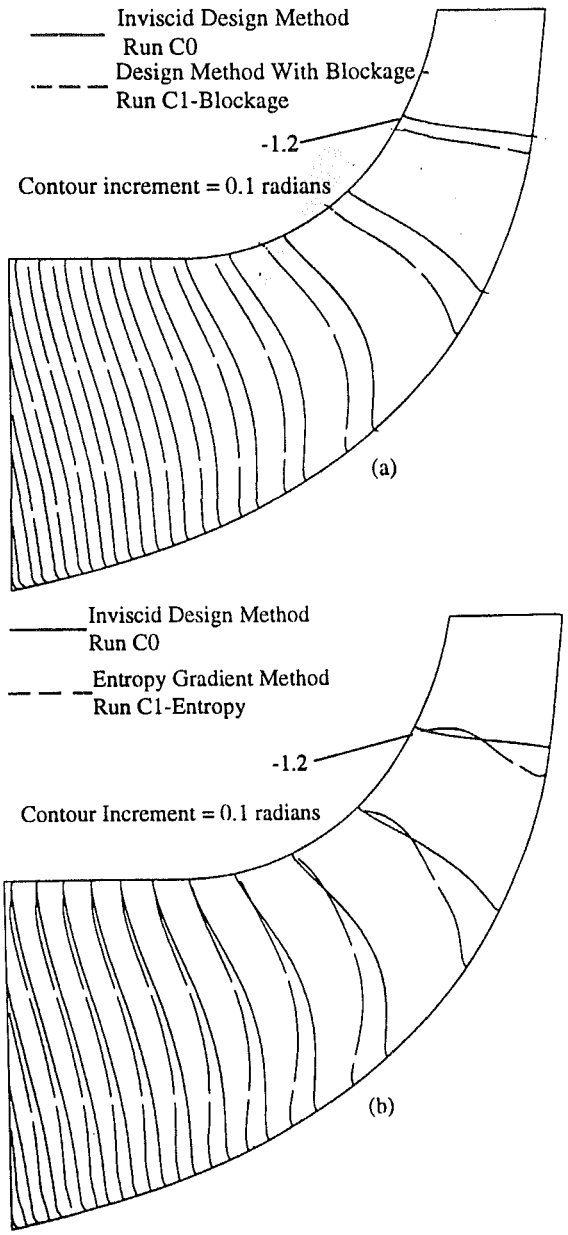

Fig. 8 Comparison of mean camber angle *f*

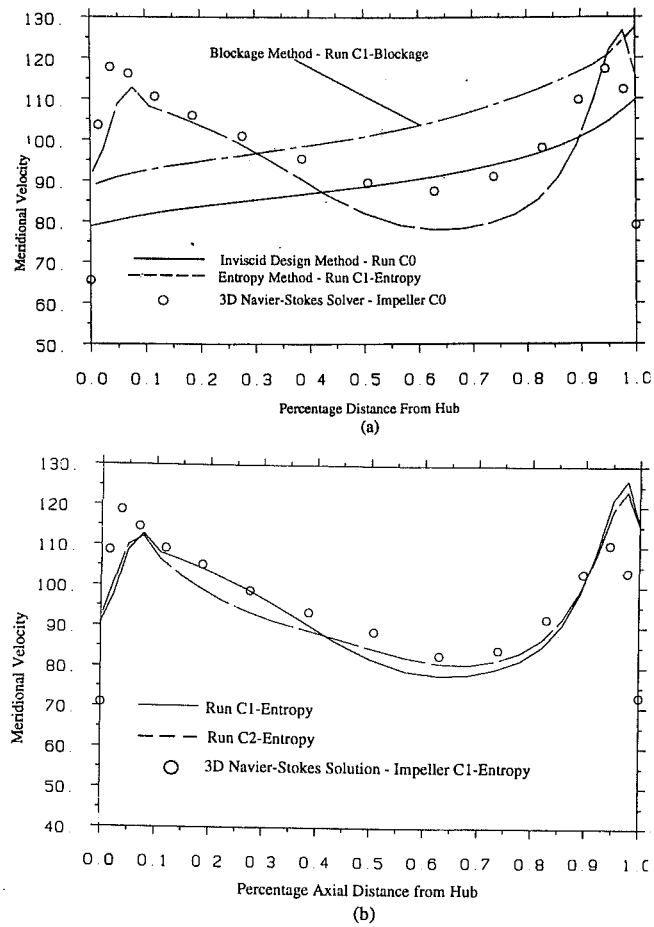

Fig. 9 Comparison of impeller exit meridional velocity

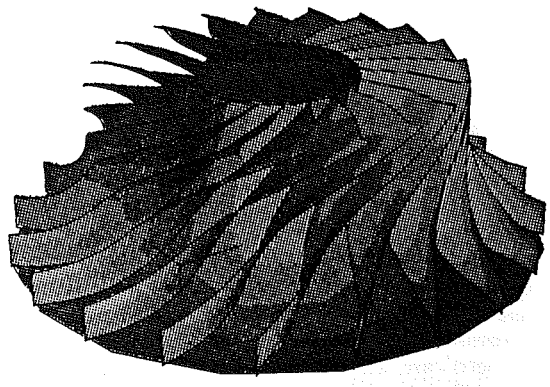

Fig. 10 Solid modeling of impeller C2-entropy

design method is compared with the mass-averaged velocity computed by the three-dimensional viscous method in Fig. 9(*a*). The circles represent the exit meridional velocity as predicted by the Dawes code for the impeller C0. As the entropy gradients and aerodynamic blockage distribution obtained from run C0 were specified to compute the geometries C1-Entropy and C1-Blockage, we can conclude that the entropy gradient method can predict the exit flow pattern with a very good degree of accuracy, while the aerodynamic blockage approach results in a fairly uniform increase in meridional velocity across the span.

In order to establish whether the flow field and the blade shapes computed by these methods are affected by extra viscous/inviscid iterations, the flows through impellers designed by the entropy gradient method (C1-Entropy) and blockage method (C1-Blockage) were computed by using the viscous method and the whole process was repeated. The effect of extra viscous/inviscid iterations on the flow field and blade shape was found to be relatively small. For example in Fig. 9(*b*) the exit meridional velocity for the entropy gradient designs C2-Entropy and C1-Entropy are compared, where only a small difference between the exit velocity can be observed. As expected, the extra iteration has resulted in a better correlation between the Dawes prediction of the exit meridional velocity and that predicted by the design method. A summary of the results of the iterations is presented in Table 1. A solid modeling of the geometry of impeller C2-Entropy is presented in Fig. 10. All the data presented in Table 1 were obtained from the three-dimensional viscous method. The results indicate that in this low-pressure application, the incorporation of viscous effects does not seem to make a very significant contribution to the design of the blade geometry, and they may perhaps be neglected.

However, the flow through this low-pressure impeller was fully attached, as velocity vector plots in Fig. 7 indicate. Therefore, in order to investigate the case where significant viscous

Table 2 Summary of results of viscous/inviscid interactions: high-speed impeller design

Run	m (kg/s)	V_θ (m/s)	Loss (%)
HS0	7.183	288	19.1
HS1 - Entropy	7.10	326	14.8
HS2 - Entropy	7.22	329.7	16.1
HS1 - Blockage	7.16	321.8	19.4
HS2 - Blockage	7.12	320	18.9

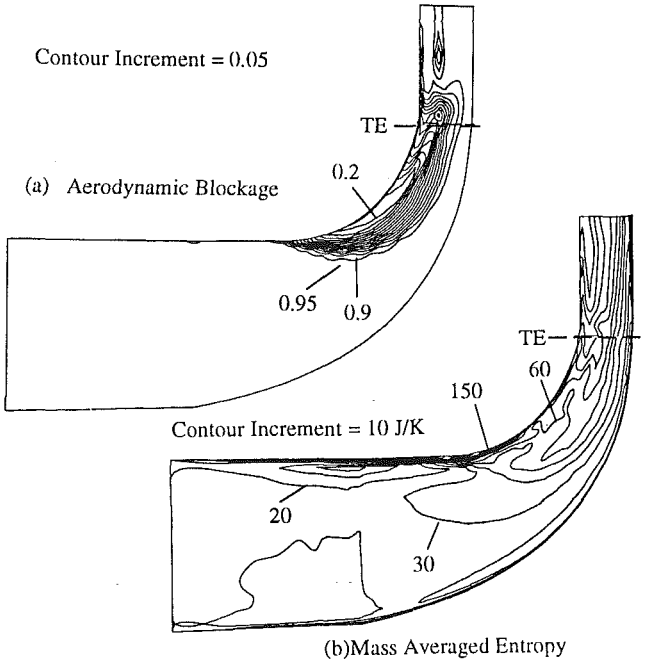

Fig. 11 Contours of aerodynamic blockage and entropy

effects, including gross boundary layer separation, are present, a generic high pressure ratio transonic compressor was designed. This compressor had exactly the same meriodional geometry and tangential thickness distribution as the original Eckardt impeller; however, the rotational speed was increased to 23,000 rpm and all velocity triangles were scaled by the ratio of blade tip speed. The design mass flow rate through the impeller was now 7.156 kg/s, the Mach number based on tip speed and inlet stagnation temperature was 1.42 and the stagnation pressure ratio of 4.4. The same loading distribution as the low speed case was specified and the value of V_θ at exit was set to 332 m/s.

The inputs above were then used in the inviscid versions of the design method to compute the geometry. The maximum relative Mach number on the shroud suction surface was predicted to be 1.15 by the inviscid method. As before, the flow through this geometry was computed by the three-dimensional N-S method. The computed aerodynamic blockage and mass-averaged entropy distribution are presented in Fig. 11. The overall distributions are similar to the low-speed case. However, in this case in a region on the shroud on the meridional bend the blockage factor is as low as 0.2, i.e., only 20 percent of flow passage is available to the flow. Furthermore, the maximum entropy is now 150 J/K in this region. The Mach number contours near the shroud surface predicted by the three-dimensional Navier–Stokes method, shown in Fig. 12, indicate that there is strong shock system near the leading edge, which causes a gross boundary layer separation, which is the main cause of the dramatic increase in losses. A summary of

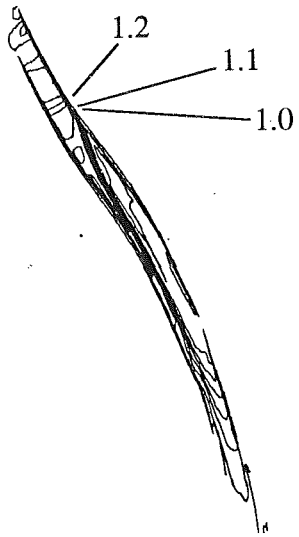

Fig. 12 Predicted Mach number distribution near the shroud

the results of this calculation is presented in Table 2 (Run HS0), where we can see that the losses in the impeller alone amount to almost 19 percent. Furthermore, the exit tangential velocity predicted by the viscous method is about 13 percent less than the designed value (288 m/s versus 332 m/s). This is particularly important because in the low-speed case, where the flow was fully attached, the predicted $V_{\theta 2}$ was almost the same as the specified value, indicating that very little slip was present. In this case, however, the gross boundary separation has resulted in a significant amount of slip in the impeller.

The blockage distribution and entropy gradients described above were then used in the corresponding versions of the design program. The wrap angle distribution computed by each method is presented in Figs. 13(a,b). Also shown in these figures are the wrap angles distributions computed by the inviscid version of the design method. The corresponding exit meridional velocities are compared with three-dimensional Navier–Stokes results in Fig. 14. The flows through these geometries were then computed by the three-dimensional N–S method, the overall results of which are summarized in Table 2. Despite the differences in geometry both methods seem to be able to account for the viscous losses, so that the actual (or predicted) exit swirl velocity is now very close to the specified values. An interesting feature of the results for impeller HS1-Entropy is the reduction in loss from 19.1 to 14 percent. This reduction in loss can be contributed to the changes in the geometry near the tip, which have reduced the shock strength and therefore the resulting shock losses. However, the viscous results still indicate that a shock-induced boundary layer separation is present near the inlet to the impeller. From a practical point of view, it is of course possible to eliminate the shock wave by appropriate adjustments to the blade loading.

6 Conclusions

A method for the three-dimensional design of centrifugal compressors has been developed, in which the viscous effects are accounted for by using a inviscid/viscous procedure. The viscous effects are incorporated by either specifying an aerodynamic blockage distribution or the entropy gradients in the machine. The results indicate that the entropy gradient approach can fairly accurately represent the viscous effects in the machine, including the effect of accumulation of low-momentum fluids by secondary flows and loss generation by shock waves.

The application of the method to a low pressure ratio compressor indicates that by specifying the loading distribution it

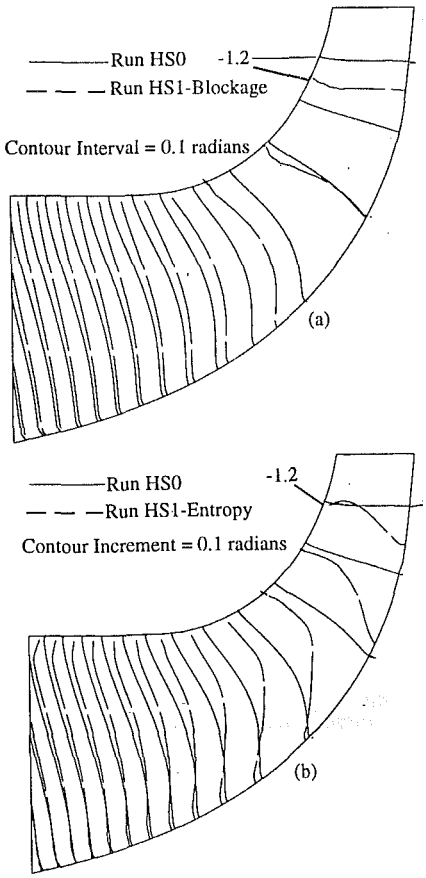

Fig. 13 Comparison of mean camber angle *f*

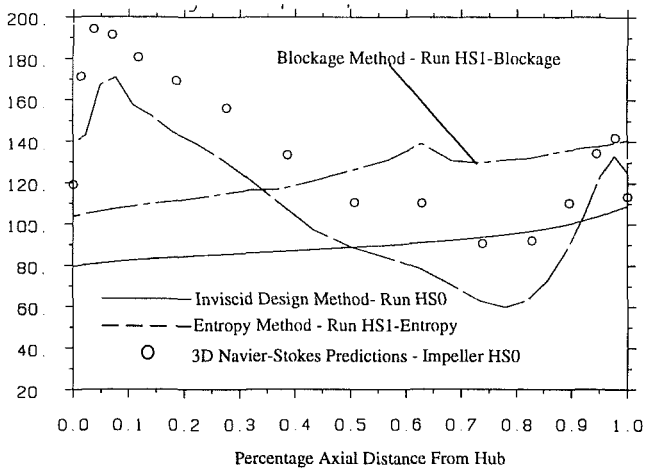

Fig. 14 Comparison of exit meridional velocity

is possible to design impellers with controlled diffusion, especially on the shroud suction surface. This in turn has resulted in an impeller free from flow separation and the results indicate that in this case inclusion of the viscous effects does not result in any obvious improvement in overall parameters such as efficiency and pressure rise. An interesting feature of the results is that the inviscidly designed impeller in fact shows very little slip, i.e., the actual exit swirl velocity is very close to that specified.

In the case of a high pressure ratio (transonic) compressor, however, the exit tangential velocity for the impeller designed by the three-dimensional inviscid method was found to be 13 percent lower than the specified value. This was because the strong shockwave/boundary layer interaction resulted in a gross boundary layer separation. By including the viscous losses, it was possible to account for these effects and thereby design an impeller with a exit tangential velocity very close to that specified.

In conclusion this inverse design method not only enables one to optimize the Mach number distributions in the impeller but it can also be used to design impellers with very high slip factors (approaching unity) and thereby provide compact designs with higher performance. Furthermore, the method can also be used to control secondary flows in the impeller. One such successful application of this method for controlling secondary flows will be reported in the near future.

Acknowledgments

The author is indebted to Professor J. D. Denton and Dr. W. N. Dawes of the Whittle Laboratory at Cambridge University, who made their codes available for the present study, and Professor W. R. Hawthorne for his comments on section 2.4. The help of Mr. M. Roddis is obtaining a solid model of the designed impeller is gratefully acknowledged.

References

Baldwin, B., and Lomax, H., 1978, "Thin Layer Approximation and Algebraic Model for Separated Turbulent Flows," AIAA Paper No. 78-257.

Borges, J. E., 1990, "A Three-Dimensional Inverse Design Method in Turbomachinery: Part I—Theory," ASME JOURNAL OF TURBOMACHINERY, Vol. 112, pp. 346–354.

Brandt, A., 1977, "Multi-level Adaptive Solution to Boundary Value Problems," *Mathematics of Computation*, Vol. 31, No. 138, pp. 333–390.

Casey, M. V., Dalbert, P., and Roth, P., 1992, "The Use of 3D Viscous Flow Calculations in the Design and Analysis of Industrial Centrifugal Compressors," ASME JOURNAL OF TURBOMACHINERY, Vol. 114, pp. 27–37.

Dang, T. Q., and Wang, T., 1992, "Design of Multistage Turbomachinery Blading by the Circulation Method: Actuator Duct Limit," ASME Paper No. 92-GT-286.

Dang, T. Q., 1993, "A Fully Three-Dimensional Inverse Method for Turbomachinery Blading in Transonic Flows," ASME JOURNAL OF TURBOMACHINERY, Vol. 115, pp. 354–361.

Dawes, W. N., 1988, "The Development of a 3D Navier–Stokes Solver for Application to All Types of Turbomachinery," ASME Paper No. 88-GT-70.

Denton, J. D., 1983, "An Improved Time Marching Method for Turbomachinery Flow Calculations," ASME *Journal of Engineering for Power*, Vol. 105, p. 514.

Denton, J. D., 1986, "The Use of a Distributed Body Force to Simulate the Viscous Effects in 3D Flow Calculations," ASME Paper No. 86-GT-144.

Dring, R. P., 1984, "Blockage in Axial Compressors," ASME *Journal of Engineering for Gas Turbines and Power*, Vol. 106, pp. 712–714.

Eckardt, D., 1976, "Detailed Flow Investigation Within a High Speed Centrifugal Compressor Impeller," ASME *Journal of Fluids Engineering*, Vol. 98, pp. 390–402.

Eckardt, D., 1980, "Flow Field Analysis of Radial and Backswept Centrifugal Compressor Impellers—Part I. Flow Measurements Using a Laser Velocimeter," *Performance Prediction of Centrifugal Pumps and Compressors*, Gopalakrishnan, ed., ASME publication, pp. 77–86.

Ghaly, W. S., 1990, "A Parametric Study of Radial Turbomachinery Blade Design in Three-Dimensional Subsonic Flow," ASME JOURNAL OF TURBOMACHINERY, Vol. 112, pp. 338–345.

Goto, A., 1992, "Study of Internal Flows in a Mixed-Flow Pump Impeller at Various Tip Clearances Using Three-Dimensional Flow Calculations," ASME JOURNAL OF TURBOMACHINERY, Vol. 114, pp. 373–382.

Hawthorne, W. R., 1974, "Secondary Vorticity in Stratified Compressible Fluids in Rotating Systems," CUED/A-Turbo/TR 63.

Hawthorne, W. R., Tan, C. S., Wang, C., and McCune, J. E., 1984, "Theory of Blade Design for Large Deflections: Part I—Two Dimensional Cascades," ASME *Journal of Engineering for Gas Turbines and Power*, Vol. 106, pp. 346–353.

Horlock, J. H., 1971, "On Entropy Production in Adiabatic Flow in Turbomachines," ASME *Journal of Basic Engineering*, Vol. 93, pp. 587–593.

Krain, H., 1988, "Swirling Impeller Flow," ASME JOURNAL OF TURBOMACHINERY, Vol. 110, pp. 122–128.

Marsh, H., 1966, "A Digital Program for the Through Flow Fluid Mechanics in an Arbitrary Turbomachine Using a Matrix," ARC R&M, No. 3509.

Roddis, M., and Zangeneh, M., 1993, "A Method for the Inverse Design of Ducted Propulsors in Axisymmetric Shear Flow," to be published in *Transactions of Royal Inst. of Naval Architects.*

Tan, C. S., 1981, "Vorticity Modelling of Blade Wakes Behind Isolated Rotors," ASME *Journal of Engineering for Power*, Vol. 103, No. 2.

Tan, C. S., Hawthorne, W. R., Wang, C., and McCune, J. E., 1984, "Theory of Blade Design for Large Deflections: Part II—Annular Cascades," ASME *Journal of Engineering for Gas Turbines and Power*, Vol. 106, pp. 354–365.

Wu, C., 1955, "A General Theory of Three Dimensional Flow in Subsonic and Supersonic Turbomachines of Axial, Radial and Mixed Flow Types," NACA TN-2604.

Zangeneh, M., 1990, "Three Dimensional Design of a High Speed Radial-Inflow Turbine by a Novel Design Method," ASME Paper No. 90-GT-235.

Zangeneh, M., 1991, "A Compressible Three Dimensional Blade Design Method for Radial and Mixed Flow Turbomachinery Blades," *Int. J. Numerical Methods in Fluids*, Vol. 13, pp. 599–624.

Zangeneh, M., 1992, "An Inverse Design Method for Radial Turbomachines," VKI Lecture series, Radial Turbines, 1992-5, Belgium.

APPENDIX

Equation (24) in the transformed (ξ, η) curvilinear computational plane takes the following form:

$$\Psi_\eta \bar{\Omega}_{f\xi} - \Psi_\xi \bar{\Omega}_{f\eta} + \bar{\Omega}_f[\Psi_\eta R_\xi - \Psi_\xi R_\eta] + (\Psi_\eta B_\xi - \Psi_\xi B_\eta) + \frac{1}{r}(y_\eta \Psi_\xi - y_\xi \Psi_\eta) = \left(\frac{\rho}{\rho_i}\right) Br[(s_\eta T_\xi - s_\xi T_\eta) + y_\eta (F_{fr})_\xi - y_\xi (F_{fr})_\eta + X_\eta (F_{fz})_\xi - X_\xi (F_{fz})_\eta]$$

where $R = \ln(\rho_i/\rho)$ and F_{fr} and F_{fz} are the radial and axial components of the dissipative body force.

C. M. Rhie

R. M. Zacharias

D. E. Hobbs

K. P. Sarathy

B. P. Biederman

C. R. Lejambre

D. A. Spear

Pratt & Whitney,
United Technologies Corporation,
East Hartford, CT 06108

Advanced Transonic Fan Design Procedure Based on a Navier-Stokes Method

A fan performance analysis method based upon three-dimensional steady Navier-Stokes equations is presented in this paper. Its accuracy is established through extensive code validation effort. Validation data comparisons ranging from a two-dimensional compressor cascade to three-dimensional fans are shown in this paper to highlight the accuracy and reliability of the code. The overall fan design procedure using this code is then presented. Typical results of this design process are shown for a current engine fan design. This new design method introduces a major improvement over the conventional design methods based on inviscid flow and boundary layer concepts. Using the Navier-Stokes design method, fan designers can confidently refine their designs prior to rig testing. This results in reduced rig testing and cost savings as the bulk of the iteration between design and experimental verification is transferred to an iteration between design and computational verification.

Introduction

The design of advanced transonic fans is a very challenging task due to the complex flow phenomena encountered at design and off-design conditions. The flow speed varies from low to high Mach numbers, there are leading edge bow shocks and standing normal surface shocks, shock/boundary layer interactions, separation, and wakes. A Navier-Stokes procedure is required to predict these complex flow situations.

The basic technology ingredients of modern Navier-Stokes computational methods, such as turbulence and geometric modeling, three-dimensional mesh generation, and numerical algorithms were developed in the 1970s and early 1980s. These ingredients were refined and made more robust through the 1980s and were ready for design application for many turbomachinery flows by the beginning of the 1990s [1-7]. However, the most important step in the transition from development to design is the validation process. This validation process not only refines physical and numerical models but also defines the *envelope* in which the models can be reliably used for a design.

This paper summarizes the validation study conducted for the fan application, which was based on the building block approach: The physical complexity of the computations was increased in discrete steps, beginning with simple two-dimensional compressor cascade cases, moving to unswept three-dimensional fans, swept three-dimensional fans, and finally three-dimensional fans with part-span shrouds and core/duct flow splitters. Numerous questions regarding the effect of the computational grid, boundary conditions, turbulence modeling, convergence and turnaround time on the calculated flow field were answered during the validation process. The resulting Navier-Stokes procedure was demonstrated to be very reliable and practical in support of design activities.

Computational Method

Governing Equations. The governing equations are the continuity equation, the Reynolds-averaged Navier-Stokes equations, and the Reynolds-averaged energy equation in mass-weighted variables. The turbulent viscosity and turbulent conductivity are introduced to model the Reynolds stress and the Reynolds heat flux terms. The turbulent viscosity and turbulent conductivity are determined by the two-equation κ-ϵ turbulence model. The near-wall regions are modeled either by wall functions, or the VanDriest near-wall formulation of Dash et al. [8]. The flows are assumed to be fully turbulent in the present work. Additional equations are the perfect gas and enthalpy-temperature relations.

Numerical Modeling. To solve the governing differential equations numerically, it was convenient first to transform them to an arbitrary curvilinear coordinate system. Using standard transformation formulae, the continuity, momentum, energy, and turbulence equations can be expressed as general transport equations in a linearized form as

$$\frac{1}{J}\{[\rho G_1\phi]_\xi + [\rho G_2\phi]_\eta + [\rho G_3\phi]_\zeta\} = \frac{1}{J}\{[J\Gamma\alpha_1\phi_\xi]_\xi + [J\Gamma\alpha_2\phi_\eta]_\eta + [J\Gamma\alpha_3\phi_\zeta]_\zeta + S\} + S^\phi \quad (1)$$

Contributed by the International Gas Turbine Institute and presented at the 38th International Gas Turbine and Aeroengine Congress and Exposition, Cincinnati, Ohio, May 24-27, 1993. Manuscript received at ASME Headquarters March 17, 1993. Paper No. 93-GT-323. Associate Technical Editor: H. Lukas.

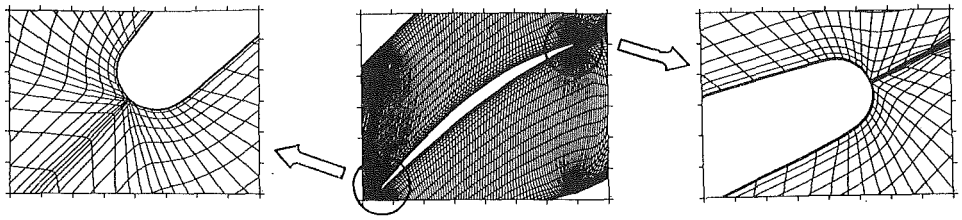

Fig. 1(*a*) Grid detail near leading edge

Fig. 1(*b*) Grid detail near trailing edge

where ξ, η, ζ are arbitrary curvilinear coordinates; ϕ represents any one of the scalar dependent variables, Γ, effective viscosity; J, the Jacobian of the transformation; G_1, G_2, G_3, are the linearized contravariant velocity components in the ξ, η, ζ coordinate directions, respectively (convective fluxes normal to grid surfaces); and S is a source term, which appears for nonorthogonal coordinate systems.

The conservation form of the general transport equation, eq. (1), is integrated over the control volume. The necessary quantities on the cell boundaries are linearly interpolated between adjacent grid nodes. As a result, second-order-accurate centered differencing is achieved.

Since the cross-stream discretization should be able to capture strong shocks, a smart dissipation scheme previously developed in [9] is used. The approach is to use the limiting grid cell Reynolds number method for automatic adaption in dissipation level. The present dissipation scheme uses a concept similar to the flux limiters to control the antidiffusive term in Total Variation Diminishing (TVD) schemes.

Solution Algorithm. A preliminary velocity field is first obtained from the momentum equations with a preliminary pressure field. Since this preliminary velocity field does not satisfy the continuity equation, pressure correction equations are solved to establish new velocity and pressure fields that satisfy the continuity equation. The momentum and continuity equations are coupled through this pressure correction procedure. A three-step pressure correction procedure previously proposed by Rhie [9, 10] is used. Then, the energy and turbulence scalar equations are each solved in turn. These equations are solved using the successive line underrelaxation procedure.

Boundary Conditions. For transonic compressible flow calculation, the absolute total pressure, absolute total temperature, and absolute flow angle fields are specified at the inlet, and the static pressure field is specified at the exit. At the exit, typically a simple one-dimensional radial equilibrium condition is applied to form a radial pressure profile while maintaining the prescribed static pressure level at a fixed radial location. For the energy equation, an adiabatic condition is used for all calculations.

Grid Generation

In order to capture the flow physics important to fan designers, namely bow shocks, shock boundary layer interactions, separations, and wakes, proper positioning of the computational grid is crucial.

The three-dimensional grid generation system links to a common airfoil section database, extracts the stacking sections, and generates two-dimensional computational meshes on axisymmetric surfaces using an elliptic grid fill technique. The grid is filled out in the radial direction by performing spline fits and evaluations in the radial direction. Endwalls are defined as axisymmetric surfaces.

For this study, H-grids were used for all three dimensional computations and C-grids were used for all two-dimensional computations. A typical grid for a three-dimensional calculation is 100 in the axial direction, 30 in the circumferential direction, and 36 in the radial direction for a total of 108,000 grid points. For complex geometries including part-span shroud, splitter, and tip clearance, the grid is increased up to a total of 350,000 grid points.

The current grid generation procedure has evolved based on the flow solver accuracy and resolution requirements, coupled with design accuracy requirements. We have broken down the areas where the grid has the largest effect on the accuracy and robustness of the solution into basic categories discussed in the following sections.

Airfoil Leading Edge. It is critical to have enough grid points on the airfoil leading edge to resolve the stagnation point and accompanying pressure rise, and subsequent re-acceleration. For a fan, which generally has a very thin leading edge, this means points have to be clustered very tightly around the airfoil leading edge. A minimum of 16 uniformly distributed grid points are located around the leading edge, which begin to rapidly spread out away from the leading edge. A typical fan leading edge detail is shown in Fig. 1(*a*).

Airfoil Trailing Edge. Since real rounded trailing edges are used in the present fan computation, it is necessary to resolve the viscous trailing edge flow field properly in order to match trailing edge static pressure values without a Kutta condition model. In practice this means that a minimal resolution of 16 points around the trailing edge should be employed as shown in Fig. 1(*b*).

Chordwise Distribution on the Airfoil Surface. It is necessary to maintain a reasonable chordwise distribution of grid points on the airfoil in a fan computation in order to resolve the shock/boundary layer effects on the suction surface. Knowing that the present solver will capture shocks in three grid points, it has been determined that a minimum of 60 grid points, distributed uniformly along most of the blade chord, will do an adequate job of resolving the shock/boundary layer effects.

Nomenclature

G_1, G_2, G_3 = curvilinear velocity components
J = Jacobian in the coordinate transformation
S = source term in finite difference equation
α_1, α_2, α_3 = metric coefficients
Γ = effective diffusion coefficient
κ, ϵ = turbulence kinetic energy and dissipation rate
ξ, η, ζ = curvilinear coordinate components
ρ = density
ϕ = general transport equation scalar quantity

Subscripts

1, 2, 3 = references to coordinate direction

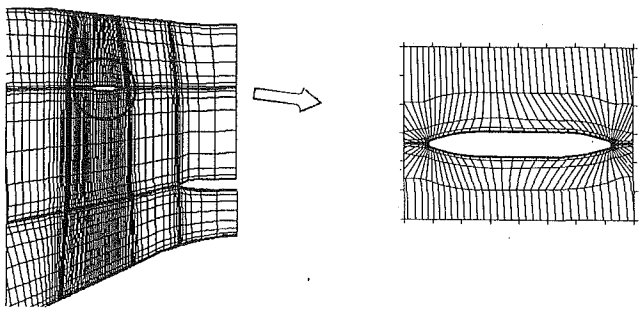

Fig. 2 Grid detail for part-span shroud

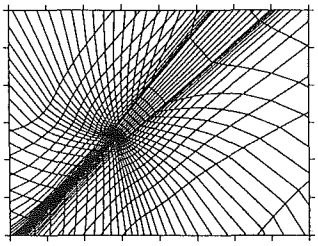

Fig. 3 Tip clearance grid near blade tip

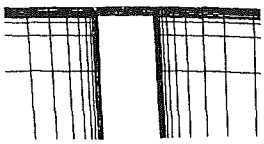

Fig. 4 Tip detail of front view of fan

Circumferential Distribution. The proper placement of grid points adjacent to the solid surfaces is crucial to the success of the fan calculation. In order to model the viscous effects that affect the fan performance, it is necessary to resolve the boundary layer. This requires the first grid point off the solid surface to be placed at $y^+ < 2$ when using the κ–ϵ turbulence model integrated to the wall, or $30 < y^+ < 300$ when using the κ–ϵ model with wall functions. In general, integration to the wall is preferred to resolve the detailed flow structure near the wall.

Splitter and Shroud Leading and Trailing Edges. Fan core/duct splitters and part-span shrouds are incorporated into the computational mesh by locally distorting the axisymmetric, radially varying grid-sheets to flow around the splitters and shrouds. This technique results in two coincident grid surfaces upstream of the splitter and shroud, and downstream of the shroud. Round leading and trailing edges are installed into the part-span shroud resulting in the mesh of Fig. 2. A cusped leading edge is used for the core splitter.

Radial Mesh Distribution. The hub and tip boundary layer resolution requirements are identical to the airfoil surface requirements outlined above. Wall functions are adequate for high aspect ratio fans where secondary flows are small, while integration to the wall is required for low aspect ratio fans, or for calculations involving hub or tip clearance.

Tip Clearance Grids. The tip clearance grid is considered a subset of the normal H mesh. For each axisymmetric grid sheet, the interior of the airfoil is filled in with grid as shown in Fig. 3. The grid inside of the blade is "blocked out," or rendered impenetrable within the flow solver, and "activated," or declared penetrable within the blade tip gap. This technique allows for the correct blunt-edged definition of the blade tip, as shown by the tip, detail of a front view of the fan grid in Fig. 4.

In the clearance gap, radial distribution of grid is carefully controlled in order to position a grid sheet precisely at the tip of the airfoil, and to place an adequate number of grid points within the tip clearance gap, which is in a minimum of five points from suction surface to pressure surface, and five points from the tip of the blade to the endwall. Therefore the mesh point count dedicated to the tip clearance region is typically 60 chordwise by 5 circumferentially by 5 radial, or 1500 total.

Initial and Boundary Conditions

An Euler solver [11] initializes the flowfield for the Navier–Stokes solver. As the inviscid mesh serves as the basis for the viscous mesh, the inviscid flow field serves as the basis for the viscous flow field. After each inviscid axisymmetric grid sheet is refined for the viscous calculation, the inviscid flow field is interpolated onto the new mesh by using bilinear interpolation.

In practice, the designer would run one or more speed lines, which are curves of the exit-to-inlet total pressure ratio as a function of corrected flow at a given corrected rotation speed. Conditions are analyzed from the maximum flow or "choked flow" to the stall line. The choked flow condition converges fastest, so the designer would calculate this point first by setting a suitably low exit static pressure value, and march up the speed line toward stall by successively raising the back pressure on converged solutions.

Convergence Monitoring

Two general criteria related to convergence must be satisfied before a calculation is declared converged: numerical and physical convergence.

Numerical Convergence. This relates to the numerical accuracy of the solution, specifically the convergence of the governing equations (continuity, momentum, energy, and turbulence). Both the maximum and average residuals of these equations are monitored. The average residuals must drop four orders of magnitude, and the maximum residuals must drop two orders of magnitude. Global conservation errors for continuity, momentum and energy equations should be less than 0.1 percent when normalized by the total inlet fluxes.

Physical Convergence. This criterion is more intuitive. In a general sense, the physical aspects of the flow field are converged when they stop changing with iteration count. The fan designer monitors the physical parameters in a hierarchical order, beginning with the first-order parameters (mass flow, static pressure, etc.) and continuing through second-order parameters (total pressure, skin friction, etc.).

The inlet-to-exit mass flow rate distribution must not vary more than 0.1 percent; there must be no nonphysical mass sources or sinks. The meridional distribution of absolute total pressure must vary in a reasonable way. There must be no nonphysical rise or fall of total pressure. The designer normally monitors a rotor trailing edge plane total pressure field and declares the convergence when the radial distribution of the circumferentially mass-averaged total pressure no longer changes with iteration. The convergence of these parameters usually takes 800 iterations for a choked flow field and increases to 2000 iterations or more for a stalled flow field.

Postprocessing

Both graphic and performance postprocessing analysis are available. Additionally, a quantitative performance postprocessor was developed for fan applications that performs mass integrations along both computational and physical surfaces in order to determine property profiles.

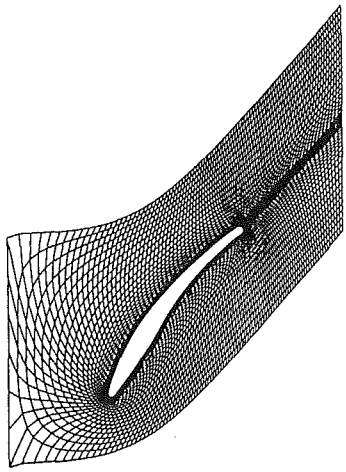

Fig. 5 Computational grid for Cascade D

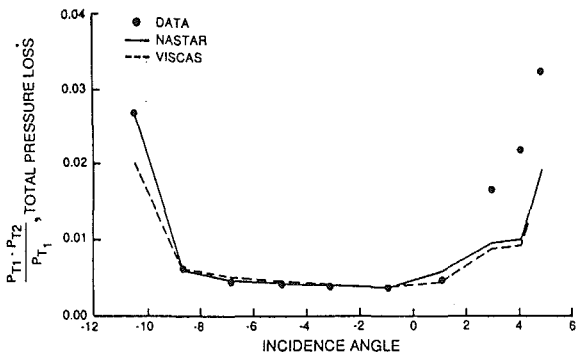

Fig. 6 Total pressure loss at various incidence angles (inlet Mach = 0.6)

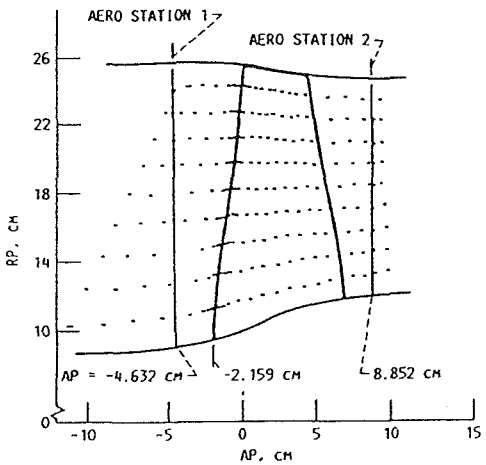

Fig. 7 Aerodynamic survey locations

Validation

This section presents the results of an extensive validation study performed using the present Navier–Stokes solver, NASTAR. The purpose of the study was to substantiate the computational capability in predicting fan performance. This validation effort is done in three steps:

1 Loss prediction capability is tested with two-dimensional compressor cascades by comparing the present results with experimental data and the results of another proven state-of-the-art Navier–Stokes code.

2 Effect of turbulence model variation on design parameters such as total pressure loss profile is studied to determine the most suitable model for three-dimensional fans.

3 Radial profile prediction capability is tested in three-dimensional fans by comparing the present results with a conventional streamline data model based on conventional far downstream rake data and laser-Doppler velocity experimental data.

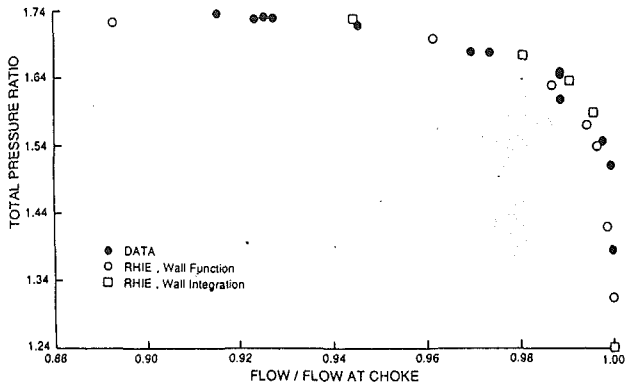

Fig. 8 Total pressure ratio as function of flow at design speed

Two-Dimensional Compressor Validation. In this section, NASTAR is applied to a two-dimensional subsonic compressor cascade and compared to data and to the VISCAS procedure of Davis, et al. [12], which demonstrated the ability to predict total pressure loss by substantially reducing the numerical smoothing while ensuring a stable solution. In order to establish confidence in NASTAR, it was crucial to demonstrate the same capability. The case shown in this section is the subsonic Cascade D operated at an inlet Mach number of 0.6. Figure 5 shows the airfoil geometry and a 196×33 **C**-type grid used. Both calculations were performed on the identical computational mesh shown in Fig. 5 using wall integrations. Figure 6 shows a comparison between the two calculations and the data for the downstream mass-averaged total pressure loss as a function of the incidence of the incoming flow. The design condition is at an incidence of -3 deg. This figure shows that both solvers match the measured loss well over the entire incidence range. The agreement between NASTAR and VISCAS established a high confidence level in the ability of NASTAR to calculate two-dimensional flow fields. In the present NASTAR study, the numerical dissipation model was optimized to minimize the artificial numerical loss. This dissipation level was then frozen for the rest of the validation studies. The total pressure loss level calculated using an *H*-type grid with the same grid density did not change.

Three-Dimensional Fan Validation

Rotor-67 Fan. Navier–Stokes analysis of NASA Lewis low aspect ratio Rotor 67 fan [13, 14] has been carried out at various operating conditions at design speed and compared to experimental data. The aerodynamic survey locations are shown in Fig. 7. Plots of fan maps obtained from two computations using different near-wall turbulence models and the data using mass flow normalized to choke flows indicate good agreement shown in Fig. 8. The computed choked mass rate was 1 percent lower than the data for both calculations. There was no tip clearance in this application. In this study, the effect of near-wall turbulence modeling near the blade surfaces was investigated, where the wall function and wall integration techniques are compared to the data. The wall integration directly resolves the laminar and buffer layers with finer grid without using the law of the wall. The wall integration method predicted slightly higher total pressure ratios than the wall function method due

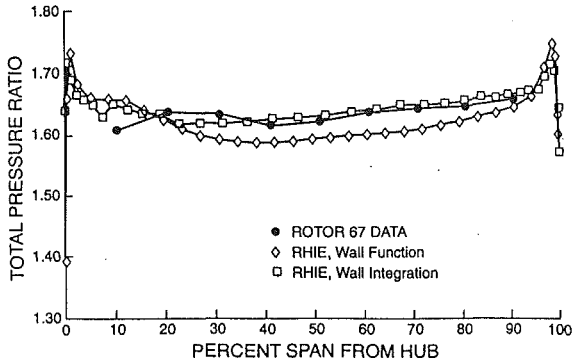

Fig. 9 Spanwise total pressure ratio profile at peak efficiency condition

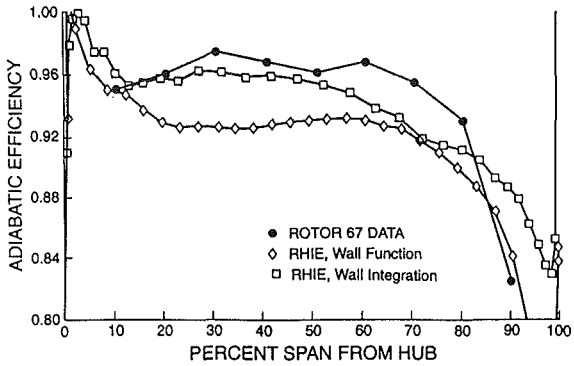

Fig. 10 Spanwise adiabatic efficiency profile at peak efficiency condition

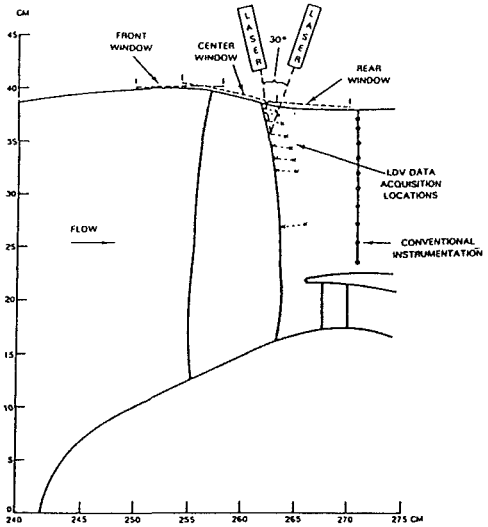

Fig. 11 Aerodynamic survey locations

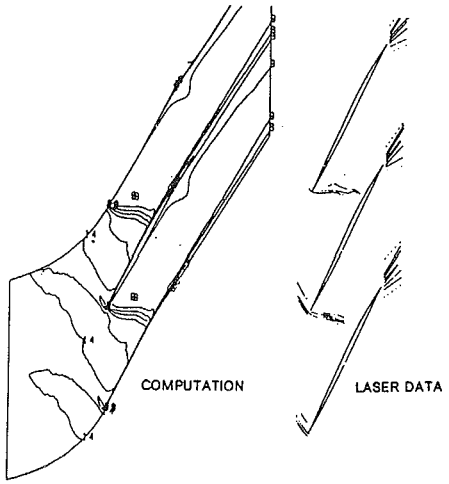

Fig. 12 Comparison of Mach contours between computation and laser data

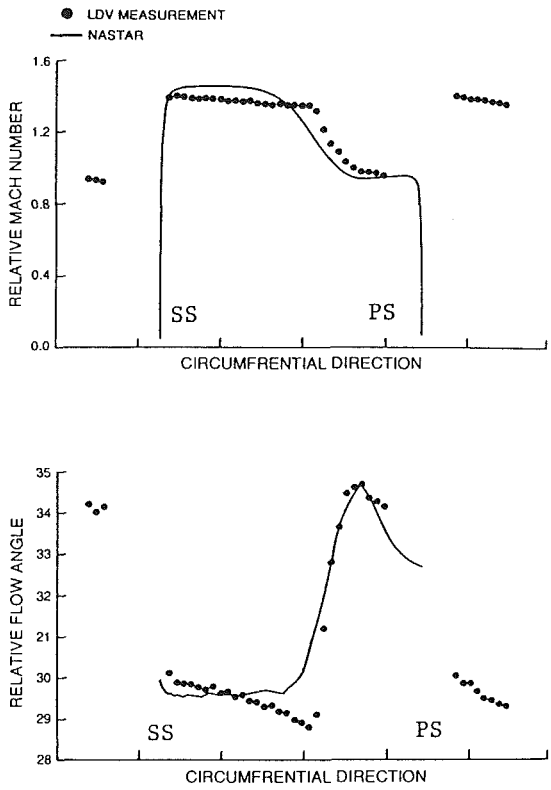

Fig. 13 Comparison of local Mach number and flow angle at 85 percent span/30 percent chord

to a better resolution of the boundary layer and the trailing edge separation. A detailed comparison of the data and the two near-wall treatments is shown in Figs. 9 and 10, where the circumferentially mass-averaged total pressure ratio and adiabatic efficiency are plotted as a function of radius at a station downstream of the trailing edge. These figures indicate that the wall integration method does a better job of matching the data than the wall function method, which suggests that the wall integration method should be used for design computations. A total of 108,000 grid points are used for both calculations. The grid stretching was different only in the blade-to-blade direction between two grids due to the boundary layer resolution requirement.

TS-27 Fan. Navier–Stokes analysis of a TS-27 fan tested under a NASA Lewis program has been carried out at peak efficiency at design speed. Extensive laser-Doppler velocimeter (LDV) data are available including documentation of interblade and intrablade velocities [15]. Figure 11 shows aerodynamic survey locations. Analysis was carried out with the wall integration method but without tip clearance using a $125 \times 35 \times 35$ grid. The Mach number contours are compared between the NASTAR computation and the LDV data in Fig. 12, where it is shown that the intrablade shock position is well captured by the computation. Intrablade Mach number and relative angle profiles are compared at 85 percent span/30 percent chord location in Fig. 13. The solution is slightly smeared due to the coarseness of the grid but it shows good

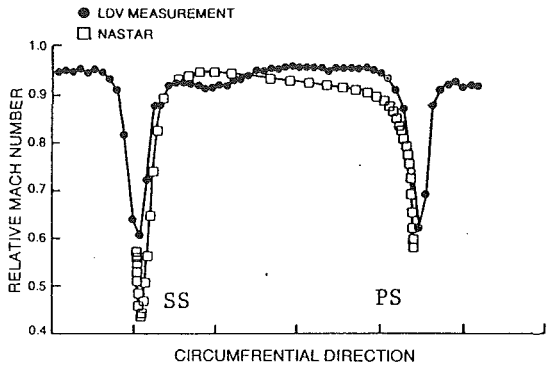

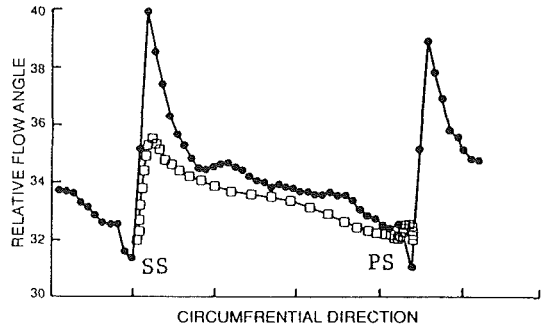

Fig. 14 Comparison of local Mach number and flow angle at 85 percent span/105 percent chord

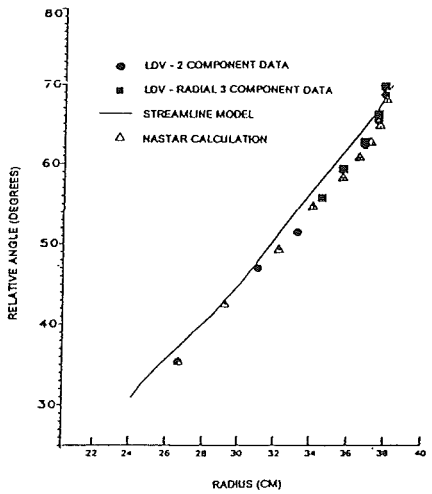

Fig. 15 Comparison of spanwise flow angle profile at 105 percent chord, peak efficiency

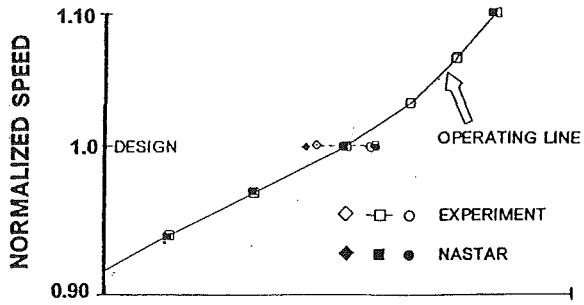

Fig. 16 Flow at low, design, and high rotor speeds

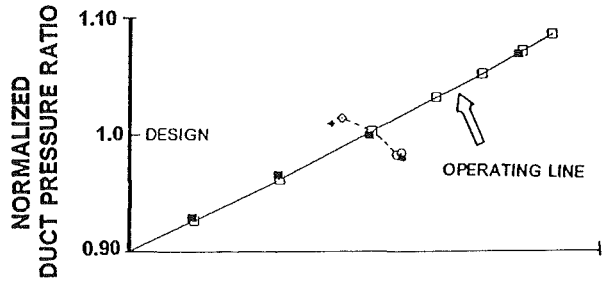

Fig. 17 Flow and total pressure ratio at low, design, and high rotor speeds

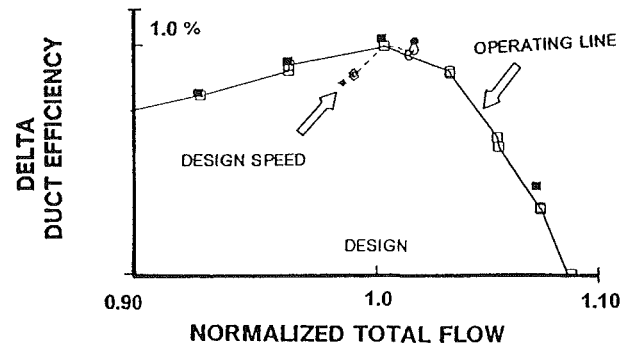

Fig. 18 Fan efficiency along the operating line and for the design speedline

comparison with the LDV data. The same profiles are compared for the blade wake at 85 percent span/105 percent chord location in Fig. 14. The computation shows a slightly lower minimum Mach number in the wake, even though it does a good job of capturing the wake characteristics. Similar trends are observed in other wake predictions including the two-dimensional calculations above. This shortcoming in the wake prediction may be due to the present wake turbulence modeling. A standard κ–ϵ turbulence model is used for the wake. The spanwise angle profile at 105 percent chord location is compared to the data and streamline model in Fig. 15. A substantial improvement over the streamline model prediction is shown.

Numerous other fan validation calculations demonstrated that the NASTAR code predicts the flow capacity, speedline shape, and the efficiency lapse rate on a consistent basis including a highly swept fan (NAFCOT [16]). Comparisons of spanwise profiles were also encouraging with the code predicting the pressure and temperature profile level and shape. This enables the designer to assess the performance differences between two designs.

Validation for Design Application

The primary aerodynamic requirement of an engine fan design is to meet the design point conditions for mass flow, total pressure ratio, and rotor speed at the peak efficiency conditions. Important off-design conditions must also be considered in the overall optimization. These include lower and higher rotor speed points along the engine operating lines associated with low and high power and the stall line points. The NASTAR code has demonstrated the capability to match overall fan performance along an operating line and along a speedline. The detailed flow field predictive capability of the NASTAR code is also used by the designer to optimize the fan blade shape radially by bringing the various fan blade airfoil sections to peak efficiency at the fan design point condition.

The configuration analyzed is a high aspect ratio blade with a part-span damper, duct/core flow splitter, and tip clearance. For this calculation, wall integration was used on a total grid

of 350,000 points. The result of the mass flow, speed, total pressure ratio, and efficiency analysis are shown in Figs. 16–18 relative to the experimental data taken from an engine in an altitude test facility. Figure 16 shows the rotor speed and flow relation at low, design, and high rotor speeds. At the design speed, the speedline is also defined by a series of three analysis points. Figure 17 shows the total pressure ratio and flow at low, design, and high rotor speeds. The comparisons in Figs. 16 and 17 show that the accuracy of the NASTAR analysis for this particular application is ± 0.5 percent flow on the operating line. The fan efficiency is shown in Fig. 18 along the operating line and for the design speedline. The comparison shows that the fan peak efficiency does in fact occur on the operating line and that the NASTAR analysis predicts this efficiency variation. Predicted near peak efficiency level is low by 0.2 percent relative to the experimental data.

Application to Current Products

The NASTAR code was applied during the design and development of the current PW4060 engine fan. Relying on the NASTAR code, rather than adhering to conventional design rules, an optimal fan design resulted with predicted performance superior to the previously tested engine fan. Engine testing of the new fan followed in an altitude test facility. Relative to the previously tested fan, the new design showed an increase of 0.5 percent in fan bypass duct adiabatic efficiency. In addition, the improved fan hub section performance provided more favorable aerodynamic inlet condition to the core low-speed compressor, resulting in a 1 percent increase in low compressor efficiency. This radially optimized fan also reduced positive inlet flow incidence at the tip, which resulted in a 3 percent increase in the transonic stall flutter boundary. The aerodynamic design changes were fully consistent with structural and engine installation requirements, permitting this new blade to go into immediate production for the PW4060 engine.

Conclusion

This paper describes the advanced capability of a Navier–Stokes procedure applied to fan designs. A number of comparisons between the experimental data and the computations during the validation phase demonstrated that the NASTAR code can accurately capture global performance levels at various operating conditions. The comparison of radial profiles also showed very good correlations. The success of the validation effort gained substantial credibility for NASTAR and pushed the code from the development stage into the fan design system.

The NASTAR code gives the designers the flexibility to evaluate a design. The use of the NASTAR code reduces the number of design/test iterations and allows the designer to analyze high risk unconventional types of designs. Preliminary screening of new concepts can now be accomplished without rig testing. This is a major change compared to the old design procedure where fan designs depended heavily on iterations between fan tests and designs.

References

1 Dawes, W. N., "A Numerical Analysis of the Three-Dimensional Viscous Flow in a Transonic Compressor Rotor and Comparison With Experimental Data," ASME JOURNAL OF TURBOMACHINERY, Vol. 109, 1987, pp. 83–90.

2 Von Backstrom, T. W., "Dawes and Denton Codes Applied to a Transonic Compressor Rotor," ASME Paper No. 90-GT-304, June 1990.

3 Adamczyk, J. J., Celestina, M. L., and Greitzer, E. M., "The Role of Tip Clearance in High-Speed Fan Stall," ASME JOURNAL OF TURBOMACHINERY, Vol. 115, 1993, pp. 28–39.

4 Hah, C., and Reid, L., "A Viscous Flow Study of Shock-Boundary Layer Interaction, Radial Transport, and Wake Development in a Transonic Compressor," ASME JOURNAL OF TURBOMACHINERY, Vol. 114, 1992, pp. 538–547.

5 Chima, R. V., "Viscous Three-Dimensional Calculations of Transonic Fan Performance," AGARD 77th Symposium on CFD Techniques for Propulsion Applications, Paper No. 21, NASA TM 103800, May 1991.

6 Weber, K. F., and Delaney, R. A., "Viscous Analysis of Three-Dimensional Turbomachinery Flows on Body Conforming Grids Using an Implicit Solver," ASME Paper No. 91-GT-205, June 1991.

7 Jennions, I. K., and Turner, M. G., "Three-Dimensional Navier–Stokes Computations of Transonic Fan Flow Using an Explicit Flow Solver and an Implicit κ–ϵ Solver," ASME JOURNAL OF TURBOMACHINERY, Vol. 115, pp. 261–272.

8 Dash, S. M., Beddini, R. A., Wolf, D. E., and Sinha, N., "Viscous/Inviscid Analysis of Curved Sub- or Supersonic Wall Jets," *AIAA J.*, Vol. 23, 1985, pp. 12–13.

9 Rhie, C. M., and Stowers, S. T., "Navier–Stokes Analysis for High Speed Flows Using a Pressure Correction Algorithm," *AIAA J. of Propulsion and Power*, Nov.–Dec. 1988, pp. 564–570.

10 Rhie, C. M., "Pressure Based Navier-Stokes Solver Using the Multigrid Method," *AIAA J.*, Vol. 27, No. 8, Aug. 1989, pp. 1017–1018.

11 Ni, R. H., and Bogoian, J. C., "Prediction of 3D Multi-stage Turbine Flow Field Using a Multi-grid Euler Solver," AIAA Paper No. 89-0203, 1989.

12 Davis, R. L., Hobbs, D. E., and Weingold, H. D., "Prediction of Compressor Cascade Performance Using a Navier–Stokes Technique," ASME JOURNAL OF TURBOMACHINERY, Vol. 110, 1988, pp. 520–531.

13 Strazisar, A. J., Wood, J. R., Hathaway, M. D., and Suder, K. L., "Laser Anemometer Measurements in a Transonic Axial-Flow Fan Rotor," NASA TP 2879, Nov. 1989.

14 Fottner, L., ed., "Test Cases for Computation of Internal Flows in Aero Engine Components," AGARD-AR-275, 1990, pp. 165–213.

15 Norton, J. M., Hobbs, D. E., Williams, R. D., House, R. D., and Harvey, W. B., "Energy Efficient Engine Hollow Fan Blade Technology, Vol. 1—Shroudless High Aspect Ratio Fan Rig, Part 2—Laser Doppler Velocimeter Test," NASA Contract Report 182221, Nov. 1989.

16 Neubert, R. J., Hobbs, D. E., and Weingold, H. D., "Application of Sweep to Improve the Efficiency of a Transonic Fan, Part 1—Design," Paper No. AIAA 90-1915, July 1990.

Detailed Flow Measurements and Predictions for a Three-Stage Transonic Fan

W. J. Calvert

A. W. Stapleton

Defence Research Agency,
Pyestock, Farnborough,
Hampshire, United Kingdom

Detailed flow measurements were taken at DRA Pyestock on a Rolls-Royce three-stage transonic research fan using advanced laser transit velocimetry and holography techniques to supplement the fixed pressure and temperature instrumentation. The results have been compared with predictions using the DRA S1-S2 quasi-three-dimensional flow calculation system at a range of speeds. The agreement was generally encouraging, both for the overall performance and for details of the internal flow such as positions of shock waves. Taken together with the computational efficiency of the calculations and previous experience on single-stage transonic fans and core compressors, this establishes the S1-S2 system as a viable design tool for future multistage transonic fans.

Introduction

The importance of computational methods in increasing the aerodynamic performance of turbomachinery and reducing development times and costs is now widely recognized. In order to gain the maximum benefit from the methods it is essential that careful validation/calibration is carried out (*a*) to assess the accuracy of the predictions and, if necessary, to allow the methods to be modified to improve the accuracy, and (*b*) to enable some understanding of previous designs to be gained and translated into the framework of the new technique. Acceptable levels of performance have been achieved in the past using empirically based methods, together with extensive development programs, and it would be extremely wasteful to ignore this hard-won experience.

Multistage transonic fans with fixed geometry are arguably the most difficult type of compressor to study. They clearly cannot be modeled by a low-speed experiment. The blade rows are generally closely spaced for optimum performance and this, together with the high flow Mach numbers, precludes obtaining accurate measurements with conventional traverse probes. The blading is usually close to choking, which makes the performance extremely sensitive to axial matching. Finally, the axial matching changes considerably at different speeds so that the blade sections have to operate over a wide range of conditions.

Several CFD techniques have been developed that can calculate the detailed flow and performance of multiple transonic blade rows (e.g., Adamczyk, 1985; Dawes, 1992). However, few applications to compressors have been published so far. This probably reflects both the difficulty of the problem and the computation times involved (Mulac and Adamczyk, 1992).

The objectives of the work presented in this paper were to take detailed flow measurements in an advanced multistage transonic fan, and to assess and calibrate the DRA S1-S2 calculation system for this type of compressor. The unit chosen as the test vehicle was a three-stage Rolls-Royce research fan with fixed geometry and a split flow delivery system (see Fig. 1), as might be used for an advanced RB199-type military engine. Inlet tip diameter was approximately 0.75 m. The fan was fitted with a special casing for the tests at DRA Pyestock to allow laser velocimetry and holography measurements to be taken of the flows within the blade rows. These measurements, together with data taken on a previous build at Rolls-Royce using fixed instrumentation—casing static pressure tappings, stator leading edge pressure and temperature probes, and downstream rakes—have been compared with predictions from the S1-S2 system, concentrating on operating conditions corresponding to engine cruise and maximum speed.

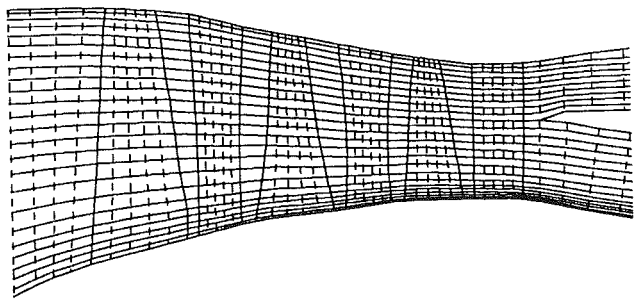

Fig. 1 Annulus and streamline pattern at maximum speed point

Laser Measurement Techniques

As with all optical measurement techniques, both the velocimetry and the holography were constrained by the test environment. Figure 2 shows the test rig with the windows fitted. The pipe-work surrounding the windows was for the window washing system. With the window size being limited by mechanical constraints, optical access for both systems was

Contributed by the International Gas Turbine Institute and presented at the 38th International Gas Turbine and Aeroengine Congress and Exposition, Cincinnati, Ohio, May 24-27, 1993. Manuscript received at ASME Headquarters February 12, 1993. Paper No. 93-GT-9. Associate Technical Editor: H. Lukas.

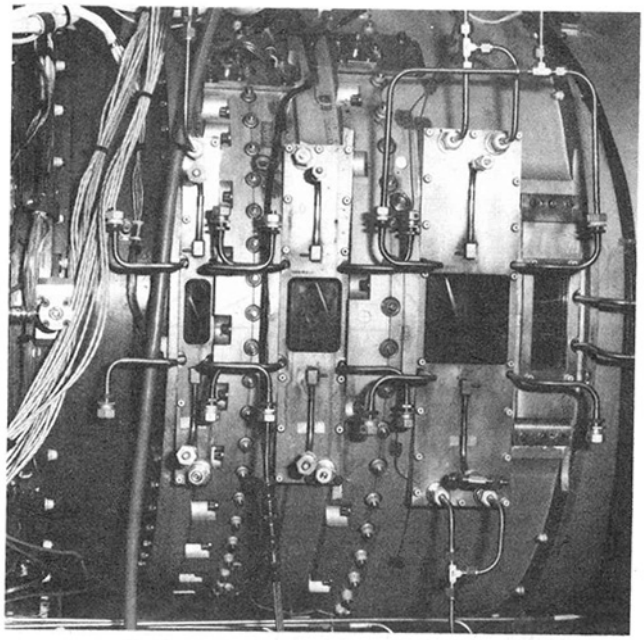

Fig. 2 Fan casing showing laser windows

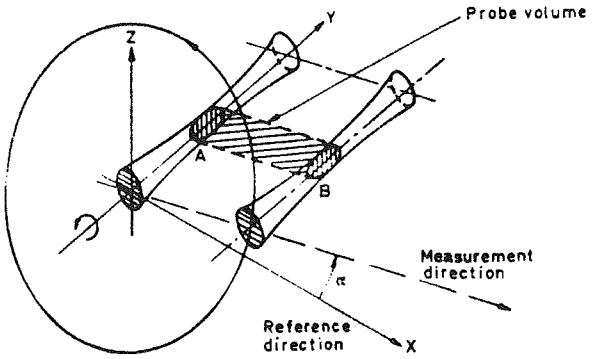

Fig. 3 Schematic of L2F measurement technique

difficult. Oil contamination on the windows also generated significant problems and in the worst case prevented measurements from being taken.

The Laser Velocimetry System. The velocimeter used for these tests was a laser-dual-focus (L2F) system similar to that described by Schodl (1980). The basic principles behind this form of velocimetry are fairly straightforward and a schematic diagram is shown in Fig. 3. Two parallel, highly focused light beams form a probe volume within the compressor airflow. The diameter of each beam at the focus is about 10 μm and the separation distance can be between 250 and 500 μm depending upon the selected transmitting optics. For these tests a focal length of 430 mm was used, which gave a beam separation of 365 μm. The resulting angle between the two transmission beams was approximately 6 deg and the included angle of the receiving optics was approximately 13 deg.

The L2F system measures the time of flight of fine particles (either naturally occurring or deliberately introduced into the flow) traveling between the on-axis beam, A, and the off-axis beam, B. This is done by correlating the pulses of reflected light that occur when a particle passes through the spots. As the diameter of the spots is small compared to their separation, most correlated pulses will only occur when the spots are aligned with the flow direction. The off-axis beam can be rotated around the on-axis one and so, by taking many time-of-flight measurements over a range of different measurement directions (typically 60), a two-dimensional probability histogram

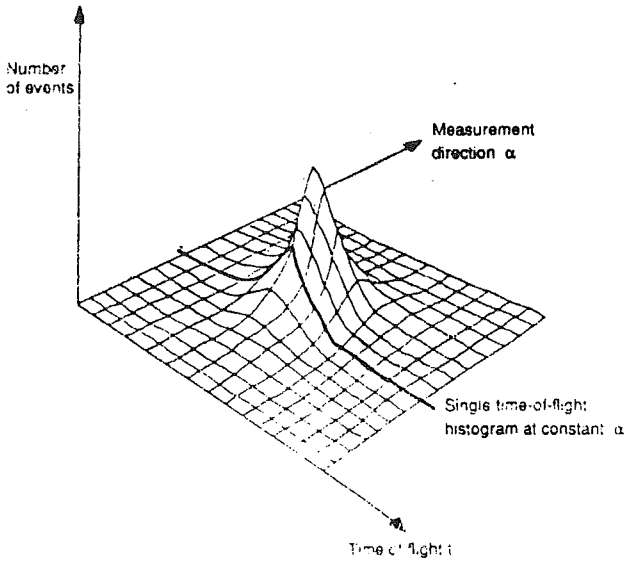

Fig. 4 Two-dimensional probability histogram constructed from measured L2F data

can be produced (Fig. 4). From this the average absolute flow velocity and flow angle at the measurement position can be calculated along with an estimate of the turbulence. As the rotor sweeps past the probe volume, data can be acquired in 16 individual measuring locations (time windows) across the rotor passage. This technique can be used to obtain data within a specific blade passage or an average for all blade passages. However, the increased collection time required to obtain measurements in a single blade passage means that it is not usually practical to collect anything other than average values.

Two sets of laser viewing windows were used, a flat set and a curved set. Curved windows produce less interference with the air flow because discontinuities in the casing geometry are reduced. However, curved windows distort the laser beams and result in significant measurement uncertainties at large probe volume immersions. For this reason plane parallel windows, which do not distort the beams, were used for all measurements except in the tip region.

Flow Seeding Methods. Laser velocimetry measurements rely upon light being scattered back from small particles traveling within the airflow. These particles must be large enough to provide a reasonable level of reflected light but, at the same time, must be small enough to follow the flow correctly. The concentration of particles must be sufficient to give a high data rate. Natural seeding from dust and pollen particles is unreliable as the size and quantities vary considerably from day to day. For this reason it is common practice to add artificial seeding to the airflow.

Flow seeding was carried out on this rig using an oil mist generator, which had previously been found to produce particles of a suitable size (i.e., up to 0.5 μm). Seeding was injected into the compressor air flow using a 10-mm-dia, circular cross-sectional, "hockey stick" probe. This probe was mounted on a traverse system located approximately 0.75 m upstream of the first rotor. Both the traverse system and the seeding generator were operated from the facility control room, with the traverse gear providing movement in the radial and yaw directions. In addition, the section of the inlet ducting that held the seeding probe could be rotated, by hand, from within the test cell. This combination of radial, circumferential, and yaw movement enabled seeding to be directed to the optimum location for each traverse in turn.

Measurement Accuracy. The laser velocimetry data were analyzed using the technique developed by Schodl (1980). This

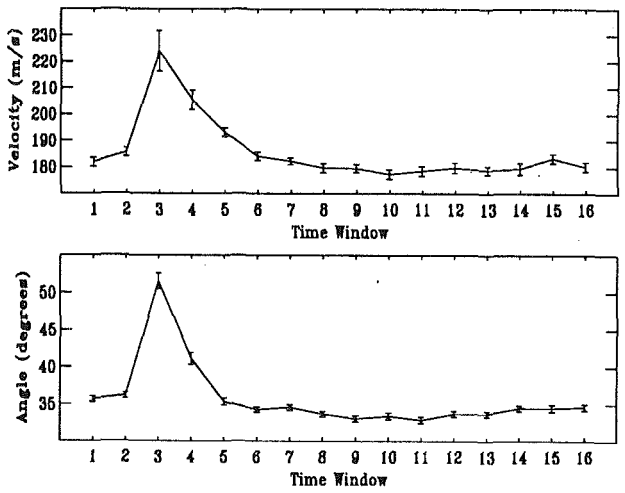

Fig. 5 Measurement uncertainty at rotor 1 exit, cruise, 70 percent blade height

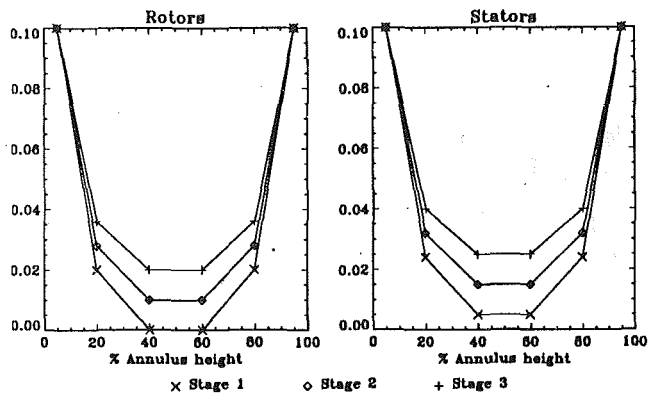

Fig. 6 Extra loss coefficients for S1-S2 prediction

replaces the two-dimensional frequency distribution (Fig. 4) with two one-dimensional distributions (called marginal distributions) in terms of numbers of events versus time of flight and spot rotation angle, respectively. As a result the mathematics are simplified and the amount of data required to define the distributions satisfactorily is reduced. The small errors introduced have been shown by Schodl to be less than 1 percent of the velocity components and less than 5 percent of the turbulence intensity for turbulence levels up to 20 percent.

Figure 5 gives an example of the typical analysis errors generated by the L2F system. It shows the measured absolute values of velocity and flow angle at a single measurement point at the exit from the first rotor. The horizontal axes show the 16 time windows into which the rotor pitch is divided. At each measurement location the number of time-of-flight measurements taken was the same, but the measurement time increased toward the rear of the machine. This was due to increased window contamination and more limited optical access. These led to more flare and a lower signal-to-noise ratio, and hence a lower data rate. For the present tests, measurement times (including data processing and movement to the next location) were between 4 and 6 minutes per point.

The analysis errors shown in Fig. 5 are about ± 1.8 m/s and ± 0.4 deg, except in the region of the rotor wake where the errors are larger due to increased turbulence. Behind rotor 2 the errors in the free-stream region were a little larger, typically ± 2.5 m/s and ± 0.6 deg. This increase is comparatively modest, bearing in mind the problems of greater oil contamination, increased free-stream turbulence due to the wakes from the upstream stators, and "turbulence" due to the different number of blades in rotors 1 and 2. In areas of severe oil contamination or very high flow turbulence these measurement uncertainties can be much higher and, at times, unacceptable. Within rotor 3, where measurement conditions were worst, collection time increased dramatically due to low signal-to-noise ratios, and errors were typically of the order of ± 6 m/s and ± 1.5 deg. This, combined with limited data coverage due to the small window size and severe oil contamination, resulted in measurements within the third rotor being abandoned.

The Laser Holography System. The laser holography measurements were conducted by personnel from the Rolls-Royce Advanced Research Laboratory. The system used a pulsed Ruby laser, the light from which was inserted upstream of the viewing window and reflected off the inside of the inlet duct, which had been painted white for this purpose. A full description of the technique is given by Parker (1990). A novel feature of the experiments on this rig was the successful attempt to obtain holograms of the second rotor by inserting the laser light through the first rotor window and reflecting it up off the first stator platform.

S1-S2 Calculation System

The DRA S1-S2 calculation system has been developed over a number of years to provide a technique capable of predicting both the overall performance and the internal flow of a wide range of compressors. The system consists of three main parts:

(*i*) The S1BYL2 inviscid-viscous interaction technique (Calvert, 1982) calculates the blade-to-blade (S1) flow of a number of sections along the span of each row in the compressor.

(*ii*) The SC90 streamline curvature throughflow method (developed from the code due to Ginder, 1984, by Dunham et al., 1990) calculates the passage-averaged hub-to-tip or meridional (S2) flow for the whole compressor, using the blade element data from (*i*).

(*iii*) A blade geometry routine calculates the intersections between specified axisymmetric stream surfaces from (*ii*) and the three-dimensional blade shapes, and hence produces revised data for S1BYL2.

A semi-automatic version of the system is described by Calvert and Ginder (1985). This has now been automated with all three parts incorporated into a single computer program.

The S1BYL2 technique produces *a priori* predictions for the blade element performance, including features such as shock wave/boundary layer interactions, and so no empirical input is required for blade deviation angles or for blade profile and shock losses. However, losses arising from secondary flows, annulus wall boundary layers, spanwise mixing, and tip clearance are not predicted by the current S1-S2 treatment. Therefore appropriate distributions of extra loss must be specified as an input. These were based on previous experience with single-stage fans (e.g., Calvert, 1991), with a small allowance for spanwise mixing and blade row interaction effects (Fig. 6). (Note: Spanwise mixing was not expected to have a major effect on the performance of this fan and so spanwise mixing terms were not included in the throughflow solution. However, smoothing of up to 0.4 deg was applied to the deviation angles of rotor 1 at the maximum speed condition to avoid a slight spanwise instability between the S1 sections.) The only other empirical input required is the level of annulus blockage, which was increased by 1/2 percent per blade row from a value of 2 percent at inlet. Additional blockage of up to 2 percent was included at the interblade planes within rotor 3 to allow for the snubber (or part-span clapper) on this row, and there was assumed to be a residual effect of 1 percent downstream of the row. The parameters listed above were held constant for all predictions of the fan.

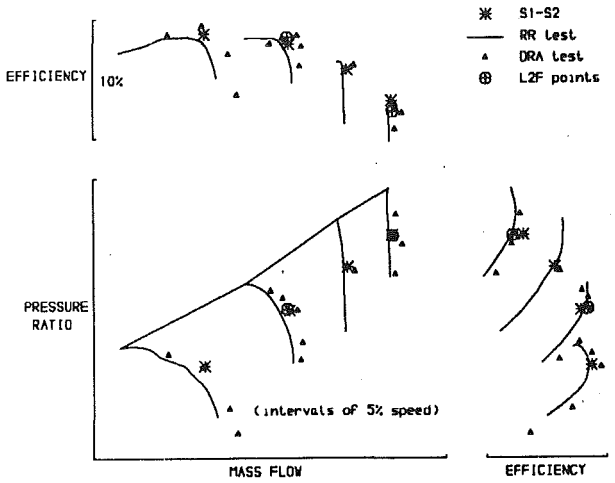

Fig. 7 Fan overall performance characteristics

The general features of the S1-S2 calculations were similar to those employed previously for single-stage fans. Thus the S2 throughflow method employed curved calculating planes at the leading and trailing edges of each of the six blade rows and four interblade planes were equally spaced in between. A total of 25 streamlines were used, 15 in the core flow and 11 in the bypass. The annulus and a typical streamline pattern are shown in Fig. 1. Blade-to-blade (S1) calculations were carried out at six sections per blade row, at heights of 5, 20, 40, 60, 80, and 95 percent, respectively. The grids for the inviscid flow part of these S1 calculations employed 119 planes in the axial direction, with 81 points equally spaced between leading and trailing edges, and up to 21 points in the pitchwise direction. Blade geometry was provided by Rolls-Royce in the form of profile coordinates on plane sections and small corrections were made to allow for the changing amount of untwist with speed.

The standard convergence criteria were adopted for the solutions: viz., S1 and S2 relative flow angles agreeing to within ± 0.1 deg, and streamtube thickness variations, blockage, and total pressure levels agreeing to ± 0.1 percent for all the blade-to-blade sections.

The computer power required for the S1-S2 system is very modest by modern standards, and solutions can be obtained on a low-cost workstation such as a VAXstation 4000 model 60. The time required for a complete solution of the three-stage fan is highly dependent on the difficulty of the blade section operating conditions and the closeness of the initial S2 solution to the final prediction, but it is of the order of 25 hours CPU on the VAXstation (or about 6 hours on an IBM RS6000 model 350 workstation).

Comparisons With Conventional Measurements

The measured overall performance characteristics for the fan at high speeds are shown in Fig. 7, together with the S1-S2 predictions along a typical engine working line. There are differences of about 1/2 percent in mass flow and 1/2 percent in efficiency between the tests at Rolls-Royce and the initial calibration at DRA. These might be due to the different casings for the laser test, to slight changes in the inlet flow between the two facilities, or to differences in the absolute accuracy of the two facilities. The differences disappeared during the laser tests as the blading became dirty. The S1-S2 solutions agree with the test results to within this level of uncertainty, and it is encouraging that the variation in efficiency with speed is modeled correctly without any changes to the end losses assumed.

The laser velocimetry measurements were taken at conditions

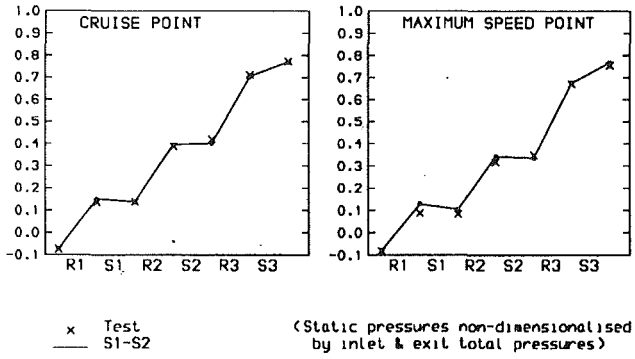

Fig. 8 Casing static pressure distributions

approximating cruise and maximum speed, and the comparisons between test and calculation will concentrate on these two points.

Casing Static Pressure Levels. The predicted casing static pressure levels from the S1-S2 solutions are compared with the test values in Fig. 8. The data are plotted in the form of coefficients relative to the inlet total pressure and the rise in total pressure, so that the effect of any difference in overall total pressure ratio is reduced. The predictions generally agree well with the test data at all positions along the casing at both operating conditions, suggesting that the predicted axial matching is about right. In particular it should be noted that the increase in the nondimensional pressure rise across rotor 3 with increasing speed is correctly modeled, and also the slight reduction in the pressure rise across rotor 1.

Stator Leading Edge Instrumentation. Two stator blades in each stage of the fan were fitted with 10 sensors to measure either total pressure or total temperature. In addition there were comprehensive rake systems in the core and bypass duct approximately 3 1/2 chords downstream of stator 3 trailing edge, which indicate the exit radial profiles of total pressure and temperature as well as allowing the overall performance to be deduced.

The radial profiles of total pressure, total temperature, and the corresponding adiabatic efficiencies are shown in Fig. 9. This type of presentation gives the most direct comparison with the measurements, but it masks the fact that the resulting mean efficiencies for stator 1/rotor 2 and for stator 2/rotor 3 are unbelievably high (i.e., close to 100 percent at the cruise point), whereas that for rotor 1 seems rather low. This illustrates the difficulty of obtaining high-accuracy measurements within this type of compressor. Given the uncertainty about the exact levels of the measured data, the agreement between prediction and test is generally considered to be reasonable. Some spanwise mixing of the flow is apparent from the flattening of the measured temperature profiles between the inlet to stator 3 and the downstream rakes, which the current calculation system does not model.

A common feature of both operating conditions is that the measured total pressure, and hence efficiency, tended to fall near the inner wall of the bypass delivery duct. This was probably caused by high incidence levels onto the splitter between the core and bypass ducts. The present S1-S2 system cannot model the pressure loss because the throughflow treatment assumes that the flow downstream of stator 3 is isentropic. However, the high incidence onto the splitter is illustrated by the predicted streamline pattern in Fig. 1.

Comparisons With Laser Velocimetry

For the following comparisons, the velocities measured by the laser velocimeter were converted into Mach numbers using (*a*) the measured inlet temperature for the inlet radial trav-

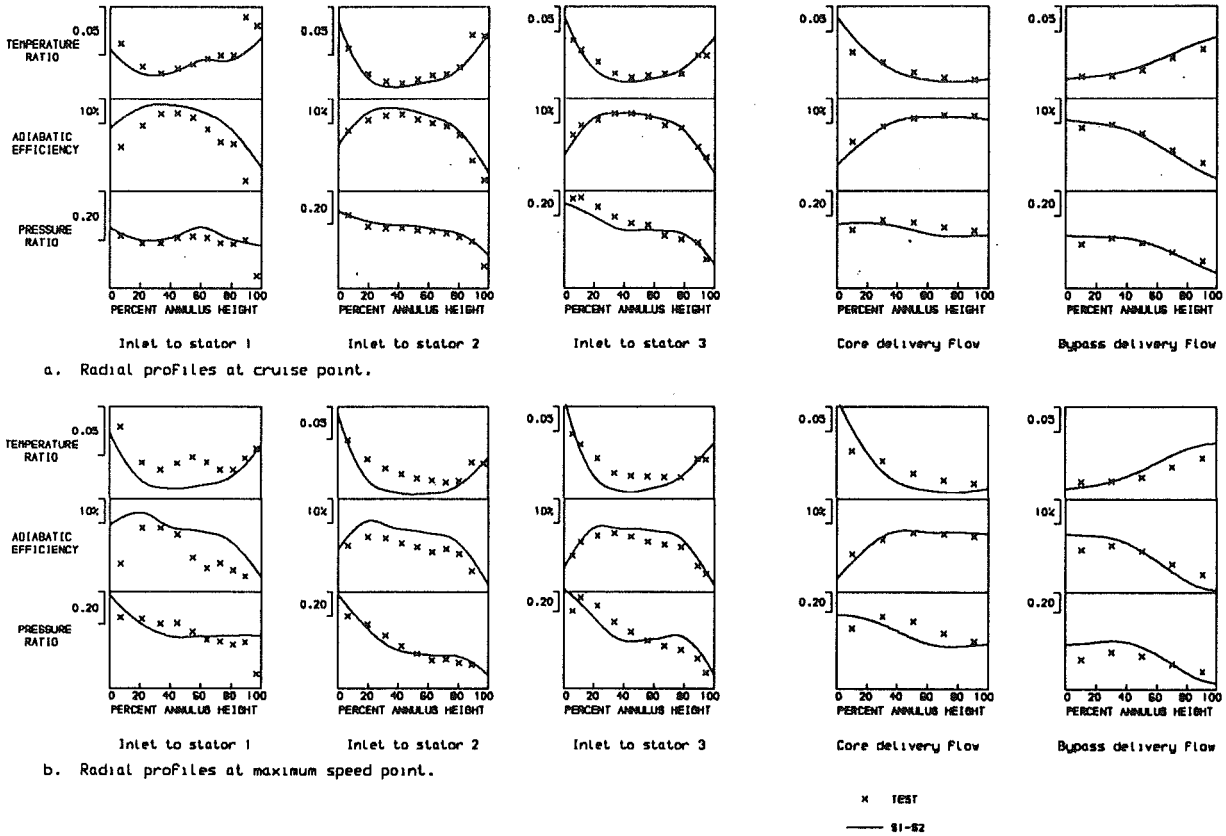

Fig. 9 Comparisons with stator leading edge and exit rake data

erses, (*b*) the measured inlet temperatures and swirl velocities and the Euler work equation for the rotor 1 traverses, and (*c*) the temperatures measured at stator 1 leading edge, the predicted exit swirl from stator 1, and the Euler work equation for rotor 2. It has already been noted that the stator 1 temperature measurements may not be very accurate, but the Mach number levels are relatively insensitive to this.

Inlet Radial Traverses. The agreement between the pitchwise-averaged laser measurements and prediction at the inlet traverse plane approximately one axial chord upstream of the first rotor is generally good at both operating conditions, i.e., within 0.01 on axial Mach number. However, the laser data indicated a larger casing boundary layer than measured by the inlet boundary layer rake. This discrepancy has not been explained: On the one hand the boundary layer rake data seem more plausible, but on the other the laser measurements were double-checked during the tests.

A noticeable feature of the laser measurements is a pitchwise variation of about ±6 percent on absolute Mach number over the outer half of the annulus, presumably due to shock waves from rotor 1. The S1BYL2 solutions do not model this very well, even with a finer grid and extended upstream flow field, but it is thought that the resulting errors in predicted blade section performance are small.

The measurements indicated a mean inlet swirl of about 1 deg across most of the annulus, whereas the S1-S2 solutions assumed zero swirl. There is no obvious reason for the inlet system on the DRA facility to produce any bulk inlet swirl and it was therefore decided not to change the S1-S2 solutions. The effect on the calculations would be quite small.

Rotor Exit Radial Traverses. The laser velocimeter was generally successful in obtaining complete traverses downstream of rotors 1 and 2 at both operating conditions. However, some gaps occurred in the wake region, and the resolution of the blade wakes was insufficient to allow accurate mixed-out values to be calculated for comparison with the predicted values in the S2 throughflow solution. In order to avoid this problem it is useful to compare the average free-stream values (see Fig. 10). The laser data were derived by mass flow averaging the pitchwise data at the points where the relative flow velocities were greater than 95 percent of the average of all the pitchwise points. For this averaging, the local static pressure and the rotor inlet total temperature and swirl velocity were assumed to be constant across the blade pitch. The S1BYL2 data are the mass-flow-averaged values of the inviscid flow at the traverse plane, corrected to remove the component of flow in the direction of the laser beams (which the laser does not measure). The S1BYL2 mixed-out values are also shown for information.

At the cruise point the agreement between prediction and test is very encouraging for both rotor 1 and 2 (Figs. 10*a*, *b*). The only significant discrepancy for rotor 1 occurs near the tip where the measurements may be indicating the presence of the casing boundary layer. There seems to be more scatter for the measurements at rotor 2 exit. A contributing factor to this is that the points nearest the tip were taken at a different time and with a different inclination of the laser beams, which would tend to reduce the measured flow angles and increase the measured flow Mach numbers (the corrections to the S1BYL2 data assumed a constant beam inclination at all positions).

At the maximum speed point there are differences between predicted and measured absolute flow angles for rotor 1 near 40 percent height and in the tip region (Fig. 10*c*). At this condition the relative flow across the blade pitch was partly supersonic near the tip, with shock waves present at the traverse plane. This means that it is difficult to distinguish between measurements in the free-stream and wake regions of the flow. The simple rule of discarding points with relative velocities less than 95 percent of the average will produce overestimates of the mean free-stream relative Mach number and underestimates of the absolute flow angle, and this explains much of

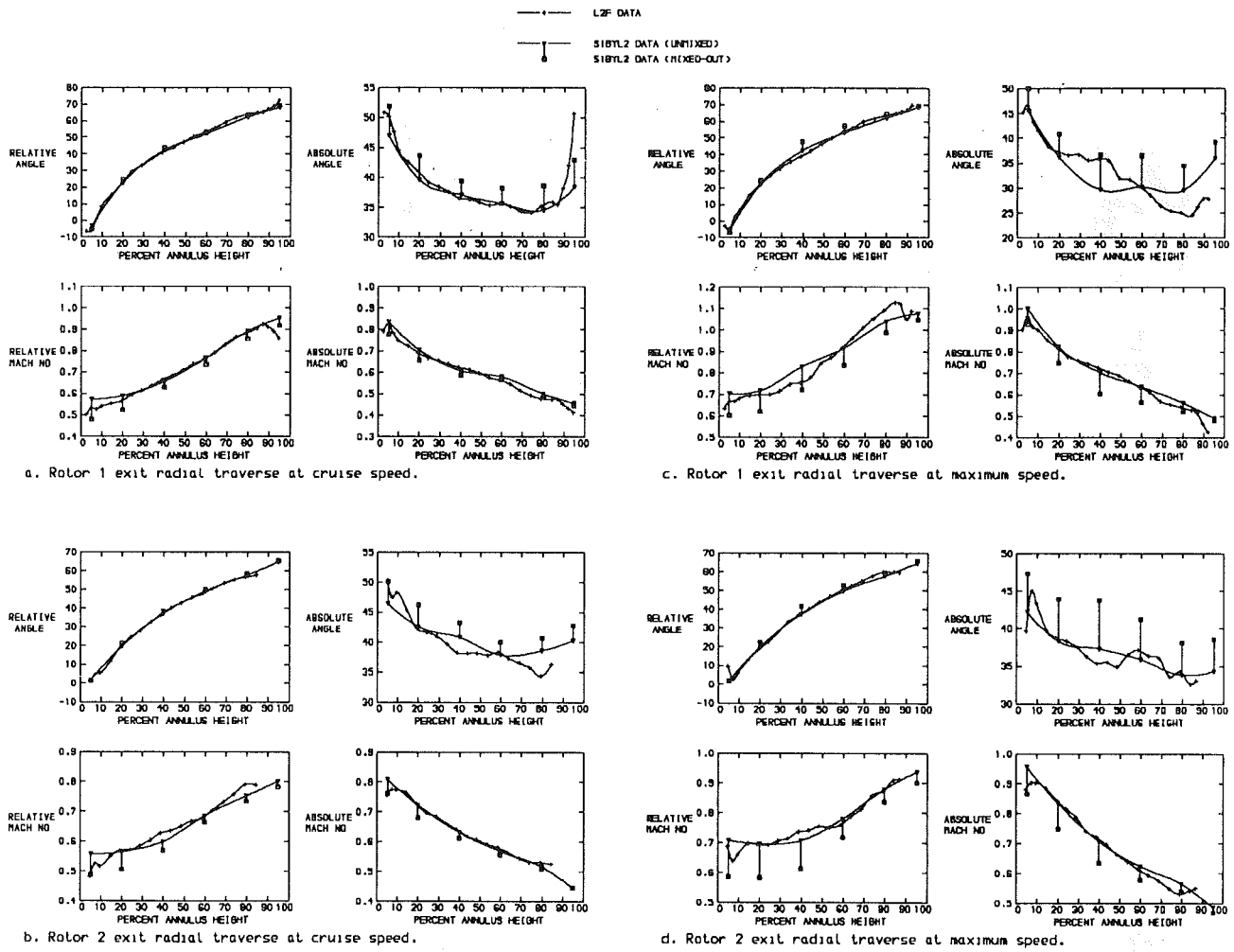

Fig. 10 Comparisons with L2F radial traverses at rotor exit

the discrepancy between prediction and test over the outer 30 percent of the annulus. At rotor 2 exit (Fig. 10*d*) the agreement is better.

An interesting feature of all four comparisons is that rotor deviations over the outer half of the annulus tend to be underestimated. The discrepancies are small, but they contrast with traditional radial deviation corrections (e.g., Robbins et al., 1965), which reduce the levels of deviation over the outer part of rotor rows. There is little evidence to support the increases in deviation that are sometimes assumed near the hub of fan rotors.

Rotor Axial Traverses. Three axial traverses were obtained in rotor 1 and two in rotor 2 at both operating conditions. The results in rotor 1 are of greater interest since the shock waves were stronger and the changes in shock position with speed larger, and the coverage of the blade passage by the laser measurements was also better. The contours of relative Mach number deduced from the measurements at 70 and 85 percent span for the two conditions are shown in Fig. 11, together with the corresponding S1BYL2 predictions. The blanked-out regions on the test plots indicate the areas where no measurements were possible; the approximate positions of the blade sections are also indicated to facilitate comparisons.

The main features that should be compared are shock positions and Mach number levels. The shapes of the contour lines, except at shock waves, are less important since they tend to be very sensitive to small errors in the data and they can sometimes change significantly if a different value is chosen for the contour level. Also care must be taken to allow for the restricted coverage of the test data in the blade leading edge region due to oil contamination on the windows.

At the cruise condition the agreement between prediction and test is generally good. Shock positions match up well and the Mach number levels are reasonably predicted. The re-acceleration of the passage flow near the pressure surface is also correctly modeled.

At maximum speed the shock was significantly farther back in the blade passage. The shock wave/boundary layer interaction was stronger, causing the shock diffusion to be more spread out near the blade suction surface, and the flow re-accelerated to supersonic speeds downstream of the shock near the pressure surface. All these features were correctly predicted by the S1-S2 calculations. The presence of an oblique shock wave running into the blade passage from the leading edge can be detected in both measurements and predictions, but it is weak and not very clear.

In some of the comparisons, the Mach numbers immediately downstream of the main shock wave are slightly underestimated. The discrepancies are quite small, typically about 0.05, and they disappear downstream as indicated by the comparisons with the rotor exit traverses. They probably occur because the real shock was more oblique than predicted: In this context it should be remembered that the S1 solutions assume that the shock front is normal to the stream surface, whereas it is generally slightly swept.

Comparisons With Laser Holography

Holographic flow visualization was carried out in the first

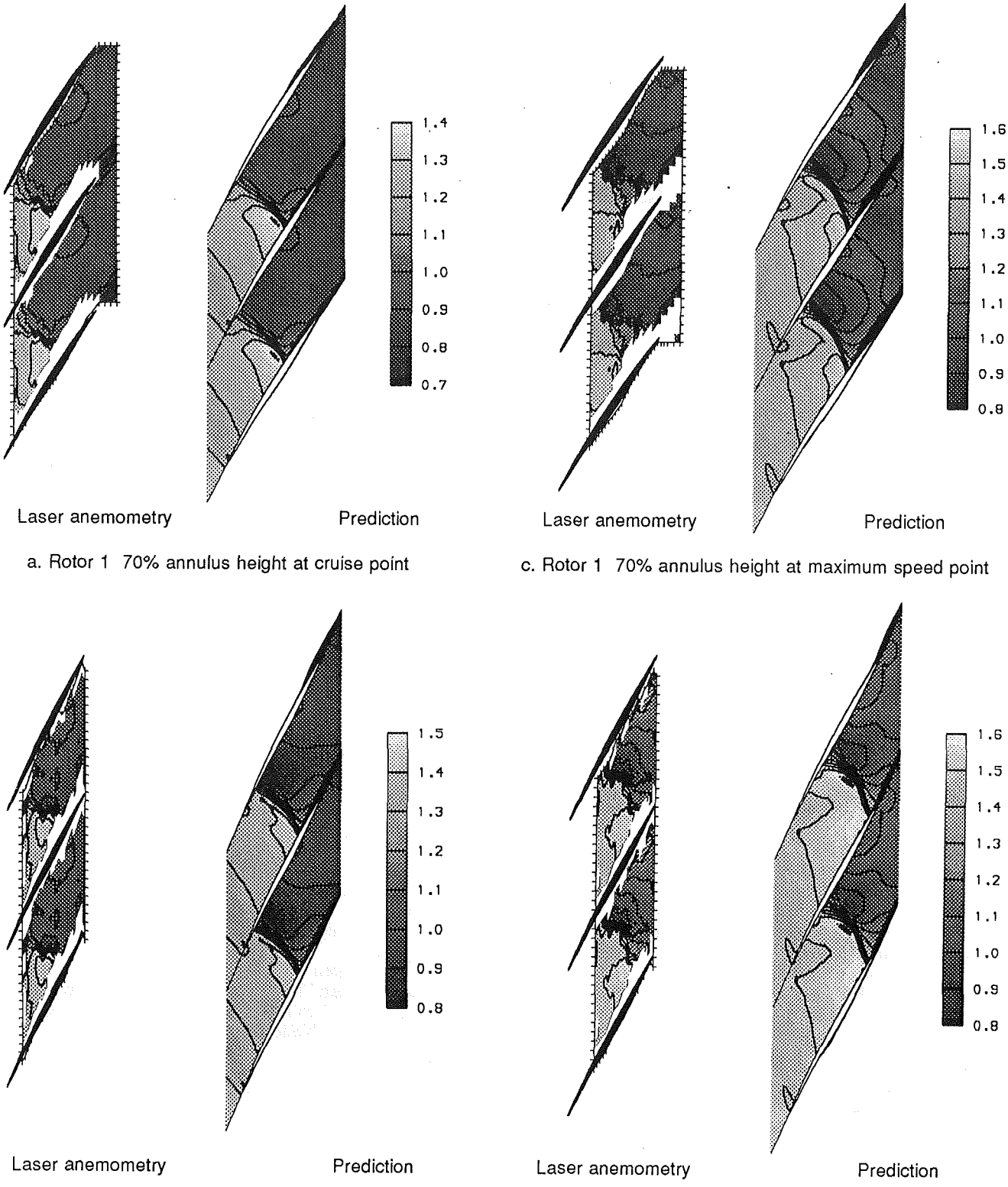

Fig. 11 Comparisons of relative Mach number contours in rotor 1

two rotors of the fan and around 100 holograms with useful information were obtained. As for the laser velocimetry measurements, the contamination of the viewing windows with oil gave some problems and it probably reduced the extent to which shock waves were visible inboard of the blade tip region.

The holograms needed to be viewed directly in order to interpret them properly, and great care was needed in identifying the spanwise positions of the visible flow features. Observations were generally consistent with the flow features measured by the laser velocimeter and predicted by the S1-S2 system. In particular they confirmed the change in shock structure for the tip of rotor 1, from a normal shock at inlet to the

blade passage at the lowest speed studied, to an oblique shock from the blade leading edge running back into the passage and past the trailing edge of the adjacent blade at the highest speed. However, it was clear than in some cases the most visible feature in the holograms was not the most important feature in the flow field. For example, the oblique shock wave at the blade tip tended to dominate the holograms at the higher speeds, but it was actually quite weak and only showed up on the Mach number contours if the contour interval was small.

Conclusions

Detailed flow measurements have been taken at two operating conditions in an advanced three-stage transonic fan, using a two-spot laser velocimeter and laser holography. The measurements, together with data from the fan conventional instrumentation, have been compared with predictions from an S1-S2 calculation system. The empirical input required by the calculations (i.e., levels of annulus blockage and extra losses to allow for blade-end effects) was based on previous experience and held constant at both conditions. The agreement obtained was encouraging. Overall performance was well predicted and the internal flows generally agreed with the measurements to within the accuracy of the data. However, there were some discrepancies due to basic limitations in the S1-S2 technique.

As a result of the comparisons made above, and previous experience with single-stage transonic fans (e.g., Calvert et al., 1987) and multistage core compressors (e.g., Ginder, 1991), it is believed that the current S1-S2 technique is a viable design tool for future multistage transonic fans. The technique is well-suited to design optimization, since it allows blade sections to be studied individually and then incorporated into the complete compressor environment using the same system. Two or more operating conditions can be considered during the optimization in order to allow the requirements for cruise and high-speed performance to be balanced.

Acknowledgments

The fan studied is a Rolls-Royce research unit and the initial calibration was carried out at Rolls-Royce, Bristol. The authors wish to thank Messrs. D. V. Roberts and M. Reeves of Rolls-Royce for providing the fan geometry and carrying out the laser holography, and their colleagues at DRA Pyestock for their help during the laser test program.

This work was jointly funded by the UK Ministry of Defence and Department of Trade and Industry.

References

Adamczyk, J. J., 1985, "Model Equation for Simulating Flows in Multistage Turbomachinery," ASME Paper No. 85-GT-226.

Calvert, W. J., 1982, "An Inviscid-Viscous Interaction Treatment to Predict the Blade-to-Blade Performance of Axial Compressors With Leading Edge Normal Shock Waves," ASME Paper No. 82-GT-135.

Calvert, W. J., and Ginder, R. B., 1985, "A Quasi-Three-Dimensional Calculation System for the Flow Within Transonic Compressor Blade Rows," ASME Paper No. 85-GT-22.

Calvert, W. J., Ginder, R. B., and Lewis, G., 1987, "Performance of a Civil Fan Rotor Designed Using a Quasi-Three-Dimensional Calculation System," *Proc I Mech E*, Paper No. C257/87.

Calvert, W. J., 1991, "Application of the RAE S1BYL2 Method to the AGARD WG18 Compressor Test Cases," AGARD-CP-510.

Dawes, W. N., 1992, "Toward Improved Throughflow Capability: The Use of Three-Dimensional Viscous Flow Solvers in a Multistage Environment," ASME JOURNAL OF TURBOMACHINERY, Vol. 114, pp. 8–17.

Dunham, J., et al., 1990, "A New Turbomachinery Throughflow Program Using the Streamline Curvature Method," unpublished RAE Report.

Ginder, R. B., 1984, "A Streamline Curvature Throughflow Calculation for Transonic Axial-Flow Compressors, Including Stations Within the Blade Row," *Proc I Mech E*, Paper No. C65/84.

Ginder, R. B., 1991, "Design and Performance of Advanced Blading for a High-Speed HP Compressor," ASME Paper No. 91-GT-374.

Mulac, R. A., and Adamczyk, J. J., 1992, "The Numerical Simulation of a High-Speed Axial Flow Compressor," ASME JOURNAL OF TURBOMACHINERY, Vol. 114, pp. 517–527.

Parker, R. J., 1990, "Practical Developments in Holographic Interferometry," *Aero. J. of the Royal Aero. Soc.*, Mar., pp. 91–98.

Robbins, W. H., Jackson, R. J., and Lieblein, S., 1965, "Blade Element Flow in Annular Cascades," Chap. VII, NASA SP36.

Schodl, R., 1980, "A Laser-Two-Focus (L2F) Velocimeter for Automatic Flow Vector Measurements in the Rotating Components of Turbomachines," *Measurement Methods in Rotating Components of Turbomachinery*, B. Lakshminarayana, ed., ASME, New York, pp. 139–147.

K. J. Kutz

T. M. Speer

MTU Motoren- und Turbinen-Union
München GmbH,
Dachauer Strasse 665,
D-80976 Munich 50,
Federal Republic of Germany

Simulation of the Secondary Air System of Aero Engines

This paper describes a computer program for the simulation of secondary air systems. Typical flow system elements are presented, such as restrictors, tappings, seals, vortices, and coverplates. Two-phase flow as occurring in bearing chamber vent systems is briefly discussed. An algorithm is described for the solution of the resulting nonlinear equations. The validity of the simulation over the engine operation envelope is demonstrated by a comparison with test results.

1 Introduction

Moore (1975) reviewed the importance of the secondary air system for the safety, reliability, and performance of an aero engine and the corresponding design problems.

To meet the increasing demands of engine design, improved simulation tools are required for the prediction of the air system behavior over a variety of operating conditions.

This paper reviews a computer program for the simulation of secondary air systems. It shows the modeling of an air system as a network of pipes and chambers and presents the physical relations governing it. This is followed by a presentation of typical flow system elements, such as restrictors, tappings, seals, vortices, and cover plates. Two-phase flow as occurring in bearing chamber vent systems is briefly discussed.

Thereafter, the algorithm is described for the solution of the resulting nonlinear equations. This involves the decoupling of the pipes and several nested levels of iterations, which refer to the computation of mass flows through flow elements, pipe flows, nodal pressures, and chamber temperatures.

Furthermore, existence and uniqueness of the solution are shown for the fixed temperature case.

The validity of the simulation over the engine operation envelope is demonstrated by a comparison with test results.

A predecessor of the simulation program presented has been described by Suntry (1963). This included, however, only a few, simple flow elements and lacked the capability of temperature computation. The same is true for the programs of Rose (1978) and Miedema and Westgeest (1981) (the latter deals only with incompressible flow).

2 Modeling of an Air System

An air system of a modern jet engine, which can become rather complicated, is shown in Fig. 1. It is best represented by a *network* diagram (Fig. 2). There is a flow exchange between the main air stream and the secondary air system at the boundary nodes. The internal nodes of the network in most cases physically represent *chambers* of some volume in the engine. The various flow paths shown in the network diagram in the following are referred to as pipes, although physically they do not always resemble real pipes.

The task is to compute the flows in the lines and the pressures in the chambers once the boundary pressures and temperatures are given. It may also involve the evaluation of temperatures in the chambers due to mixing of different air streams or heat transfer at hot engine components.

In the following section the governing equations for the air system network as a whole are presented. This is followed by a description of some problems of computing pipe flow in an air system. Finally, a review is given of the flow elements encountered in the network, especially for those typical for a turbo engine.

3 Governing Equations for the Network

For each of the N chambers or internal nodes (see Fig. 3) the law of conservation of mass applies. For steady-state conditions it takes the form

$$\sum_{i \in A_k} m_i = 0. \tag{1}$$

Here A_k denotes the set of all pipes adjacent to node k.

If mixing temperatures are also to be computed in the system, the law of conservation of energy must be applied to each chamber:

$$\sum_{i \in A_k} m_i h(T_i^k) + Q_k = 0. \tag{2}$$

Q is a possible heat input into a chamber or pipe, e. g., by convection, which for the sake of simplicity is assumed to be added to the chamber.

Unless otherwise stated, each flow temperature T_i equals the temperature of the internal or boundary node at its inlet.

In general, mass flow m_i of pipe i,

$$m_i = f_i(PC, TC), \tag{3}$$

is a function of all unknowns (and of boundary pressures and temperatures, the dependency upon which is not shown in this notation).

Normally, there is no coupling between pipes other than by

Contributed by the International Gas Turbine Institute and presented at the 37th International Gas Turbine and Aeroengine Congress and Exposition, Cologne, Germany, June 1-4, 1992. Manuscript received by the International Gas Turbine Institute February 4, 1992. Paper No. 92-GT-68. Associate Technical Editor: L. S. Langston.

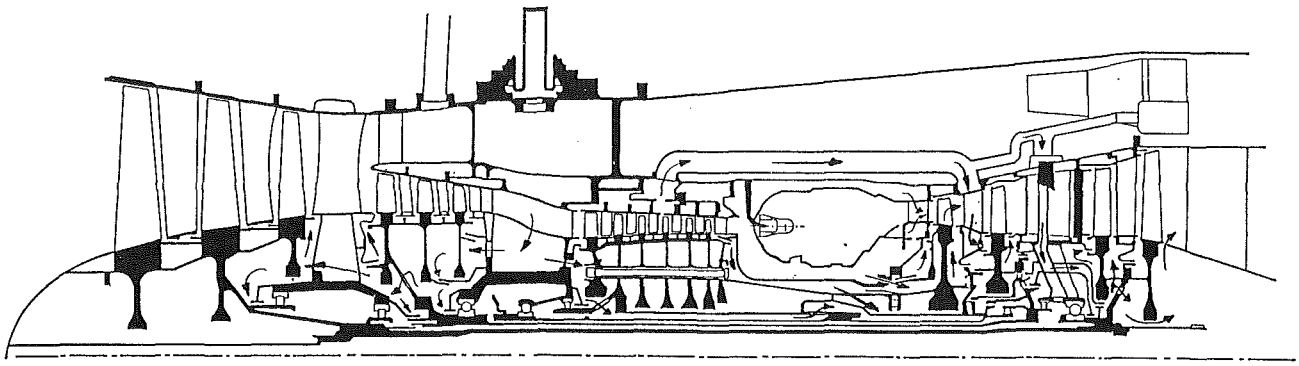

Fig. 1 Air system of a modern jet engine

mass and enthalpy flow, which is taken into account in Eqs. (1) and (2). (Some exceptions such as branches and swirl generators are presented later.) Then, Eq. (3) reduces to a function

$$m_i = f_i(P_{IN_i}, P_{OUT_i}, T_i), \tag{4}$$

where P_{IN_i} and P_{OUT_i} are the inlet and outlet pressures of pipe i, respectively; these can be nodal or boundary values. This includes as a special case a fixed prescribed value m_i, e. g., for a flow that is known by measurement.

We look for values of PC and TC such that Eqs. (1)–(3) hold.

Let pipe i contain n flow elements. We denote the pressure at the outlet of the jth element by $P_{i,j}$ (for $j<n$ this is the inlet pressure of the subsequent element; further $P_{i,n}=P_{OUT_i}$) and $P_{i,0}=P_{IN_i}$. Each element is modeled by a function

$$m = f_{i,j}(P_{IN}, P_{OUT}, T_{IN}). \tag{5}$$

Now, the n equations

$$m_i = f_{i,j}(P_{i,j-1}, P_{i,j}, T_{i,j-1}) \quad j=1, \ldots, n \tag{6}$$

must hold simultaneously for the unknown values of mass flow m_i and intermediate pressures $P_{i,1}, \ldots, P_{i,n-1}$.

Although the flow phenomena encountered in internal air systems are mostly two or three dimensional, in the scope of such a network computer code they have to be treated as one dimensional. Flow conditions and fluid properties in an area of interest have, therefore, to be considered as representative mean values. The flow correlations employed are usually derived by simplified theoretical approaches with empirical correction coefficients obtained from experiments or, as Zimmermann (1990) suggested, CFD computations.

Altogether, Eqs. (1), (2), and (6) describe a system of $2N+L$ nonlinear equations for N chamber pressures and N chamber temperatures, M pipe flows and $L-M$ intermediate pressures. For actual networks (e. g., $L=260$, $M=116$, $N=50$) this corresponds to 360 unknowns.

Nomenclature

A = set of indices of pipes adjacent to a node
c = absolute velocity
C_d = discharge coefficient = $(m_{actual}/m_{ideal}$
D = diameter
F = vector of mass balance defects
f, g = functions
h = enthalpy
j = number of flow element
J = Jacobian matrix of function $F(PC)$
k, l = node numbers
L = number of flow elements
l = length, thickness
M = number of pipes/flows
Ma = Mach number
m = mass flow
N = number of chambers/internal nodes
n = number of elements in a pipe
P = pressure
PC_k = pressure at chamber k
$PC=(PC_1, \ldots, PC_N)^T$ = vector of unknown chamber pressures
P_{IN}, P_{OUT} = inlet and outlet pressure, respectively
Re = Reynolds number
Q_k = heat input into chamber k
T_i = temperature of flow i
TC_k = temperature of chamber k
$TC=(TC_1, \ldots, TC_N)^T$ = vector of unknown chamber temperatures
T_i^k = temperature of flow i close to node k
T_{IN} = inlet temperature
u = circumferential velocity
v = velocity
w = relative velocity
x = transformed variable
ϵ = belongs to (set theory)
ΔP = pressure difference
θ = flow angle
ρ = density
$\zeta, \bar{\zeta}$ = loss coefficient

Subscripts

i = refers to pipe/flow
k, l = refers to chamber
i, j = refers to jth flow element of pipe i
0, 1, 2 = pipe references of branches
$0 \rightarrow i$ = pertaining to flow direction
1, 2 = inlet and outlet, respectively
red = reduced
s, t = static, total
t, ax = tangential, axial

Superscripts

T = transposed
$-$ = refers to new iterative value
0 = initial guesstimate

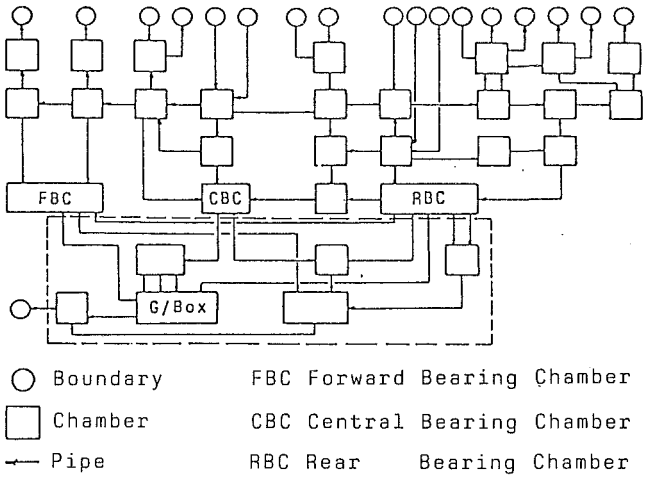

Fig. 2 Air system network for a modern jet engine

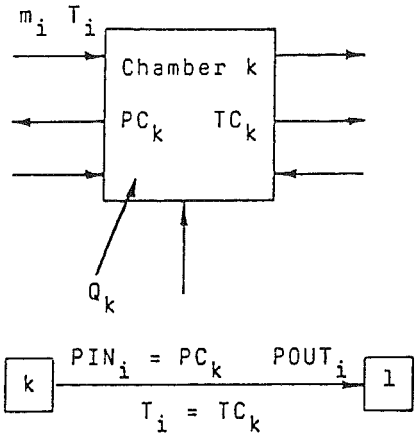

Fig. 3 Notation of nodes and pipes

A possible change of temperature over a pipe as a consequence of energy input, e. g., by vortices or heating, is accounted for by introducing additional:

$$T_{i,j} = g_{i,j}(P_{i,j-1}, P_{i,j}, T_{i,j-1}) \quad j = 1, \ldots, n \qquad (7)$$

for each element, which relate its inlet and outlet temperature. This gives additional L unknown intermediate temperatures, resulting in 620 unknowns altogether for the above example. These are computed in the course of the calculation of pipe flows (cf. Section 7.3) by a variant of the algorithm described.

4 Problems of Pipe Flow Computation

In a pipe containing many flow elements in series, the pressure normally steadily drops from the inlet to the exit of the pipe. With increasing flow or overall pressure ratio over the pipe, choking may occur at some restriction within the flow path. Choking can also be deliberately caused by a suitably sized restriction as a means to limit or meter the flow.

The possibility of choking influences the procedure for computing flow in pipes with more than one flow element. Whereas in the subcritical case the flow in a restriction is determined by both up- and downstream conditions, only the upstream ones set the flow in the choked case. The downstream pressure then depends only on the conditions at the downstream end of the pipe. A computation procedure was, therefore, selected that starts at the end of the pipe and proceeds against the flow direction.

Among the flow elements occurring in air system networks, there are some having different loss characteristics when flow direction reverses, as e. g., sudden enlargements, T-pieces,

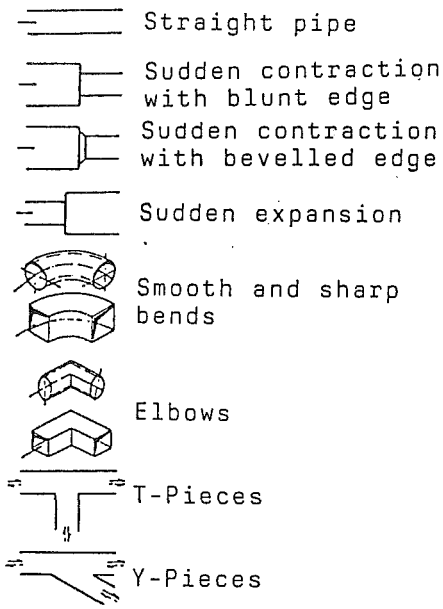

Fig. 4 Flow elements with dynamic head losses

nozzles. When a complicated network is analyzed at off-design conditions, or when effects of failures or seal wear are investigated, flow reversal can occur in some of the branches. If such a branch contains one of the above "asymmetric" flow elements, the appropriate characteristic for reversed flow would have to be used.

However, reversal of flow in a branch of an air system is usually undesirable and requires rectifying design measures anyway. Therefore, the quantitative error caused by the use of the same characteristic for both flow directions is deemed acceptable, since only the *indication* of a flow reversal is important.

5 Flow System Elements

The secondary air system of an engine can be divided into two subsystems: the internal system supplying cooling and sealing air, and the system for venting of the bearing chambers to a near ambient pressure.

The latter usually comprises some internal and external pipework and thus contains the more "classical" flow elements such as pipes, bends, branches (T and Y-pieces), pipe inlets and outlets.

The total pressure losses of these elements are commonly expressed as a multiple of the dynamic head, i.e., by a loss coefficient ζ.

For the calculation of these loss coefficients a variety of information is available in the literature (Ward Smith, 1980; Miller, 1978; Idel'chick, 1986). The pertinent calculation methods are stored in a subroutine library, which can easily be extended. Figure 4 shows the currently available elements. A complication encountered in the vent system is the occurrence of air/oil mixtures; consequently, methods for computing two-phase flow are required. The approach adopted in the present program is discussed later.

The elements typical for the internal air system are mainly restrictors and seals.

Restrictors can be divided into tappings, such as holes or slots in a wall parallel to the main flow direction, and rotating holes. Common to these elements is that the flow is described by the gas dynamic flow function and a discharge coefficient C_d. Since the dynamic head generated in the vena contracta is not recovered downstream of a restrictor, the static pressure

downstream has to be considered as the total pressure at the inlet of the following element.

In addition to the above "basic" flow elements, the modeling of an air system requires further elements. These comprise elements for the conversion of the conditions of state from an absolute to a relative system of reference and for the description of swirling flow, which is modeled by vortices.

Cover plates serve for the supply of rotor blade cooling air. Although they are composed from the above elements they are worth mentioning, since in addition to mass flow and pressure their description involves also the swirl generated by preceding elements.

In the following, the loss correlations of some of the typical flow elements mentioned above are highlighted.

5.1 Basic Flow Elements

5.1.1 Branches. Branches, such as T and Y-pieces, are special flow elements, since their incorporation into the air system program has a direct impact on the structure of the main iteration process as shown later. They may be used for either dividing or combining flow. The customary definition to account for the pressure losses of dividing flow and its modeling in the air system program is presented in Fig. 5 (for combining flow the indices have to be interchanged).

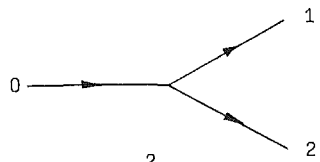

$\Delta P_{0\to i} = \zeta_{0\to i}\rho_0 v_0^2/2$ with

$\zeta_{0\to i} = \zeta_{0\to i}(v_1/v_0,\ v_2/v_0,\ \text{geometry})$

$i = 1, 2$

a) Definition of Pressure Loss Coefficient

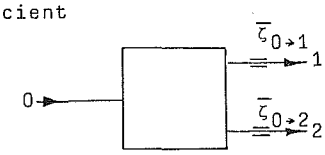

$\Delta P_{0\to i} = \bar{\zeta}_{0\to i}\rho_i v_i^2/2$ with

$\bar{\zeta}_{0\to i} = \zeta_{0\to i}\rho_0/\rho_i(v_0/v_i)^2$

$i = 1, 2$

b) Modelling in the Network

Fig. 5 Branching flow

Figure 5(*a*) indicates two things;

- In addition to the geometry, the pressure losses are dependent on the ratios of the velocities in the branches and in the mainstream.
- The pressure losses in the branches are dependent on the velocity in the mainstream.

In the scope of the main network program, however, flow, and hence velocity are assumed to depend only on the pressures at the ends of the pipe,as Eq. (4) shows. The equations have, therefore, been modified as shown in Fig. 5(*b*). Since the loss is now referred to the total head of the branch considered, each branch can be computed on its own. The loss coefficients are determined from the result of the preceding iteration loop and kept constant during the actual loop. An example for the loss coefficients of a T-piece is given in Fig. 6.

Figure 6 shows that under certain conditions there may be a rise of the total pressure in the mainstream of a T-piece instead of a pressure loss. This is opposite to the normal characteristic of a flow element and may lead to convergence problems of the main iteration algorithm. The branch must, therefore, contain additional flow elements that enforce an overall branch characteristic of rising flow with rising pressure ratio. Such an arrangement, however, exists in practical applications.

5.1.2 Restrictors. Orifices and Nozzles. Orifices and nozzles are used in the air system wherever flow metering or pressure adjustment is required: for example, the metering of cooling flow to turbine blades or the setting of bearing load controlling pressures. Furthermore, nozzles provide the required preswirl for feeding turbine blade cooling systems. For nozzles, therefore, not only the mass flow has to be computed, but also the flow velocity, which is used as an input to a flow element farther downstream (preswirl nozzle).

The discharge coefficient of orifices is influenced by a variety of factors such as Reynolds number (Miller and Kneisel, 1973), inlet corner radiusing (Benedict et al., 1975), orifice length (Lichtarovicz et al., 1965), and compressibility (Bragg, 1960; Ward Smith, 1979). The above effects, except for compressibility, have been combined into a procedure for circular orifices by McGreehan and Schotsch (1988).

Preswirl nozzles for cover plate systems are often of a very special shape, and due to the arrangement of the nozzles in a ring, there are interactions between the jets. There is very little information on C_d values of such nozzles in the literature. The C_d's for these configurations are, therefore, mostly determined by rig tests. Figures 7(*a*, *b*) present the characteristic of a stationary orifice showing the effect of geometry and compressibility and of a radial preswirl nozzle, respectively.

Tappings and rotating holes. Tappings serve to bleed air from the engine mainstream to feed the secondary air system.

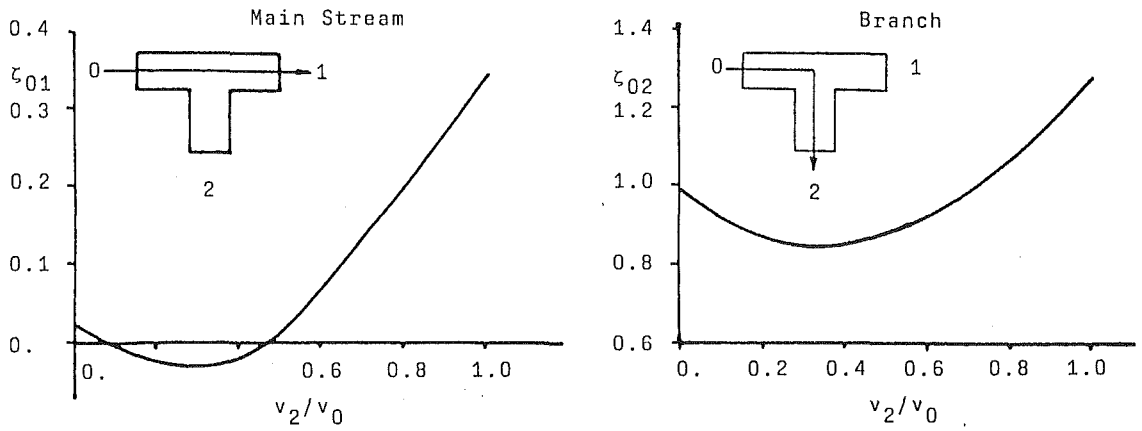

Fig. 6 Loss coefficients of a T-piece

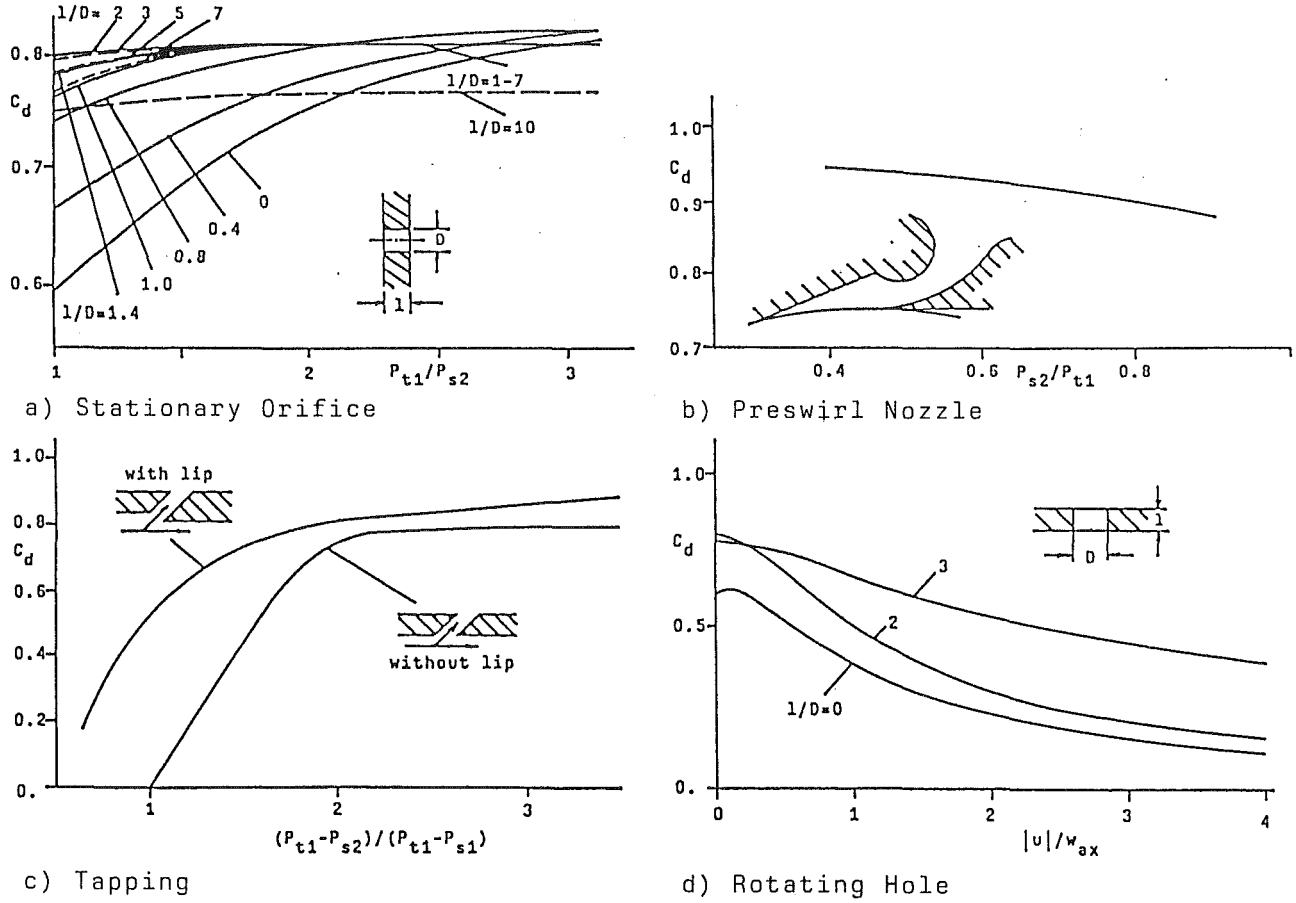

Fig. 7 Characteristics of restrictors

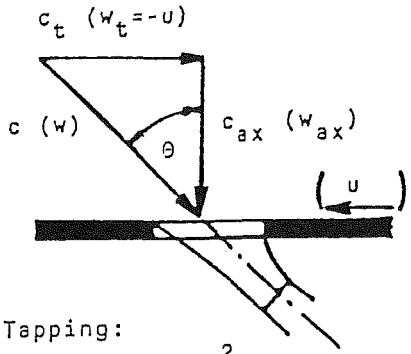

Tapping:

$$\frac{P_{t1} - P_{s2}}{P_{t1} - P_{s1}} = \frac{c^2}{c_t^2} = \frac{1}{\sin^2\Theta}$$

Rotating Hole:

$$\frac{w_t}{wax} = \frac{|u|}{w_{ax}} = \tan\Theta$$

Fig. 8 Flow situation at tapping/rotating hole

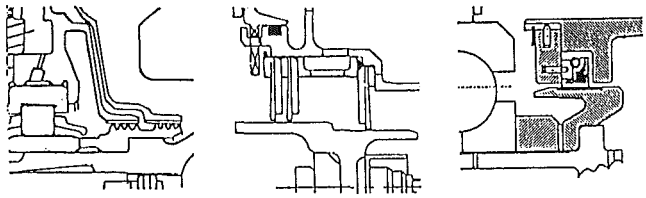

Fig. 9 Seal types

The characteristic feature is that the flow is taken through an orifice in a wall parallel to the main flow direction. In many cases orifices are rotating in shafts or disks to convey air from a stationary into a rotating system, e.g., into the feed system for rotor blade cooling.

In principle the flows for the tapping and the rotating hole are similar. Figure 8 shows the velocity triangle for a tapping, or a rotating hole, in a thin wall. The only difference is that for the rotating hole the velocities are denoted in the relative system.

A simple theory for orifices in thin walls shows that the main parameter controlling C_d is the downstream flow angle θ, which can be described by the ratio c_t/c_{ax} in the absolute system or by $|u|/w_{ax}$ in the relative system.

When the velocities are expressed by the total and static pressures of the mainstream, respectively, the branch downstream of the orifice the flow angle can be shown to depend on a pressure parameter $(P_{t1}-P_{s2})/(P_{t1}-P_{s1})$.

This parameter is very convenient for tappings, which often operate at values close to 1 (flow angles near 90 deg). Although derived from incompressible flow relations and for orifices in thin walls, experience shows that it also correlates C_d for tappings in thick walls and for mainstream Mach numbers up to 0.5. Moreover, it also correlates data for such tappings as slots in thick walls with or without a lip. Figure 7(*c*) presents an example for circumferential slots in a thick wall and shows the beneficial effect of a lip on C_d.

For rotating holes, where the flow angle may also be small, the velocity ratio is more convenient, because u is given by the

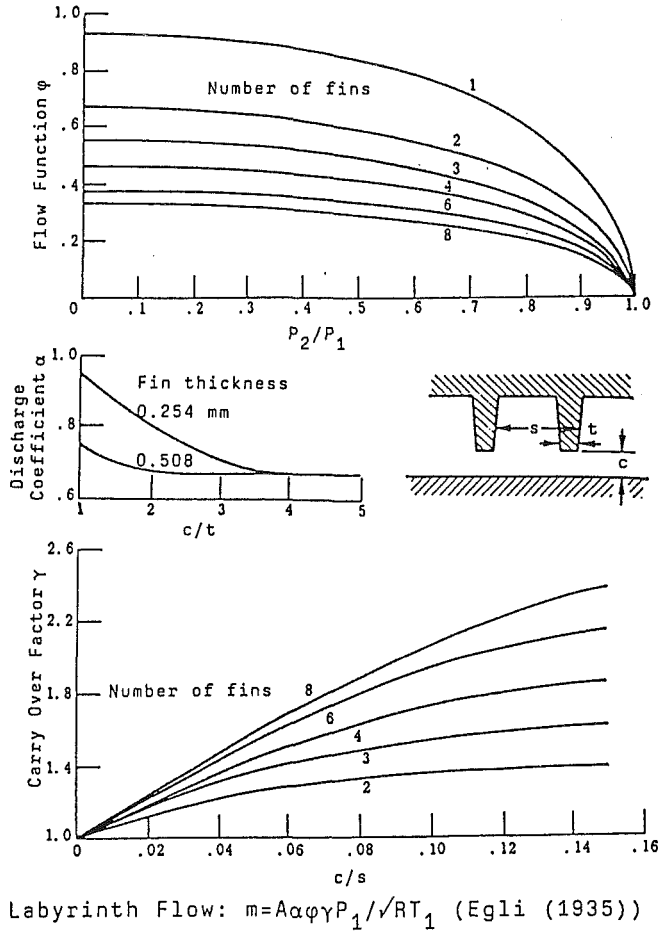

Fig. 10 Labyrinth characteristic (taken from Zuk, 1976)

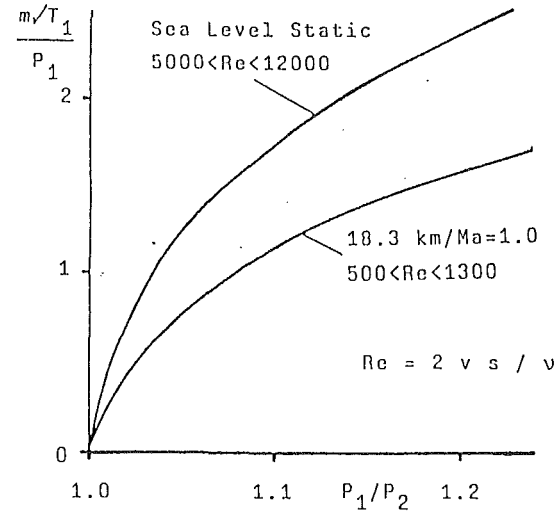

Fig. 11 Effect of Re number on labyrinth seal

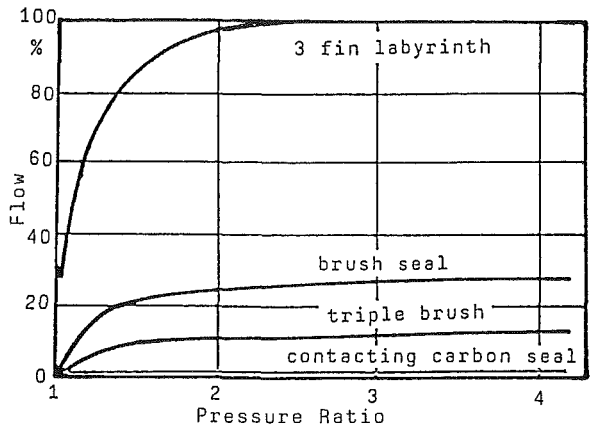

Fig. 12 Comparison between different seal types

shaft or disk speed. The axial velocity has to be derived from the static pressures both up and downstream of the orifice. A typical characteristic of a rotating hole including the effect of wall thickness is given on Fig. 7(*d*).

5.1.3 Seals. Due to their reliability, labyrinth seals (Fig. 9*a*) are the most frequently used seals in turbomachinery. Because of their simplicity, in the main straight through labyrinths are selected especially where small seal gaps can be realized. In areas where superior sealing is required, as at the exit of high-pressure compressors with larger diameters and hence larger clearances, stepped labyrinth seals are preferred.

Leakage prediction is based upon the principle of a number of restrictions in series. In the chamber between two adjacent seal fins, the kinetic energy built up in the seal gap is dissipated by a vortex. Leakage is primarily dependent on the gap width, the number of seal fins, and the discharge coefficient of the seal gaps. Since the dissipation of the jet is not 100 percent efficient, Egli (1935) introduced the concept of the carry over factor. Above influences are summarized in Fig. 10 from a paper of Zuk (1976). Usually engine companies have considerable experience with labyrinth seals and use their own empirical corrections to Egli's formula. An important parameter to be taken into account especially at high altitude operation of an engine is the effect of Reynolds number on C_d, as Fig. 11 shows.

Brush seals (Fig. 9*b*) are a relatively new seal concept and offer the advantage of being less susceptible to shaft excentricity, thermal and centrifugal growth of the rotor compared to a labyrinth seal, due to the elasticity of the bristles. The seal effectiveness depends on the density and the thickness of the packing of the bristles. The sealing quality is superior to that of labyrinth seals (Fig. 12). These seals can be applied up to considerably large diameters and thus can replace labyrinth seals at many locations of the engine. Since there is no theory yet available for the leakage prediction of brush seals, for air system calculations they are usually represented by an equivalent labyrinth seal based on test experience.

Carbon seals (Fig. 9*c*) can be either of the contacting or noncontacting type. For contacting seals there is no procedure for leakage prediction available. One has to recourse to experimental characteristics, which have to be fed into the program. For noncontacting seals as clearance seals or hydrodynamically balanced seals an approximate theory suitable for the application in an air system program is available for leakage determination (Zuk, 1972).

This theory describes the flow as of the Fanno line type and allows leakage calculation for subsonic laminar and turbulent as well as for choked flow conditions. Carbon seals offer a superior sealing quality as shown on Fig. 12. Their application, however, is limited to relatively small diameters due to limitations of rubbing speed and pressure differential (contacting seals) or manufacturing problems (clearance seals). They are, therefore, mainly used as bearing chamber seals.

5.2 Vortices. Swirling flow is encountered in the vicinity of rotating disks or shafts. Although the actual flow field is three dimensional, in the scope of an air system program a simplified theory must be used. The pressure field in swirling flow is, therefore, simply described by vortices. Depending on the magnitude of the radial flow, and on the starting condi-

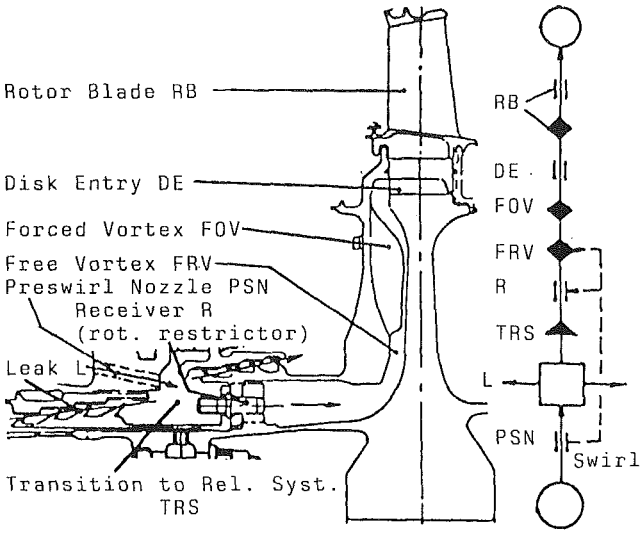

Fig. 13 Simulation of cover plate system

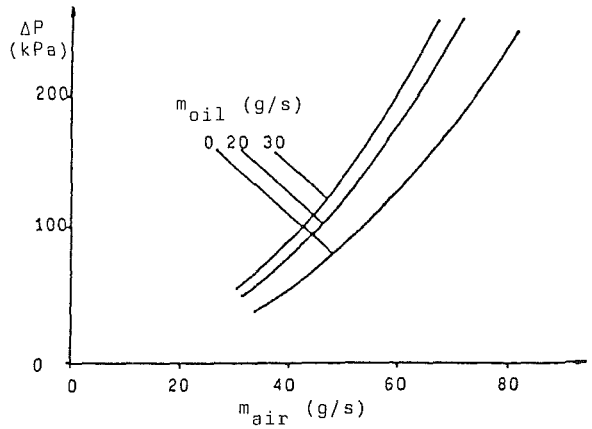

Fig. 14 Effect of oil flow on vent pipe pressure loss

tions, a free or forced vortex can be assumed. In certain cases, for example in coverplate systems, vortices are deliberately generated to increase the pressure.

For solid body vortices between rotating and stationary disks, the strength of the vortex is described by the core rotation factor, which relates vortex circumferential speed to the disk speed. This factor is of the order of 40 to 50 percent for a rotor–stator configuration. Numerous investigators (Schultz-Grunow, 1935; Daily and Nece, 1959) have shown this.

For vortices enclosed by corotating disks, the deviation from idealized behavior can be described by a "vortex effectivity," which is defined as the ratio of actual to theoretical pressure rise. This figure has either to be found from separate numerical calculations or from component rig tests.

5.3 Coverplates. As an example for the application of the aforementioned flow elements and also for the secondary interactions between elements, a coverplate is shown in Fig. 13. The system provides the cooling air for the turbine blades. Its purpose is to reduce the cooling air temperature in the relative system by strongly preswirling the flow. Seal leakage is minimized by arrangement of the preswirl nozzles at a low radius.

A cover plate can be modeled by putting the following elements in series: preswirl nozzle, rotating restrictor as receiver, a free an/or a forced vortex to account for the pressure increase due to the swirl between the corotating disks, a rotating restrictor for blade root entry, and another forced vortex and a

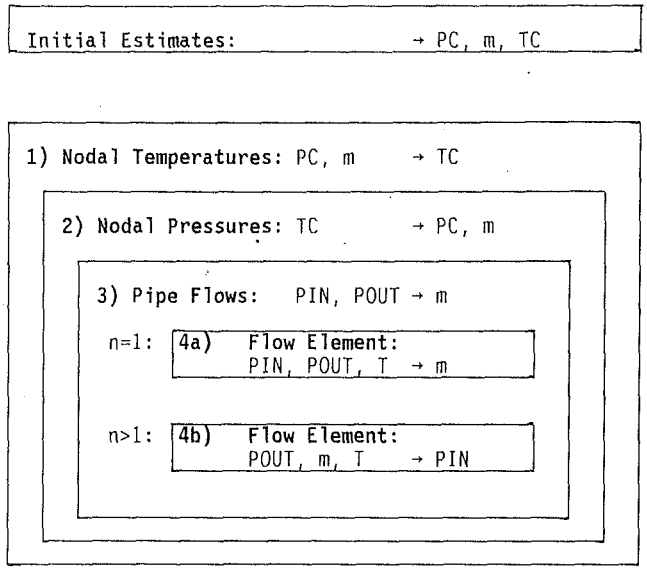

Fig. 15 Nested iterations of the computation process

restrictor to simulate the blade. The flow diagram shows that there is a secondary connection, which transmits swirl from the preswirl nozzle to the free vortex across a node in the system, thus creating an interdependence between two different branches. Rig tests have proven that this simple network closely models the behavior of a cover plate system.

6 Two-Phase Flow

The flow in vent pipes normally consists of a mixture of air and lubricating oil, which is entrained from the bearing chambers (Zimmermann et al., 1991). This oil causes a blockage of the ventlines and thus creates an additional pressure loss. Figure 14 shows how the pressure loss is increased by the vent-oil for a typical engine vent line based on engine measurement.

The concept of Lockhart and Martinelli (1949) of a two-phase multiplier is adopted to calculate these two-phase pressure losses. The two-phase multiplier is defined as the ratio of the two-phase pressure loss to the pressure loss obtained if all the fluid in the pipe were of the same phase. Although in the literature the two-phase multiplier is usually referred to the liquid phase, for the present purpose it is more practical to refer it to the gaseous phase, i.e., air, since this is the primary working fluid.

The procedures to derive the two-phase multiplier are all of a semi-empirical nature due to the complexity of the flow. The methods described in the literature are mostly set up for water/water vapor or water/air mixtures. Friedel (1978) has developed a method for computing the pressure loss of pipes based on a large amount of data. With some modifications his method is also suitable for air/oil mixtures as comparisons with engine and rig test evidence has shown (Fischer, 1990).

For pipes, orifices, smooth and sharp bends Zimmermann et al. (1991) have given procedures to evaluate the two-phase multipliers. The main problem remaining is the determination of the oil loading of the vent flow, which for the time being has to be estimated based on past engine test experience.

7 Steady-State Computation

In view of the size of the problem, it does not seem appropriate to attempt to solve all the equations simultaneously. Consequently, a hierarchical algorithm is used that exploits the topological structure of the network by decoupling pipe and element equations from each other. A rough outline of the nested iterations is given in Fig. 15.

For the sake of simplicity, let us assume that the air system contains neither branches nor swirl generators.

The algorithm starts with some initial estimates for m, PC, and TC. This will be discussed in Section 7.6.

The iteration levels are presented from the top down.

7.1 Computation of Nodal Temperature Values: ***Iteration Level 1.*** As the influence of temperatures on pressures and mass flows is relatively weak, computation of temperatures is decoupled from the other unknowns. Let us assume that m, PC, and TC satisfy Eqs. (1) and (6) (this is achieved on the lower iteration levels). If Eq. (2) also holds, the calculation is stopped. Otherwise we compute new values of enthalpies h_i from

$$\sum_{i \in A_k} m_i \bar{h}_i + Q_k = 0 \quad k = 1, \ldots, N. \tag{12}$$

As the enthalpies of all flows leaving node k satisfy

$$\bar{h}_i = h(\overline{TC}_k), \tag{13}$$

and as enthalpies are given at inlet boundary nodes, this leads to a system of M, corresponding to the number of pipes, linear equations for the enthalpies $\bar{h}_i$.

From $\bar{h}_i$, new iterative values $\overline{TC}_k$ for the chamber temperatures are computed from Eq. (13).

Although there is no theoretical proof of convergence, this algorithm has never failed to meet the desired precision within a maximum of eight iteration steps.

7.2 Computation of Chamber Pressures: ***Iteration Level 2.*** Let the nodal temperatures be fixed. These may be initial estimates or iterates from iteration level 1 or, if satisfaction of enthalpy balance, Eq. (2), is not desired, they may be fixed input values. Nodal pressures PC are computed to solve the system

$$F(PC) = \sum_{i \in A_k} m_i(PC) = 0 \quad k = 1, \ldots, N \tag{14}$$

of nonlinear equations by means of the Hybrid Method of Powell (1970), implemented by Moré et al. (1980).

This requires the computation of mass flows m_i, which enter $F(PC)$ according to Eq. (5) for any iterate PC and of the partial derivatives $\partial F_i/\partial PC_j$ (these form the $N \cdot N$ Jacobian matrix, J).

Uniqueness of Solution. From consideration of the Jacobian matrix the uniqueness of any solution can be deduced in the following way (discussion of its existence is postponed to the following paragraph). Let us consider a flow from node l to k. For the mass flow to be uniquely defined, the modeling of the flow elements must guarantee $dm/dPC \neq 0$; in fact, $dm/dPC_k < 0$ holds. This derivative dm/dPC_k contributes to the elements J_{kk} and J_{lk} of the Jacobian (with sign change); likewise for its lth column. If l (or k) denotes a boundary node, only the kth (or lth, respectively) diagonal element is influenced by that flow. Thus, J has negative diagonal elements while all others are positive. Further, the inequality

$$|J_{kk}| \leq \sum_{l \neq k} |J_{lk}| \tag{15}$$

holds for $k = 1, \ldots, N$, with strict inequality for all internal nodes that are directly connected to a boundary node by one pipe.

If there is at least one fixed boundary pressure, J is nonsingular and a so-called M matrix. (Otherwise the total problem would be undetermined.) This guarantees that any solution is unique (Ortega and Rheinboldt, 1970, pp. 55, 141).

Existence of Solution. For every internal node k the mass balance defect $F_k(PC)$ tends to infinity as $PC_k \to \infty$. If, however, PC_k approaches zero while all other pressures remain unchanged, $F_k(PC)$ decreases to a finite value because choking occurs in all pipes adjacent to node k. If now there is a fixed mass flow of sufficient magnitude given that escapes from node k, then a solution of the whole problem might not exist.

In all other cases, e.g., if only boundary pressures are prescribed and mass flows that enter the system, the existence of the solution follows from the argument above and the nonsingularity of the Jacobian matrix (Ortega and Rheinboldt, 1970, p. 137).

Practical Experience. In practice, the solution was found whenever its existence could be presupposed from physical reasons. For the reduction of mass balance defects by five orders of magnitude (starting from initial estimates) the method takes about 20 steps. For a large network this corresponds to 5 s CPU time.

7.3 Computation of Pipe Flows: ***Iteration Level 3.*** Now we consider the computation of mass flow m in pipe i for given inlet and outlet pressures P_{IN} and P_{OUT} and temperature T. If there is only one element in the pipe, m can be computed directly from the nodal values. This is done on iteration level 4. Otherwise, m and the unknown intermediate pressures $P_1, \ldots, P_n$ (we drop the index i for convenience) are found by the following algorithm:

(A) For given mass flow m, outlet pressure P_{OUT}, and temperature T compute inlet pressure $P_{IN}(m)$ such from n down to 1 (i. e., in the upstream direction) the equations

$$m = f_{i,j}(P_{j-1}, P_j, T) \tag{16}$$

for P_{j-1}.

Set $P_{IN}(m) = P_0$.

(B) Vary m according to a secant method until $P_{IN}(m)$ meets P_{IN}.

Computation of Derivatives. The performance of the Hybrid Method depends crucially on the quality of the partial derivative $\partial F_i/\partial PC_j$. As these are sums of the derivative dm/dPC, the latter have to be evaluated with care. This is done by numerical differentiation within the mass flow computation program as only then is it possible to exploit the network structure, reuse intermediate results, and adjust the increment used in computing the finite differences to each pipe.

Accelerating the Computation of "Long" Pipes. The main computational burden lies in the computation of the mass flows, especially for *long* pipes, i. e., those with many elements. During the early steps of iteration 2 all computed mass flow values of these pipes are stored and combined into a single pipe flow characteristic in the form of a curve of reduced mass flow $m\sqrt{T}/P_{IN}$ versus pressure ratio P_{IN}/P_{OUT}. During subsequent steps, this function

$$m\sqrt{T}/P_{IN} = m_{red}(P_{IN}/P_{OUT}) \tag{17}$$

is evaluated by interpolation for the given nodal values of P_{IN} and P_{OUT} resulting in values for the mass flow of a pipe with a similar characteristic, Eq. (17), as the original pipe. Partial derivatives may also be easily computed from Eq. (17).

When convergence is nearly achieved for this simplified model, its results serve as rather good starting values for the final iteration steps for the original model. Depending on the proportion of long pipes, this may save up to 40 percent of overall computation time. (A similar feature has been implemented by Rose, 1978, as was discovered by the authors at the time of writing.)

7.4 Computation of Flow Elements: ***Iteration Level 4.*** As pipes with one element and those with more elements are treated differently, one needs two routines to model each element: one to compute m from P_{IN} and P_{OUT}, and one to compute P_{IN} from m and P_{OUT}. This increases program development expenditure but saves computation time and increases precision.

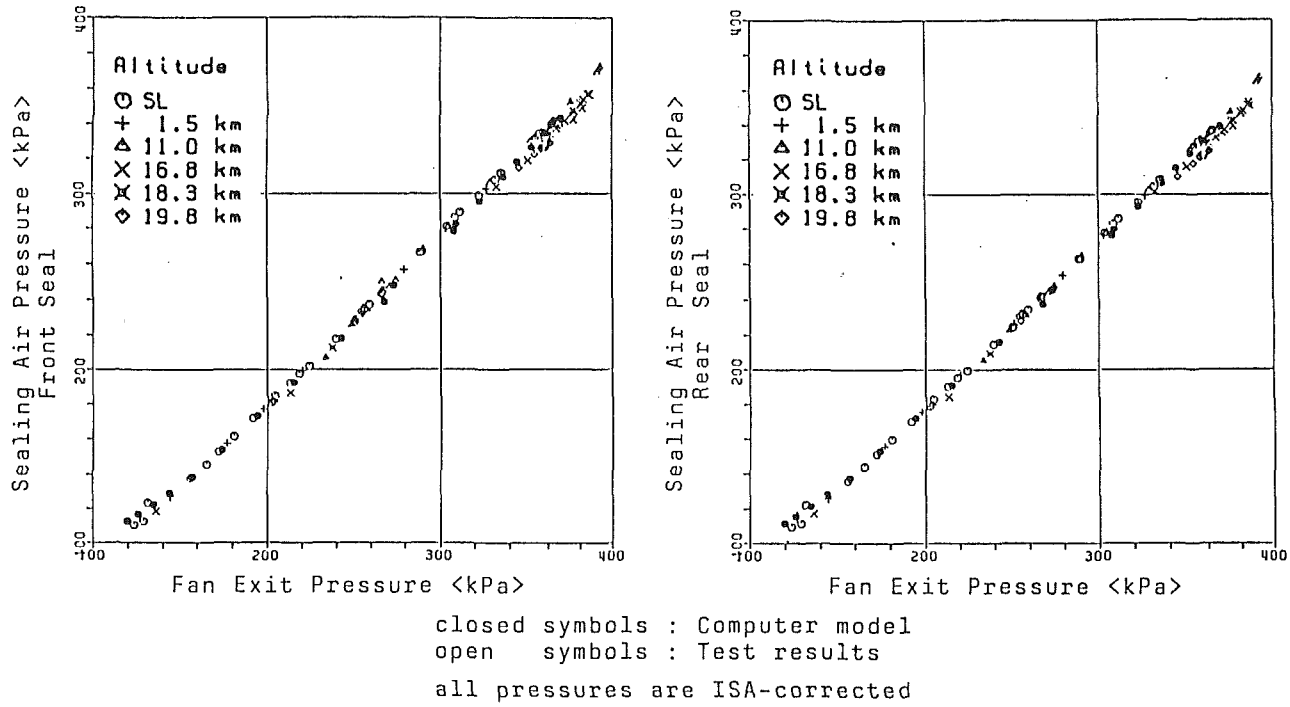

Fig. 16 Comparison between computer model and test results for rear bearing chamber sealing air pressures

For almost all types of elements Eq. (4) is implicit and must be solved iteratively for m or P_{IN}. These values are computed as precisely as possible, thus achieving smooth functions and conserving monotony, which is vital to the performance of the method.

7.5 Coupling Between Pipes. If swirl is transported from one element to another or in the presence of branches (cf. Section 5.1.1), pipes can still be treated as being decoupled for iteration levels 2 to 4 by the following method:

The corresponding transported values (swirl and loss coefficients) are "frozen" for a complete execution of iteration level 2, and they are updated with their thereby computed values after that. This necessitates execution of the outer iteration 1 even if no mixing temperatures are to be computed.

7.6 Estimating Initial Approximations. If necessary, the program computes initial estimates for internal temperatures and pressures, given their boundary values and at least one representative mass flow value.

If the boundary pressures are consistent with the prescribed flow directions, there exist internal pressure values such that the minimal ratio P_{IN}/P_{OUT} over any one pipe is maximized. The logarithms of these values are the solution of a Linear Programming (LP) problem. Maximizing P_{IN}/P_{OUT} serves to avoid nearly vanishing mass flows and their accompanying high derivatives. If the consistency condition above does not hold, the LP problem has no solution.

Given values for all mass flows, initial temperature estimates are computed in analogy to the procedure of computing new temperature iterates in Section 7.1 within iteration level 1 by solution of Eq. (12).

8 Comparison With Test Results

To highlight the validity of the computer model as an example the comparison between the simulated and measured rear bearing chamber sealing air pressures of a turbojet engine is presented on Fig. 16. The rear bearing chamber has been selected, because the sealing air, which on this engine is taken from the fan exit via total head scoops, on its way to the seals passes through a number of rotating holes in compressor disks and shafts, through vortices, and suffers from some friction pressure losses. In the end the air re-enters the mainstream rear of the low-pressure turbine.

In Fig. 16 the ISA-corrected sealing air pressures are plotted versus the corrected fan delivery pressure, which is the feeding pressure of the system. The simulated data (solid symbols) consist of a sea level static running line, some near sea level flight points, and some medium to high altitude flight points, whereas the tested data (open symbols) result from tests in an altitude test facility over a great part of the flight envelope of the engine. The simulation is based upon performance data obtained from an engine synthesis model, boundary conditions obtained from component aerodynamics, and an air system model derived from the analysis of some SLS test points.

The figure shows that the internal air system pressures when ISA corrected can be presented by a single operating line for working points all over the flight envelope, as indicated by both the simulated and the tested data. The figure further shows a good agreement between simulation and test evidence. This demonstrates that a model, which is well adapted to a few test points, can predict the air system behavior all over the flight envelope. It is to be noted, however, that this good agreement is not only the result of a careful physical modeling of the air system but also of the high quality of the cycle model and of component aerodynamics analysis.

9 Conclusions

An air system program has been set up that can model very complex networks. The CPU time for the steady-state calculation of a typical engine system consisting of a low-pressure bearing chamber sealing system, an intermediate pressure turbine cooling system, and a high-pressure turbine cooling system (with a total of 116 pipes and 50 nodes) is typically 5 s on a NAS XL100 computer.

In addition, selected geometric parameters may automatically be adjusted to meet prescribed nodal pressures values (e.g., test results or design targets).

The program has turned out to be a valuable tool for the

design of an engine air system and for the prediction of its behavior throughout the flight envelope.

The program has also been used for other networks of turbo engines, such as the feed oil system. For this application, the compressible flow relations have been replaced by those for incompressible flow. Its application is being extended to cover also transient operation of the engine.

References

Benedict, R. F., Wyler, J. S., and Brandt, G. B., 1975, "The Effect of Edge Sharpness on the Discharge Coefficient of an Orifice," ASME *Journal of Engineering for Power*, Vol. 97, No. 4, pp. 576–582.

Bragg, S. L., 1960, "Effect of Compressibility on the Discharge Coefficient of Orifices and Nozzles," *J. of Mechanical Engineering Science*, Vol. 2, No. 1, pp. 35–44.

Daily, J. W., and Nece, R. E., 1959, "Chamber Dimension Effects on Induced Flow and Frictional Resistance of Enclosed Rotating Disks," ASME *Journal of Basic Engineering*, Vol. 82, pp. XX-00.

Egli, A., 1935, "The Leakage of Steam Through Labyrinth Seals," *Trans. ASME*, Vol. 57, No. 3, pp. 115–122.

Fischer, R., 1990, "Probleme der Zweiphasenströmungen im Sperrluftsystem von Flugtriebwerken," Inst. f. Luftfahrtantriebe, Univ. Stuttgart, Germany.

Friedel, L., 1978, "Druckabfall bei der Strömung von Gas/Dampf-Flüssigkeitsgemischen in Rohren," *Chem.-Ing.-Tech.*, Vol. 50, pp. 167–180.

Idel'chik, I. E., 1986, *Handbook of Hydraulic Resistance*, 2nd ed., Hemisphere Publishing Corporation, Washington, DC.

Lichtarovicz, A., Duggins, R. K., and Markland, E., 1965, "Discharge Coefficients for Incompressible Noncavitating Flow Through Long Orifices," *J. Mech. Eng.*, Vol. 7, pp. 210–219.

Lockhart, R. W., and Martinelli, R. C., 1949, "Proposed Correlation of Data for Isothermal Two-Phase Two Component Flow in Pipes," *Chem. Engr. Progr.*, Vol. 45, No. 1, pp. 39–47.

McGreehan, W. F., and Schotsch, M. J., 1988, "Flow Characteristics of Long Orifices With Rotation and Corner Radiusing," ASME JOURNAL OF TURBOMACHINERY, Vol. 110, pp. 213–217.

Miedema, J. A., and Westgeest, B. Q. M., 1981, "Computation of Mass Flow Rates and Pressure Losses in Branched Pipeline Networks," TNO, Rep. 5173202-81-1.

Miller, D. S., 1978, "Internal Flow Systems," *BHRA Fluid Engineering*, Vol. 5.

Miller R. W., and Kneisel, O., 1973, "A Comparison Between Orifice and Flow Nozzle Laboratory Data and Published Coefficients," ASME Paper No. 73-WA/FM-5.

Moore, A., 1975, "Gas Turbine Engine Internal Air Systems: A Review of the Requirements and the Problems," ASME Paper No. 75-WA/GT-1.

Moré, J. J., Garbow, B. S., and Hillstrom, K. E., 1980, "User Guide for MINPACK-1," Argonne National Laboratory, Argonne, IL.

Ortega, J. M., and Rheinboldt, W. C., 1970, *Iterative Solution of Nonlinear Equations in Several Variables*, Academic Press, New York.

Powell, M. J. D., 1970, "A Hybrid Method for Nonlinear Equations," *Numerical Methods for Nonlinear Algebraic Equations*, P. Rabinowitz, ed., Gordon and Breach, pp. 87–114.

Rose, J. R., 1978, "FLOWNET: A Computer Program for Calculating Secondary Flow Conditions in a Network of Turbomachinery," NASA TM-73774, Lewis Research Center, Cleveland, OH.

Schultz-Grunow, F., 1935, "Der Reibungswiderstand rotierender Scheiben in Gehäusen," *ZAMM*, Vol. 15, No. 4, pp. 191–204.

Suntry, H., 1963, "Iterative Airflow Schemes," Computer Program Report 1204, Rolls-Royce Ltd., Derby, United Kingdom.

Ward Smith, A. J., 1979, "Critical Flow Metering: The Characteristics of Cylindrical Nozzles With Sharp Upstream Edges," *Int. J. Heat Fluid Flow*, Vol. 1, No. 3, pp. 123–132.

Ward Smith, A. J., 1980, *Internal Fluid Flow, The Fluid Dynamics of Flow in Pipes and Ducts*, Clarendon Press, Oxford.

Zimmermann, H., 1990, "Some Aerodynamic Aspects of Engine Secondary Air Systems," ASME *Journal of Engineering for Gas Turbines and Power*, Vol. 112, pp. 223–228.

Zimmermann, H., Kammerer, A., Fischer, R., and Rebhan, D., 1991, "Two-Phase Flow Correlations in Air/Oil Systems of Aero-Engines," ASME Paper No. 91-GT-54.

Zuk, J., 1972, "Fluid Mechanics of Noncontacting Gas Film Seals," Ph.D. Thesis, Case Western Reserve Univ.

Zuk, J., 1976, "Fundamentals of Fluid Sealing," Lewis Research Center, Cleveland, OH, NASA TN D-8151.

S. Gilham
W. S. Atkins Consultants Ltd.,
Woodcote Grove, Ashley Road,
Epsom, Surrey KT18 5BW
United Kingdom

P. C. Ivey
School of Mechanical Engineering,
Cranfield Institute of Technology,
Cranfield, Bedfordshire MK43 0AL
United Kingdom

J. M. Owen
School of Mechanical Engineering,
University of Bath,
Claverton Down, Bath BA2 7AY
United Kingdom

The Transfer of Heat by Self-Induced Flow in a Rotating Tube

This paper provides a review of recently published research on self-induced flow and heat transfer in a rotating tube, together with additional theoretical work on heat transfer to the cylindrical wall of the tube. Earlier work has shown that self-induced flow can occur when a tube, with one end open and the other sealed, is rotated about its axis: Fluid flows along the axis toward the sealed end and returns in an annular layer on the cylindrical wall. The flow and heat transfer on the end wall are similar to those associated with the so-called free disk, and measured velocity distributions in the tube and Nusselt numbers for the end wall are in good agreement with those computed from numerical solutions of the Navier–Stokes and energy equations. The Reynolds analogy is used in this paper to provide a correlation for the computed Nusselt numbers for the cylindical wall, and design correlations are provided to enable the results to be applied to anti-icing systems for the nose bullets of aero-engines.

1 Introduction

A simplified diagram of an anti-icing system for the "nose bullet" of a jet engine is shown in Fig. 1. Hot air, from the turbine-end of the engine, passes through the hollow compressor shaft, through an "anti-icing tube" and impinges on the back of the rotating nose bullet, keeping it free of ice. Unfortunately, after being exhausted through vents on the nose bullet, the hot air is ingested by the compressor, causing a loss of performance.

Rolls-Royce engineers, conducting anti-icing tests, solved the ingestion problem by sealing the vents from the nose bullet. They were surprised to see that heat transfer still occurred despite the fact that there was no longer a superposed flow of hot air along the compressor shaft. The mysterious "hot-poker effect," as it was termed, was thought to be caused by a rotating thermosyphon, and a patent was taken out for a novel anti-icing system (Rolls-Royce, 1979).

The phenomenon of self-induced flow in an isothermal constant-diameter rotating tube was discovered by Owen and Pincombe (1981) and was first reported in the scientific literature by Gilham et al. (1991a). It occurs when a tube, sealed at one end and open at the other, is rotated about its axis: Fluid flows from the open end along the axis toward the sealed end and returns in an annular boundary layer on the cylindrical wall. This phenomenon is believed to be the cause of the "hot-poker effect" referred to above. The research on self-induced flow as extended by Gilham et al. (1991b) to the case of stepped tubes representative of those found in aero-engines, and Gilham et al. (1992) considered the heat transfer to the end wall of the rotating tube.

In the present paper, the work on self-induced flow is reviewed, the problem is extended to include heat transfer through the cylindrical wall of the rotating tube, and the application to the design of anti-icing systems is considered. The review of previous work is presented in Section 2, the numerical method is described in Section 3, the heat transfer to the cylindrical wall is discussed in Section 4, and the application to design is considered in Section 5.

2 Review of Self-Induced Flow and Heat Transfer in Rotating Tubes

2.1 Experimental Apparatus. The apparatus used by Gilham et al. (1991a, b, 1992) is described briefly below, and further details are given by Ivey (1988).

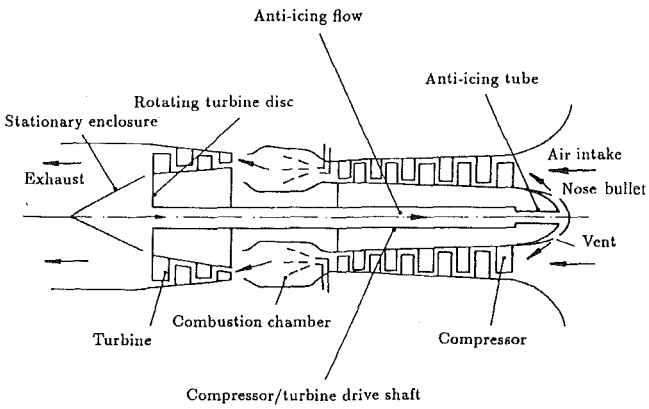

Fig. 1 Schematic diagram of a jet engine showing anti-icing system for nose bullet

Contributed by the International Gas Turbine Institute and presented at the 37th International Gas Turbine and Aeroengine Congress and Exposition, Cologne, Germany, June 1–4, 1992. Manuscript received by the International Gas Turbine Institute February 24, 1992. Paper No. 92-GT-305. Associate Technical Editor: L. S. Langston.

2.1.1 Optical Measurements. Glass tubes, of varying lengths up to 1.5 m and diameters up to 75 mm, were mounted in ball-bearing assemblies and were rotated at speeds up to 6000 rpm by means of an electric motor. One end of the rotating tube was sealed by a perspex disk, the other end opened into a stationary enclosure.

Velocity measurements were obtained by laser-Doppler anemometry (LDA) operating in the forward-scatter real-fringe mode. A 15 mW Spectra Physics He-Ne laser, Malvern Instruments transmitting optics, and a Cambridge Consultants tracking filter were used in the LDA system, and micron-size silicone oil particles were used to "seed" the air outside the stationary enclosure at the open end of the tube.

Flow visualization was conducted using a 4 W Spectra Physics argon-ion laser to produce slit illumination of an r–z plane parallel to, and coincident with, the axis of the tubes. A Concept smoke generator, which could be pulsed, was used to release clouds of micron-size oil particles into the air outside the stationary enclosure. A Canon A1 camera, operating in the "aperture-preferred mode" at F1.4, was used to take photographs with ISO 400 black and white film.

2.1.2 Heat Transfer Measurements. The heat transfer rig used a stainless-steel rotating tube, 531 mm long and 37 mm diameter, mounted in ball-bearing assemblies. One end of the tube was sealed by an end cap, housing a fluxmeter, and the other end opened into a stationary enclosure. The temperature of the air in the enclosure was varied up to 100°C by means of an electric heater, the temperature of the cylindrical wall was controlled by circulating hot air through an annulus surrounding the tube, and the exterior surface of the end wall was cooled by the impingement of jets of air at ambient temperature. The signals from thermocouples in the tube wall and on the tube axis, together with signals from the fluxmeter, were brought out through a slip-ring assembly, and the voltages were measured by a computer-controlled data logger.

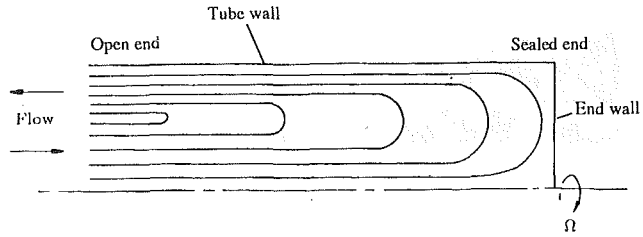

Fig. 2 Self-induced flow in a rotating tube

2.2 Isothermal Flow in Constant-Diameter Tubes. Owen and Pincombe (1981) carried out a pilot study using a glass tube, with a length-to-diameter ratio of around 27, rotating about its axis at speeds up to 2000 rpm. One end of the tube was open to the atmosphere, the other end was sealed, and a laser was used to create slit illumination.

The flow visualization revealed the recirculation shown schematically in Fig. 2. At high rotational speeds, the flow penetrated to the sealed end: the "short-tube case." At low speeds, the recirculating flow was confined to the open end: the "long-tube case." Subsequent tests revealed that the strength of the flow depended on both the rotational speed and the length-to-diameter ratio of the tube. It was presumed that the short-tube case, which had been observed under isothermal conditions, was the cause of the hot-poker effect found in the anti-icing tests referred to above.

The phenomenon of self-induced flow can be readily understood by considering an air-filled tube sealed at both ends and rotating about its axis. The air inside the tube will be in solid-

Nomenclature

a = internal radius of tube
b = outer radius of disk at open end of tube
C_m = moment coefficient = $M/\frac{1}{2}\rho\Omega^2 a^5$
C_p = specific heat at constant pressure
C_w = nondimensional mass flow rate = $m/\mu a$
E = Ekman number = $\nu/\Omega a^2$ ($= \mathrm{Re}_\phi^{-1}$)
E^* = modified Ekman number = GE
Ec = Eckert number = $\Omega^2 a^2/C_p\Delta T$
G = length-to-radius ratio = l/a
H = total enthalpy = $C_pT + \frac{1}{2}(u^2+v^2+w^2)$
k = thermal conductivity
l = length of tube
m = mass flow rate
M = frictional moment on wall
Nu = local Nusselt number = $qr/k(T_\infty - T_o)$
Nu^* = modified local Nusselt number = $qr/k(T_{o,ad} - T_o)$
Nu_{av} = average Nusselt number = $q_{av}a/k(T_\infty - T_o)_{av}$
Nu^*_{av} = modified average Nusselt number = $q_{av}a/k(T_{o,ad} - T_o)_{av}$
p = static pressure
Pr = Prandtl number = $\mu C_p/k$
q = local heat flux from fluid to wall
r = radial coordinate
R = recovery factor
Re_ϕ = rotational Reynolds number = $\Omega a^2/\nu = (\mathrm{E}^{-1})$
T = temperature
u = radial component of velocity
v = tangential component of velocity relative to a stationary frame
w = axial component of velocity
z = axial coordinate measured from open end of tube
α = thermal diffusivity = $k/\rho C_p$
β = coefficient of volumetric expansion
δ = thickness of boundary layer
ΔT = magnitude of temperature difference between fluid and wall = $|T_\infty - T_o|$
θ = nondimensional temperature = $(T - T_o)/(T_\infty - T_o)$
μ = dynamic viscosity
ν = kinematic viscosity = μ/ρ
ρ = density
τ_ϕ = tangential component of shear stress
Ω = angular speed of tube
$\mathcal{R}$ = gas constant

Subscripts

a = value at cylindrical wall, $r = a$
ad = adiabatic value
atm = atmospheric value
av = radially weighted average value
c = value in core of fluid
fd = free-disk value
flux = pertaining to fluxmeter
l = value at end wall, $z = l$
o = value at either cylindrical wall or end wall
r, ϕ, z = radial, tangential, axial directions
∞ = value at inlet to system
1, 2 = pertaining to tubes at open end and sealed end, respectively, for stepped-tube case

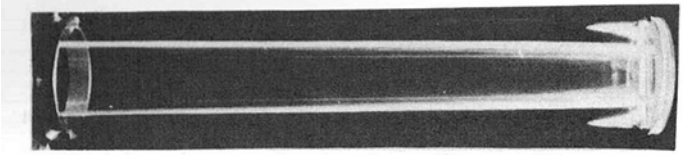

Fig. 3 Flow visualization near sealed end of tube ($G = 28.8$, $E = 6.25 \times 10^{-4}$, $t = 5.0$ s)

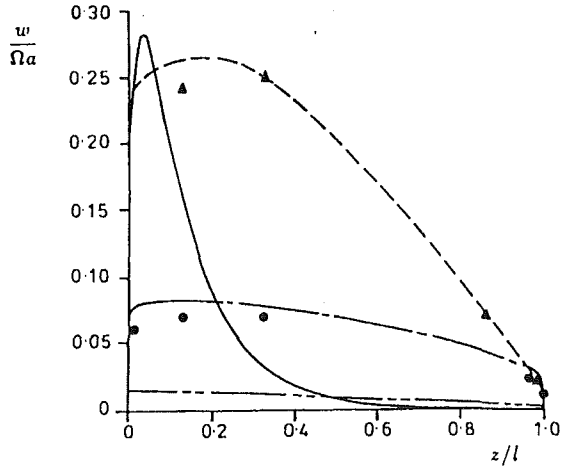

Fig. 4 (*a*) axial variation of $w/\Omega a$ at $r/a = 0$

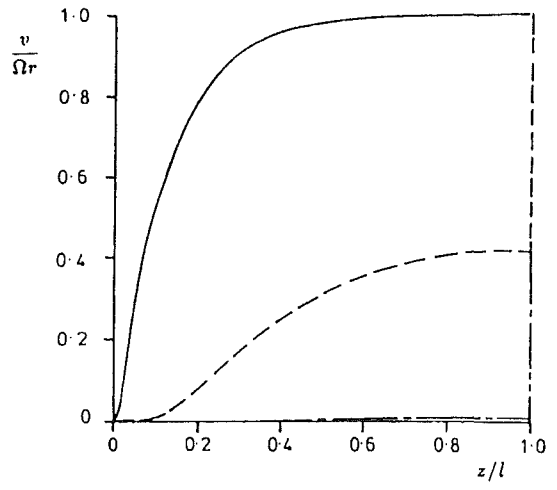

Fig. 4 (*b*) axial variation of $v/\Omega r$ at $r/a = 0.017$

Fig. 4 Effect of E^* on axial variation of velocity for $G \approx 40$. Numerical solutions: ———, $E^* = 0.2$; - - -, $E^* = 0.0266$; — - —, $E^* = 0.0027$; — - - —, $E^* = 0.0002$. Experimental data: ▲, $E^* = 0.0266$; ●, $E^* = 0.0027$.

body rotation, and the resulting centripetal acceleration will be balanced by a radial distribution of pressure. At the end walls of the tube, the axial forces due to the pressure are balanced by reactive forces on the walls. However, if one of the end walls were to be removed, the balance would be destroyed and high-pressure air near the cylindrical wall would flow axially out of the tube into the atmosphere to be replaced by an axial inflow of fresh air along the axis.

A comprehensive experimental study of self-induced flow was conducted by Ivey (1988), and a theoretical study was made by Gilham (1990). Laminar flow occurred in all the cases tested and is believed to occur inside the compressor shafts of aero-engines. Many of the results of this work for isothermal self-induced flow in a constant-diameter tube were reported by Gilham et al. (1991a), and the salient features are summarized below.

Self-induced flow depends on the Ekman number, E, and the length-to-radius ratio, G. Insight into the problem can be gained by considering the "linear equations" of motion, in which the nonlinear inertia terms in the Navier–Stokes equations, expressed in a rotating frame of reference, are assumed to be negligibly small compared with the Coriolis terms. Gilham considered the case of a rotating tube, with one end open and the other sealed, in which the fluid at the open end was in near solid-body rotation. The solutions of the linear equations showed that, for small values of the Rossby number and large values of G, the flow can be characterized by a single, modified, Ekman number E^*, where $E^* = GE$. For $E^* > 0.2$, recirculation is confined to the open end, and the axial component of velocity decays exponentially along the tube; this corresponds to the long-tube case. For $E^* < 0.2$, the flow extends to the end wall where radial outflow occurs in a Ekman layer (Ekman, 1905); this corresponds to the short-tube case. For $E^* < 0.0025$, there is an inviscid core with an Ekman layer on the end wall and a Stewartson layer (Stewartson, 1957) on the cylindrical wall of the tube.

Gilham et al. (1991a) presented numerical solutions of the Navier–Stokes equations, and described an experimental study using flow visualization and laser-Doppler anemometry. Figure 3 shows the flow visualization near the sealed end of a rotating glass tube, for $G = 28.8$ and $E = 6.25 \times 10^{-4}$ ($E^* = 0.018$). A pulse of smoke was released at the open end of the glass tube, an r–z plane was illuminated with a 4 W argon-ion laser, and a sequence of photographs was taken at five frames per second. The particular frame shown in Fig. 3 was photographed five seconds after smoke was first seen to have entered the tube. The smoke front, which appears white, has reached the end wall ($z/l = 1$), where it moves radially outward in a boundary layer, and a "tongue" of smoke can be seen returning toward the open end inside the annular boundary layer on the cylindrical wall.

Figure 4 shows the axial variation of the axial and tangential components of velocity on, or near, the axis of a rotating tube, with $G \approx 40$, for various values of E^*. The measurements were made using the apparatus described in Section 2.1, and the numerical solutions of the Navier–Stokes equations were obtained using the methods described by Gilham et al. (1991a). From Fig. 4(*a*) it can be seen that, for $E^* = 0.2$, the axial component of velocity decays rapidly with distance from the open end, and Fig. 4(*b*) shows that, for $E^* = 0.2$, the fluid is in solid-body rotation near the sealed end; this is the long-tube case referred to above. The axial decay of $w/\Omega a$ is attenuated as E^* decreases, and the short-tube case occurs for $E^* \leq 0.0266$; for $E^* = 0.0002$, there is very little rotation in the core of fluid outside the boundary layers. It should be noted that $E^* \propto (\Omega a)^{-1}$; as a consequence, *w increases*, despite the fact that $w/\Omega a$ *decreases*, as E^* is reduced.

The flow in the boundary layer on the end wall is closely related to that on an infinite disk rotating in a quiescent environment: the free disk. The von Karman equations for the free disk (von Kármán, 1921) can be obtained from the Navier–Stokes equations using the transformations:

$$F(\zeta) = \frac{u}{\Omega r},\ G(\zeta) = \frac{v}{\Omega r},\ H(\zeta) = \frac{w}{(\Omega\nu)^{1/2}},\ P(\zeta) = \frac{p}{\rho\Omega\nu} \tag{2.1}$$

where

$$\zeta = z' \left(\frac{\Omega}{\nu}\right)^{1/2} \tag{2.2}$$

and z' is the axial distance from the disk. (The definitions of G and H given above are not used outside this section of the paper.) The boundary conditions for the free disk are:

$$F(0) = 0,\ G(0) = 1,\ H(0) = 0,$$
$$F(\zeta) \to 0,\ G(\zeta) \to 0 \text{ as } \zeta \to \infty. \tag{2.3}$$

Cochran (1934) obtained the first numerical solutions of the

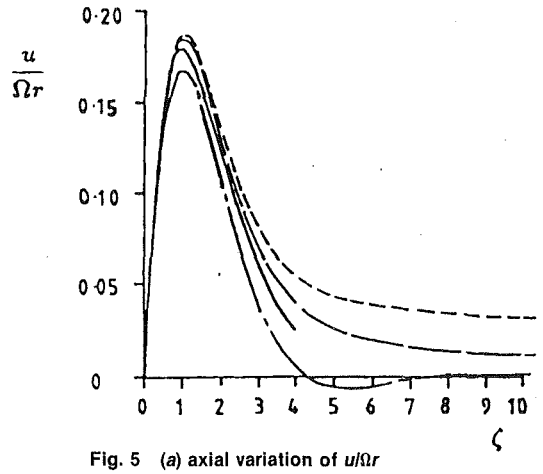

Fig. 5 (*a*) axial variation of $u/\Omega r$

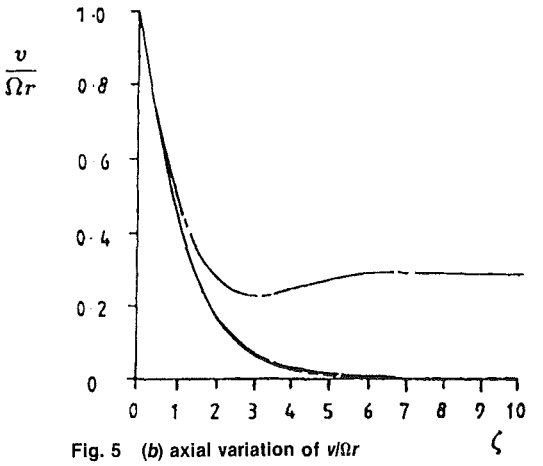

Fig. 5 (*b*) axial variation of $v/\Omega r$

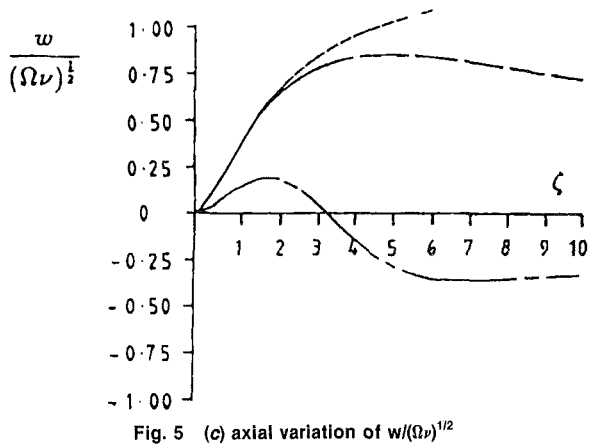

Fig. 5 (*c*) axial variation of $w/(\Omega\nu)^{1/2}$

Fig. 5 Effect of *r/a* on velocity distributions at sealed end for $G = 42.6$, $E^* = 0.0027$. Numerical solutions: ---; $r/a = 0.25$; ——, $r/a = 0.50$; — - — $r/a = 0.75$. Free-disk profiles: ——, Rogers (see Owen and Rogers, 1989).

von Karman equations and showed that $H(\zeta) \to 0.886$ as $\zeta \to \infty$. Rogers (see Owen and Rogers, 1989) obtained more accurate solutions, which are identical with those of Benton (1966), and $H(\zeta) \to 0.8845$ as $\zeta \to \infty$. Also, for the free disk, the boundary-layer thickness δ (defined by the point where $v/\Omega r = 0.01$) is given by

$$\delta \approx 5.5\left(\frac{\nu}{\Omega}\right)^{1/2}. \tag{2.4}$$

Figure 5 shows the computed variation of $u/\Omega r$, $v/\Omega r$ and $w/(\Omega\nu)^{1/2}$ with ζ, for a rotating tube with $G = 42.6$ and $E^* = 0.0027$,

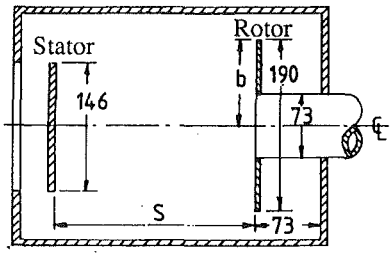

Fig. 6 (*a*) Rotor-stator system at open end (dimensions in mm)

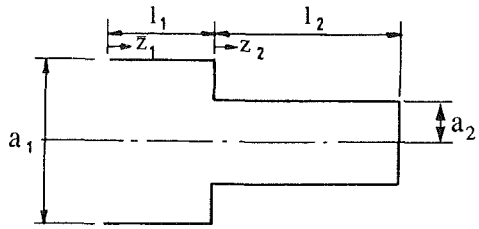

Fig. 6 (*b*) Reducing-diameter case

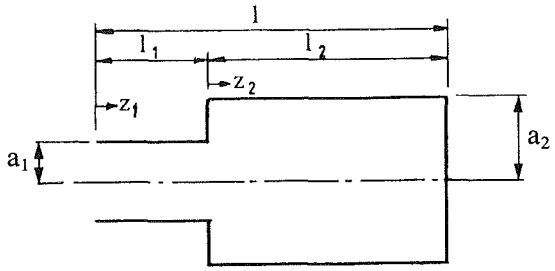

Fig. 6 (*c*) Increasing-diameter case

Fig. 6 Schematic diagram of stepped tubes and rotor-stator system tested

together with the free-disk profiles of Rogers. For small ζ, the computed values of $u/\Omega r$ are similar to the free-disk values; for $r/a \leq 0.5$, the computed values of $v/\Omega r$ are almost identical with those for the free disk for all ζ; for $r/a \leq 0.5$, the computed values of $w/(\Omega\nu)^{1/2}$ are similar to the free-disk values for small ζ. Away from the end wall, the axial component of velocity in the core of the fluid can be significantly greater than that associated with the free disk.

For a constant value of E, the radial extent over which free-disk-type flow occurs increases as E^* decreases (that is, as G decreases). However, only a fraction of the fluid entering the open end of the tube reaches the sealed end: Most is recirculated into the annular boundary layer on the cylindrical wall. The "pumping effect" creating the self-induced flow is caused mainly by the cylindrical wall, and not by the end wall, of the tube.

2.3 Isothermal Flow in Stepped Tubes. In an aero-engine, the compressor shaft is often "stepped": It changes in diameter from section to section. Also, as indicated in Fig. 1 there is a turbine disk near the open end, and this can create swirl inside the enclosure from which the hot anti-icing air is drawn. Gilham et al. (1991b) reported experiments, using the apparatus described in Section 2.1.1, involving stepped tubes as well as tubes in which a rotor-stator assembly was placed at the open end, as shown in Fig. 6, and LDA measurements of the axial component of velocity were made on the axis of the tube near the sealed end. These measurements were made for constant-diameter tubes, with and without the rotor-stator system at the open end, and for stepped tubes, for both the reducing-diameter and increasing-diameter cases. The con-

stant-diameter tube without the rotor–stator system was used as a datum with which other tubes were compared.

For the reducing-diameter case, tests were conducted for $G_2 = 28.8$, $a_2/a_1 = 0.8$, for $G_2 = 42.6$, $a_2/a_1 = 0.5$, and for $E_2 \geq 2 \times 10^{-3}$ (where the subscripts 1 and 2 refer to the tubes at the open end and sealed end, respectively). From these tests it was concluded that the flow near the sealed end of the tube was not significantly different from that for the "equivalent constant-diameter tube" (where $G = G_2$). In other words, for the conditions tested, the open-ended large-diameter tube does not appear to affect the flow near the sealed end of the small-diameter tube. It should be noted, however, that as $a_2/a_1 \rightarrow 1$, the flow must approach that for a constant-diameter tube in which $G = (l_1 + l_2)/a_2$. The "critical value" of a_2/a_1, above which the effect of the large-diameter tube becomes significant, is not known.

For the increasing-diameter case, tests were conducted for $G_1 = 22.4$, $G_2 = 25.0$, and $a_2/a_1 = 1.25$, and for $E_2 \geq 2 \times 10^{-3}$. The results were compared with a "datum" constant-diameter tube with $l = l_1 + l_2$ and $a = a_2$ ($G = 42.2$). Although the velocity near the sealed end was reduced, compared with the datum, the attenuation was found to be relatively small for $E < 3 \times 10^{-3}$. This suggests that a restriction inside the compressor shaft need not impair the anti-icing flow to the sealed end.

For the rotor–stator system, tests were conducted with a disk of outer radius $b = 95$ mm attached to a tube of inner radius $a = 36.5$ mm. A stator of 146 mm diameter was placed inside the stationary enclosure, an axial distance s from the disk, with $s/b = 0.38$ and 2.3. Measurements made for $E \geq 2.5 \times 10^{-3}$ showed that, for $s/b = 2.3$, the axial component of velocity near the sealed end of the tube was similar to that for the datum case. For $s/b = 0.38$, however, the velocity near the sealed end was typically about half that of the datum case; the reduction in self-induced flow was attributed to swirl in the air near the open end of the tube. This problem was overcome by the use of an anti-swirl device (see Ivey, 1988), which was subsequently patented (Rolls Royce, 1988).

The above-mentioned tests showed that self-induced flow could be used for anti-icing in constant-diameter or stepped tubes, with or without a rotor–stator system near the open end.

2.4 Heat Transfer to the End Wall. Gilham et al. (1992) reported a combined numerical and experimental study of the heat transfer to the end wall of a constant-diameter rotating tube. For the experimental results, the rig described in Section 2.1.2 was used; for the numerical results, solutions of the Navier–Stokes and energy equations (see Section 3) were obtained. For the computations, it was assumed that the tube walls had a temperature T_o and the air entered the system with a temperature T_∞. For the "heating case," $T_\infty = 20°C$ and $T_o = 0°C$; for the "cooling case," $T_\infty = 20°C$ and $T_o = 40°C$.

It is convenient to define the Eckert number as

$$\mathrm{Ec} = \frac{\Omega^2 a^2}{C_p \Delta T} \tag{2.5}$$

where $\Delta T = |T_\infty - T_o|$. Frictional heating, which is negligible for $\mathrm{Ec} \ll 1$, increases as Ec increases and can be significant at the small values of E^* for which many of the computations were conducted.

The influence of frictional heating on the Nusselt number can be reduced by using a "modified Nusselt number" (see Owen and Rogers, 1989) defined as

$$\mathrm{Nu}_l^* = \frac{q_l r}{k(T_{l,\,ad} - T_l)} \tag{2.6}$$

where $T_{l,\,ad}$ is the adiabatic-disk temperature.

It was shown in Section 2.2 that the flow near the end wall is related to that for the free disk. For this case,

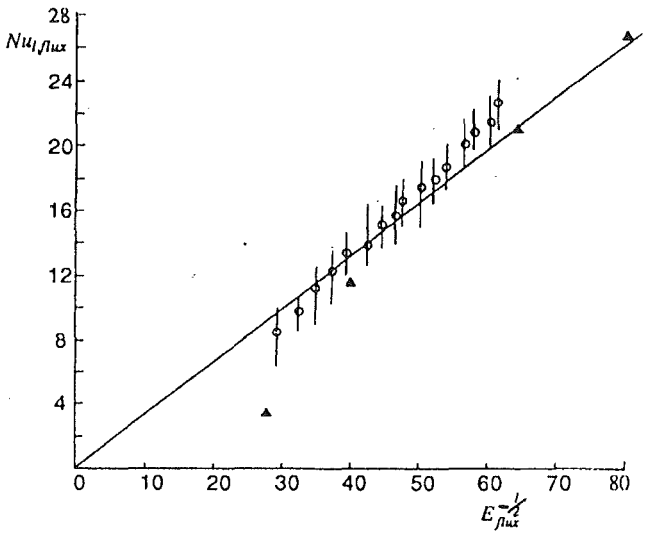

Fig. 7 Comparison between measured and computed average Nusselt numbers at the sealed end for $G \approx 30$. ▲, computed values; ○, measured values; |, experimental uncertainty; ——, Eq. (2.9)

$$T_{l,\,ad} = T_\infty + R\,\frac{\Omega^2 r^2}{2C_p} \tag{2.7}$$

where R is a recovery factor, which for air is approximated by $R = \mathrm{Pr}^{1/3}$.

Gilham et al. (1992) used the Reynolds analogy for the end wall to obtain a correlation of the computed radially weighted-average Nusselt number, $\mathrm{Nu}^*_{l,\,av}$. For $5 < G < 40$, $2 \times 10^{-4} < E^* < 2 \times 10^{-3}$ and $\mathrm{Ec} < 0.3$ (which is the range of interest for anti-icing systems), the correlation is

$$E^{1/2}\,\mathrm{Nu}^*_{l,\,av} = 0.397 - 0.824\,E^{*1/4} \tag{2.8}$$

For an isothermal free disk rotating in air, the average Nusselt number is given by Owen and Rogers as

$$E^{1/2}\mathrm{Nu}^*_{l,\,av} = 0.326 \tag{2.9}$$

It is interesting to note that, according to Eq. (2.8), the free-disk value should occur at $E^* = 5.51 \times 10^{-5}$. Although this value of E^* is outside the stated range of applicability of the correlation, Eq. (2.9) does provide a useful limiting case.

Also, from Eq. (2.8), $\mathrm{Nu}^*_{l,\,av} = 0$ when $E^* = 0.054$, which is again outside the limits of the correlation. However, for $E^* > 0.054$, where "long-tube" conditions obtain, the heat transfer at the sealed end should be governed by the relatively weak conduction and buoyancy effects inside the rotating fluid.

Equation (2.8) was obtained from computations for incompressible flow, and additional computations were carried out for compressible flow with $\beta \Delta T \leq 0.14$. It was found that buoyancy effects increase the average Nusselt number on the end wall for the "heating case," and reduce it for the "cooling case." However, for $E^* \leq 0.002$ and $\beta \Delta T \leq 0.14$, the effect of buoyancy on the Nusselt number was relatively small (< 5 percent) and could probably be ignored for most cases of engineering interest.

The average Nusselt numbers on the experimental rig were measured using a fluxmeter, of radius $a_{\mathrm{flux}} = 0.65a$, embedded in the end wall of the tube. The reference air temperature for the Nusselt numbers was based on measurements made on the axis of the tube at $z/l = 0.892$. Figure 7 shows the variation of $\mathrm{Nu}_{l,\,\mathrm{flux}}$ with $E_{\mathrm{flux}}^{-1/2}$ (where a_{flux} rather than a is used in the definitions of the Nusselt and Ekman numbers) for both the experimental and the computed results. It should be noted that the "conventional" Nusselt numbers rather than the "modified" values were used in the experiments, which were conducted for the heating case; the same definitions were used for the computed values, which were obtained assuming incom-

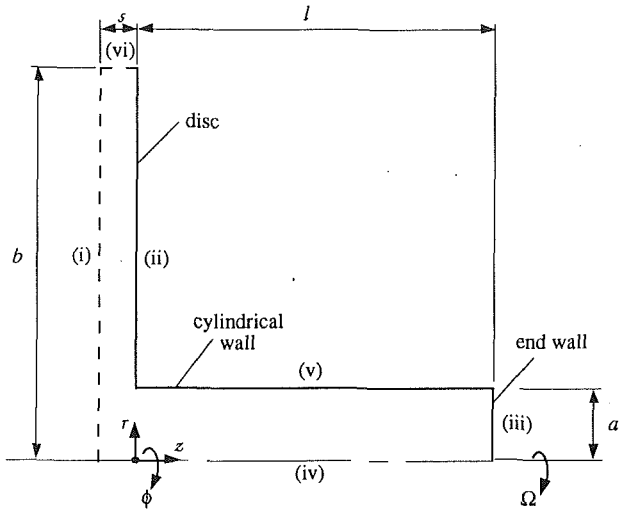

Fig. 8 Domain of integration for the rotating tube and disk (roman numerals refer to boundaries)

pressible flow. The free-disk curve corresponding to Eq. (2.9) is included for comparisons. (It should be noted that $E^{1/2}\,Nu^*_{l,\,av}$ is independent of the radius, and so Eq. (2.9) is valid for a disk, or fluxmeter, or any radius. However, E^* does depend on the radius, and so Eq. (2.8) is invalid for a fluxmeter with a radius smaller than that of the end wall; this equation is not, therefore, shown in Fig. 7.)

Figure 7 shows that, at the smaller values of $E^{-1/2}$, both the computed and the measured Nusselt numbers are lower than the free-disk curve. This is consistent with the fact that the area of the end wall exposed to the self-induced flow decreases as the Ekman number increases. At the larger values of $E^{-1/2}$, the computed Nusselt numbers become close to the free-disk curve but the measured values are higher; this might be due, in part, to buoyancy effects. The differences between the measured and computed data are, in the main, within the bounds of the experimental errors.

3 Numerical Method

3.1 Equations of Motion and Energy Equation. The equations governing the conservation of momentum, mass, and energy are given by the Navier–Stokes, continuity, and energy equations. In stationary cylindrical-polar coordinates (r, ϕ, z) assuming the flow to be steady, axisymmetric, and laminar, the equations (see Bird et al., 1960) are:

$$\frac{1}{r}\frac{\partial}{\partial r}(\rho r u^2)+\frac{\partial}{\partial z}(\rho w u)=-\frac{\partial p}{\partial r}+\frac{\rho v^2}{r}+\frac{1}{r}\frac{\partial}{\partial r}\left(\frac{4}{3}\mu r\frac{\partial u}{\partial r}\right)+\frac{\partial}{\partial z}\left(\mu\frac{\partial u}{\partial z}\right)-\frac{2}{3}\frac{u}{r}\frac{\partial \mu}{\partial r}-\frac{4}{3}\mu\frac{u}{r^2}-\frac{2}{3}\frac{\partial}{\partial r}\left(\mu\frac{\partial w}{\partial z}\right)+\frac{\partial}{\partial z}\left(\mu\frac{\partial w}{\partial r}\right) \quad (3.1)$$

$$\frac{1}{r}\frac{\partial}{\partial r}(\rho r u v)+\frac{\partial}{\partial z}(\rho w v)=-\frac{\rho u v}{r}+\frac{1}{r}\frac{\partial}{\partial r}\left(\mu r\frac{\partial v}{\partial r}\right)+\frac{\partial}{\partial z}\left(\mu\frac{\partial v}{\partial z}\right)-\frac{\mu v}{r^2}-\frac{v}{r}\frac{\partial \mu}{\partial r} \quad (3.2)$$

$$\frac{1}{r}\frac{\partial}{\partial r}(\rho r u w)+\frac{\partial}{\partial z}(\rho w^2)=-\frac{\partial p}{\partial z}+\frac{1}{r}\frac{\partial}{\partial r}\left(\mu r\frac{\partial w}{\partial r}\right)+\frac{\partial}{\partial z}\left(\frac{4}{3}\mu\frac{\partial w}{\partial z}\right)-\frac{2}{3}\frac{\partial}{\partial z}\left(\mu\frac{1}{r}\frac{\partial}{\partial r}(ru)\right)+\frac{1}{r}\frac{\partial}{\partial r}\left(\mu r\frac{\partial u}{\partial z}\right) \quad (3.3)$$

$$\frac{1}{r}\frac{\partial}{\partial r}(\rho r u)+\frac{\partial}{\partial z}(\rho w)=0 \quad (3.4)$$

$$\frac{1}{r}\frac{\partial}{\partial r}(\rho r u H)+\frac{\partial}{\partial z}(\rho w H)=\frac{1}{r}\frac{\partial}{\partial r}\left(\frac{k}{C_p}r\frac{\partial H}{\partial r}\right)+\frac{\partial}{\partial z}\left(\frac{k}{C_p}\frac{\partial H}{\partial z}\right)+S_H \quad (3.5)$$

where

$$S_H=\frac{1}{r}\frac{\partial}{\partial r}\left[\left(\mu-\frac{k}{C_p}\right)r\frac{\partial}{\partial r}\left(\frac{u^2+v^2+w^2}{2}\right)\right]+\frac{\partial}{\partial z}\left[\left(\mu-\frac{k}{C_p}\right)\frac{\partial}{\partial z}\left(\frac{u^2+v^2+w^2}{2}\right)\right]+\frac{1}{r}\frac{\partial}{\partial r}\left[\mu r\left(\frac{1}{3}u\frac{\partial u}{\partial r}-\frac{2}{3}\frac{u^2}{r}-\frac{2}{3}u\frac{\partial w}{\partial z}-\frac{v^2}{r}+w\frac{\partial u}{\partial z}\right)\right]+\frac{\partial}{\partial z}\left[\mu\left(u\frac{\partial w}{\partial r}+\frac{1}{3}w\frac{\partial w}{\partial r}-\frac{2}{3}\frac{w}{r}\frac{\partial}{\partial r}(ru)\right)\right]. \quad (3.6)$$

Here p, ρ, and μ denote pressure, density, and dynamic viscosity, respectively and (u, v, w) are the velocity components in the (r, ϕ, z) directions. The stagnation enthalpy is denoted by H $(H=C_pT+1/2(u^2+v^2+w^2))$, C_p is the specific heat capacity, which is assumed constant, and k is the thermal conductivity.

The equation of state for a perfect gas was used to calculate the density, where

$$\rho=\frac{p}{\Re T} \quad (3.7)$$

Here $\Re$ denotes the gas constant,which for air is 287 J/kgK, and T is the temperature in Kelvin.

The dynamic viscosity, μ [kg/ms], was assumed to vary according to Sutherland's law, which for air is:

$$\mu=\frac{1.46\times10^{-6}T^{3/2}}{(110+T)} \quad (3.8)$$

The thermal conductivity, k [W/mK], was evaluated according to:

$$k=\frac{\mu C_p}{\mathrm{Pr}} \quad (3.9)$$

where Pr is the Prandtl number, which was assumed constant and equal to 0.71, and $C_p=1.00$ kJ/kgK.

3.2 Boundary Conditions

3.2.1 Open End of Tube. As shown in Fig.1, in an aero-engine there is a rotating disk attached to the compressor shaft near the open end. Although Ivey (1988) found that the presence of a rotating disk at the open end of the tube had only a small effect on the measured velocity near the sealed end, the inclusion of a rotating disk in the mathematical model has the advantage of simplifying the specification of the boundary conditions near the open end. By placing the boundaries on the left-hand side of the disk, see Fig. 8, the fluid enters the system axially through boundary (i) and leaves radially through boundary (vi).

The problem can be further simplified, as described by Gilham et al. (1991a), by the use of von Kármán's (1921) equations for the "free disk." For the computations described below, the von Karman equations are assumed to apply to an annular disk, of inner radius a and outer radius b, attached to the open end of the rotating tube. Boundary (i) shown in Fig. 8 is assumed to be far enough away from the disk for the conditions at infinity to apply at $z=-s$, so that

$$u=0,\ v=0,\ p=p_{\mathrm{atm}} \text{ at } z=-s \quad (3.10)$$

where p_{atm} is the atmospheric pressure. Also, the radius of the

disk is assumed to be large enough so that the von Kármán similarity solutions (see Section 2.2) are applicable such that

$$\frac{\partial}{\partial r}\left(\frac{u}{r}\right)=0,\quad \frac{\partial}{\partial r}\left(\frac{v}{r}\right)=0,\quad \frac{\partial w}{\partial r}=0,\quad \frac{\partial p}{\partial r}=0 \qquad (3.11)$$

Equations (3.10) and (3.11) ensure that, as for the free-disk case, fluid enters the system axially through boundary (*i*) and leaves radially through boundary (*vi*).

The radius of the disk was set at $b = 5a$ and, for most cases, $s=a$, which ensured that $\delta \ll s$ where δ is given by Eq. (2.4). For the case of a solid disk, Gilham (1990) found that a value of $s=4\delta$ was sufficient to ensure that the computed velocity profiles were in good agreement with the free-disk solutions given by Owen and Rogers (1989).

3.2.2 Conditions for the Six Boundaries. All solid surfaces were assumed to be at the same temperature, $T=T_o$, and no-slip conditions were applied at these surfaces. At inlet to the system, the fluid temperature was taken to be $T=T_\infty$ (where $T_\infty=293$ K), and the free-disk conditions discussed above were used for the velocity. The atmospheric pressure was taken to be $p_{\text{atm}}=1$ bar, and all nondimensional parameters were based on properties calculated at $T=T_\infty$ and $p=p_{\text{atm}}$. For the tube axis, $r=0$, symmetry conditions were assumed for w and T.

The conditions for the six boundaries shown in Fig. 8 are given below.

(*i*) $z=-s,\ 0\le r\le b$:

$u=0,\ v=0,\ p=p_{\text{atm}},\ T=T_\infty$;

(*ii*) $z=0,\ a\le r\le b$:

$u=0,\ v=\Omega r,\ w=0,\ T=T_o$;

(*iii*) $z=l,\ 0\le r\le a$:

$u=0,\ v=\Omega r,\ w=0,\ T=T_o$;

(*iv*) $r=0,\ -s\le z\le l$:

$u=0,\ v=0,\ \dfrac{\partial w}{\partial r}=0,\ \dfrac{\partial T}{\partial r}=0$;

(*v*) $r=a,\ 0\le z\le l$:

$u=0,\ v=\Omega a,\ w=0,\ T=T_o$;

(*vi*) $r=b,\ -s\le z\le 0$:

$$\frac{\partial}{\partial r}\left(\frac{u}{r}\right)=0,\ \frac{\partial}{\partial r}\left(\frac{v}{r}\right)=0,\ \frac{\partial w}{\partial r}=0,\ \frac{\partial T}{\partial r}=0. \qquad (3.12)$$

3.3 Finite-Difference Equations. An outline of the finite-difference method is given below, and the interested reader is referred to Gilham (1990) or Gilham et al. (1991a, b) for further details. The finite-difference equations were obtained by integrating the momentum and energy equations over a control volume formed by a rectangular, nonuniform, staggered grid, as recommended by Patankar (1980) and by Patankar and Spalding (1972). The nonuniform grid was generated using a geometric progression, with a maximum "grid-expansion factor" of 1.3.

The resulting finite-difference equations were solved using the nonlinear multigrid algorithm of Vaughan et al. (1989). Underrelaxation was implemented implicitly, via the coefficients, for the momentum and energy equations and explicitly for the pressure; underrelaxation factors were in the range 0.3 to 0.8. Numerical instabilities caused by the strong coupling between the radial and tangential momentum equations were reduced by the method suggested by Gosman et al. (1976).

Computations were conducted for $5 \le G \le 40$ and $5 \times 10^{-5} \le \mathrm{E} \le 0.04$, and the number of nodes used depended on G and E. For $G=10$ and $\mathrm{E}=2\times10^{-3}$, 128 axial and 65 radial nodes were used in the tube, and 65 axial and 97 radial nodes were used in the region outside the open end. For incompressible flow, the multigrid method required 89 iterations for solution of the momentum equations, which took 672 minutes of CPU time on a VAX 8530 computer; solution of the energy equation took 29 iterations, which required 97 CPU minutes. Longer time was required for the compressible cases as the momentum and energy equation could not be uncoupled.

4 Self-Induced Flow and Heat Transfer to the Cylindrical Wall

4.1 Computed Isotherms. Figure 9 shows the computed isotherms for incompressible flow for $G=40$, $\mathrm{E}^*=2\times10^{-2}$, 2×10^{-3} and 2×10^{-4}. The nondimensional temperature, θ, is defined as:

$$\theta=\frac{T-T_o}{T_\infty-T_o} \qquad (4.1)$$

where the temperature of the air at inlet is $T_\infty=293$ K and the temperature of the solid surfaces is $T_o=313$ K. This corresponds to the "cooling case" where the air is colder than the surface of the tube ($T_\infty<T_o$). Isotherms for the "heating case" ($T_\infty>T_o$), and for other values of G, are similar to those shown in Fig. 9. Owing to the scale chosen for the figure, the steep gradients at the sealed end, where $\theta=0$, cannot be seen. This is the case for $\mathrm{E}^*=2\times10^{-3}$ and 2×10^{-4}, where the Ekman layer is very thin.

In all cases shown, heat flows from the sealed end towards the open end. For $\mathrm{E}^*=2\times10^{-2}$, where the self-induced flow is very weak, the heat transfer is mainly by conduction. For the other cases, the thermal boundary layer on the cylindrical wall becomes thinner as E^* is reduced; the same is true of the thermal boundary layer on the end wall but, as stated above, this cannot be seen owing to the scale of the figure. For $\mathrm{E}^*=2\times10^{-4}$, the temperature of the core of fluid near the axis is virtually isothermal and equal to the temperature of the air outside the tube; the isotherms shown are inside the velocity boundary layer on the cylindrical surface.

4.2 Entrained Flow and Moments on Cylindrical Wall. The flow rate at the open end of the tube exceeds that near the sealed end; most of the fluid is recirculated from the central core to the annular boundary layer on the cylindrical wall. At any axial location, the mass flow rate, m, of fluid flowing toward the sealed end (which equals that flowing toward the open end) is given by

$$m=\pi\int_0^a \rho r|w|\,dr \qquad (4.2)$$

The nondimensional flow rate, C_w, is defined as

$$C_w=\frac{m}{\mu a} \qquad (4.3)$$

and Fig. 10 shows the axial variation of the computed values of $C_w\mathrm{E}$ for $G=40$ and for various values of E^*. For $\mathrm{E}^*=0.2$, the long-tube case, $C_w\mathrm{E}$, decays to zero before the flow reaches the sealed end. For the short-tube cases, flow reaches the sealed end, and $C_w\mathrm{E}$ decreases (although C_w *increases*) as E^* decreases.

Figure 11 shows the computed variation of $(C_{w,\infty}\mathrm{E})^{-1}$ with $\mathrm{E}^{*1/2}$ for $G=40$, where $C_{w,\infty}$ is the value of C_w at the inlet of the tube. The computed results can be correlated for $2\times10^{-4} < \mathrm{E}^* < 10^{-2}$ and $G>5$ by

$$(C_{w,\infty}\mathrm{E})^{-1}=0.393\ \mathrm{E}^{*-1/2}+0.513 \qquad (4.4)$$

The nondimensional flow rate associated with a free disk is, according to Owen and Rogers (1989),

$$C_{w,fd}=2.779\ \mathrm{E}^{-1/2} \qquad (4.5)$$

It is interesting to note that as $\mathrm{E}^*\to 0$, Eq. (4.4) shows that $C_{w,\infty}\mathrm{E}\to 2.54\,\mathrm{E}^{*1/2}$, or

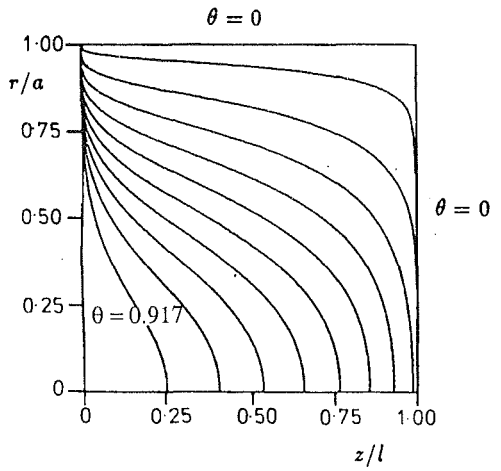

Fig. 9 (*a*) $E^* = 2 \times 10^{-2}$

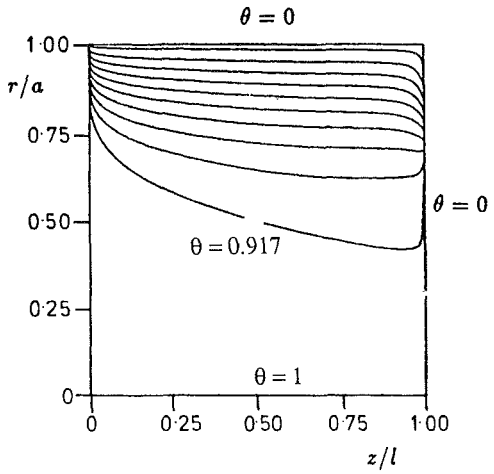

Fig. 9 (*b*) $E^* = 2 \times 10^{-3}$

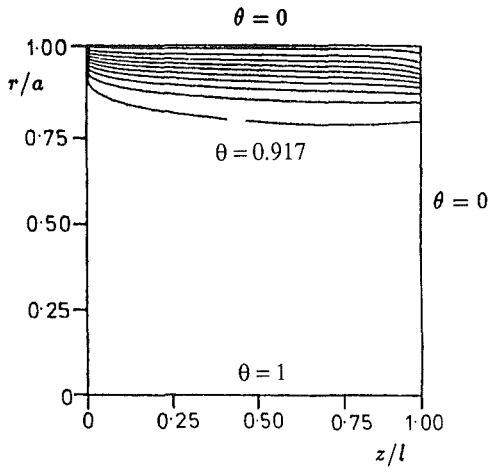

Fig. 9 (*c*) $E^* = 2 \times 10^{-4}$

Fig. 9 Effect of E^* on computed isotherms for $G = 40$: cooling case ($T_\infty < T_o$)

$$\frac{C_{w,\infty}}{C_{w,fd}} \rightarrow 0.916\, G^{1/2} \tag{4.6}$$

That is, for $G > 1.09$, $C_{w,\infty} > C_{w,fd}$: The "pumping effect" of the cylindrical wall of the tube is stronger for small values of E^* than that of the end wall.

For the cylindrical wall, the moment coefficient, $C_{m,a}$, is defined as

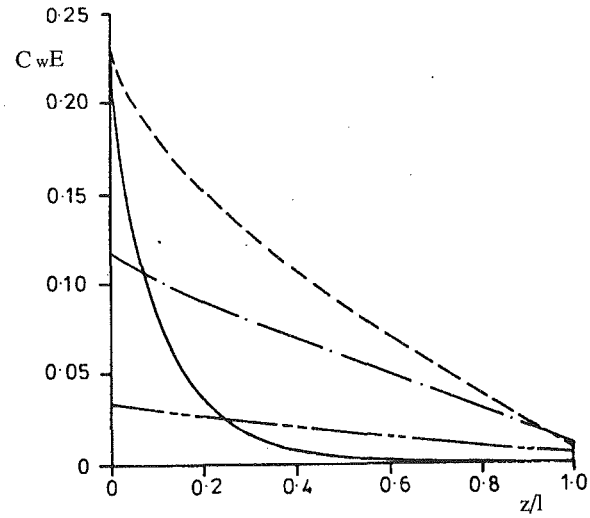

Fig. 10 Axial variation of computed values of C_wE for $G \approx 40$. ——, $E^* = 0.2$; ---, $E^* = 2.7 \times 10^{-2}$; —·—, $E^* = 2.7 \times 10^{-3}$; — - - —, $E^* = 2 \times 10^{-4}$.

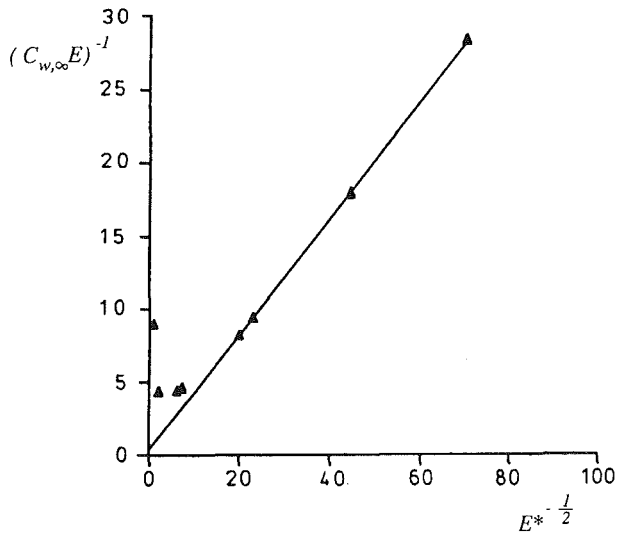

Fig. 11 Variation of $(C_{w,\infty}E)^{-1}$ with $E^{*-1/2}$. ▲, computed values for $G = 40$; ——, Eq. (4.4)

$$C_{m,a} = \frac{M_a}{1/2\rho\Omega^2 a^5} \tag{4.7}$$

where

$$M_a = 2\pi a^2 \mu \int_0^1 \left[r \frac{\partial}{\partial r} \left(\frac{v}{r} \right) \right]_{r=a} dz. \tag{4.8}$$

Figure 12 shows the variation of the computed values of $C_{m,a}E^{*-1}$ with $E^{*-1/3}$ for $G = 40$. The numerical values can be correlated for $2 \times 10^{-4} < E^* < 10^{-2}$ and $G > 5$ by

$$C_{m,a}E^{*-1} = 9.52\, E^{*-1/3} - 28.9 \tag{4.9}$$

Gilham (1990) showed that, for $E^* < 0.02$ and $G > 5$, the effect of G on the computed values of both C_wE and $C_{m,a}E^{*-1}$ was relatively small. Using the Reynolds analogy discussed below, the moment coefficients can be used to provide an estimate for the Nusselt numbers on the cylindrical wall of the tube.

4.3 The Reynolds Analogy for a Rotating Cylindrical Wall. Owen and Rogers (1989) discussed the Reynolds analogy applied to a rotating disk, and Gilham et al. (1992) applied the analogy to the end wall of a rotating tube. This section

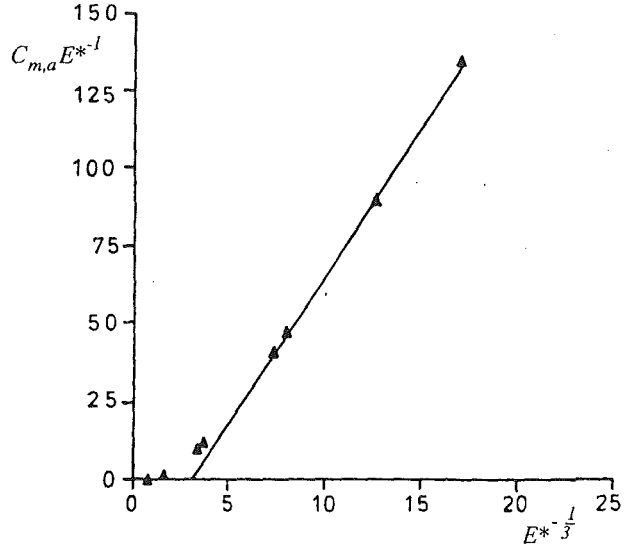

Fig. 12 Variation of computed values of $C_{m,a}E^{*-1}$ with $E^{*-1/3}$, ▲ computed values for $G=40$; —, Eq. (4.9)

considers the application of the analogy to a rotating cylindrical wall.

For incompressible flow, with $Pr=1$, Eqs. (3.2) and (3.5) can be simplified to

$$u\frac{\partial v}{\partial r}+w\frac{\partial v}{\partial z}+\frac{uv}{r}=\nu\left(\frac{\partial^2 v}{\partial r^2}+\frac{1}{r}\frac{\partial v}{\partial r}-\frac{v}{r^2}+\frac{\partial^2 v}{\partial z^2}\right) \tag{4.10}$$

$$u\frac{\partial H}{\partial r}+w\frac{\partial H}{\partial z}=\alpha\left(\frac{\partial^2 H}{\partial r^2}+\frac{1}{r}\frac{\partial H}{\partial r}+\frac{\partial^2 H}{\partial z^2}\right). \tag{4.11}$$

Consider the case where there is a boundary layer of thickness δ on the cylindrical wall and a central core of rotating fluid. When the boundary-layer thickness is small, such that $\delta \ll a$, then $v/r \ll \partial v/\partial r$ and $\partial^2/\partial z^2 \ll \partial^2/\partial r^2$, and, as $\nu=\alpha$, Eqs. (4.10) and (4.11) can be written in the common form

$$u\frac{\partial \Phi}{\partial r}+w\frac{\partial \Phi}{\partial z}=\alpha\left(\frac{\partial^2 \Phi}{\partial r^2}+\frac{1}{r}\frac{\partial \Phi}{\partial r}\right) \tag{4.12}$$

where

$$\Phi=\frac{v-\omega a}{a(\Omega-\omega)} \text{ or } \Phi=\frac{H-H_c}{H_a-H_c} \tag{4.13}$$

for Eqs. (4.10) and (4.11), respectively. Here, a is the radius of the cylinder, Ω and ω are the angular speeds of the cylinder and the fluid core, respectively, and the subscripts a and c refer to the cylindrical wall and to the core, respectively.

If the boundary conditions and initial conditions for v and H are similar, then their solutions are similar, and throughout the boundary layer

$$\frac{v-\omega a}{a(\Omega-\omega)}=\frac{H-H_c}{H_a-H_c} \tag{4.14}$$

On the cylindrical wall $u=0$, $v=\Omega a$, $w=0$, and the local heat flux, q_a, is given by

$$q_a=-k\left(\frac{\partial T}{\partial r}\right)_{r=a}=\frac{\tau_{\phi,a}}{a(\Omega-\omega)}\left[H_a-H_c-\Omega a^2(\Omega-\omega)\right] \tag{4.15}$$

where $\tau_{\phi,a}=\mu(\partial v/\partial r)_{r=a}$ is the tangential component of the shear stress at the cylindrical wall.

If it is assumed that $u, w \ll \Omega a$, then for an adiabatic wall ($q_a=0$) the surface temperature, $T_{a,ad}$, is given by

$$T_{a,ad}=T_c+\frac{a^2(\Omega-\omega)^2}{2C_p} \tag{4.16}$$

Thus, from Eqs. (4.15) and (4.16),

$$q_a=-k\left(\frac{\partial T}{\partial r}\right)_{r=a}=\frac{\tau_{\phi,a}}{a(\Omega-\omega)}C_p\left[T_a-T_{a,ad}\right] \tag{4.17}$$

The modified local Nusselt number is defined as

$$\mathrm{Nu}_a^*=\frac{q_a a}{k(T_{a,ad}-T_a)} \tag{4.18}$$

and so

$$\mathrm{Nu}_a^*=\frac{1}{\mathrm{E}}\frac{\tau_{\phi,a}}{\rho\Omega^2 a^2(1-\omega/\Omega)}. \tag{4.19}$$

If the core of fluid outside the boundary layer is nonrotating and isothermal (such that $T_c=T_\infty$, the temperature of the fluid at inlet to the tube), Eqs. (4.16) and (4.19) reduce to

$$T_{a,ad}=T_\infty+\frac{\Omega^2 a^2}{2C_p} \tag{4.20}$$

$$\mathrm{Nu}_a^*=\frac{1}{\mathrm{E}}\frac{\tau_{\phi,a}}{\rho\Omega^2 a^2} \tag{4.21}$$

and the average Nusselt number for a cylinder of length l is given by

$$\mathrm{Nu}_{a,av}^*=\frac{C_{m,a}}{4\pi \mathrm{E}^*} \tag{4.22}$$

where $C_{m,a}$ is the moment coefficient for the cylindrical wall defined by Eq. (4.7).

For nonunity Prandtl numbers, Eqs. (4.20), (4.21), and (4.22) require further modification such that

$$T_{a,ad}=T_\infty+R\frac{\Omega^2 a^2}{2C_p}, \tag{4.23}$$

$$\mathrm{Nu}_a^*=f(\mathrm{Pr})\frac{1}{\mathrm{E}}\frac{\tau_{\phi,a}}{\rho\Omega^2 a^2} \tag{4.24}$$

$$\mathrm{Nu}_{a,av}^*=f(\mathrm{Pr})\frac{C_{m,a}}{4\pi \mathrm{E}^*} \tag{4.25}$$

where $f(\mathrm{Pr})$ and the recovery factor R both depend on Pr.

4.4 Heat Transfer to the Cylindrical Wall. Figure 13 shows the computed axial variation of Nu_a for the heating case ($T_\infty > T_o$) for $G=40$ and various values of E^*. There is a sharp reduction of Nu_a near the open end of the tube, where recirculation is strongest, followed by a more gradual reduction along the tube as the boundary layer on the cylindrical wall thickens. For $\mathrm{E}^*=2\times10^{-4}$, there is a sudden rise and fall in Nu_a near the sealed end; this is caused by impingement of the radial outflow from the boundary layer on the end wall.

It can also be seen from Fig. 13 that Nu_a increases as E^* decreases. However, part of this increase is caused by frictional heating; Nu_a is not based on the adiabatic-wall temperature, and the Eckert number increases from $\mathrm{Ec}=1.15\times10^{-4}$ at $\mathrm{E}^*=2\times10^{-2}$ to $\mathrm{Ec}=1.15$ at $\mathrm{E}^*=2\times10^{-4}$. (The increase of Nu_a with decreasing E^* is smaller for the cooling case, where $T_\infty < T_o$, as frictional heating *reduces* the heat transfer from the wall to the fluid.)

By using the adiabatic-wall temperature given by Eq. (4.20), the modified average Nusselt number, $\mathrm{Nu}_{a,av}^*$, becomes virtually independent of the Eckert number for both the heating and the cooling cases. The Reynolds analogy shows that $\mathrm{Nu}_{a,av}^* \propto C_{m,a}\mathrm{E}^{*-1}$ (see Eq. (4.25)), and Fig. 14 provides evidence to confirm this relationship. The computations were carried out for $G=40$, and the solid line is given by

$$\mathrm{Nu}_{a,av}^*=0.0676\,C_{m,a}\,\mathrm{E}^{*-1} \tag{4.26}$$

which is valid for both the heating and the cooling cases. This suggests that $f(\mathrm{Pr})$ in Eq. (4.25) can be approximated, for air, by

$$f(\mathrm{Pr})=0.850\approx \mathrm{Pr}^{1/2} \tag{4.27}$$

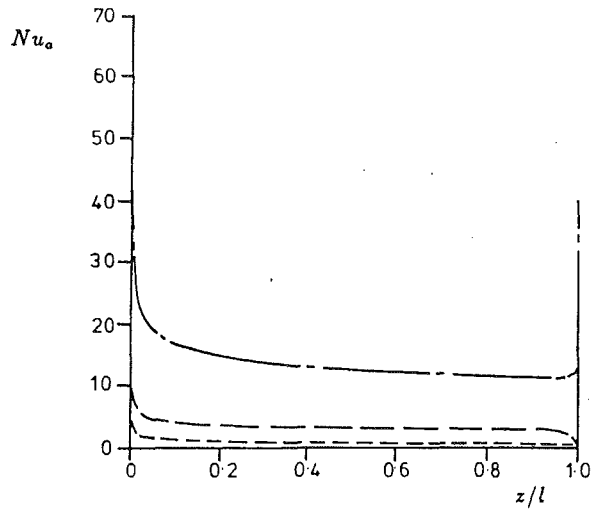

Fig. 13 Axial variation of computed value of Nu_a for $G=40$: heating case ($T_\infty > T_o$) ---, $E^*=2\times10^{-2}$; ———, $E^*=2\times10^{-3}$; — - — $E^*=2\times10^{-4}$

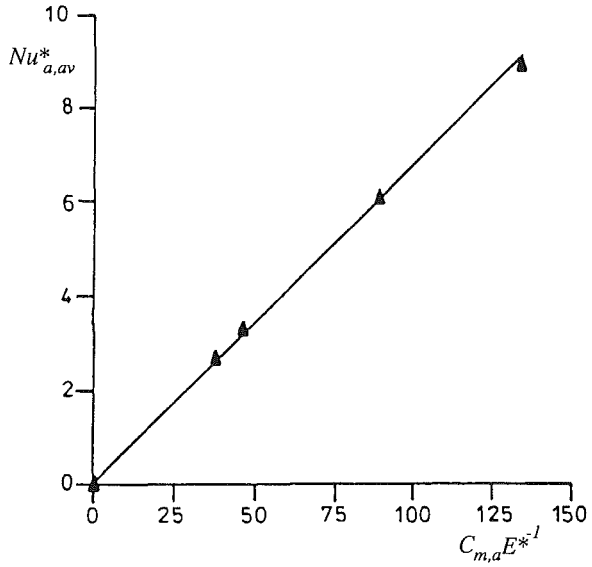

Fig. 14 Variation of $Nu^*_{a,av}$ with $C_{m,a}\,E^{*-1}$ ▲, computed values for $G=40$; ——— , Eq. (4.26)

Applying Eq. (4.26) to Eq. (4.9) gives

$$Nu^*_{a,\,av}=0.643\,E^{*-1/3}-1.95 \tag{4.28}$$

and Fig. 15 shows that Eq. (4.28) provides a good fit to the computed Nusselt numbers. This relationship should be valid over the same range as Eq. (4.9): $2\times10^{-4}<E^*<10^{-2}$ and $G>5$.

Ivey (1988) was unable to make accurate measurements of the heat flux through the cylindrical wall of the rotating tube; unlike the end wall, the cylindrical wall contained no fluxmeters. However, using measured values of the thickness of the annular boundary layer and a simple conduction model for the heat transfer, Ivey did obtain estimates of the local Nusselt numbers. Although these estimates were similar in magnitude to the computed values, no detailed comparison is possible.

An additional experimental program, with a rig instrumented to measure the small Nusselt numbers that occur for the cylindrical wall, would be required to provide a complete validation of Eq. (4.28). However, as stated in Section 2.4, computed Nusselt numbers for the end wall were in good agreement with the values measured by fluxmeters, which suggests that the computed results for the cylindrical wall are probably accurate enough for design calculations.

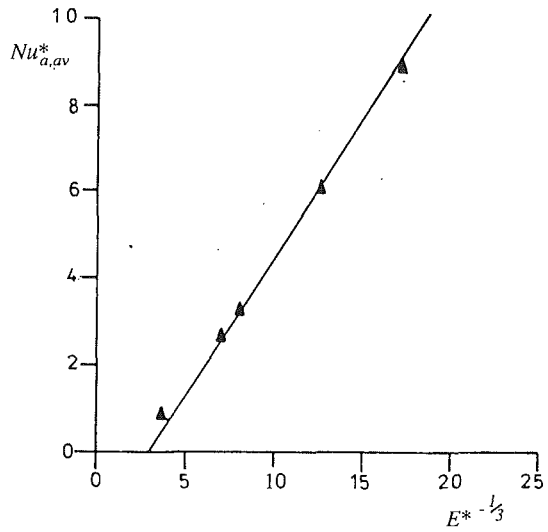

Fig. 15 Variation of $Nu^*_{a,\,av}$ with $E^{*-1/3}$ ▲, computed values for $G=40$; ——— , Eq. (4.28)

5 Application to Design of Anti-Icing Systems

5.1 Design Formulae. The information given in the preceding sections can be used for the design of anti-icing systems for the nose bullets of jet engines.

The most important parameters are the nondimensional flow rate entering (and leaving) the tube, $C_{w,\infty}$, and the modified average Nusselt numbers for the end wall, $Nu^*_{l,\,av}$, and for the cylindrical wall, $Nu^*_{a,\,av}$. The correlations given by Eqs. (4.4), (2.8), and (4.28), for a constant-diameter tube rotating in air, are rewritten below for convenience.

$$C_{w,\,\infty}=\{E(0.393\,E^{*-1/2}+0.513)\}^{-1} \tag{5.1}$$

for $G>5$, $2\times10^{-4}<E^*<10^{-2}$

$$Nu^*_{l,\,av}=E^{-1/2}\,(0.397-0.824\,E^{*1/4}) \tag{5.2}$$

for $G>5$, $2\times10^{-4}<E^*<2\times10^{-3}$, $Ec<0.3$

$$Nu^*_{a,\,av}=0.643\,E^{*-1/3}-1.95 \tag{5.3}$$

for $G>5$, $2\times10^{-4}<E^*<10^{-2}$, $Ec<1$

These correlations are for laminar flow, and no evidence of turbulent flow was observed for the ranges tested by the authors. However, as the flow on the end wall is similar to that on the free disk, transition from laminar to turbulent flow would be expected to occur for $E<5\times10^{-6}$.

The average Nusselt number for an isothermal free disk rotating in air is

$$Nu^*_{l,\,av}=0.326\,E^{-1/2} \tag{5.4}$$

and this should provide an upper bound for Eq. (5.2). This free-disk value occurs, according to Eq. (5.2), at $E^*=5.5\times10^{-5}$ (which is outside the range of validity of the correlation). For smaller values of E^*, Eq. (5.2) overestimates the free-disk value and is likely to be in error. It should be pointed out, however, that neither Eq. (5.2) nor Eq. (5.4) allows for buoyancy effects, which, as discussed in Section 2.4, can increase the Nusselt number on the end wall for the heating case above the free-disk value. Thus, Eq. (5.4) provides an approximate but not exact upper bound for the heat transfer from the end wall. (The effect of buoyancy on the computed average Nusselt number for the cylindrical wall was negligible for $\beta\Delta T\le0.14$.)

5.2 Application to Engine Data. Experimental measurements were obtained from the nose bullet of a Rolls-Royce aero-engine (Cross, 1987). The anti-icing tube (see Fig. 1) had a length-to-radius ratio of $G=28.8$, the temperatures of the

cylindrical surface of the tube and the nose bullet were 150°C and 17°C, respectively, and the Ekman number was $E = 6.3 \times 10^{-5}$. Using the measured value of the heat flux, Ivey (1988) estimated that the average Nusselt number was

$$Nu^*_{l,\,av} = 35.$$

From Eq. (5.2), with $E^* = 1.8 \times 10^{-3}$,

$$Nu^*_{l,\,av} = 29.$$

For the engine, $\beta \Delta T \approx 0.3$, which would be expected to increase the heat transfer to the nose bullet and may explain some of the discrepancy. However, considering the uncertainties and assumptions made, the agreement between the two estimates is considered to be reasonable.

It should be pointed out that, in the engine, there was a stepped tube with a reducing diameter (see Fig. 6) with $G_1 = 21$, $a_2/a_1 = 0.4$. This, as discussed in Section 2.3, should not affect significantly the conditions in the anti-icing tube, and so it is reasonable to use the correlations for a constant-diameter tube.

The above example, while of limited value, does give some confidence in the use of the correlated results.

6 Conclusions

Recently published work has shown that self-induced flow can be used to transfer heat to the sealed end of a rotating tube and to provide anti-icing for the nose bullets of aero-engines. The flow is caused by rotationally induced pressure gradients in the fluid: buoyancy effects, which can increase the heat transfer to the sealed end, are not responsible for the flow.

For the conditions tested by the authors, the flow was found to be laminar, and numerical solutions of the Navier–Stokes equations and the energy equations were in good agreement with velocity measurements inside the tube and with Nusselt numbers measured by a fluxmeter on the end wall. The flow near the end wall was shown to be similar to that associated with a free disk, although the flow rate of air entering the open end of the tube can be much greater than the free-disk entrainment rate.

The Reynolds analogy, which is applicable under certain conditions to both the end wall and the cylindrical wall, has been used to provide correlations of the computed average Nusselt numbers for the cylindrical wall. These results, together with correlations for the flow rate entering the tube and the average Nusselt numbers for the end wall, are presented in terms of the modified Ekman number, and they are valid over ranges of variables appropriate for the design of anti-icing systems in aero-engines. There are no reliable data with which to test the Nusselt numbers for the cylindrical wall, but those for the end wall agree reasonably well with the limited data available from tests on an actual anti-icing system.

Acknowledgments

The work was conducted while we were at the University of Sussex, and we wish to thank SERC and Rolls Royce plc for funding the research program.

References

Benton, E. R., 1966, "On the Flow Due to a Rotating Disc," *J. Fluid Mech.*, Vol. 24, pp. 781–800.

Bird, R. B., Stewart, W. D., and Lightfoot, E. N., 1960, *Transport Phenomena*, Wiley, New York.

Cochran, W. G., 1934, "The Flow Due to a Rotating Disc," *Proc. Cambridge Phil. Soc.*, Vol. 30, pp. 365–375.

Cross, C. P., 1987, Private Communication.

Ekman, V. W., 1905, "On the Influence of the Earth's Rotation on Ocean-Currents," *Ark. Mat. Astra Fys.*, Vol. 2, pp. 1–52.

Gilham, S., 1990, "Theoretical Study of Self-Induced Flow in a Rotating Tube," D. Phil. thesis, University of Sussex, United Kingdom.

Gilham, S., Ivey, P. C., Owen, J. M., and Pincombe, J. R., 1991a, "Self-Induced Flow in a Rotating Tube," *J. Fluid Mech.*, Vol. 230, pp. 505–524.

Gilham, S., Ivey, P. C., and Owen, J. M., 1991b, "Self-Induced Flow in a Stepped Rotating Tube," ASME Paper No. 91-GT-276; ASME *Journal of Engineering for Gas Turbines and Power*, Vol. 114, 1992, pp. 268–274.

Gilham, S., Ivey, P. C., and Owen, J. M., 1992, "Self-Induced Flow and Heat Transfer in a Rotating Tube," *Int. J. Heat Fluid Flow*, Vol. 14, pp. 27–36.

Gosman, A. D., Koosinlin, M. L., Lockwood, F. C., and Spalding, D. B., 1976, "Transfer of Heat in Rotating Systems," ASME Paper No. 76-GT-25.

Ivey, P. C., 1988, "Self-Induced Flow in a Rotating Tube," D. Phil. thesis, University of Sussex, United Kingdom.

Kármán, Th. Von, 1921, "Über laminare und turbulente Reibung," *Z. angew Math. Mech.*, Vol. 1, pp. 233–252.

Owen, J. M., and Pincombe, J. R., 1981, "Rotationally Induced Flow and Heat Transfer in Circular Tubes," Report 81/TFMRC/32, School of Engineering and Applied Sciences, University of Sussex, United Kingdom.

Owen, J. M., and Rogers, R. H., 1989, *Flow and Heat Transfer in Rotating-Disc Systems. Vol. 1: Rotor-Stator Systems*, Research Studies Press, Taunton, United Kingdom; Wiley Inc., USA.

Patankar, S. V., 1980, *Numerical Heat Transfer and Fluid Flow*, McGraw-Hill, New York.

Patankar, S. V., and Spalding, D. B., 1972, "A Calculation Procedure for Heat and Mass Transfer in Three-Dimensional Parabolic Flows," *Int. J. Heat Mass Transfer*, Vol. 15, pp. 1787–1806.

Rolls Royce Limited, 1979, "Nose Bullet Anti-icing for Gas Turbine Engines," United Kingdom Patent GB 2,046,843B.

Rolls Royce plc, 1988, "Gas Turbine Engine Anti-icing System," United Kingdom Patent Application GB 2,217,393A.

Stewartson, K., 1957, "On Almost Rigid Rotations," *J. Fluid Mech.*, Vol. 3, pp. 17–26.

Vaughan, C. M., Gilham, S., and Chew, J. W., 1989, "Numerical Solutions of Rotating Disc Flows Using a Non-linear Multigrid Algorithm," *Proc. 6th Int. Conf. on Numerical Methods in Laminar and Turbulent Flow*, Vol. 6, pp. 63–73, Pineridge Press, Swansea, United Kingdom.

Ingestion Into the Upstream Wheelspace of an Axial Turbine Stage

T. Green

A. B. Turner

Thermo-Fluid Mechanics Research Centre,
School of Engineering,
The University of Sussex,
Falmer, Brighton, BN1 9QT
Sussex, United Kingdom

The upstream wheelspace of an axial air turbine stage complete with nozzle guide vanes (NGVs) and rotor blades (430 mm mean diameter) has been tested with the objective of examining the combined effect of NGVs and rotor blades on the level of mainstream ingestion for different seal flow rates. A simple axial clearance seal was used with the rotor spun up to 6650 rpm by drawing air through it from atmospheric pressure with a large centrifugal compressor. The effect of rotational speed was examined for several constant mainstream flow rates by controlling the rotor speed with an air brake. The circumferential variation in hub static pressure was measured at the trailing edge of the NGVs upstream of the seal gap and was found to affect ingestion significantly. The hub static pressure distribution on the rotor blade leading edges was rotor speed dependent and could not be measured in the experiments. The Denton three-dimensional C.F.D. computer code was used to predict the smoothed time-dependent pressure field for the rotor together with the pressure distribution downstream of the NGVs. The level and distribution of mainstream ingestion, and thus the seal effectiveness, was determined from nitrous oxide gas concentration measurements and related to static pressure measurements made throughout the wheelspace. With the axial clearance rim seal close to the rotor the presence of the blades had a complex effect. Rotor blades in connection with NGVs were found to reduce mainstream ingestion seal flow rates significantly, but a small level of ingestion existed even for very high levels of seal flow rate.

1 Introduction

In a modern large aircraft gas turbine the proportion of core airflow bypassing the H.P. turbine nozzle guide vanes is now approaching 10 percent. Approximately half of this is used for blade and vane cooling and half for disk cooling and rim sealing. This 5 percent of core flow bleed for rotor-stator wheelspace cooling and purging represents a penalty of about 5 percent on specific fuel consumption and commercial pressures are increasing to improve rim sealing and disk cooling efficiency without compromising safety margins generally; see, for example, Campbell (1978), Moore (1975), and Haaser et al. (1988).

Research into the purging and sealing of rotor-stator wheelspaces is an interesting story of industrial and academic cooperation. Conditions inside the engine are usually complex, hostile to sensitive instrumentation, and other aspects of engine research often have a higher priority so that most rotor-stator work has been done on rigs either by engine companies in-house or by universities.

Contributed by the International Gas Turbine Institute and presented at the 37th International Gas Turbine and Aeroengine Congress and Exposition, Cologne, Germany, June 1-4, 1992. Manuscript received by the International Gas Turbine Institute February 24, 1992. Paper No. 92-GT-303. Associate Technical Editor: L. S. Langston.

Serious research into rotor-stator rim sealing has now been conducted for some 25 years with most investigations being carried out on rigs simulating just the rotor-stator wheelspace. Very little rim seal work has been reported on actual gas turbines or turbine stages built for the purpose (i.e., including both NGVs and rotor blades).

1.1 Background. One of the earliest comprehensive studies was by Bayley and Owen (1970) who examined a shrouded rotor-stator system with a simple axial clearance seal operating in a quiescent environment, i.e., with no mainstream flow above the rim seal. These workers produced a useful working correlation for the minimum dimensionless coolant flow rate ($Cw_{,\min} = \dot{m}/\mu r_o$) necessary to prevent any ingestion: $Cw_{,\min} = 0.61\, G_{ca}\, \mathrm{Re}_\theta$. This has been used for many years and engine measurements that have been reported suggested that it was not unreasonable; see, for example, Kessler et al. (1980).

Phadke and Owen (1983) extended this original work with a variety of radial clearance rim seals, again in a simple quiescent environment, and produced a similar relationship modifying the clearance ratio term but still indicating that $Cw_{,\min}$ was directly proportional to rotational Reynolds number.

Abe et al. (1979) were the first to question the validity of the Bayley and Owen correlation. They concluded from their

rig tests that the coolant flow rate necessary to prevent ingestion was independent of rotational speed and instead depended primarily on the mainstream gas velocity. These workers tested several seal geometries with a variable swirl external flow over the rim seal clearance. Nozzle guide vanes provided the swirl but "*rotor blades on the disk were not used*": The disk was driven independently by an electric motor. Abe et al. incidentally found that one type of radial clearance seal could be up to 20 times more effective than a simple axial clearance seal.

The findings of Abe et al. prompted Owen to re-examine rim sealing criteria and he proceeded to test a rotor–stator configuration employing an external mainstream flow. Phadke and Owen (1988 a, b, c) in a comprehensive series of experiments convincingly explained the differences between the original rotor–stator experiments and the "external flow" results of Abe et al. (and to a certain extent those of Kobayashi et al. (1984) although these workers obtained conflicting results). Phadke and Owen showed that mainstream ingestion through a rim seal into a wheelspace could be "rotationally dominated" or "external flow dominated" (in which pressure asymmetries in the external flow were the controlling factor) and presented correlations for both regimes. This was enlightening but it did not help the turbine designer very much since he had insufficient engine data to allow him to use the correlations and most turbine wheelspace sealing flow calculations proceeded as before, from knowledge of previous designs.

However, some of the most useful work on rotor–stator ingestion concerns the amount of ingestion that occurs when less than the minimum sealing flow rate is supplied to the wheelspace. Many workers—Abe et al. (1979), Kessler et al. (1980), Kobayashi et al. (1984), Graber et al. (1987), Haaser et al. (1988) and Dadkhah et al. (1991)—are generally agreed that a small reduction of the coolant flow below the sealing minimum does not suddenly produce catastrophically high ingestion. The contamination increases gradually in an exponential manner as the coolant flow is progressively reduced. This knowledge has been useful to the designer since for the downstream stages it is known that some mainstream ingestion can be tolerated and that small coolant flows can keep the rotor and stator temperatures within acceptable limits.

1.2 Objective. This paper presents the results of rim seal ingestion experiments using a complete model turbine stage: nozzle guide vanes and rotor blades. The upstream wheelspace of the stage was used with a simple axial clearance seal positioned immediately adjacent to the rotor disk. The measured variation of sealing effectiveness with coolant flow rate has been compared with the results obtained for the different conditions above the rim seal, the first three of which have been used by various workers over the past 25 years:

- simple quiescent environment.
- axisymmetric external mainstream flow.
- nozzle guide vanes to provide swirl and controlled external pressure asymmetry but without rotor blades.

In addition, the results of axial traverses across the wheelspace are presented to show the effect that rotor blades have on the distribution of ingestion through the wheelspace. Also, since pressure measurements are among the easiest to make under engine conditions, these are presented to indicate how wheelspace pressure and ingestion are related for the specific geometry tested.

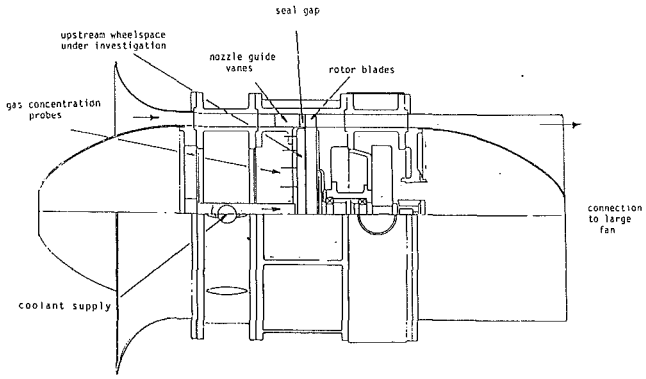

Fig. 1 General assembly of rig

2 Experimental Apparatus

A general outline of the rig is shown in Fig. 1. The model turbine stage operated in the "suction mode" with cold air being drawn through by a large centrifugal fan. The total pressure and temperature upstream of the NGVs were therefore atmospheric and the maximum stage pressure drop was 1000 mm water (9810 Pa).

The central rotor–stator assembly was supported inside the external mainstream flow annulus by eight aerodynamic struts upstream of the NGVs and eight downstream of the rotor blades. No influence of the wake from these struts was de-

Nomenclature

C_{axial} = axial component of nozzle exit
$Cw \equiv \dot{m}/\mu r_o$ = nondimensional coolant mass flow rate
$Cw_{,min}$ = minimum nondimensional flow to present ingress
C_2 = nozzle exit velocity
$G \equiv s/r_o$ = rotor-stator gap ratio
$G_{ca} \equiv sc/r_o$ = axial seal clearance ratio
$\dot{m}_c$ = coolant mass flow rate
$\dot{m}_i$ = ingress mass flow rate
p = static pressure
p_a = ambient pressure
p_e = external flow static pressure downstream of NGVs
$p^* \equiv (p - p_e) \times 1000/p_e$ = nondimensional static pressure difference
r = radial coordinate
r_o = outer radius of stator
$R \equiv r/r_o$ = nondimensional radial coordinate
$Re_\theta \equiv \rho\omega r_o^2/\mu$ = rotational Reynolds number
$Re_w \equiv \rho U_e r_o/\mu$ = external flow Reynolds number
s = axial gap between rotor and stator
sc = seal clearance
Ue = axial velocity of external flow upstream of NGVs
U_2 = velocity of rotor hub
V_2 = relative velocity onto rotor blades
z = axial coordinate
$Z \equiv z/s$ = nondimensional axial coordinate
β_2 = direction of gas velocity relative to rotor blade
η_c = coolant flow gas concentration
η_R = gas concentration at radius ratio R in wheelspace
μ = fluid viscosity
ρ = fluid density
$\phi \equiv \eta_c/\eta_R$ = nondimensional gas concentration
ω = angular speed of rotor

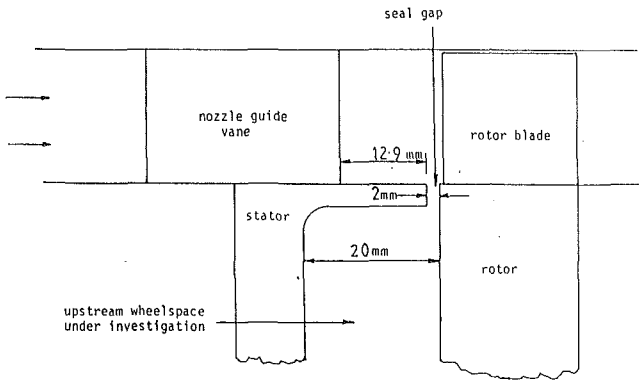

Fig. 2 Rotor-stator rim seal arrangement

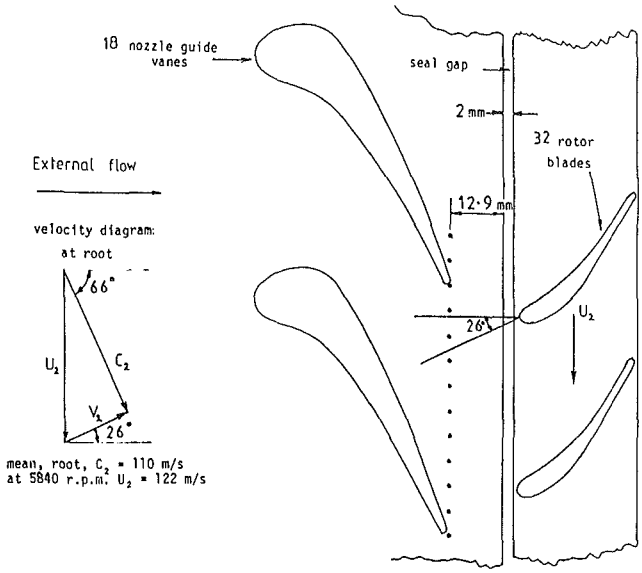

Fig. 3 Nozzle guide vane and rotor blade profiles and position of static pressure taps

tected. Precise location of the assembly was necessary for accurate control of the rim seal clearance and this was achieved by using substantial aluminum alloy castings with spigotted flanges. The rotor–stator rim seal arrangement is shown in Fig. 2.

The stator and rotor faces were completely flat and for the tests reported in this paper the wheelspace gap and the rim seal clearance were maintained constant at 20 mm and 2 mm, respectively (G = 0.1, G_{ca} = 0.01). The stator shroud diameter was 400 mm, the rotor hub diameter was 399.5 mm, and both the NGV and rotor blade span were 30 mm. The rotor blades had a true chord of 50 mm, the aspect ratio was 0.6, and solidity was 4.0. The constant diameter annulus contained 18 NGVs (20 deg pitching) individually molded from an epoxy/metal compound mounted 15.6 mm upstream of the rotor blade leading edges. The turbine had 32 untwisted constant-profile blades machined in aluminum integral with the disk to form a "blisk." The NGV and rotor blade profiles are shown in Fig. 3, which also shows the number and location of the static pressure taps at the NGV hub trailing edges.

The maximum air velocity from the nozzles was only 110 m/s. The rotor blade hub speed at the design point (5840 rpm) was 122 m/s so that the rotor incidence was 26 deg negative. The turbine design was thus far from current practice but this was done to give a high (wheelspace) rotational Reynolds number. The stage loading was very low, owing to the low expansion ratio, and the flow coefficient, C_{axial}/U_2, was 0.33. The turbine speed was controlled by an air brake, which proved less effective than expected and the lowest speed obtainable was 5890 rpm; the "runaway" speed was 6650 rpm. The turbine speed had negligible effect on the mainstream flow rate, which was controlled by the large downstream suction blower.

The sealing flow was supplied from a separate source and ranged up to about Cw = 10,000 ($Cw = \dot{m}/\eta r_o$). This represents a mean seal flow velocity to nozzle exit velocity ratio of 0.24.

3 Experimental Apparatus

3.1 Pressure. Static pressure tappings were made in the wheelspace on three radial lines at nine radius ratios, the most outer one being at R = 0.95. A single row of static pressure taps was made in the mainstream exactly on the line of the trailing edge of the nozzle guide vanes to measure the outlet static profile at the hub. This corresponded to a position 12.9 mm upstream of the edge of the rim seal and thus 15.6 mm upstream of the leading edges of the rotor blades. The pressure difference across the shroud quoted was from the wheelspace R = 0.95 position to the mean of the NGV hub trailing edge static pressures.

Total pressures upstream of the NGVs and static pressures at the interspace tip and rotor exit hub and tip were also measured. All pressures, including those across the wheelspace coolant flow orifice plate, were recorded using a microcomputer-controlled Scanivalve.

3.2 Nitrous Oxide Gas Concentration. The detection and quantification of mainstream flow ingestion were made by seeding the coolant supply to the wheelspace with approximately 450 ppm of nitrous oxide and sampling through four 1 mm bore tubes at four radial positions, R = 0.163, 0.411, 0.658, and 0.905. The sealing effectiveness Φ was determined from the mean of each of the four gas concentration measurements made at the stator surface. The sampling tubes were synchronously traversed axially across the cavity to determine the distribution and penetration of the ingestion throughout the wheelspace. The uncertainty in the gas concentration measurements, estimated at ±2 percent, was due principally to the averaging of the small rapid fluctuations in concentration experienced inside the wheelspace.

4 Experimental Results

In some rim-seal experiments run with the present rig with NGVs, but without rotor blades (Green, 1991), it was found that ingestion into the wheelspace increased as the NGVs were moved closer to the rim seal. This was not unexpected and was caused by the increased circumferential pressure asymmetry created by the mainstream flow. In these experiments at low external flow rates ingestion increased with rotational speed but at high external flow rates ingestion decreased slightly with rotational speed. However, in general rotational speed had very little effect and external pressure asymmetry behind the NGVs dominated.

For the present tests, the variation in static pressure at the NGV trailing edge (with the rotor blades present) is shown in Fig. 4. The static pressure variation at the trailing edge of the NGVs (without rotor blades present) was measured in earlier tests and gave similar results to those shown in Fig. 4.

It was not possible with these tests to measure pressures on the rotor leading edge hub surface and this is regretted since it almost certainly has an influence on ingestion by driving mainstream gas down the face of the rotor disk from regions of high pressure (with the peaks as high as the mainstream total pressure) that exist just upstream of the rotor blade leading edges. Accordingly the blade-to-blade hub pressure distribution at the rotor blade leading edge was predicted theoretically using the inviscid Denton (1985) code and is shown

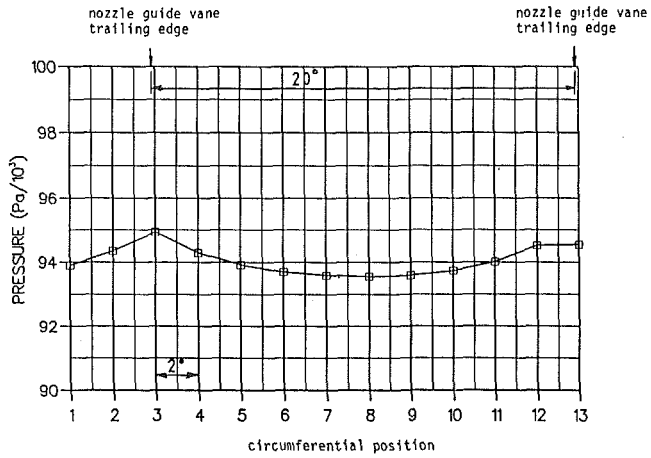

Fig. 4 Static pressures at trailing edge of nozzle guide vanes upstream axial seal; G_{ca} = 0.01; Re_w = 470,000

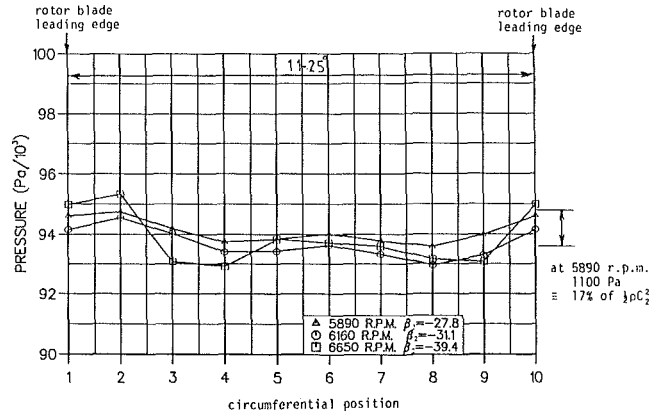

Fig. 5 Theoretical prediction (Denton) of hub static pressure 0.1 mm upstream of leading edge of rotor blades for different rotational speeds; Re_w = 470,000

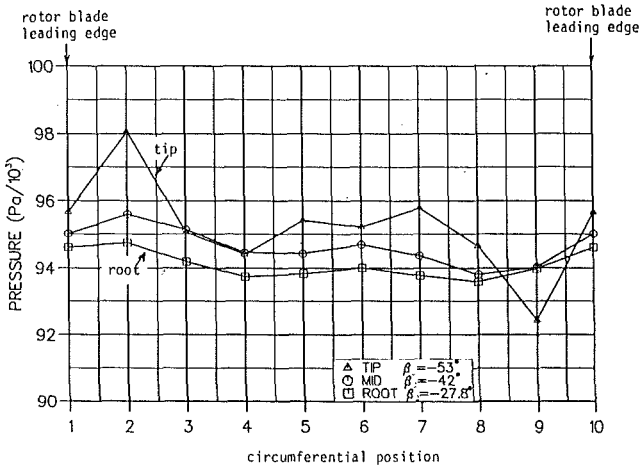

Fig. 6 Theoretical prediction (Denton) of static pressure at three radial positions, 0.1 mm upstream of leading edge of rotor blades; 5890 rpm; Re_w = 465,000

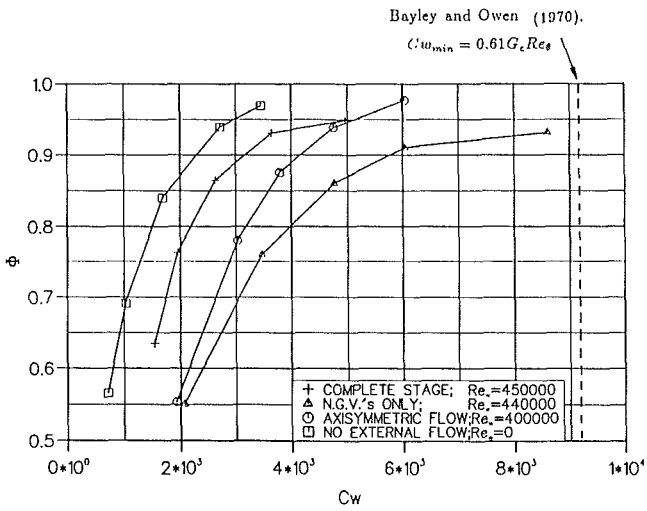

Fig. 7 Variation of sealing effectiveness with nondimensional coolant flow rate for four external flow conditions: upstream axial seal; G_{ca} = 0.01; $Re_\theta = 1.5 \times 10^6$

in Fig. 5 for several rotational speeds. With the external flow held constant lower rotational speeds (achieved by increasing the braking effect) implied smaller rotor blade incidences. These were all negative, i.e., opposed to the rotor blade motion, due to the constraints of the low pressure ratios and therefore the low velocities used in the rig. The Denton code was only used for the rotor blades with the mixed-out (measured) nozzle exit pressures and velocities used as input. In the real situation the nozzle wakes and the circumferential variation in velocity and static pressure could be significant and this can only be predicted with an unsteady three-dimensional calculation.

As expected Fig. 5 shows that the largest negative incidence on the rotor blades (minimum turbine braking) creates the largest pressure variation. Although small in absolute terms this peak-to-peak variation nevertheless represents approximately 25 percent of the stage pressure drop but only 2.5 percent of the inlet total pressure. The predicted hub maximum static pressure variation is very close to the rotor blade *relative* dynamic pressure ($1/2\rho V2/2$). For completeness Fig. 6 gives predictions of static pressure contours 0.1 mm upstream of the leading edge of the rotor blades for hub, midheight, and tip positions for a rotational speed of 5890 rpm.

Figure 7 shows the main contribution of this paper: Here the sealing effectiveness for this regular shaped wheelspace with a simple axial clearance seal is compared for four different external flow conditions. The condition of no external flow—the quiescent environment—showed the least ingestion and the condition with the NGVs alone showed most ingestion. Surprisingly, the complete stage, with NGVs and rotor blades, showed a level of ingestion closer to the condition of zero external flow, the rotationally dominated case, for the range of coolant flows used. To achieve this the rotor blades' upstream pressure distribution would seem to have the effect of smoothing out the NGVs pressure asymmetry. For interest, in Fig. 7 the prediction of Bayley and Owen for the minimum coolant flow to completely seal the wheelspace is also shown. Although the present conditions are far more complex than were originally considered by these two workers the prediction is quite reasonable—*for this seal arrangement.*

When the coolant flow is increased to approach the fully sealed condition, the physical situation appears to be rather more complex. In Fig. 8 the mean nondimensional pressure difference across the rim seal is shown to decrease to zero with increasing coolant flow, but the sealing effectiveness appears to approach a constant value of about 0.94. This cannot be accounted for by uncertainties in the gas concentration measurements and a small amount of ingestion is certainly present. The pressure difference across the shroud is defined using the *mean* of the NGV hub outlet static pressure measured some 12.9 mm upstream of the shroud edge and peaks in pressure around the circumference almost certainly still exist.

It is accepted that the pressure in the mainstream reaches

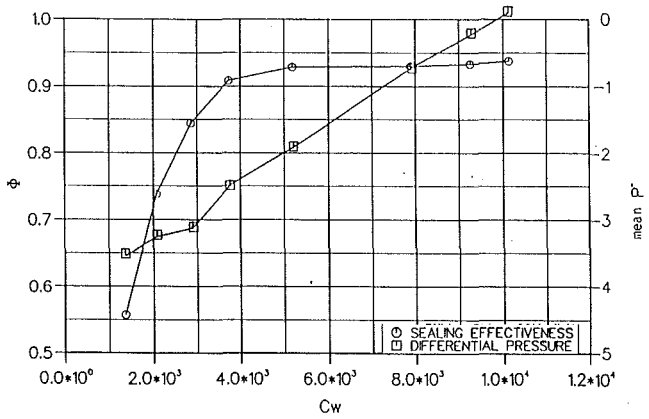

Fig. 8 Comparison of sealing effectiveness (Φ) and differential pressure (P^*) measurements in the wheelspace: upstream axial seal; G_{cs} = 0.01; Re_θ = 1,500,000; Re_w = 470,000

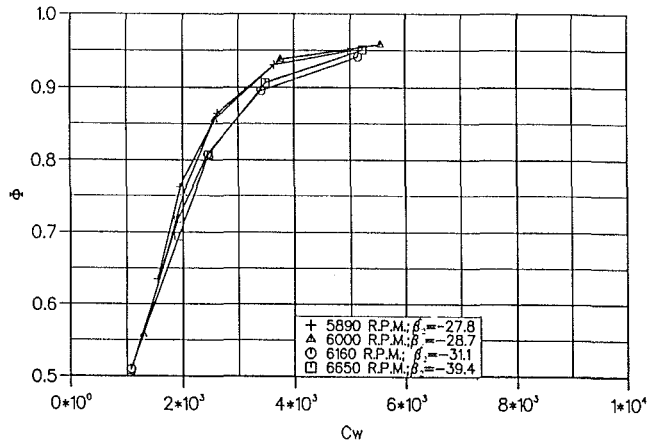

Fig. 9 Variation of sealing effectiveness with nondimensional coolant flow rate on axial turbine stage for four rotational speeds: upstream axial seal; G_{cs} = 0.01; Re_w = 470,000

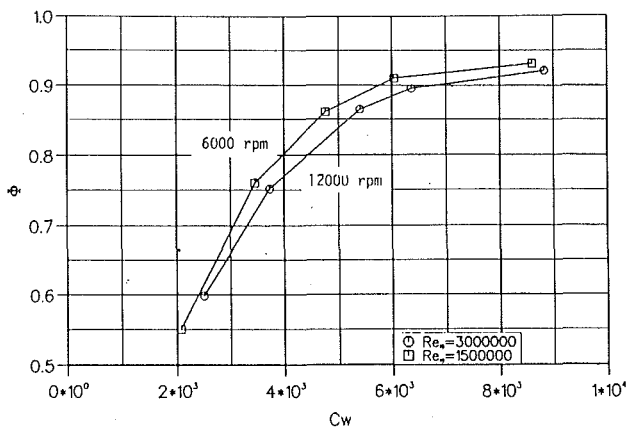

Fig. 10 Variation of sealing effectiveness with nondimensional coolant flow rate with NGVs alone in external flow: upstream axial seal; G_{cs} = 0.01; Re_w = 440,000

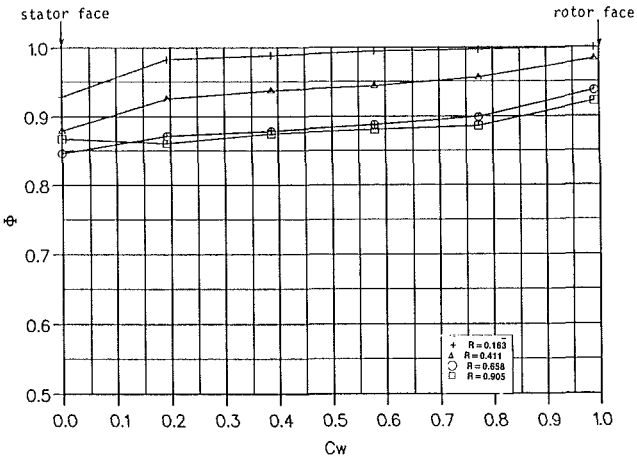

Fig. 11 Variation of sealing effectiveness with nondimensional coolant flow rate with NGVs alone in external flow (with disk driven by separate air turbine): upstream axial seal; G_{cs} = 0.01; Re_w = 440,000

the relative total pressure at the rotor blade leading edges and that this effect is felt upstream as far as three or four blade leading edge radii. Increasing the coolant flow velocity through the rim seal may possibly interact adversely with the mainstream flow in the region of the rotor blade root to create an increasingly "peaky" pressure profile above the rim seal. This could mean that rotor blades have the effect of making the mainstream flow more axisymmetric at low coolant flow rates but in making the wheelspace much more difficult to seal completely at high coolant flow rates.

Figure 9 shows the effect of rotor speed on sealing effectiveness for the complete stage. In these tests rotor blade incidence and speed are linked together (in the engine of course, incidence, speed, and mainstream mass flow are all linked). Although marginal, over this limited speed range increasing rotor speed appears to increase the ingestion rate, showing that the cavity could be more rotationally dominated than external flow asymmetry dominated.

With NGVs alone (i.e., with no rotor blades but with the rotor disk driven by a separate turbine) ingestion into the wheelspace is entirely external flow asymmetry dominated. Figure 10 shows that increasing the disk speed, for example from 6000 rpm to 12,000 rpm, increases ingestion only slightly. Comparing Figs. 9 and 10 it appears that the rotor blades reduce ingestion so that the axial position of the rim seal in the NGV–rotor blade interspace could be an important variable. Figure 11 shows the "local" sealing effectiveness distribution across the wheelspace for four different radius ratios obtained from axial traverses of the gas concentration probes from stator face to rotor face. The shapes of these distributions are identical whether rotor blades are used or not and are very similar to those obtained by Dadkhah et al. (1991). The outer radii show the presence of most ingestion, the inner radii the least with the stator face feeling slightly more effect than the rotor. It is evident from the two outer probe traverses that the outer half of the wheelspace is thoroughly "stirred up" since it produces a consistent and uniform degree of ingestion. However, at high coolant flow rates (for sealing effectivenesses greater than about 0.9) the innermost probe generally indicated slightly more ingestion than the outermost probe, with the overall concentration in the wheelspace more uniform.

5 Conclusions

The experiments reported in this paper have produced the unexpected result that over a wide range of coolant flows, the rotor blades tend to make the external flow downstream from the NGVs more axisymmetric in the region of a rim seal located close to the disk. However, with rotor blades a small residual

ingestion still occurred at high coolant flow rates. This raises the speculation that to completely seal the wheelspace the pressure underneath the seal must be increased to the mainstream total or stagnation *relative* value, which occurs as a spike at the rotor blade leading edges. This is a case of "diminishing returns," which has implications for all stages of an engine but particularly for the H.P. stages in which hot gas ingestion may contaminate any preswirled blade coolant used.

An important consideration in rim seal design would thus appear to be the positioning of the rim seal or shroud edge in relation to the NGV trailing edge and the rotor blade leading edge. For an upstream wheelspace, a location close to the rotor blades may have advantages, whereas for a downstream wheelspace, although not examined in the present tests, the rim seal edge should be positioned as far as possible downstream from the pressure asymmetry at the rotor blade trailing edges. It is for further research to determine whether radial clearance rim seals behave in the same way as the axial clearance seal used in these tests.

Although rotor speed appeared slightly to increase ingestion rates, this was evident only over a limited speed range, and since the influence of rotor speed and rotor blade incidence could not be independently examined in these tests, further work is clearly necessary to quantify this effect.

The effect of rotor blades on the distribution of ingestion inside the wheelspace was found to be negligible; any ingress appeared mostly on the stator face with the outer half of the wheelspace thoroughly "stirred up." The principal contribution of this work is the finding that rotor blades, together with NGVs, play an important role in the overall wheelspace rim design problem and that oversimplified experimental rigs operated far from engine conditions may often only serve to confuse the issue.

In these experiments the stage pressure ratio, the hub Reynolds number, the Mach number, and the rim seal design itself are quite unrepresentative of gas turbine practice. Before design rules can be established with confidence, all the influencing parameters should be examined together at conditions as close to modern engine operating levels as possible.

References

Abe, T., Kikuchi, J., and Takeuchi, H., 1979, "An Investigation of Turbine Disc Cooling (Experimental Investigation and Observation of Hot Gas Flow Into a Wheelspace)," presented at the 3rd CIMAC Conf., Vienna, Paper No. GT-30.

Bayley, F. J., and Owen, J. M., 1970, "The Fluid Dynamics of a Shrouded Disc System With a Radial Outflow of Coolant," ASME *Journal of Engineering for Power*, Vol. 92, p. 35.

Campbell, D. A., 1978, "Gas Turbine Disc Sealing System Design," AGARD Conference on Seal Technology in Gas Turbine Engine, AGARD-CP-237, London.

Dadkhah, S., Turner, A. B., and Chew, J. W., 1991, "Performance of Radial Clearance Rim Seals in Upstream and Downstream Rotor-Stator Wheelspaces," ASME Paper No. 91-GT-32; ASME JOURNAL OF TURBOMACHINERY, Vol. 114, 1992, pp. 439–445.

Denton, J. D., 1985, "The Calculation of Fully Three-Dimensional Flow Through Any Type of Turbomachine Blade Row," AGARD lecture series No. 140, 3D Computation Techniques Applied to Internal Flows in Propulsion Systems.

Graber, D. J., Daniels, W. A., and Johnson, B. V., 1987, "Disk Pumping Test," Air Force Wright Aeronaut. Lab. Report No. AFWAL-TR-87-2050.

Green, T., 1991, unpublished work, T.F.M.R.C., University of Sussex, TN96.

Haaser, F., Jack, J., and McGreehan, W., 1988, "Windage Rise and Flowpath Gas Ingestion in Turbine Rim Cavities," ASME *Journal of Engineering for Gas Turbines and Power*, Vol. 110, pp. 78–85.

Kessler, W., Frei, O., and Fahrni, F., 1980, "Experimental and Analytical Investigation of Turbine Disk Cooling," *Measurements Methods in Rotating Components of Turbomachinery*, ASME, New York, p. 327.

Kobayashi, N., Matsumoto, M., and Shizuya, M., 1984, "An Experimental Investigation of a Gas Turbine Disk Cooling System," ASME *Journal of Engineering for Gas Turbines and Power*, Vol. 106, pp. 136–141.

Moore, A., 1975, "Gas Turbine Internal Air Systems: a Review of the Requirements and Problems," ASME Paper No. 75-WA/GT-1.

Phadke, U. P., and Owen, J. M., 1983, "An Investigation of Ingress for an Air-Cooled Shrouded Rotating Disc System With Radial Clearance Seals," ASME *Journal of Engineering for Power*, Vol. 105, pp. 178–183.

Phadke, U. P., and Owen, J. M., 1988a, "Aerodynamic Aspects of the Sealing of Gas Turbine Rotor-Stator Systems, Part 1: The Behaviour of Simple Shrouded Rotating Disk Systems in a Quiescent Environment," *Int. J. Heat Fluid Flow*, Vol. 9, pp. 98–105.

Phadke, U. P., and Owen, J. M., 1988b, "Aerodynamic Aspects of the Sealing of Gas Turbine Rotor-Stator Systems, Part 2: The Performance of Simple Seals in a Quasi-axisymmetric External Flow," *Int. J. Heat Fluid Flow*, Vol. 9, pp. 106–112.

Phadke, U. P., and Owen, J. M., 1988c, "Aerodynamic Aspects of the Sealing of Gas Turbine Rotor-Stator Systems, Part 3: The Effect of Non-axisymmetric External Flow on Seal Performance," *Int. J. Heat Fluid Flow*, Vol. 9, pp. 113–117.

A Study of Rotor Cavities and Heat Transfer in a Cooling Process in a Gas Turbine

R. S. Amano
Professor,
Department of Mechanical Engineering,
University of Wisconsin,
Milwaukee, WI 53201

K. D. Wang
Stress Technology, Inc.,
Rochester, NY 14623

V. Pavelic
Professor,
Department of Mechanical Engineering,
University of Wisconsin,
Milwaukee, WI 53201

A high-temperature flow through a gas turbine produces a high rate of turbulent heat transfer between the fluid flow field and the turbine components. The heat transfer process through rotor disks causes thermal stress due to the thermal gradient just as the centrifugal force causes mechanical stresses; thus an accurate analysis for the evaluation of thermal behavior is needed. This paper presents a numerical study of thermal flow analysis in a two-stage turbine in order to understand better the detailed flow and heat transfer mechanisms through the cavity and the rotating rotor-disks. The numerical computations were performed to predict thermal fields throughout the rotating disks. The method used in this paper is the "segregation" method, which requires a much smaller number of grids than actually employed in the computations. The results are presented for temperature distributions through the disk and the velocity fields, which illustrate the interaction between the cooling air flow and gas flow created by the disk rotation. The temperature distribution in the disks shows a reasonable trend. The numerical method developed in this study shows that it can be easily adapted for similar computations for air cooling flow patterns through any rotating blade disks in a gas turbine.

1 Introduction

A high-temperature flow through a gas turbine produces a high rate of turbulent heat transfer between the flow and the turbine components. Flow impingement and recirculation are common flow phenomena in cavity flows between rotating disks and stationary nozzle disks. In this case flow impingement associates itself with higher turbulence levels, which result in highly augmented heat and momentum transfer. Therefore, a sound numerical technique for computations of flows through complex geometries as well as mathematical models that can predict such turbulent flows are needed for better understanding of the heat transfer mechanism and associated stresses through turbine components.

This paper presents a method for the computation of temperature in rotating disks and the flows in a cavity between the nozzle and blade disk by employing a finite volume method, which is combined with the nonorthogonal boundary-fitted coordinate system. It is the present purpose to clarify the heat transfer and turbulent flow pattern in a gas turbine by obtaining temperature and flow property distributions by using a computer simulation technique. The algebraic grid generation technique was used to generate grids in arbitrary shapes of disks and flow fields. Computations were performed by using the set of governing equations transformed for use on a generalized curvilinear coordinate system. Turbulent computations were made by using the k–ϵ model for the computation of turbulence stresses. Wall function boundary conditions for the k–ϵ model was developed for the evaluation of the numerical cell adjacent to the solid wall. The system of governing equations was solved transiently and the process of heat transfer was observed at different time steps until 50 minutes after start-up.

This is one of the first papers to incorporate the finite volume method transformed into the axisymmetric curvilinear coordinate system for the computations of rotating disks. Thus, the three-dimensional effect is taken into account without modeling a full three-dimensional system. The model introduced here is also unique due to its "segregation method," which is advantageous in performing computations with a smaller number of grids than are actually used in the entire solution domain.

2 Problem Specifications

Figure 1 shows the prototype of the gas turbine in the present computations. The main focus of the present research lies in the predictions of temperature and flow patterns that occur during the initial operational stage of the gas turbine. The cooling domain is illustrated in Fig. 2.

The disks are made of Alloy 901 whose thermal conductivity is 170 W/m•K and the specific heat is 881 J/kg•K. The operational rotating speed of the disks is 6825 rpm. It is assumed that this rotational speed is achieved instantaneously after the startup. The coolant air is supplied through the annularly arranged holes into the cavities. The details are shown in Table 1. The injection coolant holes at sections 1–3 are replaced by

Contributed by the International Gas Turbine Institute and presented at the 37th International Gas Turbine and Aeroengine Congress and Exposition, Cologne, Germany, June 1–4, 1992. Manuscript received by the International Gas Turbine Institute March 1992. Paper No. 92-GT-358. Associate Technical Editor: L. S. Langston.

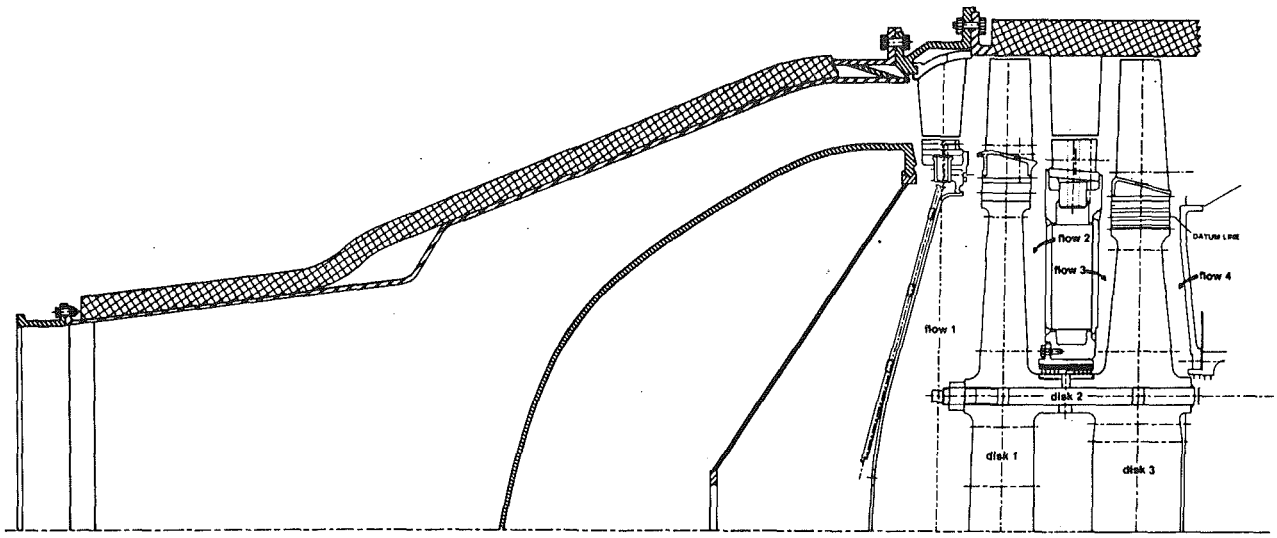

Fig. 1 Flow path in a gas turbine

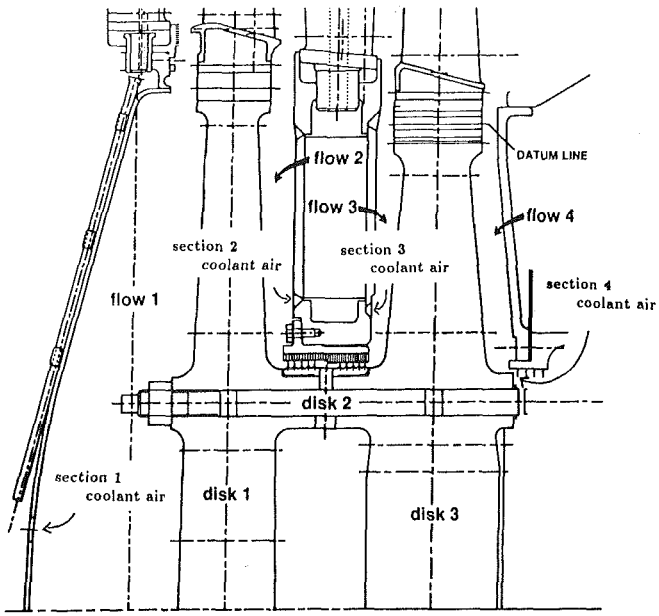

Fig. 2 Computation domain

annular slit types. This was done by setting the total cross-sectional area of the coolant air nozzles equal to the computational cross-sectional areas where annular slit nozzles were considered instead of the annularly aligned holes. In this way the computational model can be kept in an axisymmetric form

Table 1 Specifications of coolant air

Section	1	2	3	4
Location (distance from CL), (cm)	15.5	24.1	24.1	17.1
Hole diameter, (cm)	2.54	0.95	0.56	0.64
No. of holes	6	8	8	annulus type
Flow rate, (kg/sec)	0.338	0.136	0.045	0.023
Injection coolant temperature, (^oC)	332	403	403	177

and, yet, the flow rates are maintained the same as those used in actual turbines.

The mainstream temperatures above the following flow regions are:

flow1	744°C
flow2	619°C
flow3	619°C
flow4	500°C

Each computational domain requires a different set of transport equations to be solved; thus, two separate algorithms need to be coupled together. These two algorithms are installed in a single computer program and used to solve the entire domain iteratively. That is, the flow region is solved by using the full Navier–Stokes, turbulence, and thermal energy equations, whereas the temperature distribution in the disk region—a solid domain—is solved by using only the heat conduction equation. At each time step the boundary values of each domain were corrected iteratively.

Nomenclature

C_1, C_2 = constants for turbulence model
c_p = specific heat for constant pressure
G = generation rate of turbulence kinetic energy
k = turbulence kinetic energy
p = mean pressure
P = P-function
Pr = Prandtl number
Pr_t = turbulent Prandtl number
$\dot{q}''_w$ = wall heat flux
T = temperature
T_w = wall temperature
U = mean velocity in x direction
U_{IN} = inlet velocity of cooling air
V = mean velocity in r direction
W = mean velocity in θ direction
x, r, θ = cylindrical coordinates
ϵ = dissipation rate of turbulent kinetic energy
μ = absolute viscosity
μ_t = turbulent viscosity
ν = kinematic viscosity
ν_t = turbulent kinematic viscosity
ξ, η = transformed coordinates
ρ = density of fluid
τ_w = wall shear stress

Subscripts

i, j = tensor notations
ξ, η = partial derivatives with respect to ξ and η, respectively

The Mach number at the maximum speed point was only about 0.1, which was primarily due to a high-temperature gas. Due to the low Mach number in the turbine, the incompressible forms of the Navier–Stokes equations and thermal energy equation were used.

The computation for the flow field was based on quasi-three-dimensional coordinates. The mathematical models that are employed in this study are given in the next section.

3 Mathematical Models

The transport equations governing the dependent variables in the present study are given by:

Continuity Equation

$$\frac{\partial \rho}{\partial t}+\frac{\partial}{\partial x_i}(\rho U_i)=0 \tag{1}$$

Momentum Equations

$$\frac{\partial(\rho U_i)}{\partial t}+\frac{\partial \rho U_i U_j}{\partial x_j}=\frac{\partial p}{\partial x_i}+\frac{\partial}{\partial x_j}\left[\mu_{\text{eff}}\left(\frac{\partial U_i}{\partial x_j}+\frac{\partial U_j}{\partial x_i}\right)\right] \tag{2}$$

Thermal Energy, T:

$$\frac{\partial(\rho T)}{\partial t}+\frac{\partial \rho U_j T}{\partial x_j}=\frac{\partial}{\partial x_j}\left[\left(\frac{\mu}{\text{Pr}}+\frac{\mu_t}{\text{Pr}_t}\right)\frac{\partial T}{\partial x_j}\right] \tag{3}$$

Turbulence Kinetic Energy, k:

$$\frac{\partial(\rho k)}{\partial t}+\frac{\partial \rho U_j k}{\partial x_j}=\frac{\partial}{\partial x_j}\left[\left(\mu+\frac{\mu_t}{\sigma_k}\right)\frac{\partial k}{\partial x_j}\right]+\rho(G-\epsilon) \tag{4}$$

Turbulence Energy Dissipations, ϵ:

$$\frac{\partial(\rho \epsilon)}{\partial t}+\frac{\partial \rho U_j \epsilon}{\partial x_j}=\frac{\partial}{\partial x_j}\left[\left(\mu+\frac{\mu_t}{\sigma_\epsilon}\right)\frac{\partial k}{\partial x_j}\right]+\rho\left(C_1\frac{\epsilon G}{k}-C_2\frac{\epsilon^2}{k}\right) \tag{5}$$

where

$$G=\nu_t\frac{\partial U_i}{\partial x_j}\left(\frac{\partial U_i}{\partial x_j}+\frac{\partial U_j}{\partial x_i}\right) \tag{6}$$

$$\mu_{\text{eff}}=\mu+\mu_t \tag{7}$$

$$\nu_t=C_\mu\frac{k^2}{\epsilon} \tag{8}$$

The constants that appear in Eqs. (5) and (8) have the following values:

$$C_1=1.44;\quad C_2=1.92;\quad C_\mu=0.09 \tag{9}$$
$$\sigma_k=1.0;\quad \sigma_\epsilon=1.3$$

The subscripts i and j used in the above equations are the tensor index notations.

4 Grid Generation

The boundary-fitted curvilinear coordinate system was used in order to simulate the irregularly shaped boundaries originally developed by Thompson (1980) and modified by Maruszewski and Amano (1988a) for better use of internal flow computations.

In this technique the grid point locations on the left and right boundaries are given, and the grid points in the interior of the domain are computed along straight lines connecting the corresponding top and bottom boundary grid points. The method described here allows for the generation of grids with the grid line spacing next to the walls kept at a constant user-specified value.

If $(N-2)$ grid points are to be distributed along a straight line between the grid points (x_1, y_1) and (x_N, y_N), and if the spacing between the points (x_1, y_1) and (x_2, y_2) and the spacing between the points (x_{N-1}, y_{N-1}) and (x_N, y_N) is to be a user-specified value, $(\Delta s)_1$, then the expansion factors in the x and y directions are given by:

$$\beta_x=\left[1+\frac{\Delta X(\beta_x-1)}{2(\Delta x)_1}\right]^{\frac{2}{N-1}} \tag{10}$$

$$\beta_y=\left[1+\frac{\Delta Y(\beta_y-1)}{2(\Delta y)_1}\right]^{\frac{2}{N-1}} \tag{11}$$

where

$$\Delta X=x_N-x_1 \tag{12}$$

$$\Delta Y=y_N-y_1 \tag{13}$$

$$(\Delta y)_1=\text{sign}(\Delta Y)\frac{(\Delta s)_1}{\sqrt{1+\left(\frac{\Delta X}{\Delta Y}\right)^2}} \tag{14}$$

$$(\Delta x)_1=(\Delta y)_1\frac{\Delta X}{\Delta Y} \tag{15}$$

Since the equations for the expansion factors β_x and β_y cannot be solved explicitly, it is necessary to iterate. Fixed point iteration using the expressions in the form shown above was found to converge within a few iterations, and was used to generate all the grids shown here. Once the expansion factors are known, the grid point locations are given by:

$$x_n=x_1+(\Delta x)_1\frac{(\beta_x)^{n-1}-1}{\beta_x-1}\quad \text{for } n\le\frac{N+1}{2} \tag{16}$$

$$y_n=x_1+(\Delta y)_1\frac{(\beta_y)^{n-1}-1}{\beta_y-1}\quad \text{for } n\le\frac{N+1}{2} \tag{17}$$

$$x_n=x_N-(\Delta x)_1\frac{(\beta_x)^{N-n}-1}{\beta_x-1}\quad \text{for } n>\frac{N+1}{2} \tag{18}$$

$$y_n=y_N-(\Delta y)_1\frac{(\beta_y)^{N-n}-1}{\beta_y-1}\quad \text{for } n>\frac{N+1}{2} \tag{19}$$

The method shown here was found to be very efficient, and could be used for many different geometries.

5 Coordinate Transformation

Equations (2)–(5) are transformed from Cartesian coordinates (x, y) into generalized curvilinear coordinates (ξ, η). Consider the general steady-state two-dimensional transport equations in the following form:

$$\frac{\partial \rho\phi}{\partial t}+\frac{1}{r}\left[\frac{\partial(\rho U r\phi)}{\partial x}+\frac{\partial(\rho V r\phi)}{\partial r}\right]=\frac{1}{r}\left[\frac{\partial}{\partial x}\left(r\Gamma\frac{\partial\phi}{\partial x}\right)+\frac{\partial}{\partial r}\left(r\Gamma\frac{\partial\phi}{\partial r}\right)\right]+R(x, r, \theta) \tag{20}$$

where

$$\phi=U\text{: } R(x, r, \theta)=-\frac{\partial p}{\partial x}+S_u \tag{21}$$

$$\phi=V\text{: } R(x, r, \theta)=-\frac{\partial p}{\partial r}+\frac{\rho W^2}{r}-\frac{2\mu V}{r^2}+S_v \tag{22}$$

$$\phi=W\text{: } R(x, r, \theta)=-\frac{\rho VW}{r}-\frac{W}{r^2}\frac{\partial}{\partial r}(r\mu) \tag{23}$$

$$\phi=k\text{: } R(x, r, \theta)=\rho(G-\epsilon) \tag{24}$$

$$\phi=\epsilon\text{: } R(x, r, \theta)=\rho(C_1\epsilon G-C_2\epsilon^2)/k \tag{25}$$

The above equation is transformed into the following form:

$$\frac{1}{J}\frac{\partial \rho\phi}{\partial t}+\frac{1}{rJ}[(\rho\tilde{U}r\phi)_\xi+(\rho\tilde{V}r\phi)_\eta]=S(\xi, \eta)+\frac{1}{rJ}\left\{\left[\frac{\Gamma}{J}(q_1 r\phi_\xi-q_2 r\phi_\eta)\right]_\xi+\left[\frac{\Gamma}{J}(-q_2 r\phi_\xi+q_3 r\phi_\eta)\right]_\eta\right\} \tag{26}$$

where

$$\tilde{U} = Ur_\eta - Vx_\eta \tag{27}$$

$$\tilde{V} = Vx_\xi - Ux_\xi \tag{28}$$

$$q_1 = x_\eta^2 + r_\eta^2 \tag{29}$$

$$q_2 = x_\xi x_\eta + r_\xi r_\eta \tag{30}$$

$$q_3 = x_\xi^2 + r_\xi^2 \tag{31}$$

$$J = x_\xi r_\eta - x_\eta r_\xi \tag{32}$$

Equation (26) is discretized by using the finite volume method described in the following section.

6 Numerical Method

Formulation and discretization of all transport equations were performed by using the finite volume approach by breaking each equation into diffusion, convection, and source terms. The system of equations was linearized so that it could be solved iteratively by the tridiagonal matrix algorithm.

6.1 Pressure Correction Algorithm. For the pressure correction scheme the PISO (Pressure Implicit with Splitting of Operators) algorithm by Issa (1985) was employed. In the present form of equations, it is assumed that two pressure and velocity corrections are sufficient. The first pressure correction equation of PISO is identical to that used by SIMPLE (Patankar, 1980). That is, the U-component velocity correction equation is given by:

$$A_p^u U_p' = \Sigma A_{nb}^u U_{nb}' - y_\eta p_\xi' + y_\xi p_\eta' \tag{33}$$

where A's are the influence coefficients, and U' and p' are the velocity and pressure corrections. The subscript nb denotes the neighbor coefficients. If the above equation was used in the derivation of the pressure correction equation, an unmanageable equation would result. Instead, it is assumed that the velocity correction at a point is not affected by the velocity corrections of its neighbors, and thus the summation term in Eq. (33) is neglected. The velocity components are then given by:

$$U_p' = B^u p_\xi' + C^u p_\eta' \tag{34}$$

$$V_p' = B^v p_\xi' + C^v p_\eta' \tag{35}$$

where

$$B^u = \frac{-y_\eta}{A_p^u}; \quad B^v = \frac{x_\eta}{A_p^v}; \quad C^u = \frac{y_\xi}{A_p^u}; \quad C^v = \frac{-x_\xi}{A_p^v} \tag{36}$$

and the velocity corrections for U and V are:

$$U = U^* + U' \tag{37}$$

$$V = V^* + V' \tag{38}$$

The pressure correction equation is obtained by substituting Eqs. (34), (35), (37), and (38) into the discretized form of the transformed continuity equation, which is given by:

$$[\rho(Uy_\eta - Vx_\eta)]_e - [\rho(Uy_\eta - Vx_\eta)]_w + [\rho(Vx_\xi - Uy_\xi)]_n - [\rho(Vx_\xi - Uy_\xi)]_s = 0 \tag{39}$$

A second corrector step is done to ensure that the continuity and momentum equations are satisfied at the end of each iteration. The second corrector step requires the solution of a second pressure correction equation, and thus the computation time per iteration will be longer for PISO than for other algorithms. However, it requires only 60 percent of iteration with the SIMPLE algorithm (Maruszewski and Amano, 1988a).

It is reported by Maruszewski and Amano (1988a) that including the cross-derivative terms in the source term had no advantages over the method of neglecting the cross-derivative terms. It was also observed that the use of a nine-point solver ensured stability and robustness of the computational method. For the reasons mentioned above, the semi-implicit solver of Peric (1987) was employed in this study to solve the pressure correction equation.

6.2 Velocity Correction Algorithm. The Cartesian velocities U and V were corrected and contravariant velocities $\tilde{U}$ and $\tilde{V}$ were calculated using the new values of U and V rather than computing the Cartesian velocities and correcting contravariant velocities. This is because it was found that the former method gives more accurate results and is more efficient than the latter (Maruszewski and Amano, 1988b).

The velocities can be obtained by substituting the velocity corrections, U' and V', into Eqs. (37) and (38):

$$U = U^* + B^u p_\xi' + C^u p_\eta' \tag{40}$$

$$V = V^* + B^v p_\xi' + C^v p_\eta' \tag{41}$$

where B^u, B^v, C^u, and C^v are defined in the same form as Eq. (36) and where A_p^u and A_p^v are the coefficients of U_p and V_p, respectively. $\tilde{U}$ and $\tilde{V}$ were calculated using the definition of the contravariant velocities.

6.3 Boundary Conditions. At the inflow, outflow, and symmetry axis, conventional conditions are employed; prescribed values are provided at the inflow region, and zero gradients of the variable are used at the outflow region and the symmetry axis.

At the wall boundaries, including the sides and top of the disks, the wall function treatment is employed for the momentum and the turbulence kinetic energy. The dissipation rate is evaluated under the local equilibrium condition. Details of these conditions are given in Maruszewski and Amano (1988b).

6.4 Heat Transfer Coefficient. Local heat transfer coefficients are computed from:

$$h = \frac{\dot{q}_w''}{(T - T_w)} \tag{42}$$

where the wall flux rate can be determined by employing the "wall law" proposed by Jayatilleke (1969):

$$\frac{\rho c_p (T - T_w) k^{1/2}}{\dot{q}_w''} = \frac{Uk^{1/2}}{\tau_w/\rho} + P \tag{43}$$

where P is the so-called P-function:

$$P = 9.24\left[\left(\frac{\mathrm{Pr}}{\mathrm{Pr}_t}\right)^{0.75} - 1\right] \times \left[1 + 0.28 \exp\left(-0.007 \frac{\mathrm{Pr}}{\mathrm{Pr}_t}\right)\right] \tag{44}$$

The turbulent Prandtl number, Pr_t, is set equal to 0.9. The wall shear stress was evaluated through the local turbulence variations.

6.5 Numerical Procedure. In this study the "segregation" method is used; that is, each segment of the solution domain is computed one by one, such as flow1, flow2, ..., disk1, disk2, ... Thus, the memory size required for the computation is much less than the case when the entire solution domain is computed at the same time.

Since the boundary conditions at the solid wall boundary are unknown, an iterative solution technique was used. This was performed in the following steps:

1 The inlet conditions for both cooling and hot gases are provided.
2 The initial temperature distribution is set for the entire domain.
3 In the cavity flow region the momentum, turbulence, and temperature equations were solved with the given initial temperature distributions at the solid wall boundary.
4 The local heat transfer coefficients are computed for the

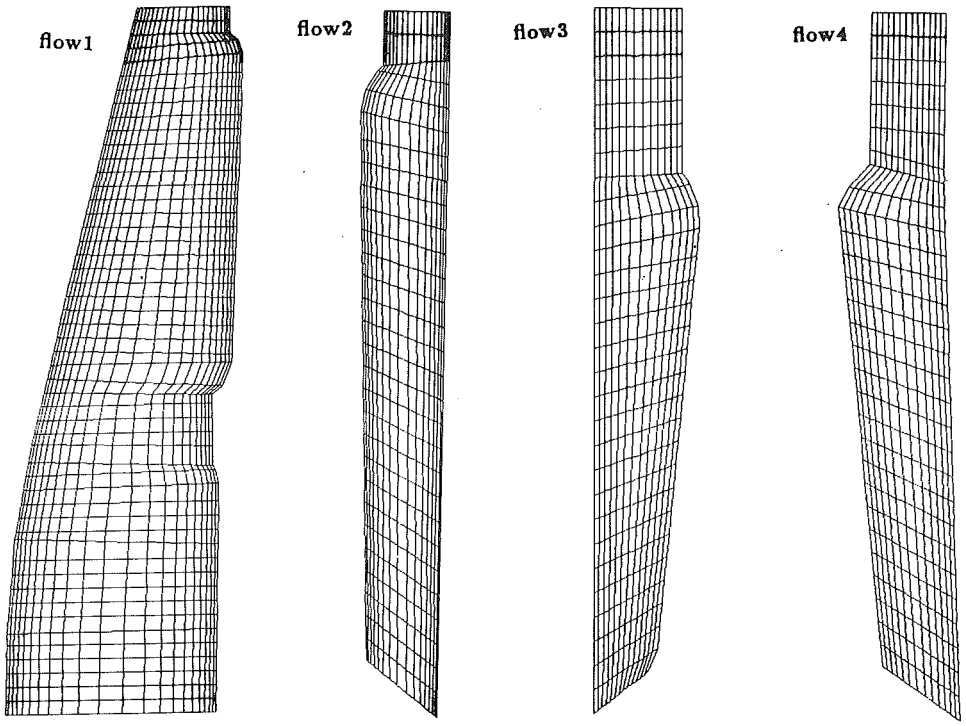

Fig. 3 Grids used for computations of cavity flows

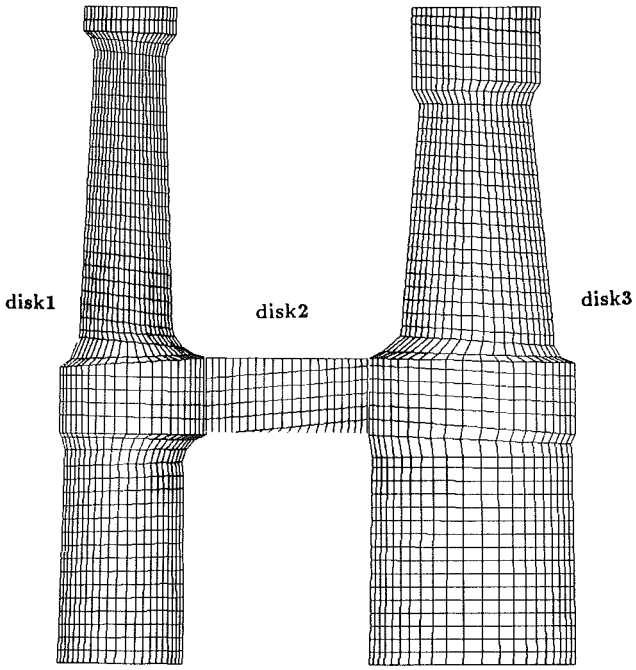

Fig. 4 Grids used for computations of rotating disks

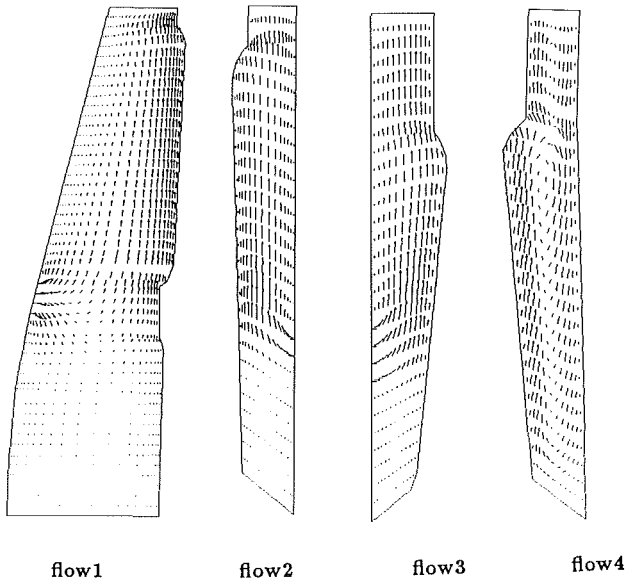

Fig. 5 Velocity vectors of cavity flows

numerical cells along the disk wall boundary by employing "the law of the wall."

5 These computed local heat transfer coefficients are used as the boundary conditions for the computation of temperature distributions in the disk region. In this manner, the temperature distributions are now determined throughout the disk. However, these temperature values may not be accurate since the local heat transfer coefficients computed in the preceding step are based on the given temperature values at the disk boundary which may be changed subject to the flow impingement. Thus, steps 4 and 5 need to be repeated with the updated temperature values as the new boundary conditions for computations in the cavity flow region and the newly computed local heat transfer coefficients as the updated boundary conditions for disk region.

6 When the interface conditions converge, the time step is advanced, and the computation proceeds until it reaches steady state. At the outlet of the flow domain, the outflow conditions are employed; that is, the zero gradients are used for the velocities and turbulence quantities, whereas zero second derivative condition is used for the pressure and temperature.

7 Results

Several grid independent tests were performed for both cav-

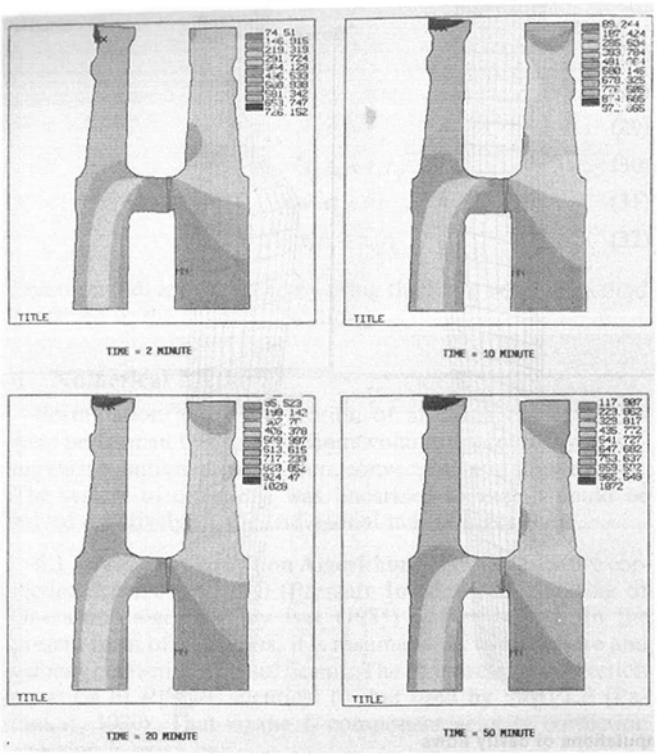

Fig. 6 Temperature contours in disks

ities and disks. 1144 grid points were employed in each computational domain for flow1 and two disks (disk1 and disk3), and 660 grid points for flow2 through flow4 and disk2. Thus, a total of 6072 grid points were employed for the present computations. These grids for cavity flows and disks are shown in Figs. 3 and 4, respectively.

Figure 5 shows the computed velocity vectors for the four cavity flows (flow1 through flow4). The cooling air is injected into the cavity at a height of 45 percent from the bottom line for flow1, flow2, and flow3 regions. As a result a higher velocity flow field occurs along the upper 60 percent of the disk surface. Flow4 shows the case of air injection at the bottom corner of the cavity, and the flow pattern is uniform along the entire disk surface.

Figure 6 shows the computed temperature contours through the disks. The figure depicts a transient heat transfer process until 50 minutes after start-up. As is expected, the heating starts at the left top corner of the first disk, and the heat is transferred through disk1 toward the symmetric line. At the same time high temperature is generated at the top portion of disk2 due to convection of heat from the hot gas in the main stream. It is observed that a local hot spot appears on disk2 just above where two disks meet. This seems to be caused by the impingement of the coolant air, which is already heated due to the convection between the hot gas entering from the main stream and the cooling air. The heated air generates higher convective heat transfer effects on the wall and thus results in slightly higher temperature than the rest of the disk area. The temperature field seems to reach steady state after 50 minutes.

8 Conclusions

1 The computations were successfully performed by using the present model for predictions of flow and temperature fields.
2 The "segregation" method is advantageous because it requires much fewer grid points in each computation than if the entire domain were computed.
3 This study can be easily extended to seek optimum cooling and cavity flow conditions.

Acknowledgments

The computations were made on a CRAY Y/MP, which is sponsored by NSF under research grant No. MSM890010N. Part of this research was supported by Stress Technology Inc.

References

Issa, R. I., 1985, "Solution of the Implicitly Discretized Fluid Flow Equations by Operator-Splitting," *Journal of Computational Physics*, Vol. 62, pp. 40–65.

Jayatilleke, C. L., 1969, "The Influence of Prandtl Number and Surface Roughness on the Resistance of the Laminar Sublayer to Momentum and Heat Transfer," *Progress in Heat and Mass Transfer*, Vol. 1, pp. 193–329.

Maruszewski, J. P., and Amano, R. S., 1988a, "Grid Generation and Its Application to Turbulent Separated Flows," *Numerical Grid Generation in Computational Fluid Mechanics*, Pineridge Press, pp. 885–894.

Maruszewski, J. P., and Amano, R. S., 1988b, "A Study of Turbulent Flow Computations in an Angled Duct With a Step," ASME FED-Vol. 66, pp. 43–47.

Patankar, S. V., 1980, *Numerical Heat Transfer and Fluid Flow*, Hemisphere Publishing Corporation, Washington, DC.

Peric, M., 1987, "Efficient Semi-implicit Solving Algorithm for Nine-Diagonal Coefficient Matrix," *Numerical Heat Transfer*, Vol. 11, pp. 251–279.

Thompson, J. F., 1980, "Numerical Solution of Flow Problems Using Body-Fitted Coordinate Systems," *Computational Fluid Mechanics*, W. Kollmann, ed., Hemisphere Publishing, Washington, DC, pp. 1–98.

V. I. Khilnani
Graduate Student.

L. C. Tsai
Graduate Student.

S. H. Bhavnani
Mem. ASME

J. M. Khodadadi
Mem. ASME

J. S. Goodling
Mem. ASME

Department of Mechanical Engineering,
Auburn University,
Auburn, AL 36849-5341

J. Waggott
Advanced Engineering and Development,
Dresser-Rand Steam Turbine,
Motor and Generator Division,
Wellsville, NY 14895

Mainstream Ingress Suppression in Gas Turbine Disk Cavities

The sealing characteristics of an air-cooled gas turbine disk cavity have been studied using laser sheet flow visualization. Experiments were performed on a simplified half-scale model of an actual gas turbine disk cavity. This type of rotor–stator geometry with a double-toothed-rim (DTR) seal at the outer periphery and a labyrinth seal at the inner periphery of the cavity has been tested for its ability in preventing ingress of hot mainstream gases. The results show good agreement with previously esimated design data. Experiments were conducted for various labyrinth seal flow rates and rotational Reynolds numbers up to 1.52 × 10^6. The effects of rotor eccentricity on minimum purge flows have also been discussed.

Introduction

Electric utilities continue to seek ways of generating their product with increasing efficiency. One concept, the Compressed Air Energy Storage (CAES), is an alternative load management technology for power generation.

In a CAES plant, air is compressed using relatively inexpensive off-peak power and stored in a large underground cavern. At periods of intermediate or peak demand, this air is mixed with fuel, combusted, and expanded through a gas expander, which in turn drives a generator. A schematic diagram of a CAES plant (Pollak, 1988) is shown in Fig. 1. It consists of a motor and a generator coupled through clutches to the compressors on one side and to a high-pressure (HP) and a low-pressure (LP) turbo-expander on the other side. The LP reheat expander operates at conditions typical of an industrial gas turbine. In this type of gas expander, temperatures entering the mainstream flow path are between 900 and 1300°C. The disks supporting the rotor and stator blades would be expensive if fabricated out of materials that can withstand such elevated temperatures. It is normal practice to supply the spaces around these disks with cooling air to maintain disk metal temperatures less than 500°C. Minimizing the cooling air required to prevent mainstream ingestion is desirable because this minimizes the thermodynamic and aerodynamic penalties associated with cooling flows.

In this study, a simplified half-scale model of the first-stage disk cavity of an air-cooled gas turbine was used to gain an insight into the flow characteristics in complex rotor–stator disk systems. This paper focuses on one major aspect of its design, i.e., the flow distribution and cooling system.

Overview

Several studies have attempted to understand the complex flow patterns in air-cooled gas turbine wheelspaces. These have concentrated on parallel flat disks with simple seal geometries. Bayley and Owen (1970) showed that for a shrouded plane rotor–stator system with simple axial rim seal, the minimum mass flow necessary to prevent ingress was proportional to the rotational Reynolds number and the shroud clearance ratio. In order to gain a better understanding of the flow structures, flow visualization techniques using smoke and lasers have been successfully used in recent years. Pincombe (1989) reported laser-based flow visualization results for rotating disk systems. The entire flow structure was studied by seeding the coolant air supply with smoke and illuminating it with a sheet of laser light. It was shown that there exists a linear relationship be-

Contributed by the International Gas Turbine Institute for publication in the JOURNAL OF TURBOMACHINERY. Manuscript received at ASME Headquarters November 1992. Associate Technical Editor: H. Lukas.

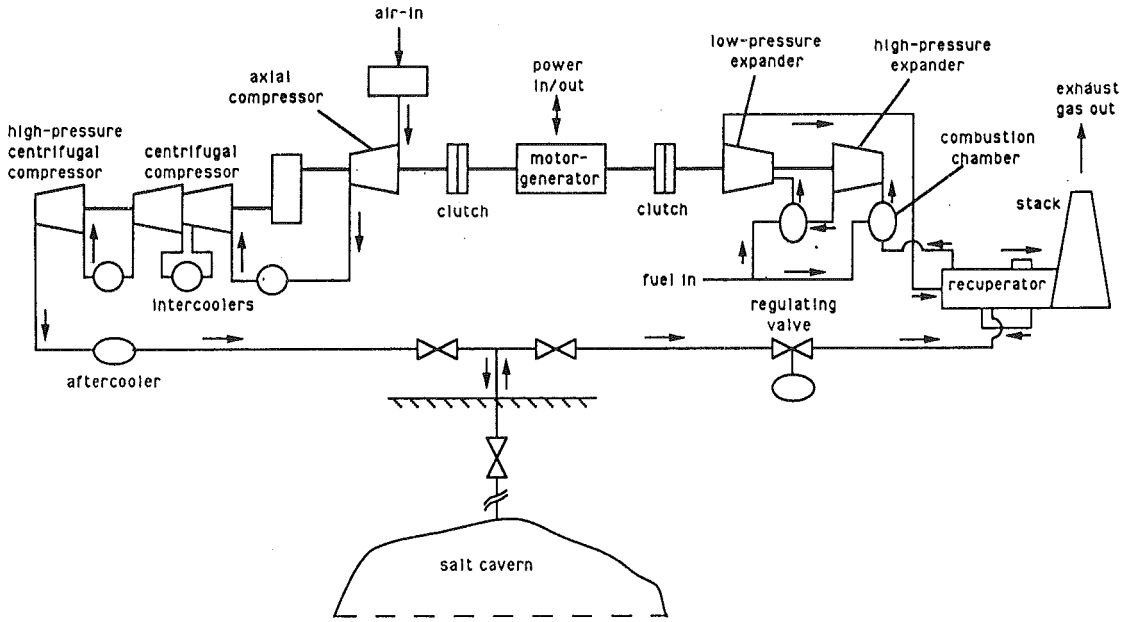

Fig. 1 Schematic diagram of a CAES plant (Pollak, 1988)

tween the minimum mass flow necessary to prevent ingress, and the rotational Reynolds number for a fixed seal clearance. Owen and Phadke (1980) reported an empirical correlation for minimum mass flow based on flow visualization and validated the results with pressure measurements. Phadke and Owen (1988a) studied the sealing characteristics of rotor–stator systems, with seven seal geometries using flow visualization, pressure and concentration measurements. It was shown that the estimates of minimum mass flow based on flow visualization were in good agreement with the values determined from the other two techniques. In a more comprehensive study, Phadke and Owen (1988b) studied the effects of external mainstream flow on the sealing characteristics of shrouded rotor–stator systems incorporating simple axial or radial clearance seals. It was found that there were two flow regimes: a rotation-dominated regime in which the minimum sealing air to prevent ingress of external fluid into the rotor–stator wheelspace increased with increasing rotational speed, and an external flow-dominated regime (in which most gas turbines operate) where the required sealing air was proportional to the external air flow and was independent of the rotational speed. Later, Phadke and Owen (1988c) concluded that increasing the circumferential pressure asymmetry in the external flow considerably increased the minimum sealing air flow.

Bhavnani et al. (1992), in their recent work, studied the fluid flow characteristics of simple geometries of gas turbine disk cavities. Minimum coolant flow rates for the prevention of ingress were determined for the case of a simple axial rim seal using flow visualization. The results compared well with previously published data. El-Oun et al. (1988) studied the sealing performance in a simplified model of an air-cooled gas turbine disk cavity with coolant air supplied through two different locations. It was concluded that the minimum throughflow rate was independent of the location where the flow was fed into the disk system.

Most of the experimental work conducted in the past concentrated on the sealing performance of simple rotor–stator systems. This paper presents a similar investigation for the geometry associated with practical gas turbines wherein the seal geometry, the cavity geometry, and the flow distribution system are complex.

Experimental Method and Procedure

Experimental Apparatus. The experimental setup was comprised of a Bridgeport milling machine, a rotor–stator disk cavity with a half-scale model gas turbine configuration, and the flow distribution system. All experiments were performed on disks mounted horizontally and spun in room air. The rotational speed could be changed continuously in a certain range up to 3000 rpm by controlling the motor voltage. The exact rotational speed of the rotor was determined by a stroboscope with an accuracy of ± 1 rpm. The configuration of the rotor–stator cavity is shown in Fig. 2. The 703-mm-dia

Nomenclature

C_w = dimensionless throughflow rate = $m/\mu R$
e = offset from central position (or eccentricity)
G = gap ratio = s/R
G_c = clearance ratio = s_c/R
G_{ca} = axial clearance ratio, s_{ca} R
G_{cr} = radial clearance ratio = s_{cr}/R
m = mass flow rate
R = outer radius of the rotor
Re_ϕ = rotational Reynolds number = $R^2\omega/\nu$
s = spacing between the rotor and the stator
s_c = seal clearance
s_{ca} = axial seal clearance
s_{cr} = radial seal clearance
α = centrifugal growth
ϵ = eccentricity ratio = e/s_{cr}
μ = dynamic viscosity
ν = kinematic viscosity
ρ = fluid density
ω = rotational speed

Subscripts

actual = actual value
design = design value
exp = experimental data
min = minimum value
seal = net flow through rim seal = (supply − suction)
suction = suction flow
supply = supply flow

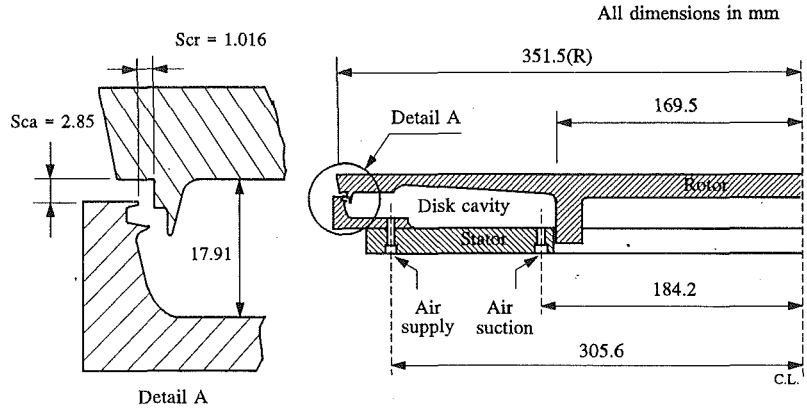

Fig. 2 The rotor-stator disk cavity with details of the double-toothed-rim seal

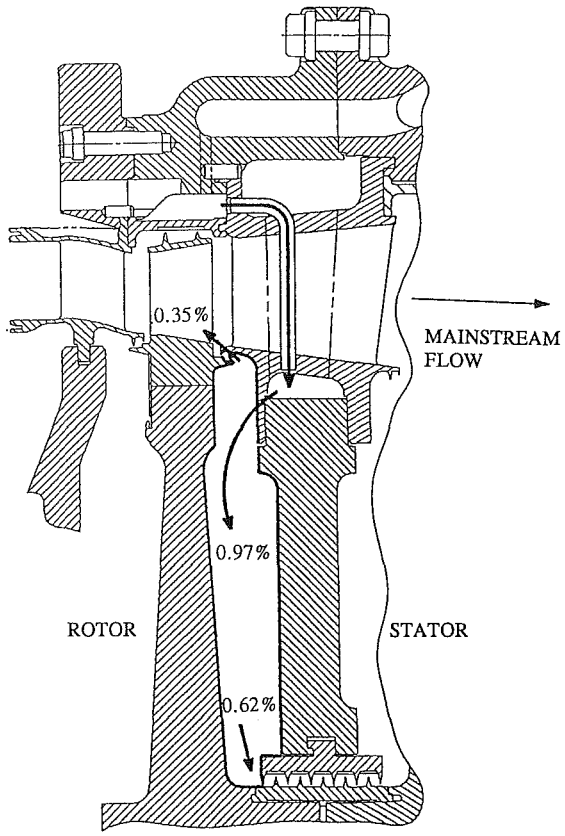

Fig. 3 Turbo-expander first-stage disk cavity with its cooling air flow distribution system (Lucas, 1990)

rotor was machined from an aluminum plate. The stator was made and assembled from two pieces of Plexiglas, an annular ring that formed a shroud, and a flat circular disk. The disk cavity was equipped with a double-toothed-rim (DTR) seal at the outer periphery and a labyrinth seal (or shaft seal) at the inner periphery of the cavity. The DTR seal was machined such that the actual (or running) radial seal clearance obtained was equal to its design value of 0.762 mm. All critical dimensions such as the rotor and stator disk shapes and the DTR seal were scaled suitably to the actual gas turbine configuration with a scale factor of 0.4866. Special care was taken to retain all features that were likely to affect the flow structure.

Flow Distribution System. The flow distribution system was designed to simulate the conditions in a gas turbine. Figure 3 shows the cross section of a first-stage disk cavity of an actual air-cooled turbo-expander, along with its cooling air flow distribution system. The cooling flows, expressed as a percentage of mainstream (external) flow, have been estimated by Lucas (1990), as the optimum disk cooling system design for this particular geometry. The majority of the cooling air is injected into the first-stage disk cavity through a set of equally spaced holes located at the outer periphery of the cavity. This cooling stream splits off into rim seal leakage flow to prevent ingress of external air and main shaft seal (or labyrinth seal) flow to provide cooling to the subsequent wheelspace of the turbo-expander. It is critical that the cooling air supply must exceed the sum of the expected rim seal leakage plus the mainshaft seal flow to avoid ingestion of mainstream gases into the disk cavity.

In the experiments, the supply flow entered the cavity through twelve discrete holes located at approximately 75 percent of the radial height of the cavity as shown in Fig. 4. The labyrinth seal was modeled by providing a suction flow at the inner periphery of the disk cavity. Both flow rates were adjusted by independent valves. The flow from the blower was first fed into an air distributor (flow distributor I) having twelve openings. These were connected to the supply holes on the stator through individual flexible tubes of equal length and common diameter to ensure even flow distribution. A turbine flow meter (FTI Model FT-20-AENA-GEA-2) was installed in the pipe connecting the blower discharge and the air distributor (flow distributor I) to monitor the supply flow rate (with an accuracy of ± 0.5 percent). The shaft seal flow was drawn into a separate air distributor (flow distributor II) and then discharged into a barrel, which was fitted with a calibrated nozzle with an accuracy of ± 1 percent. The outlet of the nozzle was connected to a domestic vacuum pump. The shaft seal flow was measured by recording the pressure difference across the nozzle using a bellows-type pressure transducer (CIC Model 5525D), with an accuracy of ± 0.0025 cm of water (± 0.25 percent of reading).

Flow Visualization. Flow visualization using smoke and laser sheet illumination was adopted for the present experimental work. The beam of a 10 mW helium–neon laser (Melles Griot, Model 05-LHP-991) was focused on a cylindrical lens (focal length of 5 mm) and the sheet of light was then directed to the transparent Plexiglas shroud. Smoke produced by a smoke generator was released adjacent to the shroud, which provided the necessary light scattering. Lamp oil from a reservoir was pressurized and passed through a coiled hypodermic tubing, which was connected to a DC power supply. Voltage was adjusted to heat the tubing and thereby produce a stream of white smoke. Details of this flow visualization arrangement are shown in Fig. 5. The technique used to discern the minimum flow rate for no ingress was to observe the flow pattern through

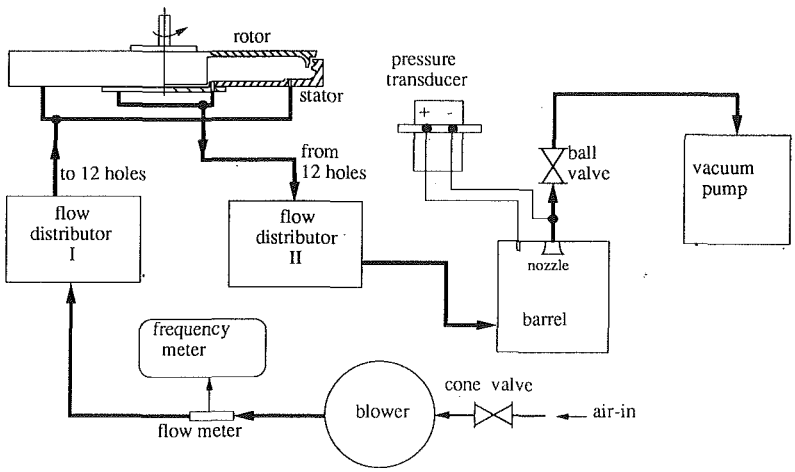

Fig. 4 Schematic diagram of the experimental air flow distribution system

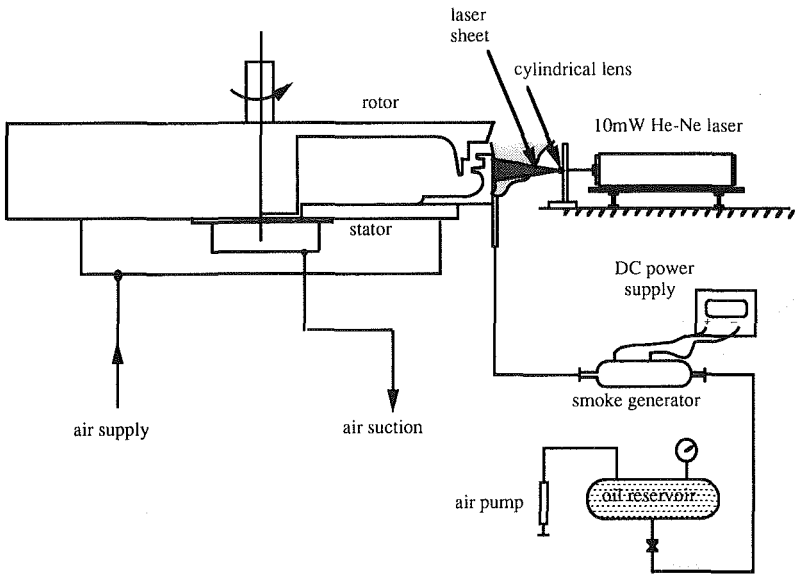

Fig. 5 Flow visualization arrangement using laser sheet illumination

the transparent Plexiglas stator while gradually increasing the air supply into the cavity. Upon observing no ingress of smoke inside the cavity, the flow rates were recorded. Repeatability tests showed that the confidence bands on the present data were 0.1 percent for Re_ϕ, and 4 percent for m_{supply} and $m_{suction}$. The latter was primarily due to the error involved in spotting ingress at the seal clearance inside the disk cavity. Further details on the experimental setup may be obtained from Khilnani (1991).

Results and Discussion

Two cases of air flow distribution system inside the disk cavity were tested:

I Air supply at the outer periphery of the cavity with labyrinth seal holes closed.

II Air supply at the outer periphery and suction through the labyrinth seal holes at the inner periphery of the disk cavity.

Case I: This case of air supply into the disk cavity with no suction through the labyrinth seal holes can be compared with the simple shrouded rotor-stator system. For the latter case, Bhavnani et al. (1992) reported an empirical correlation for minimum dimensionless throughflow rate necessary to prevent ingress:

$$C_{w,\min} = 7.822\, G_{ca}^{0.677}\, Re_\phi^{0.714} \quad (1)$$

This correlation was presented for an axial seal geometry and the cooling flow was distributed near the centerline (radius = 0). Experiments were conducted using laser-based flow visualization technique for a gap ratio $G = 0.1$ and 0.113, axial seal clearance ratios $G_{ca} = 0.0101$, 0.0144, 0.0180, and 0.0217, and rotational Reynolds numbers $Re_\phi = 5.85 \times 10^5$, 9.61×10^5, and 1.53×10^6. The experimental data are shown in Fig. 6. It was concluded that $C_{w,\min}$ is a strong function of the seal clearance and the rotational Reynolds number, but is not strongly dependent on the gap ratio.

A similar procedure was adopted to determine $C_{w,\min}$ for the complex seal geometry and a realistic flow distribution system. Experiments were conducted for a similar range of seal clearance ratios with $G_{ca} = 0.0181$ to 0.0231 and rotational Reynolds number $Re_\phi = 5.83 \times 10^5$, 9.58×10^5, and 1.52×10^6. Figure 7 shows the dependence of $C_{w,\min}$ with variations of G_{ca} and Re_ϕ. As expected, $C_{w,\min}$ increases with increase in G_{ca} and Re_ϕ. Figure 7 also shows a comparison of $C_{w,\min}$ for the simple axial rim seal with $C_{w,min}$ for the complex DTR seal. The values of $C_{w,\min}$ for the simple shrouded rotor-stator system are based

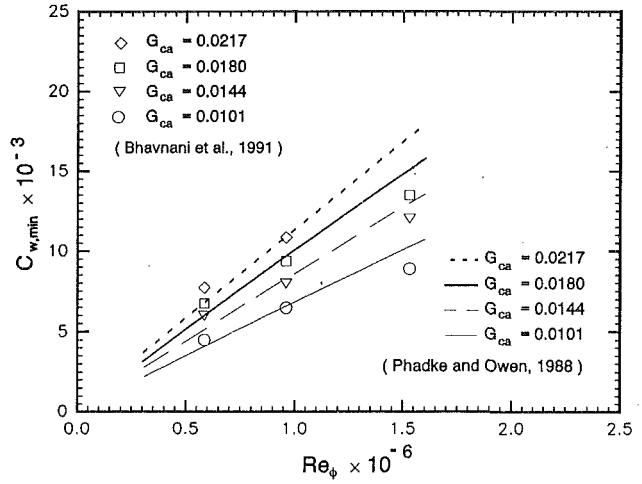

Fig. 6 $C_{w,min}$ as a function of Re_ϕ for plane rotor-stator geometry with axial rim seal (Bhavnani et al., 1992)

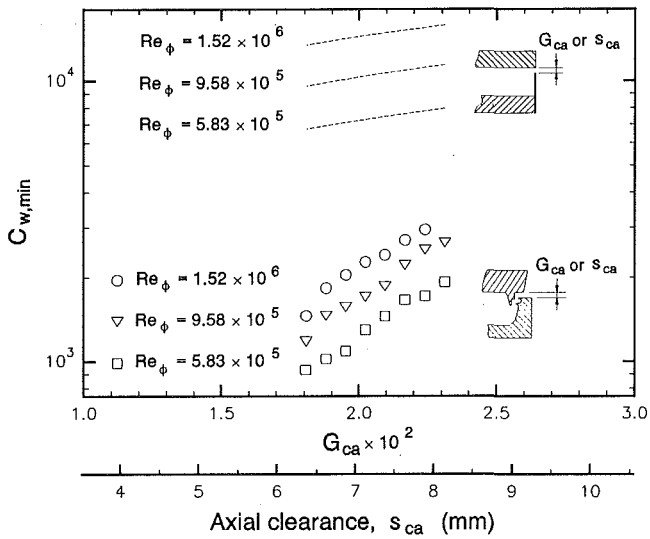

Fig. 7 Comparison of $C_{w,min}$ for the advance geometry with $C_{w,min}$ for the plane geometry

on Eq. (1) as discussed above. It is seen that for the advanced rotor–stator system, $C_{w,min}$ required to prevent ingress is much lower than that for the simple shrouded rotor–stator system at almost the same G_{ca} and Re_ϕ. This is due to the complex flow path offered by the DTR seal. This comparison indicates that the sealing behavior of the disk cavity is primarily influenced by the type of rim seal used.

Case II: In this case, the air flow distribution system was increased in complexity to simulate the conditions in an actual air-cooled gas turbine first-stage disk cavity.

Geometric similarity was achieved by fabricating a half-scale model of the rotor–stator disks as described earlier in the experimental setup. Dynamic similarity of the flow conditions inside the cavity was also achieved. Minimum mass flow rates necessary to prevent ingress for this particular geometry have been estimated by Lucas (1990) at conditions similar to those in the actual gas turbine. This designed estimate along with other properties of coolant air supply at actual gas turbine operating conditions are listed in Table 1. The estimated data were scaled to the experimental conditions by assuming a linear relationship between the mass flow rates and the rotational Reynolds number. It is seen from correlations developed in previous experimental work of other researchers (Bayley and

Table 1 Typical gas turbine operating conditions (Lucas, 1990)

Temperature	= 454 °C
Pressure	= 0.79 MPa
Dynamic viscosity, μ	= 3.336×10^{-5} Ns/m^2
Rotational Reynolds number, Re_ϕ	= 2.7×10^7
Mainstream flow	= 156 kg/s
Coolant air supply through outer holes, m_{supply}	= 0.97% of mainstream flow = 1.513 kg/s
Rim seal leakage, m_{seal}	= 0.35% of mainstream flow = 0.546 kg/s
Labyrinth seal flow, $m_{suction}$	= $m_{supply} - m_{seal}$ = 0.967 kg/s

Table 2 $C_{w,supply}$ and $C_{w,suction}$ scaled from design estimate (Lucas, 1990)

No.	$Re_\phi / 10^6$	$C_{w,supply}$	$C_{w,suction}$	$C_{w,seal}$
1.	0.276	633	406	227
2.	0.583	1337	857	480
3.	0.824	1924	1233	691
4.	0.958	2197	1408	789
5.	1.215	2836	1817	1019
6.	1.52	3486	2233	1253

Owen, 1970; Pincombe, 1989; Phadke and Owen, 1988a) that there exists a nearly linear relationship between the minimum dimensionless throughflow rate, $C_{w,min}$, and rotational Reynolds number, Re_ϕ. The present authors (Bhavnani et al., 1991) also conducted a similar investigation for a plane rotor–stator geometry equipped with an axial rim seal. The authors obtained a correlation as given by Eq. (1), which shows a slightly lower dependence of $C_{w,min}$ with Re_ϕ. Hence, a linear assumption would be a more conservative approach to determine the minimum sealing flow rate. Based on the above argument and in conjunction with Table 1, $C_{w,supply}$ and $C_{w,suction}$ were scaled to the experimental conditions using a generalized relationship of the following form:

$$(C_{w,\text{supply or suction}}/Re_\phi)_{des} = (C_{w,\text{supply or suction}}/Re_\phi)_{exp} \quad (2)$$

where the subscripts "des" and "exp" stand for design and experimental conditions, respectively. These scaled design estimates are listed in Table 2 for various rotational Reynolds numbers.

All experimental data were obtained using flow visualization to determine the minimum net flow rate required to prevent ingress of external fluid into the cavity. For a constant suction (shaft seal flow), air supply into the cavity was gradually increased while observing the flow pattern inside the cavity. Upon observing no ingress, $C_{w,supply}$ and $C_{w,suction}$ were recorded. Data points were taken at several different suction flow rates and a plot of $C_{w,supply}$ as a function of $C_{w,suction}$ was generated for six different rotational speeds as shown in Fig. 8. The results indicate that there exists a nearly linear relationship between the $C_{w,supply}$ and $C_{w,suction}$ at a fixed rotational speed. The solid lines connecting the data points were obtained using a linear least-squares best fit. The diagonal represents a physical lim-

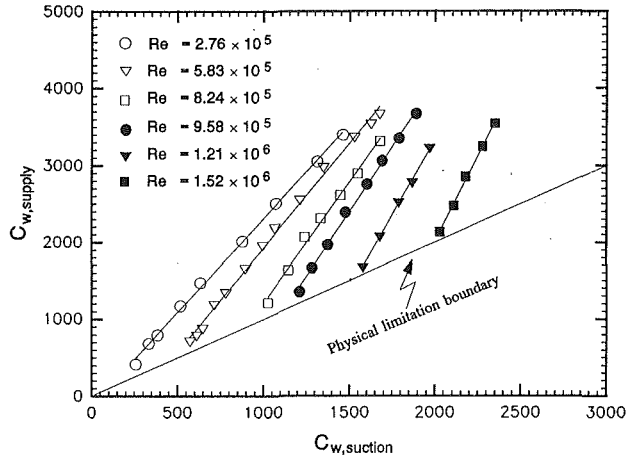

Fig. 8 $C_{w,\text{supply}}$ as a function of $C_{w,\text{suction}}$ for several values of Re_ϕ, corrected for centrifugal growth

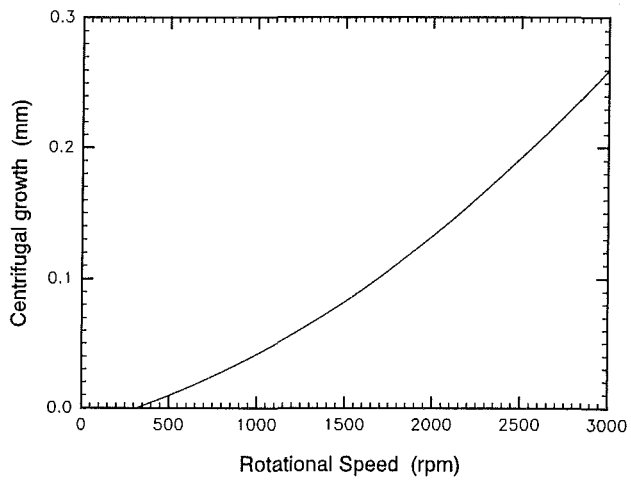

Fig. 9 Measured variation of centrifugal growth with rotational speed

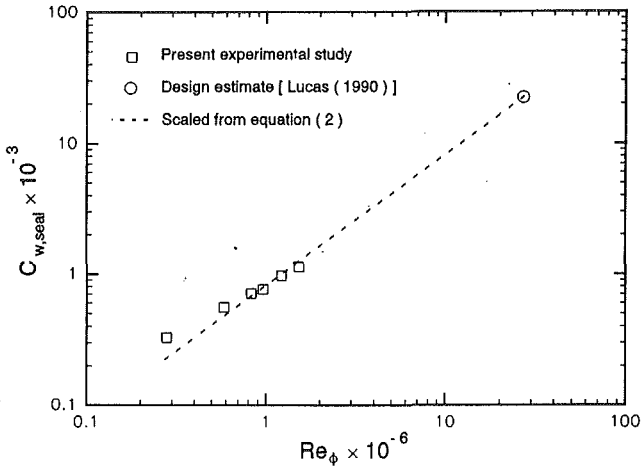

Fig. 10 Comparison of experimental data with design estimate (Lucas, 1990)

itation of this data set. Any data point below this line does not satisfy the condition of no ingress, i.e., $C_{w,\text{supply}}$ should always be greater than $C_{w,\text{suction}}$.

Correction for Centrifugal Growth. Figure 8 includes a correction for centrifugal growth. At high rotational speeds, the rotor was subject to centrifugal growth, which altered the radial seal clearance significantly. The rotor-stator geometry was fabricated such that the radial seal clearance was equal to its design value (0.762 mm) at maximum rotational speed. The centrifugal growth α, obtained experimentally, was found to be 0.254 mm at a maximum speed of 3000 rpm and negligibly small at all speeds below 300 rpm. Figure 9 shows the variation of centrifugal growth with rotational speed.

It has been well established from the preliminary experiments on a simple shrouded rotor-stator system that the minimum dimensionless throughflow rate, $C_{w,\text{min}}$, required to prevent ingress strongly depends on the seal clearance ratio, G_c. Hence, for the present case with both supply and suction throughflow streams, the net rim seal flow, $C_{w,\text{seal}}$ (i.e., $[C_{w,\text{supply}} - C_{w,\text{suction}}]$) inside the disk cavity should be corrected to account for changes in radial seal clearance. Phadke and Owen (1988b) studied the sealing performance of seven different types of rotor-stator rim seals and obtained an empirical correlation for $C_{w,\text{min}}$ for each of these types. One of the seals tested was with the stator shroud overlapping the rotor lip, which seems to be very closely related to the DTR seal in terms of its geometry and the fluid flow distribution at the seal clearance. The empirical correlation obtained for this type of seal geometry is given by:

$$C_{w,\text{min}} = C G_c^a \, \text{Re}_\phi^b \tag{3}$$

where the values of the constants C, a, and b as obtained by multiple-regression analysis are 0.224, 0.229, and 0.951, respectively.

Based on this correlation, the following correction factor was postulated:

$$(C_{w,\text{seal}})_{\text{corr}} = (C_{w,\text{seal}})_{\text{meas}} \times (G_{cr,\text{design}}/G_{cr,\text{actual}})^{0.229} \tag{4}$$

where

$(C_{w,\text{seal}})_{\text{meas}}$ = measured value obtained by flow visualization
$G_{cr,\text{design}}$ = design radial seal clearance ratio
$G_{cr,\text{actual}}$ = actual radial seal clearance ratio corrected for centrifugal growth
0.229 = exponential power associated with G_c obtained from Eq. (3) for a similar type of seal geometry (Phadke and Owen, 1988c)

For the worst case, at lowest rotational Reynolds number ($\text{Re}_\phi = 2.76 \times 10^5$), the correction in $C_{w,\text{supply}}$ for a given $C_{w,\text{suction}}$ was found to be 3 to 4 percent. As mentioned earlier, data in Fig. 8 are presented in corrected form.

The experimental data can be compared with the scaled design estimate. Using Fig. 8 in conjunction with Table 2, $C_{w,\text{suction}}$ can be determined for every $C_{w,\text{supply}}$ proportional to Re_ϕ, ensuring geometric and dynamic similarity. For example from Table 2, at $\text{Re}_\phi = 0.276 \times 10^6$ and $C_{w,\text{supply}} = 633$, the corresponding experimental value of $C_{w,\text{suction}}$ can be obtained from Fig. 8. The difference between $C_{w,\text{supply}}$ and $C_{w,\text{suction}}$ (i.e., $C_{w,\text{seal}}$) is plotted as a function of rotational Reynolds number in Fig. 10. Also shown on this plot is the design estimate for an actual gas turbine of identical disk cavity geometry from Lucas (1990). When this design estimate is scaled conservatively, as explained previously, to the rotational Reynolds numbers of the experiments, it is seen that the experimental values are quite close to the scaled design values. This confirms the adequacy of the design.

Seal Effectiveness. The type of rim seal used in a rotor-stator disk system significantly affects the minimum purge flow requirements. The DTR seal used for the present case was designed such that the lip on the rotor ensured a smooth deflection of the disk-pumped fluid toward the stator, thereby creating a curtain effect at the rim seal. This reduced the ingress

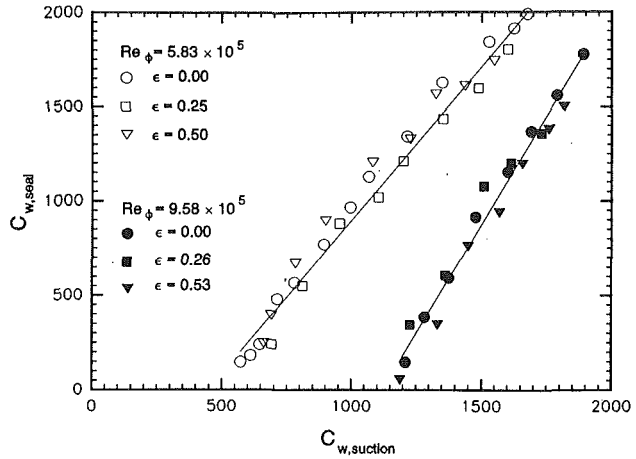

Fig. 11 Effect of seal eccentricity for $Re_\phi = 5.83 \times 10^5$ and 9.58×10^5

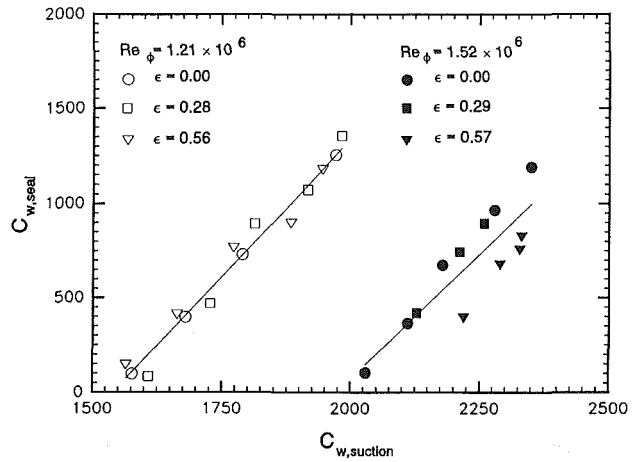

Fig. 12 Effect of seal eccentricity for $Re_\phi = 1.21 \times 10^6$ and 1.52×10^6

of the external fluid considerably. However, the rim seal effectiveness is impeded by increased supply flow. Referring to Fig. 8, with suction flow held constant, it can be seen that as Re_ϕ decreases, $C_{w,\text{supply}}$ for the no-ingress condition increases. This probably results from the supply jets disrupting the disk pumping fluid along the rotor disk face and weakening the curtain effect at the rim seal. This aspect should be considered in future design developments and the reduced seal effectiveness weighed against the enhanced surface heat transfer that may result from the impinging jets. It is expected that rim seal performance degradation would not occur if the supply flow did not impinge on the rotor disk face.

Effect of Eccentricity on Minimum Purge Flows. A gas turbine operating at high rotating speeds and temperatures may be subject to seal eccentricities. The effect of seal eccentricities on minimum purge flows was studied for this system. This was achieved by offsetting the rotor from its central position and recording the net flow inside the cavity for the "no-ingress" condition. Experiments were conducted at different values of seal eccentricity ratio, $\epsilon(\epsilon = e/s_{cr}$ where e = rotor eccentricity and s_{cr} = radial seal clearance corrected for centrifugal growth) for four rotational speeds in each case. A comparison of eccentricity data with concentric ($\epsilon = 0$) data is presented in Figs. 11 and 12. The results clearly indicate that the net flow inside the cavity does not deviate much with the degree of eccentricity. Hence, it can be concluded that the eccentricity of the rotor does not markedly affect the minimum purge flow

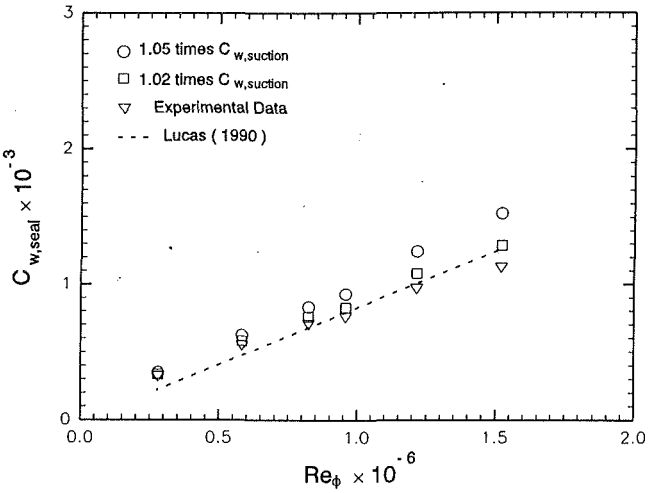

Fig. 13 Effect of increased labyrinth seal flow on minimum purge flow

requirements since the area available for ingress at the rim seal remains unchanged.

Effect of Wear on Labyrinth Seal. Due to the complex design, labyrinth seals in gas turbines sometimes do not operate at desired clearances. An assumed case of enlarged labyrinth seal was considered by increasing the suction flow rate by 2 and 5 percent of the normal flow. Corresponding values of supply flow rate were read from Fig. 10. The effect of an increase in suction flow on the minimum purge flow inside the disk cavity is presented in Fig. 13. This shows that a slight increase in suction flow rate from its designed condition (as estimated by Lucas, 1990) increases the minimum purge flow significantly. For example, at $Re_\phi = 1.52 \times 10^6$ with 2 and 5 percent increase in labyrinth seal flow, the corresponding increase in supply flow was found to be 6 and 15 percent, respectively. An increased radial inflow of air (caused due to increase in labyrinth seal flow), increases the tangential velocity with a consequent increase in the radial pressure gradient inside the disk cavity. The results in increase of sealing flow to pressurize the system and prevent ingress. It is essential that the sealing flow supplied should always be slightly higher than the minimum required to take into account the wear of the labyrinth seals.

Further studies are planned to incorporate the effects of external hot gas main flows on the sealing characteristics of DTR seals.

Conclusions

This paper has presented an experimental study on sealing performance of an air-cooled gas turbine disk cavity wherein the seal geometry, cavity geometry, and the flow distribution system are complex.

For the case of flow distribution system with air supply at the outer periphery of the cavity, results indicate that $C_{w,\text{min}}$ is a strong function of the seal clearance and the rotational Reynolds number. $C_{w,\text{min}}$ required for this case is much lower than that for the comparable simple rotor–stator system. This suggests that the seal geometry with DTR seals is very effective in preventing ingress of external fluid into the rotor-stator disk cavity. For the case with simulated labyrinth seal flow, the results confirm that there exists a linear relationship between $C_{w,\text{supply}}$ and $C_{w,\text{suction}}$ at a fixed rotational Reynolds number. The experimental results show that the design estimate (Lucas, 1990) for this type of rotor–stator geometry and flow distribution system is quite conservative.

Seal eccentricities do not have much effect on the minimum

purge flow required to prevent ingress. Contrary to this, a slight increase in the labyrinth seal flow can significantly increase the amount of rim sealing flow required.

Acknowledgments

Support of this contractual work has been provided by the Alabama Electric Cooperative, the Electric Power Research Institute, and the Dresser-Rand Corporation, and is gratefully acknowledged.

References

Bayley, F. J., and Owen, J. M., 1970, "The Fluid Dynamics of a Shrouded Disk System With a Radial Outflow of Coolant," ASME *Journal of Engineering for Power*, Vol. 92, pp. 335–341.

Bhavnani, S. H., Khodadadi, J. M., Goodling, J. S., and Waggott, J., 1992, "An Experimental Study of Fluid Flow in Disk Cavities," ASME JOURNAL OF TURBOMACHINERY, Vol. 114, pp. 454–461.

El-Oun, Z. B., Neller, P. H., and Turner, A. B., 1988, "Sealing of a Shrouded Rotor-Stator System With Preswirl Coolant," ASME JOURNAL OF TURBOMACHINERY, Vol. 110, pp. 218–225.

Khilnani, V. I., 1991, "Ingress Suppression in Gas Turbine Disk Cavities," M. S. Thesis, Auburn University, AL.

Lucas, G. M., 1990, "Thermo-Mechanical Design of the Dresser-Rand-EA-418 Low Pressure CAES Expander Secondary Flow System," IMechE, Paper No. C403/036.

Owen, J. M., and Phadke, U. P., 1980, "An Investigation of Ingress in a Simple Shrouded Rotating Disk System With a Radial Outflow of Coolant," ASME Paper No. 80-GT-49.

Phadke, U. P., and Owen, J. M., 1988a, "Aerodynamic Aspects of the Sealing of Gas Turbine Rotor–Stator System. Part 1: The Behaviour of Simple Shrouded Rotating-Disk Systems in a Quiescent Environment," *International Journal of Heat and Fluid Flow*, Vol. 9, No. 2, pp. 98–105.

Phadke, U. P., and Owen, J. M., 1988b, "Aerodynamic Aspects of the Sealing of Gas Turbine Rotor–Stator System. Part 2: The Performance of Simple Seals in an Axisymmetric External Flow," *International Journal of Heat and Fluid Flow*, Vol. 9, No. 2, pp. 106–112.

Phadke, U. P., and Owen, J. M., 1988c, "Aerodynamic Aspects of the Sealing of Gas Turbine Rotor–Stator System. Part 3: The Effect of Nonaxisymmetric External Flow on Seal Performance," *International Journal of Heat and Fluid Flow*, Vol. 9, No. 2, pp. 113–117.

Pincombe, J. R., 1989, "Gas Turbine Disk Cooling Flows," in: *Handbook of Flow Visualization*, W.-J. Yang, ed., Hemisphere Publishing Corp., Washington, DC, Chap. 33, pp. 555–576.

Pollak, R., 1988, "Status of the First U.S. CAES Plant," *EPRI Journal*, pp. 49–52.